

## PROJECT ADMINISTRATION DATA SHEET



ORIGINAL



REVISION NO. \_\_\_\_\_

Project No. E-25-659GTRI/~~STK~~DATE 5 / 31 / 84Project Director: Dr. David L. McDowellSchool/~~STK~~ MESponsor: National Science FoundationType Agreement: Grant No. MEA-8404080Award Period: From 6/15/84 To 11/30/86 \* (Performance) 2/28/87 (Reports)Sponsor Amount: This Change Total to Date

Estimated: \$ \_\_\_\_\_

\$ \_\_\_\_\_

Funded: \$ 53,559\$ 53,559Cost Sharing Amount: \$ 18,409Cost Sharing No: E-25-316Title: "Research Initiation: Hardening Rules for Nonproportional Cyclic Plasticity"

## ADMINISTRATIVE DATA

OCA Contact

Lynn Boyd x4820

1) Sponsor Technical Contact:

2) Sponsor Admin/Contractual Matters:

Clifford J. AstillWinston S. ShermanNational Science FoundationGrants OfficialDivision of Data Support ResearchNational Science FoundationAttn: Engineering Research, Grant ProgramWashington, DC 20550Washington, DC 20550(202) 357-9542(202) 357-9626Defense Priority Rating: n/aMilitary Security Classification: n/a(or) Company/Industrial Proprietary: n/a

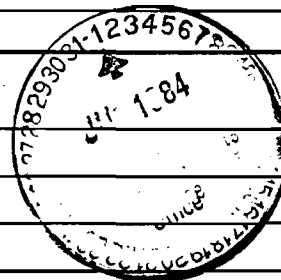
## RESTRICTIONS

See Attached NSF Supplemental Information Sheet for Additional Requirements.

Travel: Foreign travel must have prior approval — Contact OCA in each case. Domestic travel requires sponsor approval where total will exceed greater of \$500 or 125% of approved proposal budget category.

Equipment: Title vests with GIT.

## COMMENTS:

\*Includes 6 month unfunded flexibility period.

## COPIES TO:

Sponsor I.D. #02.107.000.84.049

Project Director  
Research Administrative Network  
Research Property Management  
AccountingProcurement/EES Supply Services  
Research Security Services  
Reports Coordinator (OCA)  
Research Communications (2)GTRI  
Library  
Project File  
Other NEWTON

SPONSORED PROJECT TERMINATION/CLOSEOUT SHEETDate 4-29-87Project No. E-25-659School XXX MEIncludes Subproject No.(s) N/AProject Director(s) David McDowellGTRC / XXXSponsor National Science FoundationTitle "Research Initiation: Hardening Rules for Nonproportional Cyclic Plasticity"Effective Completion Date: 11/30/86(Performance) 2/28/87

(Reports)

## Grant/Contract Closeout Actions Remaining:

☒

None

☐

Final Invoice or Final Fiscal Report

☐

Closing Documents

☐

Final Report of Inventions

☐

Govt. Property Inventory &amp; Related Certificate

☐

Classified Material Certificate

☐

Other \_\_\_\_\_

Continues Project No. \_\_\_\_\_

Continued by Project No. \_\_\_\_\_

## COPIES TO:

Project Director  
Research Administrative Network  
Research Property Management  
Accounting  
Procurement/GTRI Supply Services  
Research Security Services

## Library

GTRC

~~Research Communications (2)~~

Project File

Other Duane H.Angela DuBoseRuss EmbryHeyser~~Reports Coordinator (OCA)~~~~Other Services~~

E-25-651



GEORGIA TECH 1885-1985

DESIGNING TOMORROW TODAY

August 16, 1985

Dr. J. Weese, Director  
Division of Mechanical Engineering  
& Applied Mechanics  
NATIONAL SCIENCE FOUNDATION  
Washington, D.C. 20550

Dear Dr. Weese:

Please find enclosed a progress report for the first year of my two-year NSF initiation grant, including copies of publications produced under this support. I have addressed this report to you since Cliff Astill, my technical contact, informed me that he was going to work in another area.

Sincerely,

David L. McDowell  
Assistant Professor

DLM:lo

Enclosure(s)

**Georgia Institute of Technology**  
School of Mechanical Engineering Atlanta, Georgia 30332

PROGRESS ON NSF GRANT NO. MEA-8404080

"APPROPRIATE HARDENING RULES FOR NONPROPORTIONAL CYCLIC PLASTICITY"

Submitted To

Mechanical Engineering & Applied Mechanics Division

August 1985

Submitted by

D.L. McDowell

Assistant Professor

School of Mechanical Engineering

GEORGIA INSTITUTE OF TECHNOLOGY

Atlanta, GA 30332

Significant progress has been made during the first year of this project on understanding appropriate structures for rate-independent and rate-dependent constitutive equations for nonproportional cyclic plasticity.

A two surface theory was developed, based on Mroz kinematic hardening, with the capabilities of modeling fading memory of the maximum plastic strain excursion and additional hardening incurred during nonproportional loading. Good correlation with nonproportional block loading sequences was obtained for type 304 stainless steel.

Several nonproportional loading histories experimentally obtained by the author have been carefully examined. The superiority of a Mroz-type kinematic hardening rule was demonstrated. Furthermore, the Mroz distance vector was shown to more uniquely characterize variation of the plastic modulus function for nonproportional path segments.

In April 1985, an M.S. Thesis was completed on the subject of numerical implementation of elasto-plastic models for nonproportional plasticity. Surprisingly, it was found that numerical integration techniques previously reported most efficient for state variable theories were found least efficient for nonproportional loading.

Ongoing work in the second year of the project will include further analysis of more sophisticated isotropic and kinematic hardening rules for type 304 stainless steel at room temperature and superalloy Hastelloy-X at 649°C. The latter data has recently become available from Professor E.H. Jordan of the University of Connecticut; it was obtained under NASA sponsorship. The thrust of the second year in this program is switching to consideration of rate-dependent constitutive laws for nonproportional cyclic loading.

The following is a list of related papers produced during the first year of this grant:

1. McDowell, D.L., "A Two Surface Model for Transient Nonproportional Cyclic Plasticity: Part I - Development of Appropriate Equations," ASME Journal of Applied Mechanics, Volume 52, June 1985, pp. 298-302.
2. McDowell, D.L., "A Two Surface Model for Transient Nonproportional Cyclic Plasticity: Part II - Comparison of Theory with Experiments," ASME Journal of Applied Mechanics, Volume 52, June 1985, pp. 303-308.
3. McDowell, D.L., "An Experimental Study of the Structure of Constitutive Equations for Nonproportional Cyclic Plasticity," accepted for publication in ASME Journal of Engineering Materials and Technology, 1985.

4. McDowell, D.L., "The Significance of Nonproportional Loading Tests for Characterization of Cyclic Response of Metals." Proc. 1985 Spring Conference on Experimental Mechanics, Society for Experimental Stress Analysis, Las Vegas, June 10, 1985, pp. 229-236.
5. Sotolongo, W., and McDowell, D.L., "An Evaluation of several Constitutive Model Structures For Transient Nonproportional Cyclic Plasticity," accepted for publication in ASME Journal of Pressure Technology, August 1985.
6. Sotolongo, W., and McDowell, D.L., "On the Numerical Integration of Elasto-Plastic Constitutive Model Structures For Nonproportional Cyclic Loading," submitted for publication to Computers and Structures.

Related external presentations included the following:

1. McDowell, D.L., "Description of Nonproportional Cyclic Response," Oak Ridge National Laboratory, July 1984.
2. McDowell, D.L., "Comments on the Structure of Multiaxial Constitutive Models," Multiaxial Meeting of Fracture and Fatigue/Structural Mechanics Branches, NASA Lewis Research Center, January 22, 1985.
3. McDowell, D.L., "Some Comments on the Structure of Nonlinear Constitutive Equations for Nonproportional Cyclic Plasticity," presented at the Symposium in Honor of the Retirement of Professor JoDean Morrow of the University of Illinois, August 1984.
4. McDowell, D.L., "The Significance of Nonproportional Loading Tests for Characterization of Cyclic Response of Metals," 1985 Spring Conference on Experimental Mechanics, SEM, Las Vegas, June 10, 1985.
5. McDowell, D.L., "A Two Surface Plasticity Theory for Transient Nonproportional Cyclic Plasticity," Joint ASME/ASCE Applied Mechanics Conference, Univ. of New Mexico, Albuquerque, N.M., June 24-27, 1985.
6. McDowell, D.L., "Work in Progress on Cyclic Plastic Stress Calculation for Rail Steels," 4th ETAC Meeting, U.S. DOT Transportation Systems Center, July 16-17, 1985.

E-25-137

**FINAL REPORT**

**APPROPRIATE HARDENING RULES FOR  
NONPROPORTIONAL CYCLIC PLASTICITY**

**David L. McDowell**

**Submitted to**

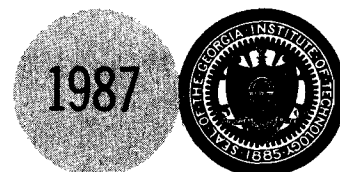
**Division of Mechanics, Structures and Materials Engineering  
National Science Foundation  
1800 G. Street, N.W.  
Washington, D.C. 20550**

**Under**

**NSF Grant No. MEA-8404080**

**March 1987**

**GEORGIA INSTITUTE OF TECHNOLOGY**  
**A UNIT OF THE UNIVERSITY SYSTEM OF GEORGIA**  
**SCHOOL OF MECHANICAL ENGINEERING**  
**ATLANTA, GEORGIA 30332**



FINAL REPORT

NSF GRANT NO. MEA-8404080

**"APPROPRIATE HARDENING RULES FOR NONPROPORTIONAL CYCLIC PLASTICITY"**

Submitted to Division of Mechanics, Structures  
and Materials Engineering

National Science Foundation  
1800 G. Street, N.W.  
Washington, D.C. 20550

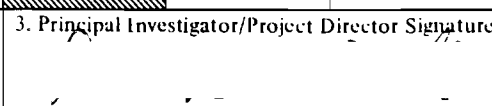
March 1987

Submitted by

DAVID L. MCDOWELL  
Assistant Professor  
The George W. Woodruff School of Mechanical Engineering  
Georgia Institute of Technology  
Atlanta, GA 30332



# APPENDIX VII

<b>NATIONAL SCIENCE FOUNDATION</b> Washington, D.C. 20550		<b>FINAL PROJECT REPORT</b> NSF FORM 98A			
PLEASE READ INSTRUCTIONS ON REVERSE BEFORE COMPLETING					
<b>PART I-PROJECT IDENTIFICATION INFORMATION</b>					
1. Institution and Address Georgia Tech Research Corporation Georgia Institute of Technology Atlanta, GA 30332-0420		2. NSF Program <b>Mechanics, Struc., and Materials Engr</b> 4. Award Period From 6/15/84 To 11/30/86		3. NSF Award Number <b>MEA-8404080</b> 5. Cumulative Award Amount <b>\$53,559</b>	
6. Project Title  <b>Appropriate Hardening Rules for Nonproportional Cyclic Plasticity</b>					
<b>PART II-SUMMARY OF COMPLETED PROJECT (FOR PUBLIC USE)</b>					
<p>The primary goal of this project was to generalize rate-independent cyclic plasticity theory to incorporate essential aspects of material behavior associated with nonproportional cyclic loading typical of many actual applications. Results obtained with the support of this grant are substantial and varied. Theoretical, experimental and numerical aspects of the problem have all been examined in great detail.</p> <p>Careful examination of nonproportional cyclic loading data revealed the inaccuracy of "classical" kinematic hardening rules. Furthermore, the importance of accurate characterization of the variation of hardening modulus was confirmed. It was shown that bounding surface theory is an appropriate constitutive framework to include these nonproportional plasticity effects. A two surface theory with Mroz-type kinematic hardening was further developed to incorporate nonproportional isotropic hardening.</p> <p>Temporal integration algorithms were examined with some important conclusions which contrast to earlier findings reported for only uniaxial or proportional loading histories. Finally, the model was incorporated in a simplified elastic-plastic rolling contact stress analysis representative of railroad wheel on rail. Agreement with experimental results indicates the importance of accurate plasticity theories for nonproportionally loaded, constrained structural calculations.</p>					
<b>PART III-TECHNICAL INFORMATION (FOR PROGRAM MANAGEMENT USES)</b>					
1.  ITEM (Check appropriate blocks)	NONE	ATTACHED	PREVIOUSLY FURNISHED	TO BE FURNISHED SEPARATELY TO PROGRAM Check (✓)      Approx. Date	
a. Abstracts of Theses		X			
b. Publication Citations		X			
c. Data on Scientific Collaborators	X N/A				
d. Information on Inventions	X N/A				
e. Technical Description of Project and Results		X			
f. Other (specify) <b>Technical papers</b>		X			
2. Principal Investigator/Project Director Name (Typed)  <b>David L. McDowell</b>		3. Principal Investigator/Project Director Signature  			4. Date <b>3/25/87</b>  <b>3/25/87</b>

## DISCUSSION OF RESULTS

The primary goal as set forth in the original proposal for this work was to generalize rate-independent plasticity theory to model essential material behaviors associated with nonproportional cyclic loading. To this end, the work conducted under support of this grant has had very significant impact.

From the theoretical standpoint, two papers were published in the ASME Journal of Applied Mechanics on a two surface cyclic plasticity model which incorporates nonproportional isotropic hardening effects and an accurate Mroz-type kinematic hardening rule. The accuracy of the model was examined by comparison with biaxial experimental results previously obtained by the author on type 304 stainless steel. As a measure of their significance, the two papers won the 1986 Alfred Noble Prize jointly awarded by ASME, ASCE, IEEE, AIMPE, and WSE for the best paper by an author under 31 years of age appearing in any of their respective journals. In addition, a paper co-authored by Dr. McDowell and an M.S. student, W. Sotolongo, explored the accuracy of several generic types of cyclic plasticity models for nonproportional loading in an ASME Journal of Pressure Vessel Technology paper; included in the comparisons were a simple single loading surface model, a two surface or bounding surface model, and a state variable or unified creep-plasticity model.

Distinct experimental contributions were also made to the development of a constitutive framework appropriate for cyclic nonproportional loading. In a 1985 ASME Journal of Engineering Materials and Technology paper, the author demonstrated the superior correlation of kinematic hardening and modulus function obtained with a two surface Mroz-type approach. The classical kinematic hardening rules of Prager and Ziegler were shown to be quite inaccurate. The tremendous importance of an accurate prescription for plastic modulus variation was clearly shown. A paper presented at the 1985 Spring Conference on Experimental Mechanics in June 1985 emphasized the importance of nonproportional loading experiments in deducing the appropriate tensorial nature of kinematic hardening; the noncollinearity of the backstress and the inelastic strain rate vector provides the additional information required to develop accurate hardening rules.

A study of nickel-base superalloy Hastelloy X subjected to high-temperature, nonproportional cyclic loading was published in 1986 in the proceedings of the 3rd Symposium on Nonlinear Constitutive Relations for High-Temperature Applications sponsored by NASA. The experimental results were obtained from Professor E. Jordan of the University of Connecticut. It was demonstrated by careful computer analysis of the data that a dynamic recovery term was absolutely essential to model the kinematic hardening under sinusoidal, out-of-phase tension-torsion loading of thin walled tubular specimens. Interestingly, Chaboche had shown in 1983 that such a recovery term was essentially equivalent to a two surface viscoplasticity model. This study was conducted with two Ph.D. students.

An evaluation of the subtleties and implications of existing nonproportional cyclic loading data will soon appear in the ASME Journal of Applied Mechanics. A companion paper which embodies the results of this

detailed analysis in a simplified model structure was published in the ASCE Journal of Engineering Mechanics in March 1987.

Beyond the realm of applied continuum mechanics, micro-mechanistic explanations were sought for the unusually pronounced cyclic hardening exhibited by austenitic stainless steels subjected to nonproportional cyclic loading. The accumulated hardening was greatly in excess of that observed in uniaxial tests at the same effective strain amplitude. Nonproportionally cycled specimens were sectioned and examined via conventional metallography, scanning and transmission electron microscopy, and x-ray diffraction. The additional cyclic hardening was found to be associated with stress- and deformation-assisted martensitic transformations which could be characterized with respect to the nonproportional loading histories. This work was conducted jointly by the author and Professor S. Antolovich of the School of Materials Engineering at Georgia Tech. The final revisions are underway for publication of this work in Metallurgical Transactions.

Another major area addressed in this work is the numerical integration of these more complex constitutive equations. In particular, the resulting equations are mathematically "stiff" in certain loading regimes and numerical accuracy and efficiency is a concern. Along with his student, W. Sotolongo, the author published a study of the efficiency and accuracy of a number of temporal integration algorithms with and without time-step control, predictor-corrector algorithms, radial return, etc. for a rate-independent bounding surface model, a rate-independent single loading surface model, and a unified creep-plasticity model. Interestingly, a higher order Runge-Kutta method with fixed time-step size was found superior. An important finding was that a simple Euler algorithm with automatic time-step size control was superior for proportional loading, but quite unacceptable for nonproportional loading; this finding contrasted with the results of previous researchers who considered only proportional loading and espoused simple Euler techniques for state variable constitutive theories.

Thus far, we have mentioned the theoretical, experimental and numerical aspects of the work conducted with support of this grant. The contributions have been significant in all three areas.

With regard to immediate practical concerns of an economic character, the two surface theory developed during this grant period was applied to the problem of elastic-plastic rolling contact of wheel on rail. Subsurface cyclic plastic deformation is a likely major contributor to the initiation and growth of corrugations in rail; it is also inextricably linked to initiation-growth of subsurface fatigue cracks. These problems are extremely costly to the railroad industry. The cyclic stress-strain field of material in the contact region varies in a highly nonproportional manner as the wheel moves past a specific point of the rail. A number of factors including wheel load, friction, braking or driving influence the cumulative inelastic deformation of the near-surface region. A computer program was written which simulated the constraints of various subsurface layers in rail in two dimensions, applied a two dimensional translating Hertzian distribution with the same mean pressure as a three dimensional distribution typical of actual rail-wheel contact geometry, and integrated a two surface-type constitutive law for cyclic plastic deformation. The results,

economically obtained with the simple model, compared favorably with measured surface deformations and with subsurface residual stress distributions obtained with very expensive finite element solutions which used over-simplified constitutive models. The co-author of this paper was Dr. G. Moyar, a consultant with the Association of American Railroads.

The following is a list of related papers produced during the grant duration:

(Copies enclosed)

1. McDowell, D. L., "A Two Surface Model for Transient Nonproportional Cyclic Plasticity: Part I - Development of Appropriate Equations," ASME Journal of Applied Mechanics, Vol. 52, June 1985, pp. 298-302.
2. McDowell, D. L., "A Two Surface Model for Transient Nonproportional Cyclic Plasticity: Part II - Comparison of Theory with Experiments," ASME Journal of Applied Mechanics, Vol. 52, June 1985, pp. 303-308.
3. McDowell, D. L., "An Experimental Study of the Structure of Constitutive Equations for Nonproportional Cyclic Plasticity," ASME Journal of Engineering Materials and Technology, Vol. 107, Oct. 1985, pp. 307-315.
4. McDowell, D. L., "The Significance of Nonproportional Loading Tests for Characterization of Cyclic Response of Metals," Proc. 1985 Spring Conference on Experimental Mechanics, Society for Experimental Stress Analysis, Las Vegas, June 10, 1985, pp. 229-236.
5. Sotolongo, W., and McDowell, D.L., "An Evaluation of Several Constitutive Model Structures for Transient Nonproportional Cyclic Plasticity," ASME Journal of Pressure Vessel Technology, Vol. 108, Aug. 1986, pp. 273-279.
6. Sotolongo, W., and McDowell, D.L., "On the Numerical Integration of Elasto-Plastic Constitutive Model Structures for Nonproportional Cyclic Loading," Computers and Structures, Vol. 24, No. 4, 1986, pp. 595-606.
7. McDowell, D.L., "An Evaluation of Recent Developments in Hardening and Flow Rules for Rate-Independent, Nonproportional Cyclic Plasticity," accepted for publication in ASME Journal of Applied Mechanics, 1986.
8. McDowell, D.L., "A Simple, Experimentally Motivated Cyclic Plasticity Model," ASCE Journal of Engineering Mechanics, Vol. 113, No. 3, March 1987, pp. 378-397.
9. McDowell, D.L., Stock, S.R., Stahl, D., and Antolovich, S.D., "Biaxial Path Dependence of Deformation Substructure of Type 304 Stainless Steel," under review for publication in Metallurgical Transactions, Aug. 1986.

10. McDowell, D.L., Moosbrugger, J., Doumi, M., and Jordan, E.H., "Some Implications for Cyclic Plastic and Viscoplastic Equations Based on Nonproportional Loading Experiments," Proc. 3rd Symposium on Nonlinear Constitutive Relations for High-Temperature Applications, NASA Lewis RC, University of Akron, Ohio, June 11-13, 1986.
11. McDowell, D.L. and Moyer, G.J., "A More Realistic Model of Nonlinear Material Response: Application to Elastic-Plastic Rolling Contact," Proc. 2nd Int. Symp. on Contact Mechanics and Wear of Rail/Wheel Systems, University of Rhode Island, Kingston, July 8-11, 1986.

Related external presentations included the following:

1. McDowell, D.L., "Description of Nonproportional Cyclic Response," Oak Ridge National Laboratory, July 1984.
2. McDowell, D. L., "Some Comments on the Structure of Nonlinear Constitutive Equations for Nonproportional Cyclic Plasticity," presented at the symposium in honor of the retirement of Professor JoDean Morrow of the University of Illinois, August 1984.
3. McDowell, D. L., "Comments on the Structure of Multiaxial Constitutive Models," Multiaxial Meeting of Fracture and Fatigue/Structural Mechanics Branches, NASA Lewis Research Center, January 22, 1985.
4. McDowell, D. L., "The Significance of Nonproportional Loading Tests for Characterization of Cyclic Response of Metals," Proc. 1985 Spring Conference on Experimental Mechanics, Society for Experimental Stress Analysis, Las Vegas, June 10, 1985, pp. 229-236.
5. McDowell, D.L., "A Two Surface Plasticity Theory for Transient Nonproportional Cyclic Plasticity," Joint ASME/ASCE Applied Mechanics Conference, Univ. of New Mexico, Albuquerque, N.M., June 24-27, 1985.
6. McDowell, D.L., "Work in Progress on Cyclic Plastic Stress Calculation for Rail Steels," 4th ETAC Meeting, U.S. DOT Transportation Systems Center, July 16-17, 1985.
7. McDowell, D.L., Moosbrugger, J., Doumi, M., and Jordan, E.H., "Some Implications for Cyclic Plastic and Viscoplastic Equations Based on Nonproportional Loading Experiments," 3rd Symposium on Nonlinear Constitutive Relations for High-Temperature Applications, NASA Lewis RC, University of Akron, Ohio, June 11-13, 1986.

8. McDowell, D.L. and Moyer, G.J., "A More Realistic Model of Nonlinear Material Response: Application to Elastic-Plastic Rolling Contact," 2nd Int. Symp. on Contact Mechanics and Wear of Rail/Wheel Systems, University of Rhode Island, Kingston, July 8-11, 1986.



The Society shall not be responsible for statements or opinions advanced in papers or in discussion at meetings of the Society or of its Divisions or Sections, or printed in its publications. Discussion is printed only if the paper is published in an ASME Journal. Released for general publication upon presentation. Full credit should be given to ASME, the Technical Division, and the author(s). Papers are available from ASME for nine months after the meeting.  
Printed in USA.

# A Two Surface Model for Transient Nonproportional Cyclic Plasticity:

## Part 1 Development of Appropriate Equations

D. L. McDowell

Assistant Professor,  
School of Mechanical Engineering,  
Georgia Institute of Technology,  
Atlanta, Ga. 30332  
Assoc. Mem. ASME

*A two surface stress space model is introduced with internal state variable repositories for fading memory of maximum plastic strain range and non-proportionality of loading. Evolution equations for isotropic hardening variables are prescribed as a function of these internal variables and accumulated plastic strain, and reflect dislocation interactions that occur in real materials. The hardening modulus is made a function of prior plastic deformation and the distance of the current stress point from the limit surface. The kinematic hardening rules of Mroz and Prager are used for the yield and limit surfaces, respectively. The structure of the model is capable of representing essential aspects of complex nonproportional deformation behavior, including direction of the plastic strain rate vector, memory of plastic strain range, cross-hardening effects, variation of hardening modulus, cyclic hardening or softening, cyclic ratcheting, and mean stress relaxation.*

### Introduction

The presence of cyclic plasticity in a multiaxial stress-strain field is a serious fatigue design consideration in the nuclear, aircraft, and ground vehicle industries [1-4]. When the stress rate is nonradial in deviatoric stress space at some interval of each loading cycle, the analysis is complicated by non-proportionality effects [5].

Nonproportional loading places additional requirements on the constitutive equations for transient cyclic plasticity. In particular, the plastic strain rate vector direction, memory of plastic strain range, magnitude of the plastic hardening modulus, and cross-hardening effects are of critical importance. The objective of this work is to introduce a two surface model based on the assumptions of time and rate-independent plasticity theory which is capable of predicting results from cyclic, nonproportional, room-temperature tests performed by the author [6, 7], including cyclic hardening effects. A companion paper demonstrates the quantitative behavior of this model for nonproportional strain cycling experiments conducted by the author on type 304 stainless steel.

Contributed by the Applied Mechanics Division for presentation at the 1985 Joint ASME/ASCE Applied Mechanics, Fluids Engineering, and Bioengineering Conference, Albuquerque, N. Mex., June 24-26, 1985 of THE AMERICAN SOCIETY OF MECHANICAL ENGINEERS.

Discussion on this paper should be addressed to the Editorial Department, ASME, United Engineering Center, 345 East 47th Street, New York, N.Y. 10017, and will be accepted until two months after final publication of the paper itself in the JOURNAL OF APPLIED MECHANICS. Manuscript received by ASME Applied Mechanics Division, April, 1984; final revision, August, 1984. Paper No. 85-APM-9.

Copies will be available until February, 1986.

### Motivation From Previous Work

**Plastic Strain Rate Direction.** With regard to the direction of the plastic strain rate vector during nonproportional cyclic loading there are two approaches. The first approach, motivated chiefly by yield surface probing experiments during nonproportional straining [8-11], requires the formulation of an anisotropic yield surface [12-15]. This surface can distort, expand, or contract to reflect deformation-induced anisotropy and isotropic hardening.

It is reasonable to assume for cyclic plasticity applications that deformation-induced anisotropy can be accounted for by a kinematic backstress  $\alpha$ . The yield surface may contract or expand but not distort. These assumptions result in a computationally more efficient form of the yield surface than most formulations that permit distortion:

$$f = f(\sigma - \alpha, R) = 0 \quad (1)$$

where  $\alpha$  is determined from the consistency condition  $\dot{f} = 0$  during plastic flow and the ratio of kinematic to isotropic hardening [16].

As usual, the conditions for plastic flow are

$$\dot{\epsilon}^p = \dot{m}(\partial f / \partial \sigma) \text{ if } f = 0 \text{ and } \dot{\sigma} : (\partial f / \partial \sigma) \geq 0 \quad (2)$$

$$\dot{\epsilon}^p = 0 \text{ otherwise} \quad (3)$$

where  $\dot{m}$  is a scalar multiplier, and  $\sigma$  is the stress tensor. Here the usual decomposition of the total small strain rate into elastic and plastic components is assumed, i.e.,  $\dot{\epsilon} = \dot{\epsilon}^e + \dot{\epsilon}^p$ . The scalar product  $\dot{\sigma}_{ij}(\partial f / \partial \sigma_{ij})$  is denoted by  $\dot{\sigma} : (\partial f / \partial \sigma)$ .

Lambda [17, 18], McDowell et al. [19, 20], and Garud [21, 22] have demonstrated the applicability of equations (1)-(3)

for proper plastic strain rate direction under conditions of nonproportional straining at cyclically stable conditions when the hardening rule is obtained from a nested surface approach. The yield surface radius  $R$  can be determined for cyclic hardening or softening from a relation that defines  $R$  as a function of accumulated plastic strain  $\eta = \int \sqrt{(\dot{\epsilon}^p : \dot{\epsilon}^p)} dt$  [23].

**Plastic Strain Range Effects.** It is well known that the evolution of the isotropic hardening parameter  $R$  depends on plastic strain range [24–26], particularly for the austenitic stainless steels. Analytical description of this dependence requires a more detailed repository for history dependence than  $\eta$ . At the very least, a measure of the metric plastic strain accumulation from a point of recent unloading is necessary [27, 28]. A plastic strain range memory parameter  $q$  was introduced by Chaboche et al. [29] and Nouailhas et al. [30] for cyclic loading. The evolution of  $q$  follows from

$$\dot{q} = \frac{1}{2} H(F) \mathbf{n} : \mathbf{n}^* \eta (2/3)^{1/2} \quad (4)$$

where  $H(F) = 1$  if  $F = 0$  and  $H(F) = 0$  if  $F < 0$ . The normal to the yield surface  $f$  at the current stress point is denoted by  $\mathbf{n}$ , where  $\mathbf{n} = (\partial f / \partial \boldsymbol{\sigma}) / \|\partial f / \partial \boldsymbol{\sigma}\|$ . The notation  $\|\partial f / \partial \boldsymbol{\sigma}\|$  denotes the norm  $(\partial f / \partial \boldsymbol{\sigma} : \partial f / \partial \boldsymbol{\sigma})^{1/2}$ . Here,  $F$  is the plastic strain memory surface defined in second invariant form by

$$F = (2/3)(\epsilon^p - \alpha^p) : (\epsilon^p - \alpha^p) - q^2 = 0 \quad (5)$$

where  $\alpha^p$  is the center of the memory surface in plastic strain space. Note that  $\mathbf{n}^*$  is the normal to the surface  $F$  at the point  $\epsilon^p$  defined by  $\mathbf{n}^* = (\partial F / \partial \epsilon^p) / \|\partial F / \partial \epsilon^p\|$ . For completely reversed uniaxial cycling,  $q$  represents half the axial plastic strain range. The surface  $F$  is shown in Fig. 1 in plastic strain space.

There is a rather severe problem with this formulation of plastic strain range memory. If an overload cycle occurs in which the plastic strain range is doubled, for example, continued cycling at the smaller strain range may not result in a saturated isotropic hardening state that corresponds to the overload cycle. Yet  $q$  would correspond to the plastic strain range of the overload cycle. The actual plastic strain range "remembered" by the material would lie somewhere between that of the small and large cycles [25, 31]. This lack of evanescence can be corrected by introduction of a fading memory term in equation (4)

$$\dot{q} = \left[ \frac{1}{2} H(F) \Gamma(2/3)^{1/2} - \Lambda(q) \right] \eta \quad (6)$$

where  $\Lambda(q)$  is the memory loss-rate function and  $\Gamma$  is a scalar to be defined later. This capability of fading memory is also necessary to allow for the possibility of readjustment of the isotropic hardening or softening response when reducing the applied strain range during cyclically stable conditions.

Expressing the flow rule in equation (2) in an equivalent form  $\dot{\epsilon}^p = (1/h) (\dot{\sigma} : \mathbf{n}) \mathbf{n}$  allows interpretation of  $h$  as a generalized plastic modulus or hardening modulus. It is particularly attractive to define  $h$  through a multiple nested surface scheme as in the approach of Mroz [32–34]. Path dependence of  $h$  and  $\epsilon^p$  is achieved through the translation of the yield and loading surfaces.

**Cross-Hardening Effects.** It is experimentally observed for a number of metals [7, 17, 30, 35] that nonproportional cycling leads to an increase in the size of the region of elastic response above that corresponding to proportional cycling at the same effective strain range. This additional isotropic hardening apparently results from increased dislocation interaction and is not included in conventional theories. Brown and Miller [35] were able to correlate this additional

hardening for out-of-phase sinusoidal straining of 1 percent Cr-Mo-V steel by introducing a rotation factor

$$RF = \frac{\text{shear strain range at 45 deg to maximum shear plane}}{\text{maximum shear strain range}} \quad (7)$$

For proportional straining, defined in this work as loading for which the total strain rate is collinear with the total strain,  $RF = 0$ . For the case of sinusoidal tension-torsion straining of a thin-walled tubular specimen with an engineering shear to axial strain amplitude ratio of  $\gamma_a / \epsilon_a = (1 + \nu)$  and a phase angle of 90 deg,  $RF = 1$ . Here,  $\nu$  is Poisson's ratio. The latter case defines every plane in the specimen wall as a maximum shear strain plane of equal shear strain range at some point in the loading cycle. The maximum shear planes rotate at a constant rate. This case also yielded the most additional cyclic hardening observed by Brown and Miller within a rather coarse matrix of phase angle and strain amplitude ratio tests.

Brown and Miller achieved a correlation coefficient of 0.836 for various phase angle and strain amplitude ratios by assuming a linear relation between cyclically stable flow stress and rotation factor based on a maximum shear stress-strain Ramberg-Osgood relation analogous to the uniaxial cyclic stress-strain curve [24].

Nouailhas et al. [30] point out that inclusion of plastic strain range dependence through the memory parameter  $q$  of equations (5) and (6) is highly insufficient to correlate the significant additional hardening of type 316 stainless steel subjected to 90 deg out-of-phase tension-torsion loading. Hence, the need to define another state variable to account for the additional hardening during nonproportional loading is well established.

McDowell [6, 7, 31] introduced an instantaneous measure  $J$  of the nonproportionality of the strain rate tensor

$$J = |\dot{\gamma}_{\max}(\epsilon) / g(\gamma_{\max}(\epsilon))| \quad (8)$$

$$\dot{\gamma}_{\max}(\epsilon) = d/dt (\epsilon_1 - \epsilon_3) \quad (9)$$

$$\gamma_{\max}(\epsilon) = (\epsilon)_1 - (\epsilon)_3 \quad (10)$$

where  $\epsilon_1, \epsilon_3$  are the largest and smallest principal strains, and  $(\epsilon)_1, (\epsilon)_3$  are the largest and smallest principal values, respectively, of the strain rate tensor at each point in time. The function  $g$  is defined by  $g(x) = 1$  if  $x = 0$ ;  $g(x) = x$  if  $x \neq 0$ .

There is a physical interpretation for this definition of  $J$ . Under conditions of proportional straining,  $\dot{\gamma}_{\max}(\epsilon) = \gamma_{\max}(\dot{\epsilon})$  and  $J = 1$ . In this case, the principal axes of strain are fixed with respect to material axes. For the case of sinusoidal tension-torsion straining of a thin-walled tubular specimen with a shear to axial strain amplitude ratio of  $\gamma_a / \epsilon_a = (1 + \nu)$  and a phase angle of 90 deg,  $\dot{\gamma}_{\max}(\epsilon) = 0$  and  $J = 0$  since  $\gamma_{\max}(\epsilon)$  is nonzero. Again, this is the case of maximum additional cyclic hardening observed experimentally by Brown and Miller. Hence,  $0 \leq J \leq 1$  with decreasing values of  $J$  indicative of higher degrees of instantaneous nonproportionality.

Since  $J$  is an instantaneous measure of nonproportionality, the degree of nonproportionality,  $\phi$ , representative of several complete cycles of loading can be expressed as a functional of  $J$  such that  $0 \leq \phi \leq 1$ ;  $\phi$  is directly analogous to  $RF$  in equation (7), but evolves continuously. A specific rate form for the state variable  $\phi$  will be proposed later.

It should also be noted that the form for  $J$  in equations (8)–(10) is valid for proportional straining or for conditions of nonproportional loading where the principal strain directions rotate continuously at some or all points of a loading cycle, as in axial-torsion tests of thin-walled tubular specimens. Nonproportional variations of principal strains with fixed principal directions will not be considered in this study.



## Description of Model

It should be noted that the formulation for memory of plastic strain range and nonproportionality of loading discussed in the previous sections are strain-based. Hence, the possibility of including these parameters in a strain space plasticity theory [36–38] appears physically meaningful. However, the memory of plastic strain range would still necessitate a separate plastic strain memory surface or analogous formulation. In addition, accurate modeling of modulus and kinematic hardening for nonproportional cyclic loading would probably require a multiple surface strain space formulation [38]. Therefore, the present paper will consider a more conventional stress space formulation for the yield surface, with the addition of a plastic strain memory surface.

A two surface, stress-space, cyclic plasticity model similar to that of Dafalias and Popov [27] and Krieg [34] is considered. This model includes plastic strain range and nonproportionality dependence in the isotropic hardening formulation. It is valid for complex, nonproportional, cyclic loading with transient hardening or softening behavior. Only small strains are considered.

The yield and limit surfaces are defined as  $f(s - \alpha, R) = 0$  and  $f^*(s^* - \alpha^*, R^*) = 0$ , respectively, where

$$f = (3/2)\xi : \xi - R^2 \quad (11)$$

$$f^* = (3/2)\xi^* : \xi^* - (R^*)^2 \quad (12)$$

where  $s = \sigma - (1/3)(\sigma : \mathbf{I})\mathbf{I}$ ,  $\xi = s - \alpha$ ,  $\xi^* = s^* - \alpha^*$ , and where  $\alpha$ ,  $R$ , and  $\alpha^*$ ,  $R^*$  denote the vector position of the center and radius of the yield and limit surfaces, respectively. The vectors  $s$  and  $s^*$  are position vectors of generic points on the yield and limit surfaces, respectively, in deviatoric stress space. The identity tensor is denoted by  $\mathbf{I}$ . The flow rule can be stated as  $\dot{\epsilon}^p = (1/h)(\dot{s} : \mathbf{n})\mathbf{n}$  if  $f = 0$  and  $\dot{s} : \mathbf{n} \geq 0$ , with  $\dot{\epsilon}^p = 0$  otherwise where  $h = (2/3)(d\sigma/d\epsilon^p)$  is determined from a stable uniaxial cyclic stress-strain curve, and  $\mathbf{n} = (\partial f / \partial s) / \|\partial f / \partial s\|$ .

To formulate hardening rules and the form of the function  $h$  for multiaxial loading, it is necessary to consider previous nonproportional cyclic loading experiments. The work of Lamba [17, 18] points to the use of a Mroz-type [32, 33] kinematic-isotropic hardening rule. The kinematic hardening rules of Prager [39] and Ziegler [40] prove to be inadequate for nonproportional cyclic loading [17, 18]. Hence, the use of two surfaces in the stress space formulation is both minimal and capable of accuracy.

The following simple hardening rules are representative of popular two surface models and can include all essential aspects of reality [23] such as cyclic hardening and softening, cyclic mean stress relaxation, and cyclic creep or ratcheting:

$$\dot{\alpha} = \dot{\mu}_\alpha \nu \quad (13)$$

$$\dot{R} = \Sigma \dot{\eta} \quad (14)$$

$$\dot{\alpha}^* = \kappa \dot{\eta} \quad (15)$$

$$\dot{R}^* = \zeta \dot{\eta} \quad (16)$$

Equations (13) and (15) define kinematic hardening of  $f$  and  $f^*$ , respectively. Isotropic hardening is defined in equations (14) and (16). In these equations,  $\nu = (s^* - s) / \|s^* - s\|$ ,  $\eta = (\dot{\epsilon}^p : \dot{\epsilon}^p)^{1/2} = \|\dot{\epsilon}^p\|$  and  $\kappa = (2/3)(d\sigma/d\epsilon^p)_\infty$  where  $d\sigma$  and  $d\epsilon^p$  are measured from a uniaxial cyclic stress-strain curve. Hence,  $\kappa$  represents the asymptotic plastic modulus. In practice,  $\kappa$  is selected to best fit the asymptotic stress-strain response. The functions  $\Sigma$  and  $\zeta$  will be discussed later.

In the Mroz rule of equation (13)  $s^*$  defined as the point on the surface  $f^*$  which has the same outward normal as the normal,  $\mathbf{n}$ , to the yield surface  $f$  at the current stress state,  $s$ :

$$s^* = \alpha^* + (R^*/R)\xi \quad (17)$$

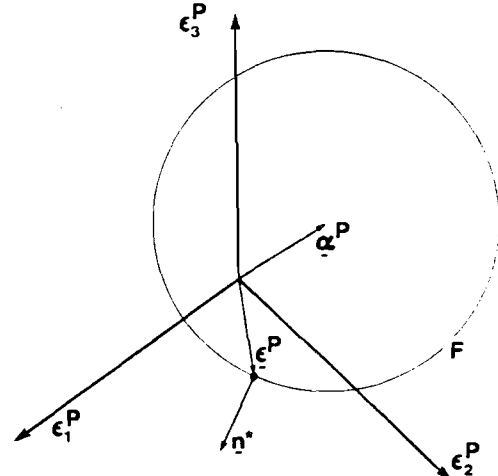


Fig. 1 Plastic strain memory surface  $F$  when the current plastic strain lies on  $F$

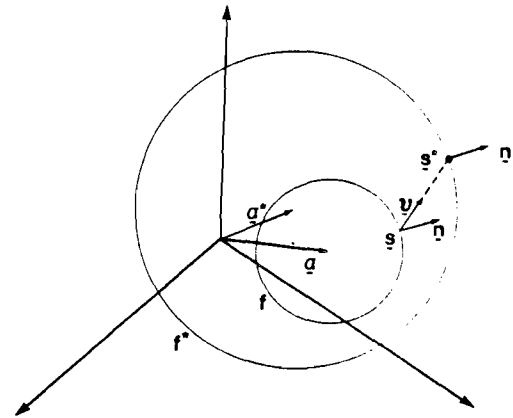


Fig. 2 Surfaces  $f$  and  $f^*$  in deviatoric stress space

The rate scalar  $\dot{\mu}_\alpha$  is determined from the consistency condition  $\dot{f} = 0$  during the plastic flow, which upon the substitution  $\dot{\alpha} = \dot{\mu}_\alpha \nu$  leads to

$$\dot{\mu}_\alpha = (\xi : \dot{s} - (2/3)\dot{R}\dot{R}) / (\xi : \nu) \quad (18)$$

The surfaces  $f$  and  $f^*$  and the parameters  $\alpha$ ,  $\alpha^*$ ,  $\mathbf{n}$  and  $\nu$  are illustrated in Fig. 2 in deviatoric stress space. The hardening modulus,  $h$ , can be expressed as a function of  $\|s^* - s\|$ . As noted by Krieg [34], the stiffness decreases as  $\|s^* - s\|$  decreases until we approach the asymptotic state characterized by  $\kappa$  at some significant level of plastic strain. In the absence of accurate knowledge of the variation of the hardening modulus during nonproportional plastic flow, it is assumed that the limit surface  $f^*$  is of primary importance in defining  $h$ . The functional relationship for  $h$  can then be determined from a stable uniaxial cyclic stress-strain curve as shown in Fig. 3. Since this curve is representative of cyclically stable response,  $\dot{R} = \dot{R}^* = 0$  and hardening is purely kinematic. The radii  $R^*$  and  $R$  determined from this uniaxial cyclic stress-strain curve will be denoted as  $\bar{R}^*(0, q)$  and  $\bar{R}(0, q)$ , respectively, where  $q$  is the maximum plastic strain amplitude in the incremental step test used to determine the curve. Small offset or deviation from linearity definitions of yield could be used. The hardening modulus could be generally written as

$$h = h(\|s^* - s\| / (\theta(R^* - R)), \kappa) \quad (19)$$

As  $\|s^* - s\| \rightarrow 0$ ,  $h \rightarrow \kappa$ . The asymptotic slope  $(2/3)(d\sigma/d\epsilon^p)_\infty$  defines  $\kappa$  as shown in Fig. 3. The radii  $R$  and  $R^*$  are the  $\Delta\epsilon^p/2 = 0$  ordinate intercepts defined by a deviation

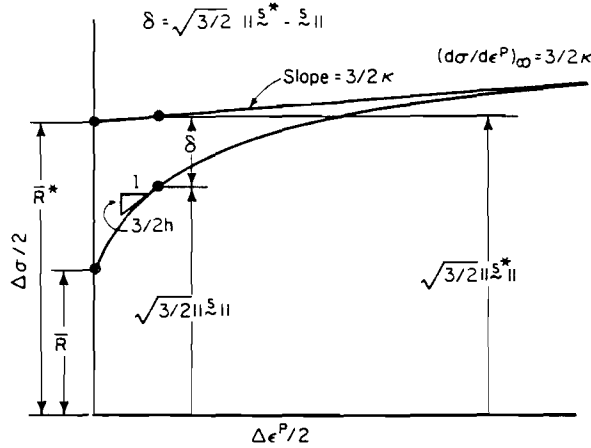


Fig. 3 Determination of parameters in two surface model from a uniaxial cyclic stress-strain curve

from linearity, perhaps, and back extrapolation of the asymptotic plastic response defined by  $\kappa$ , respectively. Thus,  $R$  is the uniaxial yield strength of the material.

The  $\theta$  parameter in equation (19) introduces memory of the most recent point of elastic unloading. It is a measure of the effects of plastic deformation accumulated during the last loading reversal. From an alternative viewpoint, it is a measure of the initial distance to the asymptotic plastic state from the point of initial yielding for the current plastic trajectory. Hence, the use of  $\theta$  has the same qualitative effect on the plastic modulus function as the delta parameter introduced by Dafalias and Popov [27] to describe the experimental observation that  $h$  is not strictly just a function of current distance from the limit surface. A simple, reasonable choice for  $\theta$  for each plastic strain trajectory would be

$$\theta = \|s_0^* - s_0\| / (R_0^* - R_0) \quad (20)$$

where all zero subscripted variables correspond to values at the most recent point of initial yielding following a change in loading direction.

The hardening rules in equations (13)–(16) allow the surfaces  $f$  and  $f^*$  to expand and translate independently without intersecting. The limit surface translates more slowly and, possibly, in a different direction than the yield surface when the stress point lies within  $f^*$ . When  $\|s^* - s\| \rightarrow 0$  and  $\dot{R} = \dot{R}^* = 0$ , the surfaces approach tangential contact and translate according to  $\dot{\alpha} \rightarrow \dot{\alpha}^* = \kappa \dot{n}$  since  $h \rightarrow \kappa$ . When  $\|s^* - s\| = 0$ , we can heuristically take  $\nu = n$ .

The use of this stress space formulation is restricted to strain-hardening behavior for which  $(\partial f / \partial s) : \dot{s} > 0$  during plastic flow, a condition almost universally met by metals of structural interest at typical cyclic strain magnitudes.

The isotropic hardening functions  $\Sigma$  and  $\zeta$  can be written as

$$\dot{R} = \mu (\bar{R}(\phi, q) - R) \psi \dot{\eta} \quad (21)$$

$$\dot{R}^* = \mu (\bar{R}^*(\phi, q) - R^*) \psi^* \dot{\eta} \quad (22)$$

where  $\bar{R}$  and  $\bar{R}^*$  represent cyclically stable values of  $R$  and  $R^*$  corresponding to the current values of state variables  $\phi$  and  $q$ . The rate of approach to the cyclically stable state is governed by  $\mu$ . The admissibility functions  $\psi$  and  $\psi^*$  place restrictions on the stable states that can actually be attained. They are necessary for complex loading because a formulation based on internal state variables that do not necessarily monotonically increase (i.e., plastic strain range  $q$  and nonproportionality of loading  $\phi$ ) implies reversibility; yet isotropic hardening is known to be largely irreversible for planar slip metals [25, 26], and nearly reversible for wavy slip materials of structural interest. In the event of nonfading memory for cyclically hardening metals,  $\psi$  and  $\psi^*$  could be represented by Heaviside functions  $u(\bar{R}(\phi, q) - R)$  and

$u(\bar{R}^*(\phi, q) - R^*)$ , respectively. In contrast, completely fading memory can be described by  $\psi = \psi^* = 1$ .

The variable  $\phi$  represents the integrated effects of mobile dislocation interactions during cycling. The evolution of  $\phi$  can be described by

$$\dot{\phi} = \mu^* (1 - J - \phi) \dot{\eta} u(1 - J - \phi_{\text{limit}}) \quad (23)$$

where  $\phi = 0$  at time  $t = 0$  or  $\dot{\eta} dt = 0$ . Inclusion of the Heaviside function  $u(1 - J - \phi_{\text{limit}})$  is based on the assumption that additional hardening due to interaction of slip systems during nonproportional loading is determined primarily by those portions of each loading cycle for which the maximum shear planes rotate during plastic flow. The threshold value  $\phi_{\text{limit}}$  may be defined as a small number in the range 0.01 to 0.03 so that virtually all deviations from proportionality are included. The calculation of  $\phi$  is insensitive to the magnitude of  $\phi_{\text{limit}}$  if  $\phi_{\text{limit}}$  is less than 0.10, particularly for moderate to severe degrees of nonproportionality of loading. For proportional straining,  $\phi = 0$ . For  $\gamma_a / \epsilon_a = (1 + \nu)$  during sinusoidal tension-torsion straining with a phase angle between applied axial and shear strains of 90 deg,  $\phi \rightarrow 1$  as  $\dot{\eta} dt \rightarrow \infty$ . The evolution of  $q$ , the plastic strain range variable, is defined by equation (6). Introducing a kinematic hardening rule for  $F$  in equation (5),

$$\dot{\alpha}^p = (H(F)/2)(\dot{\epsilon}^p : n^*) n^* \quad (24)$$

Hence, the surface  $F$  can evolve only if  $F = 0$  and  $\epsilon^p$  lies on  $F$ . Enforcing the consistency condition  $\dot{F} = 0$  during plastic flow when  $F = 0$  ( $H(F) = 1$ ),

$$(\partial F / \partial \epsilon^p) : \dot{\epsilon}^p + (\partial F / \partial \alpha^p) : \dot{\alpha}^p - 2q\dot{q} = 0 \quad (25)$$

which, after some substitution and manipulation, leads to

$$\Gamma = n^* : n + \sqrt{6} \Lambda(q) \quad (26)$$

All that remains in the isotropic hardening formulation is assignment of the functions  $\bar{R}(\phi, q)$  and  $\bar{R}^*(\phi, q)$  in equations (21) and (22). McDowell [6, 7] demonstrated the applicability of the linear form

$$\bar{R}(\phi, q) = \phi[\bar{R}(1, q) - \bar{R}(0, q)] + \bar{R}(0, q) \quad (27)$$

$$\bar{R}^*(\phi, q) = \phi[\bar{R}^*(1, q) - \bar{R}^*(0, q)] + \bar{R}^*(0, q) \quad (28)$$

where  $\bar{R}(1, q)$  and  $\bar{R}^*(1, q)$  can be obtained, for example, from the cyclic stress-strain response during proportional loading immediately following cyclically stable 90 deg out-of-phase tension-torsion loading of thin-walled tubular specimens at a shear to axial strain amplitude ratio of  $\gamma_a / \epsilon_a = (1 + \nu)$ .

## Conclusions

The proposed model, while limited in scope to time and rate-independent behavior, is significant in two respects. First, the effects of changes in plastic strain range and nonproportionality of loading are incorporated in the evolution of isotropic hardening via two additional state variables  $q$  and  $\phi$ . It is fully expected that either or both of these variables could be included in virtually any constitutive framework. Abrahamson [41] incorporated an analogous form of  $\phi$  proposed by McDowell [7] into a state variable constitutive framework valid for cyclic viscoplasticity.

It is noted that the structure of the proposed theory is capable of representing those aspects of material behavior perceived as most essential and relevant by Drucker and Palgen [23] for time-independent cyclic plasticity including erasure of memory of prior deformation by overload excursions, cyclic hardening or softening under symmetric cycles of stress or strain in the plastic range, progressive creep or ratcheting of the hysteresis response during unsymmetric cycles of stress in the plastic range, and progressive relaxation of mean stress during unsymmetric cycles of strain in the

plastic range. The accuracy of the ratcheting or mean stress relaxation capability of this model would be enhanced by admitting dependence of  $\kappa$  and  $h$  on  $(1/2)(\dot{\epsilon}:\dot{\epsilon})$ , the second invariant of deviatoric stress.

## Acknowledgments

The author wishes to acknowledge the National Science Foundation (Grant No. MEA-8404080; Program Manager, C. J. Astill) for continuing research support on the subject of this paper.

## References

- 1 Krempl, E., *The Influence of State of Stress on Low-Cycle Fatigue of Structural Materials*, ASTM STP 549, 1974.
- 2 Brown, M. W., and Miller, K. J., "Two Decades of Progress in the Assessment of Multiaxial Low-Cycle Fatigue Life," *Low-Cycle Fatigue and Life Prediction*, ASTM STP 770, 1982, pp. 482-499.
- 3 Fash, J. W., Socie, D. F., and McDowell, D. L., "Fatigue Life Estimates for a Simple Notched Component Under Biaxial Loading," to appear in ASTM STP 853.
- 4 Garud, Y. S., "MULTI-AXIAL FATIGUE: A Survey of the State of the Art," Proceedings of the ASTM/SAE Workshop on Elasto-Plastic Materials Behavior and Component Fatigue Analysis, Minneapolis, April 1980.
- 5 Laflen, J. H., and Cook, T. S., "Equivalent Damage—A Critical Assessment," NASA CR-167874, Nov. 1982.
- 6 McDowell, D. L., "On the Path Dependence of Transient Hardening and Softening to Stable States Under Complex Biaxial Cyclic Loading," *Proceedings of the International Conference on Constitutive Laws for Engineering Materials*, Desai and Gallagher, Eds., Tucson, Ariz., Jan. 1983, pp. 125-132.
- 7 McDowell, D. L., "Transient Nonproportional Cyclic Plasticity," Ph.D. thesis, Design and Materials Division, Report No. 107, Department of Mechanical and Industrial Engineering, University of Illinois at Urbana-Champaign, June 1983.
- 8 Liu, K. C., and Greenstreet, W. L., "Experimental Studies to Examine Elastic-Plastic Behaviors of Metal Alloys Used in Nuclear Structures," *Constitutive Equations in Viscoplasticity: Computational and Engineering Aspects*, AMD, ASME, Vol. 20, 1976, pp. 35-56.
- 9 Hecker, S. S., "Experimental Studies of Yield Phenomena in Biaxially Loaded Metals," *Constitutive Equations in Viscoplasticity: Computational and Engineering Aspects*, AMD, ASME, Vol. 20, 1976, pp. 1-32.
- 10 Phillips, A., Tang, J. L., and Ricciuti, M., "Some New Observations on Yield Surfaces," *Acta Mechanica*, Vol. 20, 1974, pp. 23-39.
- 11 Ohashi, Y., Kawashima, K., and Yokochi, T., "Anisotropy Due to Plastic Deformation of Initially Isotropic Mild Steel and Its Analytical Formulation," *Journal of the Mechanics and Physics of Solids*, Vol. 23, 1975, pp. 277-294.
- 12 Phillips, A., and Weng, G. J., "An Analytical Study of an Experimentally Verified Hardening Law," *ASME JOURNAL OF APPLIED MECHANICS*, Vol. 42, June 1975, pp. 375-378.
- 13 Shiratori, E., Ikegami, K., and Yoshida, F., "Analysis of Stress-Strain Relations by Use of an Anisotropic Hardening Plastic Potential," *Journal of the Mechanics and Physics of Solids*, Vol. 27, 1979, pp. 213-229.
- 14 Drucker, D. C., "Some Implications of Work Hardening and Ideal Plasticity," *Quarterly of Applied Mathematics*, Vol. 7, No. 4, Jan. 1950, pp. 411-418.
- 15 Mair, W. M., and Pugh, H., "Effect of Prestrain on Yield Surfaces in Copper," *Journal Mechanical Engineering Science*, Vol. 6, No. 2, 1964, pp. 150-163.
- 16 Newman, J. C., Jr., "Finite Element Analysis of Crack Growth Under Monotonic and Cyclic Loading," *Cyclic Stress-Strain and Plastic Deformation Aspects of Fatigue Crack Growth*, ASTM STP 637, 1977, pp. 56-80.
- 17 Lamba, H. S., "Nonproportional Cyclic Plasticity," TAM Report No. 413, Department of Theoretical and Applied Mechanics, University of Illinois at Urbana-Champaign, 1976.
- 18 Lamba, H. S., and Sidebottom, O. M., "Proportional Biaxial Cyclic Hardening of Annealed Oxygen-Free High-Conductivity Copper," *Journal of Testing and Evaluation*, ASTM, Vol. 6, No. 4, 1978, pp. 260-267.
- 19 McDowell, D. L., "Multiaxial Nonproportional Cyclic Deformation," Report No. 102, Design and Materials Division, Department of Mechanical and Industrial Engineering, University of Illinois at Urbana-Champaign, May 1981.
- 20 McDowell, D. L., Socie, D. F., and Lamba, H. S., "Multiaxial Nonproportional Cyclic Deformation," *Low-Cycle Fatigue and Life Prediction*, ASTM STP 770, 1982, pp. 500-518.
- 21 Garud, Y. S., "A New Approach to the Evaluation of Fatigue Under Multiaxial Loadings," *Proceedings, Symposium on Methods for Predicting Material Life in Fatigue*, ASME, Dec. 1979, pp. 247-263.
- 22 Garud, Y. S., "Prediction of Stress-Strain Response Under General Multiaxial Loading," *Mechanical Testing for Deformation Model Development*, ASTM STP 765, 1982, pp. 223-238.
- 23 Drucker, D. C., and Palgen, L., "On Stress-Strain Relations Suitable for Cyclic and Other Loading," TAM Report No. 443, Department of Theoretical and Applied Mechanics, University of Illinois at Urbana-Champaign, July 1980.
- 24 Landgraf, R. W., Morrow, J., and Endo, T., "Determination of the Cyclic Stress-Strain Curve," *Journal of Materials*, ASTM, Vol. 4, No. 1, Mar. 1969, pp. 176-188.
- 25 Lukas, P., and Polak, J., "Cyclic Stress-Strain Response in Low Amplitude Region," *Proceedings of the Symposium on Work Hardening in Tension and Fatigue*, AIME, Cincinnati, Nov. 1975, pp. 177-205.
- 26 Landgraf, R. W., "Cyclic Stress-Strain Responses in Commercial Alloys," *Proceedings of the Symposium on Work Hardening in Tension and Fatigue*, AIME, Cincinnati, Nov. 1975, pp. 240-259.
- 27 Dafalias, Y. F., Popov, E. P., "A Model of Nonlinearly Hardening Materials for Complex Loading," *Acta Mechanica*, Vol. 21, 1975, pp. 173-192.
- 28 Eisenberg, M. A., "A Generalization of Plastic Flow Theory With Application to Cyclic Hardening and Softening Phenomena," *ASME Journal of Engineering Materials and Technology*, Vol. 98, 1976, pp. 221-228.
- 29 Chaboche, J.-L., Dang Van, K., and Cordier, G., "Modelization of the Strain Memory Effect on the Cyclic Hardening of 316 Stainless Steel," *Proceedings of the 5th International Conference on Structural Mechanics in Reactor Technology*, Berlin, 1979.
- 30 Nouailhas, D., Policella, H., and Kaczmarek, H., "On the Description of Cyclic Hardening Under Complex Loading Histories," *Proceedings of the International Conference on Constitutive Laws for Engineering Materials*, Desai and Gallagher, Eds., Tucson, Ariz., Jan. 1983, pp. 45-49.
- 31 McDowell, D. L., and Socie, D. F., "Transient and Stable Deformation Behavior Under Cyclic Nonproportional Loading," to appear in ASTM STP 853.
- 32 Mroz, Z., "Mathematical Models of Inelastic Material Behavior," Solid Mechanics Division, University of Waterloo, Waterloo, Ontario, 1973.
- 33 Mroz, Z., "An Attempt to Describe the Behavior of Metals Under Cyclic Loads Using a More General Workhardening Model," *Acta Mechanica*, Vol. 7, 1967, pp. 199-212.
- 34 Krieg, R. D., "A Practical Two Surface Plasticity Theory," *ASME JOURNAL OF APPLIED MECHANICS*, Vol. 42, Sept. 1975, pp. 641-646.
- 35 Brown, M. W., and Miller, K. J., "Cyclic Deformation of 1 Percent Cr-Mo-V Steel Under Out-of-Phase Loads," *Fatigue of Engineering Materials and Structures*, Vol. 2, 1979, pp. 217-228.
- 36 Casey, J., and Naghdi, P. M., "On the Characterization of Strain-Hardening in Plasticity," *ASME JOURNAL OF APPLIED MECHANICS*, Vol. 48, 1981, pp. 285-296.
- 37 Casey, J., and Naghdi, P. M., "On the Nonequivalence of the Stress Space and Strain Space Formulations of Plasticity Theory," *ASME JOURNAL OF APPLIED MECHANICS*, Vol. 50, 1983, pp. 350-354.
- 38 Yoder, P. J., and Iwan, W. D., "On the Formulation of Strain-Space Plasticity With Multiple Loading Surfaces," *ASME JOURNAL OF APPLIED MECHANICS*, Vol. 48, 1981, pp. 773-778.
- 39 Prager, W., "A New Method of Analyzing Stress and Strain in Workhardening, Plastic Solids," *ASME JOURNAL OF APPLIED MECHANICS*, Vol. 23, 1956, p. 493.
- 40 Ziegler, H., "A Modification of Prager's Hardening Rule," *Quarterly of Applied Mathematics*, Vol. 17, 1959, pp. 55-60.
- 41 Abrahamson, T. E., "Modeling the Behavior of Type 304 Stainless Steel with a Unified Creep-Plasticity Theory," Ph.D. thesis, Department of Mechanical and Industrial Engineering, University of Illinois at Urbana-Champaign, 1983.



The Society shall not be responsible for statements or opinions advanced in papers or in discussion at meetings of the Society or of its Divisions or Sections, or printed in its publications. Discussion is printed only if the paper is published in an ASME Journal. Released for general publication upon presentation. Full credit should be given to ASME, the Technical Division, and the author(s). Papers are available from ASME for nine months after the meeting.  
Printed in USA.

# A Two Surface Model for Transient Nonproportional Cyclic Plasticity:

## Part 2 Comparison of Theory With Experiments

D. L. McDowell

Assistant Professor,  
School of Mechanical Engineering,  
Georgia Institute of Technology,  
Atlanta, Ga. 30332  
Assoc. Mem. ASME

*For the two surface cyclic plasticity model introduced in Part 1, methods for determination of model parameters are described. The model is specialized to axial-torsional loading of a thin-walled tubular specimen, and applied to non-proportional, room-temperature cycling of type 304 stainless steel. Computer simulations for two complex histories show good general agreement with experimental data obtained by the author.*

### Introduction

In Part 1 of this two-part paper, a two surface cyclic plasticity model was developed which includes the essential aspects of cyclic nonproportional loading. In this part, the material constants and model parameters are determined for type 304 stainless steel. The model is specialized to axial-torsional loading and compared with nonproportional, cyclic histories consisting of several sequential blocks, each consisting of different strain-controlled paths. It is shown that the model gives quantitatively good agreement for these complex histories and that the nonproportional state variable is necessary for this agreement.

Type 304 stainless steel is widely used in applications that involve cyclic nonproportional loading such as boiling water and liquid-metal-cooled fast breeder reactors and gas turbine engines. Such applications have warranted a relatively high research effort with regard to room and high-temperature cyclic deformation characteristics [1-4] related to fatigue and creep-fatigue interaction [5, 6].

### Determination of Model Parameters

Most of the parameters of the two surface model presented in companion paper can be determined from uniaxial tests. The model requires well-defined nonproportional, biaxial tests to determine saturated or cyclically stable isotropic hardening variables.

1. **Parameters  $\bar{R}(0, q)$ ,  $\bar{R}^*(0, q)$ ,  $\kappa$  and  $h$ .** The radii  $\bar{R}(0, q)$  and  $\bar{R}^*(0, q)$  of the yield and limit surfaces, respectively, can be determined from stable uniaxial cyclic stress-strain curves [7] determined at several maximum strain amplitudes across the range of interest. The strain rate of the tests should be of the same order of magnitude as that of the histories to be modeled.

It should be noted that the asymptotic slope  $(d\sigma/d\epsilon^P)_\infty = (3/2) \kappa$  is also a function of nonproportionality and strain range,  $\bar{\kappa} = \bar{\kappa}(\phi, q)$ , where  $\bar{\kappa}$  denotes the slope for cyclically stable response corresponding to current values of  $\phi$  and  $q$ . The variables  $\sigma$  and  $\epsilon^P$  are applied stress and plastic strain in the axial direction.

The function  $\bar{\kappa} = \bar{\kappa}(0, q)$  is defined by fitting the slope  $(2/3) (d\sigma/d\epsilon^P)_\infty$  of the cyclic stress-strain curves at several  $q$  values.

Having determined  $\bar{R}$ ,  $\bar{R}^*$ , and  $\bar{\kappa}$ , we can compute  $h$  from the uniaxial cyclic stress-strain curve at a selected value of  $q = q'$

$$h = \frac{2}{3} \frac{d\sigma}{d\epsilon^P} = h(\delta/\delta_0, \bar{\kappa}(0, q')) \quad (1)$$

where

$$\delta = \sqrt{3/2} \|s - s_0\| \text{ and } \delta_0 = \sqrt{3/2} \|s_0^* - s_0\| \\ = \bar{R}^*(0, q') - \bar{R}(0, q) \quad (2)$$

The quantity  $\delta$  is shown in Fig. 3 of Part 1.

2. **Parameters  $\bar{R}(1, q)$ ,  $\bar{R}^*(1, q)$ , and  $\bar{\kappa}(1, q)$ .** It is necessary to determine the  $\bar{R}(1, q)$  and  $\bar{R}^*(1, q)$  functions in equations (27) and (28) of Part 1 by running appropriate biaxial tests. Tension-torsion tests can be run at several strain amplitude levels with a phase angle between applied sinusoidal axial and engineering shear strain of 90 deg and a shear to axial strain amplitude ratio  $\gamma_a/\epsilon_a = (1 + \nu)$ . The parameters  $\bar{R}(1, q)$ ,  $\bar{R}^*(1, q)$  and  $\bar{\kappa}(1, q)$  are determined in

Contributed by the Applied Mechanics Division for presentation at the 1985 joint ASME/ASCE Applied Mechanics, Fluids Engineering, and Bioengineering Conference, Albuquerque, N. Mex., June 24-26, 1985 of THE AMERICAN SOCIETY OF MECHANICAL ENGINEERS.

Discussion on this paper should be addressed to the Editorial Department, ASME, United Engineering Center, 345 East 47th Street, New York, N.Y. 10017, and will be accepted until two months after final publication of the paper itself in the JOURNAL OF APPLIED MECHANICS. Manuscript received by ASME Applied Mechanics Division, April 1984; final revision, August, 1984. Paper No. 85-APM-10.

Copies will be available until February, 1986.

analogy to the uniaxial case from half of the hysteresis loops obtained by subsequent axial loading after reaching cyclically stable response, or from a stable cyclic effective stress-strain curve obtained by connecting effective stress points at maxima of effective strain.

**3. Parameters  $\Lambda(q)$  and  $\mu$ .** The function  $\Lambda(q)$  in equations (6) and (26) of Part 1 can be determined by running completely reversed uniaxial tests at a strain amplitude  $\epsilon_{a2}$  until cyclically stable, increasing the strain amplitude to  $\epsilon_{a1}$  for three cycles, and then decreasing to  $\epsilon_{a2}$  for 10 cycles. After decreasing to  $\epsilon_{a2}$ , the cyclic stress amplitude is compared to that corresponding to  $\epsilon_{a2}$  if cycling were continued at amplitude  $\epsilon_{a1}$ . We can heuristically define  $\Lambda(q) = Cq$ , where  $C$  is a constant, based on limited experiments. Upon decreasing the strain range to  $\epsilon_{a2}$  and integrating equation (6) of Part 1 from this point on with  $H(F) = 0$ ,

$$C = -1n[q^*/(\epsilon_{a1}^P)]/[40\epsilon_{a2}^P(3/2)^{1/2}] \quad (3)$$

where  $\epsilon_{a1}^P$  and  $\epsilon_{a2}^P$  are the plastic strain amplitudes corresponding to  $\epsilon_{a1}$  and  $\epsilon_{a2}$ , just before and after the amplitude reduction, respectively, and  $q^*$  is some plastic strain amplitude between  $\epsilon_{a1}^P$  and  $\epsilon_{a2}^P$ . From the stress-strain response after unloading from  $\epsilon_{a1}^P$  to 10 cycles of loading at  $\epsilon_{a2}^P$ , the value of  $q^*$  can be determined by setting  $\bar{R}(0, q^*) = R$  since  $\bar{R}(0, q)$  is known, for example. In general,  $\beta_i(0, \epsilon_{a2}^P) \neq \beta_i(0, q^*)$  where  $\beta_i = \bar{R}, \bar{R}^*$  and  $\bar{\kappa}$ , respectively, for  $i = 1, 2, 3$ . Note that  $q^*$  is the maximum plastic strain amplitude that is "remembered" by the material after the three cycle overload.

The parameter  $\mu$  can be approximated as a constant for a range of strain amplitudes as demonstrated in previous uniaxial and proportional biaxial tests [8, 9, 10]. In the current rate formulation for  $\phi$ , constant  $\mu^*$  may be taken to fit transient response under conditions of nonproportional loading. For uniaxial tests,  $\phi = \dot{\phi} = 0$  and  $\mu$  is easily found from tests in which the strain range is suddenly increased. Denote the values of  $\bar{R}, \bar{R}^*$ , and  $\bar{\kappa}$  pertaining to cyclically stable response at a completely reversed uniaxial strain amplitude  $q_a$  as  $\beta_i(0, q_a)$ . If the plastic strain amplitude is increased to  $q_b$  at time  $t = 0$  such that  $q_b > q_a$ , integration of equations (21) and (22) of Part 1 and equation (15) of Part 2 (to be introduced) with all  $\psi$  values equal to 1 gives

$$X_i - \beta_i(0, q_b) = [\beta_i(0, q_a) - \beta_i(0, q_b)] \exp \left[ -\mu \int_0^t \dot{\eta} dt \right] \quad (4)$$

where  $X_i = R, R^*$ , and  $\kappa$ , respectively, for  $i = 1, 2, 3$ . Since the  $\beta_i(0, q)$  functions are known from previous uniaxial tests,  $X_i$  can be determined from the hysteresis loops as a function of  $\int_0^t \dot{\eta} dt$  and a representative value for  $\mu$  can then be determined from equation (4). For simplicity, the stress amplitude could be used to determine  $\mu$  in equation (4) instead of  $X_i$  and  $\beta_i$ . If the transient response of a virgin specimen is used, the  $\beta_i(0, q_a)$  parameters in equation (4) could be replaced by initial values of  $R, R^*$ , and  $\kappa$ .

**4. Parameters  $\psi, \psi^*, \psi_\kappa$ , and  $\mu^*$ .** The form of the  $\psi, \psi^*$ , and  $\psi_\kappa$  functions in equations (21) and (22) of Part 1 and equation (15) of Part 2 must be determined for each material. Minimally, uniaxial tests would be necessary in which the strain amplitude is suddenly decreased from  $q_b$  corresponding to cyclically stable conditions to  $q_a$  where  $q_b > q_a$ . The  $\psi$  functions could be constructed from a number of such tests since  $\bar{R}, \bar{R}^*$ , and  $\bar{\kappa}$  are known in the evolution equations for  $R, R^*$ , and  $\kappa$ . Since the  $\psi$  functions may be history-dependent, it may be sufficiently accurate to heuristically assume simple forms for wavy and planar slip materials as stated in Part 1.

The choice of  $\mu^*$  can be made by fitting the rate of approach to the new cyclically stable state after switching from cyclically stable uniaxial loading. Let  $J'$  be defined as the degree of nonproportionality for the subsequent cycles

(approximated as a constant). If the effective strain range is not substantially increased or decreased, we can approximate  $q = q^*$  as a constant. Then, equations (23), (21), or (22), and (27) or (28) of Part 1 can be combined into the differential equation

$$\frac{dX_i}{d\eta} + \mu X_i = \mu(1 - J')(1 - e^{-\mu^* \eta})[\beta_i(1, q^*) - \beta_i(0, q^*)] + \mu\beta_i(0, q^*) \quad (5)$$

with the initial condition  $X_i = \beta_i(0, q^*)$  at  $\eta = 0$ . The solution to this equation is

$$X_i = \beta_i(0, q^*) + (1 - J')[\beta_i(1, q^*) - \beta_i(0, q^*)][1 + (\mu^* e^{-\mu^* \eta} - \mu e^{-\mu \eta}) / (\mu - \mu^*)] \quad (6)$$

for  $i = 1, 2, 3$ . The maximum effective stress amplitude could be used in equation (6) to determine  $\mu^*$  instead of  $X_i$  and  $\beta_i$ . The constant  $\mu^*$  can be approximated by fitting equation (6) to the observed  $X_i$  versus  $\eta$  response, since  $\mu$  is known.

### Specialization to Axial-Torsional Loading

For a thin-walled tubular section subjected to combined tension and torsion, the deviatoric stress components can be expressed in terms of the nonzero stress components  $\sigma_{11}$  and  $\sigma_{12}$  as follows:

$$s_{11} = (2/3)\sigma_{11}, s_{22} = s_{33} = -(1/2)s_{11}, s_{12} = \sigma_{12} \quad (7)$$

$$\xi_{11} = s_{11} - \alpha_{11}, \xi_{22} = \xi_{33} = -(1/2)\xi_{11}, \xi_{12} = s_{12} - \alpha_{12} \quad (8)$$

since  $\alpha_{22} = \alpha_{33} = -(1/2)\alpha_{11}$ . Also,  $s_{23} = s_{13} = \alpha_{13} = \alpha_{23} = 0$ . Here, the subscripts 1, 2, 3 denote the axial, circumferential, and radial directions of the tubular test specimen, and  $s$  is the deviatoric stress tensor.

The  $s$  and  $\alpha$  tensors are, of course, symmetric. In this case the yield surface is expressed as  $f = \sigma_{11}^2 + 3\sigma_{12}^2 - R^2 = 0$ .

The components of the normal  $n = \xi/\|\xi\|$  are  $n_{11} = \xi_{11}/P_\xi$  and  $n_{12} = \xi_{12}/P_\xi$  where  $P_\xi = ((3/2)\xi_{11}^2 + 2\xi_{12}^2)^{1/2}$  and  $n_{33} = n_{22} = -(1/2)n_{11}$ . For the case of tension-torsion loading of a thin-walled tubular specimen, the instantaneous measure of nonproportionality is expressed as

$$J = 1 + (\epsilon_{11}\dot{\epsilon}_{11}(1 + \nu)^2 + 4\epsilon_{12}\dot{\epsilon}_{12}) / [(\epsilon_{11}^2(1 + \nu)^2 + 4\epsilon_{12}^2)(\dot{\epsilon}_{11}^2(1 + \nu)^2 + 4\dot{\epsilon}_{12}^2)]^{1/2} \quad (9)$$

The kinematic hardening rule for the yield surface becomes  $\dot{\alpha}_{11} = Z(\dot{s}_{11}^* - s_{11})$  and  $\dot{\alpha}_{12} = Z(\dot{s}_{12}^* - s_{12})$  where

$$Z = [(3/2)\xi_{11}\dot{s}_{11} + 2\xi_{12}\dot{s}_{12} - (2/3)R\dot{R}] / [\xi_{11}(s_{11}^* - s_{11})(3/2) + 2\xi_{12}(s_{12}^* - s_{12})] \quad (10)$$

and  $s_{11}^* = \alpha_{11}^* + (R^*/R)\xi_{11}$ ,  $s_{12}^* = \alpha_{12}^* + (R^*/R)\xi_{12}$ . The flow rule can be written in component form as  $\dot{\epsilon}_{11}^P = (1/h)P_\xi n_{11}$  and  $\dot{\epsilon}_{12}^P = (1/h)P_\xi n_{12}$  if  $P_\xi = ((3/2)\dot{s}_{11}n_{11} + 2\dot{s}_{12}n_{12}) \geq 0$ ;  $\dot{\epsilon}_{11}^P = \dot{\epsilon}_{12}^P = 0$  otherwise. Here,  $h$  is determined from equation (1). Kinematic hardening of the limit surface  $f^*$  follows the Prager rule  $\dot{\alpha}_{11}^* = \kappa n_{11} \dot{\eta}$  and  $\dot{\alpha}_{12}^* = \kappa n_{12} \dot{\eta}$  where  $\dot{\eta} = ((3/2)(\dot{\epsilon}_{11}^P)^2 + 2(\dot{\epsilon}_{12}^P)^2)^{1/2}$ .

Isotropic and kinematic hardening rules for the plastic strain memory surface are written, respectively, as

$$\dot{q} = [((3/2)n_{11}\dot{\eta} + 2n_{12}\dot{\eta}) + \sqrt{6}\Lambda(q)](2/3)^{1/2}H(F)/2 - \Lambda(q)]\dot{\eta} \quad (11)$$

$$\dot{\alpha}_{11}^P = P_\alpha n_{11}^*, \quad \dot{\alpha}_{12}^P = P_\alpha n_{12}^* \quad (12)$$

where  $P_\alpha = H(F)((3/2)n_{11}\dot{\eta} + 2n_{12}\dot{\eta})/2$ ;  $H(F) = 1$  if  $F = 0$  and  $H(F) = 0$  if  $F < 0$ . In the preceding equations,  $\eta_{11}^* = (\epsilon_{11}^P - \alpha_{11}^P)/\Delta$  and  $\eta_{12}^* = (\epsilon_{12}^P - \alpha_{12}^P)/\Delta$  where

$$\Delta = ((3/2)(\epsilon_{11}^P - \alpha_{11}^P)^2 + 2(\epsilon_{12}^P - \alpha_{12}^P)^2)^{1/2} \quad (13)$$

Isotropic hardening rules for the yield and limit surfaces reduce to  $\dot{R} = \mu(\dot{R}(\phi, q) - R)\psi\dot{\eta}$  and  $\dot{R}^* = \mu(\dot{R}^*(\phi, q) -$

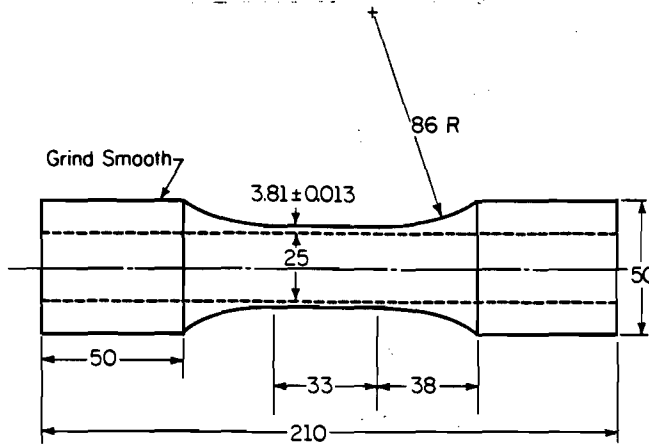


Fig. 1 Tubular biaxial specimen; dimensions in mm

$R^*)\psi^*\dot{\eta}$  where  $\phi$  evolves according to the equation

$$\dot{\phi} = \mu^*(1 - J - \phi) \dot{\eta} u(1 - J - \phi_{\text{limit}}) \quad (14)$$

with  $\phi_{\text{limit}} = 0.02$  (i.e., small) and  $q$  is obtained from integration of equation (11).

To obtain an accurate representation of the change in asymptotic plastic modulus  $\kappa$  during cyclic hardening, it is possible to write an evolution equation

$$\dot{\kappa} = \mu(\bar{\kappa}(\phi, q) - \kappa) \psi_x \dot{\eta} \quad (15)$$

where  $\psi_x$  is an appropriate admissibility function analogous to  $\psi$  and  $\psi^*$ .

Hence, we have established a set of first order evolution equations for  $\alpha$ ,  $\epsilon^p$ ,  $\alpha^*$ ,  $\eta$ ,  $q$ ,  $\alpha^p$ ,  $R$ ,  $R^*$ ,  $\phi$ , and  $\kappa$ , respectively. For a given strain or stress history, they may be integrated to give the resulting stress or strain response, respectively. For a known strain history, assuming isotropic elastic response,

$$\dot{\sigma}_{11} = E(\dot{\epsilon}_{11} - \dot{\epsilon}_{11}^p), \quad \dot{\sigma}_{12} = 2G(\dot{\epsilon}_{12} - \dot{\epsilon}_{12}^p) \quad (16)$$

Using the equations  $\dot{\epsilon}_{11}^p = (1/h) (\dot{s} : n) n_{11}$ ,  $\dot{\epsilon}_{12}^p = (1/h) (\dot{s} : n) n_{12}$ ,  $E = 2G(1 + \nu_e)$ ,  $\dot{\sigma}_{11} = (3/2)\dot{s}_{11}$ , and  $\dot{\sigma}_{12} = \dot{s}_{12}$ , we can substitute into equations (16) to obtain  $\dot{s}_{11}$  and  $\dot{s}_{12}$ , since  $\dot{\epsilon}_{11}$  and  $\dot{\epsilon}_{12}$  are known. Here,  $\nu_e$  is the value of Poisson's ratio from purely elastic response.

### Application to Complex Nonproportional Histories

**Determination of Parameters for Type 304 Stainless Steel.** A series of room-temperature, strain-controlled uniaxial and tension-torsion tests were run to determine the parameters of the two surface model for type 304 stainless steel. All specimens were heat treated at 1100°C for 40 minutes in a vacuum and furnace cooled to achieve an isotropic grain structure with an average grain diameter of 0.16 mm. A schematic of a tension-torsion specimen is shown in Fig. 1.

The biaxial tests were performed on a computer-controlled, closed-loop, servohydraulic test machine. A computer program was written so that any combination of line segments in strain space could be joined end-to-end to define a loading cycle. A block was defined as an arbitrary number of identical cycles. Furthermore, the program allowed the user to define any number of blocks, each containing a different cycle loading path. The effective strain rate  $\dot{\epsilon} = (\dot{\epsilon}_{11}^2 + 4\dot{\epsilon}_{12}^2/3)^{1/2}$  was kept constant along each segment.

Several uniaxial incremental step tests and out-of-phase step tests at maximum strain amplitudes ranging from 0.003 to 0.01 were run to establish the plastic strain range dependence of  $\bar{R}(0, q)$ ,  $\bar{R}^*(0, q)$ ,  $\bar{\kappa}(0, q)$ ,  $\bar{R}(1, q)$ ,  $\bar{R}^*(1, q)$  and  $\bar{\kappa}(1, q)$ . From four uniaxial tests at  $\dot{\epsilon} = 0.002 \text{ sec}^{-1}$ , linear

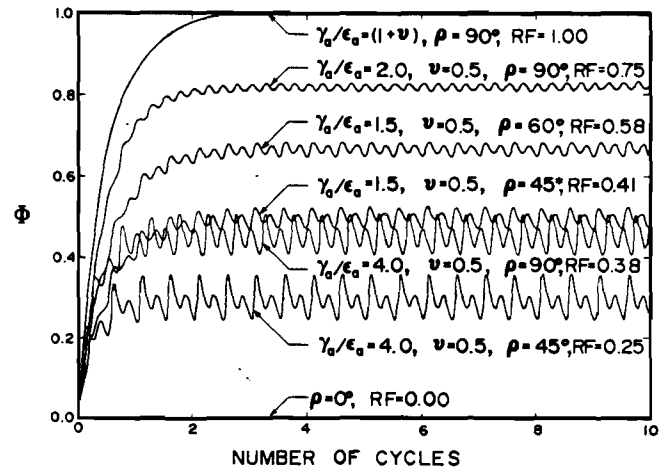


Fig. 2 Nonproportional state variable  $\phi$  versus number of cycles for sinusoidal loading with  $\epsilon_a = 0.005$  and various  $\gamma_a/\epsilon_a$  and  $\rho$  values. The rotation factor  $RF$  from Brown and Miller's theory is included for comparison in each case.

relationships were fit as a satisfactory approximation for  $\bar{R}(0, q)$ ,  $\bar{R}^*(0, q)$  and  $\bar{\kappa}(0, q)$ :

$$\bar{R}(0, q) = 171 + (q - 0.005)4000 \text{ MPa} \quad (17)$$

$$\bar{R}^*(0, q) = 295 + (q - 0.005)20690 \text{ MPa} \quad (18)$$

$$\bar{\kappa}(0, q) = 4370 - (q - 0.005)196100 \text{ MPa} \quad (19)$$

A plastic strain offset of 0.0005 was used to define yield. The hardening modulus was determined from the uniaxial cyclic stress-strain curve with  $q = 0.0068$  as

$$h = \kappa \left( 1 + (91960/\kappa) \left\{ \sinh \left\{ \frac{\|s^* - s\|}{\|s_0^* - s_0\|} \right\} \right\}^{1.1} \right) \quad (20)$$

From three sinusoidal tension-torsion tests described by

$$\epsilon = \epsilon_{11} = \epsilon_a \sin \omega t, \quad \gamma = 2\epsilon_{12} = \gamma_a \sin(\omega t - \rho) \quad (21)$$

with  $\epsilon_{22} = \epsilon_{33} = -\nu\epsilon_{11}$ ,  $\epsilon_{23} = \epsilon_{13} = 0$ ,  $\gamma_a/\epsilon_a = 1.5$  and  $\rho = 90 \text{ deg}$ ,  $\bar{R}(1, q)$ ,  $\bar{R}^*(1, q)$ , and  $\bar{\kappa}(1, q)$  were approximated by

$$\bar{R}(1, q) = 405 \text{ MPa}, \bar{R}^*(1, q) = 565 \text{ MPa}, \bar{\kappa}(1, q) = 4046 \text{ MPa} \quad (22)$$

From uniaxial tests where the strain range was increased or decreased, constants  $\mu$  and  $C$  were taken as  $\mu = 10$  and  $C = 0.6$ . The value of  $\mu^*$  was taken to be 50 based on a transition from stable proportional to nonproportional cycling. Plots of  $\phi$  versus number of cycles for the loading described in equations (21) appear in Fig. 2. For the type 304 stainless steel of this investigation,  $\psi$  and  $\psi^*$  were taken as Heaviside functions  $u(\beta_i - X_i)$  for  $i = 1$  and 2, respectively. The parameter  $\psi_x$  was taken as the Heaviside function  $u(\kappa - \bar{\kappa})$ . Significant fading memory of prior cyclically stable states was not observed even for nonproportional loading followed by proportional loading. All tests were conducted at effective strain rates ranging from  $0.001 \text{ sec}^{-1}$  to  $0.003 \text{ sec}^{-1}$ .

**Correlation of Theory With Experiments.** Results of two separate strain-controlled tension-torsion tests are reported in this investigation. Young's modulus and the shear modulus were respectively determined as  $E = 188 \text{ GPa}$  and  $G = 77 \text{ GPa}$ .

To compare the experimental results with the proposed two surface theory, the same strain histories were introduced in the constitutive equations. The specialized axial-torsional equations were integrated using a first-order predictor-corrector method [11, 12]. The state equations can be expressed as  $\dot{\mathbf{x}} = \mathbf{F}(\mathbf{x}, t)$  where

$$\mathbf{x} = \{\alpha_{11} \alpha_{12} \epsilon_{11}^p \epsilon_{12}^p \alpha_{11}^* \alpha_{12}^* \eta q \alpha_{11}^p \alpha_{12}^p R R^* \phi \kappa s_{11} s_{12}\}^T \quad (23)$$

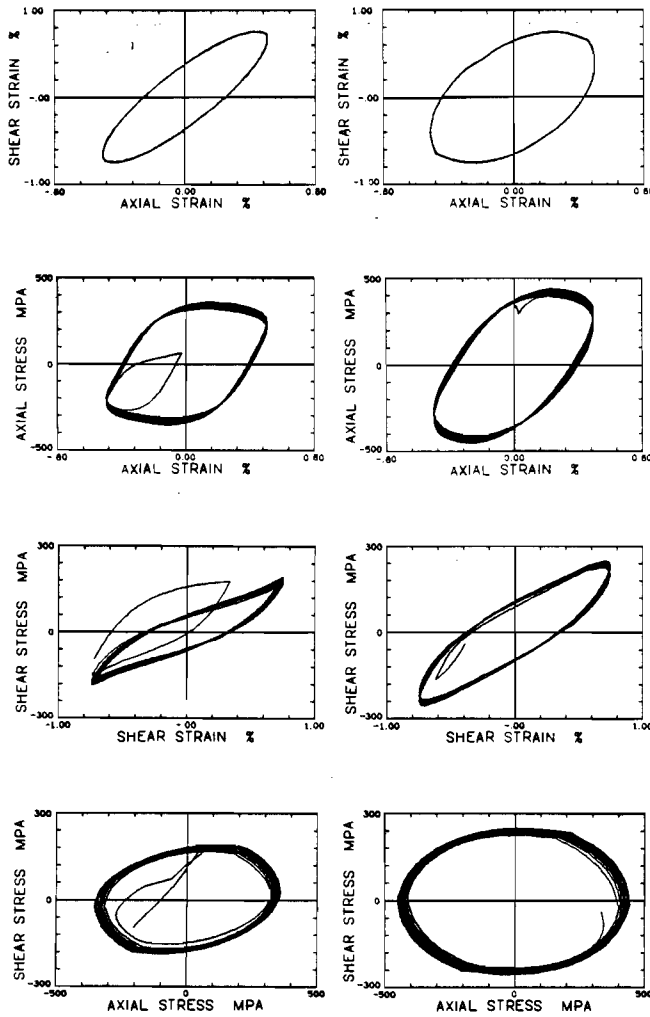


Fig. 3 Experimental results for History 1: (left column) cycles 1 to 10 of block 2, and (right column) cycles 1 to 10 of block 3

Define  $\bar{x}_{k+1}^P$  and  $\bar{x}_{k+1}^C$  as predicted and corrected values of  $\bar{x}$ , respectively, at the  $(k + 1)$ th time step. The corrector algorithm was repeated until the norm of the error vector

$$\bar{E} = \left( \sum_{i=1}^{16} (|\bar{x}_{k+1}^C - \bar{x}_{k+1}^P|_i / |\bar{x}_{k+1}^C|_i)^2 \right)^{1/2} \quad (24)$$

was acceptable where  $(\bar{x}_{k+1}^C - \bar{x}_{k+1}^P)_i$  and  $(\bar{x}_{k+1}^C)_i$  are the  $i$ th components of  $(\bar{x}_{k+1}^C - \bar{x}_{k+1}^P)$  and  $\bar{x}_{k+1}^C$ , respectively. Then, the accepted value of  $\bar{x}_{k+1}$  is  $\bar{x}_{k+1} = (4/5)\bar{x}_{k+1}^C + (1/5)\bar{x}_{k+1}^P$ . Automatic time-step control was included to reduce (increase) the time step  $\Delta t_k$  if  $\bar{E}$  was greater (less) than a selected maximum value at a selected iteration. All calculations were performed on the Georgia Tech Cyber 835.

**History 1: Specimen SS09.** This specimen was subjected to 10 cycles of a proportional incremental step test with maximum strain amplitudes of  $\epsilon_a = 0.007$ ,  $\gamma_a = 0.0105$ , and a strain rate  $\dot{\epsilon} = 0.001 \text{ sec}^{-1}$ . Subsequently, three blocks of different loading cycles were applied. Block 1 consisted of 16 cycles of proportional loading on the same maximum shear planes with  $\rho = 0^\circ$ ,  $\epsilon_a = 0.005$ , and  $\gamma_a = 0.0075$ . Block 2 consisted of 25 cycles of sinusoidal loading with  $\rho = 30 \text{ deg}$ ,  $\gamma_a = 0.0075$ , and  $\epsilon_a = 0.005$ . Block 3 consisted of 25 cycles of sinusoidal loading with  $\rho = 60 \text{ deg}$ ,  $\gamma_a = 0.0075$ , and  $\epsilon_a = 0.005$ .

The imposed cyclic strain history for blocks 2 and 3 is shown in Fig. 3 along with the experimentally observed axial stress-strain, shear stress-engineering strain and shear stress-

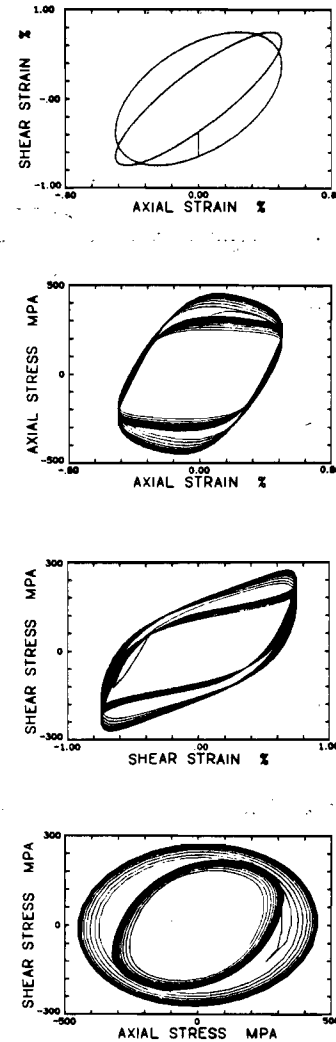


Fig. 4 Predicted results for History 1: 25 cycles of block 2 and first 10 cycles of block 3

axial stress responses. Block 1 is not included since no additional transient cyclic hardening occurred. Since data were taken in cycles 1 to 10 and geometrically increasing powers-of-two beyond cycle 10 of each block, only cycles 1 to 10 for blocks 2 and 3 appear in Fig. 3. Very little additional hardening occurred between cycles 10 and 25 [9, 10].

It should be noted that any measure of effective plastic strain range (e.g., octahedral or maximum shear) does not increase for each subsequent block, yet additional isotropic hardening occurs at the beginning of blocks 2 and 3. Computer-generated plots of the blocks 2 and 3 from two surface plasticity theory, shown in Fig. 4, demonstrate the capability of state variable  $\phi$  to correlate this additional hardening. In the analysis, the initial values  $R = 170 \text{ MPa}$ ,  $R^* = 291 \text{ MPa}$ , and  $\kappa = 4427 \text{ MPa}$  were used, based on the hysteresis loop response from the stable cycles of block 1. Cyclic hardening in each block is predicted well by the model. Since the points from numerical integration were plotted at effective strain increments of 0.0005 to 0.001 and connected by straight lines, the plotted results have a piecewise linear appearance. Of course, the time steps used in integration were considerably smaller.

For block 3, the yield and limit surfaces are in contact for most, if not all, of each cycle. The evolution of  $R$ ,  $R^*$ ,  $q$ , and  $\phi$  in the model is plotted for this history in Fig. 5 as a function of time. Note that  $q$  exhibits a general decay in each block as cyclic hardening accumulates. Also,  $\phi$  increases, as expected,

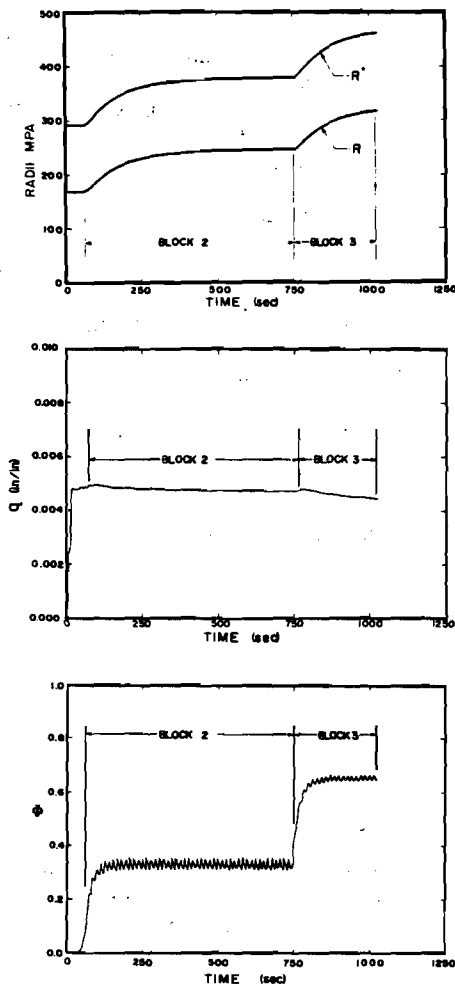


Fig. 5 Evolution of  $R$ ,  $R^*$ ,  $q$ , and  $\phi$  for blocks 2 and 3 of History 1

for each block. In the numerical integration, the norm  $\bar{E}$  of the error vector was kept below  $10^{-3}$ . Poisson's ratio in equation (9) was taken as an effective value based on the ratio of maximum effective plastic strain range to maximum effective total strain range.

To illustrate the consequences of neglecting non-proportional cross-hardening effects in the analysis, the model was used to predict the same imposed strain history with  $\phi = 0$  always. This would be the case if, as usually is done, only uniaxial test results were used as a reference in models for nonproportional histories. Figure 6 shows the responses predicted in this case for blocks 1, 2, and 3 of History 1. The lack of transient hardening in blocks 2 and 3 is noted. Hence, the use of uniaxial baseline data for non-proportional histories obviously can be quite inaccurate for this material.

**History 2: Specimen SS01.** This specimen was subjected to three blocks of dissimilar cycles. Block 1 consisted of proportional loading from the virgin state for 25 cycles with  $\epsilon_a = 0.0041$ ,  $\gamma_a = 0.006$ , and  $\dot{\epsilon} = 0.003 \text{ sec}^{-1}$ . Block 2 consisted of another 25 cycle path, introducing another discrete set of maximum shear strain planes at the same axial and shear strain amplitudes. Block 3 consisted of another 25 cycle path that joined the previous two paths by continuously rotating the maximum shear strain planes between the tips. The three blocks of loading paths are shown in Fig. 7 along with the experimentally observed axial stress-strain, shear stress-engineering strain, and shear stress-axial stress responses. All responses are from the first 10 cycles of each block with the exception of the shear-stress-axial stress

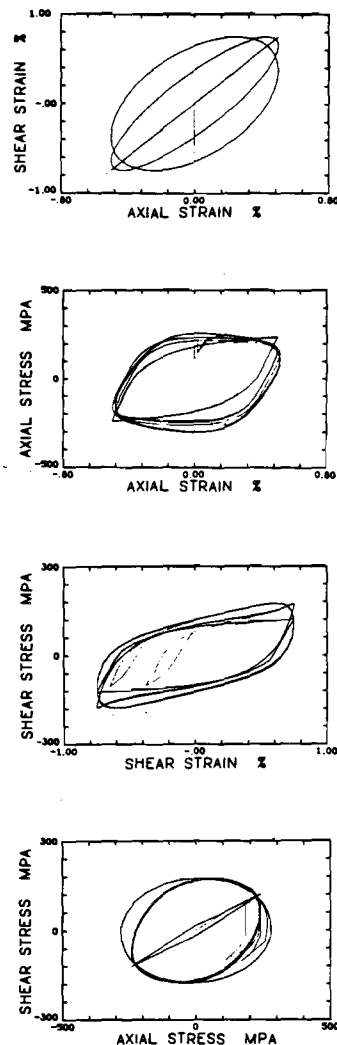


Fig. 6 Predicted results for History 1 if  $\phi = 0$ . The underestimation of hardening predicted in blocks 2 and 3 illustrates the inaccuracy of extrapolating uniaxial test results to nonproportional loading.

responses for blocks 1 and 2, which are from cycle 24. Again, little additional transient hardening was observed for cycles 10 to 25. The tips of the strain paths are numbered to denote sequence of loading. The response for block 2 was nearly stable immediately following block 1. It is clear that the stress response in block 3 is not symmetric and distortion and/or translation of the limit or large offset strain yield surface has occurred. Again, the isotropic hardening accrued in block 3 considerably exceeds that predicted by using a uniaxial cyclic stress-strain curve at the same maximum plastic strain range.

Results from the model are shown in Fig. 8 for each block. Note that the transient response in block 3 is well represented by the model, but the model predicts unloading from the limit surface near the maximum axial stress amplitude while the experimental results do not clearly reveal such a phenomenon. Hence, the peak axial stress amplitude is underestimated. The rate of hardening in block 3 is reasonably accurate, even though the loading is quite complex. In the analysis, the initial values  $R = 148 \text{ MPa}$ ,  $R^* = 192 \text{ MPa}$ , and  $\kappa = 8366 \text{ MPa}$  were used, based on the monotonic stress-strain curve for the annealed type 304 stainless steel. Initial values for all other variables were taken as zero. Again, the norm of the error vector was maintained below  $10^{-3}$ .

## Conclusions

It has been demonstrated that the proposed two surface



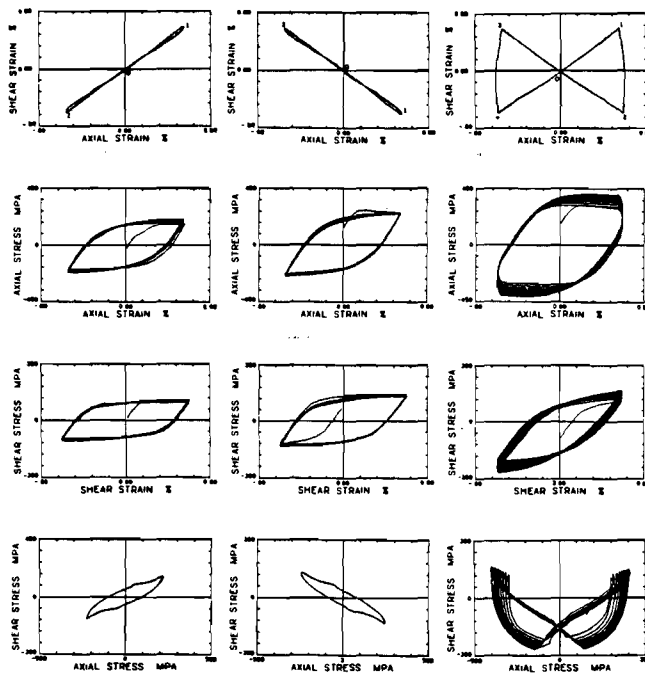


Fig. 7 Experimental results for History 2: (left column) cycles 1 to 10 of block 1, (center column) cycles 1 to 10 of block 2, and (right column) cycles 1 to 10 of block 3

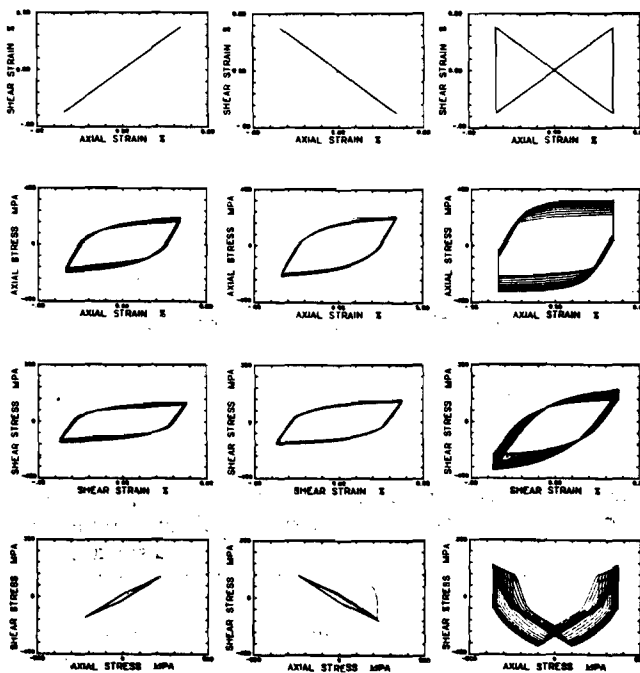


Fig. 8 Predicted results for History 2: (left column) cycles 1 to 25 of block 1, (center column) cycles 1 to 25 of block 2, and (right column) cycles 1 to 25 of block 3

theory is capable of reasonably accurate prediction of stress-strain response for complex nonproportional loading. The model combines an appropriate kinematic hardening rule based on the theory of Mroz with an isotropic hardening rule that accounts for dependence on plastic strain range and nonproportionality of loading, both of which can be significant for a number of materials of structural interest. Hence, the model is sophisticated enough to describe essential aspects of transient, cyclic, nonproportional deformation behavior.

To achieve this necessary sophistication, some concessions were made. To model plastic strain range dependence, state variables  $\alpha^p$  and  $q$  are introduced. State variables  $R^*$ ,  $\alpha^*$  and  $\kappa$  were introduced in addition to the usual variables  $R$  and  $\alpha$  to produce an acceptable description of plastic strain rate direction and hardening modulus during nonproportional plastic flow. State variable  $\phi$  was defined to account for additional isotropic hardening during nonproportional loading. Even with these additional parameters, the model is simple in the respect that the yield surface is not allowed to distort.

Methods for experimental determination of model parameters have been set forth, although there is freedom to adapt the model to peculiar characteristics of each material of interest. For example, the functions  $\Lambda(q)$ ,  $\psi$ ,  $\psi^*$ , and  $\psi_\kappa$  may be determined to any desired degree of precision. The function  $\theta$  may be selected to give smooth reloading response after unloading for small subcycles, or to accurately fit cyclic creep ratcheting response. Even with the relatively small number of tests run in this investigation to determine  $\bar{R}$ ,  $\bar{R}^*$ ,  $\bar{\kappa}$ ,  $C$ , and  $\mu$ , it is seen that the theory satisfactorily models the more complex histories of this study. No claim can be made regarding the sufficiency of experimental characterization of the  $\Lambda(q)$  and  $\psi$  functions in this study, since the histories to be predicted did not include overload sequence effects. It seems that the choice of the structure of the model is more important than exhaustive experimental characterization, as evidenced by the poor predictions obtained when  $\phi$  was neglected.

## Acknowledgments

The author wishes to acknowledge the National Science Foundation (Grant No. MEA-8404080; Program Manager, C. J. Astill) for continuing research support on the subject of this paper.

## References

- 1 Miller, A., "An Inelastic Constitutive Model for Monotonic, Cyclic, and Creep Deformation: Part II—Application to Type 304 Stainless Steel," *ASME Journal of Engineering Materials and Technology*, Vol. 98, 1976, pp. 106-113.
- 2 Liu, M. C. M., Krempl, E., and Nairn, D. C., "An Exponential Stress-Strain Law for Cyclic Plasticity," *ASME Journal of Engineering Materials and Technology*, Vol. 98, 1976, pp. 322-329.
- 3 Wu, H. C., and Yip, M. C., "Endochronic Description of Cyclic Hardening Behavior for Metallic Materials," *ASME Journal of Engineering Materials and Technology*, Vol. 103, 1981, pp. 212-217.
- 4 Eisenberg, M. A., "A Generalization of Plastic Flow Theory With Application to Cyclic Hardening and Softening Phenomena," *ASME Journal of Engineering Materials and Technology*, Vol. 98, 1976, pp. 221-228.
- 5 Koterazawa, R., and Iwata, Y., "Fracture Mechanics and Fractography of Creep and Fatigue Crack Propagation at Elevated Temperature," *ASME Journal of Engineering Materials and Technology*, Vol. 98, 1976, pp. 296-304.
- 6 Cheng, C. Y., and Diercks, D. R., "Effects of Hold Time on Low-Cycle Fatigue Behavior of AISI Type 304 Stainless Steel at 593°C," *Metallurgical Transactions*, Vol. 4, 1973, pp. 615-617.
- 7 Landgraf, R. W., Morrow, J., and Endo, T., "Determination of the Cyclic Stress-Strain Curve," *Journal of Materials*, ASTM, Vol. 4, No. 1, Mar. 1969, pp. 176-188.
- 8 Lamba, H. S., and Sidebottom, O. M., "Proportional Biaxial Cyclic Hardening of Annealed Oxygen-Free High-Conductivity Copper," *Journal of Testing and Evaluation*, ASTM, Vol. 6, No. 4, 1978, p. 260-267.
- 9 McDowell, D. L., "Transient Nonproportional Cyclic Plasticity," Ph.D. thesis, Report No. 107, Design and Materials Division, Department of Mechanical and Industrial Engineering, University of Illinois at Urbana-Champaign, June 1983.
- 10 McDowell, D. L., "On the Path Dependence of Transient Hardening and Softening to Stable States Under Complex Biaxial Cyclic Loading," *Proceedings of the International Conference on Constitutive Laws for Engineering Materials*, Desai and Gallagher, Eds., Tucson, Ariz., Jan. 1983, pp. 125-132.
- 11 Kumar, V., Morjaria, M., and Mukherjee, S., "Numerical Integration of Some Stiff Constitutive Models of Inelastic Deformation," *ASME Journal of Engineering Materials and Technology*, Vol. 102, 1980, pp. 92-96.
- 12 Hilderbrand, F. B., *Finite-Difference Equations and Simulations*, Prentice-Hall, Englewood Cliffs, N.J., 1968.

# An Experimental Study of the Structure of Constitutive Equations for Nonproportional Cyclic Plasticity

D. L. McDowell

Assistant Professor,  
School of Mechanical Engineering,  
Georgia Institute of Technology,  
Atlanta, Ga. 30332

*Three type 304 stainless steel specimens of the same geometry were subjected to complex, cyclic axial-torsional histories characterized by varying degrees of non-proportionality of straining. All tests were at room-temperature. The data from cyclically stable hysteresis loops were reduced and the direction of the plastic strain rate vector, variation of plastic hardening modulus, and direction of translation of a rate and time-independent yield surface were studied. It is shown that the independent variables in a Mroz-type formulation map the experimental results with a higher degree of uniqueness than other popular formulations studied for both the hardening modulus and direction of yield surface translation. Also, the plastic strain rate is not, in general, in the direction of the deviatoric stress or stress rate.*

## Introduction

Numerous adaptations of time and rate-independent plasticity theory have been suggested in the literature [1-7] and implemented in existing finite element codes for cyclic loading. Often these models are applied to structures subjected to nonproportional variation of stresses and strains [8]. Model constants and parameters, however, are usually obtained from uniaxial tests (proportional loading or straining).

The usual elements in a time and rate-independent plasticity theory for metals are a yield surface, a flow rule that relates increments of stress and plastic strain, and hardening rules that specify the movement of the yield surface and any shape changes during plastic flow. Experiments have revealed that nonproportional strain cycling affects all of these elements significantly. Translation and distortion of the yield locus has been shown to be highly dependent on prestrain and changes in direction of straining [9-12]. Cyclic hardening can be pronounced under conditions of highly nonproportional strain cycling [13-16], increasing the cyclic strength level significantly above that observed in uniaxial tests at the same effective plastic strain amplitude. The kinematic hardening rule and flow rule are complicated by changes in plastic strain rate direction, rendering many generalizations made from uniaxial tests inaccurate.

Recent evaluations of hardening and flow rules [17-20] have consisted of integrating a number of models for a given control history and comparing with experimentally obtained hysteresis responses. This procedure allows qualitative comparison. In this paper, an inverse approach is taken. The data from nonproportional cyclic tests are reported in reduced form and several basic proposed structures of hardening and flow rules are examined for correlative capability.

## Experimental Procedure

The material chosen for this study was type 304 stainless steel with the AISI composition shown in Table 1. Type 304 stainless steel has been widely used in high temperature applications, particularly in nuclear structures. The cyclic deformation behavior of 304 stainless steel has been extensively modeled under uniaxial conditions.

Tubular axial-torsional specimens were machined from as-received bar stock of 50.8 mm diameter as shown in Fig. 1. The experimental details appear elsewhere [15, 21, 24]. Axial

Table 1 Composition

	C	Mn	Si	Cr	Ni	Fe
AISI	0.08% max	2.0% max	1.0% max	18-20%	8-12%	Bal.
Actual	0.08	1.40	0.45	19.13	9.49	Bal.

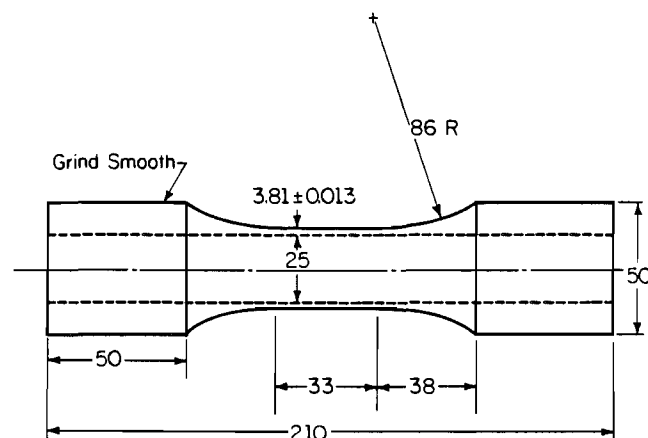


Fig. 1 Tubular axial-torsional specimen (dimensions in mm)

Contributed by the Materials Division for publication in the JOURNAL OF ENGINEERING MATERIALS AND TECHNOLOGY. Manuscript received by the Materials Division, August 13, 1984.

Table 2 Complex strain histories

SAR-101-11

BLOCK #					
	$\dot{\epsilon}(\text{sec}^{-1})$	1	2	3	4
SS01	0.003	endpoint sequence: 0 $\epsilon=0$ 1 $\epsilon=0.0041$ $\gamma=0.006$ 2 $\epsilon=0.0041$ $\gamma=0.006$ return to $\epsilon=0$	endpoint sequence: 0 $\epsilon=0$ 1 $\epsilon=0.0041$ $\gamma=0.006$ 2 $\epsilon=0.0041$ $\gamma=0.006$ return to $\epsilon=0$	endpoint sequence: 0 $\epsilon=0$ 1 $\epsilon=0.0041$ $\gamma=0.006$ 2 $\epsilon=0.0041$ $\gamma=0.006$ 3 $\epsilon=0.0041$ $\gamma=0.006$ 4 $\epsilon=0.0041$ $\gamma=0.006$ return to $\epsilon=0$	
		25 cycles	25 cycles	25 cycles	
SS09	0.001	Incremental Step Test:  $\gamma_{\theta}^{\text{MAX}}=0.007$  $\gamma_{\theta}^{\text{MAX}}=0.0105$	$\epsilon_c=0.005$ $\gamma_c^a=0.0075$ $\theta=0$	$\epsilon_c=0.005$ $\gamma_c^a=0.0075$ $\theta=30^\circ$	$\epsilon_c=0.005$ $\gamma_c^a=0.0075$ $\theta=60^\circ$
		10 cycles	16 cycles	25 cycles	25 cycles
SS04	0.002	0 $\epsilon=0$ 1 $\epsilon=0, \gamma=0.0085$ 2 $\epsilon=0, \gamma=0.0085$ 3 $\epsilon=-0.0039, \gamma=0.0057$ 4 $\epsilon=0.0039, \gamma=0.0057$ 5 $\epsilon=0.0046, \gamma=0.0039$ 6 $\epsilon=0.0046, \gamma=0.0039$ 7 $\epsilon=0.0051, \gamma=0$ 8 $\epsilon=0.0051, \gamma=0$ 9 $\epsilon=0.0046, \gamma=0.0039$ 10 $\epsilon=0.0046, \gamma=0.0039$ 11 $\epsilon=0.0039, \gamma=0.0057$ 12 $\epsilon=0.0039, \gamma=0.0057$ return to $\epsilon=0$			
		50 cycles			

$\epsilon$  Denotes sinusoidal loading with  $\epsilon = \epsilon_c \sin \omega t$ ,  $\gamma = \gamma_c \sin(\omega t - \theta)$ .

<sup>a</sup>Denotes sinusoidal loading with  $\epsilon = \epsilon_a \sin \omega t$ ,  $\gamma = \gamma_a \sin(\omega t - \theta)$ .

stress and shear stress were assumed uniform over the wall-thickness [16, 22].

Axial strain  $\epsilon$  was defined as the gage length displacement divided by the original gage length. The shear strain  $\gamma$  was obtained by dividing the angle of twist by the gage length and multiplying by the mean radius.

A computer program was written so that any combination of line segments in  $\epsilon$ - $\gamma$  strain space could be joined end-to-end to define a loading cycle. A block was defined as an arbitrary number of identical cycles. Furthermore, the program allowed the user to define any number of blocks, each containing a different cycle loading path. The effective strain rate ( $\dot{\epsilon} = (\dot{\epsilon}^2 + \dot{\gamma}^2/3)^{1/2}$  assuming a Poisson's ratio of 1/2) was kept approximately constant along each segment.

### Biaxial Loading Histories

Results of three strain-controlled axial-torsional histories are reported in this paper. All tests were conducted at room

temperature. The initial values of Young's modulus and shear modulus were determined as  $E = 188$  GPa and  $G = 77$  GPa, respectively. A summary of the three test histories appears in Table 2, including the effective strain rate and controlled axial and shear strain endpoint sequence of each block within each history.

The scope of this paper will be limited to considerations of essentially stable cyclic response, observed in the latter cycle of each block. Hence the flow rule and kinematic hardening rule may be examined in the absence of complicating effects of isotropic hardening.

**Notation.** The definition of the axial-torsional subspace follows as a subspace of Ilyushin's five-dimensional deviatoric vector space [23]. Define the stress vector as

$$\sigma = \sigma_1 \mathbf{n}_1 + \sigma_3 \mathbf{n}_3 \quad (1)$$

where

$$\sigma_1 = \sigma_{zz} = \sigma, \quad \sigma_3 = \sqrt{3}\sigma_{z\theta} = \sqrt{3}\tau$$

and  $\mathbf{n}_1$  and  $\mathbf{n}_3$  are orthonormal base vectors in the stress plane. Here,  $z$  and  $\theta$  denote the tube longitudinal and circumferential directions, respectively. Likewise, the plastic strain vector is defined by

$$\epsilon^P = \epsilon_1^P \mathbf{n}_1 + \epsilon_3^P \mathbf{n}_3 \quad (2)$$

where

$$\epsilon_1^P = \epsilon_{zz}^P, \quad \text{and} \quad \epsilon_3^P = (2/\sqrt{3})\epsilon_{z\theta}^P.$$

Note that the plastic strain rate vector is defined as

$$\dot{\epsilon}^P = \dot{\epsilon}_1^P \mathbf{n}_1 + \dot{\epsilon}_3^P \mathbf{n}_3. \quad (3)$$

The effective stress  $\bar{\sigma}$  and plastic strain rate  $\dot{\epsilon}^P$  (normalized to the axial case) are recognized as

$$\bar{\sigma} = |\sigma| = (\sigma \cdot \sigma)^{1/2} = (\sigma_1^2 + \sigma_3^2)^{1/2} \quad (4)$$

$$\dot{\epsilon}^P = |\dot{\epsilon}^P| \quad (5)$$

The total strain vector is heuristically defined as

$$\epsilon = \epsilon_1 \mathbf{n}_1 + \epsilon_3 \mathbf{n}_3 \quad (6)$$

where  $\epsilon_1 = \epsilon_{zz} = \epsilon$  and  $\epsilon_3 = (2/\sqrt{3})\epsilon_{z\theta} = \gamma/\sqrt{3}$ . The effective strain rate reported in Table 2 is then  $\dot{\epsilon} = |\dot{\epsilon}|$  since  $\gamma = 2\epsilon_{z\theta}$ .

**Hysteresis Response.** The input signals and resulting stress responses for a complete cycle near the end of selected nonproportional blocks are shown in Fig. 2. The beginning of

### Nomenclature

$D_i, D_o$  = gage length inside and outside diameters  
 $E$  = Young's modulus  
 $G$  = shear modulus  
 $P$  = axial load  
 $R, R_L$  = radii of yield and limit surfaces  
 $S_{ij}$  = deviatoric stress tensor  
 $T$  = torque  
 $W_P$  = accumulated plastic work  
 $c$  = scalar in kinematic hardening rule  
 $f, f^*$  = yield and limit surfaces  
 $h, h^*$  = plastic hardening moduli  
 $J_2$  = second invariant of deviatoric stress  
 $\mathbf{n}$  = unit vector in direction of plastic strain rate in axial-torsional subspace  
 $\mathbf{n}_1, \mathbf{n}_3$  = orthonormal unit vectors in axial-torsional subspace  
 $\mathbf{n}_{ij}$  = unit normal vector to yield surface  
 $s$  = accumulated effective stress  
 $\alpha$  = backstress vector in axial-torsional subspace  
 $\alpha_{ij}$  = backstress tensor  
 $\beta$  = phase angle  
 $\gamma$  = total engineering shear strain  
 $\gamma_a$  = total engineering shear strain amplitude

$\delta$  = distance from current stress point to corresponding limit surface point  
 $\delta_m, \delta_z$  = distance to limit surface defined by Mroz and Ziegler based approaches  
 $\epsilon, \epsilon_{zz}$  = total axial strain  
 $\epsilon_a$  = total axial strain amplitude  
 $\epsilon_{z\theta}$  = total shear strain  
 $\epsilon_{zz}^P, \epsilon_{z\theta}^P$  = axial and shear plastic strain components  
 $\epsilon^P$  = plastic strain vector in axial-torsional subspace  
 $\epsilon_1^P, \epsilon_3^P$  = components of  $\epsilon^P$   
 $\bar{\epsilon}, \bar{\epsilon}^P$  = effective total strain and plastic strain  
 $d\lambda, d\lambda^*$  = scalars in flow rule  
 $d\mu_1, d\mu_2$  = scalars in kinematic hardening rules  
 $\xi_P$  = accumulated plastic strain  
 $\sigma, \sigma_{zz}$  = axial stress  
 $\sigma_{z\theta}$  = shear stress  
 $\sigma$  = stress vector in axial-torsional subspace  
 $\sigma_{ij}$  = stress tensor  
 $\sigma_1, \sigma_3$  = components of  $\sigma$   
 $\sigma^*, \sigma^{**}$  = points on the limit surface which correspond to Mroz and Ziegler based approaches  
 $\tau$  = shear stress

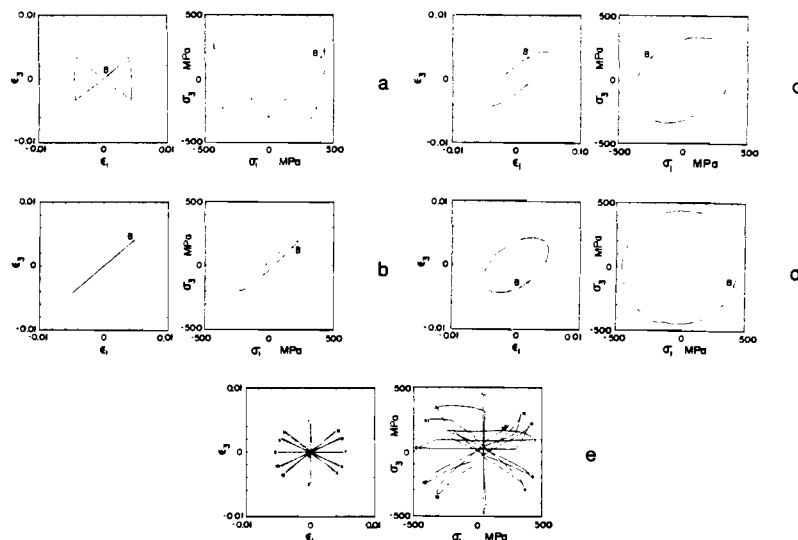


Fig. 2 Input strain cycle and resulting stress responses: (a) specimen SS01, block #3, cycle #24; (b) specimen SS09, block #2, cycle #16; (c) specimen SS09, block #3, cycle #24; (d) specimen SS09, block #4, cycle #16; and (e) specimen SS04, block #1, cycle #40

the data for each block is marked with "B" to establish a datum for later calculations of accumulated stress or strain.

It should be noted that there are path-dependent differences in the extent of cyclic hardening. For example, block #3 of specimen SS09 exhibits a saturation effective stress level which considerably exceeds that of block #2. Yet the maximum plastic shear strain amplitude of block #2 exceeds that of block #3. The transient behavior of these three histories, including the additional cyclic hardening during nonproportional strain cycling, have been previously documented [15, 24]. This paper, as previously mentioned, will not address the transient behavior.

**Plastic Strain Rate Direction.** To compute the plastic strain rate vector from the data, numerical differentiation was required. The values of axial stress, shear stress, axial strain, and shear strain of five contiguous data points were parameterized with respect to arc length  $s = \Sigma(\Delta\sigma \cdot \Delta\sigma)$  along the path. Then a parabola was least-squares fit to the five data points to form each of the smoothed functions  $\sigma(s)$ ,  $\tau(s)$ ,  $\epsilon(s)$ , and  $\gamma(s)$ , and the derivatives  $d\sigma/ds$ ,  $d\tau/ds$ ,  $d\epsilon/ds$ , and  $d\gamma/ds$  were obtained for the central (third) point. The derivative of plastic strain was computed as

$$\frac{d\epsilon^P}{ds} = \left( \frac{d\epsilon}{ds} - \frac{1}{E} \frac{d\sigma}{ds} \right) \mathbf{n}_1 + \left( \frac{d\gamma}{ds} - \frac{1}{G} \frac{d\tau}{ds} \right) \sqrt{3} \mathbf{n}_3 \quad (7)$$

and the unit normal vector in the direction of the plastic strain rate was defined by

$$\mathbf{n} = (d\epsilon^P/ds) / |d\epsilon^P/ds| \quad (8)$$

A check on the smoothness of the data was obtained by applying a first order central difference technique to each three contiguous points to obtain the derivatives for the central point [25]. This technique resulted in essentially the same results as the five-point parabola method, indicating good differentiability of the data.

To avoid the scatter in plastic strain increment direction which may occur in regions where the plastic strain increment is very small (e.g., elastic unloading), a "cutoff" value of  $|d\epsilon^P/ds|$  was used. A value of  $|d\epsilon^P/ds| = 1.4 \times 10^{-6} \text{ MPa}^{-1}$  was selected after initially plotting the histories to omit regions of unloading for which  $|d\epsilon^P/ds| < 1.4 \times 10^{-6} \text{ MPa}^{-1}$ .

Figure 3 shows the plastic strain rate direction plotted as vectors from the corresponding positions of the stress space  $\sigma_1$

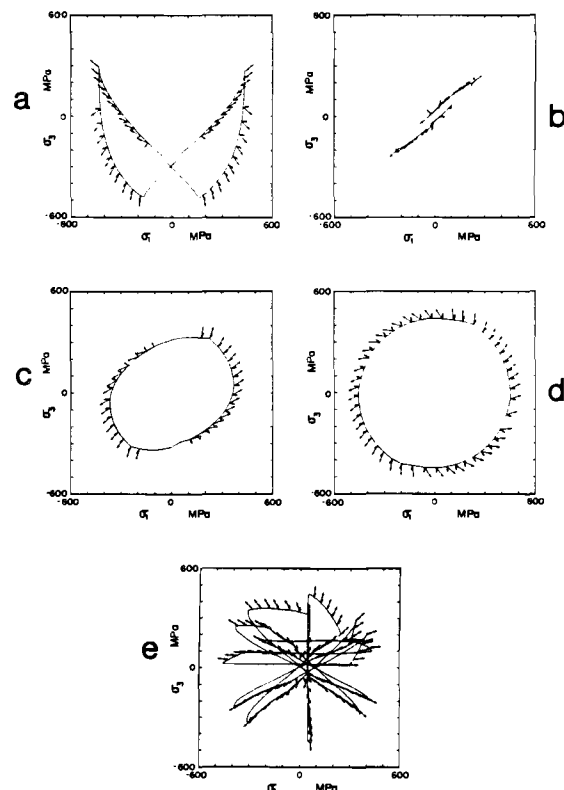


Fig. 3 Plastic strain rate and deviatoric stress directions. The longer vectors are in the direction of plastic strain rate corresponding to the points at the tail of the vectors. The shorter vectors are in the direction of deviatoric stress. The cycles correspond to: (a) specimen SS01, block #3; (b) specimen SS09, block #2; (c) specimen SS09, block #3; (d) specimen SS09, block #4; and (e) specimen SS04.

versus  $\sigma_3$  response. Note that the plastic strain rate direction is plotted at data points at approximately equal increments of accumulated stress  $s$ . The deviatoric stress (radial) direction is also plotted at the same data points with shorter vectors.

Two interesting observations are readily made. If the plastic strain rate were in the direction of deviatoric stress, as suggested by some current theories [26], then the plastic strain increment would be radial in  $\sigma_1$  versus  $\sigma_3$  space since

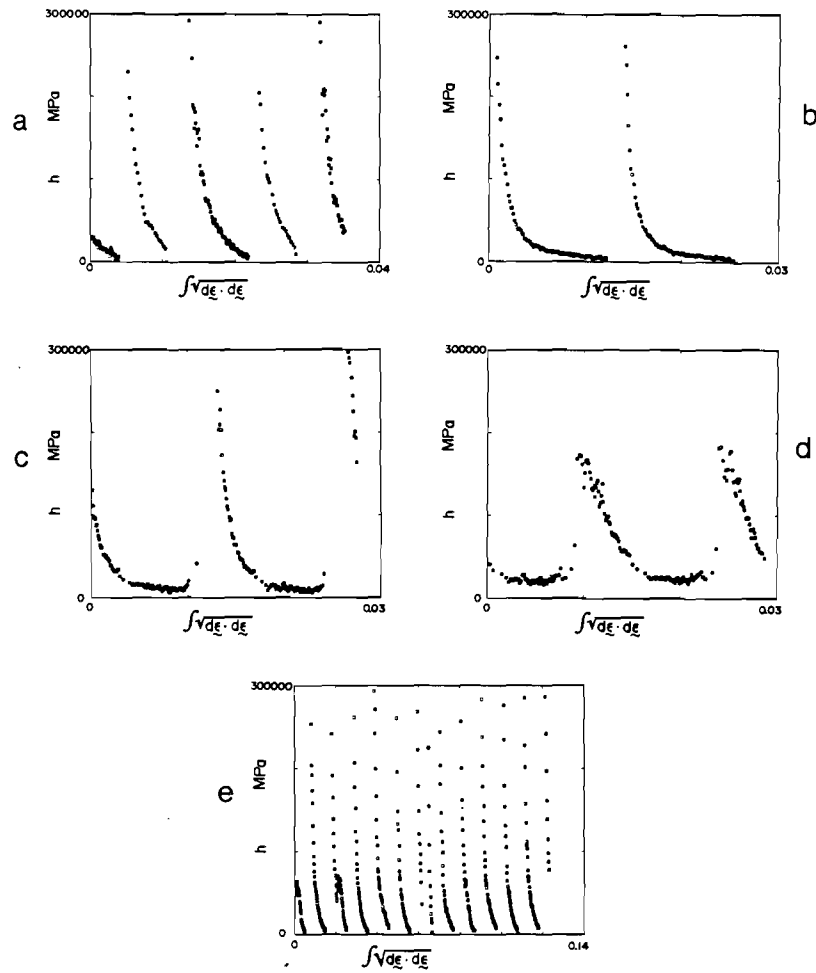


Fig. 4 Modulus  $h$  versus accumulated strain from the initial point in each cycle corresponding to: (a) specimen SS01, block #3; (b) specimen SS09, block #2; (c) specimen SS09, block #3; (d) specimen SS09, block #4; and (e) specimen SS04

$$d\epsilon_{zz}^P = d\lambda(2/3)\sigma_{zz} - d\epsilon_{zz}^P = d\lambda^* \sigma_{zz} - d\epsilon_1^P = d\lambda^* \sigma_1 \quad (9)$$

$$d\epsilon_{z\theta}^P = d\lambda \sigma_{z\theta} - 2d\epsilon_{z\theta}^P / \sqrt{3} = \frac{2}{\sqrt{3}} (3/2)d\lambda^* (\sqrt{3}\sigma_{z\theta}) / \sqrt{3} - d\epsilon_3^P = d\lambda^* \sigma_3 \quad (10)$$

If the plastic strain rate were in the direction of deviatoric stress rate, as suggested in some integral formulations [27], then the plastic strain increment would be tangent to the stress path. Figure 3 clearly shows that neither is the case for stable nonproportional cycling. Of the nonproportionally loaded specimens, only SS04, which consists of several radial paths, exhibits collinearity of the plastic strain rate and deviatoric stress.

From the data in Fig. 3, it is obvious that the normality flow rule would require at the very least a translation of a Tresca or von Mises yield surface to approximate the deformation-induced anisotropy (distortion) imparted to the yield surface under nonproportional loading. This conclusion has been drawn previously in comparison of experimental results with predictions from rate-independent cyclic plasticity theories; in this study, the experimental results only are used to invalidate the use of deviatoric stress or deviatoric stress rate in generalized (multidimensional) flow rules.

**Variation of Plastic Hardening Modulus.** The normality flow rule may be stated [28] as

$$\dot{\epsilon}_{ij}^P = \frac{1}{h} (\dot{\sigma}_{k1} n_{k1}) n_{ij} \quad (11)$$

where  $\dot{\epsilon}_{ij}^P$  is the plastic strain rate tensor,  $\dot{S}_{ij}$  is the deviatoric stress rate tensor, and  $n_{ij}$  is the unit normal vector to the yield surface in nine-dimensional stress space. Here,  $h$  defines the plastic hardening modulus.

In the reduced axial-torsional subspace, the flow rule can be stated as

$$\dot{\epsilon}^P = \frac{1}{h^*} (\dot{\sigma} \cdot \mathbf{n}) \mathbf{n} \quad (12)$$

where  $\sigma$ ,  $\epsilon^P$  and  $\mathbf{n}$  are defined by equations (1), (2), and (8), respectively. Hence,

$$h^* = \frac{\dot{\sigma} \cdot \mathbf{n}}{\dot{\epsilon}^P \cdot \mathbf{n}} \quad (13)$$

defines the hardening modulus in the subspace. For the axial-torsional loading of this study, it can be shown that  $h = (2/3)h^*$ .

Plots of  $h$  versus accumulated strain from the initial point of each path (points B in Fig. 2) are shown in Fig. 4. It is noted that the modulus exhibits variations through each nonproportional cycle, consistently approaching a value less than 10,000 MPa in the plastic regions. Hence, there appears to be an approach to an asymptotic value of  $h$  even for very complex histories.

It is useful at this point to consider criteria for correlation of the variation of hardening modulus. In practice, the slope of a uniaxial cyclic stress-plastic strain curve is fit as a function of one of these parameters. Then this functional

relationship is extended to multiaxial calculations. The validity of this approach comes into question for non-proportional loading. In this study, several previously proposed correlations will be investigated.

It is perhaps simplest to consider the modulus to be a function of effective stress [29],

$$h = h(\sqrt{3J_2}) \quad (14)$$

where  $J_2 = 1/2 S_{ij} S_{ij}$  is the second invariant to deviatoric stress. For axial-torsional loading,  $\sqrt{3J_2} = (\sigma_1^2 + \sigma_3^2)^{1/2}$ .

Another class of simple correlations for variation of modulus, more generally accepted for nonproportional loading, involve two or more nested surfaces [30-32]. These theories implicitly include kinematic hardening of the yield surface through dependence on the direction of the unit normal vector  $\mathbf{n}$  (plastic strain rate direction). In this study, the yield surface will be considered as nested within a single fixed surface of larger radius, defined as the limit surface. Such two surface theories are widely used and are computationally efficient [31-32].

Two simple models will be evaluated. Both models state that the modulus  $h$  is a function of the metric distance from the current stress point on the yield surface to a generic point on the limit surface. The models differ only in the definition of this generic point. In both cases, yield and limit surfaces are defined by von Mises forms as  $f = (\sigma - \alpha) \cdot (\sigma - \alpha) - R^2$  and  $f^* = \sigma_L \cdot \sigma_L - R_L^2$ , respectively, where  $\sigma_L$  is a point on the limit surface, and  $\alpha$  is the center of the yield surface.

In the Mroz model, the modulus is a function of the distance from the current stress point to a corresponding point  $\sigma^*$  on the limit surface with the same exterior unit normal, as shown in Fig. 5. Hence,

$$h = h(\delta_m) \quad (15)$$

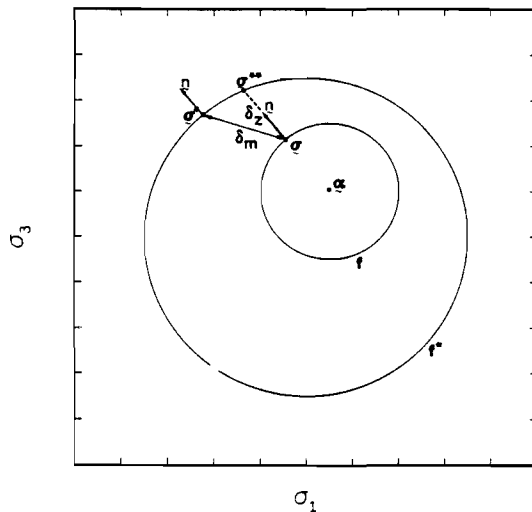


Fig. 5 Definition of  $\delta_m$  and  $\delta_z$  in two surface approaches

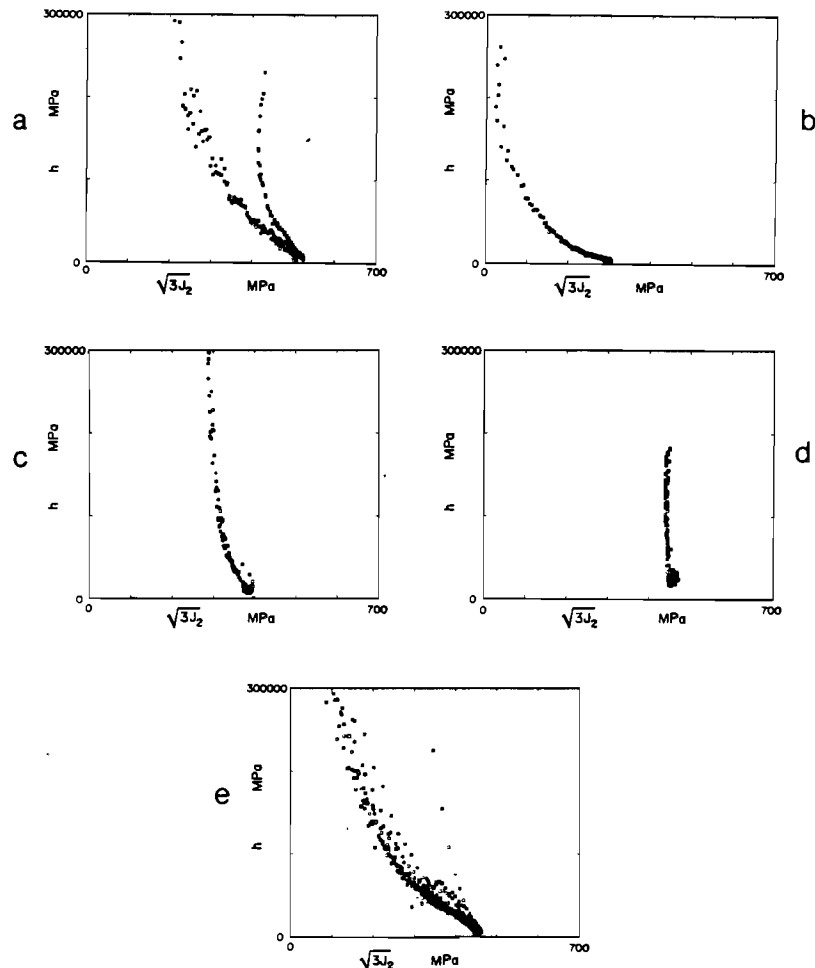


Fig. 6 Modulus  $h$  versus  $\sqrt{3J_2}$  corresponding to: (a) specimen SS01, block #3; (b) specimen SS09, block #2; (c) specimen SS09, block #3; (d) specimen SS09, block #4; and (e) specimen SS04

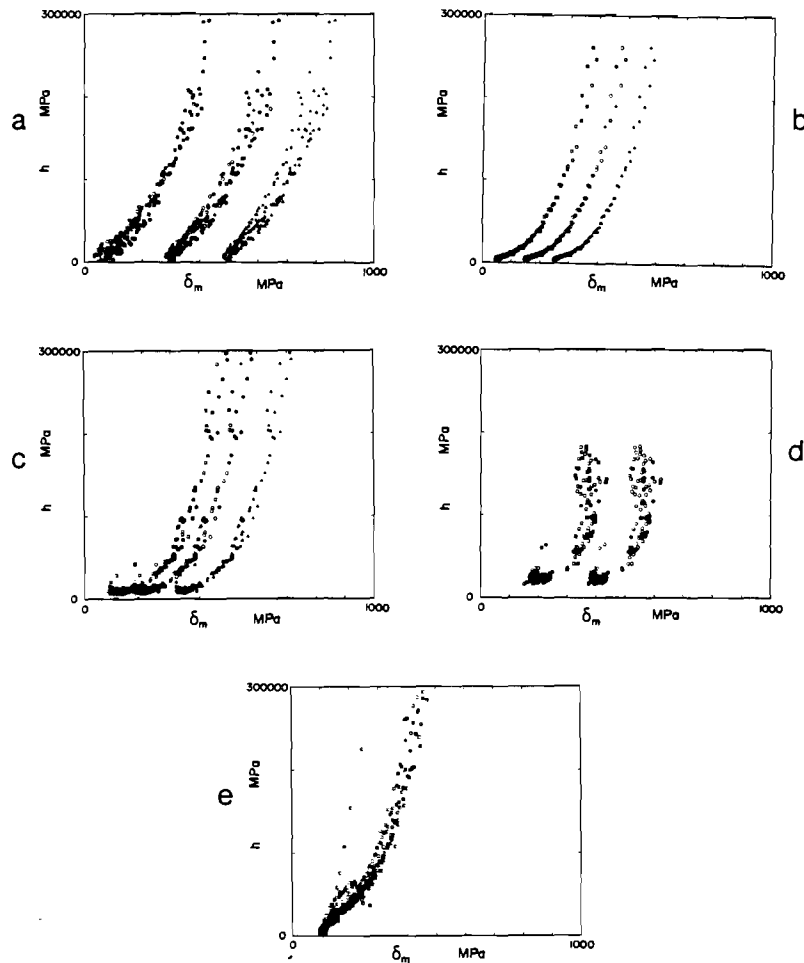


Fig. 7 Modulus  $h$  versus  $\delta_m$  for: (a) specimen SS01, block #3; squares, circles, and triangles correspond to  $R_L = 550$  MPa, 800 MPa, and 1000 MPa, respectively; (b) specimen SS09, block #2; squares, circles, and triangles correspond to  $R_L = 350$  MPa, 450 MPa, and 550 MPa, respectively; (c) specimen SS09, block #3; squares, circles, and triangles correspond to  $R_L = 450$  MPa, 550 MPa and 700 MPa, respectively; (d) specimen SS09, block #4; squares and circles correspond to  $R_L = 550$  MPa and 800 MPa, respectively; and (e) specimen SS04,  $R_L = 550$  MPa

where  $\delta_m = |(\sigma^* - \sigma)|$ . Here,  $\sigma^* = R_L n$  since the limit surface is not allowed to translate.

Some authors [32] have also proposed the use of a rule based on Ziegler kinematic hardening,

$$h = h(\delta_z) \quad (16)$$

where  $\delta_z = |\sigma^{**} - \sigma|$ . Here,  $\sigma^{**}$  is the point on limit surface defined by the intersection of the unit normal vector to the yield surface with the limit surface, as shown in Fig. 5.

It should be noted that the correlations in equations (14)–(16) are functionally identical for cyclic paths in which the deviatoric stress (stress rate) is radial always. Significant differences can exist, though, for nonproportional loading. In Figs. 6, 7, and 8, modulus  $h$  is plotted versus  $\sqrt{3}J_2$ ,  $\delta_m$ , and  $\delta_z$ , respectively. A measure of correlative capability of each can be obtained by examining the scatter of the data throughout each cycle. A good theory should collapse the data into one curve, relecting a one-to-one mapping of modulus versus the independent variable.

Note that the correlations for block #3 of specimen SS01 are not unique according to the  $\sqrt{3}J_2$  or  $\delta_z$  variables. In contrast, the Mroz approach ( $\delta_m$  in Fig. 7) consolidates the data much better. To evaluate the sensitivity of the Mroz and Ziegler based approaches to dimension of the limit surface,

three limit surface radii of 550 MPa, 800 MPa, and 1000 MPa were implemented, as seen in Figs. 7 and 8. Only small differences exist between the correlations obtained (apart from translation of curves) for the vastly different limit surface radii, indicating insensitivity to the radius parameter. Since translation of the limit surface would be of the order of the asymptotic value of  $h$  multiplied by plastic strain amplitude [32] (i.e.,  $< 50$  MPa), this effect was taken as secondary and not evaluated in this study.

Specimen SS04 is correlated equally well by the Mroz and Ziegler approaches. None of the approaches correlate one of the branches of the path. Even though the end points of the stress space response correspond roughly to proportional loading for each straining direction, there is readjustment in direction of the stress response in the plastic region. Perhaps as a result an inflection is observed in the plots of modulus shown in Fig. 6, 7, and 8.

Specimen SS09 illustrates some of the problems associated with modulus correlations for highly nonproportional cycling. As the loading becomes increasingly nonproportional, the second invariant of deviatoric stress approaches a constant value. Hence,  $\sqrt{3}J_2$  is useless for block #4, even though it is satisfactory for the proportional straining of block #2. Note that for block #4 the Ziegler

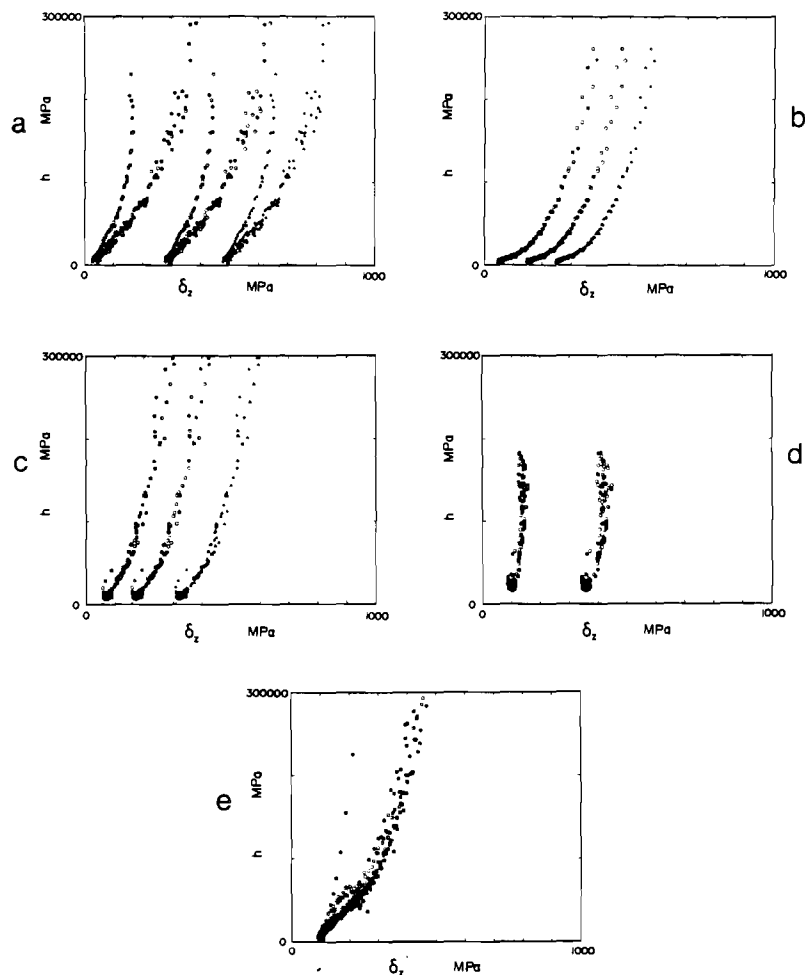


Fig. 8 Modulus  $h$  versus  $\delta_z$  for: (a) specimen SS01, block #3; squares, circles, and triangles correspond to  $R_L = 550$  MPa, 800 MPa, and 1000 MPa, respectively; (b) specimen SS09, block #2; squares, circles, and triangles correspond to  $R_L = 350$  MPa, 450 MPa, and 550 MPa, respectively; (c) specimen SS09, block #3; squares, circles, and triangles correspond to  $R_L = 450$  MPa, 550 MPa and 700 MPa, respectively; (d) specimen SS09, block #4; squares and circles correspond to  $R_L = 550$  MPa and 800 MPa, respectively; and (e) specimen SS04,  $R_L = 550$  MPa

approach is little better than  $\sqrt{3}J_2$  since  $\delta_z \cong \text{constant}$ . But the Mroz rule exhibits a significant variation of  $\delta_m$  through the cycle. Even the Mroz rule, though, exhibits a higher degree of nonlinearity than for the proportional straining of block #2. Another interesting observation regarding block #4 is the higher asymptotic value of  $h$  in the plastic region. The lowest value of  $h$  in each cycle increases from block #2 to block #4 steadily as the nonproportionality increases. This result is consistent with the Mroz rule, which allows for an increasing distance from the asymptotic limit surface (greater  $\delta_m$ ) for increasing degree of loading nonproportionality. It is also consistent with the Ziegler based rule to a lesser extent.

A second measure of the accuracy of a modulus correlation is comparison of the various nonproportional cycles with a proportional cycle. This comparison is not without some ambiguity, since the cyclically stable radii of the yield and limit surfaces may depend on the degree of nonproportionality of loading. As shown, however, the functional relationship between  $h$  and  $\delta_m$  or  $\delta_z$  is weakly dependent on the limit surface radius. Hence, it is useful to compare the correlations obtained for block #2 of specimen SS09 with the corresponding  $\sqrt{3}J_2$ ,  $\delta_m$ , and  $\delta_z$  correlations for nonproportional cycles. These comparisons are shown in Fig. 9. Note that the Mroz based correlation, while not uniformly

accurate, provides the most consistent correlation of the three. Of course, the limit surface would be required to expand with increasing nonproportionality of loading in order to maintain a "unique" mapping of  $h$  and  $\delta_m$ .

**Translation of Yield Surface.** Two kinematic hardening rules which have been widely implemented for cyclic plasticity are the Mroz [13, 28, 30] and Ziegler [13, 33] rules. According to the Ziegler rule, the center of the yield surface  $\alpha_{ij}$  moves in the direction of the vector which connects the center of the current yield surface with the current stress point,

$$d\alpha_{ij} = d\mu_1(\sigma_{ij} - \alpha_{ij}) \quad (17)$$

where  $d\mu_1$  is a scalar factor.

According to the Mroz rule for the yield surface and a stationary limit surface,

$$d\alpha_{ij} = d\mu_2(\sigma_{ij}^* - \sigma_{ij}) \quad (18)$$

where  $\sigma_{ij}^*$  is a point on the limit surface with the same exterior unit normal vector as that of the yield surface at the current stress point, and  $d\mu_2$  is another scalar proportionality factor.

Both hardening rules can be compared, at least qualitatively, by implementation in the axial-torsional subspace. In the axial-torsional subspace, the Ziegler rule in equation (17) is equivalent to Prager's rule  $d\alpha = c d\epsilon^p$  where



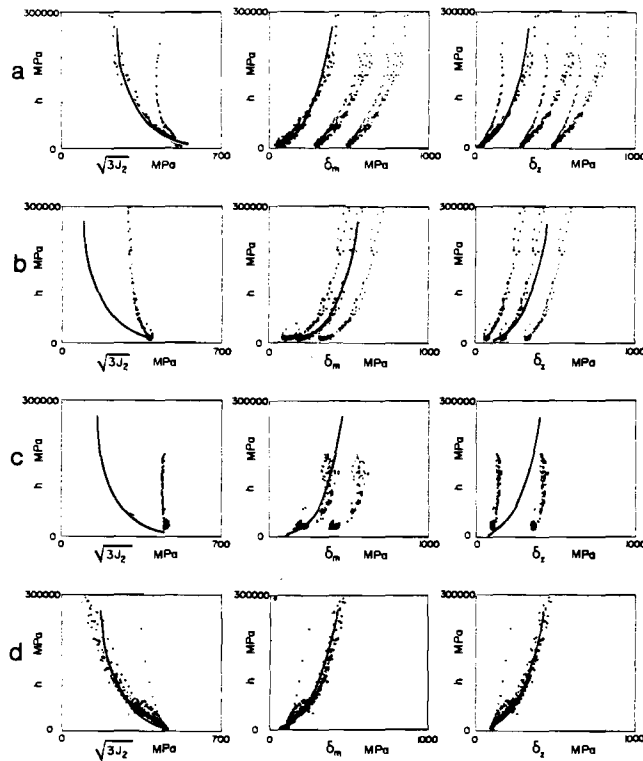


Fig. 9 Comparison of proportionally loaded block #2 of specimen SS01 with: (a) specimen SS01, block #3; (b) specimen SS09, block #3; (c) specimen SS09, block #4; (d) specimen SS04. The solid line in each case represents the corresponding data for block #2 of specimen SS09, and is translated to match each data set at the point of approach of  $h$  to some small asymptotic value.

$d\alpha = d\alpha_1 n_1 + d\alpha_2 n_2$ , and  $c$  is a scalar. Recalling that the direction of  $d\epsilon^P$  was previously found at each point for which  $|d\epsilon^P/ds| \geq 1.4 \times 10^{-6} \text{ MPa}^{-1}$ , the direction of  $d\alpha$  via Ziegler's rule is then known. For the Mroz rule,  $d\alpha$  is in the direction of  $(\sigma^* - \sigma)$ , discussed in equation (15).

Invoking the normality flow rule and a von Mises yield surface of the form  $f = (\sigma - \alpha) \cdot (\sigma - \alpha) - R^2$ , the plastic strain rate direction defines the line along which the yield surface center  $\alpha$  is located. The metric distance from the current stress point  $\sigma$  to  $\alpha$  must then equal  $R$  from the yield condition. In Fig. 10, the evolution of  $\alpha$  through a cycle is plotted as a solid line for two histories. For specimen SS01, two yield surface radii are plotted for comparison. Note that errors in calculated plastic strain rate direction are magnified in the algorithm for plotting  $\alpha$ , resulting in a somewhat wavy path. It is possible, though, to make some very important comparisons of the two hardening rules based on this data. In Fig. 10, vectors are plotted according to each rule. The ideal rule would result in vectors tangent to the path of  $\alpha$ . Inspection of Fig. 10 clearly reveals the superiority of the Mroz rule for these histories. This superiority had previously been claimed by Lamba [13, 18] by comparing experimental axial-torsional hysteresis loops with theory.

## Conclusions

For nonproportional, cyclically stable strain cycling of type 304 stainless steel specimens, the following observations are made.

1. The direction of plastic strain rate does not in general coincide with that of the deviatoric stress or deviatoric stress rate.

2. A correlation for modulus based only on the second invariant of deviatoric stress is unsatisfactory for describing the variation of modulus along different path segments within

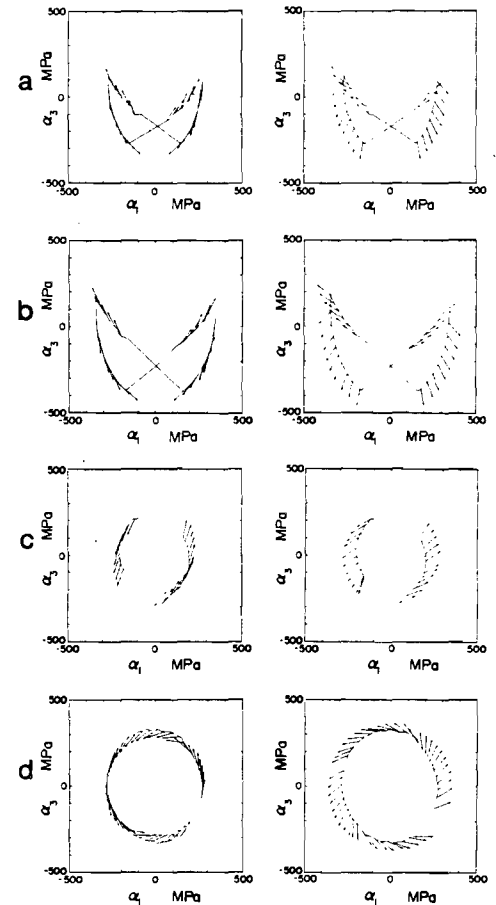


Fig. 10 Instantaneous directions of movement of  $\alpha$  via (left column) Mroz rule and (right column) Ziegler rule for (a) specimen SS01, block #3,  $R = 200 \text{ MPa}$ ; (b) specimen SS01, block #3,  $R = 100 \text{ MPa}$ ; (c) specimen SS09, block #3,  $R = 200 \text{ MPa}$ ; and (d) specimen SS09, block #4,  $R = 200 \text{ MPa}$ . For the Mroz rule,  $R_L = 550 \text{ MPa}$  was used.

the same cycle or along two distinctly different non-proportional paths.

3. A correlation for modulus based on the metric distance from the current stress point to a corresponding point on a fixed limit surface of larger radius can produce satisfactory results provided the corresponding point is properly selected. The use of a Mroz based definition of the corresponding point on the limit surface is superior to that of Ziegler based definition.

4. The Mroz kinematic hardening rule is more accurate than the Ziegler rule for nonproportional cycling.

## Acknowledgments

The support of this work by a grant from the National Science Foundation (NSF Solid Mechanics Division Grant No. MEA-8404080; Program Manager C. J. Astill) is gratefully acknowledged.

## References

- 1 Iwan, W. O., "On a Class of Models for the Yielding Behavior of Continuous and Composite Systems," *ASME Journal of Applied Mechanics*, Vol. 34, 1967, pp. 612-617.
- 2 Zienkiewicz, O. C., Nayak, G. C., and Owan, D. R., "Composite and Overlay Models in Numerical Analysis of Elasto-Plastic Continua," *Symp. Foundations of Plasticity*, ed., Sawczuk, Noordhoff, Leyden, 1973, pp. 107-123.
- 3 Jhansale, H. R., "A New Parameter for the Hysteretic Stress-Strain Behavior of Metals," *ASME JOURNAL OF ENGINEERING MATERIALS AND TECHNOLOGY*, 1975, pp. 33-38.
- 4 Kalev, I., "Cyclic Plasticity Models and Application in Fatigue Analysis," *Computers and Structures*, Vol. 13, 1981, pp. 709-716.

- 5 Eisenberg, M. A., "A Generalization of Plastic Flow Theory with Application to Cyclic Hardening and Softening Phenomena," *ASME JOURNAL OF ENGINEERING MATERIALS AND TECHNOLOGY*, Vol. 98, 1976, pp. 221-228.
- 6 Garud, Y. S., "Prediction of Stress-Strain Response Under General Multiaxial Loading," *ASTM STP 765*, 1982, pp. 223-238.
- 7 Shiratori, E., Ikegami, K., and Yoshida, F., "Analysis of Stress-Strain Relations by Use of an Anisotropic Hardening Plastic Potential," *Journal of the Mechanics and Physics of Solids*, Vol. 27, 1979, pp. 213-229.
- 8 Leis, B. N., and Laflen, J. H., "Problems in Damage Analysis Under Nonproportional Cycling," *ASME JOURNAL OF ENGINEERING MATERIALS AND TECHNOLOGY*, Vol. 102, 1980, pp. 127-134.
- 9 Liu, K. C., and Greenstreet, W. L., "Experimental Studies to Examine Elastic-Plastic Behaviors of Metal Alloys Used in Nuclear Structures," *Constitutive Equations in Viscoplasticity: Computational and Engineering Aspects*, AMD, ASME, Vol. 20, 1976, pp. 35-56.
- 10 Hecker, S. S., "Experimental Studies of Yield Phenomena in Biaxially Loaded Metals," *Constitutive Equations in Viscoplasticity: Computational and Engineering Aspects*, AMD, ASME, Vol. 20, 1976, pp. 1-32.
- 11 Phillips, A., Tang, J. L., and Ricciuti, M., "Some New Observations on Yield Surfaces," *Acta Mechanica*, Vol. 20, 1974, pp. 23-39.
- 12 Mair, W. M., and Pugh, H., "Effect of Pre-Strain on Yield Surfaces in Copper," *Journal Mechanical Engineering Science*, Vol. 6, No. 2, 1964, pp. 150-163.
- 13 Lamba, H. S., "Nonproportional Cyclic Plasticity," TAM Report No. 413, Department of Theoretical and Applied Mechanics, University of Illinois at Urbana-Champaign, 1976.
- 14 Nouailhas, D., Policella, H., and Kaczmarek, H., "On the Description of Cyclic Hardening Under Complex Loading Histories," *Proceedings of the International Conference on Constitutive Laws for Engineering Materials*, eds. Desai and Gallagher, Tucson, Ariz., Jan. 1983, pp. 45-49.
- 15 McDowell, D. L., and Socie, D. F., "Transient and Stable Deformation Behavior Under Cyclic Nonproportional Loading," to appear in *ASTM STP 853*.
- 16 Kanazawa, K., Brown, M. W., and Miller, K. J., "Cyclic Deformation of 1% Cr-Mo-V Steel Under Out-of-Phase Loads," *Fatigue of Engineering Materials and Structures*, Vol. 2, 1979, pp. 217-228.
- 17 McDowell, D. L., Socie, D. F., and Lamba, H. S., "Multiaxial Nonproportional Cyclic Deformation," *Low-Cycle Fatigue and Life Prediction*, ASTM STP 770, 1982, pp. 500-518.
- 18 Lamba, H. S., and Sidebottom, O. M., "Cyclic Plasticity for Nonproportional Paths—2. Comparison with Predictions of Three Incremental Plasticity Models," *ASME JOURNAL OF ENGINEERING MATERIALS AND TECHNOLOGY*, Vol. 100, 1978, pp. 104-111.
- 19 Hunsaker, B., Vaughan, D. K., and Stricklin, J. A., "A Comparison of the Capability of Four Hardening Rules to Predict a Material's Plastic Behavior," *ASME Journal of Pressure Vessel Technology*, Feb. 1976, pp. 66-74.
- 20 Almroth, B. O., "Evaluation of Available Technology for Prediction of Plastic Strain," *Constitutive Equations in Viscoplasticity: Computational and Engineering Aspects*, AMD, ASME, Vol. 20, 1976, pp. 201-211.
- 21 McDowell, D. L., "A Two Surface Model for Transient Nonproportional Cyclic Plasticity: Part II—Comparison of Theory with Experiments," to appear in *ASME Journal of Applied Mechanics*.
- 22 Brown, M. W., and Miller, K. J., "Biaxial Cyclic Deformation Behavior of Steels," *Fatigue of Engineering Materials and Structures*, Vol. 1, 1979, pp. 93-106.
- 23 Ilyushin, A. A., Prikl. *Mat. Mekh.*, Vol. 18, p. 641.
- 24 McDowell, D. L., "On the Path Dependence of Transient Hardening and Softening to Stable States Under Complex Biaxial Cyclic Loading," *Proceedings of the International Conference on Constitutive Laws for Engineering Materials*, eds. Desai and Gallagher, Tucson, Ariz., Jan. 1983, pp. 125-132.
- 25 Carnahan, B., Luther, H. A., and Wilkes, J. O., *Applied Numerical Methods*, Wiley, 1969, p. 128.
- 26 Bodner, S. R., and Partom, Y., "Constitutive Equations for Elastic-Viscoplastic Strain Hardening Materials," *ASME Journal of Applied Mechanics*, Vol. 42, 1975, pp. 385-389.
- 27 Valanis, K. C., and Lee, C. F., "Endochronic Theory of Cyclic Plasticity with Applications," *ASME Journal of Applied Mechanics*, Vol. 51, 1984, pp. 367-374.
- 28 Mroz, Z., "Mathematical Models of Inelastic Material Behavior," Solid Mechanics Division, University of Waterloo, Waterloo, Ontario, 1973.
- 29 Drucker, D. C., and Palgen, L., "On Stress-Strain Relations Suitable for Cyclic and Other Loading," *ASME Journal of Applied Mechanics*, Vol. 48, 1981, pp. 479-485.
- 30 Mroz, Z., "An Attempt to Describe the Behavior of Metals Under Cyclic Loads Using a More General Workhardening Model," *Acta Mechanica*, Vol. 7, 1967, pp. 199-212.
- 31 Krieg, R. D., "A Practical Two Surface Plasticity Theory," *ASME Journal of Applied Mechanics*, Vol. 42, Sept. 1975, pp. 641-646.
- 32 Dafalias, Y. F., and Popov, E. P., "A Model of Nonlinearly Hardening Materials for Complex Loading," *Acta Mechanica*, Vol. 21, 1975, pp. 173-192.
- 33 Ziegler, H., "A Modification of Prager's Hardening Rule," *Quarterly of Applied Mathematics*, Vol. 17, 1959, pp. 55-60.

# THE SIGNIFICANCE OF NONPROPORTIONAL LOADING TESTS FOR CHARACTERIZATION OF CYCLIC RESPONSE OF METALS

David L. McDowell  
Assistant Professor  
School of Mechanical Engineering  
Georgia Institute of Technology  
Atlanta, Georgia 30332  
Member of SESA

## ABSTRACT

The structure of constitutive models for cyclic plasticity is usually based on uniaxial tests. These models are then generalized to multiaxial stress-strain states assuming the combined states as equivalent uniaxial. It is shown that serious errors are introduced by this assumption for nonproportional loading. Hence, nonproportional loading tests can be helpful in determining appropriate multiaxial generalizations of theories based on a predominately uniaxial test database.

## INTRODUCTION

The usual procedure in formulating constitutive laws for the cyclic plastic behavior of materials is to

- observe cyclic stress-strain response in uniaxial tests,
- formulate a constitutive theory capable of including the essential elements of the uniaxial response,
- determine the model constants and parameters from uniaxial tests dictated by the form of the model, and
- generalize to multiaxial states of stress and strain on the basis of effective stress and strain.

In reality, proceeding from steps (a) - (c) to step (d) is a very large "jump". Furthermore, it is often done without a physical/experimental basis, particularly if the multiaxial stresses and strains vary nonproportionally. Yet this generalization from uniaxial response forms the basis of essentially all cyclic plasticity constitutive subroutines currently found in nonlinear finite element codes. Recently, formulation of fatigue crack initiation models for complex multiaxial loading [1-3] has been fueled by industrial concern for predicting fatigue life of components. Since cyclic plasticity has long been related to low-cycle fatigue life [4-6], it is obvious that application of strain-based multiaxial fatigue criteria requires accurate constitutive equations.

The purpose of this paper is to discuss inappropriate generalizations, for cyclic plasticity theories, from uniaxial test data to cyclic, nonproportional, biaxial loading. In addition, some biaxial tests will be described which can assist in the formulation of more general constitutive laws.

## SOME COMMON ASSUMPTIONS OF TIME- AND RATE-INDEPENDENT CYCLIC PLASTICITY THEORY FOR METALS

To provide a framework for this discussion, the elements of generalized time- and rate-independent theory will be outlined. For theories which employ a yield surface

$$f(\underline{\sigma} - \underline{\alpha}, R) = 0 \quad (1)$$

of relatively simple form, the deformation-induced anisotropy is described by backstress  $\underline{\alpha}$ . The characteristic dimension of the surface is denoted by  $R$ . By Drucker's postulate the associated flow rule, applicable for metals, is

$$d\underline{\epsilon}^P = d\lambda \nabla f \quad (2)$$

where  $\nabla f$  is the gradient of  $f$  in stress space and  $d\lambda$  is a scalar multiplier. Expressing the scalar multiplier in the forms

$$d\underline{\epsilon}^P = H(d\underline{\sigma} : \nabla f) \nabla f \quad (3)$$

where  $H$  is a scalar or, alternatively,

$$d\bar{\epsilon}^P = \frac{1}{h} (d\bar{\sigma} : \bar{n}) \bar{n} \quad (4)$$

where  $\bar{n} = \nabla f / \|\nabla f\|$ ,  $h$  is recognized as the plastic modulus. Of course equations (2) and (3) are applicable even for general anisotropic forms of  $f$  [7-9]. In principle, anisotropic yield surface formulations could be used to accurately model multiaxial cyclic plasticity. Extensive necessary experimental characterization by yield surface probing, difficulty in characterizing history dependence, and resulting complex analytical forms have seriously limited the use of anisotropic yield surfaces in actual applications. Since the current work seeks to explore inadequacies in common assumptions, yield surfaces of the form in equation (1) will be considered. Of course, equations (1)-(4) are applicable in any relevant stress space or subspace.

In addition to the flow rule, kinematic and isotropic hardening rules are typically specified for  $\bar{\alpha}$  and  $R$  in equation (1):

$$d\bar{\alpha} = d\mu \bar{\xi} \quad (5)$$

$$dR = \Lambda(\zeta) d\zeta \quad (6)$$

The evolution of these parameters is related by the consistency condition  $df = 0$  during plastic flow, or

$$\nabla f : d\bar{\sigma} - \nabla f : d\bar{\alpha} - (\partial f / \partial R) dR = 0 \quad (7)$$

Some of the popular forms for  $\bar{\xi}$  include

$$\text{Prager rule:} \quad \bar{\xi} = \bar{n} \quad (8)$$

$$\text{Ziegler rule:} \quad \bar{\xi} = (\bar{\sigma} - \bar{\alpha}) \quad (9)$$

$$\text{Mroz rule:} \quad \bar{\xi} = (\bar{\sigma}^* - \bar{\alpha}) \quad (10)$$

where  $\bar{\sigma}^*$  is the point on a loading or bounding surface which encloses yield surface  $f$  [10-12] with the same outward normal vector  $\bar{n}$  as that of the current stress point. For surfaces which do not have a unique mapping of normal vectors to stress points, such as the Tresca case, one may specify  $\bar{\sigma}^*$  to be a geometrically similar point on the bounding surface [13].

The Mroz rule can apply to a series of loading surfaces in a sequential manner [10-11], or can apply to a single bounding surface (e.g. two surface theories [14-18]). It is easy to rationalize the prolific implementation of the Prager and Ziegler rules, since they are quite simple and require no bounding surfaces. Furthermore, since no distinction can be made between the rules in equations (8) - (10) for uniaxial loading, there is no reason to introduce additional complexity to correlate uniaxial test databases. Yet, the Mroz rule has been found to be most accurate [14-15,19] for the general case of biaxial cyclic loading.

Typical forms for  $\zeta$  in equation (6) are [20-22]

$$\zeta = \int (\bar{\sigma} - \bar{\alpha}) : d\bar{\epsilon}^P = \int dW^{PC} \quad (11)$$

or

$$\zeta = \int (d\bar{\epsilon}^P : d\bar{\epsilon}^P)^{1/2} \quad (12)$$

where  $dW^{PC}$  is a measure of plastic work increment. Usually, no particular limits of integration are specified for equations (11) and (12) other than from the beginning of the history to the current point.

For strain-hardening response, the plastic modulus  $h$  in equation (4) is commonly expressed as

$$h = h(\rho) \quad (13)$$

The parameter  $\rho$  often appears as one of the following forms:

$$\text{linear hardening:} \quad \rho \text{ irrelevant, } h = \text{constant} \quad (14)$$

$$\text{effective stress:} \quad \rho = (3J_2)^{1/2} \quad (15)$$

$$\text{Mroz-type:} \quad \rho = \|\bar{\sigma}^* - \bar{\alpha}\| = \delta_m \quad (16)$$

$$\text{Plastic strain or work accumulation:} \quad \rho = \int dW^{PC} \text{ or } \rho = \int (d\bar{\epsilon}^P : d\bar{\epsilon}^P)^{1/2} \quad (17)$$

where  $J_2$  is the second invariant of deviatoric stress. In equation (17), the lower limit of integration is taken to correspond to the point of initial yielding in the current reversal [23]. Note that the Mroz form in equation (16) is defined in terms of a two surface theory as in Dafalias [16, 18], Krieg [17] and McDowell [14-15]. A multiple surface Mroz formulation effectively discretizes stress space into a number of sub-regions of constant plastic modulus at the expense of introducing a significant number of additional

loading surfaces and associated backstress components. Hence, for computational efficiency, the two surface form of the Mroz rule is desirable.

#### EXPERIMENTAL VALIDITY OF ASSUMPTIONS

One of the most useful tests for characterization of the uniaxial cyclic stress-strain response of metals is the incremental step test [24]. In this strain-controlled test, the applied strain range is successively increased and decreased linearly until the stress-strain response stabilizes. The resulting cyclic stress-strain curve is then used to represent stable hysteresis response.

An analogous test may be defined for tension-torsion testing of thin-walled tubular specimens. In these tension-torsion tests, the relative angle of twist and axial deformation of the gage section may be independently enforced via closed-loop, servohydraulic, computer control. The in-plane axial stress  $\sigma$  and shear stress  $\tau$  are taken to be uniform and statically determinate. Details of the specimen design, extensometry, and testing procedures are discussed elsewhere [25-26]. If sinusoidal axial and engineering shear strains are enforced with phase angle  $\beta$ ,

$$\epsilon = \epsilon_a \sin \omega t \quad (18)$$

$$\gamma = \gamma_a \sin(\omega t - \beta) \quad (19)$$

a sort of phase angle step test may be run by successively increasing  $\beta$  from 0 to 90 degrees after reaching cyclic stability at each value of  $\beta$ . Such a test was performed on initially annealed type 304 stainless steel. In Figure 1, the enforced cyclic strain path and resulting stable axial versus shear stress responses are shown for  $\beta = 0, 30$  and  $60$  degrees with  $\gamma_a/\epsilon_a = 1.5$  and  $\epsilon_a = 0.005$ . In these tests, the effective strain rate was maintained constant at  $0.001 \text{ sec}^{-1}$ . The significant extent of cyclic hardening should be noted, with a concurrent successive decrease in any measure of effective plastic strain range [25].

An increase in the value of  $\beta$  corresponds to an increase in the overall effects of nonproportionality within a cycle. McDowell et al. [27] showed in metallurgical studies that this additional hardening can be traced to an increase in the uniformity of deformation product (intensity of slip system activation) among the grains.

This phase angle step test has important implications in terms of the validity of the previously stated common assumptions of cyclic plasticity theory for metals. Figure 2 shows a plot of maximum effective stress in each cycle for the three successive blocks. The onset of additional cycle-by-cycle hardening at each step increase of  $\beta$  dictates that the  $\Lambda$  dependence on  $\zeta$  in equation (6) is not an appropriate general form. Since this additional hardening occurs without an increase in effective plastic strain range, plastic strain range dependence is not enough. An additional dependence on the nonproportionality of loading is required, i.e.

$$dR = \Lambda(\zeta, \phi) d\zeta \quad (20)$$

where  $\phi$  introduces path nonproportionality effects [28-30]. An additional variable [14-15, 25, 30] may be introduced to account for plastic strain range effects observed even in uniaxial tests.

Turning to the kinematic hardening rule, equation (5), it is easy to verify the applicability of the Prager or Ziegler rules. Since the stress-strain history was recorded on magnetic disk, the data were appropriately numerically differentiated to give  $d\sigma/ds$ ,  $d\tau/ds$ ,  $d\epsilon/ds$ , and  $d\gamma/ds$  [31], where the parametric independent variable  $s$  is the effective stress arc length along the path, i.e.

$$s = \int (d\tilde{\sigma} \cdot d\tilde{\sigma})^{1/2} \quad (21)$$

$$\tilde{\sigma} = \sigma_1 \tilde{n}_1 + \sigma_3 \tilde{n}_3 \quad (22)$$

$$\sigma_1 = \sigma \quad (23)$$

$$\sigma_3 = \sqrt{3} \tau \quad (24)$$

Equation (22) defines the stress vector  $\tilde{\sigma}$  in deviatoric axial-torsional stress subspace [31] with orthogonal base vectors  $\tilde{n}_1$  and  $\tilde{n}_3$ . Hence,

$$\frac{d\tilde{\sigma}}{ds} = \left( \frac{d\epsilon}{ds} - \frac{1}{E} \frac{d\sigma}{ds} \right) \tilde{n}_1 + \left( \frac{d\gamma}{ds} - \frac{1}{G} \frac{d\tau}{ds} \right) \frac{1}{\sqrt{3}} \tilde{n}_3 \quad (25)$$

where  $E$  and  $G$  are Young's modulus and shear modulus, respectively, and  $d\epsilon^P$  is the plastic strain increment.

The plastic strain rate direction is thus defined by equation (25). In this axial-torsional subspace, the von Mises yield condition is expressed as

$$f = (\tilde{\sigma} - \tilde{\alpha}) \cdot (\tilde{\sigma} - \tilde{\alpha}) - R^2 = 0 \quad (26)$$

At any point along the stress trajectory, the backstress  $\tilde{\alpha}$  must be located such that  $d\epsilon^P$  is collinear with  $(\tilde{\sigma} - \tilde{\alpha})$ . This follows from the normality flow rule, equation (3), applied to equation (26). Note

that  $\dot{n} = (\dot{\sigma} - \dot{\alpha})/|\dot{\sigma} - \dot{\alpha}|$  in this case so that equations (8) and (9) result in equivalent forms. If one assumes a yield surface radius, then the trajectory of  $\alpha$  is fully defined for this case, assuming  $J_2$  flow theory holds, as  $\alpha = \sigma - Rn$ . In the analysis of the data, a "cutoff" value of  $|d\epsilon^p/ds| < 1.4 \times 10^{-6} \text{ MPa}^{-1}$  was used to define regions of elastic unloading. In Figure 3, the trajectory of  $\alpha$  is plotted in stress space for an assumed yield surface radius of  $R = 200 \text{ MPa}$ . In addition, the predicted direction of backstress increment  $d\alpha$  in equations (5), (8), and (9) is plotted as a vector from the associated current backstress point. Note the significant lack of correlation with experiment, since the correct kinematic hardening rule should result in tangency of  $d\alpha$  with the trajectory of  $\alpha$ . This lack of correlation holds for virtually any assumed values of  $R$  and other conventional forms of the yield surface  $f$  (e.g. Tresca).

The Mroz kinematic hardening rule, employing a single bounding surface, results in much better correlation as seen in Figure 4. Note that  $\sigma^* = R^*n$ , where  $R^*$  is the radius of a surface  $f^* = \sigma^* \cdot \sigma^* - (R^*)^2$  which bounds the maximum stress response.

Another important result is that the plastic strain rate vector is not, in general, in the direction of either the deviatoric stress or stress rate since

$$d\epsilon^p = d\lambda_1 \sigma \quad (27)$$

$$d\epsilon^p = \lambda_2 d\sigma \quad (28)$$

as seen in Figure 5.

In the axial-torsional subspace, the flow rule is written as

$$d\epsilon^p = \frac{2}{3} \frac{1}{h} (d\sigma \cdot n) n \quad (29)$$

where  $h = 2/3 (d\sigma \cdot n)/(d\epsilon^p \cdot d\epsilon^p)^{1/2}$  is the plastic modulus. In a uniaxial test,  $h$  is simply  $2/3 d\sigma/d\epsilon^p$ . Modulus  $h$  is easily determined from the data during plastic flow since both  $d\epsilon^p/ds$  and  $d\sigma/ds$  are known. In Figure 6,  $h$  is plotted versus some of the assumed forms of  $\rho$  in equations (14)-(17). Pure dependence of  $h$  on any one of these parameters would require a uniqueness of  $h(\rho)$  regardless of path. A measure of correlative capability is the similarity of the shape of the plots for out-of-phase cycling with in-phase cycling. Clearly, the modulus is not constant, as stated in equation (14), but varies from very high ( $\rightarrow \infty$ ) to very low ( $\sim 4000 \text{ MPa}$ ) values. Nor is the modulus generally a function of effective stress as suggested in equation (15). For the 60 degree out-of-phase loading, the effective stress is approximately constant.

Accumulated plastic strain or plastic work from the most recent point of initial yielding is not satisfactory. As seen in Figure 6, the minimum value of  $h$  increases as  $\beta$  increases. Furthermore, there is essentially no elastic unloading for  $\beta = 60$  degrees or, presumably, for  $\beta > 60$  degrees. For such histories, validity of equation (17) would require that the modulus saturates monotonically to some constant value since this is the case in uniaxial or proportional loading.

The Mroz definition of  $\rho$  in equation (16), also shown in Figure 6, appears to demonstrate the highest correlation between in-phase and out-of-phase paths.

To put these results into perspective, it should be noted that differences between each of the earlier assumptions for time- and rate-independent plasticity would vanish for uniaxial loading. Only for nonproportional loading are the differences large enough to assess validity. Therefore, on the basis of uniaxial tests only, one might formulate an improper form of the constitutive equations for evaluation of structural response under nonproportionally varying boundary conditions. It would seem that nonproportional loading tests can contribute significantly to the development of a general model framework with little increase in complexity.

#### SOME IMPLICATIONS FOR RATE-DEPENDENT, UNIFIED THEORIES

An important class of rate-dependent theories currently proposed for description of cyclic plasticity and creep over a range of temperatures and strain rates are unified creep-plasticity equations. The typical structure of these equations is as follows [32]:

$$\dot{\epsilon}^i = F\left(\frac{|\dot{\sigma} - \dot{\alpha}|}{K}\right) (\dot{\sigma} - \dot{\alpha}) \quad (30)$$

$$\dot{\alpha} = h_{\alpha} \dot{\epsilon}^i - r_{\alpha} \alpha \quad (31)$$

$$\dot{K} = h_K |\dot{\epsilon}^i| - r_K K \quad (32)$$

Here,  $\dot{\epsilon}^i$  is the inelastic strain rate and  $K$  is an isotropic hardening variable. Hardening functions ( $h_{\alpha}$ ,  $h_K$ ) and recovery functions ( $r_{\alpha}$ ,  $r_K$ ) appear in these equations.

It is usual for researchers to determine both the structure and material parameters of these equations from uniaxial testing. Though the equations are highly coupled and nonlinear, one can readily choose forms for  $f$ ,  $h$ , and  $h_K$  to fit uniaxial cyclic response, neglecting recovery terms [32].

In light of earlier discussion, it is interesting to consider whether the structure of these equations is appropriate in the general case. For relatively high strain rate cycling, equation (31) is a Prager-type

translation rule. Furthermore, the function  $F$  in equation (30) was not necessarily developed to describe large rotations of the  $(\underline{\sigma} - \underline{\alpha})$  vector. More future efforts should be dedicated to evaluation of the validity of the structure of these equations for nonproportional loading.

#### SUMMARY

Virtually all of the current models for cyclic plasticity were formulated on the basis of uniaxial behavior. Sometimes, these constitutive equations are used in loading regimes which are fundamentally different from uniaxial loading. Nonproportional loading is such a regime. The following generalizations can be made for rate- and time-independent cyclic plasticity theory for metals.

- a. Mroz-type kinematic hardening rules and plastic modulus functions are appropriate.
- b. Using only accumulated plastic strain or work is not entirely appropriate for use in isotropic hardening rules.
- c. The direction of the plastic strain rate vector is some combination of deviatoric stress and stress rate directions which can be aptly prescribed by accurate backstress evolution.
- d. Nonproportional cyclic testing has an important role in placing restrictions on the structure of cyclic plasticity theory.

#### ACKNOWLEDGEMENTS

The author would like to acknowledge the National Science Foundation (NSF Solid Mechanics Division Grant No. MEA-8404080; Program Manager C. J. Astill) for support of this work.

#### REFERENCES

1. Krempl, E., "The Influence of State of Stress on Low-Cycle Fatigue of Structural Materials," ASTM STP 549, 1974.
2. Brown, M. W., and Miller, K. J., "Two Decades of Progress in the Assessment of Multiaxial Low-Cycle Fatigue Life, "Low-Cycle Fatigue and Life Prediction," ASTM STP 770, 1982, pp. 482-499.
3. Garud, Y. S., "MULTI-AXIAL FATIGUE: A Survey of the State of the Art," Proceedings of the ASTM/SAE Workshop on Elasto-Plastic Materials Behavior and Component Fatigue Analysis, Minneapolis, April 1980.
4. Coffin, L. F., Jr. and Tavernelli, J. F., "The Cyclic Straining and Fatigue of Metals," Trans. Metallurgical Soc., Am. Institute Mining, Metallurgical and Petroleum Engrs., Vol. 215, Oct. 1959, pp. 794-806.
5. Manson, S. S., and Hirschberg, M. H., "Fatigue Behavior in Strain Cycling in the Low and Intermediate Cycle Range," Tenth Sagamore Army Materials Research Conf., Sagamore, NY, Aug. 1963.
6. Morrow, J. D., and Socie, D. F., "The Evaluation of Fatigue Crack Initiation Life Prediction Methods," Proc. of Fatigue '81, Materials, Experimentation and Design in Fatigue, Soc. of Environmental Engrs., Warwick University, England, March 24-27, 1981, pp. 3-21.
7. Ohashi, Y., Kawashima, K., and Yokochi, T., "Anisotropy Due to Plastic Deformation of Initially Isotropic Mild Steel and Its Analytical Formulation," Journal of the Mechanics and Physics of Solids, Vol. 23, 1975, pp. 277-294.
8. Phillips, A., and Weng, G. J., "An Analytical Study of an Experimentally Verified Hardening Law," ASME Journal of Applied Mechanics, Vol. 42, June 1975, pp. 375-378.
9. Shiratori, E., Ikegami, K., and Yoshida, F., "Analysis of Stress-Strain Relations by Use of an Anisotropic Hardening Plastic Potential," Journal of the Mechanics and Physics of Solids, Vol. 27, 1979, pp. 213-229.
10. Mroz, Z., "An Attempt to Describe the Behaviour of Metals Under Cyclic Loads Using a More General Workhardening Model," Acta Mechanica, Vol. 7, 1967, pp. 199-212.
11. McDowell, D. L., Socie, D. F., and Lamba, H. S., "Multiaxial Nonproportional Cyclic Deformation," Low-Cycle Fatigue and Life Prediction, ASTM STP 770, 1982, pp. 500-518.
12. Mroz, Z., Mathematical Models of Inelastic Material Behaviour, Solid Mechanics Division, University of Waterloo, Waterloo, Ontario, 1973.
13. Garud, Y. S., "Prediction of Stress-Strain Response Under General Multiaxial Loading," Mechanical Testing for Deformation Model Development, ASTM STP 765, 1982, pp. 223-238.

14. McDowell, D. L., "A Two Surface Model for Transient Nonproportional Cyclic Plasticity: Part I - Development of Appropriate Equations," to appear in ASME Journal of Applied Mechanics.
15. McDowell, D. L., "A Two Surface Model for Transient Nonproportional Cyclic Plasticity: Part II - Comparison of Theory with Experiments," to appear in ASME Journal of Applied Mechanics.
16. Dafalias, Y. F., and Popov, E. P., "A Model of Nonlinearly Hardening Materials for Complex Loading," Acta Mechanica, Vol. 21, 1975, pp. 173-192.
17. Krieg, R. D., "A Practical Two Surface Plasticity Theory," ASME Journal of Applied Mechanics, Vol. 42, Sept. 1975, pp. 641-646.
18. Dafalias, Y. F., "The Concept and Application of the Bounding Surface in Plasticity Theory," Physical Non-Linearities in Structural Analysis, Int. Union of Theoretical and Applied Mechanics, Symp. Senlis, France, May 27-30, 1980, pp. 56-63.
19. Lamba, H. S., "Nonproportional Cyclic Plasticity," TAM Report No. 413, Department of Theoretical and Applied Mechanics, University of Illinois at Urbana-Champaign, 1976.
20. Drucker, D. C., and Palgen, L., "On Stress-Strain Relations Suitable for Cyclic and Other Loading," TAM Report No. 443, Department of Theoretical and Applied Mechanics, University of Illinois at Urbana-Champaign, July 1980.
21. Jhansale, H. R., "A New Parameter for the Hysteretic Stress-Strain Behavior of Metals," ASME Journal of Engineering Materials and Technology, 1975, pp. 33-38.
22. Krieg, R. D., and Key, S. W., "Implementation of a Time Independent Plasticity Theory into Structural Computer Programs," Proc. Winter Annual Meeting of ASME, Constitutive Equation Viscoplasticity: Computational and Engineering Aspects, New York, Dec. 1976, pp. 125-137.
23. Eisenberg, M. A., "A Generalization of Plastic Flow Theory with Application to Cyclic Hardening and Softening Phenomena," ASME Journal of Engineering Materials and Technology, Vol. 98, 1976, pp. 221-228.
24. Landgraf, R. W., Morrow, J., and Endo, T., "Determination of the Cyclic Stress-Strain Curve," Journal of Materials, ASTM, Vol. 4, No. 1, March 1969, pp. 176-188.
25. McDowell, D. L., "Transient Nonproportional Cyclic Plasticity," Ph.D. Thesis, Design and Materials Division, Report No. 107, Department of Mechanical and Industrial Engineering, University of Illinois at Urbana-Champaign, June 1983.
26. Waill, L. E., "Crack Observations in Biaxial Fatigue," Report No. 108, Design and Materials Division, Dept. of Mechanical and Industrial Engineering, University of Illinois at Urbana-Champaign, March 1983.
27. McDowell, D. L., Payne, R. K., Stahl, D., and Antolovich, S. D., "Effects of Nonproportional Cyclic Loading Histories on Type 304 Stainless Steel," Proceedings of the International Spring Meeting of Societe Francaise de Metallurgie, Paris, May 1984.
28. McDowell, D. L., "On the Path Dependence of Transient Hardening and Softening to Stable States Under Complex Biaxial Cyclic Loading," Proceedings of the International Conference on Constitutive Laws for Engineering Materials, Eds. Design and Gallagher, Tucson, AZ, Jan. 1983, pp. 125-132.
29. McDowell, D. L., and Socie, D. F., "Transient and Stable Deformation Behavior Under Cyclic Nonproportional Loading," to appear in ASTM STP 853.
30. Nouailhas, D., Policella, H., and Kaczmarek, H., "On the Description of Cyclic Hardening Under Complex Loading Histories," Proceedings of the International Conference on Constitutive Laws for Engineering Materials, Eds. Desai and Gallagher, Tucson, AZ, Jan. 1983, pp. 45-49.
31. McDowell, D. L., "An Experimental Study of the Structure of Constitutive Equations for Nonproportional Cyclic Plasticity," to appear in ASME Journal of Engineering Materials and Technology.
32. Cescotto, S., Leckie, F. A. and Abrahamson, E. A., "Unified Constitutive Models for Creep and Plasticity of Metals at High Temperature," Design and Materials Division, Dept. of Mechanical and Industrial Engineering, Univ. of Illinois at Urbana-Champaign, 1983.



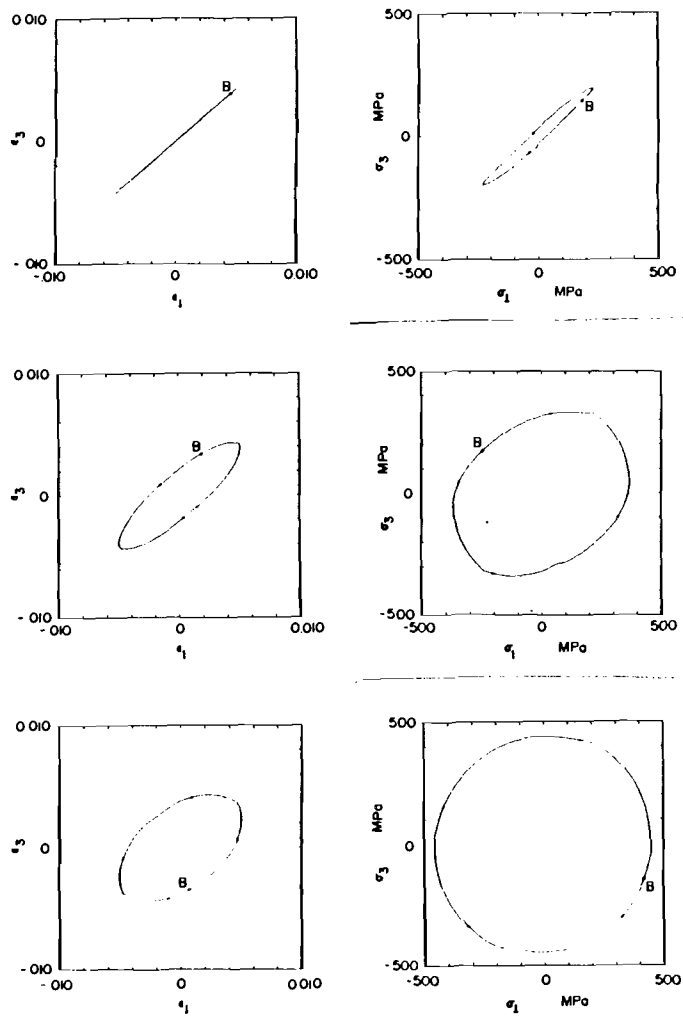


Fig. 1. Cyclic strain path imposed (left) and resulting stable axial versus shear stress responses (right) for  $\beta = 0$  (top), 30 (center), and 60 (bottom) degrees. Note that  $\epsilon_1 = \epsilon$ ,  $\epsilon_3 = \gamma/\sqrt{3}$ ,  $\sigma_1 = \sigma$ , and  $\sigma_3 = \sqrt{3} \tau$ .

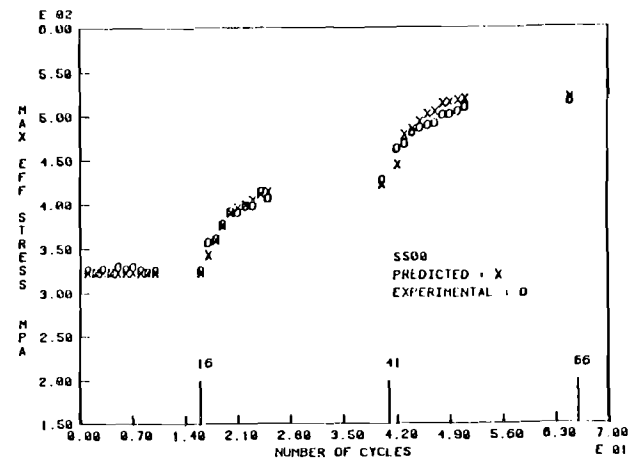


Fig. 2. Maximum shear stress (Tresca definition:  $\max(\sigma^2 + 4\tau^2)^{1/2}$ ) in each cycle for  $\beta = 0, 30$  and 60 degrees.

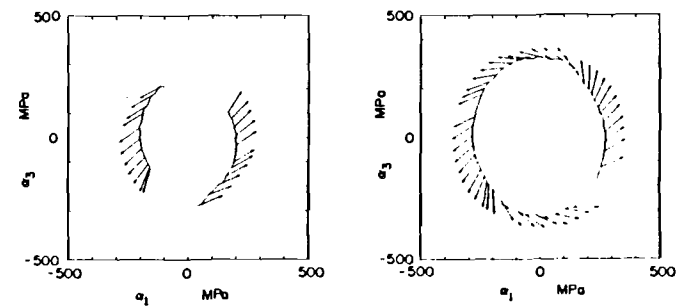


Fig. 3. Trajectory of  $\alpha$  in stress space with  $R = 200$  MPa assumed. Vectors denote direction of predicted backstress increment via Ziegler's rule. Note that  $\sigma_1$  and  $\sigma_3$  are components corresponding to  $\sigma_1$  and  $\sigma_3$ , respectively. Histories are  $\beta = 30^\circ$  (left) and  $\beta = 60^\circ$  (right).

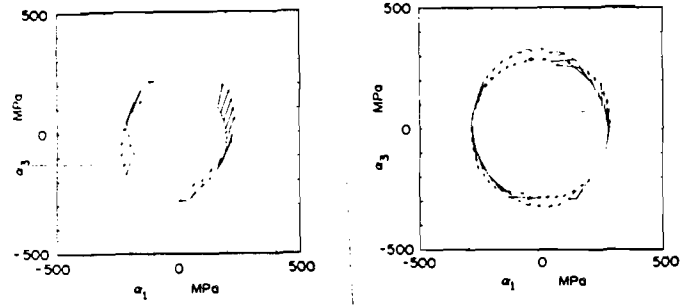


Fig. 4. Trajectory of  $\alpha$  ( $R = 200$  MPa,  $R^* = 550$  MPa) and predicted direction of backstress increment via the Mroz rule. Histories are  $\beta = 30$  degrees (left) and  $\beta = 60$  degrees (right).

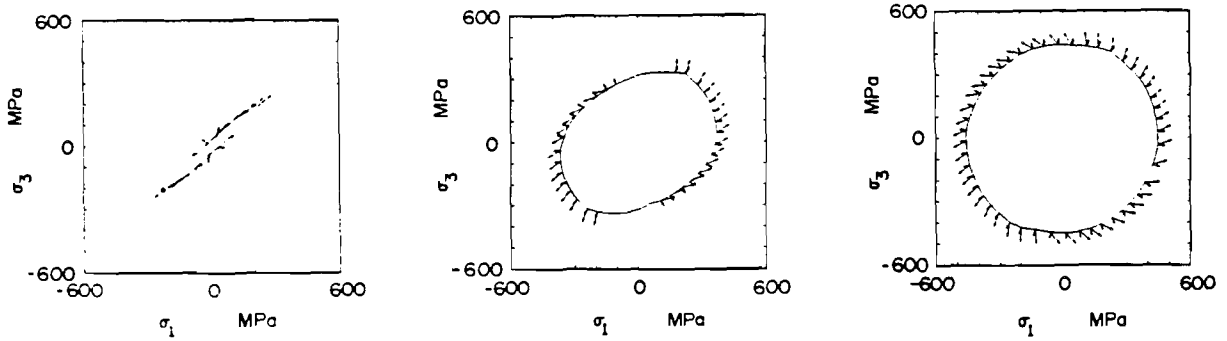


Fig. 5. Stable stress space responses for  $\beta = 0$  degrees (left),  $\beta = 30$  degrees (center), and  $\beta = 60$  degrees (right). Short vectors represent deviatoric stress direction; longer vectors are in direction of plastic strain rate.

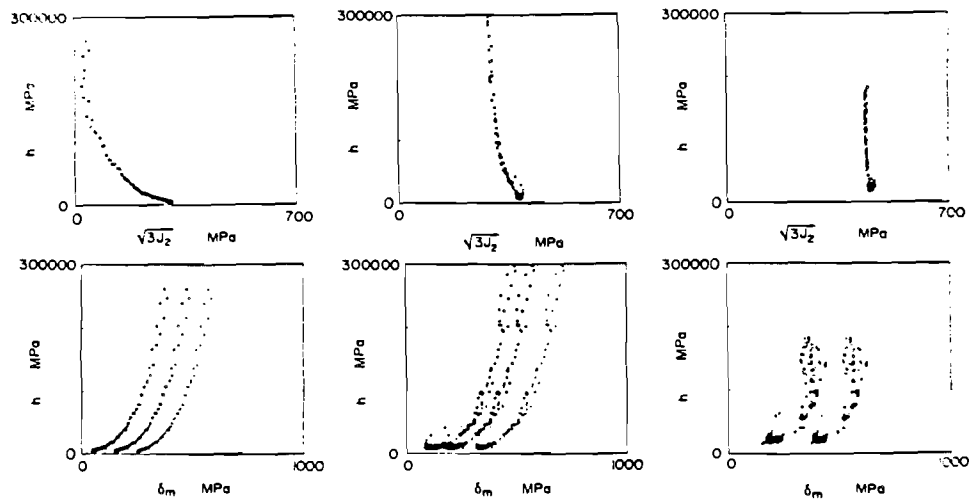


Fig. 6. Modulus  $h$  versus effective stress (top) and Mroz (bottom) definitions for  $\beta = 0$  degrees (left),  $\beta = 30$  degrees (center), and  $\beta = 60$  degrees (right). In the Mroz rule, the various curves represent different  $R^*$  values, ranging from 350 MPa to 800 MPa.

# An Evaluation of Several Constitutive Model Structures for Transient Nonproportional Cyclic Plasticity

W. Sotolongo

Graduate Research Assistant.

D. L. McDowell<sup>1</sup>

Assistant Professor.

School of Mechanical Engineering,  
Georgia Institute of Technology,  
Atlanta, Ga. 30332

*Four constitutive models for cyclic plasticity of different essential structure are evaluated under conditions of nonproportional, multiaxial loading. Drucker's one-surface theory, McDowell's two-surface theory, Krieg's one-surface theory with Radial-Return Integration Algorithm, and Abrahamson's Unified Creep-Plasticity theory are the constitutive models under consideration. Their transient hardening and stable loop responses are compared to experimental data for two nonproportional axial-torsional loading histories. Their computational efficiency is also analyzed.*

## Introduction

The study of cyclic plasticity under nonproportional loading conditions is motivated by the fact that such loading is realistic for many situations encountered in the nuclear, aircraft, and ground vehicle industries. There are several multiaxial cyclic plasticity models available in the literature [1-8]. Most of the implemented models are capable of properly modeling only uniaxial or proportional, multiaxial loadings. They are sometimes used for nonproportional straining without basis for knowing if the predicted results are accurate. This approach is less than desirable but has evolved from the lack of knowledge (experimental data) regarding nonproportional loading histories.

The goal of this study is to evaluate the correlative capability of appropriate constitutive equation structures which range from simple modified classical plasticity theories to complex modified classical plasticity theories in addition to state variable or unified theories. This study will evaluate several generic forms of proposed cyclic plasticity models for nonproportional, multiaxial loading. Four different plasticity models will be evaluated and classified based on their accuracy in predicting the stress-strain response for an axial-torsional (biaxial) stress state. It should be noted that this study does not infer that other particular models with the same generic forms are inferior; the models used were selected on the basis of the availability of multiaxial generalizations and of material constants. This test case was chosen for two reasons. There is experimental data available to serve as the reference in the model evaluation process. Also McDowell [11] has experimentally shown that these biaxial histories incorporate most of the relevant anomalous phenomena that characterizes nonproportional, multiaxial loading. In effect, such biaxial histories are

the simplest yet most appropriate step to be followed in the transition from uniaxial to nonproportional, multiaxial straining.

Realizing that there is no single, superior model structure for all applications, this study purports to comparatively clarify the regimes of applicability of each model structure for complex nonproportional loading.

## Drucker's Model

This model was presented by Drucker and Palgen [1]. Its structure is that of a modified classical, single-surface theory valid for time- and rate-independent response. Two versions were presented. The rounding corner option would predict smooth rounding of the cyclic stress-strain curves. The sharp corner option would predict the correct behavior on reloading after elastic unloading. Only the rounding corner option will be considered here.

This model uses a von Mises yield surface given by

$$f = \frac{1}{2} (s - \alpha) : (s - \alpha) - \frac{R^2}{3} = 0 \quad (1)$$

where  $s$  is the deviatoric stress tensor,  $\alpha$  is the deviatoric backstress tensor, and  $R$  is the uniaxial yield strength. In this work, the colon represents the scalar product of two tensors, e.g.,  $(s_{ij} - \alpha_{ij}) (s_{ij} - \alpha_{ij})$ .

Its associative flow rule is given by

$$\dot{\epsilon}^p = B \left( \frac{J_2}{\partial^2} \right)^N (s - \alpha) ((s - \alpha) : \dot{s}) \quad (2)$$

$$\text{if } f = 0 \text{ and } \dot{\sigma} : (\partial f / \partial \sigma) \geq 0 \quad (2)$$

$$\dot{\epsilon}^p = 0 \text{ otherwise} \quad (3)$$

where  $\dot{\epsilon}^p$  is the plastic strain rate tensor,  $\dot{\sigma}$  is the stress rate tensor,  $\dot{s}$  is the deviatoric stress rate tensor,  $B$  and  $N$  are experimentally determined material model parameters,  $J_2$  is the

<sup>1</sup>To receive all communications regarding this paper.

Contributed by the Pressure Vessels and Piping Division for publication in the JOURNAL OF PRESSURE VESSEL TECHNOLOGY. Manuscript received by the Pressure Vessels and Piping Division, September 17, 1985.

second invariant of  $s$ , and  $\bar{\sigma}$  is a normalizing stress.  $J_2$  and  $\bar{\sigma}$  are of the following form:

$$J_2 = \frac{1}{2} s:s \quad (4)$$

$$\bar{\sigma} = \sigma^* \left( 1 + \gamma \exp \left( -\frac{W^p}{W_0} \right) \right) \quad (5)$$

where

$$W^p = \int_0^t (s - \alpha) : \dot{\epsilon}^p dt \quad (6)$$

and  $\sigma^*$ ,  $\gamma$  and  $W_0$  are material dependent model parameters. Note that  $W^p$  is a monotonically increasing quantity similar, but not equivalent, to the accumulated plastic work. Isotropic hardening is achieved by effectively increasing or decreasing the plastic tangent modulus at a given stress level. The plastic modulus is essentially made a function of  $J_2$  and  $W^p$ .

A Ziegler-type kinematic hardening rule is assumed as

$$\dot{\alpha} = \frac{1}{2k^2} (s - \alpha)((s - \alpha) : \dot{s}) \quad (7)$$

where  $k$  is the material yield strength in shear. For greater details on the determination of the model parameters, the reader is referred to [1].

### McDowell's Model

This model was presented by McDowell [2, 3]. Its structure is that of a two-surface simplification [6-8] of the Mroz [9] or mechanical sublayer models [10]. It consists of a yield surface within which the material response is elastic and a limit surface that "bounds" the material response during plastic flow.

This model uses von Mises surfaces for the yield and limit surfaces of the following forms:

$$f = \frac{3}{2} (s - \alpha) : (s - \alpha) - R^2 = 0 \quad (8)$$

$$f^* = \frac{3}{2} (s^* - \alpha^*) : (s^* - \alpha^*) - R^{*2} = 0 \quad (9)$$

where  $R$  is the radius of the surface. The asterisk superscript refers to the limit surface.

The flow rule for this model is given by

$$\dot{\epsilon}^p = \frac{1}{h} (\dot{s} : n) n \quad (10)$$

where  $h$  is the plastic modulus and  $n$  is the unit normal to the yield surface given by  $n = (s - \alpha) / \|s - \alpha\|$ . Here,  $\|s - \alpha\| = ((s - \alpha) : (s - \alpha))^{1/2}$ .

For the yield surface, a Mroz-type kinematic hardening rule is assumed

$$\dot{\alpha} = \frac{\left( (s - \alpha) : \dot{s} - \frac{2}{3} R \dot{R} \right) (s^* - s)}{(s - \alpha) : (s^* - s)} \quad (11)$$

where  $\dot{\alpha}$  is the backstress rate tensor and  $\dot{R}$  represents isotropic hardening of the yield surface.  $s^*$  is the point in the limit surface having the same outward normal to the corresponding point in the yield surface at the current stress state; that is,

$$s^* = \alpha^* + (s - \alpha) \frac{R^*}{R} \quad (12)$$

For the limit surface, a Prager-Ziegler-type kinematic hardening rule is assumed as

$$\dot{\alpha}^* = \kappa \dot{\eta} n \quad (13)$$

$$\dot{\eta} = (\dot{\epsilon}^p : \dot{\epsilon}^p)^{1/2} = \|\dot{\epsilon}^p\| \quad (14)$$

where  $\kappa$  is the asymptotic modulus and  $\dot{\eta}$  is the norm of the plastic strain rate tensor.

The isotropic hardening rules for the yield and limit surfaces have been similarly defined as

$$\dot{R} = \mu (\dot{R}(\phi, q) - R) \dot{\eta} \quad (15)$$

$$\dot{R}^* = \mu (\dot{R}^*(\phi, q) - R^*) \dot{\eta} \quad (16)$$

where  $\dot{R}(\phi, q)$  and  $\dot{R}^*(\phi, q)$  correspond to the cyclically stable values of the yield and limit surface radii for given values of  $\phi$  and  $q$ , which will be defined shortly.  $\psi$  and  $\psi^*$  are functions chosen appropriately for the material being used. For non-fading memory of cyclically hardening materials, McDowell recommends to use Heaviside functions  $\psi = u(\dot{R}(\phi, q) - R)$  and  $\psi^* = u(\dot{R}^*(\phi, q) - R^*)$ . For completely fading memory, McDowell recommends  $\psi = \psi^* = 1$ .  $\mu$  is an experimentally determined scalar rate parameter. Through experimental testing, McDowell has shown that  $\dot{R}(\phi, q)$  and  $\dot{R}^*(\phi, q)$  can be expressed approximately as linear functions of the form

$$\dot{R}(\phi, q) = \phi (\dot{R}(1, q) - \dot{R}(0, q)) + \dot{R}(0, q) \quad (17)$$

$$\dot{R}^*(\phi, q) = \phi (\dot{R}^*(1, q) - \dot{R}^*(0, q)) + \dot{R}^*(0, q) \quad (18)$$

where  $\dot{R}(1, q)$ ,  $\dot{R}(0, q)$ ,  $\dot{R}^*(1, q)$ , and  $\dot{R}^*(0, q)$  can be experimentally determined. The plastic modulus and asymptotic plastic modulus are defined as

$$h = \kappa \left( 1 + \frac{91960}{\kappa} \left( \sinh \left\{ \frac{\|s^* - s\|}{\|s_0^* - s_0\|} \right\} \right)^{1.1} \right) \quad (19)$$

$$\dot{\kappa} = \mu (\dot{\kappa}(\phi, q) - \kappa) \dot{\psi}_\kappa \dot{\eta} \quad (20)$$

where  $\dot{\kappa}(\phi, q)$  corresponds to the cyclically stable values of the asymptotic modulus for given values of  $\phi$  and  $q$ , and  $s_0$  and  $s_0^*$  are values of  $s$  and  $s^*$  corresponding to the maximum value of  $\|s^* - s\|$  in the history. Parameters  $s_0$  and  $s_0^*$  are not material constants.  $\dot{\psi}_\kappa$  is an experimentally determined function. It is assumed that

$$\dot{\kappa}(\phi, q) = \phi (\dot{\kappa}(1, q) - \dot{\kappa}(0, q)) + \dot{\kappa}(0, q) \quad (21)$$

where  $\dot{\kappa}(0, q)$  and  $\dot{\kappa}(1, q)$  can be experimentally determined.

McDowell [12] has defined an instantaneous measure of nonproportionality of the loading path as

$$J = \left| \frac{\frac{d}{dt} (\epsilon_1 - \epsilon_3)}{g((\dot{\epsilon})_1 - (\dot{\epsilon})_3)} \right| \quad (22)$$

where  $\epsilon_1$  and  $\epsilon_3$  are the largest and smallest principal strains, and  $(\dot{\epsilon})_1$  and  $(\dot{\epsilon})_3$  are the largest and smallest principal strain rates. Here  $g$  is defined as  $g(x) = 1$ , if  $x = 0$  or  $g(x) = x$  if  $x \neq 0$ . To account for accumulated effects of nonproportional paths, McDowell introduced a state variable  $\phi$  which evolves according to

$$\dot{\phi} = \mu^* (1 - J - \phi) \dot{\eta} u(1 - J - \phi_{\text{limit}}) \quad (23)$$

where  $\mu^*$  is an experimentally determined scalar parameter and  $u(1 - J - \phi_{\text{limit}})$  is a Heaviside function introduced to reduce the effects of proportional path segments in the evolution of  $\phi$ .

To account for memory of maximum plastic strain range, McDowell introduced a state variable  $q$  equal to the radius of a strain memory surface in plastic strain space given by

$$F = \frac{2}{3} (\epsilon^p - \alpha^p) : (\epsilon^p - \alpha^p) - q^2 = 0 \quad (24)$$

where  $\alpha^p$  is the center of the strain memory surface in plastic strain space and  $q$  is its current radius. The kinematic hardening rule assumed was of the following form:

$$\dot{\alpha}^p = \frac{H(F)}{2} (\dot{\epsilon}^p : n^*) n^* \quad (25)$$

where  $\dot{\alpha}^p$  is the time rate of  $\alpha^p$ ,  $H(F) = 1$  if  $F = 0$  and  $H(F) = 0$  if  $F < 0$ , and  $n^*$  is the unit normal to the strain memory

surface at the current state of plastic strain. Its isotropic hardening rule was defined as

$$\dot{q} = \left( \frac{1}{2} H(F) \Gamma \sqrt{\frac{2}{3}} - \Lambda(q) \right) \dot{\eta} \quad (26)$$

where  $\Gamma$  is a scalar function and  $\Lambda(q)$  is an experimentally determined function to account for fading memory of maximum plastic strain range. It may be shown that

$$\Gamma = \mathbf{n}^* : \mathbf{n} + \sqrt{6} \Lambda(q) \quad (27)$$

For greater detail on the determination of the model parameters the reader is referred to McDowell [3].

### Kreig's Model With Radial-Return Integration Algorithm

This model was proposed by Kreig and Key [4]. Its structure is that of a modified classical theory comparable to that of Drucker's. A radial-return integration algorithm is utilized making this a very efficient material model.

This model uses a von Mises yield surface given by equation (1) with  $L = \sqrt{2/3} R$ . Kreig and Key [13] introduced a trial stress rate tensor as

$$\dot{\sigma}^{tr} = \mathbf{C} : \dot{\epsilon} \quad (28)$$

where  $\mathbf{C}$  is the fourth rank elasticity tensor and  $\dot{\epsilon}$  is the total strain rate tensor. The flow rule is expressed as

$$\dot{\epsilon}^p = \left[ \frac{1}{2G} \left( \frac{1}{1 + \frac{H'}{3G}} \right) \dot{\sigma}^{tr} : \mathbf{N} \right] \mathbf{N} \text{ if } f=0 \text{ and } \dot{\sigma}^{tr} : \mathbf{N} \geq 0 \quad (29)$$

$$\dot{\epsilon}^p = 0 \text{ otherwise} \quad (30)$$

where  $\mathbf{N}$  is the unit normal to the yield surface,  $G$  is the shear yield strength, and  $H'$  is the cyclically stable value of the experimentally determined asymptotic plastic modulus at the maximum plastic strain range of interest.

A linear combination of isotropic and Prager-type kinematic hardening is assumed as given by a model parameter  $\beta$  as follows:

$$\dot{\alpha} = \frac{2}{3} (1 - \beta) H' \dot{\epsilon}^p \quad (31)$$

$$\dot{L} = \sqrt{\frac{2}{3}} \beta H' \left( \frac{2}{3} \dot{\epsilon}^p : \dot{\epsilon}^p \right)^{1/2} \quad (32)$$

where  $\dot{L}$  is the time rate of change of  $L$ .

By letting  $\beta$  be a constant, it is essentially assumed that no saturation of the cyclic stress-strain response occurs as the material hardens or softens. Kreig's model was modified by making  $\beta$  a function of  $W^{pc}$

$$\beta = \gamma \exp \left( - \frac{W^{pc}}{W_o} \right) \quad (33)$$

where  $W^{pc}$  is defined by equation (6), and  $\gamma$  and  $W_o$  are experimentally determined model parameters.

Applying the radial-return integration algorithm to the system of differential equations given by equations (28)–(33), it becomes

$$\sigma_{n+1}^{tr} = \sigma_n + \mathbf{C} : \Delta \epsilon \quad (34)$$

$$\xi_{n+1}^{tr} = \sigma_{n+1}^{tr} - \alpha_n \quad (35)$$

$$\xi = \xi_{n+1}^{tr} - \frac{1}{3} (\text{trace } \xi_{n+1}^{tr}) \mathbf{I} \quad (36)$$

with the plastic loading case given by

$$\Lambda = \frac{1}{2G} \left( \frac{1}{1 + \frac{H'}{3G}} \right) (\|\xi\| - L_n) \quad (37)$$

$$\epsilon_{n+1}^p = \epsilon_n^p + \Lambda \mathbf{N} \quad (38)$$

$$\sigma_{n+1} = \sigma_{n+1}^{tr} - 2G\Lambda \mathbf{N} \quad (39)$$

$$\alpha_{n+1} = \alpha_n + \frac{2}{3} (1 - \beta) H' \Lambda \mathbf{N} \quad (40)$$

$$L_{n+1} = L_n + \frac{2}{3} \beta H' \Lambda \quad (41)$$

$$W_{n+1}^{pc} = W_n^{pc} + \Lambda (\sigma_{n+1} - \alpha_{n+1}) : \mathbf{N} \quad (42)$$

where  $\xi$  is a tensor approximately normal to the yield surface,  $\mathbf{I}$  is the identity tensor,  $\Delta \epsilon$  is the increment in the total strain tensor, and  $\mathbf{N} = \xi / \|\xi\|$  is the approximated unit normal to the yield surface. Subscripts  $n$  and  $n+1$  refer to the values at the beginning and at the end of the current time step.

It must be emphasized that equations (34)–(42) include Kreig's simplified model equations, the introduced modification, and the numerical integration algorithm to be used to solve this system.

### Abrahamson's Model

This is a unified creep-plasticity theory. Hence, it has a rate-dependent structure characteristic of state variable theories which reflect competition of hardening and recovery mechanisms. Such unified theories result in highly stiff systems of ordinary differential equations. Abrahamson's model was selected as representative of state variable theories since it employs the usual backstress and drag stress state variables and the evolution equations have been determined by Abrahamson for type 304 stainless steel.

Abrahamson by definition used

$$\sigma_{eff} = \left( \frac{3}{2} (s - \alpha) : (s - \alpha) \right)^{1/2} \quad (43)$$

$$\alpha_{eff} = \left( \frac{3}{2} \alpha : \alpha \right)^{1/2} \quad (44)$$

where  $\sigma_{eff}$  and  $\alpha_{eff}$  are the uniaxial equivalent values of stress and backstress, respectively.

The magnitude of the inelastic strain rate tensor is a highly nonlinear function given by

$$\dot{\epsilon}_{eff}^n = a \left( \frac{\sigma_{eff}}{K} \right)^p \quad (45)$$

where  $a$  and  $p$  are model parameters and  $K$  is the current radius of the stress surface. The flow rule is expressed as

$$\dot{\epsilon}^n = \frac{3}{2} \left( \frac{\dot{\epsilon}_{eff}^n}{\sigma_{eff}} \right) (s - \alpha) \quad (46)$$

Kinematic hardening is achieved by a function of the form

$$\dot{\alpha} = h_\alpha (\alpha_{eff}) \dot{\epsilon}^n - \frac{r_\alpha (\alpha_{eff})}{B^p} \alpha \quad (47)$$

where  $B$  is a temperature correction factor, and  $h_\alpha (\alpha_{eff})$  and  $r_\alpha (\alpha_{eff})$  are the hardening and recovery functions assumed for the material being modeled. Abrahamson showed that the following forms are appropriate for these functions:

$$h_\alpha (\alpha_{eff}) = \begin{cases} \frac{\exp(-d_2 \alpha_{eff})}{d_1} & \text{if } \dot{\epsilon}^n : \alpha \geq 0 \\ \frac{1}{d_1} & \text{if } \dot{\epsilon}^n : \alpha < 0 \end{cases} \quad (48)$$

$$r_\alpha (\alpha_{eff}) = c (\alpha_{eff})^m \quad (49)$$

where  $d_1$ ,  $d_2$ ,  $c$ , and  $m$  are experimentally determined model parameters. For room temperature cycling at relatively high strain rates, the recovery functions may be neglected.

Isotropic hardening is achieved by a function of the form

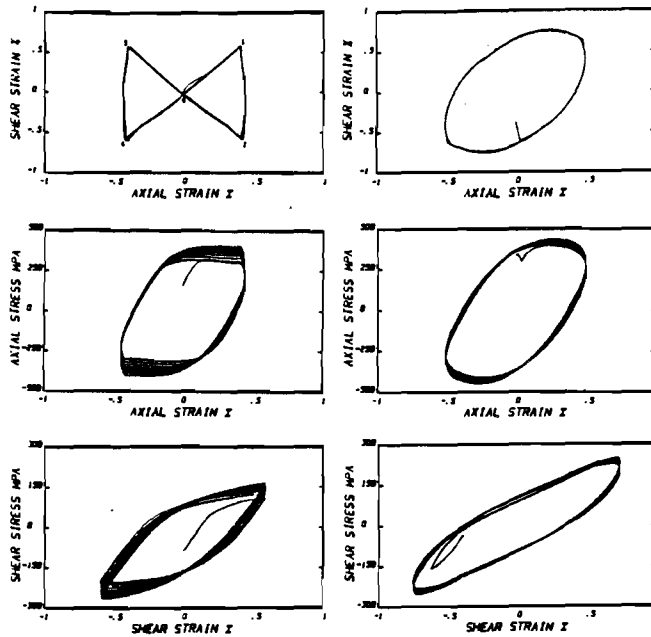


Fig. 1 Experimentally observed transient hardening responses for History I (left column) and History II (right column). Top row, input strain history; middle row, resulting axial stress-axial strain response; bottom row, resulting shear stress-shear strain response.

$$\dot{K} = \frac{H(I_{ae})}{(\psi(\phi))^{1/2}} (\psi(\phi)\alpha_{eff} - w_2(K))\dot{\epsilon}_{eff} \quad (50)$$

where  $\psi(\phi)$  accounts for nonproportionality effects,  $w_2(K)$  is a recovery term, and  $H(I_{ae})$  is an assumed function necessary to adjust the isotropic hardening rate. Based on experimental results,  $w_2(K)$  and  $H(I_{ae})$  can be expressed as

$$w_2(K) = b_1(b_2K)^{b_3} \quad (51)$$

$$H(I_{ae}) = \frac{1}{a_1 a_3 \exp(a_1(K - k_o))} \quad (52)$$

where  $b_1$ ,  $b_2$ ,  $b_3$ ,  $a_1$ ,  $a_3$  and  $k_o$  are all model parameters to be determined from experimental results.

The function  $\psi(\phi)$  was introduced by Abrahamson to his original model to account for nonproportionality effects. Abrahamson used McDowell's original formulation for the nonproportional state variable  $\phi$  [12]. In later research, McDowell [2] suggested a rate formulation for  $\phi$  as given by equation (23). The authors chose to use equation (23). Abrahamson's definition of  $\psi(\phi)$  has to be changed to the following form:

$$\psi(\phi) = \exp(4\phi) \quad (53)$$

The procedures to follow for the experimental determination of all the model parameters are explained in [5].

### Computer Analysis

A series of computer programs were written to implement the constitutive models just discussed for the axial-torsional plane-stress problem. The objective was to predict the stress-strain response of a thin-walled tubular specimen subjected to cyclic axial-torsional strain-controlled loadings that result in significant plastic deformation. Sotolongo [14] presents the simplified axial-torsional forms of the constitutive models used and the experimentally determined model parameters, modeling functions, and material constants for type 304 stainless steel, which are presented in the appendix.

With the exception of Kreig's model, all models were solved by using Gear's numerical integration algorithm. This guarantees an accurate solution and serves as an objective basis for comparison of the computational advantages or disadvantages of each model.

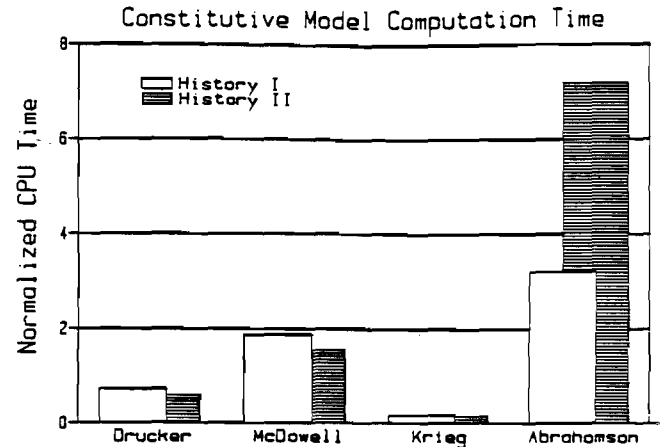


Fig. 2 Constitutive model computational efficiency for Histories I and II

Extensive experimental data on type 304 stainless steel is available in [3]. Figure 1 summarizes the relevant experimental data that will be used in this study to evaluate the material models. The applied shear strain-axial strain curves and the experimentally observed axial stress-axial strain, and shear stress-shear strain responses are shown for the transient hardening case. The tips of the transient shear strain-axial strain plots have been numbered to denote the sequence of loading. History I consists of 25 cycles of nonproportional loading with axial strain amplitude  $\epsilon_a = 0.0041$ , shear strain amplitude  $\gamma_a = 0.0060$ , and constant effective strain rate  $\dot{\epsilon}_{eff} = 0.003 \text{ s}^{-1}$ . Segments 4-1 and 2-3 are proportional; segments 1-2 and 3-4 are nonproportional. It should be noted that the extent of cyclic hardening in the first 25 cycles achieved by introducing nonproportionality effects is greatly (~70 percent) in excess of that for the uniaxial or proportional loading case [11] at the same effective plastic strain range. History II consists of 25 cycles of nonproportional sinusoidal loading with 60-deg phase angle,  $\epsilon_a = 0.0050$ ,  $\gamma_a = 0.0075$ , and  $\dot{\epsilon}_{eff} = 0.001 \text{ s}^{-1}$ . Observe the significant degree of hardening resulting from this severe nonproportional path.

To analyze the computational efficiency of the models, a nondimensional CPU time has been defined as follows:

$$CPU_N = \frac{CPU_A}{t_f} \quad (54)$$

where  $CPU_A$  is the actual CPU time taken by the Cyber 835 to solve the history under consideration and  $t_f$  is the final value of the independent variable (time) for this execution.

**Drucker's Model.** Figure 2 presents the observed computation times for the constitutive models discussed in this study. For this model, computational efficiency seems to be history-independent. The variances in normalized CPU times are rather small given that the histories are quite different. The computation times are considerably smaller than those for McDowell's and Abrahamson's models.

Figure 3 shows that for histories I and II (left and right column plots, respectively), this model greatly underestimates the additional hardening due to nonproportional loading paths. Observe that the material shows a saturated response throughout the 25 cycles. It should be noted that the model parameters for both Drucker's and Kreig's models were determined from a proportional loading history [14] at approximately the same effective total strain range as the two histories considered here. Furthermore, the initial values of dependent variables for all models corresponded to the cyclic response immediately preceding these two histories. Hence, the absence of the additional nonproportional hardening effect in Drucker's model is due to the dependence on only a monotonically increasing scalar parameter,  $W^{pc}$ , coupled with the constants  $\gamma$  and  $\sigma^*$  obtained from a proportional history.

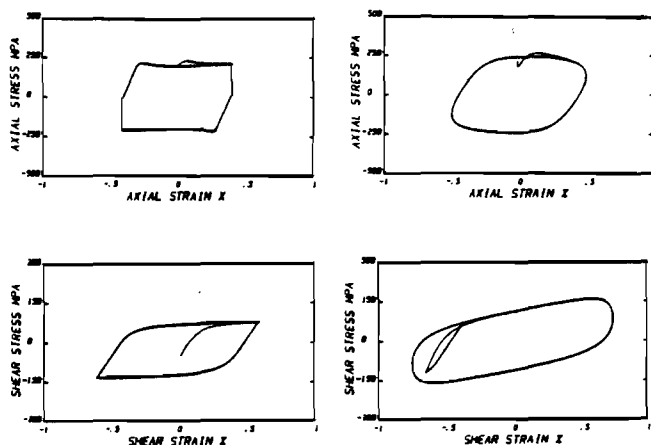


Fig. 3 Numerical solution by Drucker's model for History I (left column) and History II (right column)

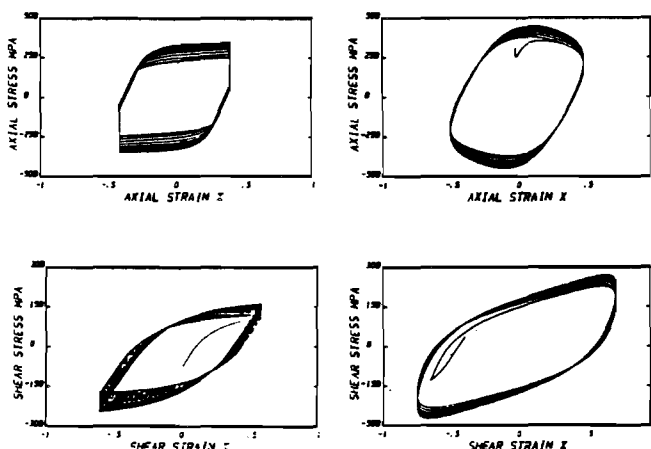


Fig. 4 Numerical solution by McDowell's model for History I (left column) and History II (right column)

The hysteresis loop shapes are predicted incorrectly; the asymptotic plastic modulus is considerably underestimated. The shear plastic strain range is overestimated by about 50 percent.

**McDowell's Model.** As seen from Fig. 2, this model's computational efficiency also seems to be history-independent. However, this model takes about twice as much computational effort compared to Drucker's model. As will be seen, the increased predictive accuracy attained might easily outweigh this disadvantage.

Figure 4 shows the numerical solution predicted by this model. Note that a significant hardening increase due to nonproportionality effects is predicted with sufficient accuracy. The cyclic response saturated within the first 10 cycles of the history. The axial stress-axial strain hysteresis loop shapes and hardening rates are accurately predicted. For the sinusoidal history, although the hardening is correctly predicted, a "flattening" of the shear stress hysteresis loops is observed resulting in an overpredicted plastic shear strain range.

**Krieg's Model.** Krieg's model's execution time is definitely history-independent as shown in Fig. 2. Note the extremely short computation times needed; this is the primary advantage of this model. Since this is the only model solved without using Gear's method, the radial-return algorithm must be responsible for this tremendous decrease in execution time. Note however that this reduction in computation time is accompanied by a sacrifice of predictive accuracy as shown next.

Figure 5 shows the predicted response for these nonproportional histories. Referring to Fig. 3 the reader will realize the many similarities between Drucker's and Krieg's predicted responses for these histories. Thus, the analysis and comments

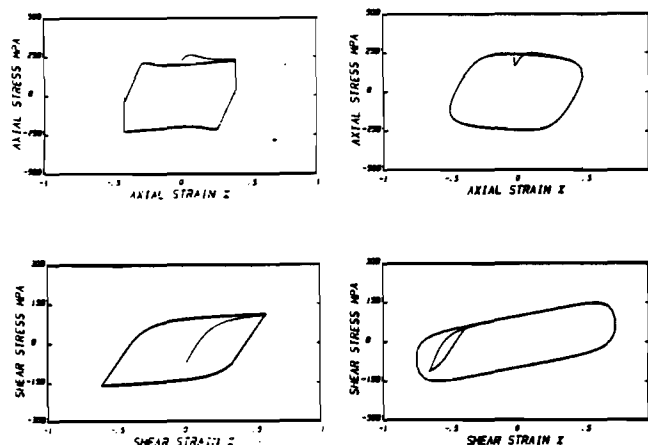


Fig. 5 Numerical solution by Krieg's model for History I (left column) and History II (right column)

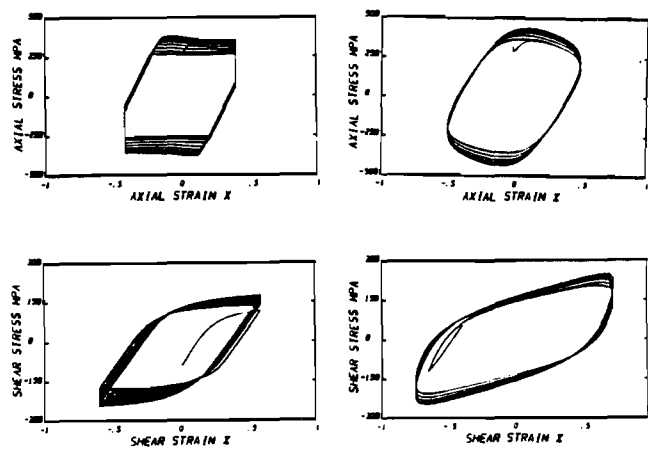


Fig. 6 Numerical solution by Abrahamson's model for History I (left column) and History II (right column)

made for Drucker's model are also valid here. In Krieg's theory, the structure of the isotropic hardening law does not include dependence on the nonproportionality of loading; only dependence on  $W^{pc}$  is included. However, Krieg's model has the advantage of being computationally extremely efficient.

It should be noted that the modification in equation (33) was made to coincide with well-known experimental observations of saturation (or approach to a cyclically stable state) of the cyclic response. It is important to realize that without this modification, isotropic hardening would accumulate unrealistically. With or without the modification, the dependence of cyclic hardening on the current level of nonproportionality [2, 3, 12] cannot be described since the response is implicitly assumed to be equivalent to the uniaxial or proportional case for this model.

**Abrahamson's Model.** Referring to Fig. 2, the reader will immediately note the large differences in CPU<sub>N</sub> as this model is integrated for nonproportional histories. Also, note that this model is extremely inefficient compared to any of the other models discussed. Since this is a generic form of unified creep-plasticity theory, this path-dependence of computational efficiency probably extends to other particular unified theories.

From Fig. 6 it is immediately seen that this model is capable of predicting nonproportional transient hardening rather accurately. Notice the sharp yielding observed in the axial stress response which results in underestimated stresses both during transient hardening and for the stable loop response. "Fattening" of the shear response results in overpredictions of the plastic strain range. The observed hysteresis loops are quite

similar to those of McDowell's model. However, McDowell's model is computationally more efficient, while Abrahamson's is more versatile since it can handle time- and rate-dependent phenomena.

### Discussion of Computer Storage Requirements

In addition to computational time, the relative amount of required computer storage for each model is a consideration. Since all models share stress, strain, backstress, and plastic strain (for fatigue analysis or cumulative deformation) as common variables, only the additional evolutionary state variables associated with each model are enumerated. Also, model constants are not compared since they would be common to all integration points in a stress analysis. The number of storage arrays stated applies to the axial-torsional subspace, but relative comparisons can be extended to higher dimensional stress spaces. In the axial-torsional subspace, only two independent components of  $\alpha$ ,  $\epsilon^p$ ,  $\alpha^*$ , or  $\alpha^p$  are necessary [2-3].

Drucker's model requires only one additional storage array for  $W^p$ . McDowell's model requires 9 ( $\alpha^*$ ,  $R$ ,  $R^*$ ,  $\kappa$ ,  $\phi$ ,  $\alpha^p$ ,  $q$ ) and Abrahamson's requires 2 ( $K$ ,  $\phi$ ). Kreig's model requires two additional storage arrays for  $W^p$  and  $L_n$ . For fair comparison, it should be noted that formulation of memory of plastic strain range, found in McDowell's model, is not represented in the other three models, nor in two-surface theory in general [6-8]. Neither is evolution of the asymptotic modulus. Hence, disregarding  $\alpha^p$ ,  $q$  and  $\kappa$ , which do not significantly alter the predictive accuracy for the loading cases considered, McDowell's model requires only five additional storage arrays. Likewise, inclusion of nonproportional isotropic hardening effects in Drucker's or Kreig's models to match experimental observations [5] would result in one more state variable (e.g.,  $\phi$ ). It must be added that the Mroz kinematic hardening rule found in McDowell's model has been shown to be more accurate for nonproportional loading than the Ziegler rule used in Drucker's formulation [2, 3, 14-16]. Also, the modulus function in the flow rule is more aptly described by a Mroz-type definition [16].

Abrahamson's model offers the best combination of accuracy and minimal storage requirements, at the expense of excess computational time and difficult experimental determination of constants and functions necessary due to the highly nonlinear coupling of the unified creep-plasticity equations. Drucker's model has predictive capability very similar to that of Kreig's model, but is not as efficient. Both Kreig's and Drucker's models do not predict the nonproportional response as accurately as McDowell's or Abrahamson's models. McDowell's model requires the most storage, but is most accurate for nonproportional loading and is less numerically stiff than Abrahamson's model.

Hence, it is apparent that gains in predictive accuracy may be accompanied by loss of numerical efficiency and ease of experimental characterization, and vice versa.

### Conclusions and Recommendations

Every model has been shown to have particular advantages and disadvantages that make them suitable or not suitable at all for specific types of applications. Thus, these models can be best evaluated and classified based on their appropriateness to solve specific types of problems which have particular priorities on the computational accuracy and efficiency required. From the facts just presented, the following recommendations can be made:

1 A simple, single-surface model (e.g., Drucker's model) should only be used for proportional loading when a relatively accurate and inexpensive solution is needed. It should not be used for modeling of nonproportional loading histories.

2 More complex, two-surface models (e.g., McDowell's model) should be used when an accurate representation of the

material response for proportional and nonproportional, multiaxial loading is required and concern with the computational costs involved is not critical.

3 A simple, single-surface model with Radial-Return Integration Algorithm (e.g., Kreig's model) should only be used as a very inexpensive but approximate way of solving the proportional, multiaxial, cyclic plasticity problem. It should not be used when nonproportionality effects are considerable.

4 Unified theories (e.g., Abrahamson's model) should be used for relatively accurate solutions under proportional and nonproportional straining. If low computational costs are of major concern, this model should not be used.

5 The two-surface model of McDowell and state variable theory of Abrahamson predict the hysteresis response most accurately, yet errors in effective plastic strain range (related to fatigue life prediction) are still seen to be as high as 50 percent under "steady-state" conditions. Work is continuing [16] to determine the source of these errors in the flow and hardening rules.

6 Selection of a material model structure obviously requires consideration of compromises between predictive accuracy, numerical integration efficiency, experimental characterization required, and required computer storage.

### Acknowledgments

The support of this work by a grant from the National Science Foundation (NSF Grant No. MEA-8404080) is gratefully acknowledged.

### References

- 1 Drucker, D. C., and Palgen, L., "On Stress-Strain Relations Suitable for Cyclic and Other Loading," *ASME Journal of Applied Mechanics*, Vol. 48, 1981, pp. 479-485.
- 2 McDowell, D. L., "A Two-Surface Model for Transient Nonproportional Cyclic Plasticity: Part I—Development of Appropriate Equations," *ASME Journal of Applied Mechanics*, Vol. 52, June 1985, pp. 298-302.
- 3 McDowell, D. L., "A Two-Surface Model for Transient Nonproportional Cyclic Plasticity: Part II—Comparison of Theory with Experiments," *ASME Journal of Applied Mechanics*, Vol. 52, June 1985, pp. 303-308.
- 4 Kreig, R. D., and Key, W. S., "Implementation of a Time-Independent Plasticity Theory into Structural Computer Programs," *Constitutive Equations in Viscoplasticity: Computational and Engineering Aspects*, eds., J. A. Stricklin and K. J. Saczalski, AMD-20, ASME, New York, 1976, pp. 125-137.
- 5 Abrahamson, T. E., "Modeling the Behavior of Type 304 Stainless Steel With a Unified Creep-Plasticity Theory," Ph.D. thesis, Department of Mechanical and Industrial Engineering, University of Illinois at Urbana-Champaign, 1983.
- 6 Dafalias, Y. F., and Popov, E. P., "A Model of Nonlinearly Hardening Materials for Complex Loading," *Acta Mechanica*, Vol. 21, 1975, p. 173-192.
- 7 Dafalias, Y. F., "The Concept and Application of the Bounding Surface in Plasticity Theory," *Physical Non-Linearities in Structural Analysis*, IUTAM Symposium, eds. Hult and Lemaitre, Senlis, France, May 27-30, 1980.
- 8 Kreig, R. D., "A Practical Two-Surface Plasticity Theory," *ASME Journal of Applied Mechanics*, Vol. 42, Sept. 1975, pp. 641-646.
- 9 Mroz, Z., "An Attempt to Describe the Behavior of Metals Under Cyclic Loads Using a More General Workhardening Model," *Acta Mechanica*, Vol. 7, 1967, pp. 199-212.
- 10 Hunsaker, B., Vaughan, D. K., and Stricklin, J. A., "A Comparison of the Capability of Four Hardening Rules to Predict a Material's Plastic Behavior," *ASME JOURNAL OF PRESSURE VESSEL TECHNOLOGY*, Feb. 1976, pp. 66-74.
- 11 McDowell, D. L., Payne, R. K., Stahl, D., and Antolovich, S. D., "Effects of Nonproportional Cyclic Loading Histories on Type 304 Stainless Steel," *Proceedings of the International Spring Meeting of Societe Francaise de Metallurgie*, Paris, May 1984, pp. 53-86.
- 12 McDowell, D. L., "Transient Nonproportional Cyclic Plasticity," Report No. 107, Design and Materials Division, Department of Mechanical and Industrial Engineering, University of Illinois at Urbana-Champaign, June 1983.
- 13 Hughes, T. J. R., "Numerical Implementation of Constitutive Models: Rate-Independent Deviatoric Plasticity," *Workshop on the Theoretical Foundation for Large-Scale Computations of Nonlinear Material Behavior*, Northwestern University, Evanston, Ill., October 24-26, 1983.
- 14 Sotolongo, W., "On the Numerical Implementation of Cyclic Elastoplastic Material Models," M.S. thesis, School of Mechanical Engineering, Georgia Institute of Technology, Feb. 1985.
- 15 Lamba, H. S., and Sidebottom, O. M., "Cyclic Plasticity for Nonproportional Paths: Part 2—Comparison with Predictions of Three-Incremental Plasticity Models," *ASME Journal of Engineering Materials and Technology*, Vol. 100, 1978, pp. 104-111.



## APPENDIX

### Drucker's Model

#### Miscellaneous Equations:

$$A = \frac{B}{(\sigma^*)^{2N}}$$

#### Model Parameters:

$$\begin{aligned} \gamma &= 0.17 & W_o &= 5.9 \text{ MPa} \\ N &= 1.35 & A &= 2.6 \times 10^{-10} \\ k &= 148.1 \text{ MPa} & \text{Units: } B &= \text{MPa}^{-3} \\ & & \sigma^* &= \text{MPa} \end{aligned}$$

#### Material Constants:

For type 304 stainless steel in the initially annealed state:  
 $\nu = 0.29$   
 $G = 75.1 \text{ GPa}$

### McDowell's Model

#### Material Modeling Functions:

For type 304 stainless steel at room-temperature:

$$\begin{aligned} \bar{R}(0, q) &= 171 + (q - 0.005)4000 \text{ MPa} \\ \bar{R}^*(0, q) &= 295 + (q - 0.005)20690 \text{ MPa} \\ \bar{\kappa}(0, q) &= 4370 - (q - 0.005)196100 \text{ MPa} \\ \bar{R}(1, q) &= 405 \text{ MPa} \\ \bar{R}^*(1, q) &= 565 \text{ MPa} \\ \bar{\kappa}(1, q) &= 4046 \text{ MPa} \\ \Lambda(q) &= 0.6q \end{aligned}$$

$$\psi = u(\bar{R}(\phi, q) - R)$$

$$\psi^* = u(\bar{R}^*(\phi, q) - R^*)$$

$$\psi_\kappa = u(\kappa - \bar{\kappa}(\phi, q))$$

where  $u(x) \equiv$  Heaviside function of  $x$  and  $\phi_{\text{limit}} = 0.02$ .

#### Material Constants:

For type 304 stainless steel in the initially annealed state:

$$\begin{aligned} \mu &= 10.0 & \nu &= 0.29 \\ \mu^* &= 50.0 & G &= 75.1 \text{ GPa} \end{aligned}$$

### Krieg's Model With Radial-Return Algorithm

#### Model Parameters:

$$\begin{aligned} W_o &= 5.9 \text{ MPa} & \gamma &= 0.35 \\ H' &= 4370 \text{ MPa} \end{aligned}$$

#### Material Constants:

For type 304 stainless steel in the initially annealed state:

$$\begin{aligned} G &= 75.1 \text{ GPa} \\ E &= 193.8 \text{ GPa} \end{aligned}$$

### Abrahamson's Model

#### Model Parameters:

For 304 stainless steel at 300°K:

$$\begin{aligned} a &= 5 \times 10^{-4} \text{ s}^{-1} & c &= 1.6 \times 10^{-8} \text{ MPa}^{-2} \text{ s}^{-1} \\ a_1 &= 0.002 \text{ MPa}^{-1} & d_1 &= 58.5 \times 10^{-6} \text{ MPa}^{-1} \\ a_3 &= 22.8 \text{ MPa} & m &= 2.0 \\ B &= 2.0 & p &= 30.0 \\ b_1 &= 0.0975 \text{ MPa} & k_o &= 126 \text{ MPa} \\ b_2 &= 0.01 \text{ MPa}^{-1} & \phi_{\text{limit}} &= 0.02 \\ b_3 &= 5.89 & d_2 &= 0.045 \text{ MPa}^{-1} \end{aligned}$$

#### Material Constants:

For type 304 stainless steel at 300°K:

$$\begin{aligned} G &= 71.1 \text{ GPa} & \nu &= 0.29 \\ E &= 173.9 \text{ GPa} & \mu^* &= 50.0 \end{aligned}$$

337-343

Analysis  
Methods  
of New

based on  
141-1157

model for  
reculation

n elastic  
9 (1981).  
n, Com-  
it analy-  
Comput.

ettram,  
stole by  
l, 60-67

ogeneity  
ll. math.

proved  
entire  
confer-

ility. J.  
94-195

and C.  
titutive

Jilbert,  
nsional  
e 210,

ties of  
ech. 6,

biaxial  
rdium.

of the

earing  
rcular  
ength.

of the  
ted by  
, pp.  
).

sment  
y and

.E. J.

defor-

tinua.

etric  
l-399

s, Jr.  
wall  
ence

## ON THE NUMERICAL INTEGRATION OF ELASTO-PLASTIC CONSTITUTIVE MODEL STRUCTURES FOR NONPROPORTIONAL CYCLIC LOADING

W. SOTOLONGO† and D. L. McDOWELL‡

School of Mechanical Engineering, Georgia Institute of Technology, Atlanta, GA 30332, U.S.A.

(Received 12 April 1985)

**Abstract**—The classical Runge-Kutta method with Gill coefficients, a non-iterative Adams predictor-corrector method, an Euler's method with automatic step-size control, an iterative Adams predictor-corrector method with automatic step-size control and Gear's method are the numerical solution algorithms considered in this study. Their computational accuracy and efficiency are evaluated for two cases of axial-torsional loading with transient, nonproportional, cyclic plasticity. The constitutive equations implemented include a modified classical single-surface theory, a two-surface theory and a unified creep-plasticity or state variable theory.

### NOTATION

$f$	yield (stress) surface
$k$	shear yield strength
$s$	deviatoric stress tensor
$W^{pc}$	accumulated plastic work
$\alpha$	center of yield (stress) surface in deviatoric stress space
$\alpha_{eff}$	uniaxial equivalent value of $\alpha$
$\epsilon, \epsilon^e, \epsilon^p$	total, elastic and plastic strain tensors, respectively
$\epsilon_{eff}$	uniaxial equivalent value of $\epsilon$
$\sigma$	stress tensor
$\sigma_{eff}$	uniaxial equivalent value of $\sigma$
$\phi$	current measure of nonproportionality
$\phi_{limit}$	threshold value of $\phi$

#### Drucker's model

$B, N, W_0, \gamma, \sigma^*$	experimentally determined model parameters
$R$	axial yield strength
$\bar{\sigma}$	plastic modulus function normalizing stress

#### McDowell's model

$f^*$	limit surface function
$F$	plastic strain memory surface
$g(x)$	$g(x) = 1$ for $x = 0$ , $g(x) = x$ for $x \neq 0$
$\beta$	plastic modulus function
$H(F)$	$H(F) = 1$ for $F = 0$ , $H(F) = 0$ for $F < 0$
$J$	instantaneous measure of nonproportionality
$n, n^*$	yield and strain memory surface unit normals, respectively
$q$	strain memory surface radius
$R, R^*$	yield and limit surface radii, respectively
$\bar{R}, \bar{R}^*$	cyclically stable values of $R$ and $R^*$
$s^*$	corresponding deviatoric stress tensor in limit surface
$u(x)$	Heaviside function of $x$
$\alpha^*$	center of limit surface in deviatoric stress space
$\alpha^p$	center of strain memory surface in plastic strain space
$\Gamma$	scalar function in evolution of $q$
$\epsilon_1, \epsilon_3$	current maximum and minimum principal strains, respectively

$(\epsilon)_1, (\epsilon)_3$	current maximum and minimum principal strain rates, respectively
$\kappa, \bar{\kappa}$	asymptotic plastic modulus and corresponding cyclically stable value
$\Lambda(q)$	memory loss-rate function
$\mu, \mu^*, \dot{\mu}_z$	rate constants
$\psi, \psi^*, \psi_\kappa$	admissibility functions in isotropic hardening rules

#### Abrahamson's model

$a_1, a_3, b_1, b_2, b_3, B, c, d_1, d_2, k_0, m, p, h_1, r_1$	experimentally determined model parameters
$H(I_{II})$	isotropic hardening rate adjusting function
$K$	stress surface radius
$Q$	instantaneous measure of nonproportionality
$w_2(K)$	recovery term in isotropic hardening function
$\epsilon^a$	inelastic strain tensor
$\epsilon_{eff}^a$	uniaxial equivalent value of $\epsilon^a$
$\psi(\phi)$	nonproportional hardening function in isotropic hardening rule

### INTRODUCTION

Transient, nonproportional cyclic plasticity problems frequently arise in automobile, aerospace and nuclear industries when mechanical components are designed to operate under stringent conditions. A balance of predictive accuracy and computational efficiency must be achieved to have success in the numerical solution of this difficult problem.

The objective of this study is to evaluate five numerical solution schemes for three generic forms of cyclic plasticity models with special attention to changes in the numerical behavior of these models when integrating proportional versus nonproportional histories. The significant coupling between material models and numerical solution schemes will be investigated in this work. This study is intended to help guide plasticity model users in the selection of

† Graduate Research Assistant.

‡ Assistant Professor. To whom all correspondence should be addressed.

the most appropriate combination of material model type and integration routine to be used for specific problems in the general area of nonproportional, multiaxial, cyclic plasticity. When dealing with structural cyclic plasticity problems via finite element analysis, a scheme which reduces time spent integrating constitutive equation subroutines by 50% can mean thousands of dollars in savings.

### CONSTITUTIVE MODEL STRUCTURES

The numerical behavior of constitutive models is determined by the structure of their equations. Three generic forms of constitutive models for cyclic plasticity will be discussed in this study. Drucker's model represents the 'simple' kinematic-isotropic, single-surface modified classical theories. McDowell's model is representative of the 'complex' two-surface theories which are a specialization of multiple loading surface theories. Abrahamsons' model is an application of a unified creep-plasticity theory to the cyclic plasticity problem. Extensive discussions of each of the models and references to models of the same generic forms are available in [1-4]; the two-surface theories and state variable theories have been shown to have capability to model nonproportional cyclic loading relatively accurately. The axial-torsional subspace forms and the experimentally determined modeling functions and parameters for each of the models are presented in [5] for type 304 stainless steel. It is not the intent of this investigation to evaluate the predictive capability of these three particular constitutive models; instead, the goal is to evaluate the efficiency of integration schemes for each of the generic structures represented by these models as a function of the nonproportionality of the loading history. Relative changes in the efficiency of integration of each of these model structures in going from proportional to nonproportional loading is particularly interesting. In many cases, one of these model structures would be selected by the numerical stress analyst who would make the choice of temporal integration scheme. Consideration of the number of model constants, parameters and computer storage requirements would be made during the selection of material model; hence, these factors are viewed as secondary in the present paper. A summary of the equations for each model will now be presented. A summary of the parameters and model constants for type 304 stainless steel at room temperature are given in the Appendix.

#### Drucker's model

##### Yield surface:

$$f = \frac{1}{2}(s - \alpha) : (s - \alpha) - \frac{R^2}{3} = 0 \quad (1)$$

##### Flow rule:

$$\dot{\epsilon}^p = B \left( \frac{J_2}{\bar{\sigma}^2} \right)^N (s - \alpha) [(s - \alpha) : \dot{s}] \quad \text{if } f = 0 \text{ and } \dot{\sigma} : (\partial f / \partial \sigma) \geq 0 \quad (2)$$

$$\dot{\epsilon}^p = 0 \text{ otherwise} \quad (3)$$

##### Isotropic hardening functions:

$$J_2 = \frac{1}{2} s : s \quad (4)$$

$$\bar{\sigma} = \sigma^* \left[ 1 + \gamma \exp \left( - \frac{W^p}{W_0} \right) \right] \quad (5)$$

$$W^p = \int_0^t (s - \alpha) : \dot{\epsilon}^p dt \quad (6)$$

##### Kinematic hardening rule:

$$\dot{\alpha} = \frac{1}{2k^2} (s - \alpha) [(s - \alpha) : \dot{s}] \quad (7)$$

#### McDowell's model

##### Yield and limit surfaces:

$$f = \frac{1}{2}(s - \alpha) : (s - \alpha) - R^2 = 0 \quad (8)$$

$$f^* = \frac{1}{2}(s^* - \alpha^*) : (s^* - \alpha^*) - R^{*2} = 0 \quad (9)$$

##### Flow rule:

$$\dot{\epsilon}^p = \frac{1}{\beta} (\dot{s} : n) n \quad (10)$$

##### Yield surface Mroz kinematic hardening rule:

$$\alpha = \frac{[(s - \alpha) : \dot{s} - \frac{2}{3} R \dot{R}](s^* - s)}{(s - \alpha) : (s^* - s)} \quad (11)$$

$$s^* = \alpha^* + (s - \alpha) \frac{R^*}{R} \quad (12)$$

##### Limit surface Prager-Ziegler kinematic hardening rule:

$$\dot{\alpha}^* = \kappa \dot{\eta} n \quad (13)$$

$$\dot{\eta} = (\dot{\epsilon}^p : \dot{\epsilon}^p)^{1/2} = \|\dot{\epsilon}^p\| \quad (14)$$

##### Yield and limit surface isotropic hardening rules:

$$\dot{R} = \mu [\bar{R}(\phi, q) - R] \dot{\eta} \quad (15)$$

$$\dot{R}^* = \mu [\bar{R}^*(\phi, q) - R^*] \dot{\eta} \quad (16)$$

$$\bar{R}(\phi, q) = \phi [\bar{R}(1, q) - \bar{R}(0, q)] + \bar{R}(0, q) \quad (17)$$

$$\bar{R}^*(\phi, q) = \phi [\bar{R}^*(1, q) - \bar{R}^*(0, q)] + \bar{R}^*(0, q) \quad (18)$$

Plastic modulus functions:

$$\beta = \kappa \left[ 1 + \frac{91960}{\kappa} \left( \sinh \left\{ \frac{\|s^* - s\|}{\|s_0^* - s_0\|} \right\} \right)^{1.1} \right] \quad (19)$$

(2)

$$\dot{\kappa} = \mu [\bar{\kappa}(\phi, q) - \kappa] \dot{\psi}_\kappa \dot{\eta} \quad (20)$$

(3)

$$\bar{\kappa}(\phi, q) = \phi [\bar{\kappa}(1, q) - \bar{\kappa}(0, q)] + \bar{\kappa}(0, q) \quad (21)$$

Nonproportional hardening state variables:

(4)

$$J = \left| \frac{\frac{d}{dt}(\epsilon_1 - \epsilon_3)}{g[(\dot{\epsilon})_1 - (\dot{\epsilon})_3]} \right| \quad (22)$$

(5)

(6)

$$\dot{\phi} = \mu^*(1 - J - \phi) \dot{\eta} u(1 - J - \phi_{\text{limit}}) \quad (23)$$

Strain memory surface:

(7)

$$F = \frac{2}{3}(\epsilon^p - \alpha^p) : (\epsilon^p - \alpha^p) - q^2 = 0 \quad (24)$$

Strain memory surface kinematic hardening rule:

$$\dot{\alpha}^p = \frac{H(F)}{2} (\dot{\epsilon}^p : n^*) n^* \quad (25)$$

Strain memory surface isotropic hardening rule:

(8)

$$\dot{q} = [\frac{1}{2} H(F) \Gamma \sqrt{\frac{2}{3}} - \Lambda(q)] \dot{\eta} \quad (26)$$

(9)

$$\Gamma = n^* : n + \sqrt{6} \Lambda(q) \quad (27)$$

Abrahamson's model

(10)

Uniaxial equivalent values:

$$\sigma_{\text{eff}} = [\frac{3}{2}(s - \alpha) : (s - \alpha)]^{1/2} \quad (28)$$

$$\alpha_{\text{eff}} = (\frac{3}{2} \alpha : \alpha)^{1/2} \quad (29)$$

(11)

Flow rule:

(12)

$$\dot{\epsilon}^n = \frac{3}{2} \left( \frac{\dot{\epsilon}_{\text{eff}}^n}{\sigma_{\text{eff}}} \right) (s - \alpha) \quad (30)$$

tening

$$\dot{\epsilon}_{\text{eff}}^n = a \left( \frac{\sigma_{\text{eff}}}{K} \right)^p \quad (31)$$

(13)

(14)

Kinematic hardening rule:

$$\dot{\alpha} = h_2(\alpha_{\text{eff}}) \dot{\epsilon}^n - \frac{r_2(\alpha_{\text{eff}})}{B^p} \alpha \quad (32)$$

(15)

(16)

(17)

(18)

$$h_2(\alpha_{\text{eff}}) = \begin{cases} \frac{\exp(-d_2 \alpha_{\text{eff}})}{d_1} & \text{if } \dot{\epsilon}^n : \alpha \geq 0 \\ \frac{1}{d_1} & \text{if } \dot{\epsilon}^n : \alpha < 0 \end{cases} \quad (33)$$

$$r_2(\alpha_{\text{eff}}) = c(\alpha_{\text{eff}})^m \quad (34)$$

Isotropic hardening rule:

$$\dot{K} = \frac{H(I_u)}{[\psi(\phi)]^{1.2}} [\psi(\phi) \alpha_{\text{eff}} - w_2(K)] \dot{\epsilon}_{\text{eff}}^n \quad (35)$$

$$w_2(K) = b_1(b_2 K)^{b_3} \quad (36)$$

$$H(I_u) = \frac{1}{a_1 a_3 \exp[a_1(K - k_0)]} \quad (37)$$

Nonproportional hardening state variables:

$$\psi(\phi) = \exp(4\phi) \quad (38)$$

where  $\phi$  is given by equation (23).

#### NUMERICAL INTEGRATION TECHNIQUES

In general, the problem is to solve an initial value problem given by a system of ordinary differential equations (system of ODEs) and the prescribed initial conditions. Mathematically this can be represented as

$$\dot{X} = F(X, t) \quad (39)$$

$$X(0) = X_0 \quad (40)$$

where  $t$  is the independent variable,  $X$  is the vector of dependent variables, and  $F$  is the vector of functions relating them.

In time- and rate-independent strain-controlled plasticity, the independent variable is the total strain tensor  $\epsilon$ . However, the authors decided to use time as the independent variable in this study since the unified creep-plasticity model (Abrahamson's) is rate- and time-dependent. This study concentrates on integration techniques suitable for accurate solution of general constitutive equations for cyclic plasticity, including multiple surface and viscoplastic theories. It should be noted that the commonly used radial-return algorithm for integrating time- and rate-independent cyclic plasticity equations was also studied in [5]; this algorithm was found to be extremely efficient for integration of combined linear kinematic-isotropic hardening within the context of a single surface theory very similar to that of Drucker *et al.* [1]. Such a theory, though, was not found to predict experimental results for cyclic nonproportional loading as accurately as the more complex multiple surface and unified creep-plasticity theories. No effort is made in this work to generalize the radial-return scheme to two-surface theory with nonlinear hardening.

Classical Runge-Kutta method with Gill coefficients

There is a whole family of Runge-Kutta methods but of particular interest is the version as modified by Gill [6]. The step-by-step procedure for the solution of a system of ODEs, denoting  $X$  at time  $t = t^n$  by  $X(t^n) = X^n$ , is given by:

$$q_0 = \begin{cases} 0 & \text{for } t^n = 0 \\ q_4^{n-1} & \text{for } t^n > 0 \end{cases} \quad (41)$$

$$\mathbf{k}_1 = h\mathbf{F}(\mathbf{X}^n, t^n) \quad (42)$$

$$\mathbf{X}_1 = \mathbf{X}^n + \frac{1}{2}(\mathbf{k}_1 - 2\mathbf{q}_0) \quad (43)$$

$$\mathbf{q}_1 = \mathbf{q}_0 + \frac{1}{2}(\mathbf{k}_1 - 2\mathbf{q}_0) - \frac{1}{2}\mathbf{k}_1 \quad (44)$$

$$\mathbf{k}_2 = h\mathbf{F}\left(\mathbf{X}_1, t^n + \frac{h}{2}\right) \quad (45)$$

$$\mathbf{X}_2 = \mathbf{X}_1 + (1 - \sqrt{\frac{1}{2}})(\mathbf{k}_2 - \mathbf{q}_1) \quad (46)$$

$$\mathbf{q}_2 = \mathbf{q}_1 + 3(1 - \sqrt{\frac{1}{2}})(\mathbf{k}_2 - \mathbf{q}_1) - (1 - \sqrt{\frac{1}{2}})\mathbf{k}_2 \quad (47)$$

$$\mathbf{k}_3 = h\mathbf{F}\left(\mathbf{X}_2, t^n + \frac{h}{2}\right) \quad (48)$$

$$\mathbf{X}_3 = \mathbf{X}_2 + (1 + \sqrt{\frac{1}{2}})(\mathbf{k}_3 - \mathbf{q}_2) \quad (49)$$

$$\mathbf{q}_3 = \mathbf{q}_2 + 3(1 + \sqrt{\frac{1}{2}})(\mathbf{k}_3 - \mathbf{q}_2) - (1 + \sqrt{\frac{1}{2}})\mathbf{k}_3 \quad (50)$$

$$\mathbf{k}_4 = h\mathbf{F}(\mathbf{X}_3, t^n + h) \quad (51)$$

$$\mathbf{X}^{n+1} = \mathbf{X}_3 + \frac{1}{6}(\mathbf{k}_4 - 2\mathbf{q}_3) \quad (52)$$

$$\mathbf{q}_4 = \mathbf{q}_3 + \frac{1}{2}(\mathbf{k}_4 - 2\mathbf{q}_3) - \frac{1}{2}\mathbf{k}_4 \quad (53)$$

where superscripts  $n-1$ ,  $n$ ,  $n+1$  refer to values at the previous time step, at the present time step, and at the desired time step increment, respectively. Note that  $h$  is the time-step size and the  $\mathbf{k}_i$ ,  $\mathbf{q}_i$ ,  $\mathbf{X}_i$  are intermediate values that do not have to be stored.

A good check on the truncation error can be obtained by keeping track of the values of  $\mathbf{q}_i^*$  at each time step [7]. Thus, the error control criterion used could be of the form

$$|\mathbf{q}_i^*| \leq h^{10} \quad t \geq 0. \quad (54)$$

Essentially, condition (54) determines the initial step-size chosen in the solution of a particular set of ODEs. Because this is a fixed step-size method,  $h$  will be constant for  $t \geq 0$ .

#### Euler's method with automatic step-size control

Euler type methods are the simplest numerical integration techniques used in the solution of systems of ODEs. According to Kumar *et al.* [8], a reasonable step-size control algorithm would involve either doubling or halving the step-size as required by some suitable error criterion and the prescribed error limits. The step-size will be controlled based on a predicted step-size  $h_p$  and the actual step-size  $h$ . Thus, for the  $n$ th step the procedure would be as follows:

1. If  $E > E_{\max}$ , replace  $h_p$  by  $h_p/2$  and recompute  $E$ .
2. If  $E \leq E_{\max}$ , let  $h = h_p$  and compute  $\mathbf{X}^{n+1}$ .
3. If  $E_{\min} \leq E \leq E_{\max}$ , let  $h_p = h$ .
4. If  $E \leq E_{\min}$ , let  $h_p = 2h$ .

$E_{\max}$  and  $E_{\min}$  are the prescribed error limits, and  $E$  is a suitable error criterion chosen by the user.

The basic Euler's method can be expressed as

$$\mathbf{X}^{n+1} = \mathbf{X}^n + h\mathbf{F}(\mathbf{X}^n, t^n). \quad (55)$$

In this study, the authors chose the following error criterion:

$$E = \left( \sum_{i=1}^N \left[ \frac{h[F_i(\mathbf{X}^n, t^n) - F_i(\mathbf{X}^{n-1}, t^{n-1})]}{X_i^n} \right]^2 \right)^{1/2} \quad (56)$$

where the  $i$  subscript refers to the  $i$ th dependent variable in the system being solved, i.e. the  $i$ th component of  $\mathbf{X}$ . Note that  $N$  is the number of dependent variables in the system.

#### Iterative Adams predictor-corrector method with automatic step-size control

The family of Adams-type predictor-corrector algorithms for solving systems of ODEs is very extensive and widely used. The predictor equation is given by

$$\mathbf{X}_p^{n+1} = \mathbf{X}^n + h\mathbf{F}(\mathbf{X}^n, t^n) \quad (57)$$

where  $h$  is the current time step-size and  $\mathbf{X}_p^{n+1}$  is the predicted vector of dependent variables. The corrector equation is given as

$$\mathbf{X}_c^{n+1} = \mathbf{X}^n + h\mathbf{F}(\mathbf{X}_p^{n+1}, t^{n+1}) - \frac{h}{2} [\mathbf{F}(\mathbf{X}_p^{n+1}, t^{n+1}) - \mathbf{F}(\mathbf{X}^n, t^n)] \quad (58)$$

where  $\mathbf{X}_c^{n+1}$  is the corrected vector of dependent variables.

Kumar *et al.* [8] recommends use of a step-size control algorithm similar to the one described for Euler's method except that an iterative algorithm for the corrector equation must be included. Thus, for the  $n$ th step the procedure would be as follows:

1. If  $E > E_{\max}$ :
  - (a) If  $m \leq m^*$ , let  $\mathbf{X}_p^{n+1} = \mathbf{X}_c^{n+1}$ ,  $m = m + 1$ , and recompute  $\mathbf{X}_c^{n+1}$  and  $E$ ;
  - (b) If  $m > m^*$ , let  $m = 0$ ,  $h_p = h_p/2$ , and recompute  $\mathbf{X}_p^{n+1}$ ,  $\mathbf{X}_c^{n+1}$ , and  $E$ ;
2. If  $E \leq E_{\max}$ , let  $h = h_p$  and compute  $\mathbf{X}^{n+1}$ ;
3. If  $E_{\min} \leq E \leq E_{\max}$ , let  $h_p = h$ ;
4. If  $E \leq E_{\min}$ , let  $h_p = 2h$

where  $m$  is the current number of corrector iterations and  $m^*$  is the maximum number of iterations allowed at a fixed time step-size.

Once convergence of the corrector equation has been achieved or the time step has been significantly reduced to keep the error within desirable bounds,

and  $E$   
r.  
as

(55)

error

(56)

ndent  
e ith  
er of

omatic

ector  
very  
on is

+1 is  
The

(58)

dent

-size  
for  
thm  
hus.  
ows:

and

ute

ons  
ed

ias  
tly  
ds.

the accepted value of the dependent variables at  $t^{n+1}$  becomes

$$\mathbf{X}^{n+1} = \frac{4}{3}\mathbf{X}_c^{n+1} + \frac{1}{3}\mathbf{X}_p^{n+1}. \quad (59)$$

The authors chose the following error criterion:

$$E = \left( \sum_{i=1}^N \left[ \frac{(\mathbf{X}_c^{n+1})_i - (\mathbf{X}_p^{n+1})_i}{(\mathbf{X}_c^{n+1})_i} \right]^2 \right)^{1/2}. \quad (60)$$

#### Non-iterative Adams predictor-corrector method

The non-iterative, explicit versions of Adams predictor-corrector methods are the most widely used for non-stiff to mildly stiff systems of ODEs. Cash [9] presents an extensive list of these methods. The authors selected a version that was shown to have a stability interval of more than twice the interval of absolute stability of any other method in its class.

The method consists of one corrector and two predictor equations. Knowing the initial conditions, the sequence of calculations would be as follows:

$$\mathbf{X}_p^{n+1} = \mathbf{X}^n + h\mathbf{F}(\mathbf{X}^n, t^n) \quad (61)$$

(57)

$$\mathbf{X}_p^{n+2} = \mathbf{X}_p^{n+1} + h\mathbf{F}(\mathbf{X}_p^{n+1}, t^{n+1}) \quad (62)$$

$$\begin{aligned} \mathbf{X}^{n+1} = \mathbf{X}^n + h \left[ \frac{1}{16}\mathbf{F}(\mathbf{X}_p^{n+2}, t^{n+2}) \right. \\ \left. + \frac{3}{8}\mathbf{F}(\mathbf{X}_p^{n+1}, t^{n+1}) + \frac{9}{16}\mathbf{F}(\mathbf{X}^n, t^n) \right] \quad (63) \end{aligned}$$

where superscripts  $n$ ,  $n+1$ , and  $n+2$  refer to values at the beginning of the present time step, at the end of the present time step, and at the end of the next time step respectively. Note the  $h$  is the time step-size (constant) and  $\mathbf{X}_p^{n+1}$  and  $\mathbf{X}_p^{n+2}$  are intermediate predictor values that must be stored.

The authors chose an overall system error estimate of the form

$$E = \left( \sum_{i=1}^N [(\mathbf{X}^{n+1})_i - (\mathbf{X}_p^{n+1})_i]^2 \right)^{1/2}. \quad (64)$$

By determining  $E$ , the appropriate initial time step-size can be chosen for a particular system of ODEs. Note that this time step-size will be kept constant and should correspond to the smallest necessary time step-size for the whole solution interval.

#### Gear's method

Gear's method is the most widely accepted numerical integration technique. It is a multiple-step, implicit, iterative, variable-order, and variable step-size method whose sophistication guarantees an accurate solution for virtually any system. Since it has become the standard ODE solver, the authors decided to use it as the reference solution technique against which all other integration methods will be compared. The mathematical details of this method are lengthy and complicated; for a detailed discussion, the reader is referred to [10].

#### COMPUTER ANALYSIS

The numerical solutions found for the axial-torsional plane-stress problem using the material models and numerical solution algorithms just presented are now described. The objective is to predict, as accurately and as efficiently as possible, the stress-strain response of a thin-walled tubular, type 304 stainless steel specimen subjected to cyclic strain-controlled, axial-torsional loadings that result in significant plastic deformation.

To analyze the computational efficiency of the integration algorithms, a non-dimensional CPU time has been defined as follows:

$$\text{CPU}_N = \frac{\text{CPU}_A}{t_f} \quad (65)$$

where  $\text{CPU}_A$  is the actual execution time for the history under consideration and  $t_f$  is the final value of the independent variable (time) for this run. Plots of the time variations of the axial and shear stress integration errors will also be shown. These errors have been defined as follows:

$$E_a(\%) = \frac{\sigma_a - \sigma_g}{\sigma_{\max}} (100) \quad (66)$$

$$E_s(\%) = \frac{\tau_a - \tau_g}{\tau_{\max}} (100) \quad (67)$$

where  $\sigma_g$  and  $\tau_g$  are the Gear's method solutions for the axial and shear stresses at given axial and shear strains respectively,  $\sigma_a$  and  $\tau_a$  are the corresponding numerical solutions (at the same axial and shear strains) by the method being considered, and  $\sigma_{\max}$  and  $\tau_{\max}$  are the largest values of axial and shear stresses calculated by Gear's method over the input history under consideration.

As previously stated, all the numerical integration techniques will be compared against the solutions calculated using Gear's numerical integration algorithm. Therefore, errors reported in this section are computed with respect to Gear's method solution (percentage of Gear's method solution normalized CPU time), not experimental results. Comparison with experimental results has been performed in other works [2-5]. The purpose of this study is to compare the performance of integration schemes as a function of structure of constitutive equations given the same initial conditions and loading history. To minimize the effects of algorithms for implementation of each constitutive model on computation time (since we want to compare integration schemes), all three sets of constitutive equations were implemented in the same subroutine structure; furthermore, the structures of the constitutive model subroutines were written as similarly as possible. Two input strain histories were used as the basis for these comparisons. History I consisted of three cycles of proportional straining from the initially annealed state with maximum

axial and shear strain amplitudes  $\epsilon_a = 0.0041$  and  $\gamma_a = 0.0060$ , respectively. The effective strain rate was kept constant at  $\dot{\epsilon}_{eff} = 0.003/\text{sec}$ . History II consisted of three cycles of sinusoidal loading with 90 degrees phase angle,  $\epsilon_a = 0.0050$ ,  $\gamma_a = 0.0075$  and  $\dot{\epsilon}_{eff} = 0.001/\text{sec}$ . Figure 4 shows the axial stress-time and the shear stress-time responses predicted for these histories using Gear's numerical integration method with McDowell's, Drucker's and Abrahamson's models. Figure 1 shows the actual values of CPU<sub>N</sub> for all the models using the reference Gear's method. The normalized CPU time seems to be insensitive to input history for McDowell's and Drucker's models. However, note the tremendous increase in execution time for Abrahamson's model when integrating non-proportional history II. So, the computation times for Abrahamson's model are greatly sensitive to the nonproportionality level of the input strain history. The reader must keep in mind this apparent path-dependence of computational efficiency since it will be shown to be an important parameter in the evaluation of the numerical solution algorithms.

#### Runge-Kutta method with Gill coefficients

Figure 2 presents computation times for this numerical method for histories I and II. Observe that for all models in both histories at least 60% reduction in CPU time is achieved compared to Gear's method. Largest computational savings are achieved for McDowell's and Abrahamson's models. Note that due to the large increase in normalized CPU time for Abrahamson's model in history II, the computational savings are in this case about 95%. Evidently, this is a very efficient integration algorithm. Figure 5 shows that axial and shear stress integration errors behave similarly in all cases. Largest errors always occur in regions of initial yielding or just after elastic unloading. Error magnitudes are kept below 1% throughout both histories except for the integration of McDowell's model for history II. It seems that an optimal time step-size was chosen since this method is both efficient and quite accurate compared to Gear's method.

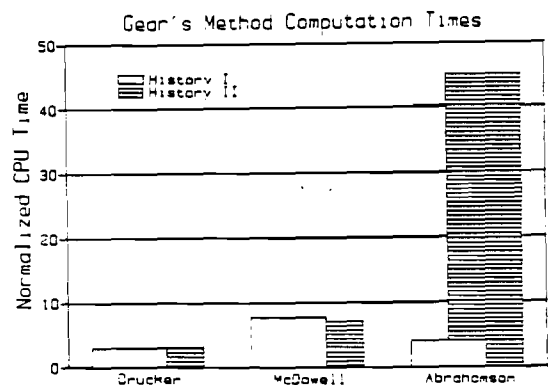


Fig. 1. Constitutive model computation times for histories I and II using Gear's numerical integration algorithm.

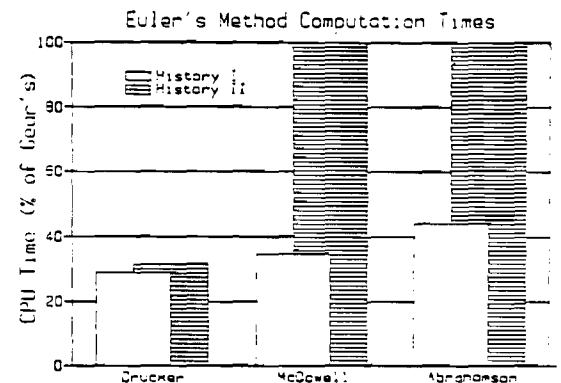
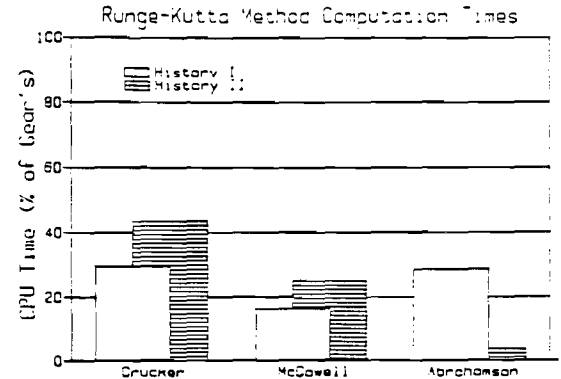


Fig. 2. Constitutive model computation times for histories I and II using Runge-Kutta and Euler's numerical integration algorithms.

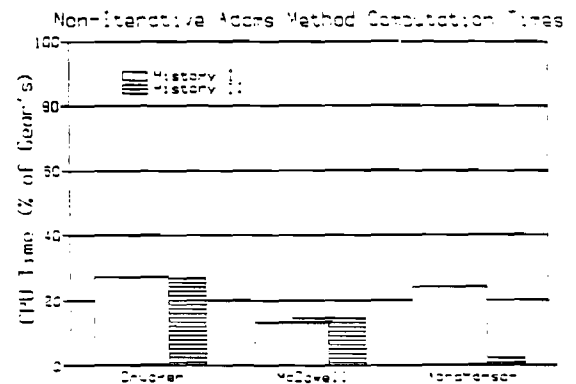
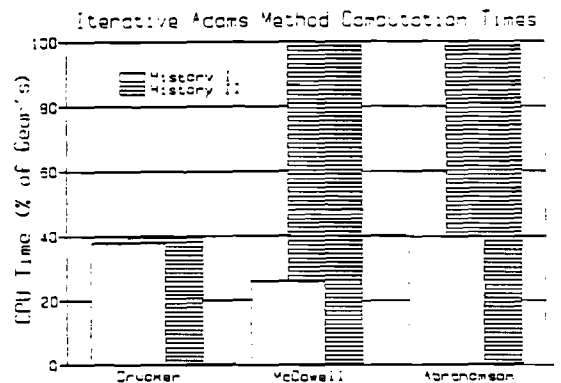


Fig. 3. Constitutive model computation times for histories I and II using iterative and non-iterative Adams predictor-corrector numerical integration algorithms.

*Euler's method with automatic step-size control*

As presented by Fig. 2, this method is quite efficient for history I (proportional history) and extremely inefficient for history II (nonproportional history) for McDowell's and Abrahamson's models. Note that the nonproportional loading CPU time as a percentage of Gear's shown in Fig. 2 for these two models is significantly in excess of 100% (~2400%); the rationale for plotting up to only 100% is that any method less efficient than Gear's is unacceptable. The fact that Euler-type methods are very efficient for proportional straining has been pointed out [8, 11] and is confirmed in this study. However, most analyses have missed the fact that, as shown here, non-proportionality of loading has a tremendous effect in

the efficiency of the numerical solution algorithm. By removing the nonproportional isotropic hardening formulation from the models of McDowell and Abrahamson, it was shown that the large effects of nonproportional straining on integration efficiency remained. McDowell's and Abrahamson's models present highly stiff regions in the integration paths which result in the very large inefficiencies of this method. Figure 6 shows that rather large errors occur for all of the cases discussed; most important of all, these errors seem to accumulate with time. It seems that this method is not very efficient for proportional histories if good accuracy must be achieved. Euler-type methods should not be used for nonproportional histories in 'complex' or unified creep-plasticity theories.

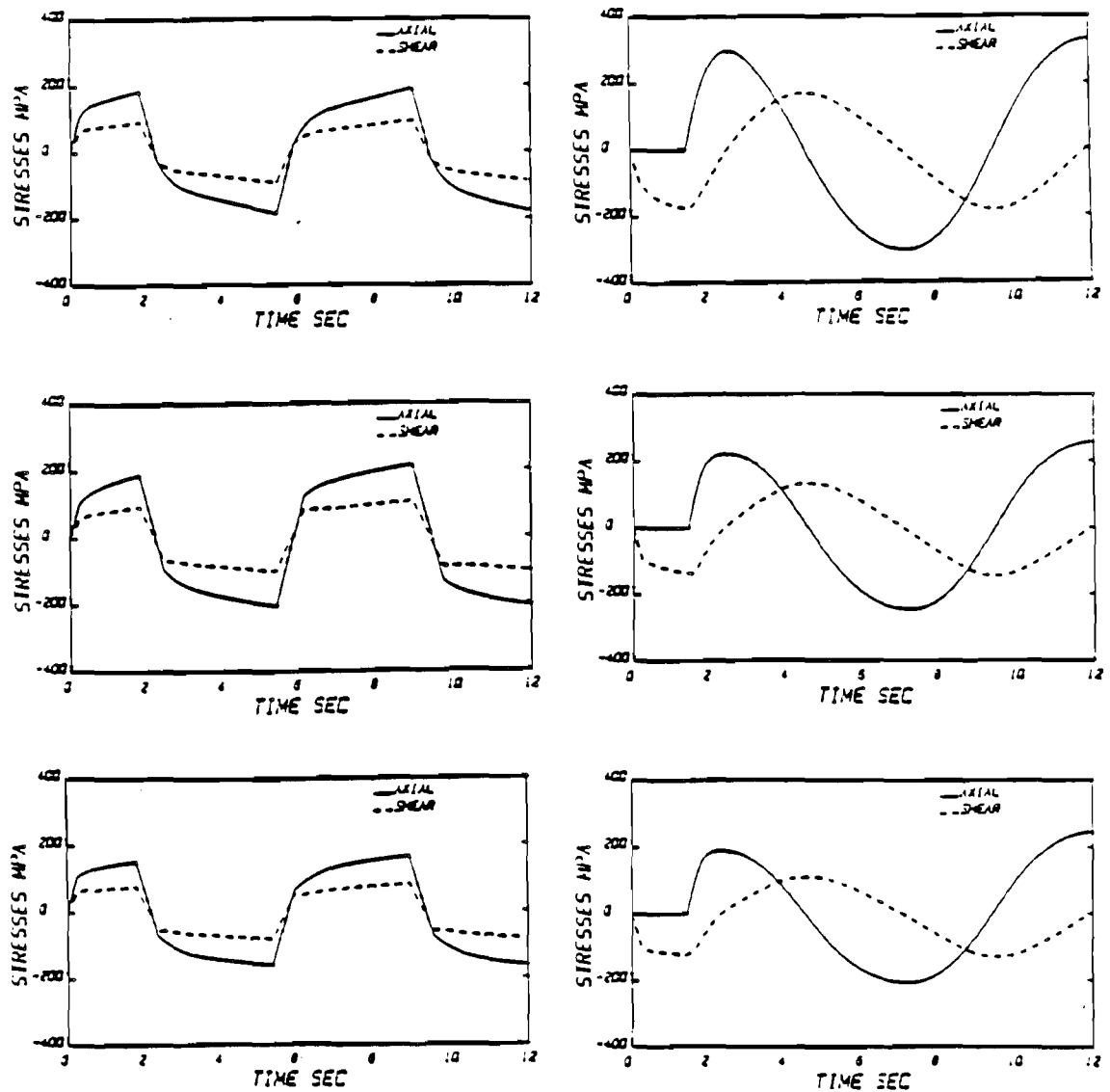


Fig. 4. Axial and shear stress vs time responses for histories I and II integrated by Gear's method. Left column, history I; right column, history II; top row, McDowell's model solution; middle row, Drucker's model solution; bottom row, Abrahamson's model solution.



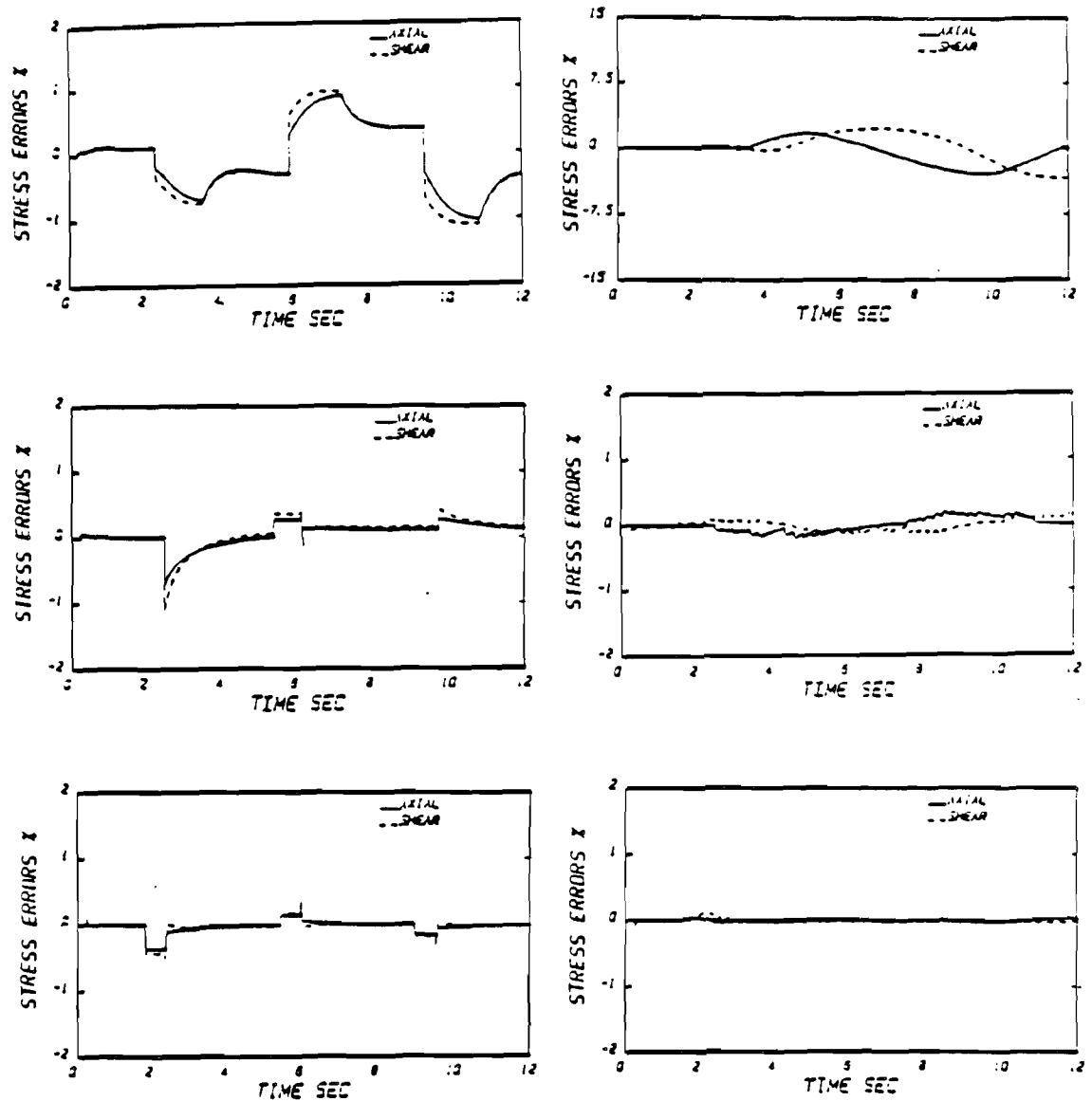


Fig. 5. Axial and shear stress errors vs time responses for histories I and II integrated by Runge-Kutta method. Left column, history I; right column, history II; top row, McDowell's model solution; middle row, Drucker's model solution; bottom row, Abrahamson's model solution.

*Iterative Adams predictor-corrector method with automatic step-size control*

Figure 3 presents the computation times observed for the cases under consideration. Comparing this figure to Fig. 2, it is seen that essentially the same behavior occurs. Figure 7 shows that, however, excellent accuracy is now achieved (comparing to Fig. 6). It seems that even though Euler-type and Iterative Adams methods behave similarly, there is an accuracy advantage to the latter which is probably due to the higher order of the integration equations used. Evidently, this method is efficient and accurate in proportional straining but quite inefficient for nonproportional loading. Once again, this is a point missed in previous analyses [8, 11].

*Non-iterative Adams predictor-corrector method*

Comparing Figs 3 and 8 with Figs 2 and 5, the reader will notice that this method is at least as efficient and as accurate as the Runge-Kutta method. Computational savings of at least 75% are now achieved while keeping integration errors below 1.5% for most of the cases. High-order, fixed step-size methods seem to have a large computational advantage over low-order, variable step-size methods in the integration of nonproportional type loadings. However, fixed step-size methods are inconvenient since some trial and error is needed to determine the optimal initial time step-size to be used in the solution of a particular problem; iteration of solutions might be necessary to determine the optimal step-size.

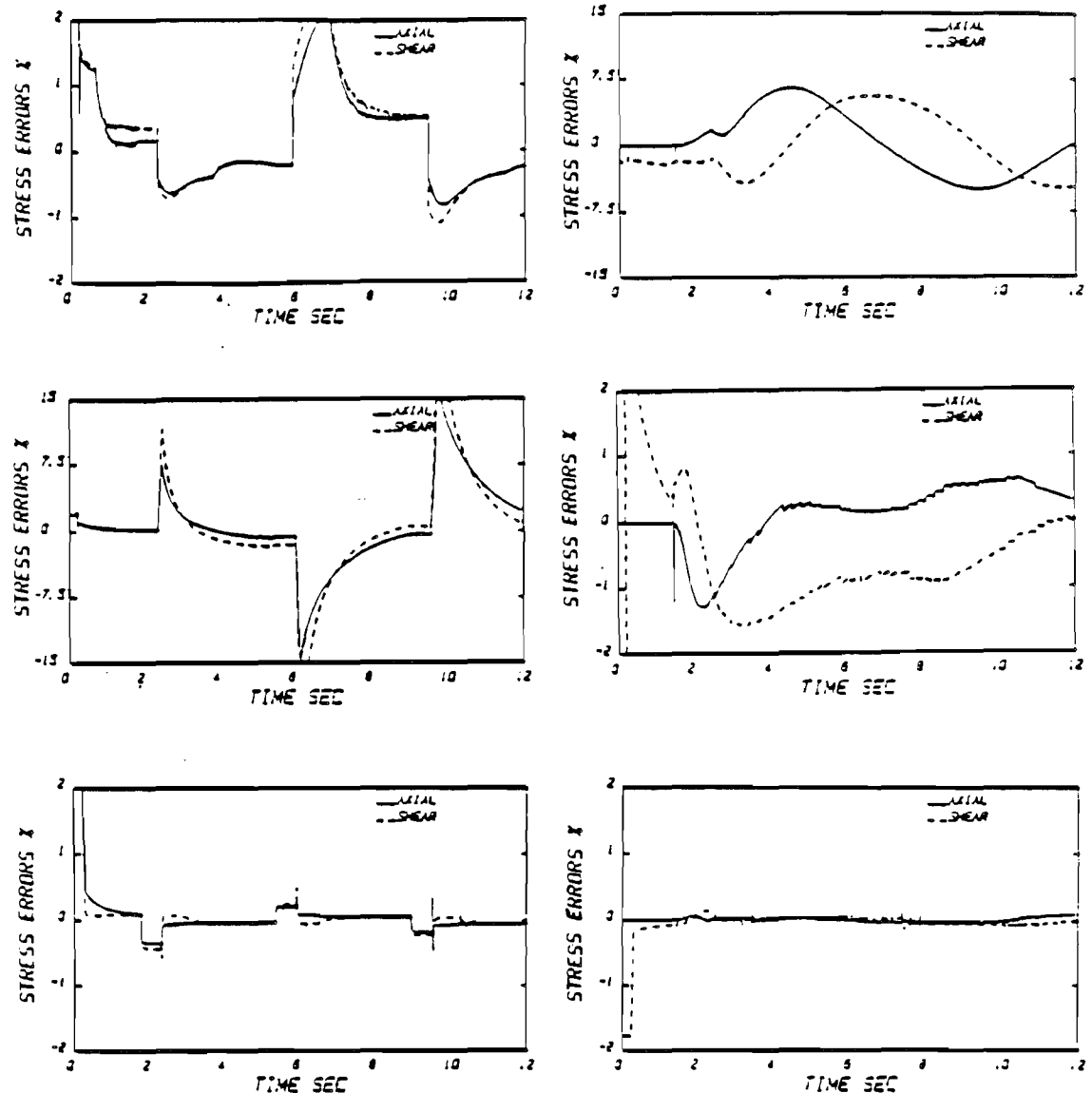


Fig. 6. Axial and shear stress errors vs time responses for histories I and II integrated by Euler's method. Left column, history I; right column, history II; top row, McDowell's model solution; middle row, Drucker's model solution; bottom row, Abrahamson's model solution.

#### DISCUSSION

Though in finite element calculations interaction of the constitutive equation integration algorithm with structural time step-size and associated iteration algorithm is an important issue, independent selection of an efficient constitutive equation integration procedure is also very important. This is especially relevant for the class of nonproportional loading problems treated in the paper.

A number of precedental studies [e.g. 8, 11, 12-15] have recently appeared in the literature regarding various temporal integration algorithms for stiff rate-independent and rate-dependent constitutive equations for cyclic loading. A conclusion of most of these studies is that an Euler method with automatic time

step-size control is most efficient. In these previous works, a key feature is that the loading paths are predominately uniaxial or one-dimensional in stress space. As was shown in this paper for several classes of constitutive models, the Euler method with automatic time step-size control may be quite efficient for uniaxial or proportional loading, but extremely inefficient for stiff constitutive equations under conditions of nonproportional multiaxial loading. For this practically important class of problems, a method with a fixed time step-size is most efficient. Based on this work, it is suggested that more consideration be given to nonproportional loading in evaluation of temporal integration schemes used in constitutive integration subroutines.

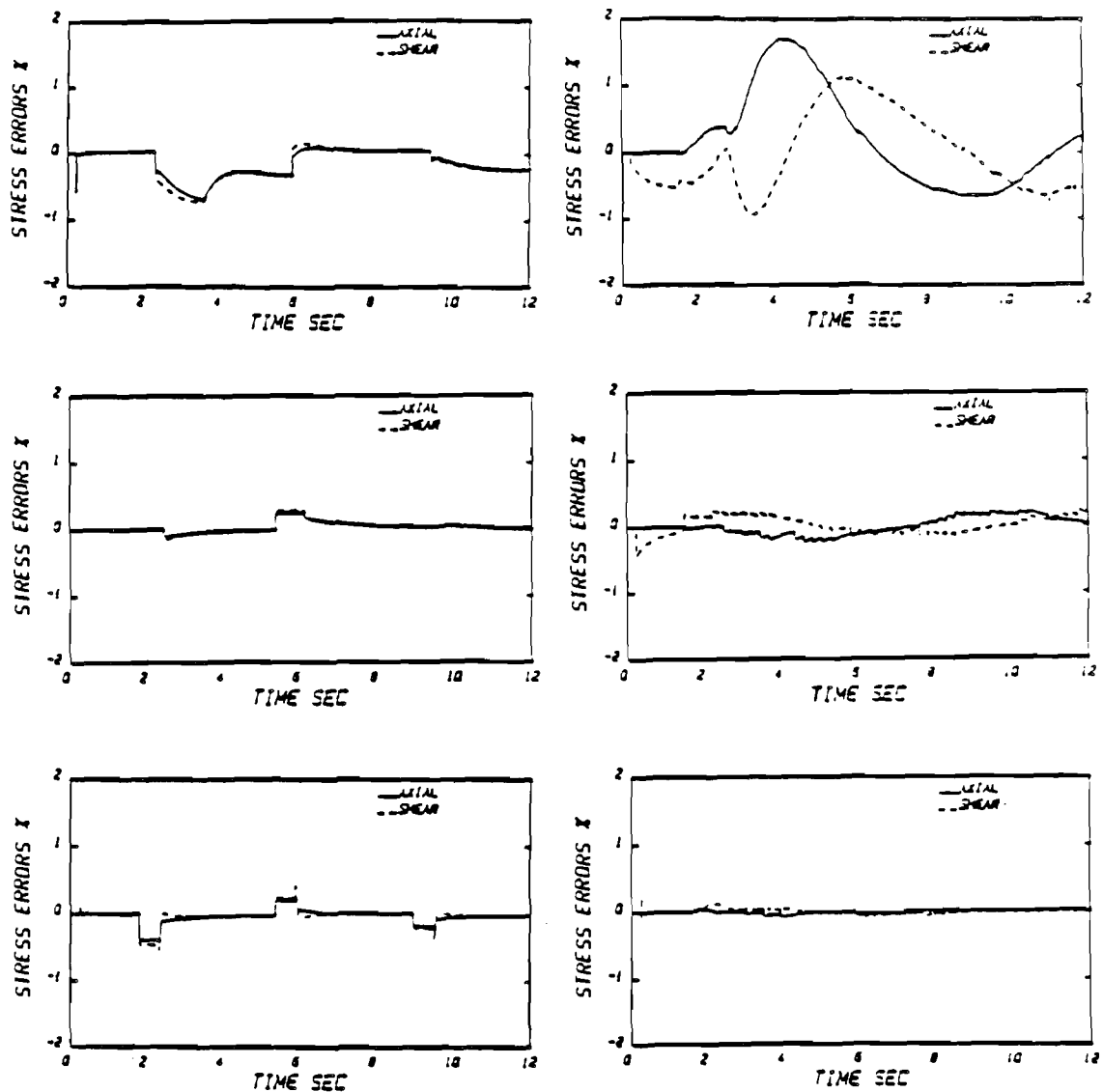


Fig. 7. Axial and shear stress errors vs time responses for histories I and II integrated by iterative Adams method. Left column, history I; right column, history II; top row, McDowell's model solution; middle row, Drucker's model solution; bottom row, Abrahamson's model solution.

#### CONCLUSIONS

Every integration routine has been shown to have particular advantages and disadvantages that make them suitable or not suitable at all for specific types of applications. Thus, these integration routines can be best evaluated based on their appropriateness to solve specific types of problems which have particular priorities on the computational accuracy and efficiency required. From the facts just presented, the following recommendations can be made:

1. Gear's method should be used for proportional or nonproportional loading when the numerical behavior of the system being solved is unknown. However, it should not be used if high computational efficiency is desired.

2. Runge-Kutta method with Gill coefficients should be used for integrating proportional and nonproportional histories for all the model structures discussed if a good estimate of the appropriate initial time step-size is available. Otherwise, iteration of trial solutions might be required to guarantee an efficient yet accurate solution.

3. Non-iterative Adams predictor-corrector method presents the same characteristics of the Runge-Kutta method and should be used under the same constraints.

4. Euler's method with automatic step-size control should only be used when integrating proportional loading histories on McDowell's and Abrahamson's models. For nonproportional loading histories and for any model expected to be rather stiff, this method

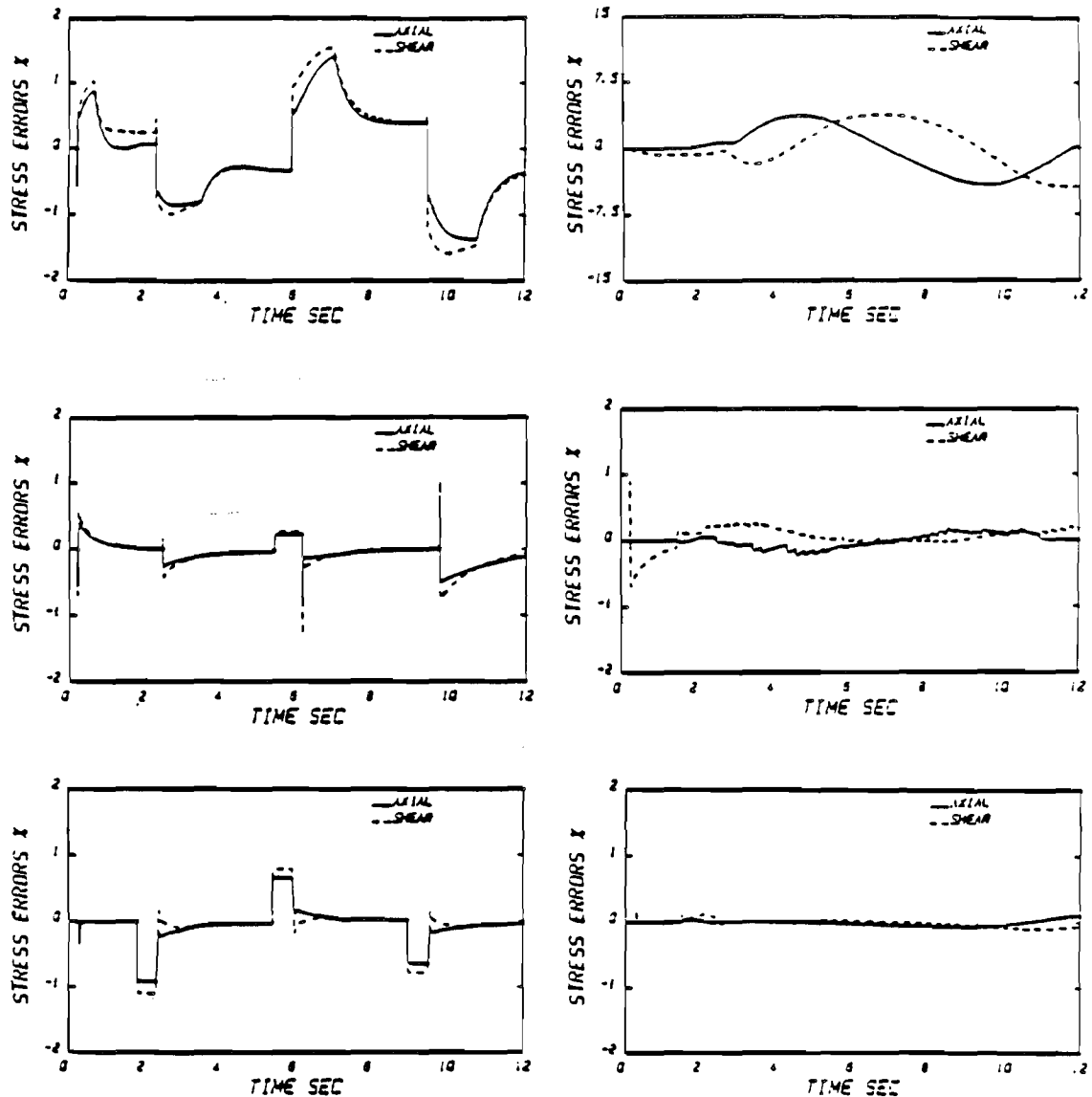


Fig. 8. Axial and shear stress errors vs time responses for histories I and II integrated by non-iterative Adams method. Left column, history I; right column, history II; top row, McDowell's model solution; middle row, Drucker's model solution; bottom row, Abrahamson's model solution.

should not be used. This conclusion is important, since it conflicts with the previously reported desirability of this method for stiff constitutive equations, surmised from proportional loading histories.

5. Iterative Adams predictor-corrector method with automatic step-size control should only be used when integrating proportional loading histories in general. For nonproportional straining, this method behaves very similar to Euler's method and, consequently, should not be used.

**Acknowledgement**—The support of this work by a grant from the National Science Foundation (NSF Grant No. MEA-8404080) is gratefully acknowledged.

#### REFERENCES

1. D. C. Drucker and L. Palgen, On stress-strain relations suitable for cyclic and other loading. *J. appl. Mech.* **48**, 479-485 (1981).
2. D. L. McDowell, A two-surface model for transient nonproportional cyclic plasticity: Part I—Development of appropriate equations. *ASME J. appl. Mech.* **52**, 298-302 (1985).
3. D. L. McDowell, A two-surface model for transient nonproportional cyclic plasticity: Part II—Comparison of theory with experiments. *ASME J. appl. Mech.* **52**, 303-308 (1985).
4. T. E. Abrahamson, Modeling the behavior of type 304 stainless steel with a unified creep-plasticity theory. Ph.D. Thesis, Department of Mechanical and Industrial Engineering, University of Illinois at Urbana-Champaign (1983).

5. W. Sotolongo, On the numerical implementation of cyclic elasto-plastic material models. M.S. Thesis, School of Mechanical Engineering, Georgia Institute of Technology (1985).
6. S. Gill, A process for the step-by-step integration of differential equations in an automatic computing machine. *Proc. Camb. Phil. Soc.* 47, 96-108 (1951).
7. H. V. Eraslan, Supplementary notes on the solution of ordinary differential equations by Runge-Kutta methods. Prepared for the One-Week Short Course in Numerical Analysis and Computer Methods, University of Tennessee Space Institute, Tullahoma, Tennessee, 13-18 January (1969).
8. V. Kumar, M. Morjaria and S. Mukherjee, Numerical integration of some stiff constitutive models of inelastic deformation. *ASME J. Engng Mater. Technol.* 102, 92-96 (1980).
9. J. R. Cash, *Stable Recursions with Applications to the Numerical Solution of Stiff Systems*. Academic Press, London (1979).
10. C. W. Gear, The automatic integration of ordinary differential equations. *Commun. ACM* 14, 176-179 (1971).
11. T. Y. Chang, J. P. Chang and R. L. Thompson, On the Numerical integration and computer implementation of viscoplastic models. Proceedings of the 2nd Symposium on Nonlinear Constitutive Relations for High Temperature Applications, NASA Lewis Research Center, 13-15 June (1984).
12. V. Kumar and S. Mukherjee, Creep analysis of structures using a new equation of state type constitutive relation. *J. Comput. Struct.* 6, 429-437 (1976).
13. K. S. Chan, S. R. Bodner, K. P. Walker and U. S. Lindholm, A survey of unified constitutive theories. Proceedings of the 2nd Symposium on Nonlinear Constitutive Relations for High Temperature Applications, NASA Lewis Research Center, 13-15 June (1984).
14. W. E. Haisler and P. K. Imbrie, Numerical Considerations in the development and implementation of constitutive models. Proceedings of the 2nd Symposium on Nonlinear Constitutive Relations for High Temperature Applications, NASA Lewis Research Center, 13-15 June (1984).
15. A. K. Miller and C. F. Shih, An improved method for numerical integration of constitutive equations of the work hardening-recovery type. *ASME J. Engng Mater. Technol.* 99-H, 275 (1977).

#### APPENDIX

##### Drucker's model

##### Miscellaneous equations

$$A = \frac{B}{(\sigma^*)^{2N}}$$

##### Model parameters

$$\begin{aligned}\gamma &= 0.17 & W_0 &= 5.9 \text{ MPa} \\ N &= 1.35 & A &= 2.6 \times 10^{-10} \\ k &= 148.1 \text{ MPa} & \text{Units: } B &= \text{MPa}^{-3} \\ & & \sigma^* &= \text{MPa}\end{aligned}$$

##### Material constants

For type 304 stainless steel in the initially annealed state:

$$\begin{aligned}\nu &= 0.29 \\ G &= 75.1 \text{ GPa}\end{aligned}$$

##### McDowell's model

##### Material modeling functions

For type 304 stainless steel at room-temperature:

$$\begin{aligned}\bar{R}(0, q) &= 171 + (q - 0.005)4000 \text{ MPa} \\ \bar{R}^*(0, q) &= 295 + (q - 0.005)20690 \text{ MPa} \\ \bar{\kappa}(0, q) &= 4370 - (q - 0.005)196100 \text{ MPa} \\ \bar{R}(1, q) &= 405 \text{ MPa} \\ \bar{R}^*(1, q) &= 565 \text{ MPa} \\ \bar{\kappa}(1, q) &= 4046 \text{ MPa} \\ \Lambda(q) &= 0.6q \\ \psi &= u[\bar{R}(\phi, q) - R] \\ \psi^* &= u[\bar{R}^*(\phi, q) - R^*] \\ \psi_\kappa &= u[\bar{\kappa}(\phi, q)]\end{aligned}$$

where  $u(x) \equiv$  Heaviside function of  $x$  and  $\phi_{\text{limit}} = 0.02$

##### Material constants

For type 304 stainless steel in the initially annealed state:

$$\begin{aligned}\mu &= 10.0 & \nu &= 0.29 \\ \mu^* &= 50.0 & G &= 75.1 \text{ GPa}\end{aligned}$$

##### Abrahamson's model

##### Model parameters

For 304 stainless steel at 300 K:

$$\begin{aligned}a &= 5 \times 10^{-4} \text{ s}^{-1} & c &= 1.6 \times 10^{-8} \text{ MPa}^{-2} \text{ s}^{-1} \\ a_1 &= 0.002 \text{ MPa}^{-1} & d_1 &= 58.5 \times 10^{-6} \text{ MPa}^{-1} \\ a_3 &= 22.8 \text{ MPa} & m &= 2.0 \\ B &= 2.0 & p &= 30.0 \\ b_1 &= 0.0975 \text{ MPa} & k_0 &= 126 \text{ MPa} \\ b_2 &= 0.01 \text{ MPa}^{-1} & \phi_{\text{limit}} &= 0.02 \\ b_3 &= 5.89 & d_2 &= 0.045 \text{ MPa}^{-1}\end{aligned}$$

##### Material constants

For type 304 stainless steel at 300 K:

$$\begin{aligned}G &= 71.1 \text{ GPa} & \nu &= 0.29 \\ E &= 173.9 \text{ GPa} & \mu^* &= 50.0.\end{aligned}$$

**An Evaluation of Recent  
Developments in Hardening  
and Flow Rules for Rate-Independent,  
Nonproportional Cyclic Plasticity**

**D.L. McDowell**  
Assistant Professor  
George W. Woodruff School of Mechanical Engineering  
Georgia Institute of Technology  
Atlanta, GA 30332

Associate Member, ASME

Revised for Publication in  
ASME Journal of Applied Mechanics

July, 1986

### ABSTRACT

The Mroz kinematic hardening rule has previously demonstrated superior capability to correlate cyclically stable nonproportional stress-strain response. In this paper, recently proposed kinematic hardening rules for single and multiple surface cyclic plasticity models are evaluated. Significant improvement over the Mroz rule, without loss of generality, is achieved with a deviatoric stress rate-dominated rule proposed by Tseng and Lee for two surface theory. Recent approaches for correlation of the modulus function and isotropic hardening are discussed. The norm of the Mroz distance vector is found to uniquely correlate the variation of plastic hardening modulus through a cycle; it is necessary to include a measure of instantaneous nonproportionality, however, to properly normalize the modulus function. A new evolution equation is offered to correlate the additional isotropic hardening observed during nonproportional loading, and several contemporary approaches are also considered.

## Introduction

With increasing emphasis on lightweight, high performance structures, there has been a corresponding rise of interest in constitutive equations for cyclic plasticity. This is true for the turbine and rocket engine, nuclear and ground vehicle industries, for example. Historically the complexity of cyclic plasticity models increased as more experimentally observed effects were reported. There has been a relatively recent emphasis (Dafalias and Popov, 1975; Dafalias, 1981; Krieg, 1975; Lamba and Sidebottom, 1978a, 1978b; McDowell, 1985a, 1985b; Nouailhas et al., 1983; Tanaka et al., 1985; Tseng and Lee, 1983) on the formulation of models for multiaxial loading. This includes consideration of nonproportional variation of the components of stress and strain referenced to material axes (nonproportional loading).

Lamba and Sidebottom (1978a, 1978b) produced data from nonproportional cyclic axial-torsional tests on OFHC copper, and showed that the kinematic hardening rule of Mroz (1967) was far superior to that of Ziegler (1959) or Prager (1956) for correlating stress-strain response during nonproportional loading. Lamba also reported a significant increase in cyclic hardening under sinusoidal out-of-phase loading, a finding that since has been reported for other materials for similar loading conditions (McDowell, 1983a; Kanazawa et al., 1979; Krempl and Lu, 1984). Prediction of the direction of plastic strain rate in general depends greatly on the kinematic hardening rule for nonproportional loading. Likewise, isotropic hardening during nonproportional loading can no longer be represented as a function of accumulated plastic strain or plastic work; it is also a function of changes in the direction of the plastic strain rate vector over a loading history (McDowell, 1985c).



Since both the direction of the plastic strain rate vector and the additional hardening during nonproportional loading are of first order importance, it is not extravagant but absolutely necessary to account for them in the cyclic plasticity model.

In this paper, experimental data from axial torsional, strain controlled, cyclic nonproportional loading tests is examined in detail for type 304 stainless steel at room temperature. Within the context of von Mises yield and loading surfaces, recently proposed approaches for kinematic hardening will be evaluated. More accurate rules are developed where necessary. Second invariant plasticity theory (i.e. von Mises) is selected as the basis for evaluation since it is of extreme practical importance to the computational plasticity community. Likewise, studies of isotropic hardening and modulus function will be based on this framework.

Results of three strain-controlled axial torsional histories are considered in this paper. All tests were conducted at room temperature. The initial values of Young's modulus and shear modulus were determined as  $E = 188$  GPa and  $G = 77$  GPa, respectively. A summary of the three test histories appears in Table I, including the effective strain rate and controlled axial and shear strain endpoint sequence of each block within each history. Details of the experimental procedures and more in-depth discussion of the experiments appear elsewhere (McDowell, 1983a, 1983b, 1985d).

Studies of kinematic hardening will be limited to consideration of essentially stable cyclic response observed in the latter cycles of each block. In this case, the kinematic hardening rules may be examined in the absence of isotropic hardening. In a later section, isotropic hardening effects and the modulus function will also be examined.

### Kinematic Hardening Rules

Previous work (Lamba and Sidebottom, 1978a, 1978b; McDowell, 1985d) has demonstrated the lack of correlation obtained with the use of either a Prager or Ziegler kinematic hardening rule for nonproportional cyclic loading, i.e.

$$\dot{\underline{\underline{\alpha}}} = \mu \dot{\underline{\underline{\epsilon}}}^P \quad (1)$$

or

$$\dot{\underline{\underline{\alpha}}} = \dot{\underline{\underline{\eta}}}(\underline{\underline{s}} - \underline{\underline{\alpha}}) \quad (2)$$

where  $\underline{\underline{s}}$  is the deviatoric stress tensor,  $\underline{\underline{\alpha}}$  is the backstress, and  $\mu$  and  $\dot{\underline{\underline{\eta}}}$  are scalar multipliers.

The superiority of a Mroz-type hardening rule, based on the concept of nested yield and loading surfaces, has been previously demonstrated. For computationally efficient two surface models with a yield surface  $f$  and enclosing limit surface  $f^*$  of the form  $f(\underline{\underline{s}} - \underline{\underline{\alpha}}, R) = 0$  and  $f^*(\underline{\underline{s}} - \underline{\underline{\alpha}}^*, R^*) = 0$ , the Mroz rule may be stated as

$$\dot{\underline{\underline{\alpha}}} = \mu_m (\underline{\underline{s}}^* - \underline{\underline{s}}) \quad (3)$$

where  $\underline{\underline{s}}^*$  is the similar point on the limit surface as shown in Fig. 1 defined by

$$\underline{\underline{s}}^* = \underline{\underline{\alpha}}^* + (R^*/R)(\underline{\underline{s}} - \underline{\underline{\alpha}}) \quad (4)$$

where  $R$  and  $R^*$  are the yield and limit surface radii, respectively.

Other kinematic hardening rules have been proposed recently which would also conceptually apply to the nonproportional loading case. Tseng and Lee (1983) proposed that the yield surface translation is related to the deviatoric stress rate direction. Their theory was motivated chiefly by the predominance of stress rate in translation of the yield locus observed in the experiments of Phillips et al. (1974, 1979). In their theory, for a stationary limit surface,

$$\dot{\underline{a}} = \mu_T \underline{\nu} \quad (5)$$

where

$$\underline{\nu} = \frac{\left[ \sqrt{\frac{2}{3}} (R^* - R) \underline{\lambda} - \underline{a} \right]}{\left\| \sqrt{\frac{2}{3}} (R^* - R) \underline{\lambda} - \underline{a} \right\|} \quad (6)$$

$$\underline{\lambda} = \frac{\underline{s} + \delta_s^* \dot{\underline{s}} / \|\dot{\underline{s}}\|}{\|(\underline{s} + \delta_s^* \dot{\underline{s}} / \|\dot{\underline{s}}\|)\|} \quad (7)$$

$$\delta_s^* = -\underline{s} : \dot{\underline{s}} / \|\dot{\underline{s}}\| + [(\underline{s} : \dot{\underline{s}} / \|\dot{\underline{s}}\|)^2 + (\frac{2}{3}(R^*)^2 - \|\underline{s}\|^2)]^{1/2} \quad (8)$$

where the scalar product is defined by  $\underline{s} : \dot{\underline{s}} = s_{ij} \dot{s}_{ij}$  for example. The norm of a second order tensor  $\underline{s}$  is denoted by  $\|\underline{s}\| = (\underline{s} : \underline{s})^{1/2}$ .

Here,  $\delta_s^*$  is the norm of the vector from the current stress point to the intersection of the deviatoric stress rate direction relative to the current stress point with the stationary limit surface  $f^*$  of the form

$$f^*(\underline{s}, R^*) = (3/2) \underline{s} : \underline{s} - (R^*)^2 \quad (9)$$

Note that  $\underline{\alpha}^* = 0$  in their formulation. Equations (5) - (9) are meant to apply to von Mises yield and limit surfaces. Note also that the rule guarantees tangency of the surfaces as  $\delta \underline{s} \rightarrow 0$  as in the Mroz rule.

Outside of the context of a multiple surface plasticity theory, one could generalize the assumed dominance of deviatoric stress rate direction with the rule

$$\dot{\underline{\alpha}} = \mu \underline{s} \dot{\underline{s}} \quad (10)$$

Another rule which has been introduced in the context of rate-dependent state variable or unified creep-plasticity theory is due to Chaboche et al. (1979),

$$\dot{\underline{\alpha}} = C[a' \dot{\underline{\epsilon}}^P - \underline{\alpha} ||\dot{\underline{\epsilon}}^P||] \quad (11)$$

where  $a'$  is a constant and  $C$  is a scalar. In Chaboche's formulation, both  $C$  and  $a'$  can be functions of the accumulated plastic strain,  $\bar{\epsilon}^P$ . In equation (11),  $C$  is determined by consistency, leaving  $a'$  freely specified. The second term, widely regarded as a dynamic recovery term, in principle can account for nonproportional loading effects since an additional directional index  $\underline{\alpha}$  is appended to the otherwise Prager-type rule. It should be noted that other investigators have proposed similar forms (Lindholm et al. 1985). It should also be noted that neither of equations (10) - (11) requires a multiple surface formulation.

The Tseng-Lee Rule in equations (5)-(8) was motivated by observation that the yield surface movement was related to deviatoric stress rate. In their

implementation of this observation, however, Tseng and Lee were constrained to ensure nesting of the yield and limit surfaces as  $\delta_s^* \rightarrow 0$ . Hence, the deviatoric stress rate direction and that of  $\underline{\nu}$  in the Tseng-Lee Rule in equation (6) are not equivalent, though  $\underline{\nu}$  much more closely follows the deviatoric stress rate direction than the Mroz rule in equation (3) for nonproportional loading.

The Tseng-Lee rule may be extended to the case of a translating limit surface by referencing to  $\underline{a}^*$  rather than the origin. The Tseng-Lee rule with nonzero  $\underline{a}^*$  is illustrated in Fig. 2.

It is possible to evaluate these rules via numerical differentiation of data from strain-controlled, axial torsional tests on thin-walled tubular specimens (McDowell, 1985d). It is convenient to make these comparisons in the axial torsional subspace.

The definition of the axial torsional subspace follows as a subspace of Ilyushin's five-dimensional deviatoric vector space (McDowell, 1985d). Define the stress vector as

$$\underline{\sigma} = \sigma_1 \underline{n}_1 + \sigma_3 \underline{n}_3 \quad (12)$$

where

$$\sigma_1 = \sigma_{zz} = \sigma, \quad \sigma_3 = \sqrt{3}\sigma_{z\theta} = \sqrt{3}\tau$$

and  $\underline{n}_1$  and  $\underline{n}_3$  are orthonormal base vectors in the stress plane. Here,  $z$  and  $\theta$  denote the tube longitudinal and circumferential directions, respectively.

Likewise, the plastic strain vector is defined by

$$\underline{\epsilon}^P = \epsilon_1^P \underline{n}_1 + \epsilon_3^P \underline{n}_3 \quad (13)$$

where  $\epsilon_1^P = \epsilon_{zz}^P$ , and  $\epsilon_3^P = (2/\sqrt{3})\epsilon_{z\theta}^P$ .

Note that the plastic strain rate vector is defined as

$$\dot{\underline{\epsilon}}^P = \dot{\epsilon}_1^P \underline{n}_1 + \dot{\epsilon}_3^P \underline{n}_3 \quad (14)$$

The effective stress  $\bar{\sigma}$  and plastic strain rate  $\dot{\bar{\epsilon}}^P$  (normalized to the axial case) are recognized as

$$\bar{\sigma} = |\underline{\sigma}| = (\underline{\sigma} \cdot \underline{\sigma})^{1/2} = (\sigma_1^2 + \sigma_3^2)^{1/2} \quad (15)$$

$$\dot{\bar{\epsilon}}^P = |\dot{\underline{\epsilon}}^P| \quad (16)$$

The total strain vector is heuristically defined as

$$\underline{\epsilon} = \epsilon_1 \underline{n}_1 + \epsilon_3 \underline{n}_3 \quad (17)$$

where  $\epsilon_1 = \epsilon_{zz} = \epsilon$  and  $\epsilon_3 = (2/\sqrt{3})\epsilon_{z\theta} = \gamma/\sqrt{3}$ . The effective strain rate reported in Table I is then  $\dot{\bar{\epsilon}} = |\dot{\underline{\epsilon}}|$  since  $\gamma = 2\epsilon_{z\theta}$ .

The plastic strain rate vector in the subspace was computed by numerical differentiation of data (McDowell, 1985d).

The axial torsional subspace can also be considered a deviatoric subspace since the second invariant of deviatoric stress can be related to  $\underline{\underline{s}} \cdot \underline{\underline{s}}$

$$\bar{\sigma} = (\underline{\underline{s}} \cdot \underline{\underline{s}})^{1/2} = \sqrt{\frac{3}{2} \underline{\underline{s}} : \underline{\underline{s}}} = \sqrt{3J_2'} \quad (18)$$

Hence, a von Mises yield surface also is circular in the subspace, i.e.

$$f = (\underline{\sigma} - \underline{\bar{\alpha}}) \cdot (\underline{\sigma} - \underline{\bar{\alpha}}) - R^2 \quad (19)$$

where  $R$  is the uniaxial yield stress and  $\underline{\bar{\alpha}}$  is the backstress in the subspace.

The associated flow rule in the subspace is given for  $f = 0$  by

$$\dot{\underline{\epsilon}}^P = \frac{1}{h} \langle \dot{\underline{\sigma}} \cdot \underline{n} \rangle \underline{n} \quad (20)$$

where  $\underline{n} = (\underline{\sigma} - \underline{\bar{\alpha}})/|\underline{\sigma} - \underline{\bar{\alpha}}|$  and  $h$  is the hardening modulus. The Macauley bracket is defined by  $\langle M \rangle = M$  if  $M \geq 0$  and  $\langle M \rangle = 0$  if  $M < 0$ . Hence,  $\dot{\underline{\epsilon}}^P$  is collinear with  $(\underline{\sigma} - \underline{\bar{\alpha}})$  for the von Mises case. A stationary limit surface  $f^*$  in the subspace, required by two surface theories, is given by

$$f^* = \underline{\sigma}^* \cdot \underline{\sigma}^* - (R^*)^2 \quad (21)$$

where  $\underline{\sigma}^*$  is a point on the limit surface.

Referring to equations (19)-(21), it is apparent that if  $R$  and  $\underline{n}$  ( $=\dot{\underline{\epsilon}}^P/|\dot{\underline{\epsilon}}^P|$ ) are known, then  $\underline{\bar{\alpha}}$  can be computed directly from

$$\underline{\bar{\alpha}} = \underline{\sigma} - R\underline{n} \quad (22)$$

for each point in the plastic range under conditions of stable or pure kinematic hardening ( $R = \text{constant}$ ). Figure 3 illustrates the imposed  $\epsilon_1$  versus  $\epsilon_3$  strain paths and resulting stable cycles of  $\sigma_1$  versus  $\sigma_3$  in the axial torsional subspace for the histories in this study, which are fully described in Table I.

In Figs. 4 - 7, the backstress path based on equation (22) is plotted as a solid line for essentially stable cycles of three nonproportional histories. In addition, vectors are plotted along these paths which represent the direction of backstress evolution predicted by the models of Mroz, Tseng-Lee, deviatoric stress rate, and that of Chaboche. These models are stated in the axial torsional subspace as

$$\text{Mroz:} \quad \dot{\bar{\alpha}} = \bar{\mu}_m (\sigma^* - \sigma) \quad (23)$$

$$\text{where} \quad \sigma^* = (R^*/R) (\sigma - \bar{\alpha}) \quad (24)$$

$$\text{Tseng-Lee:} \quad \dot{\bar{\alpha}} = \bar{\mu}_T \nu^S \quad (25)$$

$$\text{where} \quad \nu^S = \frac{(R^* - R)\lambda - \bar{\alpha}}{|(R^* - R)\lambda - \bar{\alpha}|} \quad (26)$$

$$\lambda = \frac{\sigma + \delta_\sigma \dot{\sigma}/|\dot{\sigma}|}{|\sigma + \delta_\sigma \dot{\sigma}/|\dot{\sigma}||} \quad (27)$$

and

$$\delta_\sigma = -\sigma \cdot \dot{\sigma}/|\dot{\sigma}| + [(\sigma \cdot \dot{\sigma}/|\dot{\sigma}|)^2 + ((R^*)^2 - |\sigma|^2)]^{1/2} \quad (28)$$

$$\text{Deviatoric stress rate:} \quad \dot{\bar{\alpha}} = \mu_\sigma \dot{\sigma} \quad (29)$$

$$\text{Chaboche:} \quad \dot{\bar{\alpha}} = c[a(\sigma - \bar{\alpha}) - \bar{\alpha}]|\dot{\epsilon}^P| \quad (30)$$

It should be noted that the Mroz and Tseng-Lee models require specification of  $R^*$ , the limit surface radius. Several values of  $R^*$ , including the maximum effective stress in a cycle, were used in evaluating these models.



Also, in the Chaboche model, constant  $a$  was selected as  $a = 2.3$  to provide the best fit to the data from specimen SS01, block 3. Note that the limit surface is stationary in both the Mroz and Tseng-Lee models.

Referring to Figs. 4 - 7, it is noted that degree of tangency of the vectors to the path of  $\bar{\alpha}$  provides the measure of accuracy of each model.

As discussed later, it was found that the yield surface dimension does not experience significant change, assuming  $J_2^I$  flow theory and a deviation from linearity definition of yield. Hence, a constant yield surface radius of  $R = 160$  MPa was used in all calculations for the backstress path. In contrast, the limit surface radii required for the Mroz and Tseng-Lee rules experienced significant dependence on nonproportional loading. In Figs. 4-5 it was assumed that  $R^* = \max|\bar{\sigma}| + 30$  MPa where  $\max|\bar{\sigma}|$  is the maximum cyclically stable value of effective stress in each loading block.

From Figs. 4 - 7, it is clear that some models provide a good correlation for one history, but poor correlation for others. Interestingly, the hardening rules of Mroz and Chaboche are significantly less accurate than the rules associated with deviatoric stress rate. The hardening rule of Chaboche is less accurate for the sinusoidal loading paths than the deviatoric stress rate rules. The tremendous improvement of the Chaboche rule over the Prager (1956) or Ziegler (1959) rules indicates strongly that a dynamic recovery term must be included in a single surface (Drucker and Palgen, 1981) or state variable approach (Chan et al., 1984) which uses Prager-type hardening.

It is noted that there are some differences between the directions of yield surface translation given by the Tseng-Lee rule of equation (25) and the deviatoric stress rate. The deviatoric stress rate direction provides an overall superior correlation of the backstress rate direction.

However, use of deviatoric stress rate does not ensure nesting of yield and limit surfaces in a multiple surface model. Hence, the data indicates that the Tseng-Lee rule is superior to the Mroz rule for two surface theories, yet still invokes the desired nesting feature for both proportional and non-proportional loading. The Chaboche rule is the least accurate of those studied.

### Modulus Function

Accurate assignment of the hardening modulus function  $H$  in the flow rule

$$\dot{\epsilon}^P = \frac{1}{H} \langle \dot{s} : \underline{n} \rangle \underline{n} \quad (31)$$

expressed in deviatoric stress space is extremely important for modeling nonproportional cyclic stress-strain response. In the axial torsional subspace, equation (20) is appropriate where  $H = (2/3)h$ . Modulus function  $h$  may be computed from experimental data since

$$h = \frac{(\underline{d\sigma}/ds) \cdot \underline{n}}{(\underline{d\epsilon}^P/ds) \cdot \underline{n}} \quad (32)$$

and  $\underline{d\sigma}/ds$ ,  $\underline{d\epsilon}^P/ds$ , and  $\underline{n}$  are known from numerical differentiation of data (McDowell, 1985d), where  $s = \int (\underline{d\sigma} \cdot \underline{d\sigma})^{1/2}$  is the effective stress arc length along the path.

McDowell (1985d) showed that dependence of  $h$  on the Mroz distance vector for a two surface theory

$$\delta_m = |\underline{\sigma}^* - \underline{\sigma}| \quad (33)$$

offered better correlation with nonproportional cyclic loading data than dependence on effective stress  $\sqrt{3J_2'}$ . Since dependence of  $h$  on  $\delta_m$  is assumed in two surface models with Mroz-type kinematic hardening rules, it is not surprising that such models have consistently demonstrated superior accuracy for nonproportional cyclic plasticity.

Recent advances and close examination of experimental data, however, suggest that the correlation for  $h$  can be improved. In this work, several recently proposed independent variables will be considered and compared to the performance of  $\delta_m$ .

It is now recognized (McDowell, 1985c; 1985d; Nouailhas et al., 1983) that for cyclic loading, the accumulation of inelastic strain in the history is not a sufficient independent variable for  $h$  or  $H$ . For nonproportional loading, it is clear that accumulation of plastic strain from the most recent point of elastic unloading, as suggested in earlier work (Eisenberg, 1976; Wu and Yip, 1981), is not sufficient.

For cyclic plasticity models which employ only a yield surface, nonproportionality effects can be included in the modulus function

$$H = F(\eta) + \frac{2}{3} \left( \frac{dR}{d\bar{\epsilon}^P} \right) \quad (34)$$

where  $F(\eta)$  can be a history functional of the plastic strain trajectory, including path length and direction (Dafalias, 1984), i.e.

$$F(\eta) = \bar{n}(\eta) : \frac{d}{d\eta} \int_0^\eta \zeta(\eta - \eta') \bar{n}(\eta') d\eta' \quad (35)$$

where

$$d\eta = g(\bar{\epsilon}^P) d\bar{\epsilon}^P \quad (36)$$

and  $\zeta(\eta - \eta')$  is an unspecified function.

It is noted that  $F(\eta)$  is related to the kinematic hardening rule in the general rate-independent model structure given by Dafalias (1984) for a von Mises yield surface, i.e.

$$f = \frac{3}{2} (\underline{s} - \underline{a}) : (\underline{s} - \underline{a}) - R^2 = 0 \quad (37)$$

$$L = \frac{1}{H} (\dot{\underline{s}} : \underline{n}) \quad (38)$$

$$\dot{\underline{a}} = \langle L \rangle F(\eta) \underline{\xi} / (\underline{\xi} : \underline{n}) \quad (39)$$

$$\dot{R} = \langle L \rangle \sqrt{\frac{2}{3}} dR/d\bar{\epsilon}^P \quad (40)$$

and the flow rule stated in equation (31). The reader can verify that the consistency condition is met by equations (31), (34), and (37) - (40). In equation (39),  $\underline{\xi}$  is a unit vector representing the direction of translation of the yield surface.

As pointed out by Dafalias (1984), there are two very different procedures of assigning  $H$  in equation (34). One may define  $F(\eta)$  which specifies  $H$  when  $dR/d\bar{\epsilon}^P$  is known. This is indeed a very difficult task for nonproportional loading. An alternative route is offered by the multiple loading surface approaches (Lamba and Sidebottom, 1978; Dafalias and Popov, 1975; McDowell, 1985a, 1985b; Tseng and Lee, 1983; Mroz, 1967; Tanaka et al., 1985; Dafalias, 1981) in which  $H$  is specified and  $F(\eta)$  is computed by invoking the consistency condition since  $dR/d\bar{\epsilon}^P$  is known.

The recent theory offered by Krieg and Key for nonproportional loading (Krieg and Key, 1984) is an example of the first approach. In their model,

$$\dot{\underline{\epsilon}}^P = \frac{(\underline{s} - \underline{\alpha}) : \dot{\underline{\epsilon}}}{\frac{2}{3} R^2 [1 + (Z(\beta) + B)/3G]} (\underline{s} - \underline{\alpha}) \quad (41)$$

Since

$$\dot{\underline{\epsilon}} = \dot{\underline{s}}/2G + \dot{\underline{\epsilon}}^P + (1/3)(\dot{\underline{\epsilon}}:\underline{I})\underline{I} \quad (42)$$

where  $\underline{I}$  is the identity tensor, one can show that

$$H = \frac{2}{3} [Z(\beta) + B] \quad (43)$$

where  $\beta$  in this case is defined as the scalar product of the backstress and plastic strain rate direction, i.e.

$$\beta = \underline{\alpha} : \underline{n} \quad (44)$$

Parameter B is defined as the asymptotic slope of the stress-plastic strain curve. Hence, evaluation of this approach can be made by determining the correlative capability of the  $\beta$  parameter in equations (43) - (44).

The latter approach, in which H is specified, is exemplified by the Mroz or other multiple surface approaches. This paper will investigate the capability of several parameters within the context of a two surface theory. Denoting by  $\delta$  some measure of distance from the current stress point to a point on the limit or bounding surface (i.e. asymptotic stress-strain response), H may be written as

$$H = H(\delta, \delta_{in}, H^*) \quad (45)$$

where  $\delta_{in}$  is the value of  $\delta$  at initiation of the yielding process. According to Dafalias (1981,1984),  $\delta_{in}$  provides a discrete memory parameter of the most recent unloading-reloading event. Parameter  $H^*$  is the asymptotic value of  $H$  reached at high levels of plastic strain accumulated since the most recent loading reversal. Use of  $\delta_{in}$  is necessary in a two surface model to provide a memory of prior excursions in the plastic range; in multiple surface models, this memory is provided by the presence of a series of loading surfaces, each possessing an independent backstress and radius.

A general property of the modulus function is that  $H \rightarrow H^*$  as  $\delta/\delta_{in} \rightarrow 0$  and  $H$  is large ( $\rightarrow \infty$ ) as  $\delta/\delta_{in} \rightarrow 1$ . There exists a multitude of possible forms for  $\delta$ . First consider the axial torsional subspace forms

$$\delta = \delta_m \quad (46)$$

$$\delta = \delta_{\sigma} \quad (47)$$

In Figs. 8 - 9, the correlative capability of  $\delta/A$  for each of equations (46) - (47) with cyclically stable data from five loading blocks is shown. Here,  $A$  is a parameter used to normalize  $\delta$  between 0 and 1. Parameter  $A$  is analogous to  $\delta_{in}$  as discussed above. In these three plots,  $A$  was independently selected for each form of  $\delta$  and each history to match the value of  $\delta/A$  from proportional history block 2 of specimen SS09 at  $H = 300,000$  MPa. Table II lists the values of  $A$  selected to normalize each history. Hence, the data

is normalized at high modulus values for comparison. Again, a stationary limit surface with radius

$$R^* = \max|\underline{\sigma}| + 30 \text{ MPa} \quad (48)$$

was used for determining these  $\delta$  parameters, where  $\max|\underline{\sigma}|$  is the maximum effective stress in a stable cycle for each history. Analysis of the data for widely varying values of  $R^*$ , as in an earlier paper (McDowell, 1985d), showed that the accuracy of each of these  $\delta$  parameters is very weakly dependent on  $R^*$ .

To determine the relative performance of these two measures of  $\delta$ , one can compare their ability to correlate data from several nonproportional cyclic paths. The measure of correlative capability is the uniqueness of the functional form independent of path. All data are obtained from cyclically stable cycles, so the hardening can be assumed purely kinematic, i.e.  $dR/d\bar{\epsilon}^P = 0$ . On the same basis, the Krieg-Key modulus function in equation (43) may be evaluated, considering the function  $(\bar{\alpha} \cdot n)/A$ .

Referring to Figs. 8-9, it is clear that the correlation achieved by the Mroz definition of  $\delta$  is superior to the Tseng-Lee  $\delta$  parameter. The Tseng-Lee definition of  $\delta$  exhibits a very pronounced lack of correlation in the low modulus regime. The correlative capability of both  $\delta$  parameters, though, cannot be judged entirely on the basis of Figs. 8-9 without consideration of the  $A$  values required for normalization. From Table II, it is seen that the  $A$  values are certainly not constant for each  $\delta$  parameter for all histories. In fact, there does not appear to be any relationship between  $A$  and  $R^*$  for each parameter. This result for these completely reversed nonproportional loading histories is somewhat disturbing since  $A$  and  $\delta_{1n}$  mentioned in equation (45)

should be essentially equivalent in this case. To further exemplify this point,  $\delta_m/A$  was plotted versus  $H$  with  $A = 2R^*$ ; a unique correlation was not obtained. It should be noted that several previous models for nonproportional loading based on the Mroz  $\delta$  have employed this somewhat inaccurate normalization (Lamba and Sidebottom, 1978; McDowell et al., 1982).

The correlative capability of the Krieg-Key modulus function is shown in Fig. 10, where two different definitions of  $A$  are used to normalize the data. Both definitions appear in Table II. A value of  $R = 160$  MPa was assumed in calculation of the backstress. Obviously correlation of the data is very poor using this parameter. It should be noted that the correlation is not improved when a value of  $R = 300$  MPa is used to compute backstress via equation (22).

Having evaluated the capability of several proposed parameters to correlate modulus variation during nonproportional loading, we turn to possible specific forms of equation (45) since the multiple surface (two surface, in this case) plasticity models have demonstrated superior correlation of modulus if  $\delta$  is properly selected. It has already been established in this work that normalization of  $\delta$  by a constant or by  $R^*$  or maximum effective stress will not produce satisfactory correlation. Hence, we must seek forms for  $H$  which employ a normalizing parameter which is a function of the history of loading.

Dafalias (1981, 1984) has proposed a specific form of equation (45), i.e.

$$H = \left[ 1 + g(\delta_{in}) \left( \frac{\delta/\delta_{in}}{1 - \delta/\delta_{in}} \right) \right] H^* \quad (49)$$

where  $g(\delta_{in})$  controls the slope of the stress-strain curve. Though rather elaborate rules can be devised to properly assign  $\delta_{in}$  for unloading-reloading



events, such rules will be unnecessary in this work since only completely reversed, nonproportional cyclic loading will be considered. Again, note that the precise form for  $\delta$  is left unspecified in equation (49). In fact, Tseng and Lee have used equation (49) for  $H$  along with their definition of  $\delta = \delta_s$  from equation (8).

Equation (49) has the property that  $H \rightarrow \infty$  as  $\delta \rightarrow \delta_{in}$ , i.e. at initial yielding. Also,  $H \rightarrow H^*$  as  $\delta \rightarrow 0$ , i.e. approaching the limit surface.

In Fig. 11a, the Dafalias modulus function is fit to proportional loading history SS09, block 2 with  $\delta = \delta_m$ ,  $g = 16$ ,  $\delta_{in} = 417$  MPa,  $R^* = 338$  MPa, and  $H^* = 3000$  MPa. It should be noted that a better fit could be obtained if the modulus function were nonlinear in  $(\delta_m/\delta_{in})/(1 - \delta_m/\delta_{in})$ . The best measure of usefulness of any modulus function, of course, is the capability to extend uniaxial or proportional loading test results to the nonproportional case. Figure 11b shows the correlation obtained for all histories of this study using the Dafalias function with  $g = \text{constant}$ ; the solid line is reproduced from Fig. 11a, representing proportional cycling. In all cases,  $\delta_{in}$  was defined as the maximum value of  $\delta_m$  during plastic flow for each history.

From Fig. 11, it is apparent that the correlation is satisfactory for all histories except SS09, block 4 (i.e. 60 degree out-of-phase sinusoidal loading). This history does not exhibit unloading response; hence, the normalizing parameter  $\delta_{in}$  is likely more properly determined from a reversal prior to this history. The value of  $\delta_{in} = 545$  MPa obtained for history SS09, block 3 is close to the value of  $A = 530$  MPa required for correlation with  $\delta_m$  as reported in Table II. This history points out a difficulty with a normalization procedure that depends on the initiation of yielding for nonproportional loading. In particular, it is very difficult to assign a proper definition of  $\delta_{in}$  for such histories. Also, it is important that the

modulus function fit proportional cycling data well. Other models (Chan et al., 1984) have employed an exponential or hyperbolic sine fit.

To obviate the difficulty associated with use of  $\delta_{in}$  as a normalizing parameter, another was sought which depended on current state rather than prior history. Examination of the data indicated that the quantity  $(\underline{n} \cdot \underline{n}_{\delta_m})$ , representative of the non-collinearity of the loading increment, is essential to obtaining good correlation of data in addition to a distance parameter. The best correlation is achieved by employing this quantity as a modifier of the normalizing parameter, i.e.

$$H = H^* [1 + G(\delta_{in}) \{ \sinh [k_1 D] \}^{k_2}] \quad (50)$$

where

$$D = \left\{ \frac{\delta_m}{2 - |\underline{n} \cdot \underline{n}_{\delta_m}|} \right\} \quad (51)$$

$k_1$  and  $k_2$  are constants, and  $\underline{n}_{\delta_m} = (\underline{\sigma}^* - \underline{\sigma})/\delta_m$ .

Here,  $G(\delta_{in})$  is a memory repository intended to account for unloading-reloading effects. In the axial torsional subspace, assuming  $G(\delta_{in}) =$  constant for these histories under consideration, the relationship

$$H = 3000 [1 + 16 \{ \sinh(.005D) \}^{1.75}] \text{ MPa} \quad (52)$$

is determined by fitting the response from the proportional loading block 2 of specimen SS09. All other histories are plotted in Fig. 12 using equation (52) with  $R^* = \max |\underline{\sigma}| + 30 \text{ MPa}$  in each case. Excellent correlation of the data is

obtained. Furthermore, the constants are determined only from uniaxial or equivalent proportional loading tests.

It must be stated that no claim is made here regarding the generality of any specific approach for all metals. It is important to realize, though, that any truly promising modulus function must exhibit good correlation of various nonproportional loading paths for at least one material. In this regard, the fact that one modulus function produced good correlation in this study is encouraging. Other materials, of course, must be studied to provide more perspective. The author is not aware of similar detailed evaluation of modulus functions for nonproportional cyclic loading of other materials.

### Isotropic Hardening

It is now widely recognized (McDowell, 1983; Kanazawa et al., 1979; Krempl and Lu, 1984) that the extent of isotropic hardening may depend on the nonproportionality of loading. Austenitic stainless steels, for example, exhibit a tremendous cumulative increase in flow stress under nonproportional biaxial loading relative to stable uniaxial cycling. This effect is certainly evident in the biaxial histories of this study, as presented elsewhere (McDowell, 1983). In fact, 90 degree out-of-phase sinusoidal, axial torsional, strain-controlled loading results in nearly a 100 percent increase in effective flow stress over the uniaxial case at the same effective plastic strain range.

McDowell (1985a, 1985b) introduced a measure of nonproportionality of loading  $\phi$  which entered into the isotropic hardening rule for a scalar variable,  $\kappa$ , i.e.

$$\dot{\kappa} = \bar{\mu} \left[ \bar{\kappa}(\phi, q) - \kappa \right] \left( \dot{\epsilon}^P : \dot{\epsilon}^P \right)^{1/2} \quad (53)$$

Note that the cyclically stable state,  $\bar{\kappa}$ , is dependent upon the nonproportionality of the loading path and plastic strain range, reflected by  $\phi$  and  $q$ , respectively.

This measure of nonproportionality resulted in good correlation of sinusoidal nonproportional biaxial loading (McDowell, 1985b). It resulted in  $\phi$  values of  $0 \leq \phi \leq 1$  such that  $\phi = 0$  for proportional straining, and  $\phi = 1$  for 90 degree out-of-phase sinusoidal, axial torsional straining with a shear to axial strain amplitude ratio of  $\gamma_a/\epsilon_a = (1+\nu)$ . There are several reservations which require development of another approach. First, this approach applies only to cases where the principal axes of strain continuously rotate at some point during the loading cycle. Secondly, this approach does not provide good correlation of square loading paths or nonproportional loading paths other than sinusoidal. Thirdly, calculation of  $\phi$  is based on total strain and strain rate; from a mechanistic viewpoint, nonproportionality of plastic strain rate should more closely relate to increased activation and interaction of slip systems and, hence, additional isotropic hardening.

Several alternate approaches for nonproportional isotropic hardening have been suggested recently. Bodner and Partom (Lindholm et al., 1985) and Walker (Lindholm et al., 1985) have introduced isotropic hardening rules intended to account for additional nonproportional hardening. Both approaches, however, assume a unique cyclically stable state independent of the degree of nonproportionality of the path. This prediction of saturation to a single limiting value of  $\kappa$  is not supported by experiments (McDowell, 1983; Kanazawa et al., 1979; Krempl and Lu, 1984). In Fig. 13, the maximum effective stress in each cycle,  $\max|\sigma|$ , is plotted versus the accumulated plastic strain  $\int (d\epsilon^P)$ .

$d\epsilon^P)^{1/2}$  for loading blocks from each of the three histories of this study. It is noted that the cyclically stable state depends greatly on the nonproportionality of the loading path. This behavior is the key feature of nonproportional loading.

We now turn to development of an appropriate isotropic hardening rule which includes dependence of the hardening rate and final state on the nonproportionality of the loading history. For correlation of the final state a number of parameters were investigated, including  $(\underline{n} : \dot{\underline{s}}/||\dot{\underline{s}}||)$ ,  $((\underline{s}/||\underline{s}||) : (\dot{\underline{s}}/||\dot{\underline{s}}||))$  (e.g. Bodner et al., Lindholm et al., 1985) and  $(\underline{n} : \underline{s}/||\underline{s}||)$ . None demonstrated correlation of data with the exception of  $(\underline{N} : \underline{n})$ , where  $\underline{N}$  is the unit normal vector in the direction of  $\epsilon^P$  at the point of maximum plastic strain excursion in the current loading block. We may unambiguously define a loading block as a repeated assemblage of identical cycles or combination of cycles and subcycles. Careful examination of data led to the following plastic strain-based parameter:

$$\phi^* = \left[ \frac{\pi}{\pi-2} \right] \left| \left( \frac{\pi-2}{\pi} \right) - \left| \Lambda - \frac{2}{\pi} \right| \right| \quad (54)$$

where

$$\Lambda = \frac{1}{\int_{t_B}^t ||\dot{\underline{\epsilon}}^P|| dt} \int_{t_B}^t |\underline{N} : \dot{\underline{\epsilon}}^P| dt \quad (55)$$

and  $\underline{N} = \underline{\epsilon}^{P*}/||\underline{\epsilon}^{P*}||$  where  $\underline{\epsilon}^{P*}$  is the plastic strain at the maximum value of  $||\underline{\epsilon}^P||$  in the current loading block. The time at the initiation of the current loading block is given by  $t_B$ . Similar to  $\phi$ , it can be shown that  $\phi^* = 0$  for proportional loading and  $\phi^* = 1$  for 90 degree out-of-phase sinusoidal,

axial-torsional loading with  $\gamma_a/\epsilon_a = \sqrt{3}$  and  $\nu = 1/2$ . From a physical viewpoint,  $\Lambda$  represents the plastic strain averaged component of the inelastic strain rate in the maximal plastic strain direction. Since it is defined as an averaged non-collinearity of plastic strain, it should relate more fundamentally to isotropic hardening micro-mechanisms.

An appropriate evolution equation for an isotropic hardening variable  $\kappa$  is

$$\dot{\kappa} = \mu_0 \left[ \kappa_0 + K(\phi^*)^{m(1+\phi^*)} - \kappa \right] \left( \dot{\epsilon}^P : \dot{\epsilon}^P \right)^{1/2} \quad (56)$$

where  $\mu_0$  and  $m$  are constants, and  $K$  is at most a function of plastic strain range (McDowell, 1985a). Parameter  $\kappa_0$ , also a function of plastic strain range, is the uniaxial cyclically stable value of  $\kappa$ . Note the nonlinear dependence of the final state  $(\kappa_0 + K(\phi^*)^{m(1+\phi^*)})$  on  $\phi^*$ .

Figure 14 demonstrates the correlation obtained for the various loading blocks of this study between the cyclically stable value of maximum effective stress in a cycle,  $\max|\underline{\sigma}|$ , and  $(\phi^*)^{m(1+\phi^*)}$ ; the implicit assumption in this plot that  $K = \text{constant}$  is justifiable since the effective plastic strain ranges for all these histories are nearly equivalent. The correlation is quite good considering the differences in nonproportional loading paths considered.

In Fig. 15, assuming  $\kappa = \max|\underline{\sigma}|$  in each cycle, the values of  $\kappa$  from the histories of this study are normalized and plotted versus accumulated plastic strain,  $\int |\dot{\epsilon}^P| dt$ , in each associated loading block. The normalization of  $\max|\underline{\sigma}|$  in Fig.15 is made between the initial and final values of  $\max|\underline{\sigma}|$  in

each cycle for each loading block. Interestingly, most of the histories essentially follow the hardening response observed for the proportional straining of initially annealed material in block 1 of history SS01. This is true of histories for which the principal strain directions rotate continuously (e.g. block 3 of SS01, blocks 3-4 of SS09). However, the rate of hardening observed for specimen SS04 in Fig. 15 is significantly lower than that of the other blocks. This behavior can possibly be related to the fact that plastic strain is accumulated in this history along discrete sets of principal directions. Hence, the hardening rate may be dependent on directional accumulation of plastic strain. It should be noted that this hardening rate behavior could not be correlated with either of the Bodner-Partom or Walker rate approaches. In fact, none of the parameters mentioned earlier in conjunction with correlation of the level of isotropic hardening were viable in correlating the reduced hardening rate of specimen SS04. In view of the correlation which can be achieved for the other histories via the simple approach in equation (56) and the fact that hardening rate is a second order effect compared to the extent of hardening, it may not be necessary to include dependence of the hardening rate coefficient on the nonproportionality of loading. Certainly, more data is desirable to include such dependence.

As a final point, it should be noted that in general it is necessary to allow continuous evolution of  $\bar{N}$  between successive loading blocks. An example would be a number of cycles of axial loading followed by torsional cycling. Experimentally, some additional hardening is observed in such cases (McDowell, 1983; Krempf and Lu, 1984). Instantaneous re-definition of  $\bar{N}$  to the current proportional cycling block would be incompatible with this observation. From a micro-mechanical viewpoint, the values of the resolved shear stresses on slip planes within each grain have certainly changed, and a latent hardening

effect is quite reasonably expected.

Isotropic Hardening - Evolution of Yield Surface  
or Modulus Function?

The maximum effective stress in a cycle relates closely to  $R^*$ , the radius of a limit surface in a two surface theory. In general, both the yield and limit surfaces can isotropically harden. Isotropic hardening of the yield surface is usually associated with changes in the small offset yield strength after accounting for kinematic hardening. Likewise, isotropic hardening of the limit surface is associated with changes in the flow stress at relatively large plastic strain levels.

It is interesting to consider that the modulus function  $H$  can also be a repository for isotropic hardening. In fact, it is difficult to separate changes in the modulus function from growth of the yield surface defined by a plastic strain offset on the basis of uniaxial tests. Nonproportional cyclic loading tests are quite helpful in this regard since it is possible to determine the position of the center of any assumed yield surface form by backward extrapolation of the plastic strain rate direction after abrupt changes in loading direction. Since for stable cycling hardening is purely kinematic, one should not observe abrupt changes in the yield surface center after an unloading-reloading sequence in a different direction for a simple von Mises yield surface. From plots of backstress for several nonproportional loading blocks it was observed that  $R = 160$  MPa results in the smoothest path of  $\bar{\alpha}$ . Since  $R = 148$  MPa is the yield strength of the virgin annealed material, defined by a deviation from linearity (McDowell, 1985b), it is clear that very little of the isotropic hardening can be attributed to growth of a small



offset or deviation from linearity defined yield surface; rather, it must be accommodated in the modulus function through an isotropic variable associated with limit, not yield, behavior. In a two surface theory this corresponds to growth of the limit surface. As a result, the kinematic hardening variable will exhibit increased magnitude during nonproportional hardening.

This result is of considerable importance for this material, since the extent of isotropic hardening is relatively exceptional. It is somewhat fortuitous from a modeling standpoint, since it infers that the domain of purely elastic behavior for a rate-independent material response is less influenced in magnitude by complex loading than the domain of plastic behavior. Again, perspective must be maintained since only one material has been analyzed. Certainly, though, this result warrants study in other materials under complex nonproportional loading.

Of course, the objection may be made that anisotropic deformation of the yield surface may lead to a perceived abrupt change in  $\alpha$  as observed for larger assumed yield surface radii. However, it is observed that the anisotropic deformation of the yield surface (Shiratori et al., 1979; Hecker, 1976) is strongly a function of the offset plastic strain yield definition. Anisotropy is much more pronounced for small offset definitions of yield. Since nearly all computational codes for initially isotropic, rate-independent metals employ a simple yield surface, usually of von Mises form, it is worthwhile to experimentally investigate the integrity and extension of such an approach; the bounding surface approach, in particular, offers the capability to model anisotropic plastic flow via the modulus function although the yield surface is a simple form.

## Conclusions

Analysis of nonproportional cyclic loading data for type 304 stainless steel at room temperature has revealed some interesting results.

1. The kinematic hardening rule for von Mises yield and limit surfaces is more accurately prescribed by a deviatoric stress rate rule which provides for nesting than a Mroz rule.
2. If a Prager-type kinematic hardening rule is used in either a state variable or single loading surface theory, a dynamic recovery term must be included to correlate nonproportional data. The accuracy of such an approach, though, was found inferior to that of the two surface theory with a deviatoric stress rate-type rule.
3. A modulus function based on the distance from the current stress point to the limit surface in the direction of deviatoric stress rate does not correlate nonproportional loading data uniquely.
4. A modulus function based on a Mroz distance vector can be improved by including in the normalization the scalar product of the plastic strain rate direction with the Mroz vector. Proper definition of  $\delta_{in}$  as proposed by Dafalias appears to be a very difficult task for nonproportional loading.
5. A modulus function is proposed which correlates the data from several different nonproportional histories quite well. It is determined entirely from uniaxial or proportional loading tests.

6. A more general isotropic hardening rule is proposed which correlates the observed additional hardening. It is found that, within the context of second invariant plasticity theory, the isotropic hardening is predominantly associated with growth of an isotropic limit surface rather than the yield surface.

#### Acknowledgments

The author wishes to acknowledge the National Science Foundation for support of this research.

## REFERENCES

- Chaboche, J.L., Dang-Van, K., and Cordier, G., 1979, "Modelization of Strain Memory Effect on the Cyclic Hardening of 316 Stainless Steel," Trans. 5th SMIRT, L 11/3, Berlin.
- Chan, K.S., Bodner, S.R., Walker, K.P., and Lindholm, U.S., 1984, "A Survey of Unified Constitutive Theories," Proc. 2nd Symp. on Nonlinear Constitutive Relations for High Temperature Applications, NASA Lewis Research Center, June 13-15.
- Dafalias, Y.F., 1981, "The Concept and Application of the Bounding Surface in Plasticity Theory," Physical Non-Linearities in Structural Analysis, Eds. J. Hult and J. Lemaitre, IUTAM Symposium, Senlis, France, Springer Verlag, pp. 56-63.
- Dafalias, Y.F., and Popov, E.P., 1975, "A Model of Nonlinearly Hardening Materials for Complex Loading," Acta Mechanica, Vol. 21, pp. 173-192.
- Dafalias, Y.F., 1984, "Modeling Cyclic Plasticity: Simplicity Versus Sophistication," Mechanics of Engineering Materials, Eds. Desai and Gallagher, John Wiley and Sons, pp. 153-178.
- Drucker, D.C. and Palgen, L., 1981, "On Stress-Strain Relations Suitable for Cyclic and Other Loading," ASME Journal of Applied Mechanics, Vol. 48, pp. 479-485.
- Eisenberg, M.A., 1976, "A Generalization of Plastic Flow Theory with Application to Cyclic Hardening and Softening Phenomena," ASME Journal of Engineering Materials and Technology, Vol. 98, pp. 221-228.
- Hecker, S.S., 1976, "Experimental Studies of Yield Phenomena in Biaxially Loaded Metals," Constitutive Equations in Viscoplasticity: Computational and Engineering Aspects, AMD, ASME, Vol. 20, pp. 1-32.
- Kanazawa, K., Brown, M.W., and Miller, K.J., 1979, "Cyclic Deformation of 1% Cr-Mo-V Steel Under Out-of-Phase Loads," Fatigue of Engineering Materials and Structures, Vol. 2, pp. 217-228.
- Krempf, E., and Lu, H., 1984, "The Hardening and Rate-Dependent Behavior of Fully Annealed AISI Type 304 Stainless Steel Under Biaxial In-Phase and Out-of-Phase Strain Cycling at Room Temperature," ASME Journal of Engineering Materials and Technology, Vol. 106, pp. 376-382.
- Krieg, R.D., 1975, "A Practical Two Surface Plasticity Theory," ASME Journal of Applied Mechanics, Vol. 42, pp. 641-646.
- Krieg, R.D., and Key, S.W., 1984, "On the Accurate Representation of Large Strain Non-Proportional Plastic Flow in Ductile Metals," Proc. ASME Winter Annual Meeting, Constitutive Equations: Macro and Computational Aspects, New Orleans, pp. 41-52.

Lamba, H.S., and Sidebottom, O.M., 1978a, "Cyclic Plasticity for Nonproportional Paths: Part 1 - Cyclic Hardening, Erasure of Memory, and Subsequent Strain Hardening Experiments," ASME Journal of Engineering Materials and Technology, Vol. 100, pp. 96-103.

Lamba, H.S., and Sidebottom, O.M., 1978b, "Cyclic Plasticity for Nonproportional Paths: Part 2 - Comparison with Predictions of Three Incremental Plasticity Models," ASME Journal of Engineering Materials and Technology, Vol. 100, pp. 104-111.

Lindholm, U.S., Chan, K.S., Bodner, S.R., Weber, R.M., Walker, K.P., and Cassenti, B.N., 1985, "Constitutive Modeling for Isotropic Materials," NASA CR-174980, SwRI-7476/30.

McDowell, D.L., 1983a, "On the Path Dependence of Transient Hardening and Softening to Stable States Under Complex Biaxial Cyclic Loading," Proceedings of the International Conference on Constitutive Laws for Engineering Materials, Eds. Desai and Gallagher, Tucson, AZ, pp. 125-132.

McDowell, D.L., 1983b, "Transient Nonproportional Cyclic Plasticity," Report No. 107, Design and Materials Division, Dept. of Mechanical and Industrial Engineering, University of Illinois at Urbana-Champaign.

McDowell, D.L., 1985a, "A Two Surface Model for Transient Nonproportional Cyclic Plasticity: Part I - Development of Appropriate Equations," ASME Journal of Applied Mechanics, Volume 52, pp. 298-302.

McDowell, D.L., 1985b, "A Two Surface Model for Transient Nonproportional Cyclic Plasticity: Part II - Comparison of Theory with Experiments," ASME Journal of Applied Mechanics, Volume 52, pp. 303-308.

McDowell, D.L., 1985c, "The Significance of Nonproportional Loading Tests for Characterization of Cyclic Response of Metals," Proc. 1985 Spring Conference on Experimental Mechanics, Society for Experimental Stress Analysis, Las Vegas, pp. 229-236.

McDowell, D.L., 1985d, "An Experimental Study of the Structure of Constitutive Equations for Nonproportional Cyclic Plasticity," ASME Journal of Engineering Materials and Technology, Vol. 107, pp. 307-315.

McDowell, D.L., Socie, D.F., and Lamba, H.S., 1982, "Multiaxial Nonproportional Cyclic Deformation," ASTM STP 770, pp. 500-518.

Mroz, Z., 1967, "An Attempt to Describe the Behaviour of Metals Under Cyclic Loads Using a More General Workhardening Model," Acta Mechanica, Vol. 7, pp. 199-212.

Nouailhas, D., Policella, H., and Kaczmarek, H., 1983, "On the Description of Cyclic Hardening Under Complex Loading Histories," Proceedings of the International Conference on Constitutive Laws for Engineering Materials, Eds. Desai and Gallagher, Tucson, AZ, pp. 45-49.

Phillips, A., and Lee, C.W., 1979, "Yield Surfaces and Loading Surfaces. Experiments and Recommendations," International Journal of Solids and Structures, Vol. 15, pp. 715-729.

Phillips, A., Tang, J.L, and Ricciuti, M., 1974, "Some New Observations on Yield Surfaces," Acta Mechanica, Vol. 20, pp. 23-39.

Prager, W., 1956, "A New Method of Analyzing Stresses and Strains on Work-Hardening Plastic Solids," ASME Journal of Applied Mechanics, Vol. 23, pp. 493-496.

Shiratori, E., Ikegami, K., and Yoshida, F., 1979, "Analysis of Stress-Strain Relations by Use of an Anisotropic Hardening Plastic Potential," Journal of the Mechanics and Physics of Solids, Vol. 27, pp. 213-229.

Tanaka, E., Murakami, S., and Ooka, M., 1985, "A Constitutive Model of Cyclic Plasticity in Multiaxial Non-Proportional Loading," L 2/4, SMIRT 8.

Tseng, N.T., and Lee, G.C., 1983, "Simple Plasticity Model of the Two-Surface Type," ASCE Journal of Engineering Mechanics, Vol. 109, No. 3, pp. 795-810.

Wu, H.C., and Yip, M.C., 1981, "Endochronic Description of Cyclic Hardening Behavior for Metallic Materials," ASME Journal of Engineering Materials and Technology, Vol. 103, pp. 212-217.

Ziegler, H., 1959, "A Modification of Prager's Hardening Rule," Quarterly of Applied Mathematics, Vol. 17, pp. 55-60.

### List of Figures

- Fig. 1 Surfaces  $f$  and  $f^*$  in deviatoric stress space.
- Fig. 2 Tseng-Lee kinematic hardening rule for nonzero  $\underline{\underline{a}}^*$ .
- Fig. 3 Imposed  $\epsilon_1$  versus  $\epsilon_3$  strain paths and resulting cyclically stable stress subspace responses for: (a) block 2, specimen SS09, (b) block 3, specimen SS09, (c) block 4, specimen SS09, (d) block 3, specimen SS01, and (e) block 1, specimen SS04.
- Fig. 4 Correlation achieved by Mroz rule for stable cycles from (top) block 3, specimen SS09, (center) block 4, specimen SS09, and (bottom) block 3, specimen SS01.
- Fig. 5 Correlation achieved by Tseng-Lee rule for stable cycles from (top) block 3, specimen SS09, (center) block 4, specimen SS09, and (bottom) block 3, specimen SS01.
- Fig. 6 Correlation achieved by deviatoric stress rate rule for stable cycles from (top) block 3, specimen SS09, (center) block 4, specimen SS09, and (bottom) block 3, specimen SS01.
- Fig. 7 Correlation achieved by Chaboche rule for stable cycles from (top) block 3, specimen SS09, (center) block 4, specimen SS09, and (bottom) block 3, specimen SS01.
- Fig. 8 Correlation of  $H$  versus  $\delta/A$  for Mroz definition of  $\delta$ . Stars, squares, circles, plus signs and x's correspond to data from stable cycles of block 2-4 of specimen SS09, block 3 of specimen SS01, and block 1 of specimen SS04, respectively.
- Fig. 9 Correlation of  $H$  versus  $\delta/A$  for Tseng-Lee definition of  $\delta$ .

- Fig.10 Correlation of  $H$  versus Krieg-Key modulus parameter  $(\bar{\alpha} \cdot n)/A$  for (top)  $A = \max|\underline{\sigma}|$  in cycle and (bottom)  $A = \max(\bar{\alpha} \cdot n)$  in cycle.
- Fig.11 Dafalias modulus function with  $\delta = \delta_m$  (a) fit to proportionally loaded, stable cycle from block 2, specimen SS09, and (b) resulting correlation of data from other nonproportional histories with this function.
- Fig.12 Correlation of  $H$  versus  $D$ . Solid line is that obtained by fitting proportional loading data from specimen SS09, block 2.
- Fig.13 Maximum effective stress in each cycle versus accumulated plastic strain for several loading blocks including block 3, specimen SS09 (squares), block 4, specimen SS09, (circles), block 1, specimen SS04 (plus signs), block 1, specimen SS01 (stars), and block 3, specimen SS01 (x's).
- Fig.14 Correlation of isotropic hardening achieved using state variable  $\phi^*$  for several nonproportional loading blocks. The value of  $\max|\underline{\sigma}| \approx 550$  MPa was reported by Krempf and Lu (1984) for 90 degree out-of-phase loading (i.e.  $\phi^* = 1$ ).
- Fig.15 Normalized maximum effective stress in each cycle versus accumulated plastic strain for several loading blocks. Normalization is between the initial and stable values of  $\max|\underline{\sigma}|$  for each loading block. Symbols correspond to the same histories as in Fig. 13.



TABLE I  
Complex Strain Histories  
Block Number

	$\dot{\epsilon}$ (sec <sup>-1</sup> )	1	2	3	4
SS01	0.003	endpoint sequence: 0 $\epsilon=\gamma=0$ 1 $\epsilon=0.0041$ $\gamma=0.006$ 2 $\epsilon=-0.0041$ $\gamma=-0.006$ return to $\epsilon=\gamma=0$	endpoint sequence: 0 $\epsilon=\gamma=0$ 1 $\epsilon=0.0041$ $\gamma=-0.006$ 2 $\epsilon=-0.0041$ $\gamma=0.006$ return to $\epsilon=\gamma=0$	endpoint sequence: 0 $\epsilon=\gamma=0$ 1 $\epsilon=0.0041$ $\gamma=0.006$ 2 $\epsilon=0.0041$ $\gamma=-0.006$ 3 $\epsilon=-0.0041$ $\gamma=0.006$ 4 $\epsilon=-0.0041$ $\gamma=-0.006$ return to $\epsilon=\gamma=0$	
		25 cycles	25 cycles	25 cycles	
SS09	0.001	Incremental Step test: $\epsilon_a^{\max}=0.007$ $\gamma_a^{\max}=0.0105$	$\epsilon_a=0.005$ $\gamma_a=0.0075$ $\theta=0$	$\epsilon_a=0.005$ $\gamma_a=0.0075$ $\theta=30^\circ$	$\epsilon_a=0.005$ $\gamma_a=0.0075$ $\theta=60^\circ$
		10 cycles	10 cycles	25 cycles	25 cycles
SS04	0.002	0 $\epsilon=\gamma=0$ 1 $\epsilon=0, \gamma=0.0085$ 2 $\epsilon=0, \gamma=-0.0085$ 3 $\epsilon=-0.0039, \gamma=0.0057$ 4 $\epsilon=0.0039, \gamma=-0.0057$ 5 $\epsilon=-0.0046, \gamma=0.0039$ 6 $\epsilon=0.0046, \gamma=-0.0039$ 7 $\epsilon=0.0051, \gamma=0$ 8 $\epsilon=-0.0051, \gamma=0$ 9 $\epsilon=0.0046, \gamma=0.0039$ 10 $\epsilon=-0.0046, \gamma=-0.0039$ 11 $\epsilon=0.0039, \gamma=0.0057$ 12 $\epsilon=-0.0039, \gamma=-0.0057$ return to $\epsilon=\gamma=0$			
		50 cycles			

\*Denotes sinusoidal loading with  $\epsilon = \epsilon_a \sin \omega t$ ,  $\gamma = \gamma_a \sin(\omega t - \theta)$ .

TABLE II

Values of A for Modulus Parameter Normalization

History	Two Surface & Parameters			Kreig-Key*	
	A (MPa)		R* (MPa)	A (MPa)	
	$\delta_m$	$\delta_{\dot{\sigma}}$		max   $\sigma$	max ( $\bar{\alpha} \cdot n$ )
SS09, Block #2	440	440	338	308	140
SS09, Block #3	530	360	429	399	230
SS09, Block #4	530	330	500	470	300
SS04, Block #1	465	470	494	464	300
SS01, Block #3	480	530	555	525	360

\* R = 160 MPa

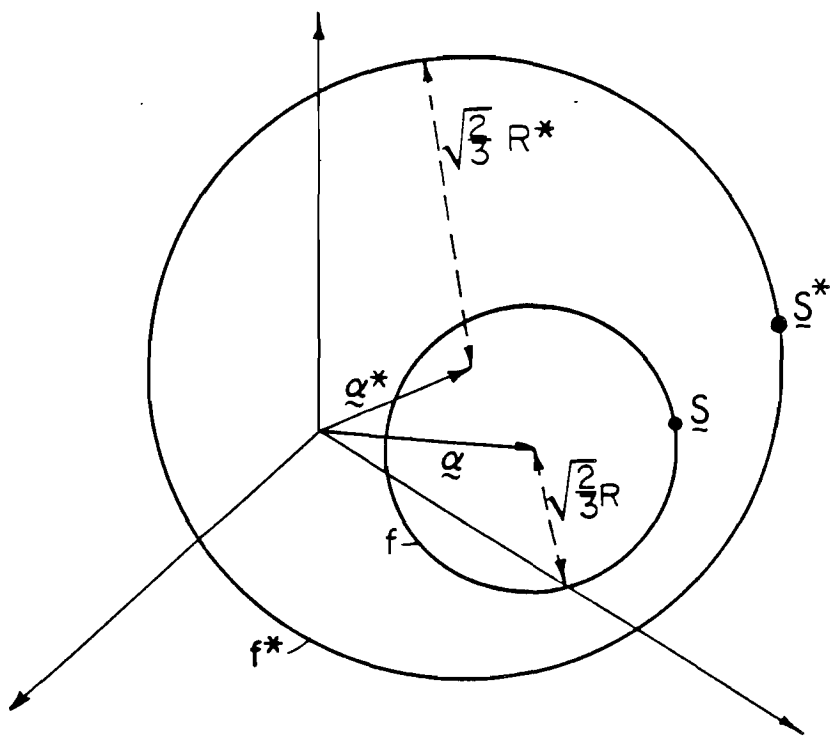


Fig 1

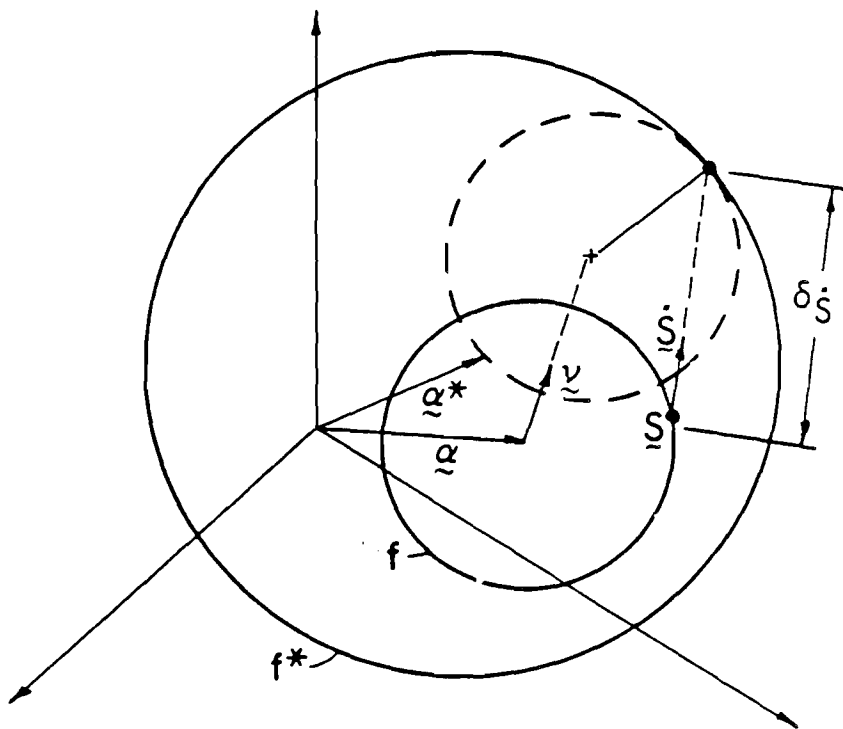


Fig. 2

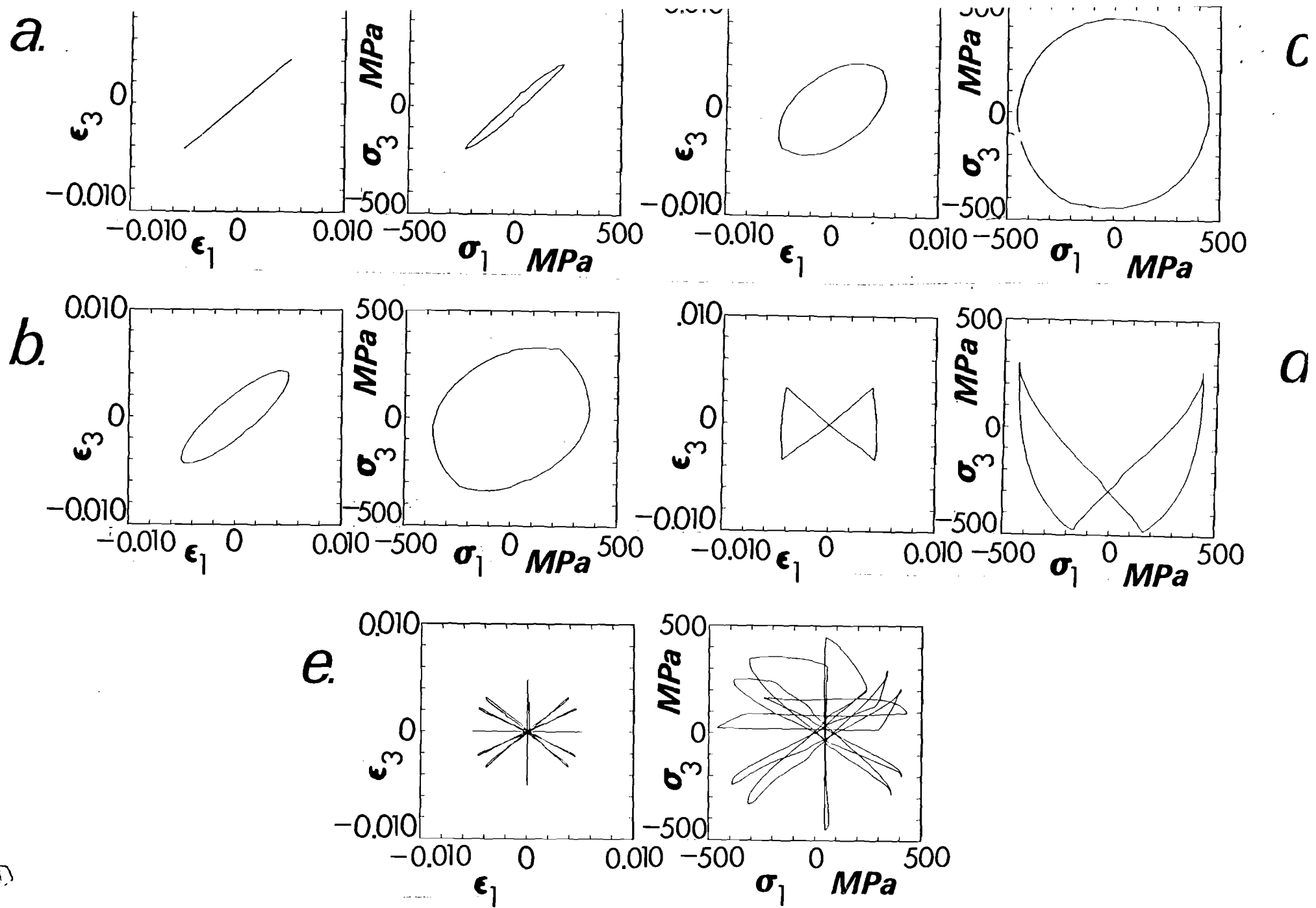


Fig. 3

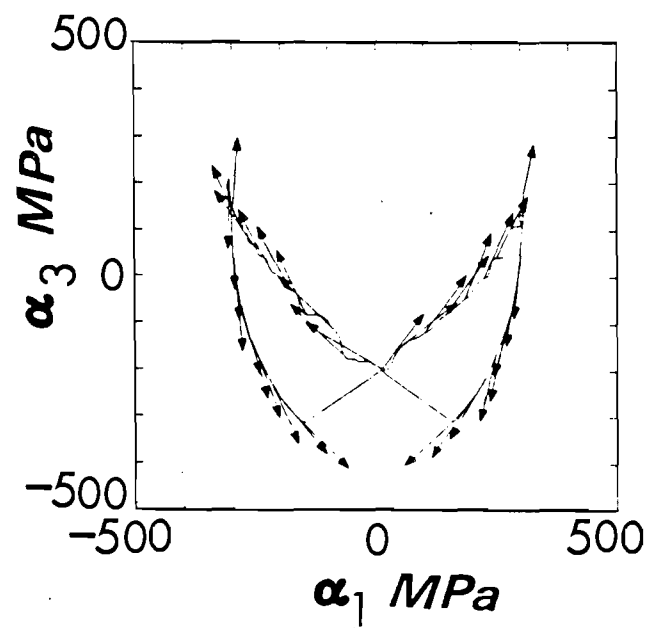
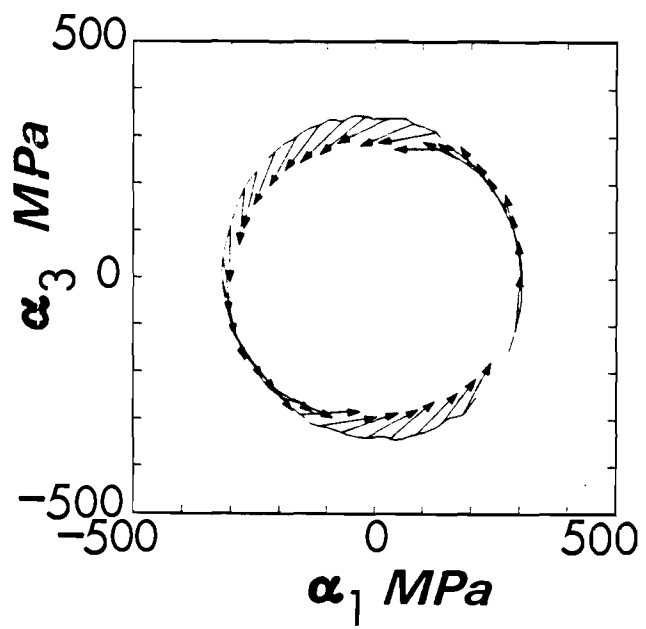
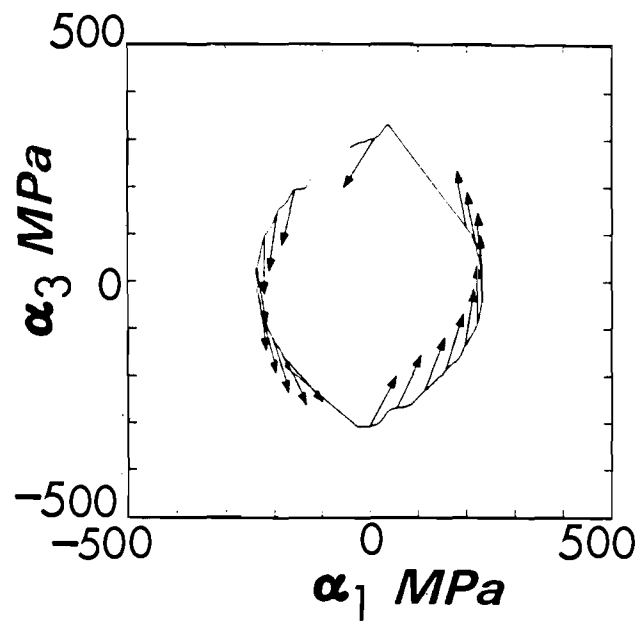


Fig. 4.

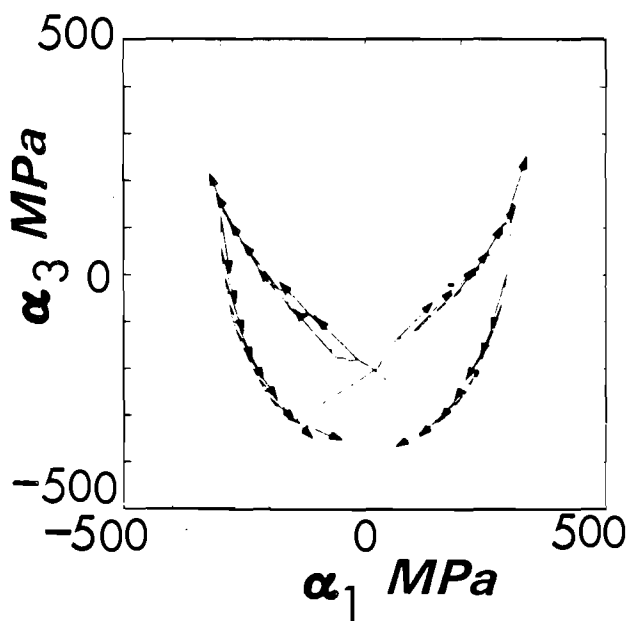
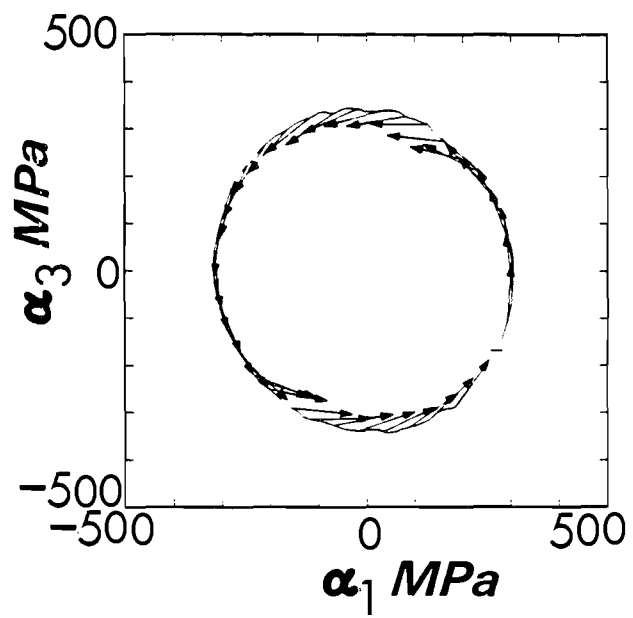
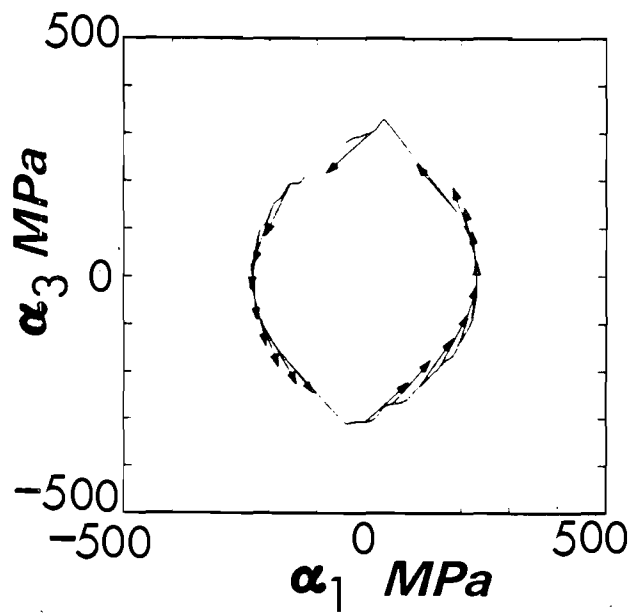


Fig. 5

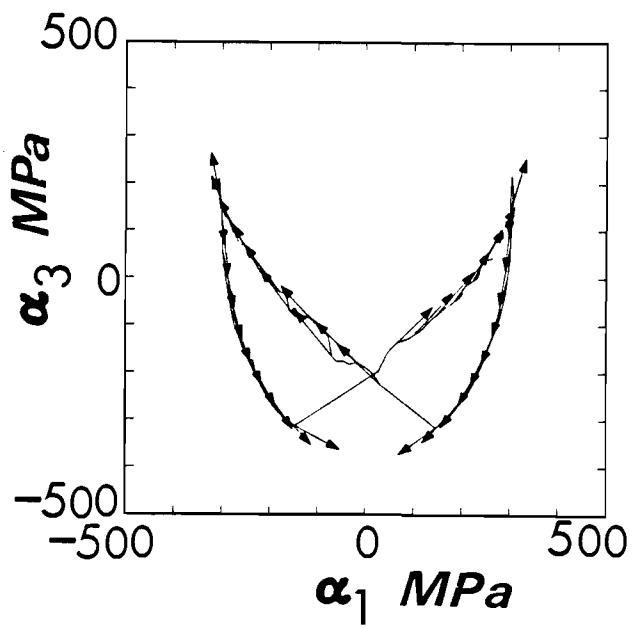
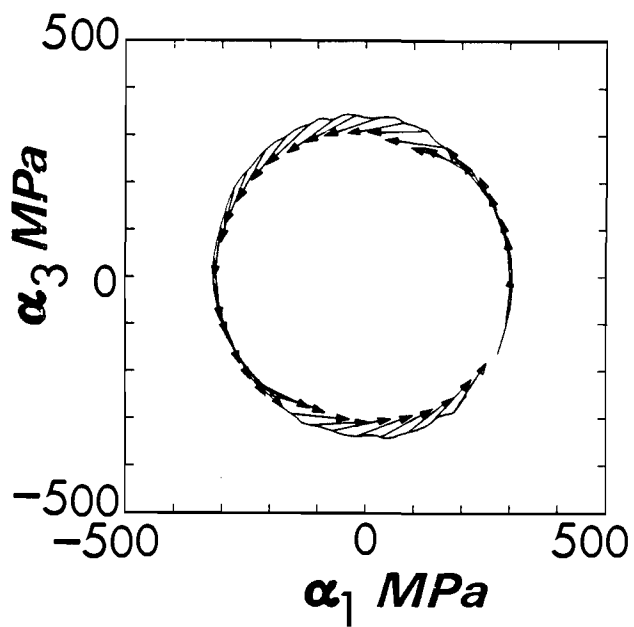
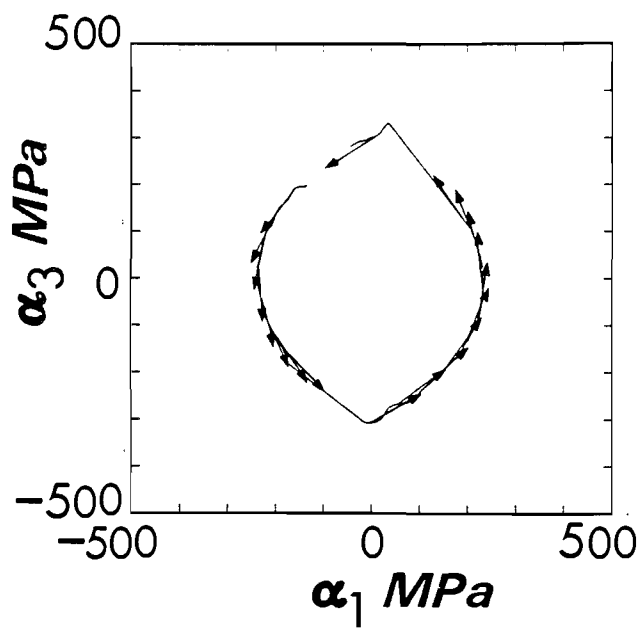


Fig. 6



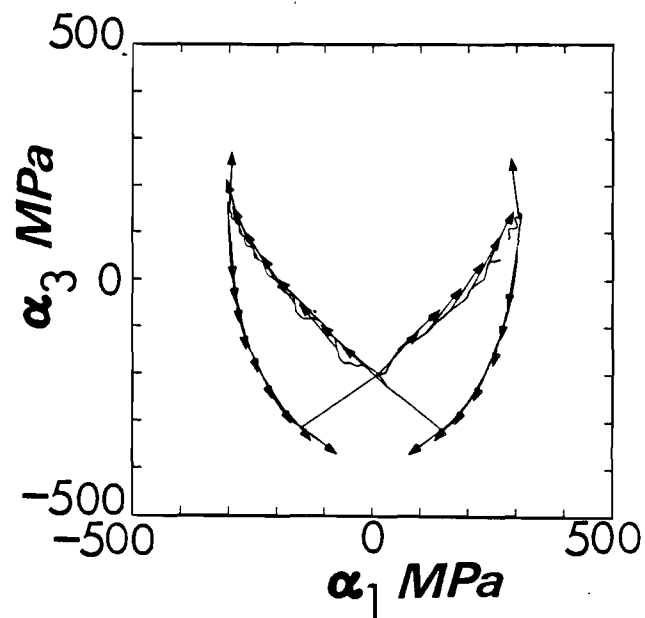
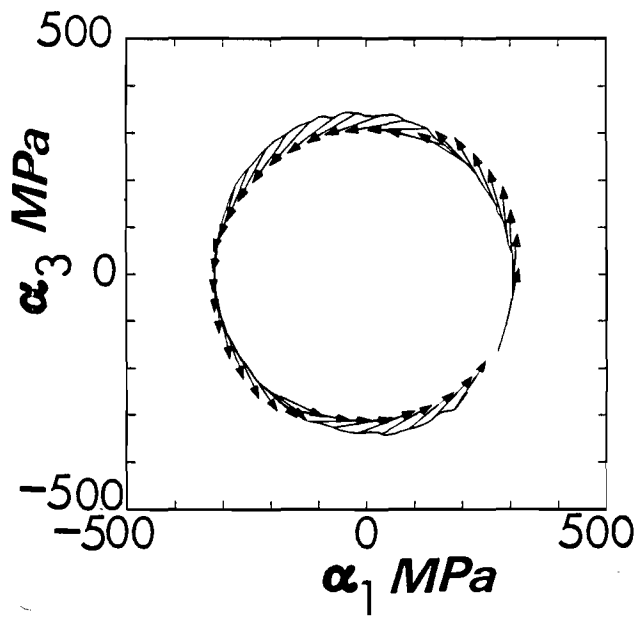
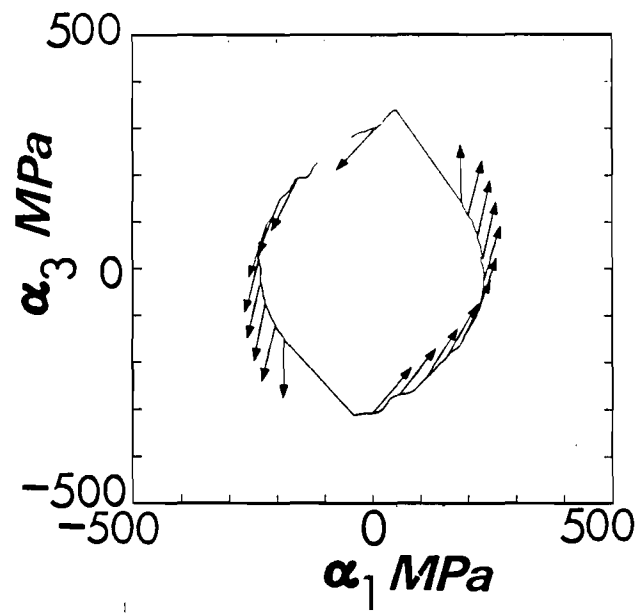
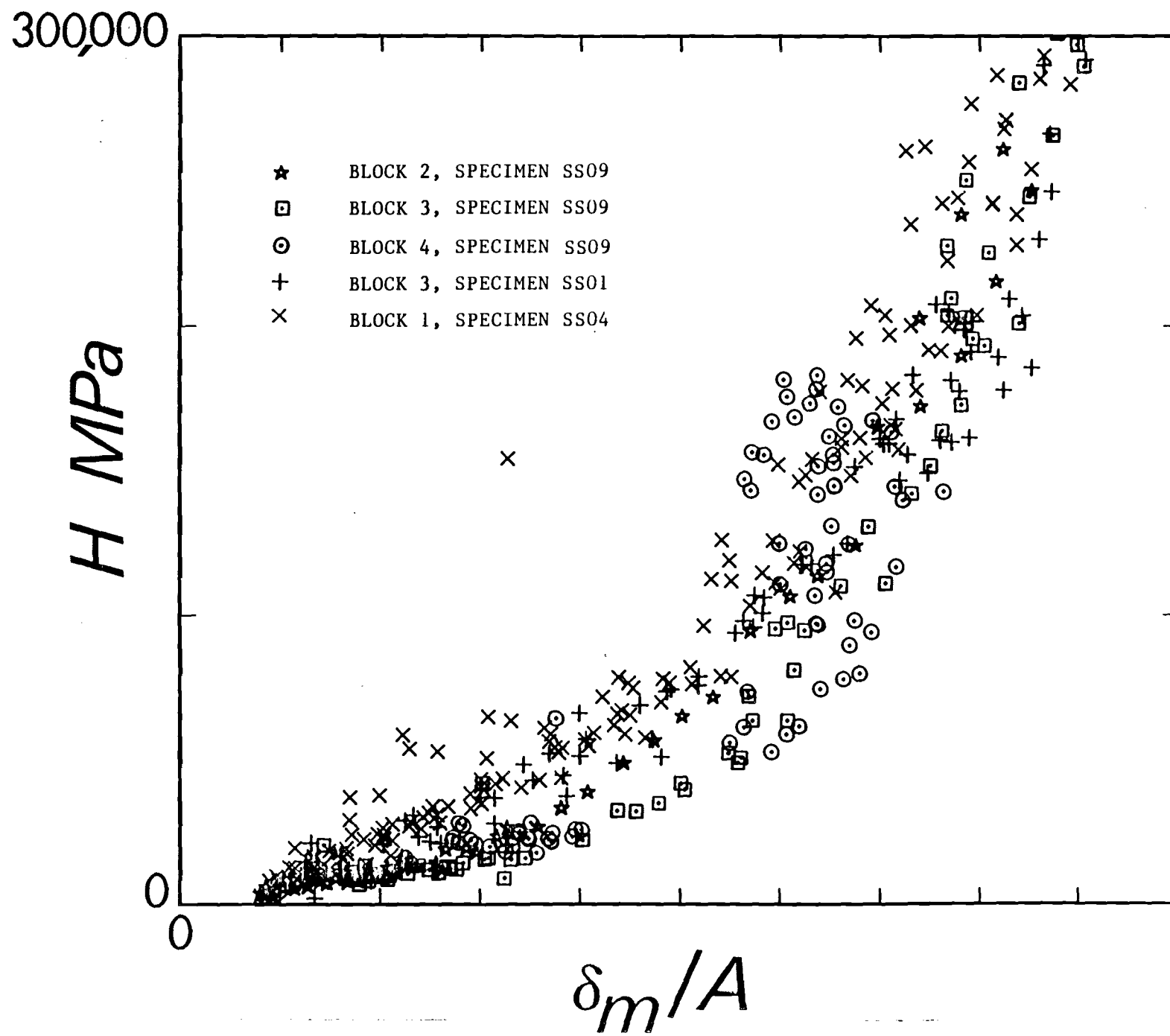


Fig. 7



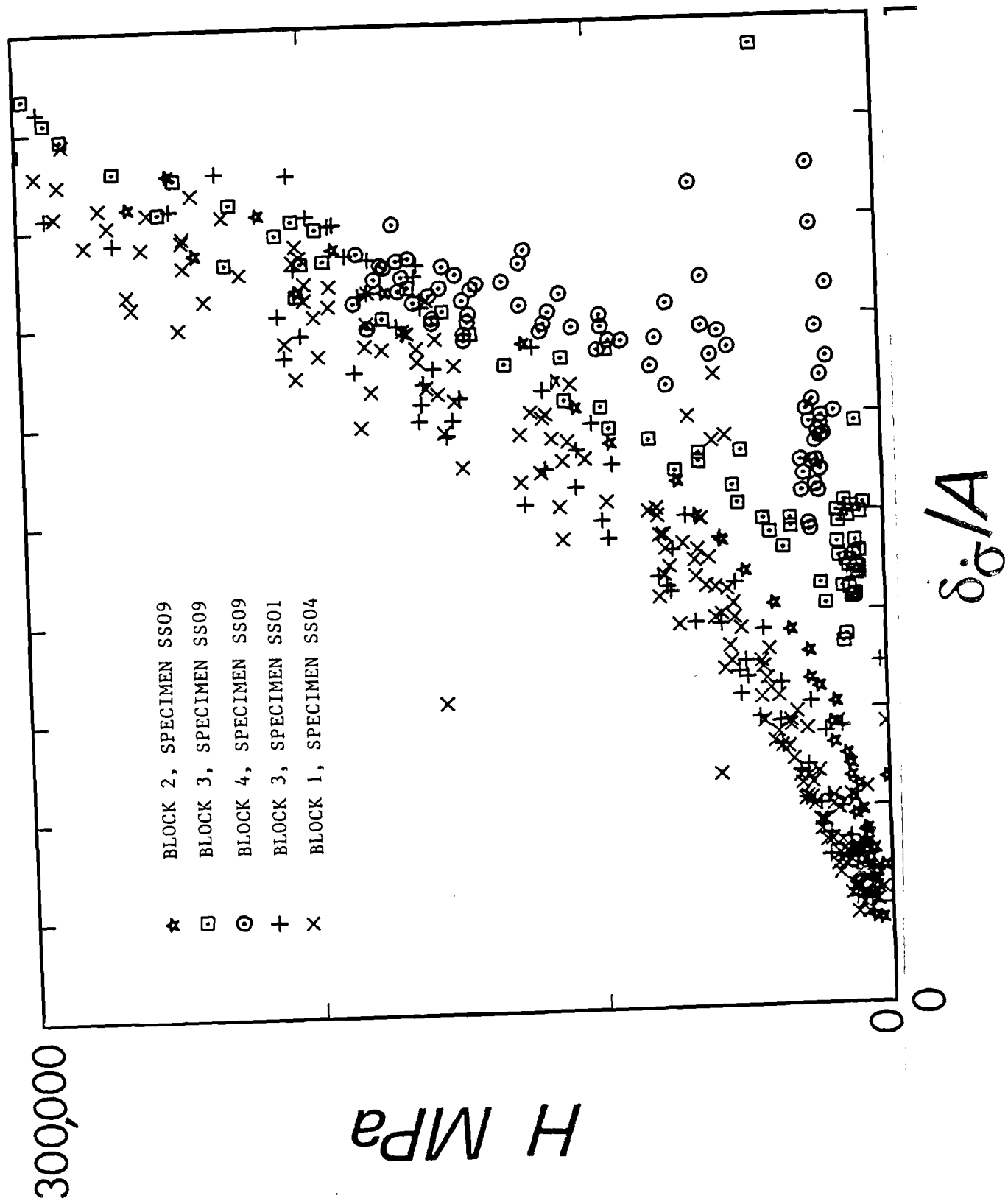


Fig. 9

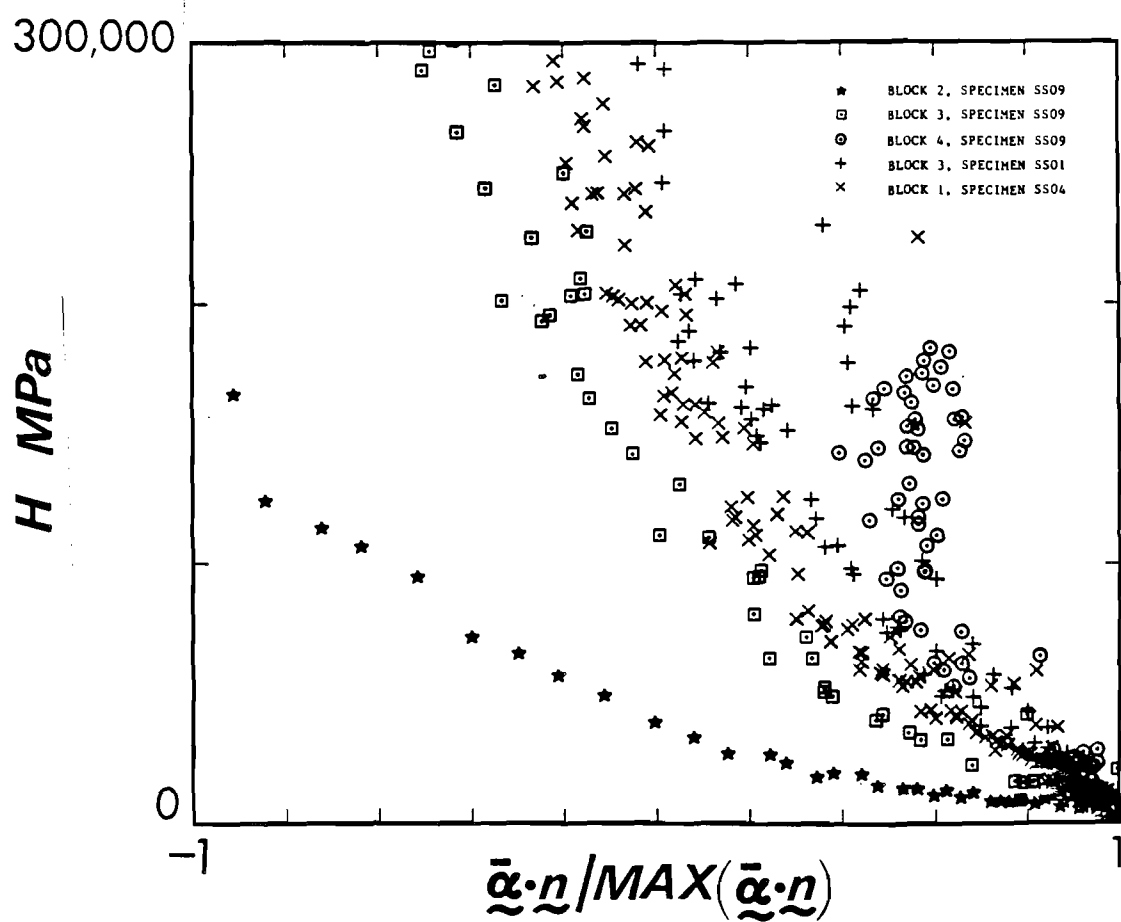
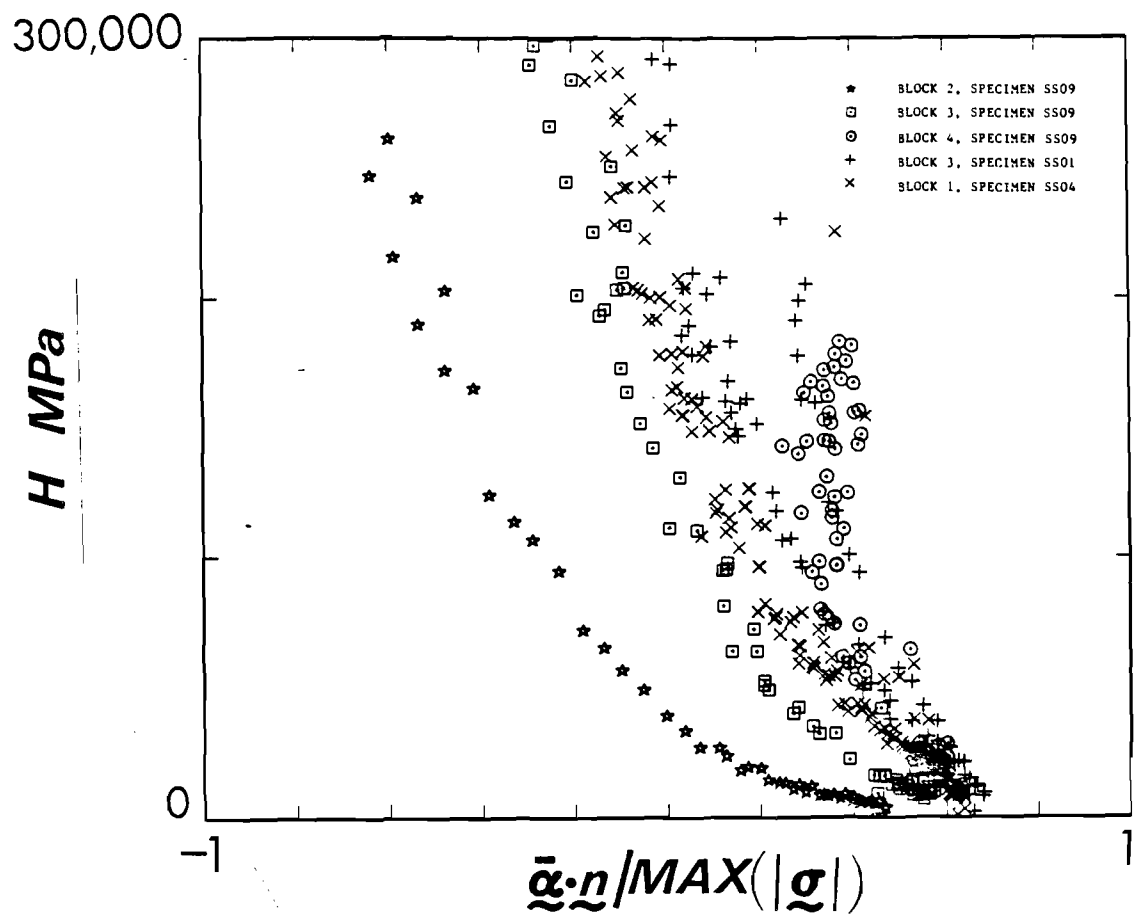
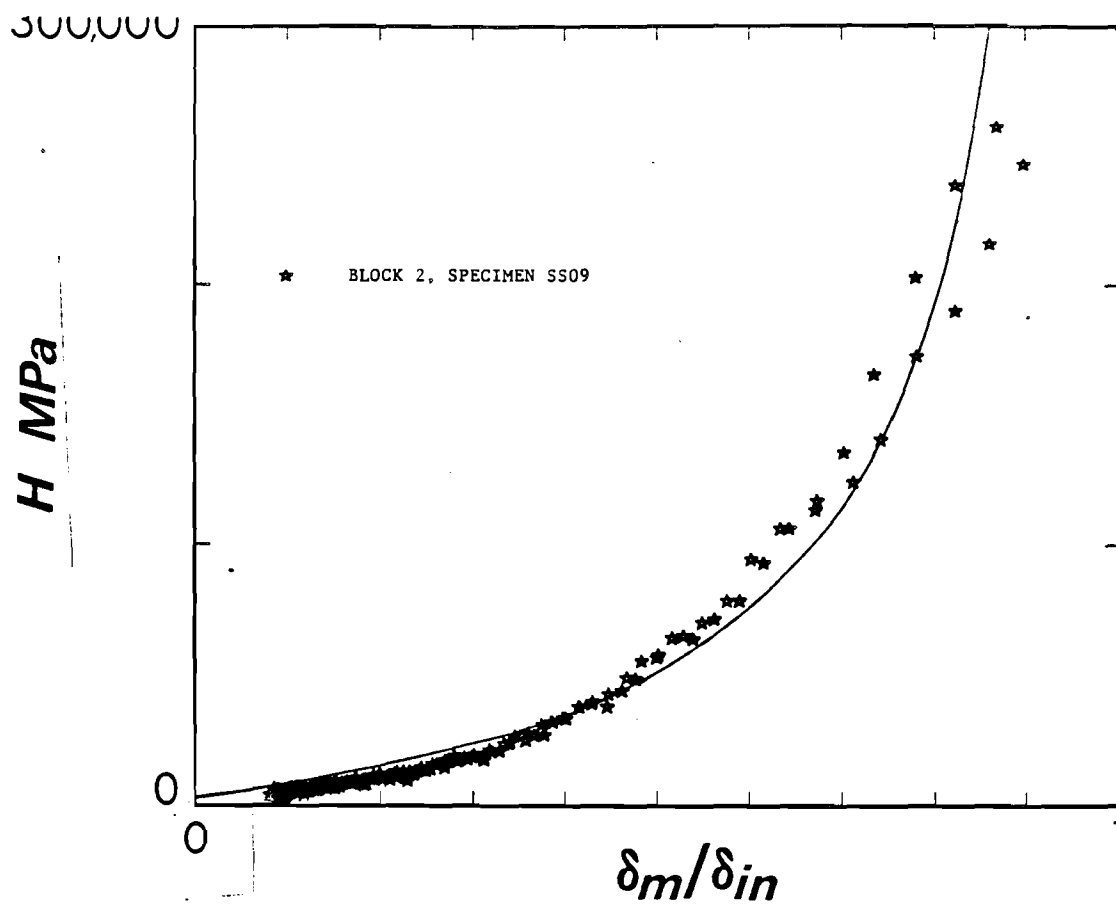


Fig. 10

*a.*



*b.*

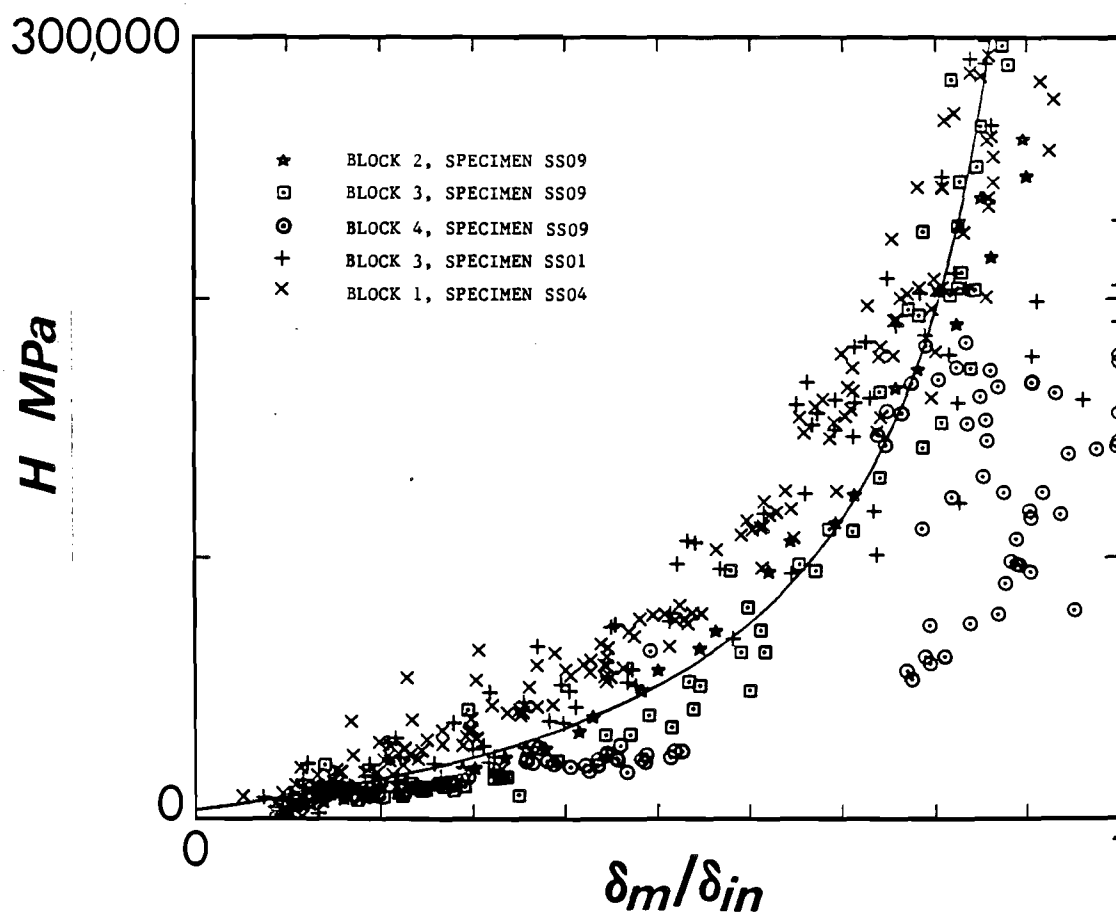


Fig. 11

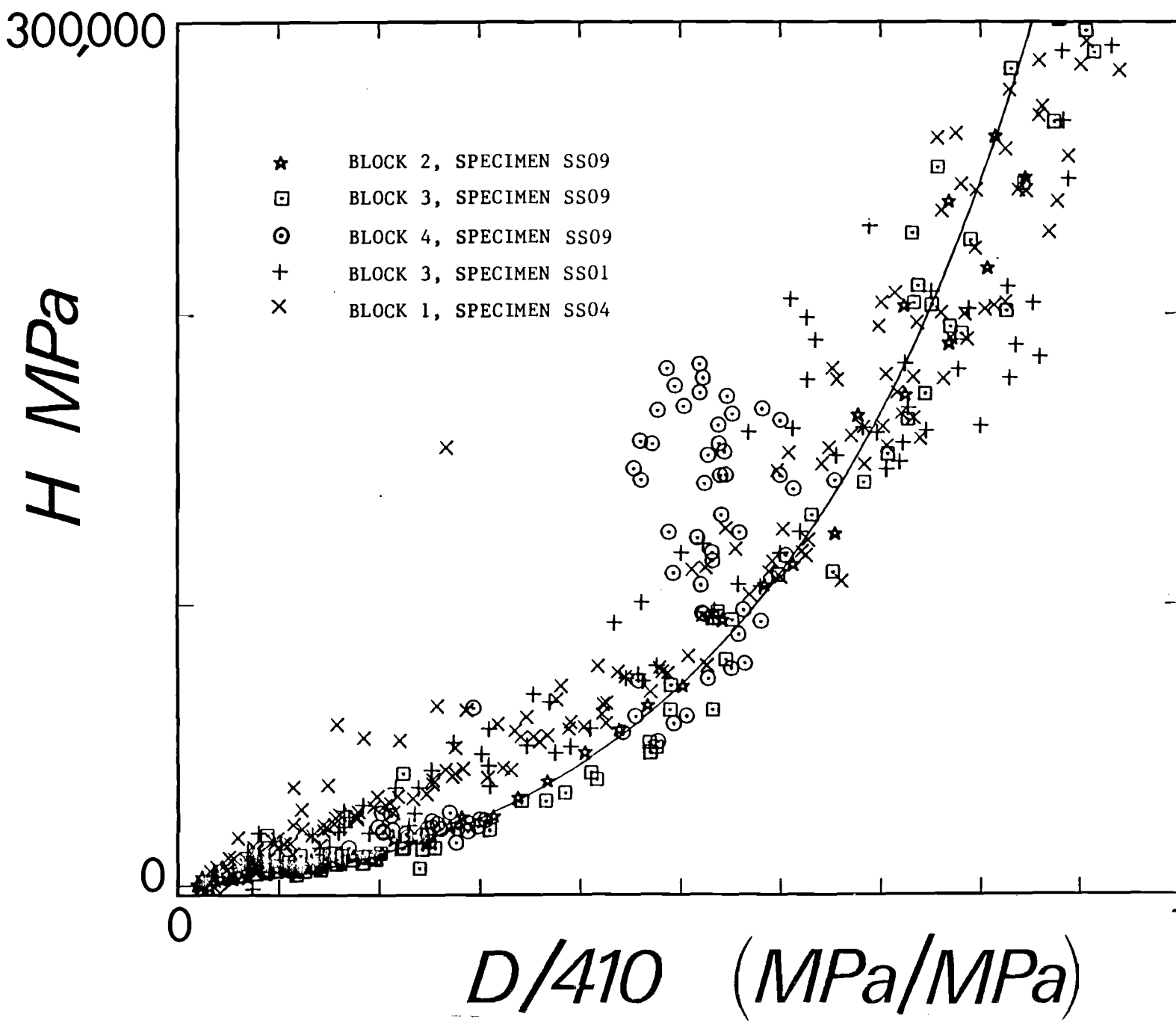


Fig 12

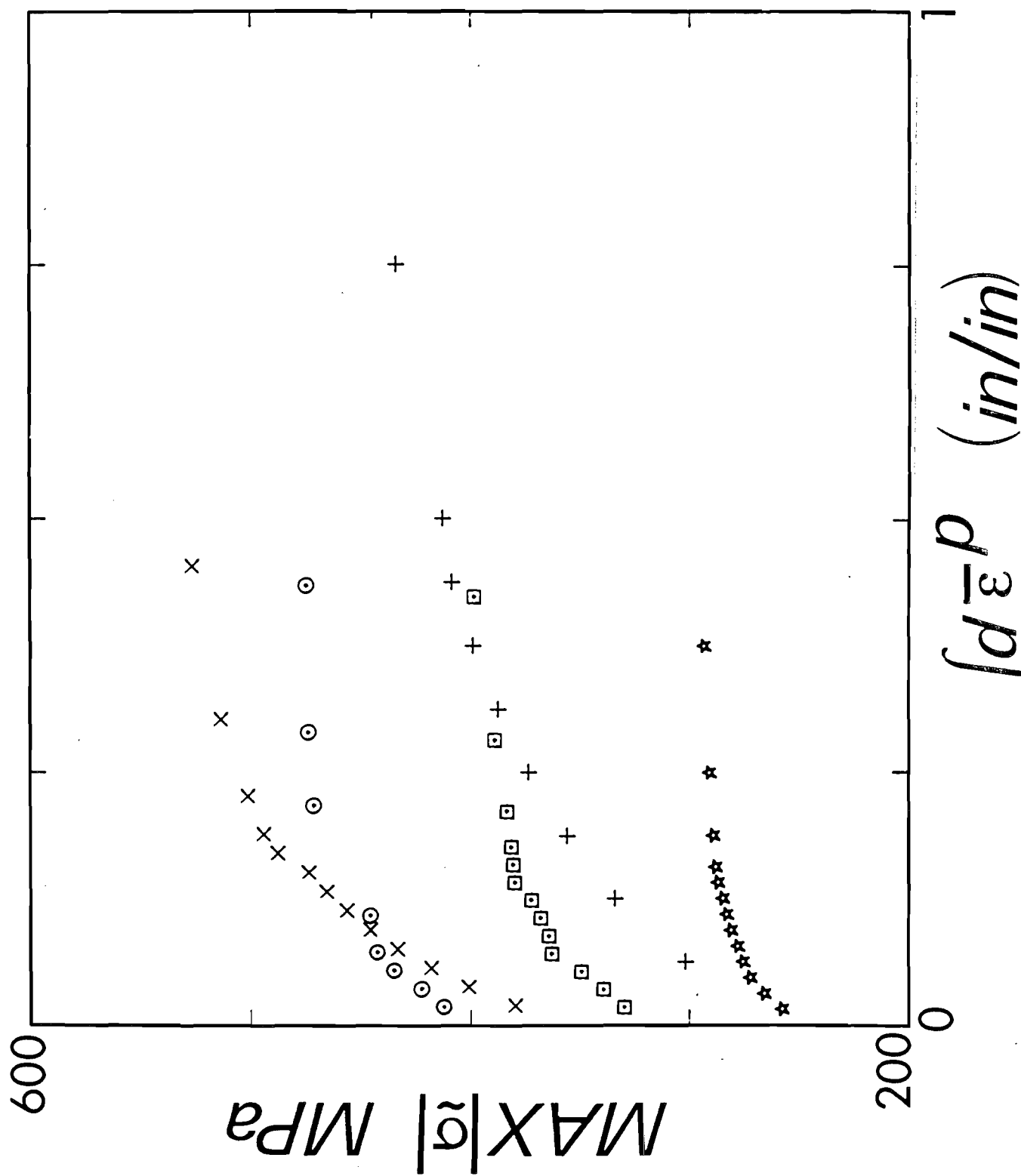
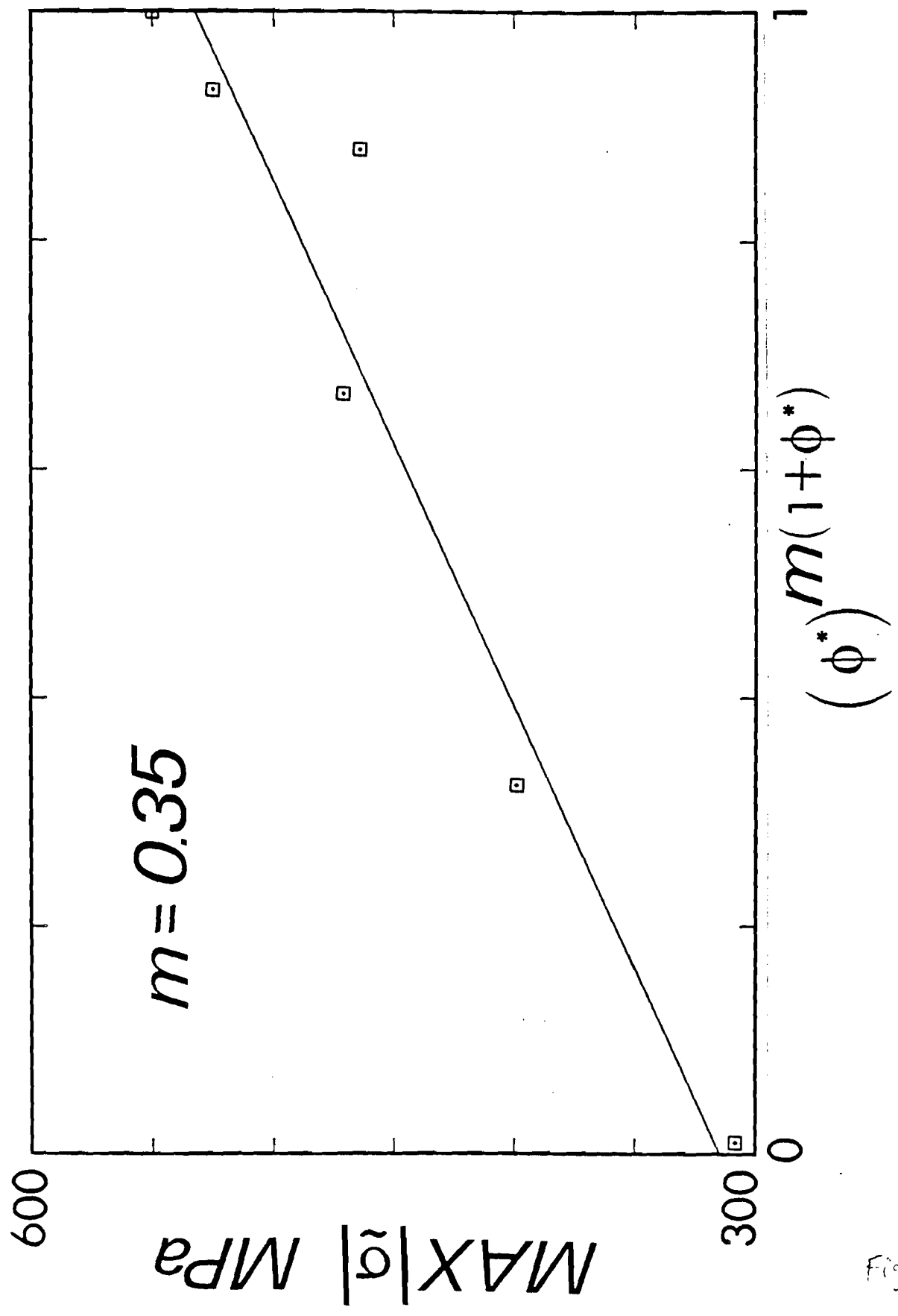


Fig. 13





# SIMPLE EXPERIMENTALLY MOTIVATED CYCLIC PLASTICITY MODEL

By David L. McDowell<sup>1</sup>

**ABSTRACT:** A two-surface cyclic plasticity theory is presented with refinements based on analysis of nonproportional cyclic plasticity data. It is shown that the model accurately correlates nonproportional cyclic stress-strain response, yet the model structure is simplified compared to previous models. New contributions include a more general isotropic hardening rule that reflects additional nonproportional hardening, and a more accurate plastic modulus representation for nonproportional loading. A kinematic hardening rule is used, which reflects experimental observations of backstress translation direction being related to deviatoric stress rate. Transient stress-strain behavior from four axial torsional nonproportional loading blocks is predicted.

## INTRODUCTION

With the increasing emphasis on lightweight, high-performance structures, there has been a corresponding rise of interest in constitutive equations for cyclic plasticity. This is true for the turbine and rocket engine, nuclear and ground vehicle industries, for example. Historically, the complexity of cyclic plasticity models increased as more experimentally observed effects were reported. There has been a relatively recent emphasis (Dafalias 1975, 1981; Krieg 1975; Lamba and Sidebottom 1978b; McDowell 1985c, 1985d; Nouailhas, et al. 1983; Ohno 1982; Tanaka, et al. 1985; Tseng and Lee 1983) on the formulation of models for multiaxial loading.

Lamba (1978a, 1978b) produced data from nonproportional cyclic axial-torsional tests on OFHC copper, and showed that the kinematic hardening rule of Mroz (1967) was far superior to that of Ziegler (1959) or Prager (1956) for correlating stress-strain responses during nonproportional loading. Lamba also reported a significant increase in cyclic hardening under sinusoidal out-of-phase loading, a finding that since has been reported for other materials for similar loading conditions (Kana-zawa, et al. 1979; Krempl and Lu 1984a; McDowell 1983a, 1983b, 1984). Prediction of the direction of plastic strain rate in general depends greatly on the kinematic hardening rule for nonproportional loading. Likewise, isotropic hardening during nonproportional loading can no longer be represented as a function of accumulated plastic strain or plastic work; it is also a function of changes in the direction of the plastic strain rate vector over a loading history (Dafalias 1984; McDowell 1985a, 1985b).

The Mroz kinematic hardening rule was originally proposed for a set of nested loading surfaces surrounding the yield surface (Mroz 1967). Since then, two surface theories have been proposed (Dafalias 1975, 1981; Krieg 1975; McDowell 1985c, 1985d) that assign the modulus in the plas-

<sup>1</sup>Asst. Prof., George W. Woodruff School of Mech. Engrg., Georgia Inst. of Tech., Atlanta, GA 30332.

Note.—Discussion open until August 1, 1987. To extend the closing date one month, a written request must be filed with the ASCE Manager of Journals. The manuscript for this paper was submitted for review and possible publication on March 13, 1986. This paper is part of the *Journal of Engineering Mechanics*, Vol. 113, No. 3, March, 1987. ©ASCE, ISSN 0733-9399/87/0003-0378/\$01.00. Paper No. 21321.

tic region as a function of the distance from the current stress point to a similar point on a surrounding limit or bounding surface. In general, kinematic and isotropic hardening rules are proposed for both the yield and limit surfaces.

Recent analysis of nonproportional data has indicated that some of the assumptions of previous two-surface models are not entirely accurate. The Mroz kinematic hardening rule can be improved by admitting dominance of the deviatoric stress rate (McDowell 1986; Tseng and Lee 1983). Correlation of the modulus function in the plastic regime can be improved by consideration of the instantaneous degree of nonproportionality in addition to the distance from the stress point to a similar point on the limit surface. Additional isotropic hardening effects during nonproportional loading can be correlated with a weighted measure of the changes in plastic strain rate direction during a cycle of loading. Furthermore, isotropic hardening can be exclusively associated with growth of the limit surface and, as a consequence, the modulus function.

## MODEL DEVELOPMENT

Modifications of classical models based on a single yield surface (Chaboche, et al. 1979; Drucker and Palgen 1981; Eisenberg 1976), though generally simple, do not accurately describe variation in hardening modulus, kinematic hardening, nor isotropic hardening (McDowell 1985a) for cyclic nonproportional histories.

Multiple- or nested-surface models (Krieg 1975; Lamba and Sidebottom 1978a, 1978b; McDowell 1985c, 1985d) which use the Mroz rule or some comparable nesting rule tend to perform accurately for nonproportional loading. Economical two-surface theories have been proposed (Dafalias 1975, 1981; Krieg 1975; Lamba and Sidebottom 1978b; McDowell 1985c, 1985d) which use an analytical representation of the hardening modulus in the regime of plastic deformation. These previously proposed two-surface theories assigned the plastic modulus as a function of the distance from the current stress point to a similar point on a bounding or limit surface. The models of Dafalias, et al. (1975, 1981), McDowell (1985c, 1985d), Tseng and Lee (1983), and Lamba, et al. (1978a, 1978b), use the concept of an asymptotic modulus, and enforce tangency of contact between yield and limit surfaces in the asymptotic regime. This paper will introduce a simplified model structure, conforming to results of detailed analysis of nonproportional cyclic data, which accurately describes the essential aspects of plastic flow and hardening.

## MODEL STRUCTURE

Only time-rate-independent plasticity will be considered. Deformation-induced anisotropy is represented by inclusion of backstress  $\alpha$  in the yield surface

$$f = \frac{3}{2} (\mathbf{s} - \boldsymbol{\alpha}) : (\mathbf{s} - \boldsymbol{\alpha}) - R^2 \dots \dots \dots (1)$$

where  $\mathbf{s}$  is the deviatoric stress tensor  $\mathbf{s} = \boldsymbol{\sigma} - (1/3)(\boldsymbol{\sigma} : \mathbf{I})\mathbf{I}$  and  $R$  is the

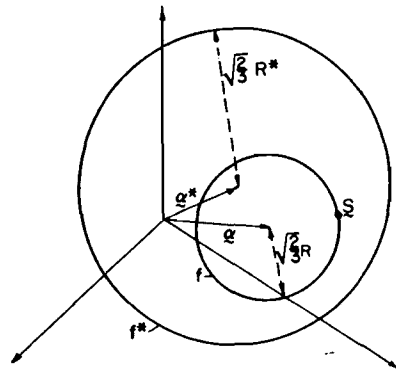


FIG. 1.—Surfaces  $f$  and  $f^*$  in Deviatoric Stress Space

yield stress normalized to the uniaxial case. The identity tensor is denoted by  $I$ . The flow rule is stated as

$$\dot{\epsilon}^P = \frac{1}{h} (\dot{s} : n) n \quad \text{if } f = 0 \quad \text{and} \quad \dot{s} : n \geq 0 \quad (2)$$

$$\dot{\epsilon}^P = 0 \quad \text{otherwise} \quad (3)$$

where the unit normal vector  $n = (s - \alpha) / \|s - \alpha\|$ , and the scalar product  $\dot{s}_{ij} n_{ij}$  is denoted by  $\dot{s} : n$ . The notation  $\|s - \alpha\|$  denotes the norm  $[(s - \alpha) : (s - \alpha)]^{1/2}$ . Here, the usual decomposition of the total small strain rate into elastic and plastic components is assumed, i.e.,  $\dot{\epsilon} = \dot{\epsilon}^e + \dot{\epsilon}^P$ . In Eq. 2,  $h$  is the hardening modulus.

Now define a limit surface  $f^*$  which encloses or bounds the yield surface

$$f^* = \frac{3}{2} (s - \alpha^*) : (s - \alpha^*) - (R^*)^2 \quad (4)$$

where  $R^*$  is the limit surface radius normalized to the uniaxial case. Surfaces  $f$  and  $f^*$  are shown in Fig. 1 in deviatoric stress space.

Kinematic and isotropic hardening rules will next be introduced for both the yield and limit surfaces. Careful analysis of nonproportional cyclic test data (McDowell 1986) shows that a variation of the Mroz kinematic hardening rule is more accurate for two surfaces. This variation, first suggested by Tseng and Lee (1983), was motivated by the observation that yield surface movement was dominated by the direction of deviatoric stress rate. Implementation of this observation in a two-surface theory must still provide for tangential nesting of the yield and limit surfaces at the asymptotic state.

As proposed by Tseng and Lee, modified here for inclusion of translation of the limit surface (i.e.,  $\alpha^* \neq 0$ ):

$$\dot{\alpha} = \mu \nu \quad (5)$$

$$\text{where } \nu = \frac{\left[ \sqrt{\frac{2}{3}} (R^* - R) \lambda - (\alpha - \alpha^*) \right]}{\left\| \sqrt{\frac{2}{3}} (R^* - R) \lambda - (\alpha - \alpha^*) \right\|} \quad (6)$$

$$\lambda = \frac{s + \delta_s \frac{\dot{s}}{\|\dot{s}\|} - \alpha^*}{\left\| \left( s + \delta_s \frac{\dot{s}}{\|\dot{s}\|} - \alpha^* \right) \right\|} \quad (7a)$$

$$\text{and } \delta_s = - (s - \alpha^*) : \frac{\dot{s}}{\|\dot{s}\|} + \left\{ \left[ (s - \alpha^*) : \frac{\dot{s}}{\|\dot{s}\|} \right]^2 + \frac{2}{3} (R^*)^2 - \|s - \alpha^*\|^2 \right\}^{1/2} \quad (7b)$$

According to this kinematic hardening rule, illustrated in Fig. 2, the instantaneous direction of translation of the yield surface is toward the position the yield surface would assume if nested with tangential contact at the point of intersection of the deviatoric stress rate direction (with respect to the current stress point) with the limit surface.

It was shown by McDowell (1985a) that the Mroz rule, given by

$$\dot{\alpha} = \mu_M (s^* - s) \quad (8)$$

$$s^* = \alpha^* + (s - \alpha) \left( \frac{R^*}{R} \right) \quad (9)$$

was more accurate for a yield surface and stationary limit surface ( $\alpha^* = 0$ ) than a Prager or Ziegler rule for cyclically stable, nonproportional, strain-controlled, axial torsional cycles imposed on tubular type 304 stainless steel specimens at room temperature. In Fig. 3, the direction

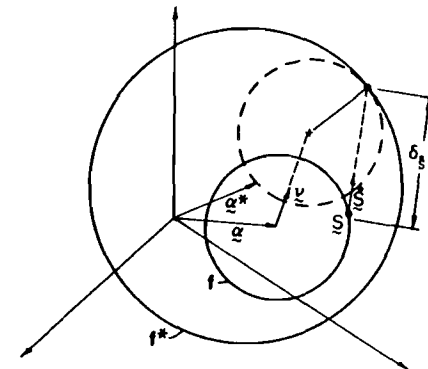


FIG. 2.—Tseng-Lee Kinematic Hardening Rule for Nonzero  $\alpha^*$

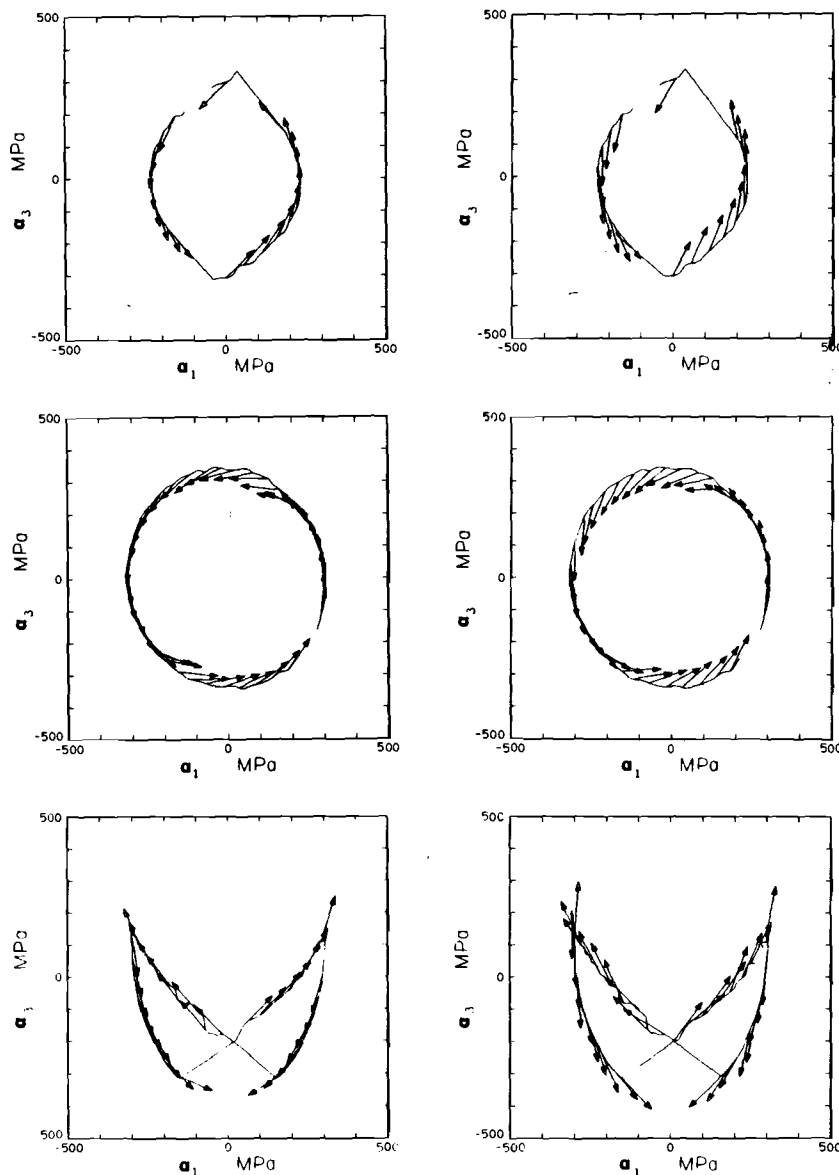


FIG. 3.—Comparison of Tseng-Lee (Left Column) and Mroz (Right Column) Kinematic Hardening Rules in Axial Torsional Subspace for Three Strain-Controlled Histories: (Top) 30° Out-of-Phase Sinusoidal; (Center) 60° Out-of-Phase Sinusoidal; (Bottom) Nonproportional "Bow Tie"-Shaped Path

of translation predicted by Eqs. 3–7 is compared to the Mroz model in Eqs. 8–9, with  $\alpha^* = 0$  and  $R^*$  slightly greater than the maximum effective stress in each stable cycle, i.e.:

$$R^* = \max \left( \frac{3}{2} \mathbf{s} : \mathbf{s} \right)^{1/2} + 30 \text{ MPa} \dots \dots \dots (10)$$

for three nonproportional loading blocks reported in detail elsewhere (McDowell 1985a, 1985d). In Fig. 3, the solid line is the backstress path in the axial torsional subspace computed by backward extrapolation by a distance  $R = 160$  MPa from the current stress point along the plastic strain rate direction; hence, the yield surface form given in Eq. 1 is assumed where the plastic strain rate is radial by normality. The axial torsional subspace is defined by

$$\sigma = \sigma_1 \mathbf{n}_1 + \sigma_3 \mathbf{n}_3 \dots \dots \dots (11)$$

where  $\sigma_1 = \sigma$  and  $\sigma_3 = \sqrt{3}\tau$ . Hence, Eq. 1 reduces to

$$f = (\sigma - \bar{\alpha}) \cdot (\sigma - \bar{\alpha}) - R^2 \dots \dots \dots (12)$$

where  $\bar{\alpha}$  is the backstress in the subspace. Eqs. 5–9 likewise are written in the subspace for comparison in Fig. 3.

It is noted that the accuracy of the kinematic hardening rule is measured by tangency of predicted backstress rate direction with the path of  $\bar{\alpha}$ . In Fig. 3, arrows are plotted along the backstress paths in the directions predicted by the Mroz and Tseng-Lee rules. It is evident that the Tseng-Lee rule provides a more accurate description. As will be discussed later, the use of  $R = \text{constant}$  for all of these histories is warranted by analysis of data.

In Eq. 5,  $\dot{\mu}$  must be determined from the consistency condition

$$\dot{f} = \left( \frac{\partial f}{\partial \mathbf{s}} \right) : \dot{\mathbf{s}} - \left( \frac{\partial f}{\partial \mathbf{s}} \right) : \dot{\mu} \mathbf{v} + \left( \frac{\partial f}{\partial R} \right) \dot{R} = 0 \dots \dots \dots (13)$$

during plastic flow. Unlike previous two-surface models which allow growth in  $R$ , in this work we take  $\dot{R} = 0$  so that

$$\dot{\mu} = \dot{\mathbf{s}} : \frac{\mathbf{n}}{(\mathbf{v} : \mathbf{n})} \dots \dots \dots (14)$$

The condition  $\dot{R} = 0$  is motivated by a study of changes in direction of the plastic strain rate vector following nonproportional unloading or abrupt changes in the direction of total strain rate or deviatoric stress rate vectors (McDowell 1986). According to Eqs. 1–3, the direction of plastic strain rate, along with continuity in the evolution or growth of  $R$ , implies the position of  $\alpha$ . In other words,  $\alpha$  cannot experience a significant instantaneous "jump" in location in this theory due to only an abrupt change in loading direction. This assertion provides a means to estimate  $R$  by analysis of data before and after an abrupt, nonproportional change in loading direction. It is found that evolution of  $R$  can be neglected (at least for the available data), and the yield surface retains its original dimension as a first order approximation if yielding is defined as deviation from linearity. This finding is embodied in a simple theory

of Drucker and Palgen (1981), and is seemingly confirmed by nonproportional yield probing experiments (Hecker 1976; Liu and Greenstreet 1976; Mair and Pugh 1964; Phillips, et al. 1974) in which the yield surface is found to distort but not appreciably expand on a cycle-by-cycle basis.

Since the kinematic hardening is best represented within the framework of the current theory by constant  $R$ , isotropic hardening is best represented by evolution of  $R^*$  and consequential evolution of the modulus function  $h$  in the flow rule. It should be noted (Krempf, et al. 1984b) that the backstress in nonproportional loading for state variable (time- and rate-dependent) theories has been shown to exert more dominant influence than the drag stress, a variable analogous to yield surface radius in the current theory.

Next, we introduce kinematic and isotropic-hardening rules for limit surface  $f^*$ :

$$\dot{\alpha}^* = \kappa \dot{\eta} \quad (15)$$

$$\text{and } \dot{R}^* = c[(R_0 + K\Lambda^{m(1+\Lambda)}) - R^*] \dot{\eta} \quad (16)$$

where  $\dot{\eta} = (\dot{\epsilon}^P : \dot{\epsilon}^P)^{1/2}$ ; and  $R_0$ ,  $\kappa$ ,  $c$ ,  $K$ , and  $m$  are material parameters. Constant  $R_0$  is the cyclically stable uniaxial value of  $R^*$ .  $R_0$  and  $K$  can depend on the plastic strain range (McDowell 1985c, 1985d), if such dependence is significant. Rate constant  $c$  may be selected to fit transient response, and can be determined from the hardening response in uniaxial tests. Likewise,  $\kappa$  can be determined from the response of uniaxial or biaxial stress-controlled ratcheting tests, since ratcheting response depends heavily on  $\alpha^*$  and the form of the modulus function to be discussed later. Mean stress relaxation response also is influenced strongly by  $\alpha^*$  and the modulus function, and could serve as a reference.

Constants  $K$  and  $m$  pertain to the additional isotropic hardening which occurs during nonproportional loading. State variable  $\Lambda$  describes the nonproportionality of the loading path. For uniaxial or proportional strain-controlled cycling ( $d\epsilon_{ij}^P = C\epsilon_{ij}^P$ , where  $\epsilon_{ij}^P$  are components of the plastic strain tensor),  $\Lambda = 0$ . For nonproportional cycling,  $0 < \Lambda \leq 1$ . Hence,  $K$  in Eq. 16 is the maximum increase of strength observed in nonproportional cycling, and  $m$  provides nonlinear weighting necessary to match experimental results for intermediate hardening levels. As pointed out by McDowell (1983a, 1983b, 1984), Kanazawa, et al. (1979), and Krempf and Lu (1984a), the extent of nonproportional isotropic hardening depends on loading history.

From axial torsional tests on thin-walled tubular specimens, it has been shown that the case of sinusoidal straining:

$$\epsilon = \epsilon_a \sin \omega t \quad (17)$$

$$\gamma = \gamma_a \sin (\omega t - \rho) \quad (18)$$

with  $\rho = 90^\circ$  and  $\gamma_a/\epsilon_a \approx 1.5$  to  $\sqrt{3}$ , results in the maximum extent of additional isotropic hardening in this biaxial case (Kanazawa, et al. 1979; McDowell 1983a, 1983b, 1984); hence,  $\Lambda = 1$  for this case. Sufficient experimental data is not available for triaxial cycling to determine possible further hardening due to stressing in a third direction. Previously, a total strain rate formulation for  $\Lambda$  (McDowell 1985c, 1985d) was proposed which accurately correlated biaxial loading cases in which the maximum shear

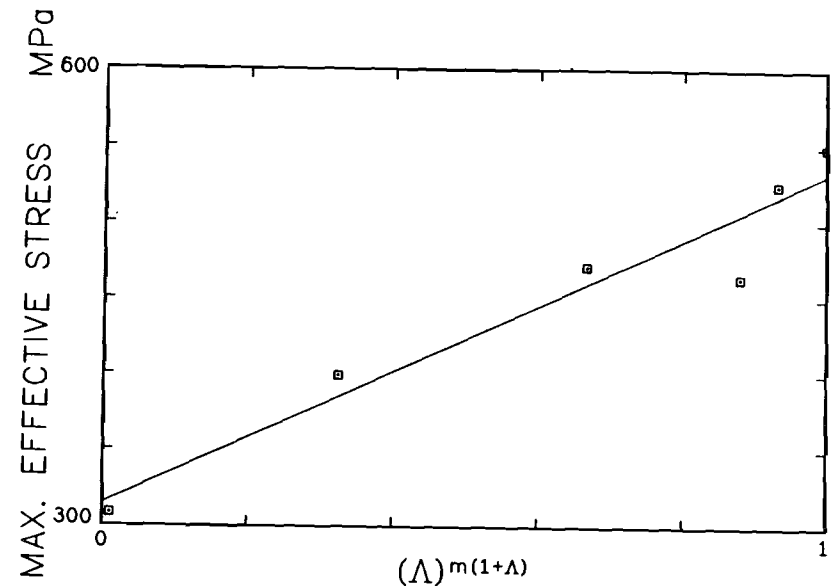


FIG. 4.—Maximum Effective Stress in Stable Cycles versus Nonproportional Hardening Parameter with  $m = 0.35$

strain planes rotated continuously. A more simple, general isotropic hardening rule is presented in this paper. Define evolution of variables  $\phi_1$  and  $\phi_2$ , and  $\bar{n}$  as:

$$\dot{\phi}_1 = [N : \dot{\epsilon}^P] u(t - t_B) \quad (19)$$

$$\dot{\phi}_2 = \|\dot{\epsilon}^P\| u(t - t_B) = \dot{\eta} u(t - t_B) \quad (20)$$

where  $N = \bar{n}/\|\bar{n}\|$ ;  $(d/dt)\bar{n} = A(\mathbf{n}^* - N)\|\dot{\epsilon}^P\|$ ;  $t_B$  = time denoting point of initiation of current loading block  $B$  ( $B = 1, 2, \dots$ );  $u(t - t_B)$  is the unit step function; and  $\mathbf{n}^*$  is the unit normal vector  $\dot{\epsilon}^P/\|\dot{\epsilon}^P\|$  at the maximum value of  $\|\dot{\epsilon}^P\|$  in the current block, i.e.,  $t \geq t_B$ . We may define a loading block as a repeated assemblage of identical cycles or combination of cycles and subcycles. This definition is unambiguous; a variable loading history would be considered as one block, for example. Initial values at the beginning of the first block, for a virgin material, can be stated as  $\phi_1 = \phi_2 = 0$  and  $\bar{n} = \mathbf{n}^* = \mathbf{n}(t = t_i) = \dot{\epsilon}^P/\|\dot{\epsilon}^P\|$  at  $t = t_i$ , where  $t_i$  corresponds to initiation of yielding.

At any point in a given block  $B$  (i.e.,  $t > t_B$ ), define  $\Lambda$  as

$$\Lambda = \left| 1 - \left( \frac{\pi}{\pi - 2} \right) \left( \phi - \frac{2}{\pi} \right) \right| \quad (21)$$

It should be noted that  $\phi = \phi_1/\phi_2$  is the ratio of the plastic strain accumulated in the primary loading direction to the total plastic strain accumulated in the current block. For proportional straining,  $\phi_1/\phi_2 \rightarrow 1$  and  $\Lambda \rightarrow 0$ . For  $90^\circ$  out-of-phase axial torsional loading with  $\gamma_a/\epsilon_a = \sqrt{3}$  and, Poisson's ratio of  $1/2$  (fully plastic),  $\phi_1/\phi_2 \rightarrow 2/\pi$  and  $\Lambda \rightarrow 1$ .

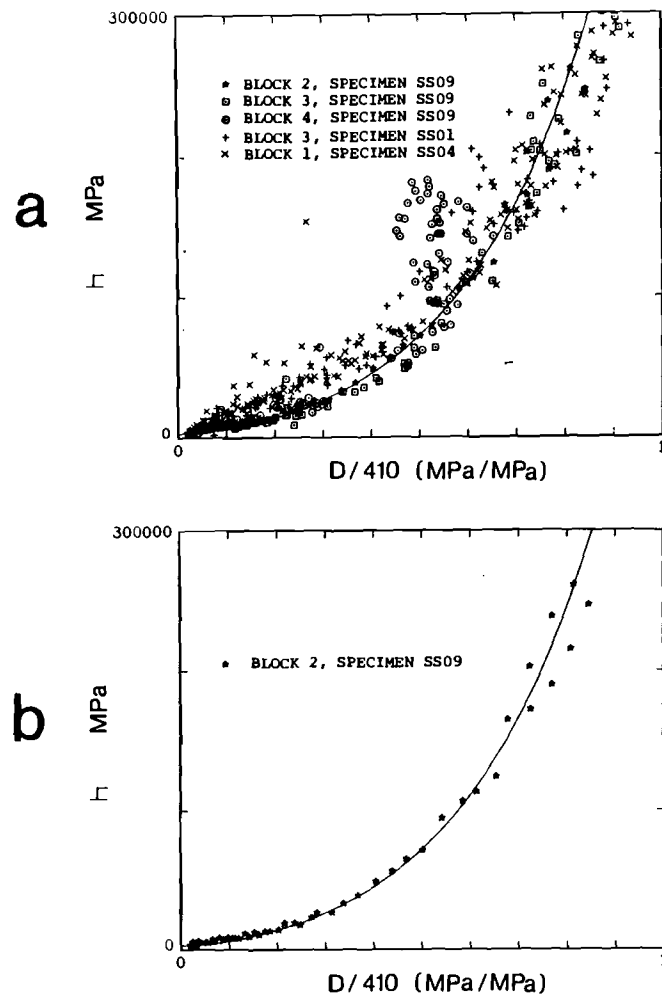


FIG. 5.—Correlation of Hardening Modulus Based on Eq. 29 for: (a) Stable Cycles from Four Different Nonproportional Loading Blocks; for (b) Stable Cycle from Proportional Loading Block, to Which Modulus Function Was Fit

The reference direction for computing nonproportionality, defined as  $N$ , is allowed to evolve upon switching to a new loading block. This vector rotates toward  $n^*$ , i.e., the direction of maximum plastic strain excursion in the current loading block. The rate of rotation to  $n^*$  is determined by  $A$ . This evolution is necessary to match experimental observations of a small amount of hardening upon switching from one proportional path to another "proportional" path. The extent of additional hardening predicted upon switching from cyclic tension to cyclic torsion, for example, is related to  $A$ . For large values of  $A$ ,  $N$  approaches  $n^*$  rapidly.

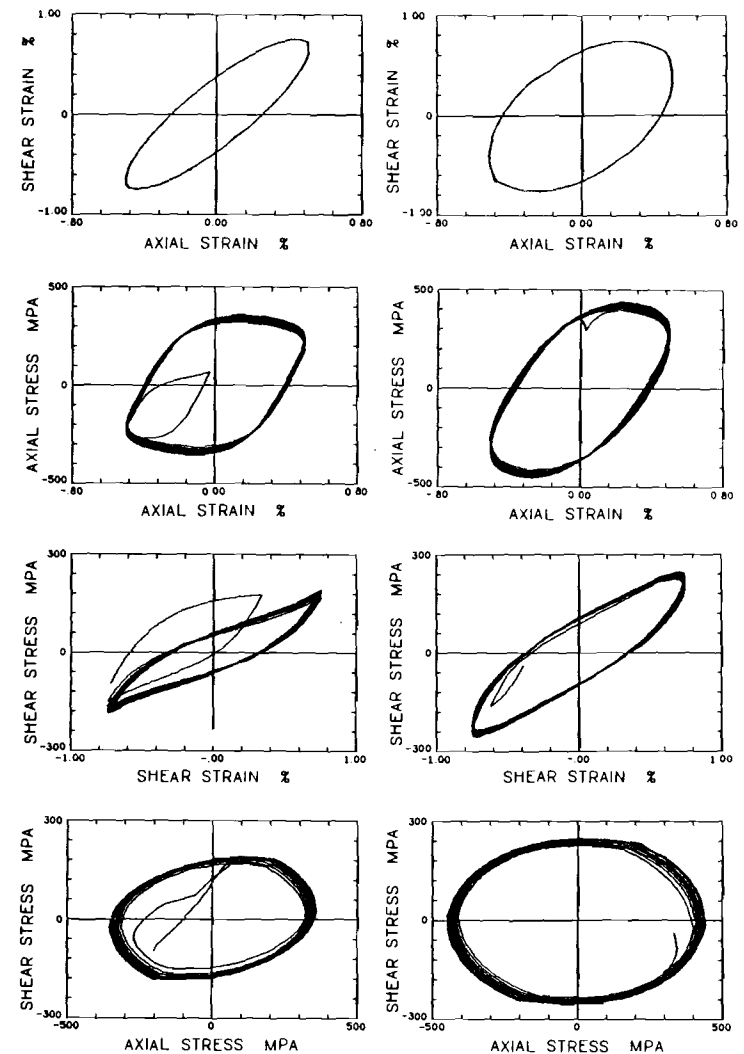


FIG. 6.—Experimental Results for History 1: (Left Column) Cycles 1 to 10 of Block 2; (Right Column) Cycles 1 to 10 of Block 3

As another point of detail, retention of memory or prior hardening states, commonly observed for planar-slip metals (McDowell 1983b, 1985c, 1985d), can be included in the equation, Eq. 16, for  $R^*$ , i.e.:

$$\dot{R}^* = c[(R_0 + K\Lambda^{m(1+\Lambda)}) - R^*] u(R_0 + K\Lambda^{m(1+\Lambda)} - R^*) \dot{\gamma} \dots \dots \dots (22)$$

where again  $u(\ )$  is the unit step function.

Saturated values of  $\Lambda^{m(1+\Lambda)}$  for five axial torsional nonproportional loading blocks of tubular type 304 stainless steel specimens at room temperature (McDowell 1985a) are shown in Fig. 4, along with the corre-

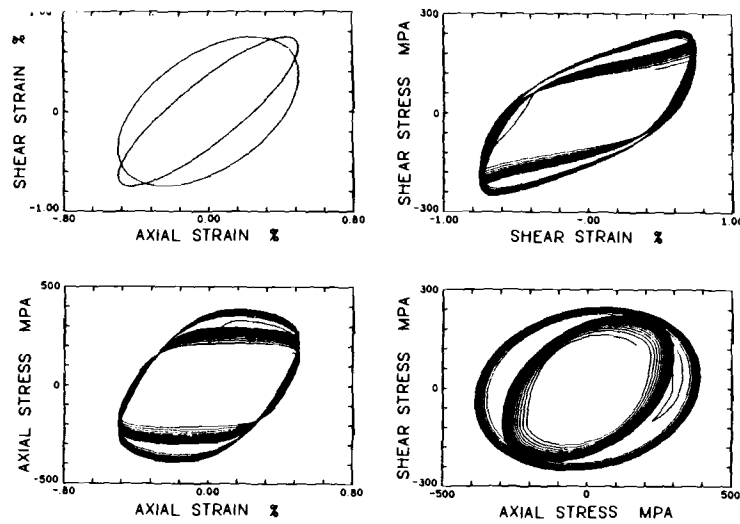


FIG. 7.—Predicted Results for History 1: 25 Cycles of Block 2 and First 10 Cycles of Block 3

sponding maximum values of  $[(3/2) s:s]^{1/2}$  in each block. Note that for  $m = 0.35$ , the maximum effective stresses are essentially linear with  $\Lambda^{m(1+\Lambda)}$ . It should also be mentioned that the scalar product of unit vectors in the deviatoric stress rate and deviatoric stress direction,  $\dot{s}:s$  (Lindholm, et al. 1985), was investigated for possible correlative capability of non-proportional hardening, but did not properly correlate the data for loading other than proportional or  $90^\circ$  out-of-phase sinusoidal.

Finally, the modulus function  $h$  must be described accurately for non-proportional loading. McDowell (1985a) has shown that dependence on effective stress (Drucker and Palgen 1981) is not valid for nonproportional cycling. The goal is to suggest an analytic form of representation of  $h$  which can be determined from uniaxial tests, but accurately applied to nonproportional loading. Recent two-surface theories (Krieg 1975; Lamba and Sidebottom 1978b; McDowell 1985c, 1985d) have proposed a dependence on the Mroz distance vector

$$h = h\left(\frac{\delta}{\delta_{in}}, \delta_{in}\right) \dots \dots \dots (23)$$

$$\text{where } \delta = \left\| \alpha^* + \left(\frac{R^*}{R}\right)(s - \alpha) - s \right\| \dots \dots \dots (24)$$

$\delta_{in}$  is the value of  $\delta$  at the beginning of the current reversal. Here,  $\delta$  is the norm of the vector from the current stress point to a similar point (same  $n$ ) on the limit surface during plastic flow. Use of the  $\delta_s$  parameter in Eq. 7 for modulus correlation gave poor results, particularly in the low modulus regime (McDowell 1986). The explicit dependence on  $\delta_{in}$  in Eq. 23 is introduced primarily to account for more appropriate initial reloading response (Dafalias 1981) in the plastic range. Dependence of

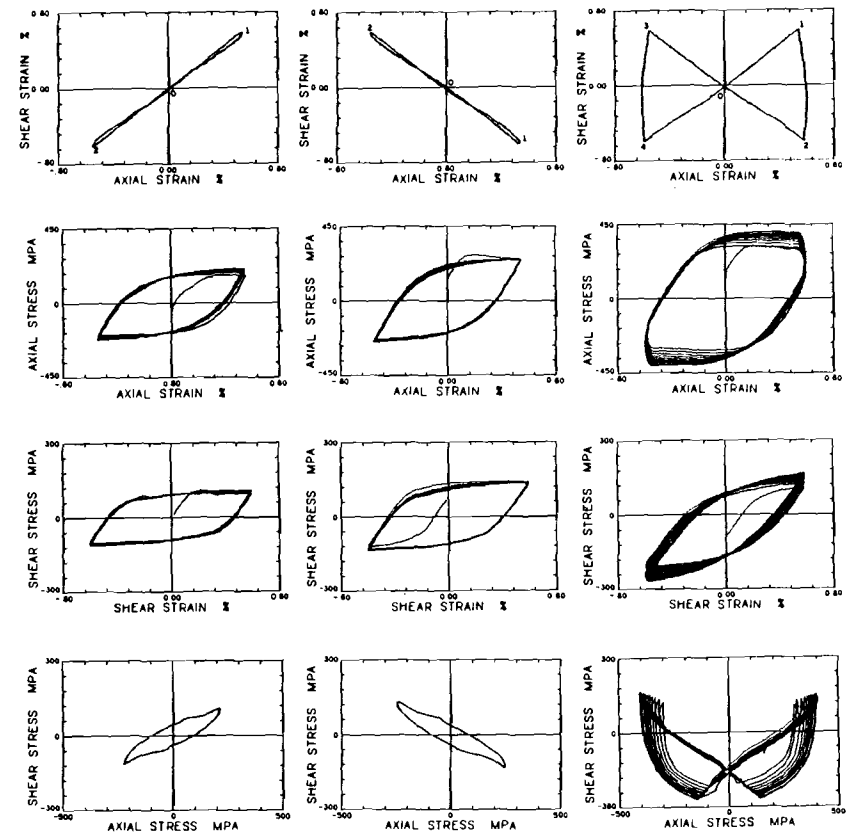


FIG. 8.—Experimental Results for History 2: (Left Column) Cycles 1 to 10 of Block 1; (Center Column) Cycles 1 to 10 of Block 2; (Right Column) Cycles 1 to 10 of Block 3

$h$  on  $(\delta/\delta_{in})$  describes the transition from the elastic state to asymptotic plastic flow.

Dafalias has suggested the form (1975,1981):

$$h = \kappa \left[ 1 + F(\delta_{in}) \left( \frac{\delta}{\delta_{in} - \delta} \right) \right] \dots \dots \dots (25)$$

which gives the proper values of  $h$  at initial yielding ( $h \rightarrow \infty$ ) and asymptotic loading ( $h \rightarrow \kappa$ ) in the plastic regime. The linear dependence on  $\delta/(\delta_{in} - \delta)$  in Eq. 25 does not precisely match data for stable proportional cycling of type 304 stainless steel. Also, definition of  $\delta_{in}$  for nonproportional loading is a problem. Defining  $\delta_{in}$  as the value of  $\delta$  at the initiation of plastic flow did not result in good normalization of the data, nor did definition of  $\delta_{in}$  as the maximum value of  $\delta$  within a cycle (McDowell 1986). It has also been shown that defining  $\delta_{in} = R^*$  results in poor normalization of data (McDowell 1986).

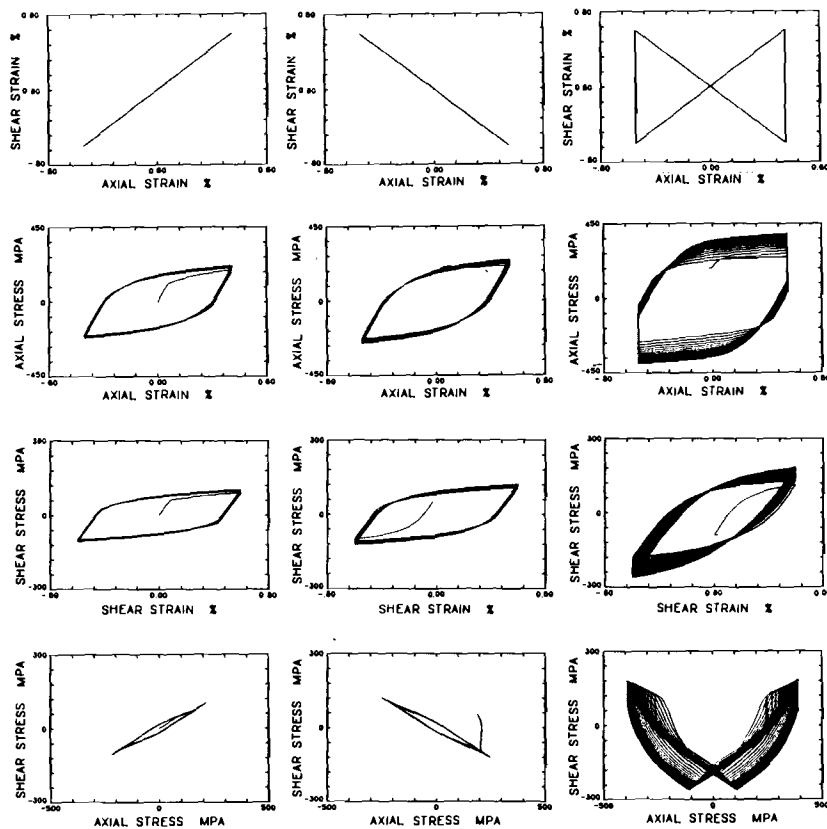


FIG. 9.—Predicted Results for History 2: (Left Column) Cycles 1 to 25 of Block 1; (Center Column) Cycles 1 to 25 of Block 2; (Right Column) Cycles 1 to 25 of Block 3

Another description of modulus variation for nonproportional cyclic data analyzed by the writer is given by

$$h = \kappa [1 + k_1 \{\sinh(k_2 D)\}^{k_3}] \dots \dots \dots (26)$$

$$\text{where } D = \left( \frac{\sqrt{\frac{3}{2}} \delta}{2 - |\mathbf{n} : \mathbf{n}_b|} \right) \dots \dots \dots (27)$$

and  $k_1$ ,  $k_2$ , and  $k_3$  are constants. Here

$$\mathbf{n}_b = \frac{\mathbf{s}^* - \mathbf{s}}{\|\mathbf{s}^* - \mathbf{s}\|} \dots \dots \dots (28)$$

and  $\mathbf{s}^*$  is given by Eq. 9. It is important to note in Eq. 27 that the product  $|\mathbf{n} : \mathbf{n}_b|$  serves to normalize data from various nonproportional loading

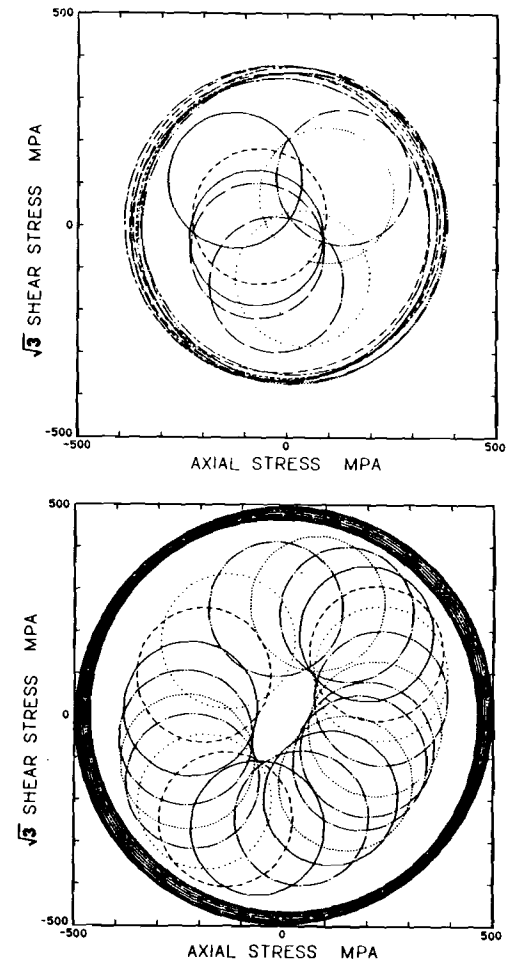


FIG. 10.—Yield and Limit Surface Movement for: (Top) Early Cycle In Block 3 of History 2; (Bottom) Stable Cycle In Block 3 of History 1

histories. For uniaxial or proportional loading,  $\mathbf{n} : \mathbf{n}_b = 1$  and  $D = \sqrt{3/2} \delta$ . Since  $k_2 = \text{constant}$  in Eq. 26, this modulus function does not employ an additional variable such as  $\delta_{in}$  to normalize the data, which is highly desirable.

Fig. 5(a) shows the accuracy of this modulus function in correlating the variation of hardening modulus for four axial torsional nonproportional loading histories imposed on tubular type 304 stainless steel specimens at room temperature (McDowell 1985a) which have significantly different values of  $R^*$ . Data from a cycle of proportional loading is also included for comparison. It is apparent that a fit to the proportional loading data is sufficient for description of nonproportional response, i.e.:

$$h = 3,000 \{1 + 16 [\sinh(0.005 D)]^{1.75}\} \dots \dots \dots (29)$$

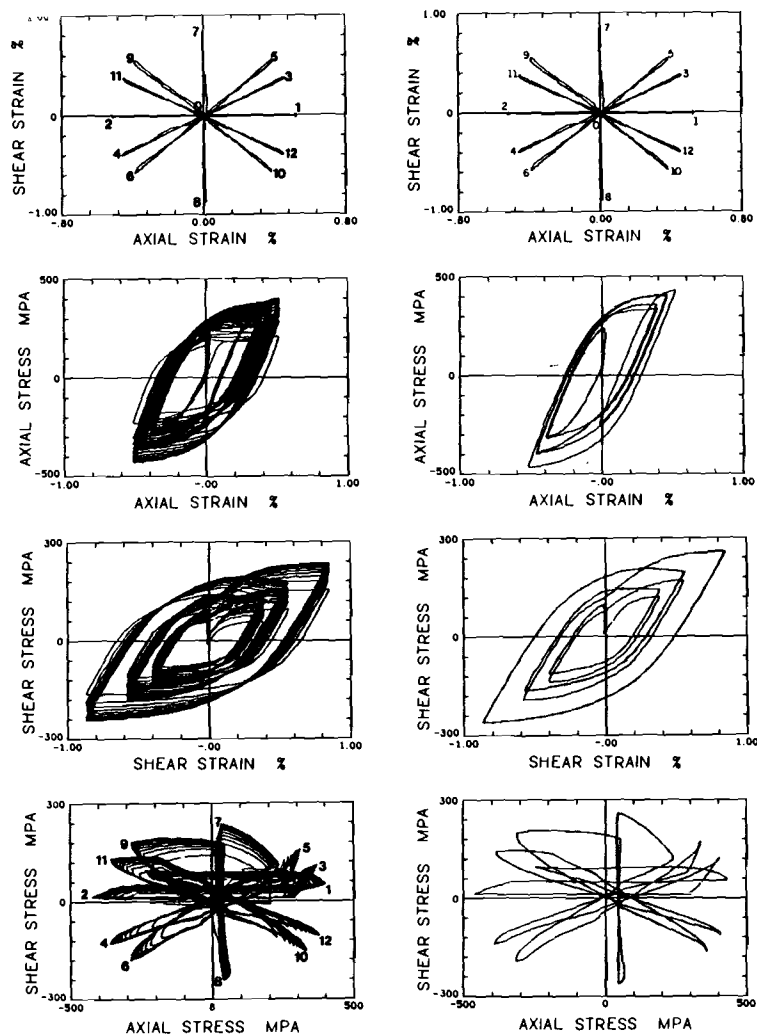


FIG. 11.—Experimental Results for History 3: (Left Column) Cycles 1 to 10; (Right Column) Cycle 40

as shown in Fig. 5(b). This function was used to compute the solid line appearing in Fig. 5(a). Hence, a uniaxial cyclic stress-strain curve would be sufficient to determine the constants in Eq. 26.

Eq. 26 is a power law function of  $\sinh(k_2 D)$ . Due to this form,  $h$  is finite at initial yielding. This results in a small discontinuity in slope in transition from elastic to elastic-plastic response. The magnitude of this discontinuity is small, and yielding is relatively smooth. Another qualification must be stated regarding Eq. 26. For accurate unloading-reloading response sufficiently far into the plastic regime (i.e., small  $\delta$ ), it might be appropriate to include influence of  $\delta_m$  to more accurately model

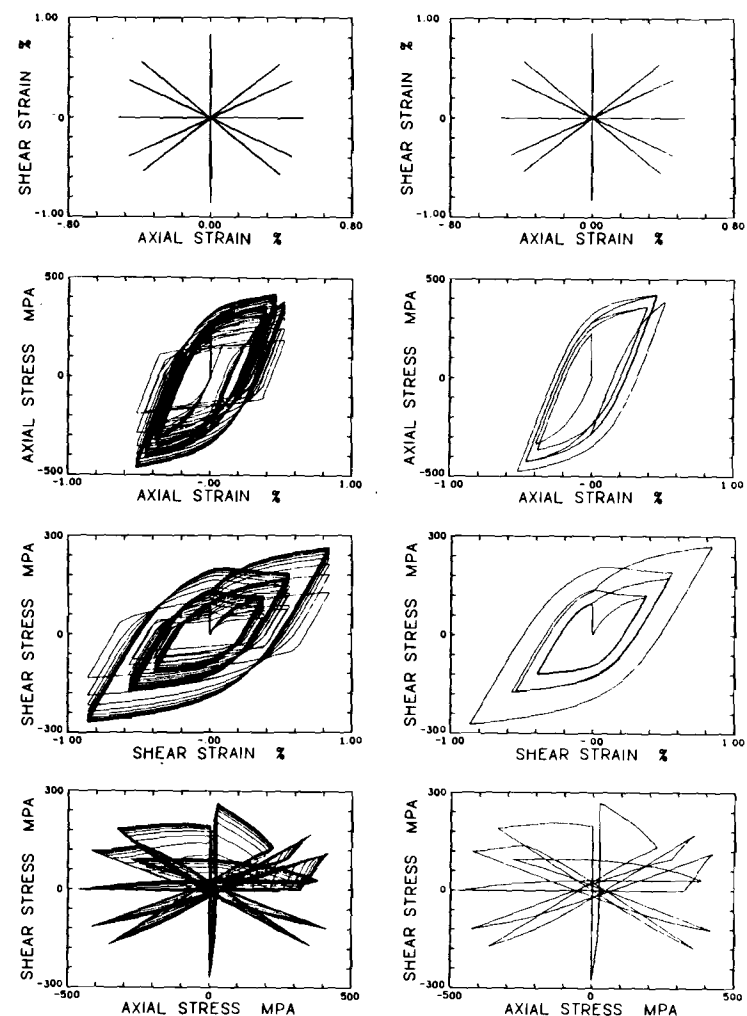


FIG. 12.—Predicted Results for History 3: (Left Column) Cycles 1 to 10; (Right Column) Cycle 40

influence of plastic deformation during the previous reversal, i.e.:

$$h = \kappa [1 + G(\delta_m) \{\sinh(k_2 D)\}^{k_3}] \dots \dots \dots (30)$$

where  $G(\delta_m)$  monotonically decreases as  $\delta_m$  increases, and is weakly dependent on  $\delta_m$  for moderately large  $\delta_m$  values. In the experiments to be reported in this paper, however, the loading is completely reversed so that  $\delta_m$  is moderately large for each reversal; hence, approximating  $G(\delta_m)$  as constant is reasonable.

#### CORRELATION WITH EXPERIMENTS

The theory was tested against several nonproportional cyclic loading



blocks imposed on annealed AISI type 304 stainless steel. Experimental details may be found elsewhere (McDowell 1983a, 1983b, 1985c, 1985d, 1984). From uniaxial tests,  $R = 160$  MPa,  $R_0 = 310$  MPa,  $c = 5$ ,  $\kappa = 3,000$  MPa,  $k_1 = 16$ ,  $k_2 = 0.005$ , and  $k_3 = 1.75$ . From sinusoidal axial torsional tests,  $K = 245$  MPa,  $m = 0.35$ , and  $A = 250$ .

The equations were reduced to the case of axial torsional loading of thin-walled tubular specimens to compare with the experiments (McDowell 1985d).

Results of three separate strain-controlled tension-torsion tests are reported in this investigation. Young's modulus and the shear modulus were respectively determined as  $E = 188$  GPa and  $G = 77$  GPa.

To compare the experimental results with the proposed two-surface theory, the same strain histories were introduced in the constitutive equations. The specialized axial torsional equations were integrated using a Runge-Kutta method with Gill coefficients (Eraslan 1969; Sotolongo 1985) and a very small time step-size to ensure negligible cumulative error. All calculations were performed on the Georgia Tech Cyber 855.

**History 1: Specimen SS09.**—Details of this history may be found elsewhere (McDowell 1985d). Two blocks of loading are discussed in this paper. Fig. 6 shows the experimental results. Predictions appear in Fig. 7. Note the good correlation achieved for additional hardening. Cyclic hardening is predicted well by the model. The initial value of  $R^*$  was 291 MPa (McDowell 1985d).

**History 2: Specimen SS01.**—Again, refer to McDowell (1985d) for details of this history. Three consecutive loading blocks are presented; experimental and predicted results appear in Figs. 8 and 9, respectively. In the analysis, the initial value  $R^* = 285$  MPa was used. Initial values for all other variables were taken as zero. Note the excellent agreement between experimental and predicted results.

The movement of the yield surface within the translating limit surface is illustrated in Fig. 10 for two loading blocks. Note the tangency at the point of nesting of the yield and limit surfaces.

**History 3: Specimen SS04.**—This specimen was subjected from the virgin state to 50 cycles of the path shown in Fig. 11 with

$$\dot{\epsilon} = \left( \dot{\epsilon}^2 + \frac{\dot{\gamma}^2}{3} \right)^{1/2} = 0.002 \text{ sec}^{-1} \dots \dots \dots (31)$$

The experimentally observed responses from cycles 1–10 and cycle 40 are also shown in Fig. 11. Note that the accumulation of hardening is again greatly in excess of the uniaxial case.

As observed in Fig. 12, the shape of the predicted hysteresis responses accurately fits the experimentally observed responses for cycles 1–10 and cycle 40. The extent of additional hardening is somewhat overestimated by the model. An initial value of  $R^* = 192$  MPa was used in the analysis, corresponding to the monotonic response.

## SUMMARY AND CONCLUSIONS

A simple two-surface model has been presented. Most of the model constants can be determined from uniaxial tests. The model structure

reflects in-depth analysis of actual cyclic nonproportional data and, consequently, can correlate the response well. New contributions include incorporation of an improved kinematic hardening rule for two-surface theory, a more realistic representation of isotropic hardening through limit surface evolution and modulus function, a more general plastic strain-based isotropic hardening formulation for nonproportional cyclic loading, and a normalization procedure for the modulus function which reflects nonproportionality of the next plastic strain increment.

## ACKNOWLEDGMENT

The author is grateful for the support of the National Science Foundation (Grant No. MEA-8404080) in this work.

## APPENDIX I.—REFERENCES

- Chaboche, J.-L., Dang-Van, K., and Cordier, G. (1979). "Modelization of the strain memory effect on the cyclic hardening of 316 stainless steel." *Trans. 5th SMiRT*, L 11/3, Berlin, Germany.
- Dafalias, Y. F. (1981). "The concept and application of the bounding surface in plasticity theory." *Physical non-linearities in structural analysis*, J. Hult and J. Lemaitre, Eds., IUTAM Symposium, Senlis, France, Springer Verlag, 56–63.
- Dafalias, Y. F. (1984). "Modeling cyclic plasticity: Simplicity versus sophistication." *Mechanics of engineering materials*, Desai and Gallagher, Eds., Wiley, New York, N.Y., 153–178.
- Dafalias, Y. F., and Popov, E. P. (1975). "A model of nonlinearly hardening materials for complex loading." *Acta mechanica*, 21, 173–192.
- Drucker, D. C., and Palgen, L. (1981). "On stress-strain relations suitable for cyclic and other loading." *J. Appl. Mech.*, ASME, 48, 479–485.
- Eisenberg, M. A. (1976). "A generalization of plastic flow theory with application to cyclic hardening and softening phenomena." *J. Engrg. Mats. Tech.*, ASME, 98, 221–228.
- Eraslan, H. V. (1969). "Supplementary notes on the solution of ordinary differential equations by Runge-Kutta methods." Prepared for the *One-week short course in numerical analysis and computer methods*, Univ. Tennessee Space Inst., Tullahoma, Tenn.
- Hecker, S. S. (1976). "Experimental studies of yield phenomena in biaxially loaded metals." *Constitutive equations in viscoplasticity: Computational and engineering aspects*, AMD, ASME, New York, N.Y., 20, 1–32.
- Kanazawa, K., Brown, M. W., and Miller, K. J. (1979). "Cyclic deformation of 1% Cr-Mo-V steel under out-of-phase loads." *Fatigue of engineering materials and structures*, 2, 217–228.
- Krempel, E., and Lu, H. (1984). "The hardening and rate-dependent behavior of fully annealed AISI type 304 stainless steel under biaxial in-phase and out-of-phase strain cycling at room temperature." *J. Engrg. Mat. Tech.*, ASME, 106, 376–382.
- Krempel, E., McMahon, J. J., and Yao, D. (1984). "Viscoplasticity based on over-stress with a differential growth law for the equilibrium stress." *Proc., 2nd Symposium on Nonlinear Constitutive Relations for High Temperature Applications*, NASA Lewis Research Center, Cleveland, Ohio.
- Krieg, R. D. (1975). "A practical two surface plasticity theory." *J. Appl. Mech.*, 42, 641–646.
- Lamba, H. S., and Sidebottom, O. M. (1978a). "Cyclic plasticity for nonproportional paths: Part 1—Cyclic hardening, erasure of memory, and subsequent strain hardening experiments." *J. Engrg. Mats. Tech.*, ASME, 100, 96–103.
- Lamba, H. S., and Sidebottom, O. M. (1978b). "Cyclic plasticity for nonproportional paths: Part 2—Comparison with predictions of three incremental plas-

- ticity models." *J. Engrg. Mats. Tech.*, ASME, 100, 104-111.
- Lindholm, U. S., Chan, K. S., Bodner, S. R., Weber, R. M., Walker, K. P., and Cassenti, B. N. (1985). "Constitutive modeling for isotropic materials." NASA CR-174980, SwRI-7476/30, NASA.
- Liu, K. C., and Greenstreet, W. L. (1976). "Experimental studies to examine elastic-plastic behaviors of metal alloys used in nuclear structures." *Constitutive equations in viscoplasticity: Computational and engineering aspects*, AMD, ASME, New York, N.Y., 20, 35-56.
- Mair, W. M., and Pugh, H. (1964). "Effect of pre-strain on yield surfaces in copper." *J. Mech. Engrg. Sci.*, 6(2), 150-163.
- McDowell, D. L. (1983a). "On the path dependence of transient hardening and softening to stable states under complex biaxial cyclic loading." *Proc. Int. Conf. Constitutive Laws for Engrg. Mats.*, Desai and Gallagher, Eds., Tucson, Ariz., 125-132.
- McDowell, D. L. (1983b). "Transient nonproportional cyclic plasticity." *Report No. 107. Design and Materials Div., Dept. of Mech. and Indust. Engrg., Univ. of Illinois at Urbana-Champaign, Ill.*
- McDowell, D. L. (1985a). "An experimental study of the structure of constitutive equations for nonproportional cyclic plasticity." *J. Engrg. Mats. Tech.*, ASME, 107, 307-315.
- McDowell, D. L. (1985b). "The significance of nonproportional loading tests for characterization of cyclic response of metals." *Proc. 1985 Spr. Conf. on Exper. Mech.*, Soc. for Experimentl. Stress Anal., Las Vegas, Nev., 229-236.
- McDowell, D. L. (1985c). "A two surface model for transient nonproportional cyclic plasticity: Part I—Development of appropriate equations." *J. Appl. Mech.*, ASME, 52, 298-302.
- McDowell, D. L. (1985d). "A two surface model for transient nonproportional cyclic plasticity: Part II—Comparison of theory with experiments." *J. Appl. Mech.*, ASME, 52, 303-308.
- McDowell, D. L. (1986). "An evaluation of recent developments in hardening and flow rules for rate-independent, nonproportional cyclic plasticity." *J. Appl. Mech.*, ASME.
- McDowell, D. L., Payne, R. K., Stahl, D., and Antolovich, S. D. (1984). "Effects of nonproportional cyclic loading histories on type 304 stainless steel." *Crack initiation under complex loadings*, French Metallur. Soc., Paris, France, 53-86.
- Mroz, Z. (1967). "An attempt to describe the behaviour of metals under cyclic loads using a more general workhardening model." *Acta mechanica*, 7, 199-212.
- Nouailhas, D., Policella, H., and Kaczmarek, H. (1983). "On the description of cyclic hardening under complex loading histories." *Proc. Int. Conf. Constitutive Laws for Engrg. Mats.*, Desai and Gallagher, Eds., Tucson, Ariz., 45-49.
- Ohno, N. (1982). "A constitutive equation of cyclic plasticity with a non-hardening strain region." *J. Appl. Mech.*, ASME, 49, 721-727.
- Phillips, A., Tang, J. L., and Ricciuti, M. (1974). "Some new observations on yield surfaces." *Acta mechanica*, 20, 23-39.
- Prager, W. (1956). "A new method of analyzing stresses and strains on work-hardening plastic solids." *J. Appl. Mech.*, ASME, 23, 493-496.
- Sotolongo, W. (1985). "On the numerical implementation of cyclic elasto-plastic materials models." thesis presented to the School of Mechanical Engineering, Georgia Institute of Technology, at Atlanta, Georgia, in partial fulfillment of the requirements for the degree of Master of Science.
- Tanaka, E., Murakami, S., and Ooka, M. (1985). "A constitutive model of cyclic plasticity in multiaxial non-proportional loading." *L 2/4, SMirt 8*, Berlin, Germany.
- Tseng, N. T., and Lee, G. C. (1983). "Simple plasticity model of the two-surface type." *J. Engrg. Mech.*, ASCE, 109(3), 795-810.
- Ziegler, H. (1959). "A modification of Prager's hardening rule." *Quart. Appl. Math.*, 17, 55-60.

- $A, c$  = rate coefficients;
- $D$  = normalized modulus parameter;
- $f, f^*$  = yield and limit surfaces, respectively;
- $h$  = hardening modulus;
- $K$  = maximum additional hardening;
- $k_1, k_2, k_3$  = constants in modulus function;
- $m$  = constant in isotropic hardening rule;
- $\mathbf{n}$  = unit vector in plastic strain rate direction;
- $\mathbf{n}_1, \mathbf{n}_3$  = orthonormal unit vectors in axial torsional subspace;
- $\bar{\mathbf{n}}, \mathbf{N}, \mathbf{n}^*$  = vectors associated with isotropic hardening rule;
- $R, R^*$  = radii of yield and limit surfaces, respectively;
- $R_0$  = uniaxial or proportional cyclically stable value of  $R^*$ ;
- $\mathbf{s}$  = deviatoric stress tensor;
- $\mathbf{s}^*$  = corresponding point on limit surface;
- $t_B$  = time at initiation of loading block  $B$ ;
- $u$  = unit step function;
- $\alpha, \alpha^*$  = center of yield and limit surfaces, respectively;
- $\bar{\alpha}$  = center of yield surface in axial torsional subspace;
- $\gamma, \gamma_a$  = total engineering shear strain and amplitude, respectively;
- $\delta, \delta_m$  = norm of Mroz distance vector and initial value, respectively;
- $\epsilon, \epsilon_a$  = total axial strain and amplitude, respectively;
- $\epsilon, \epsilon^e, \epsilon^p$  = total, elastic, and plastic strain tensors, respectively;
- $\eta$  = norm of accumulated plastic strain;
- $\kappa$  = asymptotic value of hardening modulus;
- $\Lambda$  = nonproportional hardening state variable;
- $\lambda$  = vector in kinematic hardening rule;
- $\dot{\mu}, \dot{\mu}_M$  = scalar multipliers;
- $\mathbf{v}$  = unit vector in kinematic hardening rule;
- $\rho$  = phase angle;
- $\sigma$  = axial stress;
- $\boldsymbol{\sigma}$  = stress vector in axial torsional subspace;
- $\sigma_1, \sigma_3$  = components of  $\boldsymbol{\sigma}$ ;
- $\tau$  = shear stress;
- $\phi, \phi_1, \phi_2$  = quantities related to isotropic hardening rule; and
- $\omega$  = angular frequency.

## APPENDIX II.—NOTATION

The following symbols are used in this paper:

BIAXIAL PATH DEPENDENCE OF DEFORMATION SUBSTRUCTURE OF  
TYPE 304 STAINLESS STEEL

D.L. McDowell  
Assistant Professor  
School of Mechanical Engineering  
Associate Director, Fracture and Fatigue Research Laboratory

S.R. Stock  
Assistant Professor  
School of Materials Engineering

D. Stahl  
Graduate Research Assistant  
Fracture and Fatigue Research Laboratory

S.D. Antolovich  
Professor of Metallurgy  
School of Materials Engineering  
Director, Fracture and Fatigue Research Laboratory

Georgia Institute of Technology  
Atlanta, Georgia 30332-0100

Submitted to "Metallurgical Transactions"

April, 1986

## ABSTRACT

Though martensitic transformations in austenitic stainless steels have been studied rather thoroughly for uniaxial monotonic and cyclic loading, data are scant for biaxially loaded specimens. In particular, recent experiments have indicated significant increase in cyclic hardening for nonproportionally loaded specimens. In this paper, a link is made between the additional hardening and microstructural uniformity of transformation product. This link is expressed through a micromechanical viewpoint via increased latent hardening associated with rotation of the principal stress and plastic strain rate directions.

## INTRODUCTION

Changes in loading path, including strain range and loading direction, can affect cyclic deformation at both microscopic and macroscopic levels [1-5]. This study was undertaken to investigate these effects on type 304 stainless steel using axial-torsional specimens tested at room temperature and subjected to proportional and nonproportional loading sequences at controlled effective strains and strain rates. Subsequent to testing, specimens were examined by advanced metallographic techniques to identify deformation substructures.

It has been observed in several experimental studies [4-6] that nonproportional strain cycling results in cyclic hardening beyond the extent observed in uniaxial tests at the same effective strain range. For materials which cyclically harden markedly in uniaxial tests, such as the stainless steel in the current investigation, the additional hardening can be quite pronounced during nonproportional strain cycling. There is evidence to indicate that materials which cyclically soften during uniaxial tests may harden during nonproportional cycling [4].

Logically, a link should exist between cyclic deformation substructure within each grain and polycrystalline stress-strain response. If the deformation substructure and any associated transformation products are dependent upon a rotation of the stress field with respect to each grain, then the extent of isotropic hardening observed in the polycrystalline material should reflect this dependence, and vice-versa.

## EXPERIMENTAL PROCEDURES

### Material

This material chosen for this study was type 304 stainless steel with the AISI composition shown in Table I. This FCC material exhibits a plastic

strain range dependent transformation from metastable austenite to BCT  $\alpha'$ -martensite during cycling [7-8] in addition to  $\epsilon$ -martensite, an HCP form which is associated with the formation of stacking faults on {111} slip planes [9-10]. The stacking fault energy of type 304 stainless steel is low ( $\approx 23$  mJ/m<sup>2</sup> [11]), resulting in formation of wide stacking faults and planar slip at room temperature. As a consequence of these factors, type 304 stainless steel exhibits marked cyclic hardening response dependent on applied strain range and nonproportionality of loading in the plastic region [12].

Type 304 stainless steel has been widely used in high temperature applications, particularly in nuclear structures.

#### Specimens

Tubular axial-torsional specimens were machined from as-received bar stock of 50.8 mm diameter as shown in Fig. 1. The wall-thickness to outside diameter ratio of 0.11 was found necessary from experience to prevent buckling for cyclic loading at significant levels of plastic strain. From finite element analysis and strain gage work, the variation in axial strain along the gage length was less than three percent.

Uniaxial specimens were machined from radial and longitudinal directions of the bar stock with a gage diameter of 3 mm, approximately that of the axial-torsion specimen wall. Five monotonic tension tests in the longitudinal direction resulted in a mean true fracture strength of 612 MPa with a standard deviation of  $\pm 7$  MPa. The mean percent reduction in area for the longitudinal specimens was 64.8% with a standard deviation of  $\pm 5.7\%$ . The corresponding values of mean true fracture strength and percent reduction in area for four radial specimens were 628 MPa and 56.3%, with standard deviations of  $\pm 1$  MPa and  $\pm 4.0\%$ , respectively.

In addition, completely reversed, strain-controlled fatigue tests were run on five specimens machined in the longitudinal direction and six specimens machined in the radial direction at comparable strain ranges. The stable cyclic stress amplitudes for radial and longitudinal specimens were essentially the same for a given strain amplitude  $\epsilon_a$ . The results are shown in Table II. From the tensile and fatigue tests, it is apparent that anisotropy effects in the axial-torsional specimens are minor, particularly since these specimens were machined from as-received stock.

A set of uniaxial and axial-torsional specimens were heat-treated at 1100°C for 40 minutes in a vacuum and furnace cooled to achieve the relatively isotropic grain structure shown in Fig. 2 with an ASTM grain size number of 4. There were approximately 25 grains across the wall-thickness of the axial-torsional specimen shown in Fig.1. Note the polishing marks in Fig.2; the specimens were intended primarily for cyclic deformation testing, and a fine grit was not used in the polishing process.

#### Testing Procedure

The biaxial, strain-controlled tests were performed on an axial-torsional load frame with axial and torsional cyclic load capacities of  $\pm 50$  kips and  $\pm 20$  in-kips, respectively. The system was stiffened to decrease lateral torsional frame deflection. A PDP 11-23 processor/interface was used for independent servohydraulic, closed-loop control of axial and torsional deflection or load channels and for simultaneous data acquisition.

An internal extensometer [13] was placed inside the specimen with a gage length of 25.4 mm. A linear variable differential transformer (LVDT) was used to measure axial displacement between contact points at the gage length, while a rotary variable differential transformer (RVDT) measured the relative angle of twist. Extensometer backlash and interaction between axial and torsional

channels were negligible. The deviation from linearity for both axial and shear displacement channels was less than one percent of full-scale. Alignment was verified over a wide range of axial and rotational movements of the servohydraulic ram with respect to the fixed crosshead.

Axial strain  $\epsilon$  was defined as the gage length displacement divided by the original gage length. The shear strain  $\gamma$  was obtained by dividing the angle of twist by the gage length and multiplying by the mean radius.

Axial stress  $\sigma$  and shear stress  $\tau$  were calculated from the axial load  $P$  and torque  $T$  as

$$\sigma = 4P/(\pi(D_o^2 - D_i^2)) \text{ and} \quad (1)$$

$$\tau = 12T/(\pi(D_o^3 - D_i^3)), \quad (2)$$

with the assumption that the stresses are uniform across the wall-thickness.  $D_o$  and  $D_i$  are the gage section outside and inside diameters, respectively. This assumption obviously involves some error, but the deformation theory of plasticity cannot be used to estimate the stress distribution of nonproportional loading. Brown and Miller [4,14] showed that the error in maximum shear stress,

$$\tau_{\max} = [\tau^2 + (\sigma/2)^2]^{1/2}, \quad (3)$$

is small for proportional loading and for nonproportional loading, particularly if there is significant cyclic plasticity present.

A computer program was written so that any combination of line segments in  $\epsilon$ - $\gamma$  strain space could be joined end-to-end to define a loading cycle. A



block was defined as an arbitrary number of identical cycles. Furthermore, the program allowed the user to define any number of blocks, each containing a different cycle loading path. The effective strain rate ( $\dot{\epsilon} = (\dot{\epsilon}_x^2 + \dot{\epsilon}_y^2/3)^{1/2}$ ), assuming a Poisson's ratio of 1/2, was kept constant along each segment.

The computer program was written to accomplish the following objectives:

- (a) Permit generation of a number of successive blocks of different non-proportional cyclic paths interactively with the computer. A desired effective strain rate was specified and the entire history plotted prior to running the actual test.
- (b) Run initial shear and axial modulus checks at small elastic strains to compute G and E prior to the imposed history.
- (c) Impose the strain history generated in objective (a) on the specimen and acquire data for the first 10 cycles of every block and geometrically increasing (powers of two) cycles starting at cycle 10. Load and gage length deflection data for both channels were sampled and stored on a floppy disk at increments of effective strain specified by the user. Typically, 50 to 100 sets of data were stored for each one percent increment of effective strain.

#### BIAXIAL LOADING HISTORIES

Results of three separate strain-controlled axial-torsional histories are reported in this paper. All tests were conducted at room temperature. The initial values of Young's modulus and shear modulus were determined as  $E = 188$  GPa and  $G = 77$  GPa, respectively. A summary of each of these three test

histories appears in Table III, including the effective strain rate and controlled axial and shear strain endpoint sequence of each block within each history.

#### Specimen SS01

Specimen SS01 was subjected starting from the virgin state to the eight block sequence listed in Table III. The axial-torsional strain history and hysteresis loops sampled near the end of each loading block are shown in Figs. 3 through 7.

Several interesting observations can be made regarding the deformation behavior. Consider first blocks 1 and 2 depicted in Fig. 3. The cyclic axial and shear stress amplitudes  $\sigma_a$  and  $\tau_a$  in cycle 24 of block 1, when combined via von Mises effective stress,  $\sigma = (\sigma_a^2 + 3\tau_a^2)^{1/2}$ , or Tresca effective stress,  $\sigma_{eff} = (\sigma_a^2 + 4\tau_a^2)^{1/2}$ , correspond closely to a point on the cyclic stress-strain curve determined from a uniaxial incremental step test on a specimen with the same heat treatment [6]. This equivalence, of course, is not surprising since the straining is proportional.

Upon switching to block 2, however, the cyclic stress amplitudes in block 2 noticeably increased over those of block 1. Yet the plastic strain amplitudes of both axial and shear responses in block 2 were less than those of block 1. This is evidence of latent or anisotropic hardening (cross hardening) which occurred in the first two blocks. Several experimental studies have been conducted [15-17] in which the "yield surface" is determined by strain probing techniques at various points along a strain-controlled, nonproportional loading path. Typically, these studies have concentrated on one type of loading path applied for several cycles. In the present study, the effects of cross hardening are examined by virtue of the hysteresis response.

Continuing into blocks 3 and 4, as seen in Fig. 4, a significant degree of additional cross hardening is apparent. Any measure of effective plastic strain range decreases from block 1 to block 2 to block 3. In particular, the maximum range of plastic shear strain on any plane in the specimen wall decreases from  $\Delta\gamma^p_{\max} = 0.0136$  in block 1 to  $\Delta\gamma^p_{\max} = 0.0123$  in block 3 [6]. Yet the peak effective stress increased significantly in each block, particularly in block 3. Figure 5 shows the increase in the maximum value of Tresca effective stress, i.e., maximum value of  $(\sigma^2 + 4\tau^2)^{1/2} = \max \sigma_{\text{eff}}$ , in a number of sampled cycles in the first three blocks. Data are reported for the first 10 cycles and cycle 24 of each block. The maximum effective stress increased in each block. Note that most of the transient hardening occurred in the first 10 cycles of each block. Since the maximum effective stress in block 1 corresponds approximately to that of uniaxial cyclic deformation at the same plastic strain range, the extent of additional hardening is quite significant.

It is also clear that the additional cross hardening is path-dependent, and the concept of the "universal" cyclic stress-strain curve in the conventional sense has little meaning. The cyclic strain path of block includes the paths from blocks 1 and 2 by connecting them at peak endpoints. Along the segments of the path where axial strain is approximately constant, the maximum shear strain planes rotated continuously in the specimen wall. Hence, the principal strains (and stresses) rotated continuously during these portions of the cycle.

The loading paths in blocks 4 and 5, shown in Figs. 4 and 6, did not result in significant transient hardening or softening behavior. The material retained memory of the loading of blocks 2 and 3 and did not readjust to a response characteristic of the proportional straining from the virgin state seen in block 1. This memory of additional cyclic hardening (interaction of

slip systems) during nonproportional cycling is perhaps most directly related to the low stacking fault energy of type 304 stainless steel; high stacking fault energy metals (i.e. those that exhibit wavy slip), in contrast, tend to readjust to the stress amplitude corresponding to the current strain range independent of loading sequence in uniaxial test [18-19].

Blocks 6 and 7, shown in Figs. 6 and 7, were a repeat of blocks 4 and 5 with an increase of strain amplitudes by a factor of 1.5. Again, no significant additional transient hardening was observed. Of course, the stress amplitudes were higher than those of blocks 4 and 5 since the strain amplitudes were increased. For type 304 stainless steel, the extent of additional cyclic hardening is more strongly dependent on nonproportionality of loading than on plastic strain range. This observation was also made for nonproportional strain cycling of type 316 stainless steel by Nouailhas et al [20].

Finally, in block 8 the strain cycle of block 3 was again imposed. The hysteresis response is nearly identical to that of block 3 as seen in Fig. 7. Only a small component of additional hardening beyond block 3 was observed in block 8; examination of the transient response in the first 10 cycles of block 8 shows that the rate of hardening in block 8 was essentially equal to that of the latter cycles in block 3.

#### Specimen SS09

This specimen, from the virgin state, was subjected first to 10 cycles of a 10 level incremental step test with maximum axial and shear strain amplitudes of 0.007 and 0.0105, respectively, as shown in Table III. Plots of the tenth cycle hysteresis loops are shown at the top of Fig. 8. In addition, uniaxial incremental step tests were conducted on specimens with the same heat-treatment at several maximum strain ranges. Solid curves in Fig. 8 show

the monotonic and cyclic stress-strain curves for maximum plastic strain amplitudes of 0.0045 and 0.0068 in incremental step tests. For comparison with the uniaxial tests, the axial and shear stress and strain peaks at each level in the first block of specimen SS09 are plotted in the form of Tresca and von Mises effective stresses and strains. The Tresca and von Mises effective plastic strain shown in Fig. 8 are defined, respectively, as

$$\epsilon_{eff}^P = ((\epsilon^P)^2 + (4/9) (\gamma^P)^2)^{1/2} \text{ and} \quad (4)$$

$$\bar{\epsilon}^P = ((\epsilon^P)^2 + (1/3) (\gamma^P)^2)^{1/2}. \quad (5)$$

The Tresca and von Mises effective stresses were defined earlier. Note that the effective stress-strain response in block 1 is essentially equivalent to the uniaxial case. The stress amplitudes are slightly higher for the uniaxial case primarily because they are reported after 40 to 50 complete cycles.

Block 2 for specimen SS09 consisted of continued cycling along the proportional path of the incremental step test in block 1 with  $\epsilon_a = 0.005$  and  $\gamma_a = 0.0075$ . No additional hardening was observed.

In blocks 3 and 4, the specimen was subjected to the same applied axial and shear strain amplitudes as in block 2, but with sinusoidal variation of applied strain components. The phase angle  $\beta$  between applied axial and shear strains, expressed through the equations

$$\epsilon = \epsilon_a \sin \omega t \text{ and} \quad (6)$$

$$\gamma = \gamma_a \sin(\omega t - \beta), \quad (7)$$

was sequentially increased from 0° to 30° (block 2 to 3) and from 30° to 60° (block 3 to 4).

The strain histories for blocks 2 through 4 and resulting 24th cycle hysteresis loops are shown in Table III and Figs. 9 and 10. Note that the degree of nonproportionality of loading increased sequentially from block 2 to block 4, and the resulting maximum Tresca effective stress in a cycle also increased sequentially. This block-by-block increase in cyclic strength level cannot be attributed to an increase in any measure of effective plastic strain range; in fact, the maximum range of plastic shear strain on any plane in the specimen wall decreases sequentially from  $\Delta\gamma_{\max}^P = 0.0166$  in block 2 to  $\Delta\gamma_{\max}^P = 0.0146$  in block 4.

A plot of maximum Tresca effective stress in each cycle is presented in Fig. 11. It is quite interesting that an increase in the degree of nonproportionality is analogous to an increase in strain range from cyclically stable conditions in a uniaxial test. As for specimen SS01, this significant degree of additional cyclic hardening in the absence of an increase in effective plastic strain range points to increased activation of and interaction between slip systems as likely mechanisms. During nonproportional cycling, it is likely that more slip systems in more grains have favorable Schmid factors during a loading cycle than for proportional straining. The deformation substructures and martensitic transformations for these specimens are examined in a later section.

Finally, after block 4, specimen SS09 was subjected to sinusoidal strain cycling with  $\epsilon_a = 0.005$ ,  $\gamma_a = 0.0075$  and  $\beta = 90^\circ$ . After eight or nine cycles, the specimen pulled out of the grips and the data were not transferred to magnetic disk as intended. An x-y recording indicated that additional hardening did occur in both axial and shear stress responses, presumably approaching that of 90° out-of-phase step tests reported earlier by one of the authors

[3,6], i.e.,  $\max \sigma_{eff} \approx 600$  MPa. For  $\beta = 90^\circ$  with  $\gamma_a/\epsilon_a = 1.5$ , every plane in the specimen wall is a plane of equal maximum shear strain range during some point in each loading cycle, and the maximum shear strain planes rotate continuously (assuming Poisson's ratio is 1/2). Kanazawa, Brown, and Miller [4] observed that this case resulted in the maximum extent of additional cyclic hardening for 1% Cr-Mo-V steel, as did Lamba [5] for OFHC copper.

#### Specimen SS06

This specimen was subjected to 22 consecutive alternating blocks of completely reversed axial straining or shear straining with an effective strain rate of  $\dot{\epsilon} = 0.002 \text{ sec}^{-1}$ , as shown in Table III. Block 1 consisted of 40 cycles with axial and shear strain amplitudes of  $\epsilon_a = 0.0075$  and  $\gamma_a = 0$  respectively. Block 2 consisted of 40 cycles with axial and shear strain amplitudes of  $\epsilon_a = 0$  and  $\gamma_a = 0.01125$ , respectively. Hence the effective strain range for block 2 was within 13% of that for block 1. Each successive set of two consecutive blocks after block 2 simply repeated blocks 1 and 2.

After the first several blocks, there was negligible cyclic hardening. The axial stress and plastic strain amplitudes for block 11 were  $\sigma_a = 465$  MPa and  $\epsilon_a^P = 0.005$ , respectively. The shear stress and plastic shear strain amplitudes for block 10 were  $\tau_a = 255$  MPa and  $\gamma_a = 0.0074$ , respectively. These values were cyclically stable. For blocks 5 and 6, for example, the stress amplitudes were  $\sigma_a = 450$  MPa and  $\tau_a = 255$  MPa, respectively. It should also be noted that, due to the large plastic strain amplitudes, the shear stress was negligibly small during axial cycling and vice versa. It is important to note that for each type of loading block, the effective cyclically stable stress amplitude significantly exceeded that of the uniaxial cycle stress strain curve.

## PHYSICAL EXAMINATION OF SPECIMENS

Type 304 stainless steel can form both  $\epsilon$ -martensite as well as  $\alpha'$ -martensite as a result of deformation, in addition to developing dislocation arrays. Deformed specimens were examined using conventional optical and SEM microscopy to delineate  $\epsilon$ -martensite (or planar slip bands) while x-ray techniques were used to detect the presence of  $\alpha'$ -martensite. In addition, replication techniques were employed to follow the development of deformation marks on the surface of specimens during the course of cycling.

## RESULTS AND DISCUSSION

### Correlation of Cyclic Hardening with Deformation Substructure

As mentioned previously, type 304 stainless steel exhibits a plastic strain range dependent transformation from metastable austenite to  $\alpha'$ -martensite and  $\epsilon$ -martensite in uniaxial tests. These transformations account, in part, for the marked degree of cyclic hardening observed in uniaxial tests in which strain range is increased significantly from a prior cyclically stable state.

The BCT  $\alpha'$ -martensite provides a significant barrier to dislocation movement. Likewise, the HCP  $\epsilon$ -martensite forms a platelet structure on  $\{111\}$  slip planes in association with the presence of stacking faults and would also be expected to significantly increase the difficulty of slip on intersecting  $\{111\}$  slip planes. To correlate cyclic hardening behavior, it is essential to consider the history dependence of these transformation products in addition to dislocation-dislocation interactions and accumulated dislocation density.

Formation of  $\alpha'$ - and  $\epsilon$ -martensite structures was studied for each multi-axial specimen. Presence of  $\alpha'$ -martensite was determined by x-ray diffraction



while  $\epsilon$ -martensite was determined by optical microscopy. The initial structure is seen in Fig. 12 which shows typical austenite grains of 304 stainless steel, many of which are highly twinned.

During deformation, it is possible to form 3 classes of deformation debris:

1. slip bands composed of dislocation arrays,
2.  $\epsilon$ -martensite which is hexagonal in form and
3.  $\alpha'$ -martensite which is BCT.

The first two products essentially form in response to the maximum shear stress and there is little or no effect of the normal stresses or the dilational component. The  $\epsilon$ -martensite may form because of the low stacking fault energy of the austenitic matrix and the relationship of the HCP  $\epsilon$  to the FCC  $\gamma$  matrix. It is expected that the amount of  $\alpha'$ -martensite would depend on both the shear and normal stresses as described elsewhere [21].

In Fig. 13, some deformation product\* in SS09 is seen. Note the clearly defined shear planes and the effects of the twinned regions which either change the slip direction or completely inhibit it. Similar structures were seen for other types of cycles. However, there were significant differences in the distribution of deformation product. Specimen SS09 was subjected to 90° out-of-phase cycling such that every plane in the specimen experienced the maximum shear strain range. As a consequence, the density of deformation debris was a maximum. This is seen by comparing Fig. 14 to Fig. 15. In Fig. 15 only two sets of slip planes experienced the maximum shear strain range and the density of deformation debris (slip band traces) was less than seen in Fig. 14.

---

\*We will not distinguish between  $\epsilon$ -martensite and planar arrays of extended dislocations.

For specimen SS06, which was subjected to alternating pure axial and pure torsional blocks, deformation was studied during testing using cellulose acetate replica techniques. Again, the deformation debris responds to the maximum shear strain and diamond-like figures could be seen to develop on the surface, presumably being defined by the maximum shear strain planes in axial and torsional loading as seen in Fig. 16 for two different blocks.

The specimens were also examined by x-ray diffraction subsequent to testing to determine if  $\alpha'$ -martensite was present. The nonproportional loading subjects more slip planes to a higher normal strain per cycle for a given maximum shear strain range and thus favors  $\alpha'$  formation from a thermodynamical basis [21]. Associated with an  $\alpha'$ -martensitic transformation is (a) an invariant shear strain  $\gamma_s$  and (b) a dilatation  $\epsilon_n = \Delta V/V_0$ , where  $V_0$  is the volume prior to transformation. Consider the work done by the applied stress on the martensitic transformation with respect to a potential habit plane,

$$U = \sigma_n \epsilon_n + |\tau_s| \gamma_s \quad (8)$$

where  $\sigma_n$  is the normal stress to the habit plane and  $|\tau_s|$  is the absolute magnitude of the resolved shear stress on this plane. Note that the sign of  $\tau_s$  is irrelevant but  $\sigma_n$  assists the transformation when positive. Note also that  $\epsilon_n$  and  $\gamma_s$  are constants that depend on the martensite type and the alloy composition.

For an Fe-30% Ni alloy the values are  $\gamma_s = 0.20$  and  $\epsilon_n = 0.05$  [21]. Since high positive values of  $U$  will assist transformation on the potential habit plane associated with  $\tau_s$  and  $\sigma_n$ , it is useful to consider the maximum value of  $U$  and the associated material plane at each point for the three loading histories of this study. Higher maximum values of  $U$  and a more

uniform distribution of associated planes in the specimen wall should each correlate with a greater extent of  $\alpha'$  transformation, and hence with the additional hardening observed in the nonproportional tests.

Figure 17 displays plots of the maximum value of  $U$  and the associated plane in the specimen wall during a cycle for selected blocks of nonproportional histories SS01 and SS09. The calculations were performed using values of  $\sigma_n$  and  $\tau_s$  obtained from the data by transformation to each potential habit plane in the specimen wall. Then  $U$  was computed from equation (8). The maximum value of  $U$  with respect to direction at each point in the cycle is denoted by  $U_{\max}$  and the corresponding plane by angle  $\phi$  measured positive counter-clockwise from the longitudinal specimen axis. Note that the peaks of the maximum  $U$  values are slightly higher for block 2 of specimen SS01 than for block 1, as is the maximum effective stress in a stable cycle. However, the potential habit planes associated with these  $U_{\max}$  values are not well distributed with respect to  $\phi$  and would imply a smaller amount and more inhomogeneously distributed  $\alpha'$  product. Nonproportional loading block 3 of specimen SS01 exhibits significantly higher peak and average  $U_{\max}$  values which are associated with a more uniform angular distribution of potential habit planes.

Likewise, it is readily seen that increasing degrees of nonproportionality of loading in blocks 2-4 of specimen SS09 correspond to increasing peak and average  $U_{\max}$  values within a cycle, as well as more uniform angular distribution of corresponding potential habit planes. Note that the range and peak values of  $U_{\max}$  within the more highly nonproportional loading blocks are approximately equal for both histories, reflecting that the extent of additional hardening is quite similar for the two cases.

The hypothesis that formation of  $\alpha'$ -martensite is directly related to the additional isotropic hardening would seem to make a great deal of sense based on the more uniform distribution of potential habit planes for the nonproportional loading blocks. This hypothesis must be tested, however, by measurement of the amount of  $\alpha'$ -martensite formed for each history. X-ray diffraction analysis using standard techniques [22] revealed significantly different levels of  $\alpha'$ -martensite, with specimen SS09 exhibiting the highest degree of transformation. At least three different regions of each specimen were examined, and the volume fraction of  $\alpha'$ -martensite was examined for each specimen by using two angles of incidence of the x-ray beam. The diffraction results obtained at the two different angles of incidence were equivalent, indicating lack of texture. In Fig. 18, the maximum shear stress for each specimen history is plotted versus the average volume percent  $\alpha'$ -martensite determined from the average of the two diffraction analyses. Both maximum shear stress and percent  $\alpha'$ -martensite are normalized by the values associated with specimen SS09. Clearly, there is no direct correlation between  $\alpha'$ -martensite formation and the extent of additional isotropic hardening.

It therefore does not appear that formation of  $\alpha'$ -martensite is the dominant mechanism for the tremendously increased resistance to cyclic plastic flow which is observed experimentally. This result suggests that formation of  $\epsilon$ -martensite associated with slip bands may more strongly influence the hardening behavior. Certainly, the increased grain-by-grain uniformity of deformation product mentioned earlier for specimen SS09 conforms with the observed maximum extent of hardening.

The influence of  $\epsilon$ -martensite formation on hardening behavior is an entirely plausible one from the standpoint of micromechanics. Since  $\epsilon$ -martensite is associated with slip planes and may be viewed as an extended stacking

fault, it is intimately related to plastic flow on the associated slip system. As more slip systems are activated by comparable Schmid stresses during nonproportional loading, accumulation of additional plastic strain and associated deformation product should be expected. When this occurs, increased resistance is offered against movement of dislocations on intersecting slip planes. Hence, a full latent hardening effect is produced.

The contribution of  $\epsilon$ -martensite and slip band-related processes to cyclic hardening may be reckoned on a micromechanical basis. Following the framework of Asaro [23] and Hutchinson [24], directed primarily toward textural anisotropy effects in finite deformation, one possible form for a latent hardening description is

$$h_{\alpha\beta} = qh + h(1-q)\delta_{\alpha\beta}, \quad (9)$$

where  $h_{\alpha\beta}$  are slip plane hardening rates which relate the rate of increase of critical Schmid stress on each  $\alpha$  slip system with shearing rates on all active  $\beta$  systems

$$\dot{\tau}_c^{(\alpha)} = \sum_{\beta=1}^n h_{\alpha\beta} |\dot{\gamma}^{(\beta)}|, \quad (10)$$

where  $\dot{\gamma}^{(\beta)} > 0$  only for active systems. In Eq. (9),  $h = h(\Gamma)$  and  $\delta_{\alpha\beta} = 1$  if  $\alpha = \beta$ ;  $\delta_{\alpha\beta} = 0$  if  $\alpha \neq \beta$ . The value of  $q$  governs the rate of hardening on secondary slip systems. The quantity  $\Gamma$  represents the cumulative shear for all slip systems, i.e.

$$\Gamma = \sum_{\alpha=1}^n \int |\dot{\gamma}^{(\alpha)}| dt, \quad (11)$$

and hence is a scalar measure of the extent of plastic deformation. If  $q=1$ , then  $h_{\alpha\beta} = h(\Gamma)$  and hardening is purely isotropic, i.e. lacking of cross-hardening effect. For  $q > 1$ , secondary slip systems may harden at a higher rate than the primary system. The off-diagonal terms represent latent hardening; diagonal terms represent self-hardening. It is probable that the transformation to  $\epsilon$ -martensite on  $\{111\}$  slip planes contributes to a high value of  $q$  for 304 stainless steel. It is also quite probable that  $q$  is strongly related to stacking fault energy, since a wavy slip mode results in a more homogeneous state of deformation than a planar slip mode.

It should be noted that the hardening rule in Eq. (10) is sensitive to changes in orientation of the applied strain rate tensor. The hardening rule in Eqs. (9) and (10) is the micromechanical analogy to the phenomenological formulation of an anisotropic plastic potential for a polycrystal. The possibility of using a single crystal data to predict the extent of hardening for cases of nonproportional straining of a polycrystal is intriguing. Certainly, it is necessary to consider the physical mechanisms which produce the seemingly anomalous cyclic hardening observed for the material of this study.

## CONCLUSIONS

The distribution of deformation products has been shown to be a function of loading path for type 304 stainless steel subjected to nonproportional cyclic loading. Furthermore, the effective stress amplitude in these tests correlates with the homogeneity and extent of deformation products in the polycrystalline structure.

It has also been demonstrated that there is a fundamental interaction between material and stress state. The stress state that is imposed causes certain features of the material's potential deformation morphology to be manifested. These features in turn affect shear and tensile stresses in a strain-controlled test. This mechanics/materials interaction must be taken into account if reliable constitutive models of deformation under complex loading are to be developed [25-27]. Uniaxial tests by themselves may be incapable of developing all deformation substructures (depending on the material) and thus the results of such tests should be put in perspective when applied to multiaxial conditions.

The role of  $\alpha'$ -martensite formation on the exceptional nonproportional cyclic hardening behavior of type 304 stainless steel, though appealing, does not appear to be a dominant one. Micrographs indicate that heterogeneity of  $\epsilon$ -martensite and slip band deformation products are a function of nonproportionality of loading and may more directly correlate with hardening. A micromechanical interpretation of latent hardening related to slip band processes has been offered.

#### Acknowledgments

Dr. McDowell is grateful for the support of the National Science Foundation (Grant No. MEA-8404080) in this work.

### List of References

1. Zamrik, S.Y. and Frishmuth, R.E., "The Effects of Out-of-Phase Biaxial-Strain Cycling on Low-Cycle Fatigue," *Experimental Mechanics*, pp. 204-208 (1973).
2. Leis, B.N., and Laflen, J.H., "Problems in Damage Analysis Under Nonproportional Cycling," *J. Engr. Matls. Tech.*, Vol. 102, pp. 127-134 (1980).
3. McDowell, D.L., "On the Path Dependence of Transient Hardening and Softening to Stable States Under Complex Biaxial Cyclic Loading," *Proceedings of the International Conference on Constitutive Laws for Engineering Materials*, Eds. Desai and Gallagher, Tucson, AZ, pp. 125-132 (1983).
4. Kanazawa, K., K.J. Miller and M.W. Brown, "Cyclic Deformation of 1 percent Cr-Mo-V Steel under Out-of-Phase Loads," *Fatigue of Engineering Materials and Structures*, Vol. 2, pp. 217-228, 1979.
5. Lamba, H.S., "Nonproportional Cyclic Plasticity," TAM Report No. 413, Department of Theoretical and Applied Mechanics, University of Illinois of Urbana-Champaign, 1976.
6. McDowell, D.L., "Transient Nonproportional Cyclic Plasticity," Report No. 107, Design and Materials Division, Department of Mechanical and Industrial Engineering, University of Illinois at Urbana-Champaign, June 1983.
7. Kestenbach, H.J., and Meyers, M.A., *Met. Trans.*, 7A (1976), p. 1943.
8. Bressaneelli, J.P., and Moskowitz, A., *Met. Trans. ASM*, 59, p. 223 (1966).
9. Maxwell, P.C., Goldberg, A., and Shyne, J.C., *Met. Trans.*, 5, p. 1305 (1974).
10. Mangonon, P.L., and Thomas, G., *Met. Trans.*, 1, p. 1577 (1970).
11. Kestenbach, H.J., *Phil. Mag.*, 36 p. 1509 (1977).
12. McDowell, D.L., and Socie, D.F., "Transient and Stable Deformation Behavior under Cyclic Nonproportional Loading," *ASTM STP 853*, pp. 64-87 (1985).
13. Waill, L.E., "Crack Observations in Biaxial Fatigue," Report No. 108, Design and Materials Division, Department of Mechanical and Industrial Engineering, University of Illinois at Urbana-Champaign, March 1983.
14. Brown, M.W., and Miller, K.J., "Biaxial Cyclic Deformation Behavior of Steels," *Fatigue of Engineering Materials and Structures*, Vol. 1, pp. 93-106 (1979).



15. Liu, K.C., and Greenstreet, W.L., "Experimental Studies to Examine Elastic-Plastic Behaviors of Metal Alloys Used in Nuclear Structures," Constitutive Equations in Viscoplasticity: Computational and Engineering Aspects, AMD, ASME, vol. 20, pp. 35-56 (1976).
16. Hecker, S.S., "Experimental Studies of Yield Phenomena in Biaxially Loaded Metals," Constitutive Equations in Viscoplasticity: Computational and Engineering Aspects, AME, ASME, Vol. 20, pp. 1-32 (1976).
17. Phillips, A., Tang, J.L., and Ricciuti, M., "Some New Observations on Yield Surfaces," Acta Mechanica, Vol. 20, pp.23-39 (1974).
18. Lukas, P., and Polak, J., "Cyclic Stress-Strain Response in Low Amplitude Region," Proceedings of the Symposium on Work Hardening in Tension and Fatigue, AIME, Cincinnati, pp. 177-205 (1975).
19. Landgraf, R.W., "Cyclic Stress-Strain Responses in Commercial Alloys," Proceedings of the Symposium on Work Hardening in Tension and Fatigue, AIME, Cincinnati, pp. 240-259 (1975),
20. Nouailhas, D., Policella, H., and Kaczmarek, H., "On the Description of Cyclic Hardening under Complex Loading Histories," Proceedings of the International Conference on Constitutive Laws for Engineering Materials, Eds. Desai and Gallagher, Tucson, AZ, pp. 45-49 (1983).
21. Patel, J.R., and M. Cohen: Acta Met., 1, p. 531 (1953).
22. H.P. Klug and L.E. Alexander, X-ray Diffraction Procedures for Polycrystalline and Amorphous Materials, Second Edition, Chapter 7, John Wiley & Sons (1974).
23. Asaro, R.J., "Crystal Plasticity," J. Appl. Mech., Vol. 50, pp. 921-934 (1983).
24. Hutchinson, J.W., "Elastic-Plastic Behavior of Polycrystalline Metals and Composites," Proc. Roy. Soc., Series A, Vol. 319, pp. 247-272 (1976)..
25. McDowell, D.L., "A Two Surface Model for Transient Nonproportional Cyclic Plasticity: Part I - Development of Appropriate Equations," ASME Journal of Applied Mechanics, Vol. 52, pp. 298-302 (1985).
26. McDowell, D.L., "A Two Surface Model for Transient Nonproportional Cyclic Plasticity: Part II - Development of Appropriate Equations," ASME Journal of Applied Mechanics, Vol. 52, pp. 303-308 (1985).
27. McDowell, D.L., "The Significance of Nonproportional Loading Tests for Characterization of Cyclic Response of Metals," Proc. 1985 SEM Spring Conf. on Experimental Mechanics," Las Vegas, pp. 229-236 (1985).

## LIST OF FIGURES

- Figure 1 Tubular axial-torsional specimen. Dimensions in mm.
- Figure 2 Grain structure of heat-treated type 304 stainless steel.
- Figure 3 Applied strain path and resulting hysteresis response for (left column) block 1, cycle 24, and (right column) block 2, cycle 24; specimen SS01.
- Figure 4 Applied strain path and resulting hysteresis response for (left column) block 3, cycle 24, and (right column) block 4, cycle 24; specimen SS01.
- Figure 5 Maximum value of Tresca effective stress in each cycle for blocks 1 through 3 for specimen SS01.
- Figure 6 Applied strain path and resulting hysteresis response for (left column) block 5, cycle 24, and (right column) block 6, cycle 24; specimen SS01.
- Figure 7 Applied strain path and resulting hysteresis response for (left column) block 7, cycle 24, and (right column) block 8, cycle 24; specimen SS01.
- Figure 8 Comparison of tenth cycle biaxial incremental step test for specimen SS09 (top) with uniaxial incremental step test results. The solid curves represent the uniaxial cyclic stress-strain curves after 40 to 50 cycles for  $\Delta\epsilon^P/2 = 0.0068$  (upper) and  $\Delta\epsilon^P/2 = 0.0045$  (lower), respectively.
- Figure 9 Applied strain path and resulting hysteresis response for (left column) block 2, cycle 16, and (right column) block 3, cycle 24; specimen SS09. Note that several corresponding points are numbered in the stress and strain space trajectories.
- Figure 10 Applied strain path and resulting hysteresis responses for block 4, cycle 24; specimen SS09. Note that several corresponding points are numbered in the stress and strain space trajectories.
- Figure 11 Maximum value of Tresca effective stress in cycle for blocks 2 through 4 for specimen SS09.
- Figure 12 Initial structure of 304 stainless steel used in this study. Specimen taken from grip section.
- Figure 13 Deformation debris in specimen SS09. Note the planar deformation products and their spatial orientation dependence on grain and twin structures.

- Figure 14    Deformation debris in specimen SS09. Note the relatively homogeneous distribution of deformation product.
- Figure 15    Deformation substructure of specimen SS01. Note the reduced homogeneity of deformation product compared to specimen SS09.
- Figure 16    Surface structure of specimen SS06 delineated by replica. In (a) the specimen is shown after 6 blocks while in (b) it is shown after 16 blocks. In (b) the surface is more highly deformed than in (a).
- Figure 17    Maximum values of  $U$  through a cycle versus corresponding angular position of associated potential habit planes for (left column) blocks 1 (top), 2 (middle), and 3 (bottom) of specimen SS01, and for (right column) blocks 2 (top), 3 (middle), and 4 (bottom) of specimen SS09.
- Figure 18    Correlation of maximum Tresca effective stress in a stable cycle with the measured volume percent of  $\alpha'$ -martensite. Note that both axes are normalized by values corresponding to specimen SS09, which exhibited maximum additional hardening and volume fraction  $\alpha'$ -martensite.

TABLE I. Composition of 304 SS (w/o)

	C	Mn	Si	Cr	Ni	Fe
AISI	0.08%	2.0%	1.0%	18-20%	8-12%	Bal.
ACTUAL	0.05%	1.40%	0.45%	19.13%	9.49%	Bal.

Table II. Summary of Uniaxial Fatigue Tests

Specimen Type		$\epsilon_a$	$N_f$
Longitudinal	Radial		
x		0.004	4800
x		0.0016	Run-out
x		0.003	47600
x		0.0035	4300
x		0.0035	3300
	x	0.0155	750
	x	0.005	2930
	x	0.004	7300
	x	0.004	7700
	x	0.0035	4300
	x	0.0035	13700

### Table III. Complex Strain Histories

[illegible]

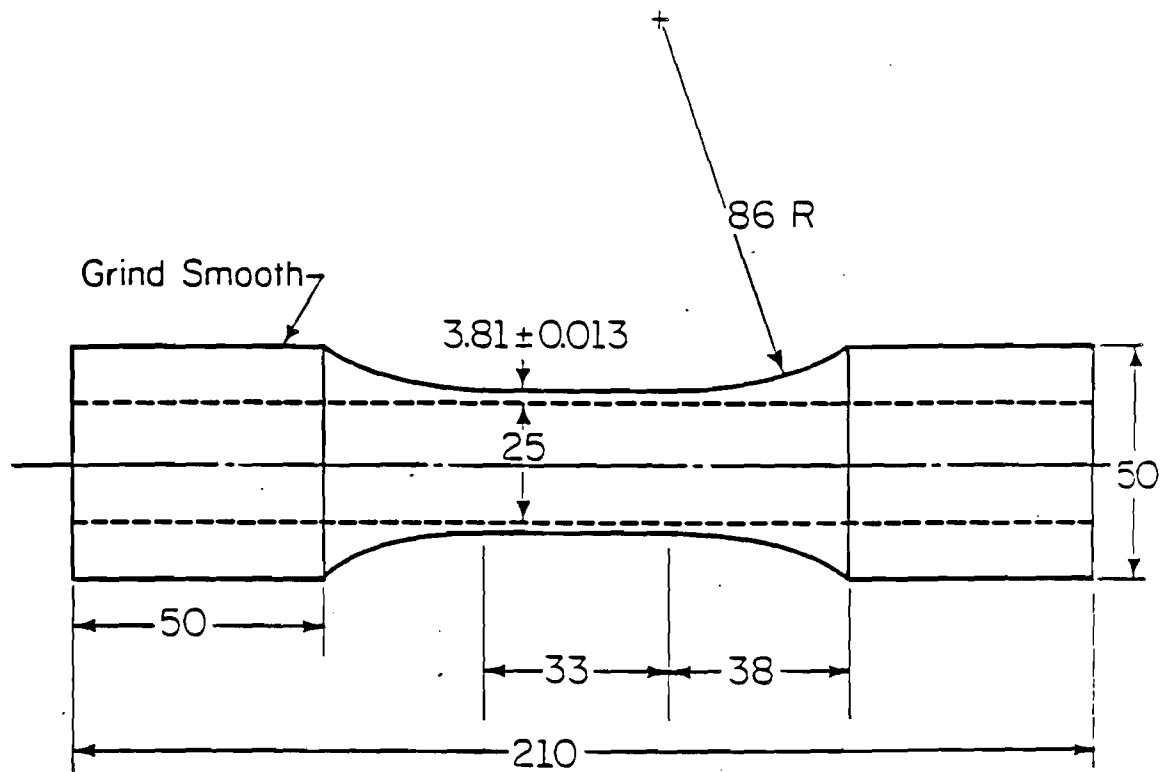
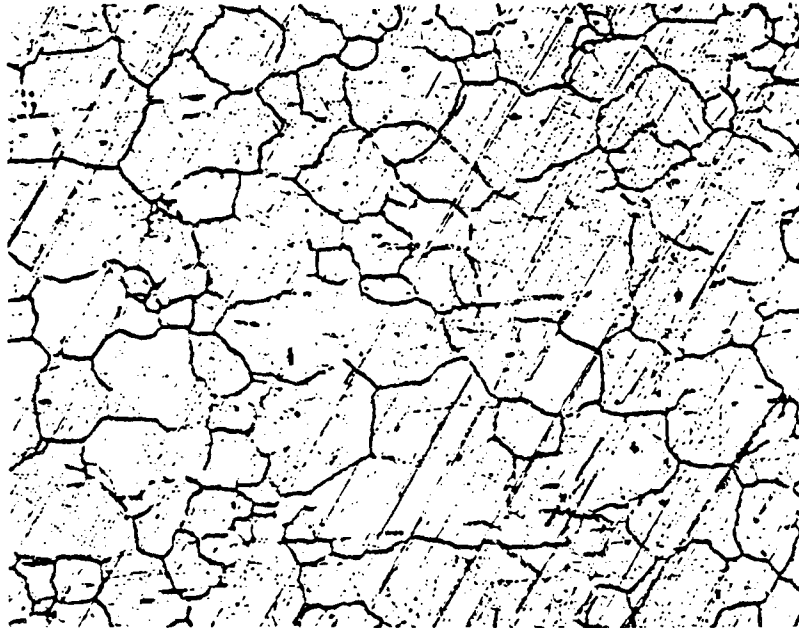


Figure 1      Tubular axial-torsional specimen.      Dimensions in mm.



1mm

Figure 2      Grain structure of heat-treated type 304 stainless steel.



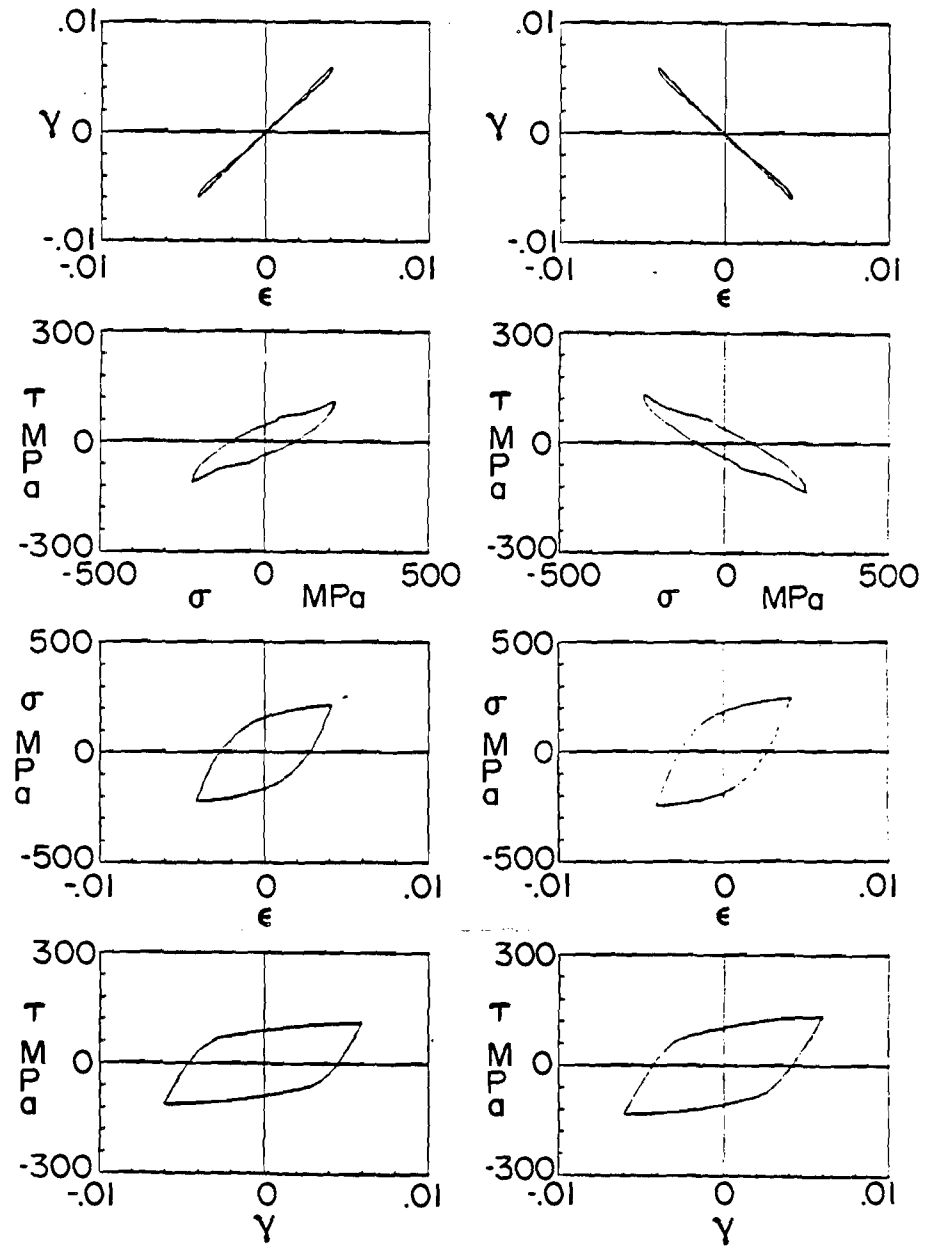


Figure 3 Applied strain path and resulting hysteresis response for (left column) block 1, cycle 24, and (right column) block 2, cycle 24; specimen SS01.

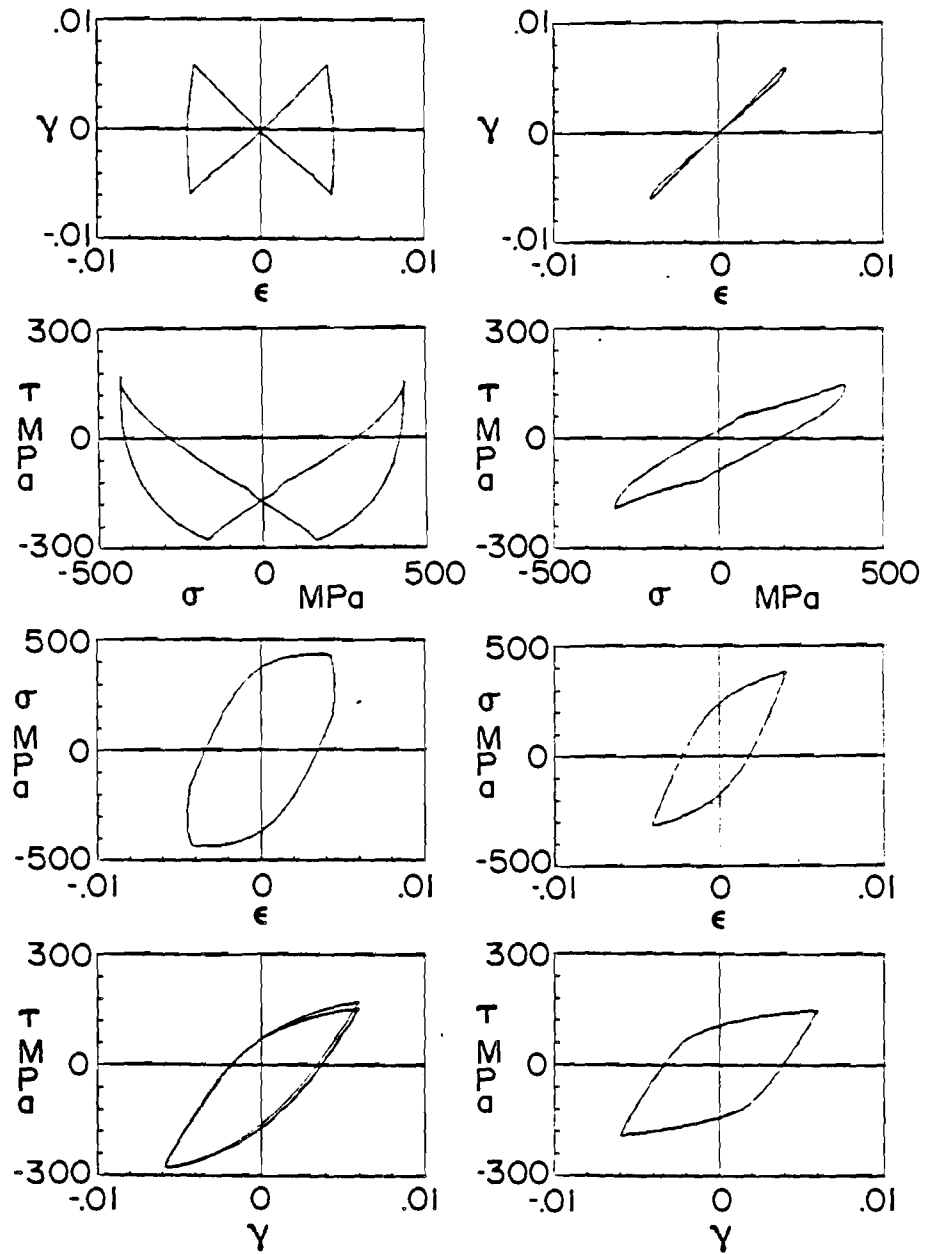


Figure 4 Applied strain path and resulting hysteresis response for (left column) block 3, cycle 24, and (right column) block 4, cycle 24; specimen SS01.

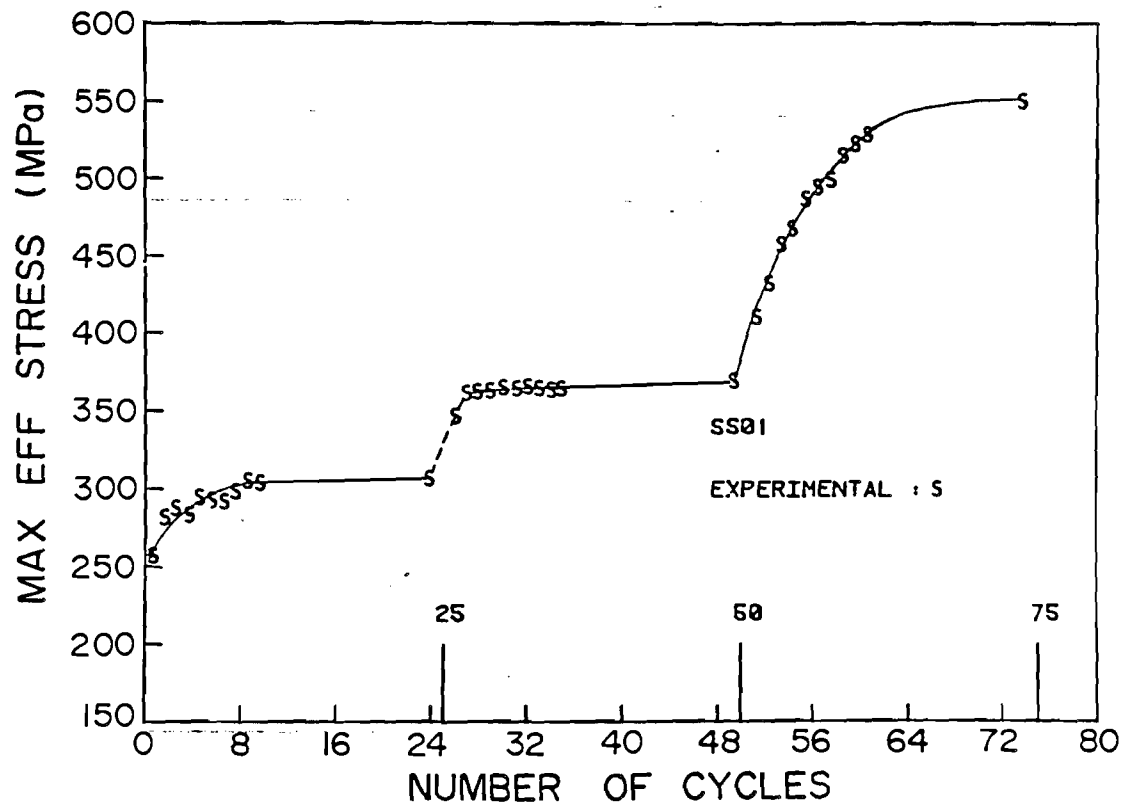


Figure 5

Maximum value of Tresca effective stress in each cycle for blocks 1 through 3 for specimen SS01.

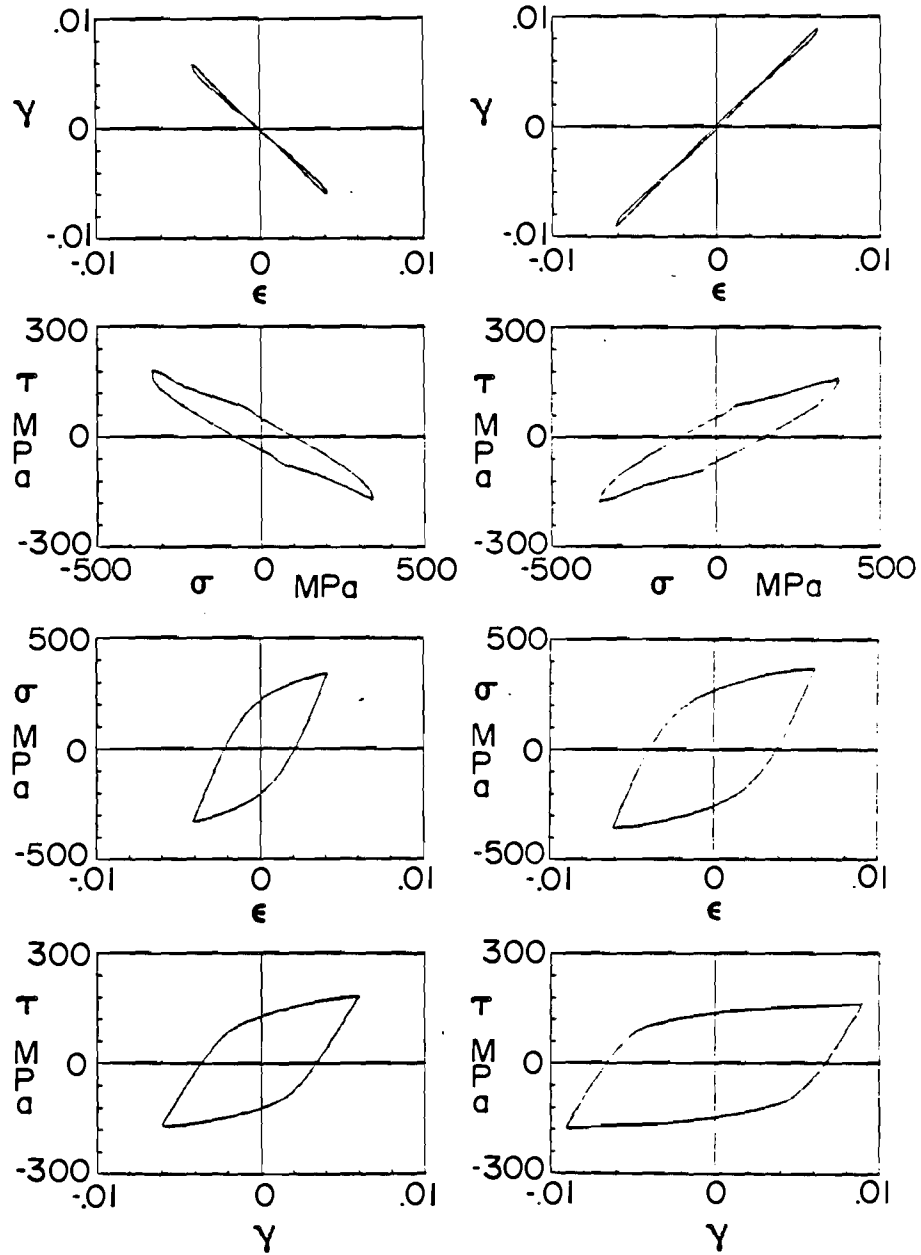


Figure 6 Applied strain path and resulting hysteresis response for (left column) block 5, cycle 24, and (right column) block 6, cycle 24; specimen SS01.

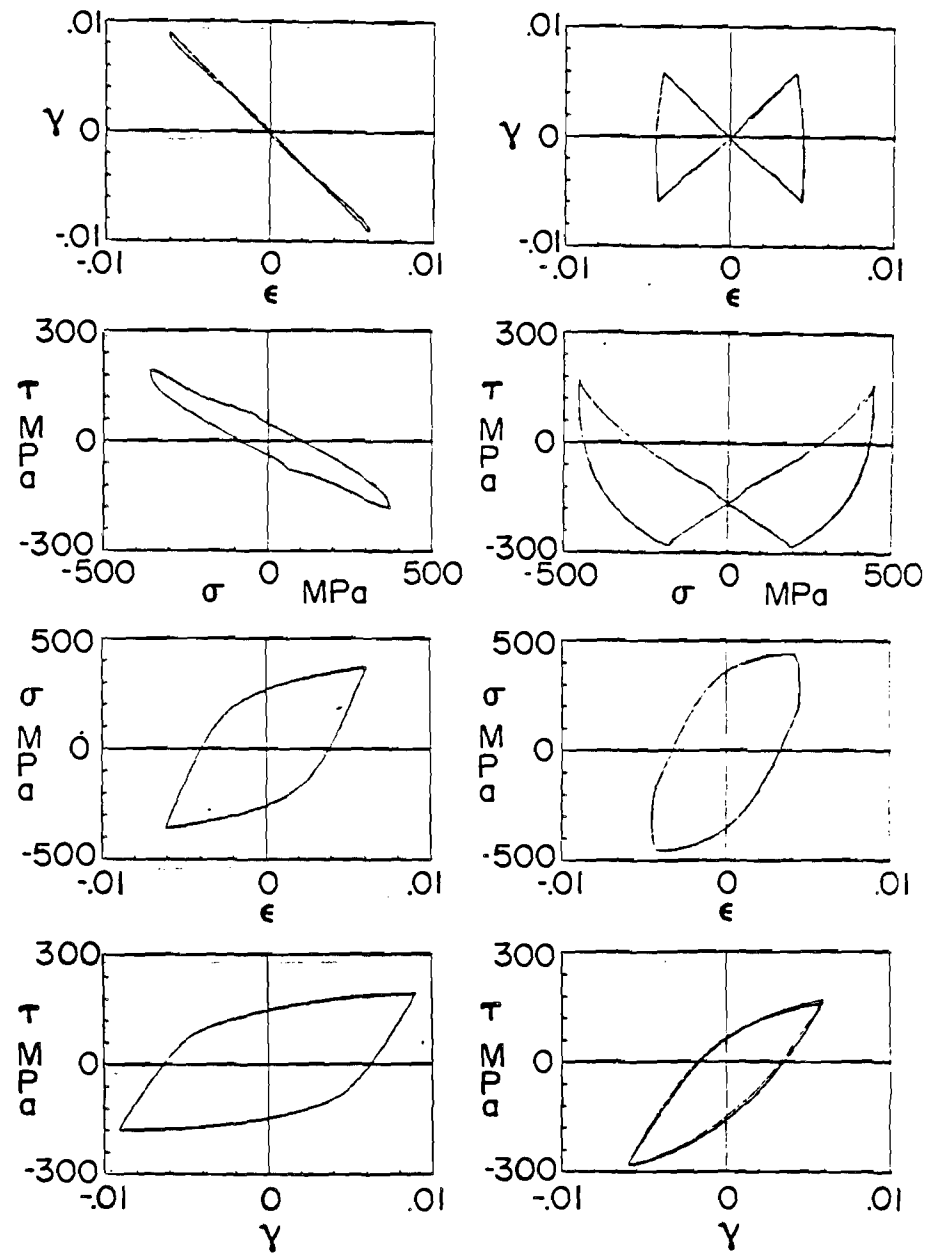


Figure 7

Applied strain path and resulting hysteresis response for (left column) block 7, cycle 24, and (right column) block 8, cycle 24; specimen SS01.

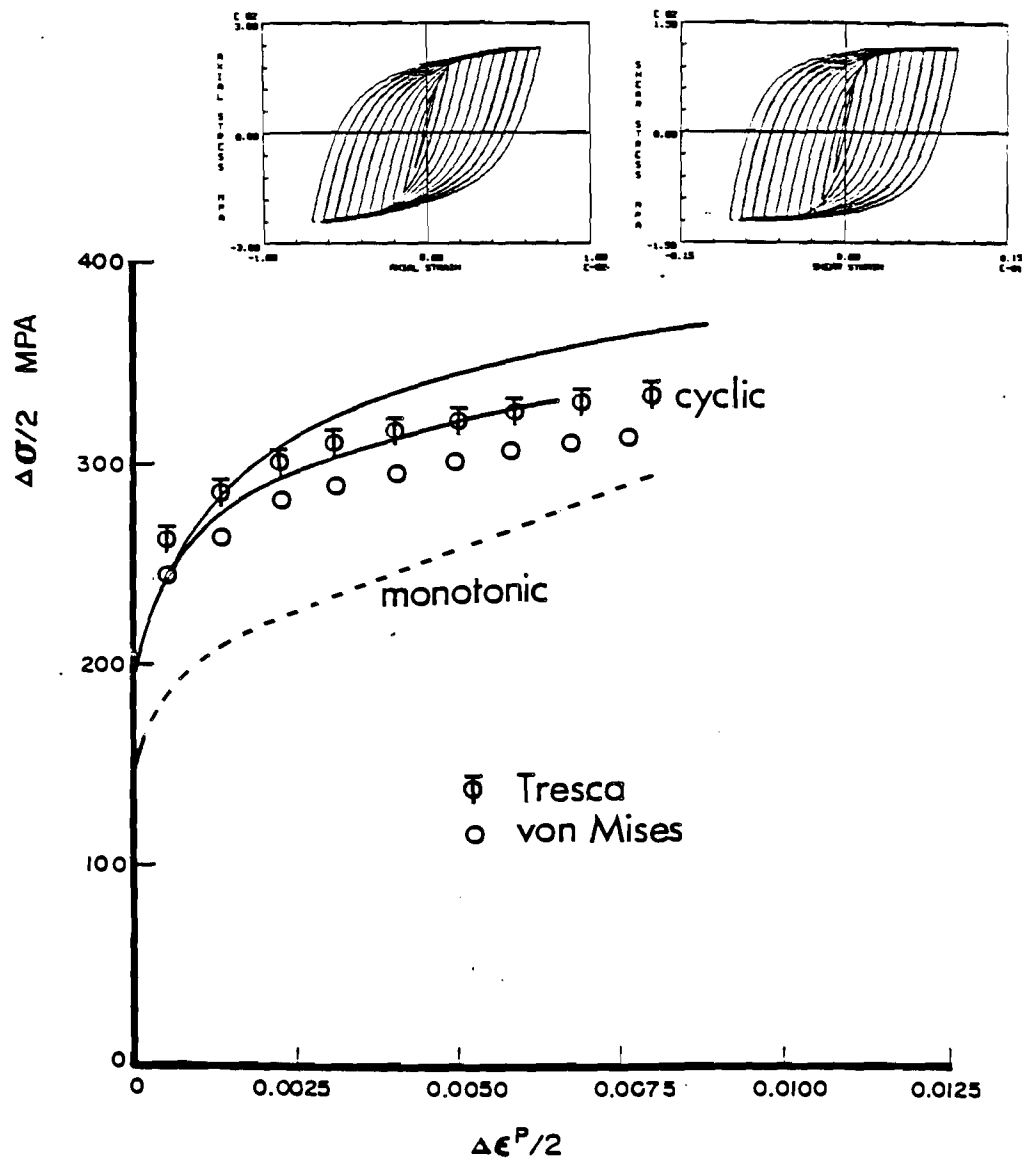


Figure 8

Comparison of tenth cycle biaxial incremental step test for specimen SS09 (top) with uniaxial incremental step test results. The solid curves represent the uniaxial cyclic stress-strain curves after 40 to 50 cycles for  $\Delta\epsilon^P/2 = 0.0068$  (upper) and  $\Delta\epsilon^P/2 = 0.0045$  (lower), respectively.

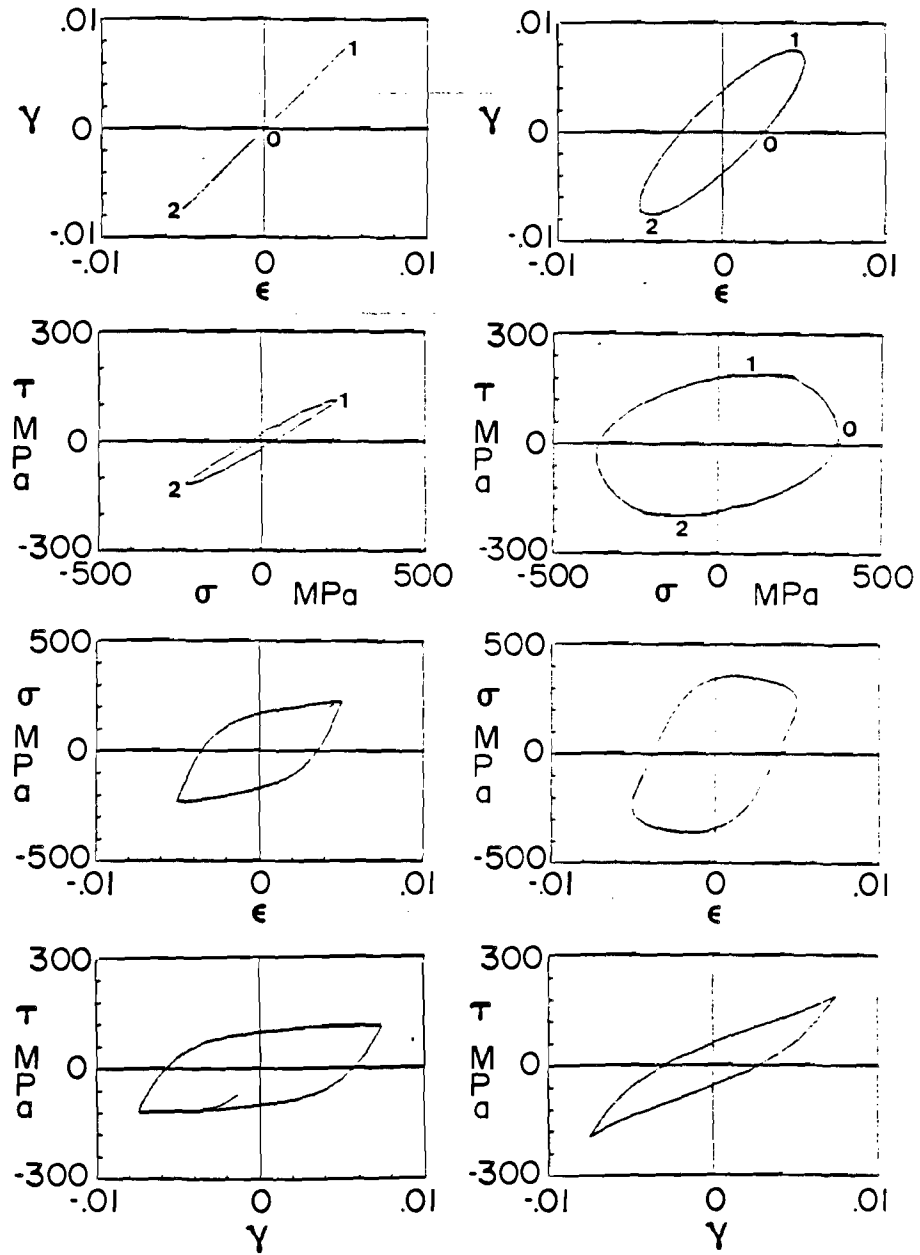


Figure 9

Applied strain path and resulting hysteresis response for (left column) block 2, cycle 16, and (right column) block 3, cycle 24; specimen SS09. Note that several corresponding points are numbered in the stress and strain space trajectories.

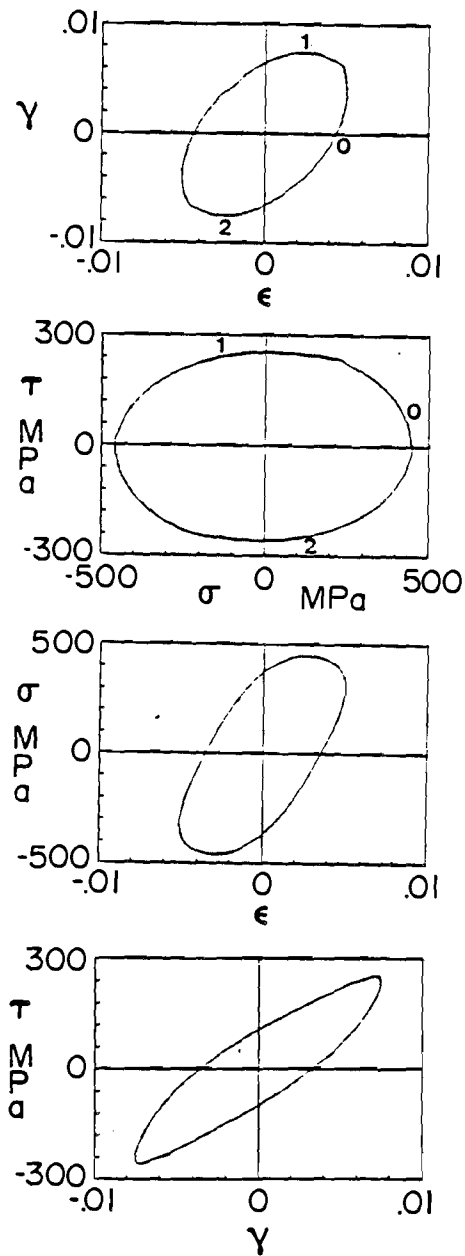


Figure 10

Applied strain path and resulting hysteresis response for block 4, cycle 24; specimen SS09. Note that several corresponding points are numbered in the stress and strain space trajectories.



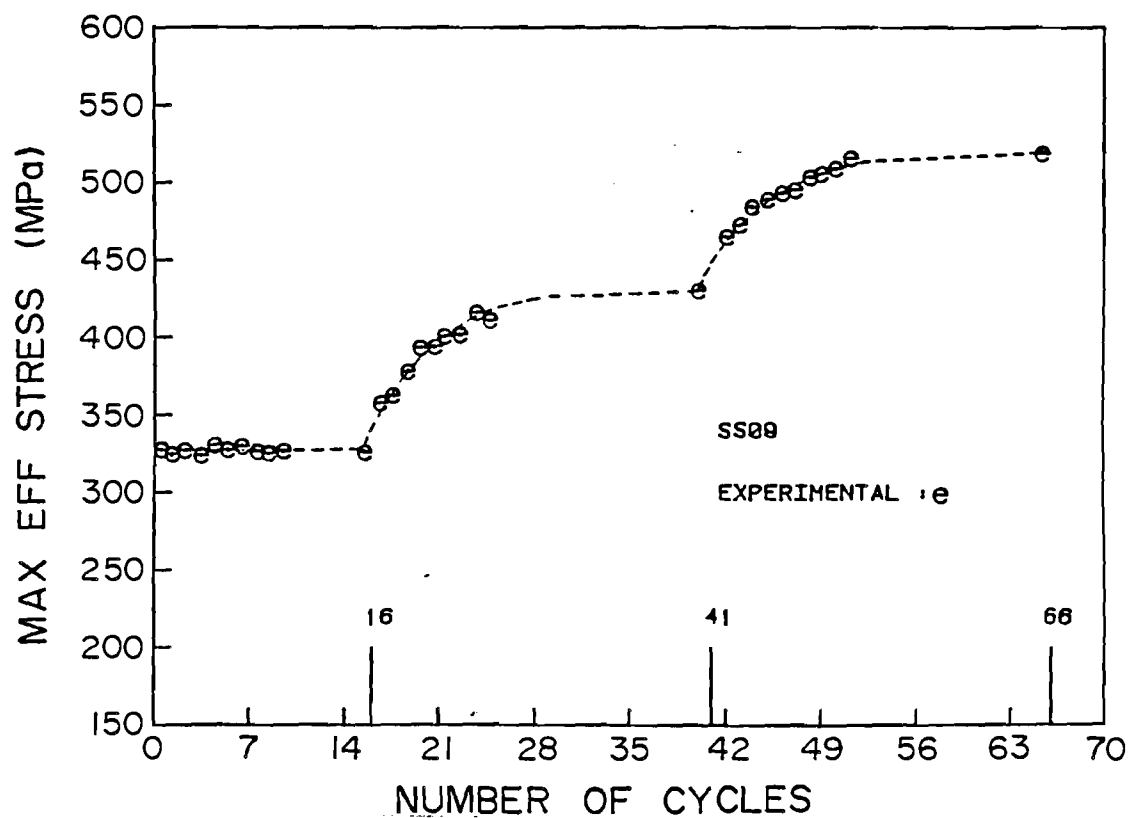


Figure 11

Maximum value of Tresca effective stress in each cycle for blocks 2 through 4 for specimen SS09.

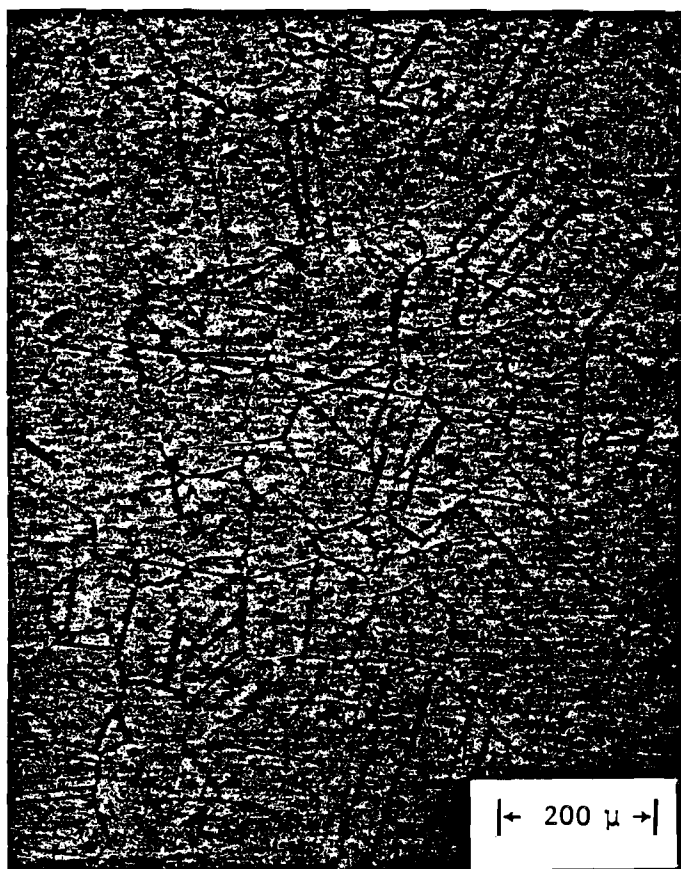


Figure 12

Initial structure of 304 stainless steel used in this study. Specimen taken from grip section.

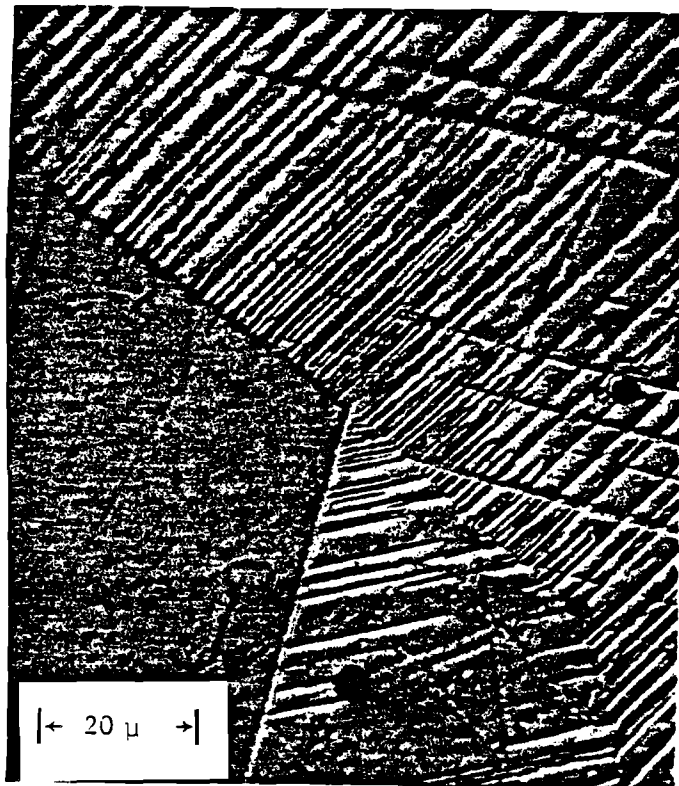


Figure 13 Deformation debris in specimen SS09. Note the planar deformation products and their spatial orientation dependence on grain and twin structures.



Figure 14 Deformation debris in specimen SS09. Note the relatively homogeneous distribution of deformation product.

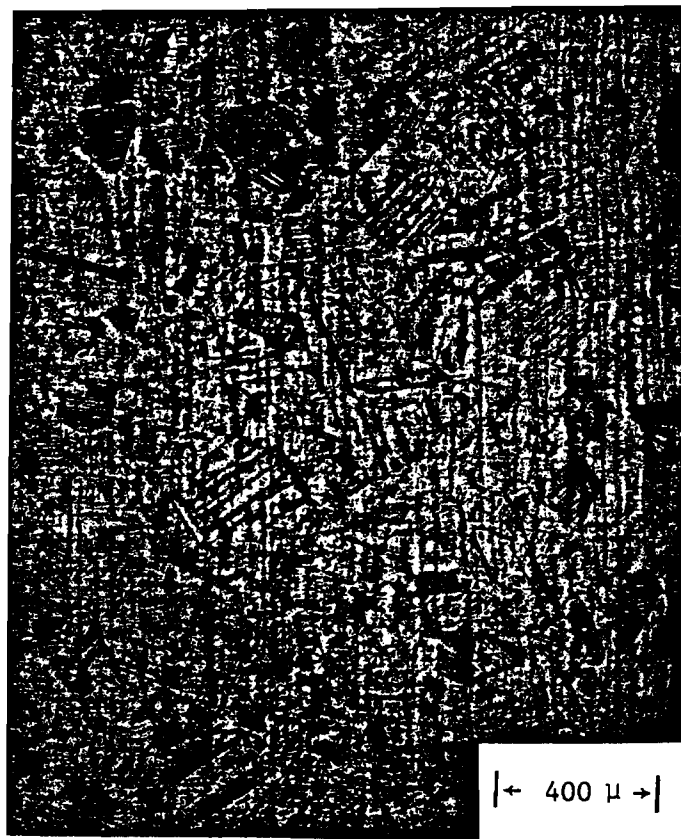


Figure 15 Deformation substructure of specimen SS01. Note the reduced homogeneity of deformation product compared to specimen SS09.



a



b

Figure 16

Surface structure of specimen SS06 delineated by replica. In (a) the specimen is shown after 6 blocks while in (b) it is shown after 16 blocks. In (b) the surface is more highly deformed than in (a).

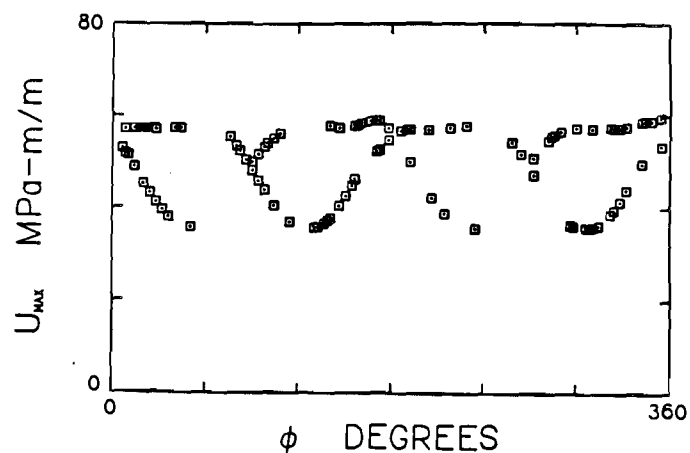
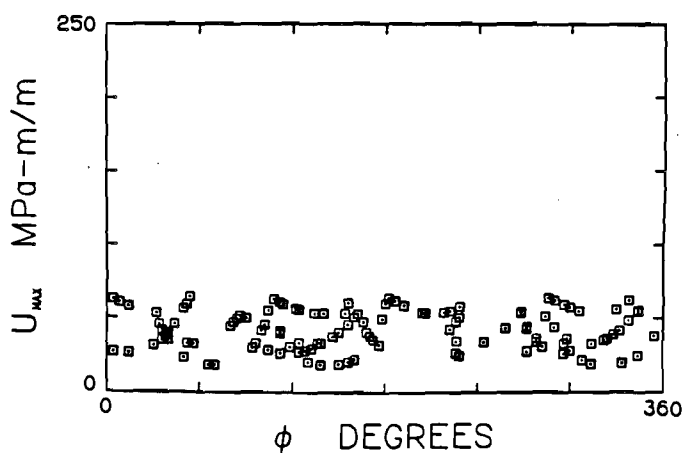
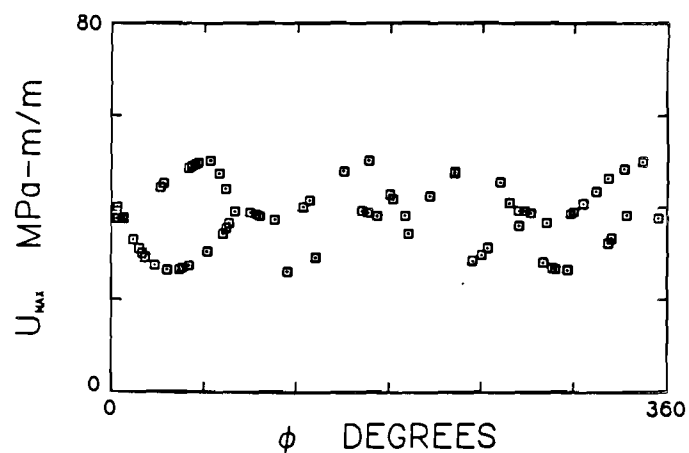
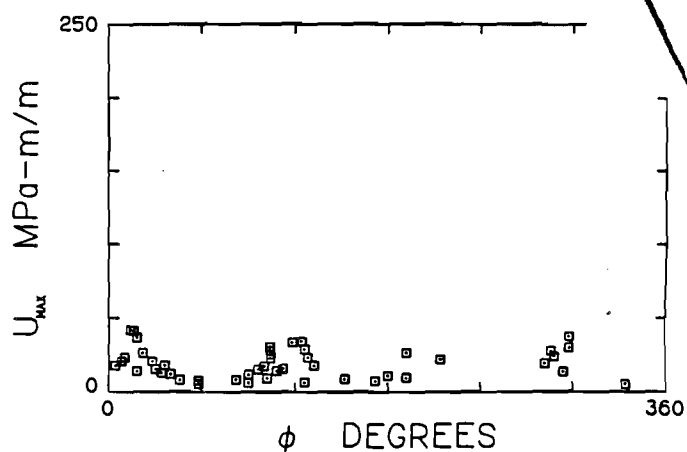
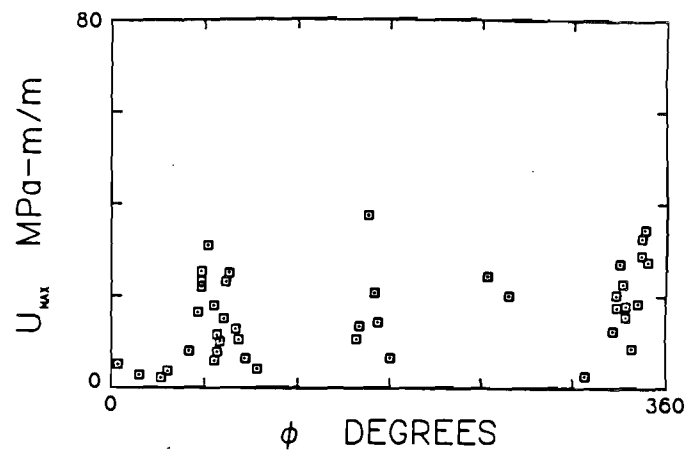
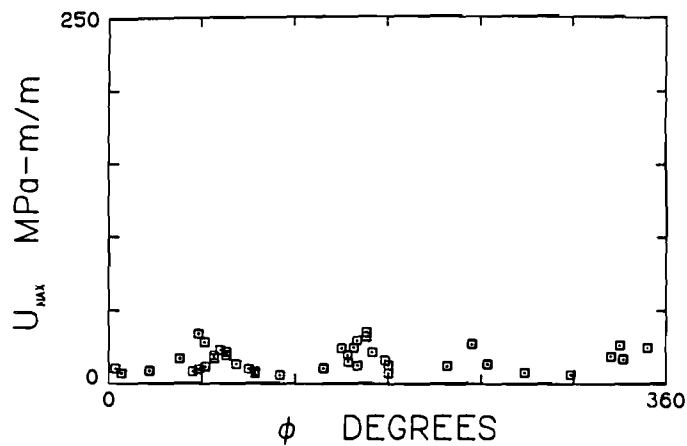


Figure 17 Maximum values of  $U$  through a cycle versus corresponding angular position of associated potential habit planes for (left column) blocks 1 (top), 2 (middle), and 3 (bottom) of specimen SS01, and for (right column) blocks 2 (top), 3 (middle), and 4 (bottom) of specimen SS09.

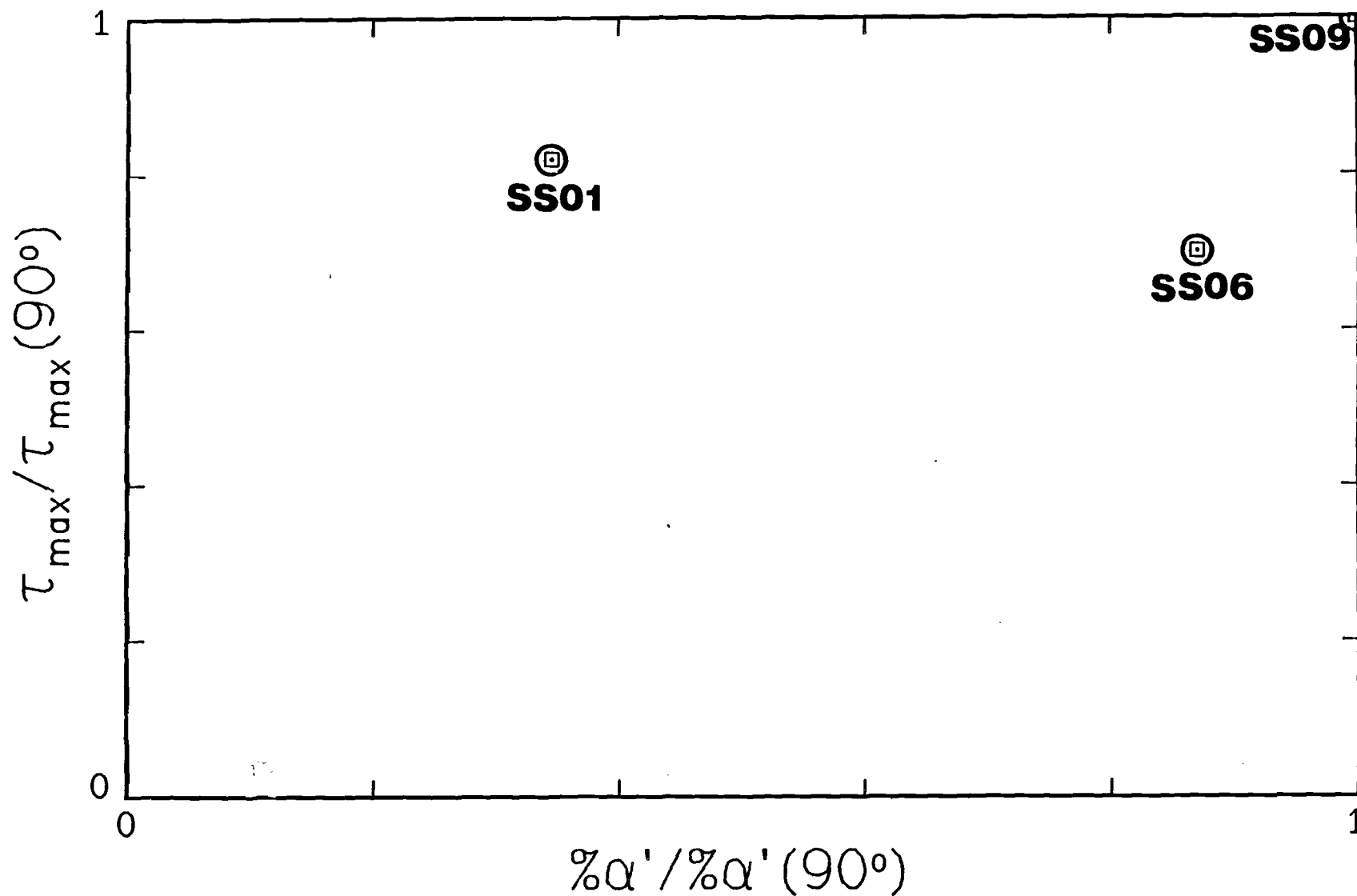


Figure 18 Correlation of maximum Tresca effective stress in a stable cycle with the measured volume percent of  $\alpha'$ -martensite. Note that both axes are normalized by values corresponding to specimen SS09, which exhibited maximum additional hardening and volume fraction of martensite.



# Some Implications for Cyclic Plastic and Viscoplastic Equations Based on Nonproportional Loading Experiments

D. L. McDowell<sup>1</sup>, J. Moosbrugger<sup>1</sup>, M. Doumi<sup>1</sup>, and E. H. Jordan<sup>2</sup>

Presented at 3rd Symposium on Nonlinear Constitutive Relations for High-Temperature Applications, NASA, University of Akron, June 11-13, 1986.

## Introduction

A number of different formulations exist for state variable or "unified" creep-plasticity theory [1-10]. There is, however, a common isothermal framework for many of these models which include backstress, e.g.

$$\dot{\underline{\epsilon}}^n = f(||\underline{s} - \underline{\alpha}||, \kappa) (\underline{s} - \underline{\alpha}) \quad (1)$$

$$\dot{\underline{\alpha}} = h_{\alpha} \dot{\underline{\epsilon}}^n - r_{\alpha} \underline{\alpha} \quad (2)$$

$$\dot{\kappa} = h_{\kappa} ||\dot{\underline{\epsilon}}^n|| - r_{\kappa} \kappa \quad (3)$$

where  $h_{\alpha}$  and  $h_{\kappa}$  are scalar hardening functions,  $r_{\alpha}$  and  $r_{\kappa}$  are scalar recovery functions,  $\underline{\alpha}$  is the backstress,  $\kappa$  is the drag stress,  $\underline{s}$  is deviatoric stress,  $\dot{\underline{\epsilon}}^n$  is the inelastic strain rate, and  $||\dot{\underline{\epsilon}}^n|| = [\dot{\underline{\epsilon}}^n : \dot{\underline{\epsilon}}^n]^{1/2}$ .

---

<sup>1</sup> School of Mechanical Engineering, Georgia Institute of Technology, Atlanta, GA 30332

<sup>2</sup> Mechanical Engineering, University of Connecticut, Storrs, CT 06268

It is usual to first select hardening and recovery functions which encompass relevant uniaxial phenomenological behavior, and then to fit the associated material constants to this data using appropriate multivariate error minimization procedures. There is a somewhat prevalent assertion among existing theories that the directional index for the hardening term in equation (2) is the inelastic strain rate, i.e.

$$\dot{\underline{\xi}} = \dot{\underline{\epsilon}}^n \quad (4)$$

Several theories [2-3, 11-12] include a dynamic recovery term with  $\underline{\alpha}$  as the directional index, i.e.

$$\dot{\underline{\xi}} = \dot{\underline{\epsilon}}^n - h_a^{-1} h_D \underline{\alpha} ||\dot{\underline{\epsilon}}^n|| \quad (5)$$

where  $h_D$  is a scalar dynamic recovery function. Uniaxial testing alone is insufficient to validate the directional index of the dynamic recovery term since  $\underline{\alpha}$  is collinear with  $\dot{\underline{\epsilon}}^n$ . This collinearity is also likely responsible for the absence of the dynamic recovery term in many theories.

An important attribute of multiaxial nonproportional loading is the non-collinearity of  $\dot{\underline{\epsilon}}^n$  and  $\underline{\alpha}$ . As will be shown in this paper, the need for the dynamic recovery term can be established from cyclic nonproportional biaxial tests. Furthermore, it is possible to comment on the relative magnitude of the direct hardening and dynamic recovery coefficients and to assess the accuracy of the direct hardening and dynamic recovery directional indices based on selected tests. Axial-torsional experiments conducted with two different materials will be discussed.

### Definition of Axial-Torsional Subspace

The definition of the axial-torsional subspace follows as a subspace of Ilyushin's five-dimensional deviatoric vector space [13]. Define the stress vector as

$$\sigma = \sigma_1 \underline{n}_1 + \sigma_3 \underline{n}_3 \quad (6)$$

$$\sigma_1 = \sigma_{zz} = \sigma, \quad \sigma_3 = \sqrt{3}\sigma_{z\theta} = \sqrt{3}\tau$$

and  $\underline{n}_1$  and  $\underline{n}_3$  are orthonormal base vectors in the stress plane. Here,  $z$  and  $\theta$  denote the tube longitudinal and circumferential directions, respectively. Likewise, the plastic strain vector is defined by

$$\underline{\epsilon}^n = \epsilon_1^n \underline{n}_1 + \epsilon_3^n \underline{n}_3 \quad (7)$$

where

$$\epsilon_1^n = \epsilon_{zz}^n, \text{ and } \epsilon_3^n = (2/\sqrt{3})\epsilon_{z\theta}^n$$

Note that the plastic strain rate vector is defined as

$$\dot{\underline{\epsilon}}^n = \dot{\epsilon}_1^n \underline{n}_1 + \dot{\epsilon}_3^n \underline{n}_3 \quad (8)$$

The effective stress  $\bar{\sigma}$  and plastic strain rate  $\dot{\bar{\epsilon}}^n$  (normalized to the axial case) are recognized as

$$\bar{\sigma} = |\underline{\sigma}| = (\underline{\sigma} \cdot \underline{\sigma})^{1/2} = (\sigma_1^2 + \sigma_3^2)^{1/2} \quad (9)$$

$$\frac{\dot{\bar{\epsilon}}^n}{\bar{\epsilon}} = \frac{|\dot{\underline{\epsilon}}^n|}{|\underline{\epsilon}^n|} \quad (10)$$

The total strain vector is heuristically defined as

$$\epsilon = \epsilon_1 \tilde{n}_1 + \epsilon_3 \tilde{n}_3 \quad (11)$$

where  $\epsilon_1 = \epsilon_{zz} = \epsilon$  and  $\epsilon_3 = (2/\sqrt{3})\epsilon_{z\theta} = \gamma/\sqrt{3}$ . The effective strain rate is then  $\dot{\tilde{\epsilon}} = |\dot{\tilde{\epsilon}}|$  since  $\gamma = 2\epsilon_{z\theta}$ .

#### AISI TYPE 304 STAINLESS STEEL AT ROOM TEMPERATURE

As reported elsewhere [14-18], thin-walled tubular specimens were subjected to strain-controlled axial-torsional histories with  $\dot{\tilde{\epsilon}} = \text{constant}$ . The strain paths for three different loading blocks are shown in Figure 1 along with the resulting stress subspace responses near the end of each loading block. Paths (b) and (c) in Figure 1 correspond to 30 and 60 degree out-of-phase sinusoidal loading. In all cases, the stress subspace responses are essentially cyclically stable.

It should be noted that there are path-dependent differences in the extent of cyclic hardening. For example, path (c) exhibits a saturation effective stress level which considerably exceeds that of block (b). Yet the maximum plastic shear strain amplitude of path (b) exceeds that of path (c). The transient behavior of these three histories, including the additional cyclic hardening during nonproportional strain cycling, have been previously documented [14-15]. This paper will not address the transient behavior since it is concerned with kinematic hardening.

#### Kinematic Hardening

For these room-temperature, constant effective strain rate tests, rate-independent plasticity is an acceptable idealization. By normality, the inelastic strain rate in the axial-torsional subspace is given by

$$\dot{\underline{\epsilon}}^n = \dot{\lambda}(\underline{\sigma} - \underline{\alpha}) \quad (12)$$

with the assumed yield surface form

$$f = (\underline{\sigma} - \underline{\alpha}) \cdot (\underline{\sigma} - \underline{\alpha}) - R^2 = 0 \quad (13)$$

where  $\dot{R} = 0$  during the stable latter cycles of each block just discussed. We may express evolution of  $\underline{\alpha}$  with or without a dynamic recovery term in equation (5), i.e.

$$\dot{\underline{\alpha}} = \mu_1 \dot{\underline{\epsilon}}^n \quad (14)$$

or

$$\dot{\underline{\alpha}} = \dot{\mu}_2 (\mu_3 \dot{\underline{\epsilon}}^n - \underline{\alpha} |\dot{\underline{\epsilon}}^n|) \quad (15)$$

where  $\mu_1$  and  $\mu_2$  are determined from the consistency condition and  $\mu_3$  is an unspecified scalar function.

Assuming  $R$ , the path of  $\underline{\alpha}$  may be computed from experimental results if  $\dot{\underline{\epsilon}}^n$  is known. To compute the plastic strain rate vector from the data, numerical differentiation was required. The values of axial stress, shear stress, axial strain and shear strain of five contiguous data points were parameterized with respect to arc length  $s = \Sigma(\Delta \underline{\sigma} \cdot \Delta \underline{\sigma})$  along the path. Then a parabola was least-squares fit to the five data points to form each of the smoothed functions  $\sigma(s)$ ,  $\tau(s)$ ,  $\epsilon(s)$ , and  $\gamma(s)$ , and the derivatives  $d\sigma/ds$ ,  $d\tau/ds$ ,  $d\epsilon/ds$ , and  $d\gamma/ds$  were obtained for the central (third) point. The derivative of plastic strain was computed as

$$\frac{d\tilde{\epsilon}^n}{ds} = \left( \frac{d\tilde{\epsilon}}{ds} - \frac{1}{E} \frac{d\sigma}{ds} \right) \tilde{n}_1 + \left( \frac{d\gamma}{ds} - \frac{1}{G} \frac{d\tau}{ds} \right) \sqrt{3} \tilde{n}_3 \quad (16)$$

and the unit normal vector in the direction of the plastic strain rate was defined by

$$\tilde{n} = (d\tilde{\epsilon}^n/ds) / |d\tilde{\epsilon}^n/ds| \quad (17)$$

A check on the smoothness of the data was obtained by applying a first order central difference technique to each three contiguous points to obtain the derivatives for the central point [16]. This technique resulted in essentially the same results as the five-point parabola method, indicating good differentiability of the data.

The hardening rules in equations (14)-(15) can be compared, at least qualitatively, by implementation in the axial-torsional subspace. Since  $\tilde{\epsilon}^n$  is collinear with  $(\tilde{\sigma} - \tilde{\alpha})$  in the subspace,

$$\tilde{\alpha} = \tilde{\sigma} - R \tilde{n} \quad (18)$$

and the predicted directions of backstress are given by

$$\tilde{n}_D = \tilde{n} \quad (19)$$

and

$$\tilde{n}_{D+DR} = \bar{\mu}_3 (\tilde{\sigma} - \tilde{\alpha}) - \tilde{\alpha} \quad (20)$$

where  $\tilde{n}_D$  and  $\tilde{n}_{D+DR}$  are vectors representative of direct hardening with or without dynamic recovery, i.e. equations (14) and (15), respectively. Since  $\tilde{n}$

and  $\underline{\alpha}$  are known from equations (17) - (18), equations (19) - (20) can be compared if  $\bar{\mu}_3$  is selected to best fit data.

In Figure 2, the backstress path is plotted assuming R. Vectors are periodically plotted along the path representing the directions expressed in equations (19) - (20). Note that  $\bar{\mu}_3 = 2.3$  was selected to provide the best fit to path (a) in Figure 2. Though  $\bar{\mu}_3$  may be a function of plastic strain range [11], this dependence is not herein considered. The degree of tangency of these vectors to the path of  $\underline{\alpha}$  provides the measure of accuracy for each rule. It should be noted that the presence of the dynamic recovery term is essential to obtain good correlation with data.

#### HASTELLOY-X AT 649°C

Experiments were conducted by Jordan on thin-walled tubular specimens. Experimental details can be found elsewhere [19]. Essentially stabilized cyclic responses are considered in this work. Two strain-controlled histories are reported in Figure 3. The two 90° out-of-phase sinusoidal histories were imposed at 649°C with an engineering shear to axial strain amplitude ratio of 3/2. In this case, each plane in the specimen wall experiences the same shear strain range and the maximum shear strain planes rotate at constant angular velocity. This type of history has also been observed to produce the maximum extent of cyclic hardening for austenitic stainless steel [14-18, 20] and Cr-Mo [21] alloys in addition to OFHC copper [22-23].

#### Backstress Evolution in the Rate-Dependent Case

The general deviatoric stress form of the flow rule which incorporates the kinematic hardening variable of Prager is chosen. As given by Chan et al. [9]

$$\dot{\underline{\epsilon}}^n = \lambda (\underline{s} - \underline{\alpha}) \quad (21)$$

where

$$\lambda = \left[ \frac{\dot{\underline{\underline{\epsilon}}}^n : \dot{\underline{\underline{\epsilon}}}^n}{(\underline{\underline{s}} - \underline{\underline{\alpha}}) : (\underline{\underline{s}} - \underline{\underline{\alpha}})} \right]^{1/2} \quad (22)$$

In equations (21) and (22)  $\dot{\underline{\underline{\epsilon}}}^n$  is the inelastic strain rate,  $\underline{\underline{s}}$  is the deviatoric stress and  $\dot{\underline{\underline{\epsilon}}}^n : \dot{\underline{\underline{\epsilon}}}^n$  denotes the scalar product of the inelastic strain rate tensor. Often referred to as the "backstress" or "equilibrium stress," the kinematic hardening variable  $\underline{\underline{\alpha}}$ , as pointed out by Chan et al. [9], can account for directional hardening, non-coaxiality of the inelastic strain rate with the deviatoric stress, and effects such as reversed creep and relaxation through zero stress when the quantity  $(\underline{\underline{s}} - \underline{\underline{\alpha}})$  is negative. In the context of rate-independent plasticity,  $\underline{\underline{\alpha}}$  represents the current origin of a translating yield surface in stress space. A general form for the evolution equation for the backstress is

$$\dot{\underline{\underline{\alpha}}} = \underline{\underline{h}} \dot{\underline{\underline{N}}} - \underline{\underline{d}} \dot{\underline{\underline{M}}} \quad (23)$$

where  $\underline{\underline{h}}$  and  $\underline{\underline{d}}$  are, in general, tensors which operate on indices  $\dot{\underline{\underline{N}}}$  and  $\dot{\underline{\underline{M}}}$ . Equation (23) represents the case for isothermal, relatively high strain rate deformation where static thermal recovery is negligible. The first and second terms represent, in a phenomenological sense, direct hardening and dynamic recovery, respectively. Typical specializations of equations (23) are

$$\underline{\underline{h}} = h_0 \quad (24)$$

$$\underline{\underline{d}} = d_0 \quad (25)$$



where  $h_0$  and  $d_0$  are scalar constants for the isothermal case and

$$\dot{\tilde{N}} = \dot{\tilde{\epsilon}}^n \quad (26)$$

$$\dot{\tilde{M}} = ||\dot{\tilde{\epsilon}}^n|| \dot{\tilde{a}} \quad (27)$$

### Determination of Backstress History

In the axial-torsional subspace, equations (21)-(23) can be written as

$$\begin{Bmatrix} \dot{\tilde{\epsilon}}_1^n \\ \dot{\tilde{\epsilon}}_3^n \end{Bmatrix} = \left[ \frac{(\dot{\tilde{\epsilon}}_1^n)^2 + (\dot{\tilde{\epsilon}}_3^n)^2}{(\sigma_1 - a_1)^2 + (\sigma_3 - a_3)^2} \right]^{1/2} \begin{Bmatrix} \sigma_1 - a_1 \\ \sigma_3 - a_3 \end{Bmatrix} \quad (28)$$

with

$$\begin{Bmatrix} \dot{\tilde{a}}_1 \\ \dot{\tilde{a}}_3 \end{Bmatrix} = \begin{bmatrix} h_{11} & h_{13} \\ h_{31} & h_{33} \end{bmatrix} \begin{Bmatrix} \dot{\tilde{\epsilon}}_1^n \\ \dot{\tilde{\epsilon}}_3^n \end{Bmatrix} - |\dot{\tilde{\epsilon}}^n| \begin{bmatrix} d_{11} & d_{13} \\ d_{31} & d_{33} \end{bmatrix} \begin{Bmatrix} a_1 \\ a_3 \end{Bmatrix} \quad (29)$$

where  $\dot{\tilde{N}}$  and  $\dot{\tilde{M}}$  are given in equations (26) and (27).

With the stress response obtained from a biaxial, strain-controlled test, the strain history can be differentiated as described earlier (but with respect to time instead of effective stress arc length) and equation (28) can be written for each of  $N$  discrete times,  $t_i$ , as

$$\tilde{a}_i = \sigma_i - |\sigma_i - \tilde{a}_i| \tilde{n}_i, \quad i = 1, 2, 3, \dots, N \quad (30)$$

where  $\tilde{n} = \dot{\tilde{\epsilon}}^n / |\dot{\tilde{\epsilon}}^n|$ . Equation (30) is nonlinear and does not possess a unique solution. Writing equation (30) as a fixed point iteration

$$\underline{\alpha}_i^{K+1} = \underline{\sigma}_i - |\underline{\sigma}_i - \underline{\alpha}_i^K| \underline{n}_i \quad (31)$$

where  $\underline{\alpha}^K$  is the  $K^{\text{th}}$  iterate of  $\underline{\alpha}$ , convergence is obtained if  $\underline{\alpha}^{K+1} \rightarrow \underline{\alpha}^\infty$ . However,  $\underline{\alpha}^\infty$  will depend, in general, on the initial guess  $\underline{\alpha}^*$ . Thus, a possible path for the backstress,  $\underline{\alpha}(t)$ , can be obtained such that  $\underline{\alpha}_i = \underline{\alpha}_i^*$  if a reasonable scheme for selecting  $\underline{\alpha}_i^*$  is chosen. Figure 4 shows the backstress paths calculated using the iteration in equation (31) for the two 90° out-of-phase histories, choosing  $\underline{\alpha}_i^* = b \underline{\sigma}_i$  where  $b$  was taken as 0.5, 0.6, 0.75 and 0.95 respectively. One can readily show that  $\underline{\alpha}_i$  will converge to  $\underline{\sigma}_i - (1-b)|\underline{\sigma}_i| \underline{n}_i$  after one iteration. As can be seen in Figure 4 each represents a reasonable potential backstress path for the 90° out-of-phase histories. Figure 5 shows the direction of  $\underline{\sigma} - \underline{\alpha}$  and  $\underline{n}$  at a discrete number of stress points for the larger strain amplitude test.

#### Determination of the Kinematic Hardening Rule

With a possible backstress path,  $\underline{\alpha}(t)$ , known as a discrete set of  $\underline{\alpha}_i$ , the backstress history can be differentiated in the manner described for the strain history to obtain  $\dot{\underline{\alpha}}_i$  at each  $t_i$ . With  $\dot{\underline{\alpha}}_i$  known for each discrete time  $t_i$ , we may form the corresponding residual  $R_i$ , i.e.

$$R_i = h \dot{\underline{\epsilon}}_i^n - d |\dot{\underline{\epsilon}}_i^n| \underline{\alpha}_i - \dot{\underline{\alpha}}_i \quad (32)$$

Then, the sum of the squared residuals can be minimized to obtain least squares estimates of  $h$  and  $d$ .

#### Case I

If  $h = h_0$  and  $d = d_0$  is chosen, then a least-squares fit based on equation (32) yields

$$\begin{bmatrix} F_{11} & F_{12} \\ F_{21} & F_{22} \end{bmatrix} \begin{bmatrix} h_0 \\ d_0 \end{bmatrix} = \begin{bmatrix} F_1 \\ F_2 \end{bmatrix} \quad (33)$$

where

$$F_{11} = \sum_{i=1}^N \left[ (\dot{\epsilon}_{1i}^n)^2 + (\dot{\epsilon}_{3i}^n)^2 \right], \quad (34)$$

$$F_{12} = F_{21} = \sum_{i=1}^N - \left[ (\dot{\epsilon}_{1i}^n a_{1i} + \dot{\epsilon}_{3i}^n a_{3i}) |\dot{\epsilon}_i^n| \right], \quad (35)$$

$$F_{22} = \sum_{i=1}^N \left[ (a_{1i}^2 + a_{3i}^2) |\dot{\epsilon}_i^n|^2 \right], \quad (36)$$

$$F_1 = \sum_{i=1}^N \left[ \dot{a}_{1i} \dot{\epsilon}_{1i}^n + \dot{a}_{3i} \dot{\epsilon}_{3i}^n \right], \quad (37)$$

$$\text{and } F_2 = \sum_{i=1}^N - \left[ (a_{1i} \dot{a}_{1i} + a_{3i} \dot{a}_{3i}) |\dot{\epsilon}_i^n| \right]. \quad (38)$$

## CASE II

Choosing  $h_{11} = h_1$ ,  $h_{33} = h_3$  with  $h_{13} = h_{31} = 0$  and  $d_{11} = d_1$ ,  $d_{33} = d_3$  with  $d_{13} = d_{31} = 0$  yields two systems of equations for a least squares fit,

$$\sum_{i=1}^N \begin{bmatrix} (\dot{\epsilon}_{\ell i}^n)^2 & -\dot{\epsilon}_{\ell i}^n a_{\ell i} |\dot{\epsilon}_i^n| \\ -\dot{\epsilon}_{\ell i}^n a_{\ell i} |\dot{\epsilon}_i^n| & (a_{\ell i} |\dot{\epsilon}_i^n|)^2 \end{bmatrix} \begin{bmatrix} h_{\ell} \\ d_{\ell} \end{bmatrix} = \sum_{i=1}^N \begin{bmatrix} a_{\ell i} \dot{\epsilon}_{\ell i}^n \\ -a_{\ell i} \dot{a}_{\ell i} |\dot{\epsilon}_i^n| \end{bmatrix}$$

where  $\ell = 1$  or  $\ell = 3$ .

Table 1 summarizes results obtained for the cases outlined above for the two 90° out-of-phase histories (with  $b = .5, .6, .75$  and  $.95$ ).

A clearer assessment of the accuracy of the kinematic hardening rules obtained for the two cases is shown in Figure 6. Here, the backstress history obtained using Euler integration is plotted, along with  $\underline{\sigma} - \underline{\alpha}$  and the direction of the plastic strain rate emanating from (or referenced to) the stress point. Shown are the results obtained for case I and case II for  $b = 0.6$  by integrating the kinematic hardening rule using the constants reported in Table 1. Note that the direction of the plastic strain rate is that determined by differentiating the strain history and the direction of  $\underline{\sigma} - \underline{\alpha}$  is that obtained by integrating the kinematic hardening rules determined from the least squares fits. Thus, the non-collinearity of the plastic strain rate direction with  $\underline{\sigma} - \underline{\alpha}$  in Figure 6 is an indication of the accuracy of the correlations for  $\underline{\dot{\epsilon}}$ .

From examination of the results reported in Table 1, two important observations are made. First, it is noted that the ratio  $h_1/h_3$  approaches unity for  $b$  in the range of  $0.5 < b < 0.6$  for both the large and small strain amplitude tests. Further,  $h_1 \approx h_3 \approx h_0$  for both tests at  $b = 0.6$ . Conversely, it is noted that the ratio  $d_1/d_3$  does not approach unity in either history and  $d_1 \neq d_3 \neq d_0$ . Furthermore, it is noted that use of a tensor operator (e.g. Case II) in the dynamic recovery term appears to result in a more realistic integrated backstress path, as observed in Figure 6. The ratio  $d_1/d_3$  is larger for the small strain amplitude test. These observations motivate some speculative assertions about the structure of the kinematic hardening rule and imply the particular utility of the 90° out-of-phase test.

From the observation that a scalar direct hardening function,  $h = h_0$ , is found for  $b = 0.6$  for both tests, it is asserted that  $\dot{\underline{N}} = \underline{\dot{\epsilon}}^{11}$  is a satisfactory index for the direct hardening term in the evolution of backstress. This

being the case, it is further asserted that it is desirable to find an index,  $\dot{\underline{M}}$ , such that  $\underline{d}$  is a scalar in the dynamic recovery term. The determination of a tensor valued  $\underline{d}$  for general stress space would be a difficult task and the mechanistic basis of such an approach would have to be justified. To this end it is proposed that

$$\dot{\underline{M}} = |\dot{\underline{\epsilon}}^n|(\underline{\alpha} - \underline{\alpha}^*). \quad (40)$$

Equation (40) implies that dynamic recovery occurs in a direction opposite the backstress referenced to some current state  $\underline{\alpha}^*$ , as opposed to the zero state ( $\dot{\underline{M}} = |\dot{\underline{\epsilon}}^n|\underline{\alpha}$ ). A possible approach, then, would be to investigate plausible choices for  $\underline{\alpha}^*$  in hope that one would yield a correlation such that  $\underline{d}$  is a scalar when  $\underline{h}$  is a scalar with  $\dot{\underline{N}} = \dot{\underline{\epsilon}}^n$ . For example, Walker [24] has proposed

$$\dot{\underline{M}} = \left[ \underline{\alpha} - \underline{\alpha}_0 - n_1 \underline{\epsilon}^n \right] |\dot{\underline{\epsilon}}^n| \quad (41)$$

where  $\underline{\alpha}_0$  is a backstress offset,  $\underline{\epsilon}^n$  is the inelastic strain, and  $n_1$  is a material constant.

In Walker's formulation in the full deviatoric stress space,

$$\underline{\alpha}_0 = -K_0 \underline{I} + 3K_0 \underline{\epsilon}^n \cdot \underline{\epsilon}^n / ||\underline{\epsilon}^n : \underline{\epsilon}^n||^2 \quad (42)$$

where  $K_0$  provides for a difference in tensile and compressive response as observed for Hastelloy-X. In equation (42),  $\underline{I}$  is the identity tensor. While  $\underline{\alpha}_0$  provides for asymmetric tensile-compressive response, the term  $n_1 \underline{\epsilon}^n$  in equation (41) serves as a reference direction for  $\underline{\alpha}$  as the directional index

for dynamic recovery since the principal axes of  $\underline{\epsilon}^n$  rotate during nonproportional loading. It should be noted that the response of type 304 stainless steel, reported in this paper, obviously requires an additional reference term, albeit a second order effect, for good correlation of all data; in this case, however, the  $\underline{\alpha}_0$  term is not required since the completely reversed response is symmetric. Since Walker [24] has determined his model constants for Hastelloy-X at 648°C, it is interesting to compare these constants with those of this study. According to Walker, the evolution equation for  $\underline{\alpha}$  may be written in the axial-torsional subspace as

$$\dot{\underline{\alpha}} = h_w \dot{\underline{\epsilon}}^n - d_w (\underline{\alpha} - \underline{\alpha}_0) |\dot{\underline{\epsilon}}|^n \quad (43)$$

at 648°C where  $\underline{\alpha}_0$  is reduced to the subspace from the six dimensional form given in equation (42). Since the magnitude of  $\underline{\alpha}_0$  is small compared to that of  $\underline{\alpha}$ , we may to first order compare  $h_w$  and  $d_w$  with  $h_0$  and  $d_0$  of Case I of this study:

$$h_w = 155,180 \text{ MPa}$$

$$d_w = 781$$

It is clear that both values are of the same order of magnitude as those reported in Table 1 for  $h_0$  and  $d_0$ . Including  $\underline{\alpha}_0$  in equation (42) for specimen #21 with  $b = 0.6$  results in a correlated  $K_0$  value of 7.5 MPa in contrast to the value of -13.8 MPa reported by Walker [24]. Certainly  $\underline{\alpha}_0$  is of secondary importance in comparison to  $\underline{\alpha}$  in the dynamic recovery term. It is quite

possible that the difference in the  $K_0$  values arises from experimental scatter in the  $90^\circ$  out-of-phase tests, which is of the same order of magnitude as  $K_0$ .

Following the assertions stated above, the data of Table 1 would also indicate that the scalars  $h_0$  and  $d_0$  are strong functions of the effective inelastic strain rate or, alternatively, the effective backstress or over-stress. It is noted that various workers have made the direct hardening function to depend on such scalar functions as  $(\bar{s} - \bar{\alpha}) : \bar{\alpha}$  [25] or the effective inelastic strain [11,26], and the dynamic recovery function to depend on such invariants as the effective inelastic strain path length [11,24,26], and the effective inelastic strain rate [2-3]. Those theories incorporating effective inelastic strain path length have hardening functions [11] and dynamic recovery functions [11,24,26] which saturate to a limiting value, independent of the backstress or inelastic strain rate magnitude.

The fortuitous nature of the  $90^\circ$  out-of-phase tests discussed herein is that the effective deviatoric stress and effective inelastic strain rate are approximately constant throughout a cycle as demonstrated in Figures 7 - 8. In contrast, these quantities vary significantly throughout a cycle for a proportional history. For the  $90^\circ$  out-of-phase test, this characteristic leads to backstress histories such that the effective backstress and over-stress are approximately constant throughout a cycle. Thus, a series of  $90^\circ$  out-of-phase tests with  $\Delta\gamma/\Delta\epsilon = 3/2$  would provide a means for assessing the functional dependence of the hardening functions,  $h_0$  and  $d_0$ , in addition to investigation of  $\bar{\alpha}^*$ . Future work will be directed towards identification of an appropriate constraint on  $\bar{\alpha}$  which produces a single acceptable path for each level of a  $90^\circ$  out-of-phase test series.

## Conclusions

From cyclic, strain-controlled, nonproportional tests on type 304 stainless steel and Hastelloy-X, the following statements may be made:

1. A dynamic recovery term is essential to properly model the backstress evolution.
2. From analysis of Hastelloy-X data obtained at 649°C, the inelastic strain rate appears to be a satisfactory directional index for direct hardening, but the backstress appears to be an inappropriate directional index of dynamic recovery.
3. Sinusoidal, 90° out-of-phase axial torsional tests can be very useful in aiding determination of backstress evolution functions, including both directional indices and scalar hardening functions, by virtue of the associated approximately constant magnitudes of overstress, inelastic strain rate, and effective stress in addition to the relatively fixed degree of noncollinearity between the direct hardening and dynamic recovery directional indices. Such tests have previously been associated with the study of nonproportional hardening effects but have more far ranging applications. For example, the magnitude of direct hardening and dynamic recovery coefficients can be estimated from a single 90° out-of-phase test. Furthermore, these estimates may be made without recourse to fitting a set of uniaxial tests and can be derived for a range of strain amplitudes typical of actual applications. Relevance of directional indices can also be assessed.



### Acknowledgments

Professor McDowell would like to acknowledge the support of the U.S. National Science Foundation (NSF MEA-840 4080). Professor Jordan conducted the experiments on Hastelloy-X with the support of a grant from NASA (NAG 3-160).

TABLE 1 -- RESULTS OF ANALYSES OF THE TWO 90° OUT-OF-PHASE HISTORIES  
HASTELLOY-X at 649°C; E = 156 GPa, G = 61 GPa

Specimen # 20  $|\dot{\epsilon}|_{av} = 6.20 \times 10^{-4} \text{ sec}^{-1}$

$$|\sigma|_{av} = 354 \text{ MPa}$$

	b = 0.5	b = 0.6	b = 0.75	b = 0.95
$h_1$	590250	695645	894621	1299100
$h_3$	596865	613755	674015	836185
$h_0$	512287	564304	674781	899441
$d_1$	1376	1724	2223	2897
$d_3$	128	415	820	1382
$d_0$	633	911	1304	1851
$h_1/d_1$	429	404	402	431
$h_3/d_3$	4663	1478	822	605
$h_0/d_0$	809	619	517	486
$h_1/h_3$	0.99	1.13	1.32	1.49
$d_1/d_3$	10.75	4.15	2.71	2.10
$ \sigma-a _{av}$	177	141	88	17.7
$ a _{av}$	248	263	293	340

Specimen # 21  $|\dot{\epsilon}|_{av} = 2.32 \times 10^{-3} \text{ sec}^{-1}$

$$|\sigma|_{av} = 522 \text{ MPa}$$

	b = 0.5	b = 0.6	b = 0.75	b = 0.95
$h_1$	235090	291513	404846	610520
$h_3$	251030	283847	348822	468800
$h_0$	229734	270395	351393	498893
$d_1$	472	604	807	1083
$d_3$	271	355	982	655
$d_0$	364	464	614	817
$h_1/d_1$	498	483	502	564
$h_3/d_3$	926	800	724	717
$h_0/d_0$	631	583	572	611
$h_1/h_3$	0.94	1.03	1.16	1.30
$d_1/d_3$	1.74	1.70	1.67	1.65
$ \sigma-a _{av}$	261	209	131	26
$ a _{av}$	336	366	420	501

## References

1. Perzyna, P., "The Constitutive Equations for Rate Sensitive Plastic Materials," Quarterly of Applied Mechanics, Volume 20, 1963.
2. Miller, A., "An Inelastic Constitutive Model for Monotonic, Cyclic and Creep Deformation, Part I: Equation Development and Analytical Procedure," J. Eng. Mat. and Technology, Trans. ASME, Volume 98, 1976.
3. Miller, A., "An Inelastic Constitutive Model for Monotonic Cyclic and Creep Deformation: Part II: Application to Type 304 Stainless Steel," J. of Eng. Mat. and Technology, Trans. ASME, Volume 98, 1976.
4. Robinson, D.N., "A Unified Creep-Plasticity Model for Structural Metals at High Temperature," ORNL/TM-5669, Oct. 1978.
5. Krieg, R.D., Swearengen, J.C. and Rohde, R.W., "A Physically-based Internal Variable Model for Rate-Dependent Plasticity," Inelastic Behavior of Pressure Vessels and Piping Components, Montreal, 25-29 June, 1978, edited by T.Y. Chang and E. Krempl.
6. Lagneborg, R., "A Modified Recovery-Creep Model and its Evaluation," Metal Science Journal, Volume 6, 1972.
7. Ponter, A.R.S., and Leckie, F.A., "Constitutive Relationships for the Time-Dependent Deformation of Metals," J. of Eng. Mat. and Technology, Trans. ASME, Volume 98, 1976.
8. Hart, E.W. "Constitutive Relations for Non-Elastic Deformations of Metals," J. of Eng. Mat. and Technology, Trans. ASME, Volume 98, 1976.
9. Chan, K.S., Bodner, S.R., Walker, K.P., and Lindholm, U.S., "A Survey of Unified Constitutive Theories," Proc. 2nd Symp. on Nonlinear Constitutive Relations for High Temperature Applications, NASA Lewis Research Center, June 13-15, 1984.
10. Allen, D.H. and Beek, J.M., "On the Use of Internal State Variables in Thermoviscoplastic Constitutive Equations," Proc. 2nd Symp. on Nonlinear Constitutive Relations for High Temperature Applications, NASA Lewis Research Center, June 13-15, 1984.
11. Chaboche, J.L., Bulletin de L'Academie des Sciences, serie des Science Techniques, Vol. XXV, No. 1, 1977, p.33.
12. Lee, D., and Zaverl, F., Jr., Acta Met., Vol. 26, No. 11, 1975, p. 385.
13. Ilyushin, A.A., Prikl. Mat. Mekh, Vol. 18, p.641.
14. McDowell, D.L., "On the Path Dependence of Transient Hardening and Softening to Stable States Under Complex Biaxial Cyclic Constitutive Laws for Engineering Materials, Ed. Desai and Gallagher, Tucson, AZ, Jan, 1983, pp. 125-132.

15. McDowell, D.L., and Socie, D.F., "Transient and Stable Deformation Behavior Under Cyclic Nonproportional Loading," ASTM STP 853, 1985, pp. 64-87.
16. McDowell, D.L., "An Experimental Study of the Structure of Constitutive Equations for Nonproportional Cyclic Plasticity," ASME Journal of Engineering Materials and Technology, Vol. 107, 1985, pp. 307-315.
17. McDowell, D.L., "A Two Surface Model for Transient Nonproportional Cyclic Plasticity: Part I - Development of Appropriate Equations," ASME Journal of Applied Mechanics, Volume 52, June 1985, pp. 298-302.
18. McDowell, D.L., "A Two Surface Model for Transient Nonproportional Cyclic Plasticity: Part II - Comparison of Theory with Experiments," ASME Journal of Applied Mechanics, Volume 52, June 1985, pp. 303-308.
19. Jordan, E.H., Elevated Temperature Biaxial Fatigue, NASA CR 175009, Oct. 1985.
20. Krempl, E., and Lu, H., "The Hardening and Rate-Dependent Behavior of Fully Annealed AISI Type 304 Stainless Steel Under Biaxial In-Phase and Out-of-Phase Strain Cycling at Room Temperature," ASME Journal of Engineering Materials and Technology, Vol. 106, 1984, pp. 376-382.
21. Kanazawa, K., Brown, M.W., and Miller, K.J., "Cyclic Deformation of 1% Cr-Mo-V Steel Under Out-of-Phase Loads," Fatigue of Engineering Materials and Structures, Vol. 2, 1979, pp. 217-228.
22. Lamba, H.S., and Sidebottom, O.M. "Cyclic Plasticity for Nonproportional Paths: Path 1 - Cyclic Hardening, Erasure of Memory, and Subsequent Strain hardening Experiments," ASME Journal of Engineering Materials and Technology, Vol. 100, 1978, pp. 96-103.
23. Lamba, H.S., and Sidebottom, O.M., "Cyclic Plasticity for Nonproportional Paths: Part 2 - Comparison with Predictions of Three Incremental Plasticity Models," ASME Journal of Engineering Materials and Technology, Vol. 100, 1978, pp. 104-111.
24. Walker, K.P., Research and Development Program for Nonlinear Structural Modeling with Advanced Time-Temperature Dependent Constitutive Relationships, NASA CR-165533, Nov. 1981.
25. Krieg, R.D., and Key, S.W., "On the Accurate Representation of Large Strain Non-Proportional Plastic Flow in Ductile Metals," Proc. ASME Winter Annual Mtg., Constitutive Equations: Macro and Computational Aspects, New Orleans, Dec. 1984, pp. 41-52.
26. Chaboche, J.L., Dang-Van, K., and Cordier, G., "Modelization of Strain Memory Effect on the Cyclic Hardening of 316 Stainless Steel," Trans. 5th SMIRT, L 11/3, Berlin, 1979.

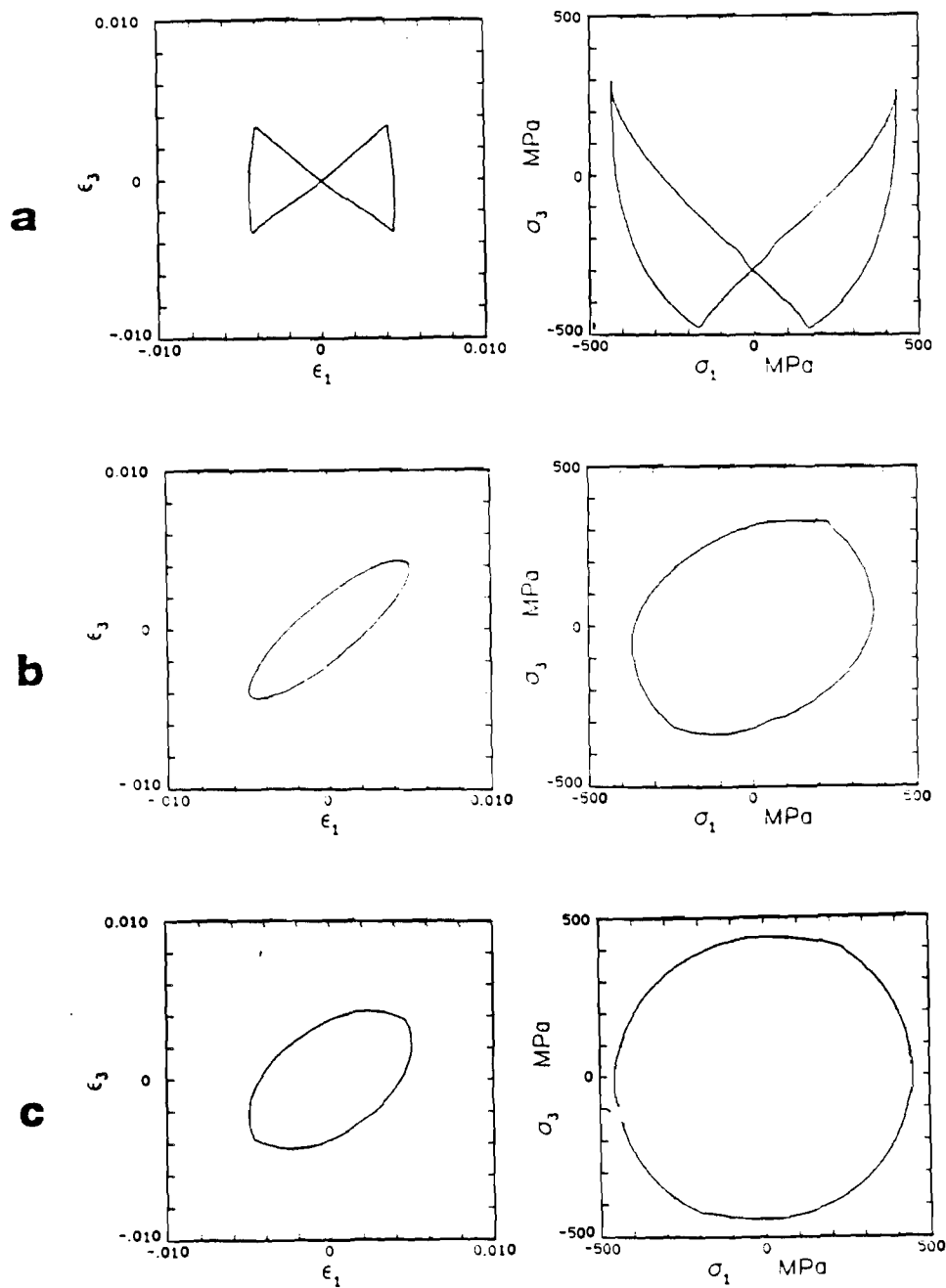


Fig. 1 Controlled axial-torsional strain paths (left column) and resulting stable stress subspace responses for type 304 stainless steel at room temperature: (a)  $\dot{\epsilon} = 0.003 \text{ sec}^{-1}$ , (b) 30° out-of-phase sinusoidal with  $\Delta\gamma/\Delta\epsilon = 1.5$ ,  $\dot{\epsilon} = 0.001 \text{ sec}^{-1}$ , and (c) 60° out-of-phase sinusoidal with  $\Delta\gamma/\Delta\epsilon = 1.5$ ,  $\dot{\epsilon} = 0.001 \text{ sec}^{-1}$ .

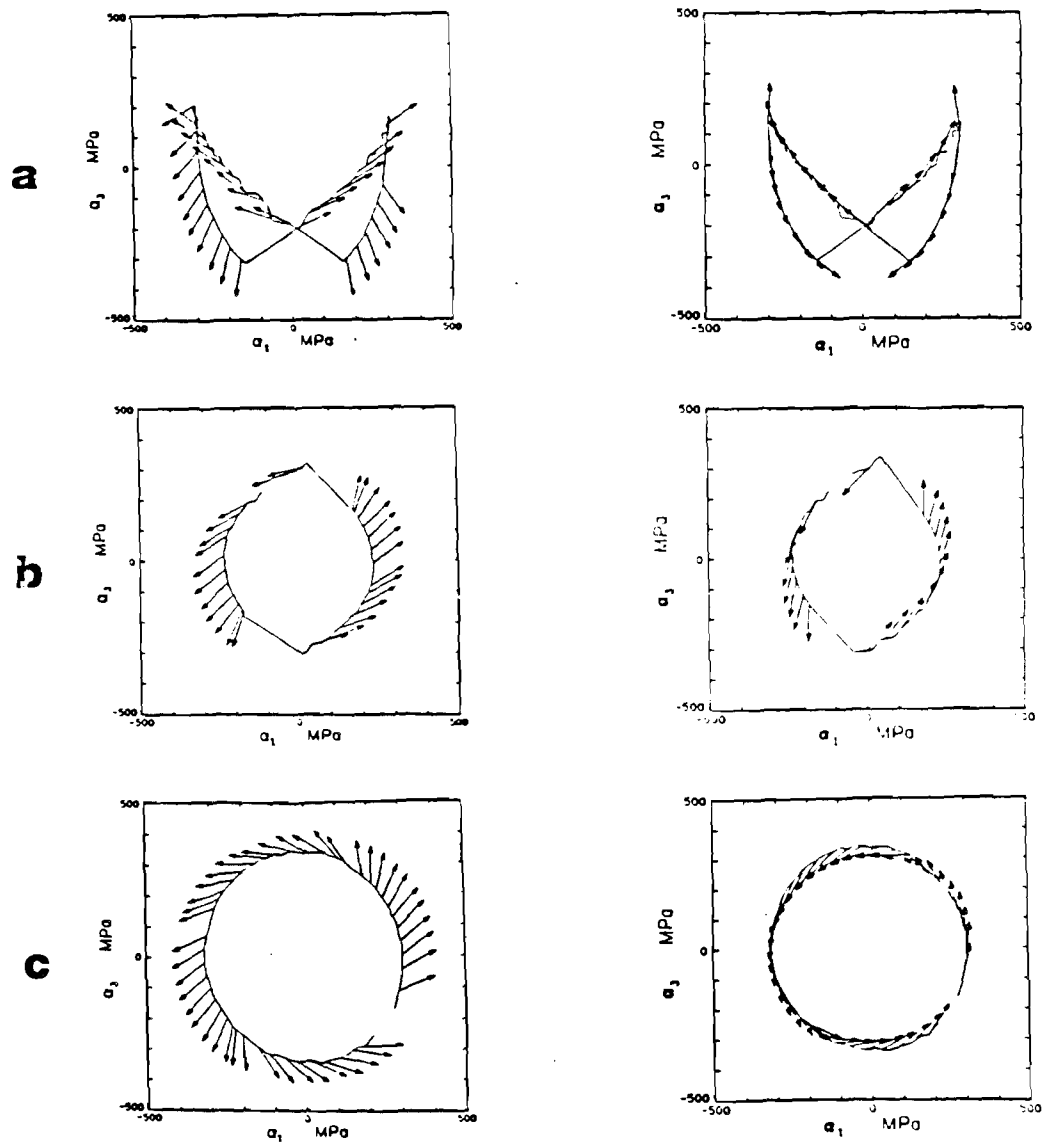


Fig. 2 Backstress rate directions predicted by Equation (19) (left column) and Equation (20) (right column) for the three histories of Fig. 1.  $R = 160$  MPa in all cases. Note the accuracy increase due to the dynamic recovery term in the right column.

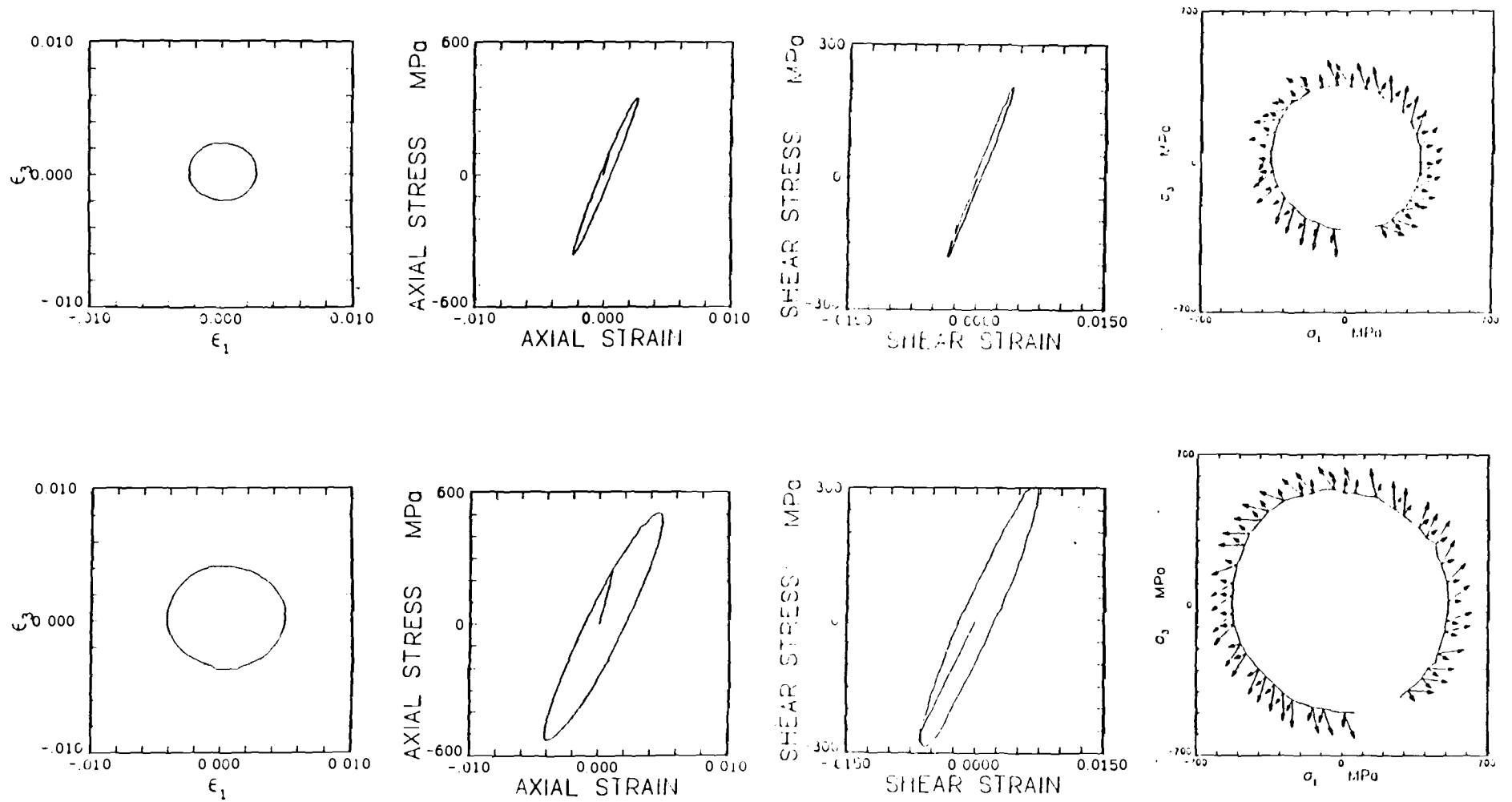


Fig. 3 Controlled axial-torsional strain paths and corresponding responses for Hastelloy-X. Two 90° out-of-phase sinusoidal histories with  $\Delta\gamma/\Delta\epsilon = 1.5$  and a frequency of 0.25 Hz. Note that the strain amplitudes are smaller for Specimen #20 (top row) than for Specimen #21 (bottom row).

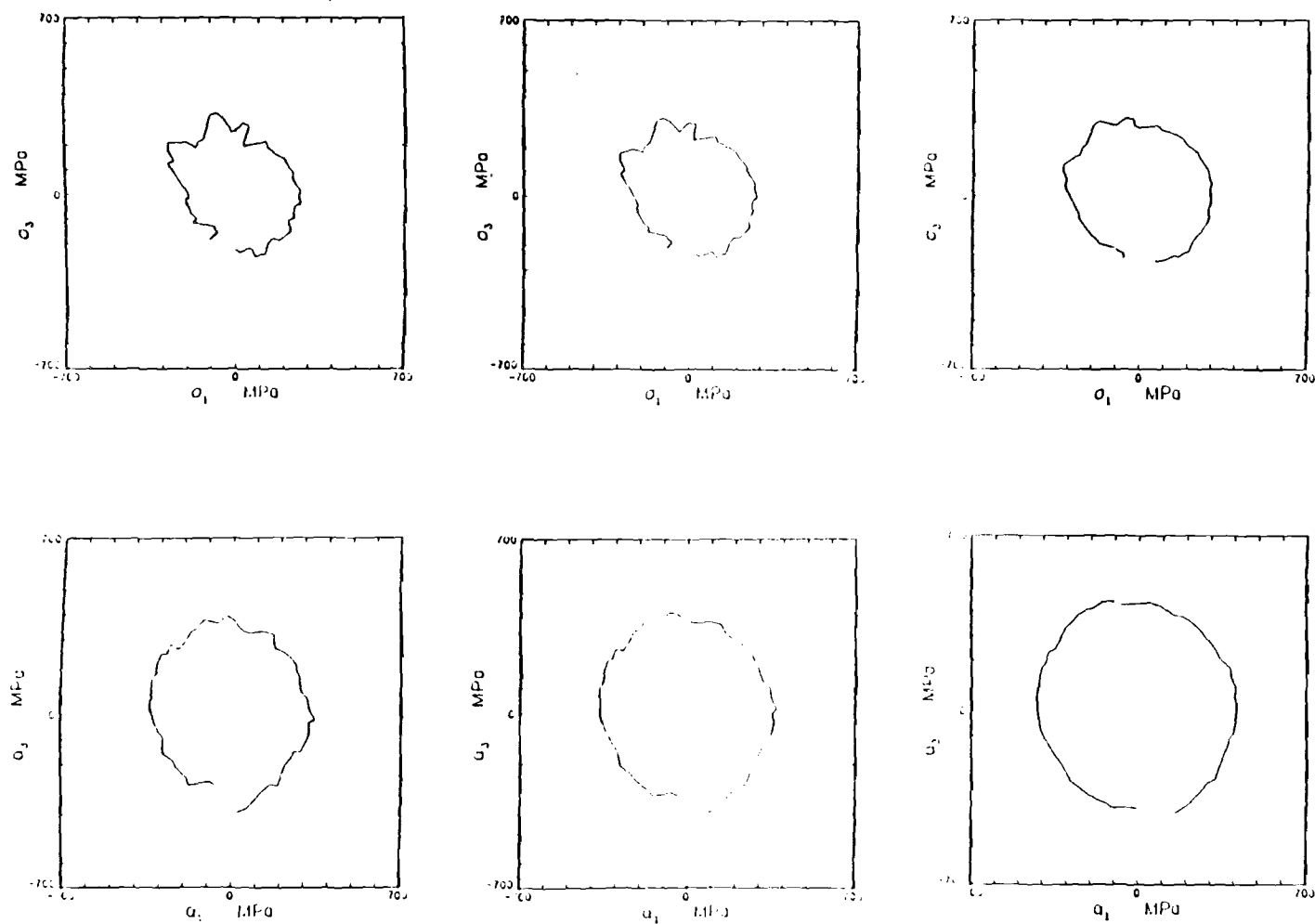
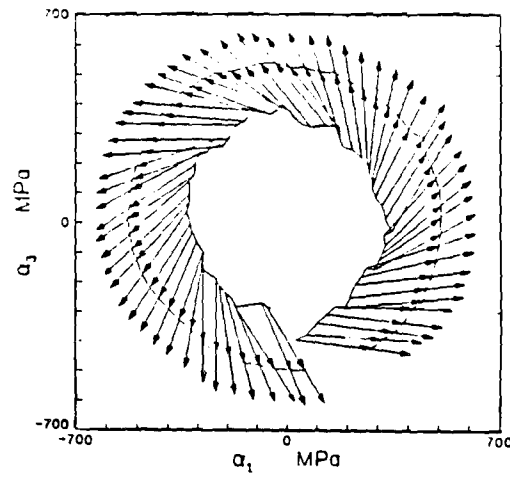
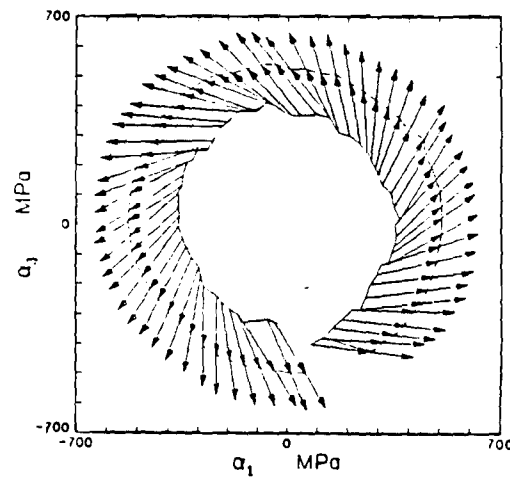


Fig. 4 Backstresses for 90° out-of-phase specimens computed from fixed-point iteration for (top row) Specimen #20 and (bottom row) Specimen #21. Initial values of backstress correspond to (left column)  $b=0.5$ , (center column)  $b=0.6$ , and (right column)  $b=0.75$ .

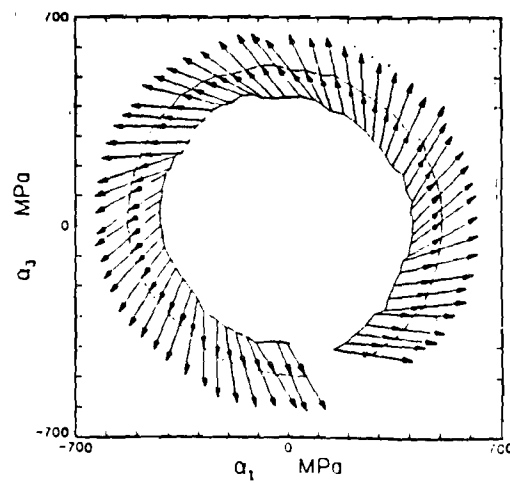




$b=0.5$



$b=0.6$



$b=0.75$

Fig. 5 Direction  $\eta$  of plastic strain rate (short vectors) and computed overstress vectors  $(\sigma - \alpha)$  for discrete points along path of Specimen #21. Note the collinearity of  $(\sigma - \alpha)$  and  $\eta$  which arises from the iteration procedure.

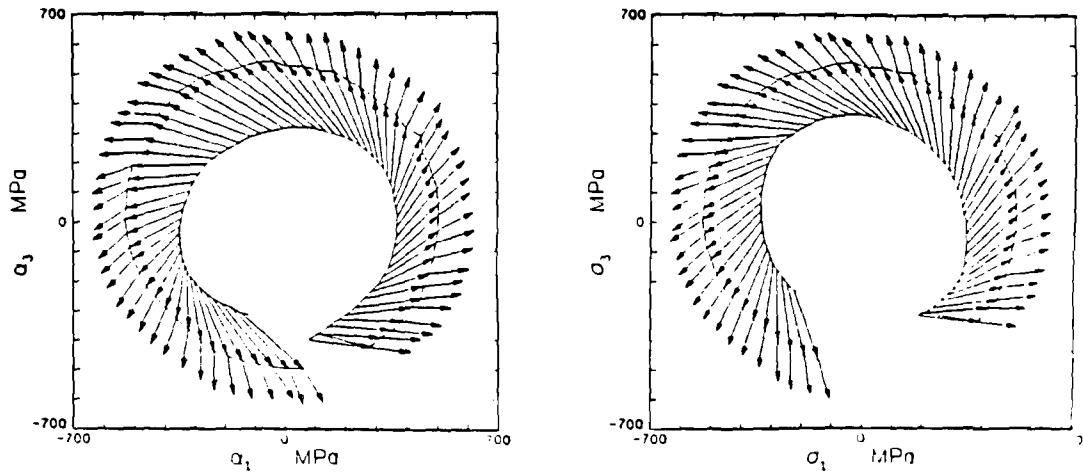


Fig. 6 Direction  $\underline{n}$  (short vectors) and associated overstress vectors  $(\underline{\sigma} - \underline{\alpha})$  for Specimen #21 with  $\underline{\alpha}$  obtained by Euler integration of (left) scalar direct hardening and dynamic recovery coefficients and (right) tensor valued coefficients. In each case, the initial value of  $\underline{\alpha}$  corresponded to  $b = 0.6$ . Note that the non-collinearity of  $\underline{n}$  and  $(\underline{\sigma} - \underline{\alpha})$  in each case arises from error in the backstress evolution rule and/or experimental scatter.

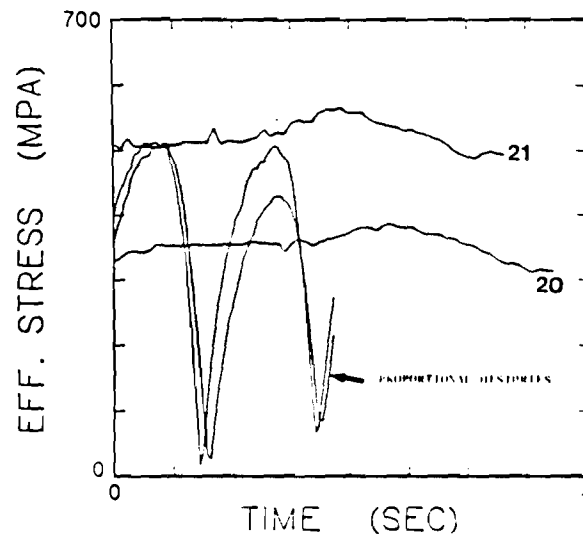


Fig. 7 Effective stress  $\bar{\sigma}$  versus time for Specimens #20-21. Two room temperature proportional loading histories are included for comparison of variation within a cycle.

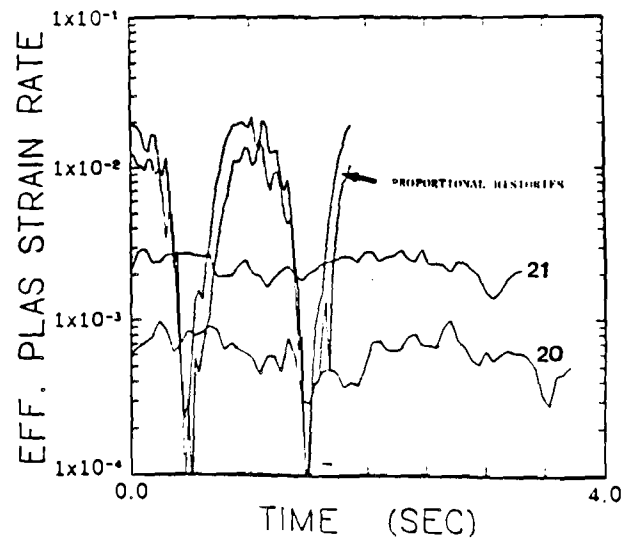


Fig. 8 Effective plastic strain rate  $|\dot{\epsilon}^p|$  versus time for Specimens #20-21. Two room temperature proportional loading histories are included for comparison of variation within a cycle.

A MORE REALISTIC MODEL OF  
NONLINEAR MATERIAL RESPONSE:  
APPLICATION TO ELASTIC-PLASTIC  
ROLLING CONTACT

D. L. McDowell  
Assistant Professor  
George W. Woodruff School of Mechanical Engineering  
Georgia Institute of Technology  
Atlanta, Georgia 30332

G. J. Moyer  
Moyer Technical Services, Inc.  
2711 B Curtiss St.  
Downers Grove, Illinois 60515

Submitted for Presentation at the Second International Symposium  
on Contact Mechanics and Wear of Rail/Wheel Systems, July 8-11,  
1986, University of Rhode Island, Kingston, Rhode Island 02881.

## ABSTRACT

Considerable analysis and experimental verifications have been conducted to determine the loading and material conditions (e.g. wheel load, friction, contact configuration, metallurgy, wear, etc.) which lead to progressive deformation in rail. Yet the onset of corrugations in rail has not been suitably explained [1]. One very important contributing element to the explanation of corrugation is likely to be the development of a constitutive model which more realistically reflects material flow behavior under nonproportional loading conditions.

This study concentrates on the prediction of cyclic plastic flow in rolling contact. Previous numerical solutions for subsurface deformation in rail have concentrated primarily on solution algorithms which incorporate realistic boundary conditions and satisfaction of equilibrium at each passage of the wheel. The material model, in contrast, has typically included a very simple, isotropic yield condition without work hardening and an associated flow rule. Much insight has been gained recently via multiaxial experiments into cyclic plasticity models appropriate for nonproportional loading typical of rolling contact. This research has revealed that even combined isotropic hardening and kinematic hardening models of the Prager or Ziegler type do not accurately predict cyclic plastic strains in combined tension and torsion applied nonproportionally. Therefore, inclusion of work hardening and deformation-induced anisotropy in a modified classical plasticity model is not enough to ensure accurate prediction of stress and strain at each point within a highly nonproportional rolling contact stress field. It follows that an elastic-perfectly plastic material model is potentially quite inaccurate for this case.

In this paper, a two surface cyclic plasticity theory is discussed. The theory includes a Mroz-type kinematic hardening rule, an accurate representation of work hardening, and transient cyclic hardening or softening. The Mroz rule and two surface theory have previously been shown by McDowell and others to be accurate for nonproportional loading.

As a demonstration of the potential for use of such a material model for elastic-plastic rolling contact, the model is implemented in a very simple, approximate numerical scheme for two dimensional plane strain line contact of a rigid cylinder with a semi-infinite half-space. A Hertzian contact stress

distribution, including tangential traction proportional to the normal pressure, is translated repeatedly across the half-space to represent the rolling contact of wheel on rail. Several peak Hertzian pressures were included in the study.

### CUMULATIVE PLASTIC DEFORMATION UNDER NONPROPORTIONAL LOADING

A distinction is made in this work between proportional and nonproportional loading. proportional loading is defined as loading for which the deviatoric stresses and stress rates are radial. Nonradial variation of deviatoric stresses will be termed nonproportional loading. In analogy, for strain-controlled loading, proportionality of the controlled total strain components results in proportional straining. Hence,

$$\dot{s}_{ij} = \dot{\lambda}_s s_{ij}^* \quad (1)$$

$$\dot{\epsilon}_{ij} = \dot{\lambda}_\epsilon \epsilon_{ij}^* \quad (2)$$

where  $s_{ij} = \sigma_{ij} - (1/3)\delta_{ij}\sigma_{kk}$  are the deviatoric stress components,  $\epsilon_{ij}$  are the total strain components,  $\dot{\lambda}_s$  and  $\dot{\lambda}_\epsilon$  are scalars, and  $s_{ij}^*$  and  $\epsilon_{ij}^*$  are constant second order tensors.

In uniaxial tests in which the applied stress range has a nonzero mean, cyclic ratcheting is observed in the direction of the mean stress [2-3]. The ratcheting may at first accelerate (cyclic softening conditions) or decelerate (cyclic hardening conditions). A cyclically stable state may be reached in which ratchet strain accumulates equally per cycle or ceases due to hardening.

There are numerous investigations of uniaxial cyclic strain ratcheting reported in the literature; unfortunately, this information is not entirely relevant to the more complex case of nonproportional multiaxial loading. The literature which does exist for multiaxial loading is primarily for tension-torsion of thin-walled tubular and torsion-bending specimens. Though these experiments are more restrictive than the general rolling contact problem in terms of coverage of stress space regimes, they do have some important similarities. First, in a very general sense, the rolling contact stress field is essentially one of compressive normal stress with alternating shear

stress variation. Tension-torsion tests of thin-walled tubular specimens with a fixed tensile or compressive axial stress and reversed shear stress at least qualitatively capture the essence of rolling contact stress field variation.

As pointed out by Moyar and Morrow [4], even though the contact stress is reduced due to plastic deformation, ratcheting occurs due to the nonproportional variation of stresses, cyclic softening, etc. Description of such phenomena requires an understanding of inherent cyclic-dependent material behavior in the absence of macroscopic stress or strain gradients. Experimental results [4-8] on thin-walled tubular specimens have shown that significant axial strain accumulation can be produced by alternating torsion in the presence of a constant axial stress (nonproportional loading). This accumulation can even occur at cyclic effective stress amplitudes which would produce no continued ratchet strain if applied proportionally.

Early tension-torsion experiments on aluminum and copper solid or thin-walled tubular specimens were performed by Moyar and Sinclair [4-5], Feltner and Sinclair [6], and Coffin [7]. Benham [8] demonstrated cumulative axial elongation under steady tension, reversed torsion for tubular axial-torsional mild steel specimens in initially normalized and cold-worked conditions. In general, higher rates of axial creep were observed for higher alternating shear conditions. Benham also reported significant cyclic accumulation of axial strain in reversed bending tests with superposed steady axial tension. Final failure occurred by either gross plastic deformation or fatigue.

Ronay and Freudenthal [9-10] investigated "second-order" effects of axial strain accumulation under pure torsional cycling for initially isotropic, strain hardening metals. Bell [11] later showed that these effects could be accounted for using finite strain considerations. Hence, the second-order effects reported by Ronay and others in torsional testing are not viewed as important to prediction of cumulative deformation under complex loading since they are not essentially due to inherent material behavior and can be accounted for by using an appropriate finite strain analysis.

More recently, Harvey et al. [12-13] and Shiratori et al. [14] have investigated axial (torsional) cyclic strain accumulation under reversed



torsional (axial) loading with superposed steady axial (shear) loads. The emphasis of their work is accurate modeling of deformation-induced anisotropy via deformation of the yield surface; ratcheting behavior is then accurately correlated for mild steel and 60/40 brass. Again, results were consistent with previous experiments. Both groups have shown that detailed modeling of the axial-torsional ratcheting behavior under nonproportional loading requires consideration of deformation-induced anisotropy, which is entirely neglected by classical isotropic hardening theories and not suitably described by popular Prager/Ziegler type kinematic hardening rules for the yield surface. It should be noted that the work of Shiratori et al. on 60/40 brass also includes cyclic creep of a thin-walled tube under conditions of cyclic axial load superposed on steady internal pressure.

## Review of Nonproportional Cyclic Plasticity Experiments

There has been a progression of experimental interest in plastic flow under nonproportional loading. Most of the experimental work from 1950 to 1975 dealt with characterization of initial anisotropy (e.g. [15-18]), changes in plastic strain rate direction due to abrupt changes in loading direction (e.g. [19-24]), effects of pre-strain on the yield locus and direction of the plastic strain rate (e.g. [16-18, 25]), and history dependence of the yield surface upon nonproportional load reversals (e.g. [26-29]). Virtually all of these experiments dealt in a very detailed manner with the initial loading response and just a few, if any, additional reversals of load. Hence, they established knowledge of the appropriate representation of initial anisotropy and limited deformation-induced anisotropy, and the superiority of the flow theory of plasticity for general nonproportional loading.

It was not until the 1970's that experimental studies were conducted in earnest for nonproportional cyclic loading with the intent to characterize cyclic hysteresis response. The work of Lamba and Sidebottom [30-31] is the first known to the authors regarding transient and stable cyclic behavior under nonproportional loading conditions. They subjected annealed, thin-walled tubular OFHC copper specimens to several nonproportional, strain-controlled loading paths until cyclic stability was reached. Axial and torsional hysteresis loops were stored on magnetic tape. Lamba found that the material's memory of past plastic deformation history can be erased by a single large excursion into the plastic range. Conversely, influence of prior overloads dominates subsequent lower amplitude cycling. Another important observation was that additional isotropic cyclic hardening occurred upon switching to nonproportional cycling from cyclically stable axial cycling; for 90 degrees out-of-phase sinusoidal loading ( $\beta = 90$  degrees,  $\gamma_a/\epsilon_a \approx 1.5$ )

$$\epsilon = \epsilon_a \sin \omega t \quad (3)$$

$$\gamma = \gamma_a \sin (\omega t - \beta) \quad (4)$$

Lamba observed a 40% increase in stress amplitudes after switching back to axial cycling. This significant effect had not been previously observed nor included in kinematic-isotropic plasticity theory.

Later experiments by Kanazawa et al. [32], Krempl et al. [33], and Ohashi et al. [34] confirm observations made by Lamba for stainless steels and for 1% Cr-Mo-V steel. McDowell [35-37] and Kanazawa et al. [32] have shown that the additional isotropic hardening can be correlated if an additional variable is introduced to account for changes in strain rate direction. All of these experiments demonstrated that the uniaxial cyclic stress-strain curve was not entirely capable of representing the actual state of hardening encountered for highly nonproportional histories. The experiments of Lamba, Ohashi, Krempl, and McDowell demonstrate that cyclic plastic flow is quite repeatable under nonproportional loading. In recent papers, McDowell has demonstrated that good description of nonproportional cyclic plasticity may be achieved, even during transient cyclic hardening or softening, if appropriate generalized hardening and flow rules are used; furthermore, the uniaxial cyclic stress-strain curve may still be quite useful for characterizing plastic flow if supplemented by properties obtained from biaxial, nonproportional loading tests.

McDowell [38-39] also has shown that the plastic strain rate direction for nonproportional cycling does not correspond to that predicted by classical theories or by combined kinematic-isotropic hardening theories using Prager or Ziegler kinematic hardening rules. The inaccuracy of these commonly used rules is quite dramatic for complex loading. Typically, the extent of cyclic hardening in uniaxial, torsional, or combined proportional loading tests can be related to the accumulation of plastic strain. The experiments of McDowell have shown that this is not the case for nonproportional variation of stresses and strains within a cycle.

These experiments, though relatively few in number, have substantially increased our knowledge of elastic-plastic material behavior relevant to the nonproportional stress-strain state in rolling contact. To date, the authors are not aware of similar experimental work performed on rail steels.

### Appropriate Cyclic Plasticity Theory

The cyclic plastic flow which occurs in rolling contact and other nonproportional loading problems is indeed a very complex, history-dependent phenomenon. Models which seek to predict or correlate only one aspect of the response (e.g. completely reversed cyclic hysteresis response) may not be adequate for other important aspects (e.g. cyclic strain accumulation). Likewise, models which may accurately describe both reversed cyclic response and cyclic ratcheting for only uniaxial tests may be quite inadequate for correlating nonproportional response. Accordingly, any model to realistically be considered for cyclic plastic flow in rolling contact must demonstrate the capability to model nonproportional loading suitably. In this work, we restrict our consideration to time- and rate-independent material response characteristic of rail steels.

The phenomenon of strain ratcheting may involve very small cyclic plastic strain accumulation during each nonproportional loading cycle. Experiments [26-29] clearly show that the actual yield locus or surface in stress space distorts significantly even under proportional stressing; hence, any change in loading direction may actually result in yielding prior to that predicted by simple isotropic, kinematic or combined plasticity models which employ classical von Mises or Tresca yield surfaces, e.g.

$$\text{(von Mises)} \quad f = (3/2) (s_{ij} - \alpha_{ij})(s_{ij} - \alpha_{ij}) - R^2 = 0 \quad (5)$$

$$\text{(Tresca)} \quad f = \max_{i,j} |(\sigma_i - \alpha_i) - (\sigma_j - \alpha_j)| - R = 0 \quad (6)$$

where  $s_{ij}$  and  $\alpha_{ij}$  are deviatoric stress and backstress, shown in Figure 1, and  $\sigma_i$  and  $\alpha_i$  are principal values of stress and backstress. Note that  $\alpha_{ij}$  is the center of yield surface which represents kinematic hardening.  $R$  is the yield strength in uniaxial loading. Kinematic hardening is represented by changes in  $\alpha_{ij}$ . Isotropic hardening (cyclic hardening or softening) is represented by evolution of  $R$ , e.g.

$$\dot{R} = g(\bar{\epsilon}^P) \dot{\bar{\epsilon}}^P \quad (7)$$

$$\dot{\epsilon}^P = \left[ \frac{2}{3} \dot{\epsilon}_{ij}^P \dot{\epsilon}_{ij}^P \right]^{1/2} \quad (8)$$

and  $g$  is some unspecified function.

The concept of the yield surface requires that there is no increment of plastic strain if the stress point lies within the yield surface, i.e.

$$d\epsilon_{ij}^P = 0 \text{ if } f < 0 \quad (9)$$

If the stress point reaches the yield surface, then plastic flow can occur by a normality flow rule [40] if the stress rate has no inward component to the yield surface, i.e.

$$d\epsilon_{ij}^P = \begin{cases} \frac{1}{h} (d\sigma_{kl} n_{kl}) n_{ij} & \text{if } f=0 \text{ and } d\sigma_{kl} n_{kl} \geq 0 \\ 0 & \text{otherwise.} \end{cases} \quad (10)$$

where  $n_{ij}$  is the unit normal vector to the yield surface,  $\sigma_{kl}$  are true stress components, and  $h$  is the plastic hardening modulus, analogous to the slope of the stress versus plastic strain curve in a uniaxial test. During plastic flow, the yield surface must deform, translate, and expand or contract such that the stress point  $\sigma_{ij}$  remains on the yield surface (consistency condition  $f = df = 0$  if  $d\epsilon_{ij}^P d\epsilon_{ij}^P > 0$ ). It can readily be seen in Figure 2 that reyielding will occur at different points ( $C'$ ,  $C''$ ,  $C'''$ ) with different exterior unit normal vector orientations ( $\underline{n}'$ ,  $\underline{n}''$ ,  $\underline{n}'''$ ). Both combined kinematic-isotropic and pure isotropic hardening models overpredict the domain of elastic behavior and give somewhat inaccurate specification of the direction of the plastic strain rate. These considerations are particularly important for cyclic plasticity (and strain ratcheting behavior) under nonproportional loading when the reversed plasticity (or cyclic strain accumulation rate) is small. Such loading is fairly typical of rolling contact under moderate to heavy hauling conditions where there are relatively few setup cycles with significant reversed plasticity followed by near "shakedown" to progressive plastic deformation of quite small cycle-by-cycle magnitude. Of course, if the radius of the intermediate von Mises yield

surface is defined by a smaller offset yield point, it will more accurately represent initial reyielding and flow direction. The intermediate yield surface shown in Figure 2 would be typical of a 0.1% or 0.2% offset definition of yield.

It should be noted that if only proportional loading is of concern, then consideration of yield surface deformation is not necessary. If reyielding occurs at point D or D' in Figure 2, the direction of  $n_{ij}$  at either point is identical and accurate description of plastic flow may be achieved by either kinematic-isotropic or fully anisotropic formulations of  $f$  with a suitable function for  $h$  in equation (10). For proportional loading, the definition of yield is not even crucial since the modulus function  $h$  is very high at either of points D or D'. However, at points C', C'', or C''', definition of  $h$  is crucial since the values of  $h$  will be significantly lower in this region (higher plastic strain rate) and highly directionally dependent. This is certainly an important consideration in modeling ratcheting behavior in rolling contact; these deformation-induced anisotropic effects can result in cumulative plastic strains even when shakedown to cyclic elastic or completely reversed plastic strains is predicted using conventional isotropic or linear kinematic hardening rules.

Shiratori et al. [14] and Harvey et al. [12-13] have recognized the necessity of including anisotropic yield surface deformation to accurately model complex cyclic ratcheting tests. Shiratori and co-workers use the concept of a set of "equiplastic strain" surfaces to correlate ratcheting response for cyclic axial load (or torsion) superposed upon steady torsion (or tension), and for cyclic axial load superposed upon steady internal pressure for mild steel. In addition to predicting axial ratchet response, they were able to predict axial shortening effects at the initiation of each reversal due to deformation-induced anisotropy.

It should be noted that these approaches are the only ones in the literature known to the authors which specifically address anisotropic deformation of yield surfaces during cyclically nonproportional plastic flow, and seek to describe the problem of cumulative deformation under these conditions. Though the goal of both efforts at modeling nonproportional

racheting response has been achieved to some extent, neither is of a form general enough for arbitrary nonproportional cyclic loading since they require a definition of a preloading event which sets up some initial configuration of loading surface(s) for subsequent cycling.

From this work on anisotropic yield surfaces, it is seen that a series of loading surfaces, each corresponding to a different offset yield definition, can be defined at each point in a nonproportional loading history with respect to the point of initial preloading. Subsequent unloading and reversed loading from this point results in deformation of this configuration of loading surfaces. However the loading surfaces most affected by subsequent plastic straining are those defined by small yield offsets. In other words, the inner yield surface may deform and translate dramatically, while the outer surfaces deform and translate very little. Hence, the intermediate surfaces provide "memory" of maximal preloading events which strongly affect subsequent cyclic plastic flow for events of lesser magnitude.

This multiple surface concept for material memory was suggested by Mroz [40-41] and Iwan [42] for use in plasticity calculations. It is variously known as a layered, nested, or multiple surface approach. The model has more recently been associated primarily with Mroz, who has introduced appropriate rules for nonproportional cyclic loading. Deformation-induced anisotropy is accounted for, to first order, by allowing otherwise simple von Mises or Tresca loading surfaces to simultaneously translate (kinematic hardening) and expand or contract (isotropic hardening). During plastic flow, the stress point always remains on the innermost surface, the yield surface. The surfaces may be written as

$$f^{(k)} = f^{(k)}(\sigma_{ij} - a_{ij}^{(k)}, R^{(k)}) = 0 \quad (11)$$

$$k = 0, 1, 2, \dots, N$$

where  $f^{(0)}$  is the yield surface and  $(N + 1)$  is the total number of surfaces. Again by normality,

$$d\epsilon_{ij}^P = d\lambda \frac{\partial f^{(0)}}{\partial \sigma_{ij}} = \frac{1}{h} (d\sigma_{kl} n_{kl}) n_{ij} \quad (12)$$

where  $n_{ij} = \partial f^{(0)} / \partial \sigma_{ij} / ((\partial f^{(0)} / \partial \sigma_{mn}) (\partial f^{(0)} / \partial \sigma_{mn}))^{1/2}$ . The configuration of loading surfaces is shown in Figure 3. The kinematic hardening rule proposed by Mroz which applies to all  $(N + 1)$  surfaces is

$$d\alpha_{ij}^{(k)} = d\mu (\sigma_{ij}^{(k+1)} - \sigma_{ij}^{(k)}) \quad (13)$$

for all  $k = 0, 1, \dots, m$  surfaces which have been "touched" by the stress point and are currently in tangential contact, and

$$d\alpha_{ij}^{(k)} = 0 \quad (14)$$

for  $k = m + 1, \dots, N$  surfaces not yet reached by the stress point. The point  $\sigma_{ij}^{(k+1)}$  is defined as the similar point or point on the  $(k + 1)^{th}$  surface with the same exterior normal as that of the  $k^{th}$  surface at the current stress point. This results in tangential contact of the yield and loading surfaces at similar points. Also, isotropic hardening is expressed by

$$dR^{(k)} = c^{(k)}(\lambda) d\lambda \quad (15)$$

where  $d\lambda = (d\epsilon_{ij}^P d\epsilon_{ij}^P)^{1/2}$  and the  $c^{(k)}(\lambda)$  are hardening functions. The modulus function  $h$  in equation (12) is taken as a constant between each set of two surfaces (piecewise linear stress strain curve representation shown in Figure 3), i.e.

$$h = h^{(m)} \quad (16)$$

The function  $h$  is typically determined from the slope of a uniaxial cyclic stress-strain curve.

The multiple surface theory of Mroz has proven to be much more accurate in correlation of multiaxial nonproportional cyclic stress-strain response than conventional kinematic-isotropic theories (e.g. Prager or Ziegler



kinematic hardening), as shown by Lamba, McDowell, and others [30-31, 38-39, 43-44]. It uses relatively simple forms for the yield and loading surfaces, yet offers a good quantitative description of hysteresis response, as shown in Figure 4 for OFHC copper.

The Mroz approach offers a simplified but reasonably accurate representation of cyclic deformation-induced anisotropy. McDowell [38-39] showed that the plastic strain rate direction and modulus function are more accurately described by a Mroz-type model than by Ziegler kinematic hardening combined with a modulus function dependent on effective stress level, for example. Furthermore, it was shown that use of a uniaxial cyclic strain-curve to define "universal" material response can be quite fallacious. Additional isotropic hardening of the order of 20% to 100% is typically observed for steels and other metals, resulting in lack of validity of equation (16). Likewise, the use of accumulated plastic strain in equation (15) is not appropriate as the only independent variable since  $dR^{(k)}$  is affected also by the direction of that accumulation (c.f. [38, 45]), i.e.

$$c^{(k)} = c^{(k)}(\lambda, \phi) \quad (17)$$

where  $\phi$  reflects changes in direction of plastic straining within a cycle.

Based on these observations and the high frequency of occurrence of nonproportional loading in practical applications, it is advisable to use Mroz-type multiple surface constitutive models. Recently, several simple theories have been offered as solutions to the multiaxial cyclic plasticity problem [3, 46], but there is no evidence of consideration of experimental evidence for nonproportional loading in these models. Hence, even "first-order" characteristics such as plastic strain rate direction and modulus variation are not accurately portrayed.

Hence, experience has shown that a multiple surface approach using simple loading surface forms or an anisotropic yield surface formulation is needed to represent nonproportional deformation-induced anisotropy. The problem becomes even more crucial when cumulative plastic deformation (a "second-order effect") is to be predicted, as in the rolling contact problem. Then, it may

be necessary to combine the two approaches using a Mroz-type kinematic hardening rule with anisotropically deforming yield surfaces, as proposed by Rees [47]. The multiple surface model of Jhansale et al. [48] has attempted to include different yield strengths in tension and compression (non-Masing behavior), but was derived with uniaxial response in mind and is somewhat ad hoc with respect to general nonproportional loading. Use of a simple invariant yield surface form such as von Mises could result in a relatively inaccurate prediction of plastic strain rate direction, and hence ratchet strain accumulation, even though the cyclic stress-strain response is sufficiently modeled.

### Reduction to Two Surface Model

As discussed in the previous section, a multiple surface theory can provide a reasonably accurate estimate of plastic strain rate direction and, through  $h$ , magnitude for nonproportional loading. A much more efficient scheme is to reduce the theory to two surfaces. The inner surface is the yield surface. The outer surface, often called the limit or bounding surface, serves to bound the response. All intermediate loading surfaces are replaced by analytical forms of modulus function  $h$  and plastic strain rate direction which depend on assumed couplings between the yield and limit surfaces and additional parameters. Kreig [49] and Dafalias and Popov [50] independently suggested two surface theory. Lamba [30-31] demonstrated its potential for correlation of nonproportional cyclic hysteresis response. Tseng and Lee [51] have also demonstrated correlation for the same data and for uniaxial cyclic creep and mean stress relaxation.

In a somewhat general form, two surface theory can be expressed as (see Figure 5):

$$\text{yield surface: } f(\sigma_{ij} - \alpha_{ij}, R) = 0 \quad (18)$$

$$\text{limit surface: } f^*(\sigma_{ij}^* - \alpha_{ij}^*, R^*) = 0 \quad (19)$$

$$\text{flow rule: } d\epsilon_{ij}^P = \begin{cases} \frac{1}{h} (d\sigma_{kl} n_{kl}) n_{ij} & \text{if } f=0 \text{ and } d\sigma_{kl} n_{kl} \geq 0 \\ 0 & \text{otherwise} \end{cases} \quad (20)$$

kinematic hardening rules:

$$\text{yield surface: } d\alpha_{ij} = d\mu(\sigma_{ij}^* - C\sigma_{ij}) \quad (21)$$

$$\text{limit surface: } d\alpha_{ij}^* = d\mu^* \nu_{ij} \quad (22)$$

isotropic hardening rules:

$$\text{yield surface: } dR = \xi(\lambda, \phi, q) (d\epsilon_{ij}^P d\epsilon_{ij}^P)^{1/2} \quad (23)$$

$$\text{limit surface: } dR^* = \xi^*(\lambda, \phi, q)(d\epsilon_{ij}^P d\epsilon_{ij}^P)^{1/2} \quad (24)$$

$$\text{modulus function: } h = h(\delta, \delta_{in}, h_\infty) \quad (25)$$

where  $\delta = ((\sigma_{ij}^* - \sigma_{ij})(\sigma_{ij}^* - \sigma_{ij}))^{1/2}$ .  $\delta_{in}$  is the initial value of  $\delta$  upon loading into the plastic regime, and  $h_\infty = h$  (asymptotic value) when  $\delta = 0$ .  $\sigma_{ij}^*$  is a generic stress point on the limit surface defined as the similar point as the current stress point on the yield surface. If a Mroz-type rule is used, then  $\sigma_{ij}^* = \alpha_{ij}^* + (R^*/R)(\sigma_{ij} - \alpha_{ij})$ , and  $C = 1$ .

McDowell [52-53] has introduced the variables  $\phi$  and  $q$  in the isotropic hardening formulation to reflect additional isotropic hardening during nonproportional loading and plastic strain range effects, respectively. He has used simple von Mises surfaces in equations (18)-(19), a modulus function fit to a uniaxial cyclic stress-strain curve, a Mroz-type rule for  $d\alpha_{ij}^*$ , a Prager rule ( $d\alpha_{ij}^* = h_\infty d\epsilon_{ij}^P$ ) for  $d\alpha_{ij}^*$ , and results of sinusoidal, strain-controlled axial-torsional tests to determine the hardening functions  $\xi$  and  $\xi^*$  in equations (23) and (24) for type 304 stainless steel. Good agreement has been obtained with nonproportional cyclic loading experiments as seen in Ref. [53].

Dafalias [54] has proposed a general form for the modulus function

$$h = h_\infty \left[ 1 + g(\delta_{in}) \left( \frac{\delta}{\delta_{in} - \delta} \right) \right] \quad (26)$$

based on behavior of mild steel, where  $g(\delta_{in})$  is introduced to accurately account for unloading-reloading behavior in the plastic range, one aspect of multiple surface models which is not automatically retained upon the reduction to two surfaces.

None of the previous work on two surface theories has specifically addressed the issue of cyclic strain ratcheting under nonproportional loading. Though they predict such phenomena, these models do not necessarily model ratchet rates precisely since the use of simple loading surfaces precludes anisotropic yield surface deformation. Two surface models do give

experimentally consistent results, however, in terms of direction of ratchet strain, stabilization to steady state ratcheting, cessation of ratcheting, and transient effects of cyclic hardening or softening. To more precisely model ratchet rates under nonproportional loading, it may be necessary to modify the modulus function slightly based on further experimental results or to employ anisotropic yield and loading surfaces.

## Perspectives on Some Previous Solutions for Cumulative Deformation in Rolling Contact

The work of K.L. Johnson and associates [60-62] has laid a solid foundation for understanding progressive deformation and shakedown in rolling contact. The Merwin-Johnson shakedown analyses with and without tangential tractive forces [60-61] have defined regions of shakedown and continued elastic-plastic deformation as a nondimensionalized function of Hertzian normal pressure divided by shear yield strength. Later finite element analyses [63-64] have somewhat refined the solution via better approximation of equilibrium and constraint conditions. These analyses have been concerned with the first few cycles of cumulative plastic deformation to determine whether or not shakedown would occur.

Several significant features relevant to cumulative deformation have been neglected in these analyses. Realistic strain hardening behavior has not been included. An elastic-perfectly plastic material model is quite crude; the extent and nature of plastic deformation for such models is entirely dependent on the constraint of surrounding material without regard for inherent material response. In reality, the phenomenon of ratcheting is very much a result of both constraint and material response. As seen in this paper, however, merely specifying some ad hoc form for strain-hardening in typical constitutive equations used in finite element analyses would be unsatisfactory for predicting ratcheting response accurately under nonproportional loading typical of rolling contact. It is the structure of the constitutive equations which is critical in modeling the ratcheting response. Nonproportional tests are necessary to determine this structure.

The work of Megahed [65], primarily concerned with ratcheting in structures subjected to thermal constraint, considered several hardening rules: perfectly plastic, linear kinematic hardening, and linear isotropic hardening. Even for the constrained unidirectional loading conditions of his study, large differences were seen between the regions of shakedown, reversed plasticity, and progressive plastic deformation predicted by the various rules. While the prediction of shakedown limit was similar using either linear kinematic hardening or perfect plasticity, the ratchet rates were shown

to be highly dependent on the strain hardening in the material model. Transient cyclic isotropic hardening or softening behavior results in large differences between perfectly plastic and linear kinematic hardening. It should be noted at this point that none of the three material models considered by Megahed would be suitable for nonproportional cyclic loading, and his loading program (two-bar structure) was based on uniaxial response. It would be expected that the differences among material models would be considerably greater for constrained nonproportional plasticity in terms of shakedown, reversed plasticity and ratcheting rates.

Accurate constitutive equations for nonproportional cyclic plasticity are a necessary tool for understanding the cumulative plastic deformation component of rail ratcheting and corrugation. Other factors such as the dynamics of rail-wheel interaction [66-68] and wear [69] are also potentially important components of this problem which are coupled with cumulative plastic deformation. In the next section, a simple demonstration will be offered to examine the potential of a two surface Mroz-type theory for cyclic deformation in rolling contact.

# DEMONSTRATION OF APPLICABILITY OF TWO SURFACE THEORY TO RAIL/WHEEL CONTACT

As an illustration of the capability of two surface theory for modeling cumulative deformation under nonproportional loading, the rolling contact of a cylinder on a semi-infinite half-space is considered. Both cylinder and half-space have the same elastic properties. It is assumed for the sake of simplicity that the normal pressure distribution in the contact region is two-dimensional Hertzian, and that tangential tractions in this region are proportional to the normal pressure, i.e.

$$p = p_0 \sqrt{1 - (x/a)^2} \quad (27)$$

$$q = q_0 \sqrt{1 - (x/a)^2} \quad (28)$$

where  $q_0 = \mu p_0$ , and  $\mu$  is the coefficient of friction. The coordinate system is shown in Figure 6, along with the normal and tractive pressure distributions. It should be noted that the assumption that tangential tractions proportional to normal pressure occur over the entire contact area is not generally correct, since regions of stick and slip are shown to occur [62, 66, 70]. However, for purposes of demonstration, it is adequate to consider the effect of tractive forces without regard for interfacial stick-slip conditions.

From Smith and Liu [71] and Poritsky [72], the linear elastic solution for stresses in the half-space are:

$$\begin{aligned} \sigma_{xx}^* = & -\frac{p_0}{\pi} z \left\{ \frac{a^2 + 2x^2 + 2z^2}{a} \phi^* - \frac{2\pi}{a} - 3x\beta^* \right\} \\ & - \frac{q_0}{\pi} \left\{ (2x^2 - 2a^2 - 3z^2)\beta^* + 2\pi \frac{x}{a} + 2(a^2 - x^2 - z^2) \frac{x}{a} \phi^* \right\} \end{aligned} \quad (29)$$



$$\sigma_{zz}^* = \frac{-p_0}{\pi} z [a\phi^* - x\beta^*] - \frac{q_0}{\pi} z^2 \beta^* \quad (30)$$

$$\tau_{xz}^* = \frac{-p_0}{\pi} z^2 \beta^* - \frac{q_0}{\pi} \left\{ \left[ a^2 + 2x^2 + 2z^2 \right] \frac{z}{a} \phi^* - 2\pi \frac{z}{a} - 3x\beta^* \right\} \quad (31)$$

where

$$\phi^* = \frac{\pi}{A} \frac{(1 + \sqrt{B/A})}{\sqrt{B/A} \sqrt{2\sqrt{B/A} + \left[ \frac{A + B - 4a^2}{A} \right]}} \quad (32)$$

$$\beta^* = \frac{\pi}{A} \frac{(1 - \sqrt{B/A})}{\sqrt{B/A} \sqrt{2\sqrt{B/A} + \left[ \frac{A + B - 4a^2}{A} \right]}} \quad (33)$$

$$A = (a + x)^2 + z^2 \quad (34)$$

$$B = (a - x)^2 + z^2 \quad (35)$$

and  $a$  = half contact width.

The normal stress  $\sigma_{yy}^*$  is given by

$$\sigma_{yy}^* = \nu(\sigma_{xx}^* + \sigma_{zz}^*) \quad (36)$$

and the shear stresses  $\sigma_{yx}^* = \sigma_{zy}^* = 0$ . Here, plane strain conditions are assumed. The Hertzian pressure  $p_0$  is related to the contact force  $F$  per unit width in the  $y$  direction by

$$p_0 = \left( \frac{2F}{\pi a} \right) \quad (37)$$

For the sake of illustration, it will be assumed that a given material point at a selected depth is subjected to a Hertzian distribution with tractive forces moving at velocity  $V$  as shown in Figure 6. Furthermore, as a first order approximation, the elastic stress field will be assumed to apply for stresses  $\sigma_{zz}$  and  $\tau_{xz}$  during each passage of the contact patch. A finite

element analysis or other approximate technique would be necessary for the rigorous elastic-plastic solution of this problem. The recent finite element analysis of Bhargava et al. [63] resulted in very similar conclusions as the Merwin-Johnson [60] and Johnson-Jefferis [61] approximate analyses.

Using an elastic-perfectly plastic constitutive model and a modified Hertzian pressure distribution to account for plasticity, Bhargava et al. showed that  $\sigma_{zz}$  and  $\tau_{xz}$  during plastic flow do not differ much from the elastic solution at a depth of  $0.755a$ . The primary stress redistributions (residual stresses) occur for  $\sigma_{xx}$  and  $\sigma_{yy}$ . This supports the assumptions of Merwin and Johnson [60] in their classical analysis. The use of the elastic solutions for  $\sigma_{xx}$  and  $\sigma_{yy}$ , therefore, could be anticipated to result in somewhat unrealistic cyclic stress conditions for ratcheting compared to the rigorous elastic-plastic case. Furthermore, the  $x$  direction strain is constrained in the actual elastic-plastic problem. Hence, a more realistic set of constraints are provided by the assumptions:

$$\dot{\epsilon}_{xx} = 0 \quad (38)$$

$$\dot{\epsilon}_{yy} = 0 \quad (39)$$

$$\sigma_{zz} = \sigma_{zz}^*(x, z, t) \quad (40)$$

$$\tau_{xz} = \tau_{xz}^*(x, z, t) \quad (41)$$

where the  $*$  superscript refers to the elastic Hertzian solution, and  $\dot{\epsilon}_{xx}$  and  $\dot{\epsilon}_{yy}$  are total strain rates, i.e.

$$\dot{\epsilon}_{ij} = \dot{\epsilon}_{ij}^e + \dot{\epsilon}_{ij}^p \quad (42)$$

Equations (38) and (39) represent constraints on longitudinal deformation and lateral deformation (plane strain), respectively. As discussed by K.L. Johnson, residual stresses  $\sigma_{zz}$  and  $\tau_{xz}$  are zero after the load passage. Stress components  $\sigma_{xx}(x, z, t)$  and  $\sigma_{yy}(x, z, t)$  are computed by simultaneously solving equations (38) and (39), i.e.

$$\dot{\sigma}_{xx} = \frac{\nu \dot{\sigma}_{zz}(n_{yy} - n_{xx}) + \dot{\sigma}_{yy}(\nu n_{yy} + n_{xx})}{(\nu n_{xx} + n_{yy})} \quad (43)$$

$$\dot{\sigma}_{yy} = \frac{\dot{\sigma}_{zz} \left[ - \left[ \frac{n_{xx}^2}{h} + \frac{1}{E} \right] \frac{\nu(n_{yy} - n_{xx})}{(\nu n_{xx} + n_{yy})} + \left[ \frac{\nu}{E} - \frac{n_{xx} n_{zz}}{h} \right] \right] - \frac{2 \dot{\sigma}_{xz} n_{xz} n_{xx}}{h}}{\left[ \left[ \frac{n_{yy} n_{xx}}{h} - \frac{\nu}{E} \right] + \left[ \frac{n_{xx}^2}{h} + \frac{1}{E} \right] \frac{(\nu n_{yy} + n_{xx})}{(\nu n_{xx} + n_{yy})} \right]} \quad (44)$$

Here,  $\nu$  and  $E$  are the usual isotropic elastic constants.

Since the stress history is enforced, only the plastic strain rates need be computed. The plastic strain rates are given by

$$\dot{\epsilon}_{ij}^p = \begin{cases} 1/h(\dot{s}_{kl} n_{kl}) n_{ij} & \text{if } f = 0 \text{ and } \dot{s}_{kl} n_{kl} \geq 0 \\ 0 & \text{otherwise} \end{cases} \quad (45)$$

where  $\dot{s}_{kl}$  is the deviatoric stress rate  $\dot{s}_{ij} = \dot{\sigma}_{ij} - 1/3 \delta_{ij} \dot{\sigma}_{kk}$ , and  $n_{ij}$  is the unit normal vector to the yield surface. The plastic modulus function is defined as  $h$ . Yield surface  $f$  is defined as a von Mises form

$$f = (3/2)(s_{kl} - \alpha_{kl})(s_{kl} - \alpha_{kl}) - R^2 = 0 \quad (46)$$

and  $n_{ij}$  is defined by

$$n_{ij} = \frac{(s_{ij} - \alpha_{ij})}{((s_{kl} - \alpha_{kl})(s_{kl} - \alpha_{kl}))^{1/2}} \quad (47)$$

where  $\alpha_{ij}$  are the components of the yield surface center which evolve according to a Mroz rule.

$$\dot{\alpha}_{ij} = \frac{(s_{kl} - \alpha_{kl}) \dot{s}_{kl} - (2/3) R \dot{R}}{(s_{pm} - \alpha_{pm})(s_{pm}^* - s_{pm}^*)} (s_{ij}^* - s_{ij}) \quad (48)$$

Here,  $s_{ij}^*$  is a point on a limit surface  $f^*$  defined by

$$f^* = (3/2)(s_{kl}^* - \alpha_{kl}^*)(s_{kl}^* - \alpha_{kl}^*) - (R^*)^2 = 0 \quad (49)$$

where  $\alpha_{kl}^*$  are the backstress components of the limit surface. The point  $s_{ij}^*$  in equation (48), shown in Figure 5, is defined as the point on  $f^*$  with the same outward normal vector as  $n_{ij}$ , i.e.

$$s_{ij}^* = \alpha_{ij}^* + (R^*/R)(s_{ij} - \alpha_{ij}) \quad (50)$$

It is the modulus function  $h$  which accounts for much of the ratcheting description when  $\dot{\alpha}_{ij}^* \approx 0$ . The evolution of  $\alpha_{ij}^*$  permits eventual cessation of ratcheting response. Hence,

$$\dot{\alpha}_{ij}^* = \kappa(\dot{\epsilon}_{kl}^p \dot{\epsilon}_{kl}^p)^{1/2} n_{ij} \quad (51)$$

where  $\kappa$  is a coefficient which governs the rate of translation of  $\alpha_{ij}^*$  and the associated retardation of ratcheting rate.

Ordinarily, isotropic hardening rules can be specified for both  $R$  and  $R^*$ :

$$\dot{R} = \bar{\mu}(\bar{R}(\phi, q) - R)(\dot{\epsilon}_{kl}^p \dot{\epsilon}_{kl}^p)^{1/2} \quad (52)$$

$$\dot{R}^* = \bar{\mu}(\bar{R}^*(\phi, q) - R^*)(\dot{\epsilon}_{kl}^p \dot{\epsilon}_{kl}^p)^{1/2} \quad (53)$$

where  $\phi$  and  $q$  are variables which relate to additional isotropic hardening under nonproportional loading and plastic strain range, respectively [52-53]. Here,  $\bar{\mu}$  is a rate constant.

In this illustrative demonstration, isotropic hardening will be neglected since the equations are fully capable of displaying complex cyclic ratcheting response with pure nonlinear kinematic hardening. Hence,  $\dot{R} = \dot{R}^* = 0$  and the initial values of  $R$  and  $R^*$  are taken from the uniaxial cyclic stress-strain curve. Furthermore,  $\kappa$  is assumed to be zero so that steady state ratcheting response (constant ratcheting rate) is described.

The modulus function

$$h = h(\delta/\delta_{\max}, h_{\infty}) \quad (54)$$

is also determined from the uniaxial cyclic stress-strain curve. Here,  $\delta = ((s_{ij}^* - s_{ij})(s_{ij}^* + s_{ij}))^{1/2}$ ,  $\delta_{\max}$  is the maximum value of  $\delta$  in the history, and  $h_{\infty}$  is the asymptotic plastic modulus (i.e. in linear hardening region).

## Material Constants and Parameters

The rail steel selected for this demonstration is carbon steel, with uniaxial cyclic stress-strain properties reported by Park and Fletcher [74]. Cyclic strength coefficient and strain hardening exponent are reported as 281 ksi and 0.226, respectively. Other investigators report similar values for carbon rail steel [75].

The limit surface radius was selected to bound any anticipated stress response. Both  $R$  and  $R^*$  were fixed at cyclically stable uniaxial values  $R = 35$  ksi and  $R^* = 140$  ksi since no data from cyclically nonproportional tests were available for rail steels. Note that a deviation from linearity definition of yield is used instead of an offset; this permits accurate description of the cyclic response even for very small plastic strains, which is necessary in cumulative deformation problems.

The modulus function was fit by a form used by Dafalias et al. [54]:

$$h = 1400 + 1200 \left( \frac{\delta/\delta_{\max}}{1 - \delta/\delta_{\max}} \right)^{1.6} \quad (55)$$

where units of  $h$  are in ksi. A plot of  $h$  versus  $\delta$  for carbon steel appears in Figure 7.

## Definition of Contact Parameters

The contact area and Hertzian contact pressure  $p_0$  in equation (37) were determined from linear elasticity theory. To adequately represent the loading intensity, the average pressure in a three-dimensional elliptical contact patch representative of typical rail-wheel contact was equated to the average pressure in the two-dimensional Hertzian distribution for a cylinder rolling on a half-space.

From Hamrock and Brewe [73], for two convex, quadratic surfaces in contact, the major and minor radii of the contact ellipse are given by (see Figure 8):

$$a^* = \left( \frac{6\zeta PR}{K\pi E'} \right)^{1/3} \quad (56)$$

$$b^* = \left( \frac{6\zeta PRK^2}{\pi E'} \right)^{1/3} \quad (57)$$

where

$$E' = \left[ \frac{2}{\frac{1-\nu_1^2}{E_1} + \frac{1-\nu_2^2}{E_2}} \right],$$

$E_1, E_2, \nu_1, \nu_2$  = elastic properties of two bodies in contact,

$P$  = total normal load,

$$\frac{1}{R} = \frac{1}{R_x} + \frac{1}{R_y} = \left( \frac{1}{r_{ax}} + \frac{1}{r_{bx}} \right) + \left( \frac{1}{r_{ay}} + \frac{1}{r_{by}} \right),$$

$r_{ax}, r_{ay}, r_{bx}, r_{by}$  = principal radii of curvature of two solids in contact.

$$K = \text{ellipticity parameter} = \frac{b^*}{a^*} = \frac{2Z - \zeta(1 + \Gamma)^{1/2}}{\zeta(1 - \Gamma)}; \quad \Gamma = R \left( \frac{1}{R_x} - \frac{1}{R_y} \right)$$

and  $Z$  and  $\zeta$  are elliptic integrals of the first and second kind, i.e.

$$Z = \int_0^{\pi/2} \left[ 1 - \left( 1 - \frac{1}{K^2} \right) \sin^2 \phi \right]^{-1/2} d\phi$$

$$\zeta = \int_0^{\pi/2} \left[ 1 - \left( 1 - \frac{1}{K^2} \right) \sin^2 \phi \right]^{1/2} d\phi$$

The peak Hertzian pressure for this elliptical contact is given by

$$P_{0|3-D} = \frac{3}{2} \frac{P}{\pi a^* b^*} \quad (58)$$

with the average contact pressure given by

$$\bar{P}|_{3-D} = \frac{P}{\pi a^* b^*} = \frac{2}{3} P_0|_{3-D} \quad (59)$$

In the two-dimensional problem considered here (line contact of cylinders), the average pressure is given by

$$\bar{P} = \frac{F}{2a} \quad (60)$$

where  $F$  = normal load per unit width, and  $a$  is half the contact width. The value of  $a$  is expressed as

$$a = \sqrt{\frac{2F}{\pi} \left\{ \left[ \frac{1}{R_1} + \frac{1}{R_2} \right] \left[ \frac{1 - \nu_1^2}{E_1} + \frac{1 - \nu_2^2}{E_2} \right] \right\}} \quad (61)$$

where  $R_1$  and  $R_2$  represent the radii of curvature of the two cylinders in line contact [71]. Assuming  $\bar{P} = \bar{P}|_{3-D}$ ,

$$\frac{F}{2a} = \frac{P}{\pi a^* b^*} \quad (62)$$

Since  $a$  is known as a function of  $F$  from equation (61) and  $P$ ,  $a^*$ , and  $b^*$  are assumed known from the three-dimensional problem we may solve for  $F$  from equation (62). Then we can solve for  $p_0$  in equation (37), and we have a rational estimate for maximum Hertzian pressure in the illustrative model.

For typical wheel on rail [73] as shown in Figure 8, the parameters are

$$r_{ax} = 19.8''$$

$$K = 0.71$$

$$r_{ay} = \infty$$

$$\zeta = 1.3526$$

$$r_{bx} = \infty$$

$$Z = 1.8508$$

$$r_{by} = 11.8''$$

$$E_1 = E_2 = 30 \times 10^3 \text{ ksi}$$

$$\nu_1 = \nu_2 = 0.3$$



For the cylinder rolling on the half space,  $R_1 = 19.8"$  and  $R_2 = \infty$ . Hence,

$$a^* = 0.093P^{1/3} \quad (63)$$

$$b^* = 0.066P^{1/3} \quad (64)$$

$$F = 1.229 \times 10^{-3} P^2 / (a^*)^4 \quad (65)$$

$$p_0 = 16.28 \sqrt{F} \quad (66)$$

$$a = 0.0391 \sqrt{F} \quad (67)$$

where  $P$  is in kips and  $a$  is in inches. Thus, given a contact load  $P$ , we may compute  $p_0$  and  $a$  values that relate to the "equivalent" two-dimensional line contact problem with the same average contact pressure as that of a realistic railroad wheel-rail contact.

#### Details of Computer Analysis

A FORTRAN computer program was written to calculate the accumulation of plastic strain with each passage of the contact region. Since the ratcheting is steady state for the most part after the first few cycles in the analysis, 20 cycles were imposed for each loading condition. A cycle is defined as the movement of the center of the contact region from  $-30a$  to  $+30a$  with respect to material point in question. The material point is specified by  $\bar{z}$  as shown in Figure 6. At each increment of the contact region, the stresses in equations (29) - (36) were imposed. The constitutive equations were integrated using a Runge Kutta technique with Gill Coefficients [59], which maintains a small error per time step. Time was taken as the independent variable, even though the constitutive equations are time- and rate-independent.

## RESULTS AND DISCUSSION

Recognizing that equilibrium is not met by the preceding simple assumptions, comparison with elastic-plastic finite element results is intended to be of only a qualitative nature. Some very revealing aspects regarding the rate of inherent material response can, however, be drawn from this comparison.

In Figure 9, results are presented for the accumulation of subsurface plastic shear strain,  $\gamma_{xz}^P$ , and residual stress,  $\sigma_{xx}$ , for only applied normal tractions ( $\mu=0$ ). Note that results at the end of the 15th and 20th cycles (load passages) are reported. In the plots,  $k = 20.2$  ksi and  $G = 11,500$  ksi. This value of  $k$  corresponds to

$$k = \frac{R}{\sqrt{3}} \quad (68)$$

where  $R$  is the uniaxial yield strength. Peak Hertzian pressures were evaluated, ranging from  $2\sqrt{3} \leq p_0/k \leq 5\sqrt{3}$ . This corresponds to wheel loads in the range  $1.2 \leq P \leq 18.7$  kips. Note that the shear strains are plotted as negative to conform in sign to the coordinate system employed by Bhargava et al [63].

It is interesting to note that the phenomenon of forward shear is predicted for the higher  $p_0/k$  values. Finite element results obtained by Bhargava et al [63] are also reported in Figure 9. Though the residual stress and strain distributions are of similar character, there are several differences. First, the cyclic shear strain accumulation in the current model is an order of magnitude smaller. Experimental results are of the same order of magnitude. Secondly, the magnitude of the positive subsurface shear strains are a significantly higher fraction of the maximum negative shear strains than in the finite element results. The smaller ratchet strains are probably attributable to the material workhardening in the current model. The second observation is possibly due to lack of equilibrium in the model and/or

the rather stringent assumption of instantaneous zero x-direction total strain rate. Note that the magnitude and sense of the residual stresses are comparable in each case.

An important result of the current analysis is the relative magnitude of peak Hertzian pressure for which ratcheting ceases, i.e. shakedown. From Figure 9 it is apparent that shakedown is evident for  $p_0/k \approx 2\sqrt{3}$ . A "shakedown limit" is reached somewhere between  $p_0/k = 2\sqrt{3}$  and  $2.5\sqrt{3}$ . It must be emphasized that the definition of  $k$  based on deviation from linearity produces a conservative shakedown limit. Larger values of  $k$  based on work hardening would lead to even smaller values of shakedown limit. It is recalled that both the Merwin-Johnson [60] and Bhargava et al [63] analyses found a shakedown limit of  $p_0/k \approx 3.5 - 4.0$ , which is corroborated by the value of  $p_0/k \approx 3.5$  found in this study. It should also be noted that the shape of the shear stress-strain hysteresis loops predicted by the model were very similar to that computed by finite element analysis.

Since the stresses and strains are reasonably well predicted by this model for the case of zero tangential tractions, it is interesting to introduce effects of driving and braking tangential tractions. A tangential traction representative of braking was first introduced by assuming  $\mu = 0.3$  such that  $q_0 = 0.3 p_0$ . Plots of 15th and 20th cycle residual stress and shear strain are shown in Figure 10 for  $P_0/k$  values of  $2.5\sqrt{3}$  and  $3.5\sqrt{3}$ . Note the significantly enhanced backward shear compared to the same cases with zero tangential traction. In contrast, application of a driving tangential traction with  $q_0 = -0.3 p_0$  results in significant forward shear as shown in Figure 11.

Hence it is clear that driving and braking conditions introduce quite different subsurface plastic flow. Also, any variation of lubrication conditions along the rail can result in a longitudinal gradient of subsurface shear strain, normal strain and residual stress.

Based on these results, it appears that the role of inherent material work hardening response is an important one with respect to accurate prediction of ratchet strain per cycle. The qualitative model herein, based on

an accurate cyclic plasticity model and representative kinematic constraints, captures the essence of the subsurface response. It is interesting to note that integration of this simple model required only 1 - 2 CPU seconds per complete cycle for each depth on a Cyber 990. This contrasts to the 7 - 24 CPU hours required by the Bhargava finite element solution on a VAX 11-780.

There are, of course, a few reservations about the preceding analysis. First, equilibrium is neglected. Secondly elastic Hertzian stresses are assumed for  $\sigma_{zz}$  and  $\tau_{xz}$ ; this assumption should not lead to significant error in the shakedown regime. Thirdly, the constraint that the total strain rate in the x direction is zero is somewhat stringent. Finally, cyclic hardening or softening have not been accounted for; one of the advantages of the two surface cyclic plasticity theory is the ease with which these effects can be introduced [52-53].

### CONCLUSIONS

A sophisticated, two-surface cyclic plasticity theory, known to accurately correlate nonproportional cyclic plasticity experiments, has been introduced into a qualitative model of two dimensional rolling contact representative of wheel on rail. It has been demonstrated that the subsurface residual stresses and shear strains agree qualitatively with rigorous finite element analysis and with the Merwin-Johnson model, both of which assume perfectly plastic response. Furthermore, the shakedown limit is comparable to these analyses. The magnitude of subsurface plastic shear strain accumulation in the present model is, however, significantly less than either analysis, in agreement with experimental results. These findings suggest that accurate representation of the work hardening response and kinematic hardening rule for cyclic nonproportional loading can significantly enhance solution of cyclic strain accumulation in a rolling contact stress field.

## REFERENCES

1. Daniels, L.E. and N. Blume, "Rail Corrugation Growth Performance," Proc. 2nd Intl. Heavy Haul Railway Conf., Sept. 25-30, 1982.
2. Lamba, H.S. and O.M. Sidebottom, ASTM Journal of Testing and Evaluation, Vol. 6, No. 4, 1978, pp. 260-267.
3. Drucker, D.C. and L. Palgen, ASME Journal of Applied Mechanics, Vol. 48, 1981, pp. 479-485.
4. Moyar, G.J. and J. Morrow, "Surface Failure of Bearings and Other Rolling Elements, " Bulletin 468, Engineering Experiment Station, University of Illinois at Urbana-Champaign, Vol. 62, No. 35, Nov. 1964.
5. Moyar, G.J. and G.M. Sinclair, "Cyclic Strain Accumulation Under Complex Multiaxial Loading," Proc. Intl. Conf. on Creep, Inst. of Mechanical Engineers, London and New York, 1963, p.47.
6. Feltner, C.E. and G.M. Sinclair, Joint Intl. Conf. on Creep, Book 2, sessions 3-9, London, 1963.
7. Coffin, L.F. Jr., ASME Journal of Basic Engineering, Vol. 82, No. 3, 1960, p. 671.
8. Benham, P.P., International Journal of Mechanical Sciences, Vol. 7, 1965, pp. 81-86.
9. Ronay, M., International Journal of Solids and Structures, Vol. 3, 1967, pp. 167-176.
10. Freudenthal, A.M. and M. Ronay, Proc. Royal Society, A292, No. 14, 1966.
11. Bell, J.F., Archives of Rational Mechanics Analysis, Vol. 84, No. 2, 1983, pp. 139-170.
12. Harvey, S.J., Adkin, P. and P.J. Jeans, Fatigue of Engineering Materials and Structures, Vol. 6, No. 1, 1983, pp. 89-99.
13. Bright, M.R. and S.J. Harvey, "Cyclic Strain Induced Creep-Non-linear Problems in Stress Analysis, Applied Science Publishers, 1977.
14. Shiratori, E., Ikegami, K. and F. Yoshida, Journal of the Mechanics and Physics of Solids, Vol. 27, 1979, pp. 213-229.
15. Hill, R., Mathematical Theory of Plasticity, Oxford University Press, 1950.
16. Frederking, R.M. and O.M. Sidebottom, ASME Journal of Applied Mechanics, March 1971, pp. 15-22.
17. Hu, L.W., ASME Journal of Applied Mechanics, Vol. 23, 1956, pp. 444-450.

18. Hu, L.W. and J. Marin, ASME Journal of Applied Mechanics, Vol. 22, No. 1, 1955, pp. 77-85.
19. Ohashi, Y., Kawashima, K. and T. Yokochi, Journal of the Mechanics and Physics of Solids, Vol. 23, 1975, pp. 277-294.
20. Phillips, A., ASME Journal of Applied Mechanics, Dec. 1952, pp. 496-500.
21. Krempf, E. and H. Lu, Mechanics of Materials, Vol. 2, 1983, pp. 183-192.
22. Hecker, S.S., Acta Mechanica, Vol. 13, 1972, pp. 69-86.
23. Moon, H., Acta Mechanica, Vol. 23, 1975, pp. 49-63.
24. Gill, S.S. and J. Parker, ASME Journal of Applied Mechanics, March 1959, pp. 77-87.
25. Mair, W.M. and H.L.D. Pugh, Journal of Mechanical Engineering Science, Vol. 6, No. 2, 1964, pp. 150-163.
26. Hecker, S.S., "Experimental Studies of Yield Phenomena in Biaxially Loaded Metals," Proc. of Winter Annual Mtg. of ASME, Stricklin and Saczalski, Eds., New York, NY, Dec. 5-10, 1976, pp. 1-34.
27. Liu, K.C. and W.L. Greenstreet, "Experimental Studies to Examine Elastic-Plastic Behaviors of Metal Alloys Used in Nuclear Structures," Proc. of Winter Annual Mtg. of ASME, Stricklin and Saczalski, Eds., New York, NY, Dec. 5-10, 1976, pp. 35-56.
28. Phillips, A., Tang, J.-L. and M. Ricciuti, Acta Mechanica, Vol. 20, 1974, pp. 23-39.
29. Naghdi, P.M., Essenburg, F. and W. Koff, ASME Journal of Applied Mechanics, June 1958, pp. 201-209.
30. Lamba, H.S. and O.M. Sidebottom, ASME Journal of Engineering Materials and Technology, Vol. 100, 1978, pp. 96-103.
31. Lamba, H.S. and O.M. Sidebottom, ASME Journal of Engineering Materials and Technology, Vol. 100, 1978, pp. 104-111.
32. Kanazawa, K., Miller, K.J. and M.W. Brown, Fatigue of Engineering Materials and Structures, Vol. 2, 1979, pp. 217-228.
33. Krempf, E. and H. Lu, Journal of Engineering Materials and Technology, Vol. 106, No. 4, 1984, pp. 376-382.
34. Ohashi, Y., Tanaka, E. and M. Ohoka, ASME Journal of Engineering Materials and Technology, 1984.
35. McDowell, D.L., "Transient Nonproportional Cyclic Plasticity," Design and Materials Div. Report No. 107, Dept. of Mechanical and Industrial Engr., University of Illinois at Urbana-Champaign, June 1983.

36. McDowell, D.L. and D.F. Socie, "Transient and Stable Deformation Behavior Under Cyclic Nonproportional Loading," ASTM STP 853, 1985, pp. 64-87.
37. McDowell, D.L. and D.F. Socie, "On the Path Dependence of Transient Hardening and Softening to Stable States Under Complex Biaxial Cyclic Loading," Proc. Intl. Conf. on Constitutive Laws for Engineering Materials, Eds. Desai and Gallagher, Tucson, AZ, Jan. 1983, pp. 125-132.
38. McDowell, D.L., "An Experimental Study of the Structure of Constitutive Equations for Nonproportional Cyclic Plasticity," ASME Journal of Engineering Materials and Technology, Oct. 1985, Vol. 107, pp. 307-315.
39. McDowell, D.L., "The Significance of Nonproportional Loading Tests for Characterization of Cyclic Response of Metals," SESA (SEM) Spring Conf., Las Vegas, Nevada, June 1985.
40. Mroz, Z., Mathematical Models of Inelastic Material Behaviour, Solid Mech. Div., University of Waterloo, Waterloo, Ontario, 1973.
41. Mroz, Z., Acta Mechanica, Vol. 7, 1969, pp. 199-212.
42. Iwan, W.D., ASME Journal of Applied Mechanics, Vol. 34, 1967, pp. 612-617.
43. Garud, Y.S., "A New Approach to the Evaluation of Fatigue under Multiaxial Loadings," Proc. Symp. on Methods for Predicting Materials Life in Fatigue, ASME, Dec. 1979, pp. 247-263.
44. McDowell, D.L., Socie, D.F. and H.S. Lamba, ASTM STP 770, 1982, pp. 500-518.
45. Nouailhas, D., Policella, H., and H. Kaczmarek, "On the Description of Cyclic Hardening Under Complex Loading Histories," Proc. Intl. Conf. on Constitutive Laws for Engineering Materials, Eds. Desai and Gallagher, Tucson, AZ, Jan. 1983, pp. 45-49.
46. Naghdi, P.M. and D.J. Nikkel, Jr., ASME Journal of Applied Mechanics, Vol. 51, No. 3, 1984.
47. Rees, D.W.A., Acta Mechanica, Vol. 52, July 1984, pp. 15-40.
48. Jhansale, H.R. and S.K. Sharma, "Inelastic Behavior of Structural Metals under complex Cyclic Loadings," Paper No. 77-366, AIAA/ASME 18th Structures, Struc. Dynamics and Materials Conf., San Diego, CA, March 21-, 23, 1977.
49. Krieg, R.D., ASME Journal of Applied Mechanics, Vol. 42, Sept. 1975, pp. 641-646.

50. Dafalias, Y.F. and E.P. Popov, *Acta Mechanica*, Vol. 21, 1975, pp. 173-192.
51. Tseng, N.T. and G.C. Lee, *Journal of Engineering Mechanics*, Vol. 109, No. 3, June 1983, pp. 795-810.
52. McDowell, D.L., "A Two Surface Theory for Nonproportional Cyclic Plasticity--Part 1: Development of Appropriate Equations," *ASME Journal of Applied Mechanics*, Vol. 52, June 1985, pp. 298-302.
53. McDowell, D.L., "A Two Surface Theory for Nonproportional Cyclic Plasticity--Part 2: Comparison of Theory with Experiments," *ASME Journal of Applied Mechanics*, Vol. 52, June 1985, pp. 303-308.
54. Dafalias, Y.F., "The Concept and Application of the Bounding Surface in Plasticity Theory," *IUTAM Symp. on Physical Non-Linearities in Structural Analysis*, Senlis, France, Eds. J. Hult and J. Lemaitre, 1981, pp. 56-63.
55. McDowell, D.L., "A Simple, Experimentally Motivated, Nonproportional Cyclic Plasticity Model," submitted to *ASCE Journal of Engineering Mechanics*, March 1986.
56. Phillips, A. and G.J. Weng, *ASME Journal of Applied Mechanics*, June 1975, pp. 375-378.
57. Chan, K.S., Bodner, S.R., Walker, K.P. and U.S. Lindholm, "A Survey of Unified Constitutive Theories," 2nd symp. on Nonlinear Constitutive Relations for High Temperature Applications, Cleveland, Ohio, June 1984.
58. Cescotto, C.S. and F.A. Leckie, "Determination of Unified Constitutive Equations for Metals at High Temperature," *Proc. Intl. Conf. on Constitutive Laws for Engineering Materials*, Eds. Desai and Gallagher, Tucson, AZ, Jan. 1983, pp. 105-111.
59. Sotolongo, W. "On the Numerical Implementation of Cyclic Elasto-Plastic Material Models," M.S. Thesis, School of Mechanical Engineering, Georgia Inst. of Technology, February 1985.
60. Merwin, J.E. and K.L. Johnson, *Proc. Instn. Mech. Engrs.*, Vol. 177, No. 25, 1963, pp. 676-690.
61. Johnson, K.L. and J.A. Jefferis, "Plastic Flow and Residual Stresses in Rolling and Sliding Contact," *Proc. Symp. on Fatigue in Rolling Contact*, Inst. Mech. Engrs. London, 1963.
62. Johnson, K.L., "One Hundred Years of Hertz Contact," *proc. Instn. Mech. Engrs.*, Vol. 196, 1982.
63. Bhargava, V., G.T. Hahn and C.A. Rubin, *ASME Journal of Applied Mechanics*, Paper 84-WA/APM-43, 1984



64. Martin, G.C. and W.W. Hay, "The Influence of Wheel-Rail Contact-Forces on the Deformation of Rail Steels," Paper 72-WA/RT-8, ASME, New York, 1972.
65. Megahed, M.M., International Journal of the Mechanical Sciences, Vol. 23, 1981, pp. 169-182.
66. Kalker, J.J., "Review of Wheel-Rail Rolling Contact Theories," Proc. Winter Annual Meeting of ASME, The General Problem of Rolling Contact, Chicago, IL, Nov. 16-21, 1980, pp. 77-92.
67. Clark, R.A. and P. Foster, "Mechanical Aspects of Rail Corrugation Formation," presented at Corrugation Symposium, Technical University of Berlin, June 1983.
68. Clark, R.A. Dean, P.A., Elkins, J.A. and S.G. Newton, Journal of Mechanical Engineering Science, Inst. of Mech. Engrs., Vol. 24, No. 2, 1982, pp. 65-75.
69. Kumar, S. and R. Margasahayam, "A Parametric and Experimental Analysis of Friction, Creep and Wear for Wheel and Rail on Tangent Tracks," Proc. Winter Annual Meeting of ASME, The General Problem of Rolling Contact, Chicago, IL, Nov. 16-21, 1980, pp. 139-156.
70. Kumar, S., Garg, V.K. and B. Annigeri, "Adhesion and Creep Zone Investigation of Planar Elastic Steel on Steel Contacts with Friction - A Finite Element Analysis," Proc. Winter Annual Meeting of ASME, The General Problem of Rolling Contact, Chicago, IL, Nov. 16-21, 1980, pp. 107-119.
71. Smith, J.O. and G.K. Liu, ASME Journal of Applied Mechanics, Vol. 21, 1953, pp. 157-166.
72. Poritsky, H., ASME Journal of Applied Mechanics, Vol. 18, 1950, pp. 191-210.
73. Hamrock, B.J. and D. Brewe, ASME Journal of Lubrication Technology, Paper No. 81-Lub-54, presented at the ASLE-ASME Joint Lubrication Conf., New Orleans, Oct. 1981.
74. Park, Y.J. and F.B. Fletcher, "Fatigue Behavior and Fracture Toughness of Standard Carbon and High Strength Rail Steels," Proc. 2nd Intl. Heavy Haul Railway Conf., Sept. 25-30, 1982.
75. Scutti, J.J., Pelloux, R.M. and R. Fuquen-Moleno, Fatigue of Engineering Materials and Structures, Vol. 7, No. 2, 1984, pp. 121-135.
76. Laufer, E.E., Ghonem, H., Kalousek, J. and D.H. Stone, "Aspects of Plastic Deformation and Fatigue Damage in Pearlitic Rail Steel," Proc. 2nd Intl. Heavy Haul Railway Conf., Sept. 25-30, 1982.
77. Moyar, G.J., Personal Communication, March 14, 1985.

78. McDowell, D.L., "Methodology of the Out-of-phase Incremental Step Test," presented at the ASTM Fall Meeting of Committee E.09 on Fatigue, St. Louis, MO, Oct. 1981.

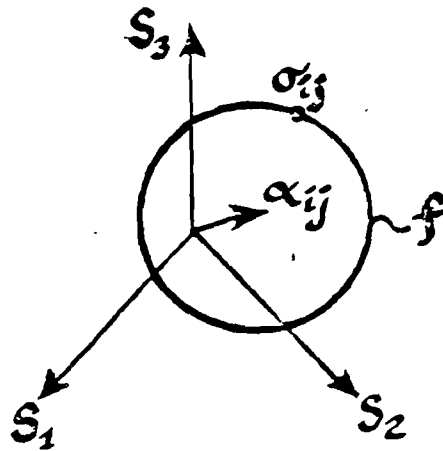


Fig.1 Von Mises yield surface in the deviatoric stress plane.

— Pure isotropic  
— Combined Iso-Kin  
--- Actual

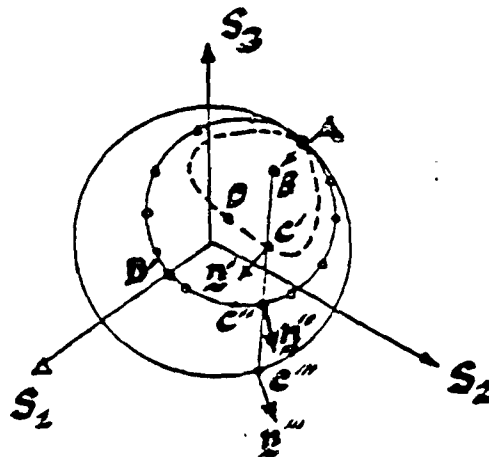


Fig.2 Effect of functional form of yield surface on nonproportional plastic flow.

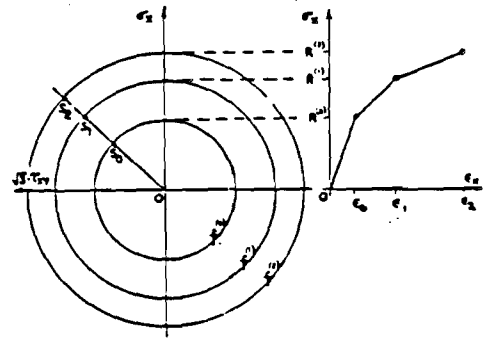


Fig.3 Initial configuration of loading surfaces, based on Mroz model, derived from cyclic stress-strain curve (from Garud [43]).

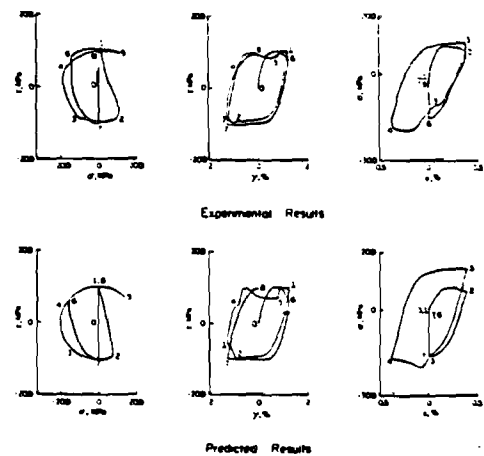


Fig.4 Experimental (top row) and predicted (bottom row) results for nonproportional cyclic loading of OFHC copper (from McDowell et al. [44]).

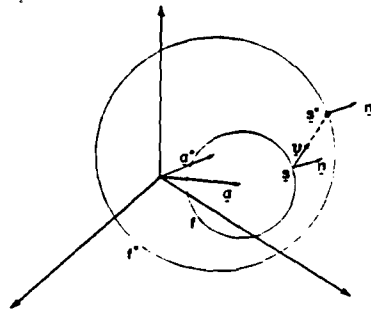


Fig.5 Von Mises yield and limit surfaces in the deviatoric stress plane.

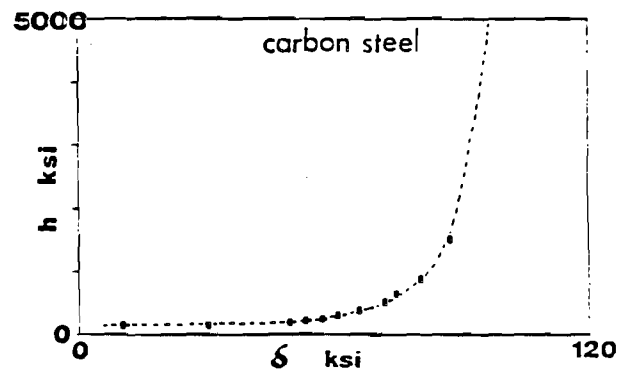


Fig.7 Modulus function  $h$  versus norm of Hroz distance vector  $\delta$  for carbon rail steel.

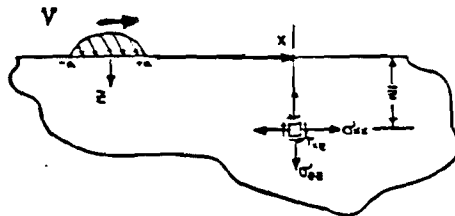


Fig.6 Coordinate frame for moving contact area with respect to a fixed material element at  $z = \bar{z}$ .

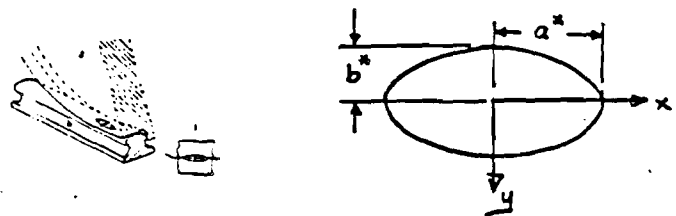


Fig.8 Typical wheel/rail contact geometry (left, from Hamrock and Brewe [73]), and definition of  $a^*$  and  $b^*$  (right).

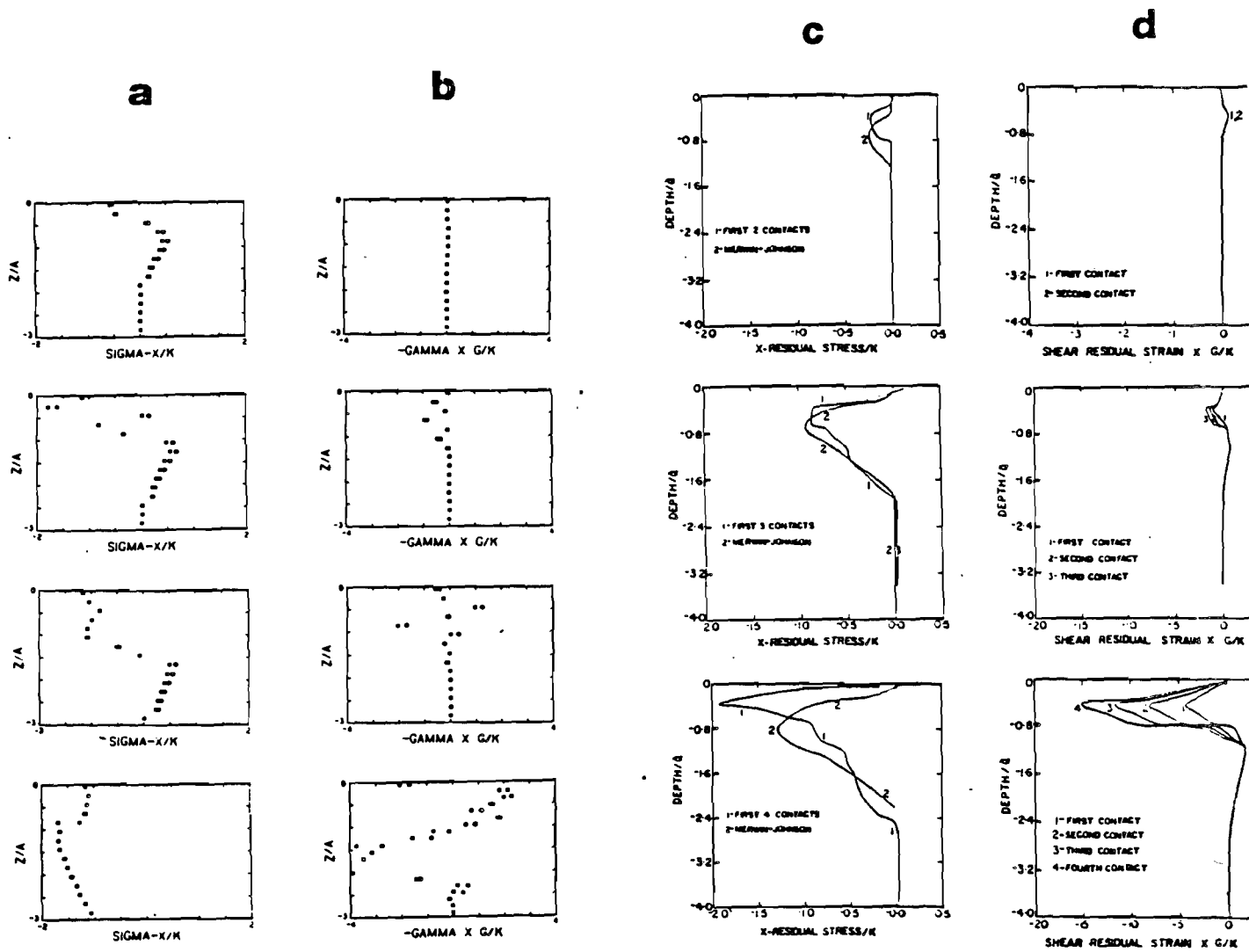


Fig.9 Predictions of two surface model (columns (a) and (b)) for  $\mu=0$  and  $p_0/k=2\sqrt{3}$ ,  $2.5\sqrt{3}$ ,  $3\sqrt{3}$ , and  $5\sqrt{3}$ , respectively, from top to bottom. Bhargava et al [63] finite element results appear in columns (c) and (d) for  $p_0/k=3.5$ ,  $4.35$ , and  $5.0$ , respectively, from top to bottom.

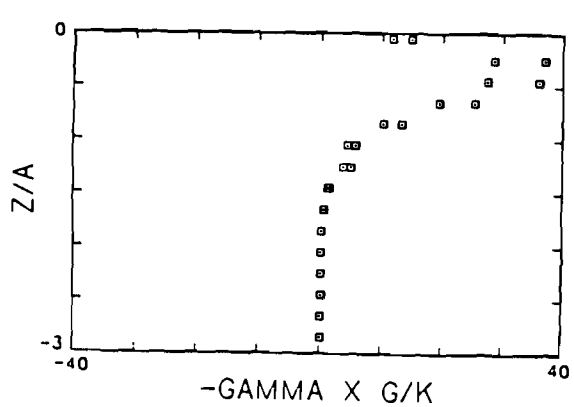
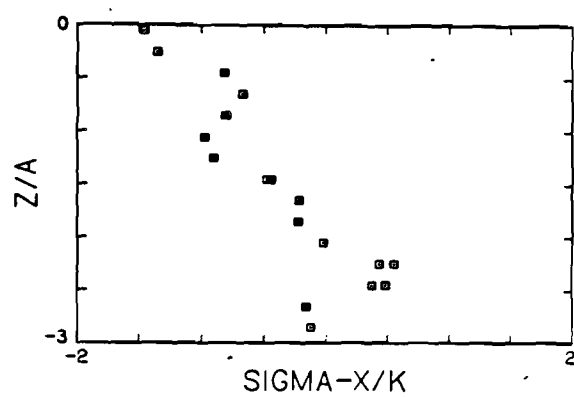
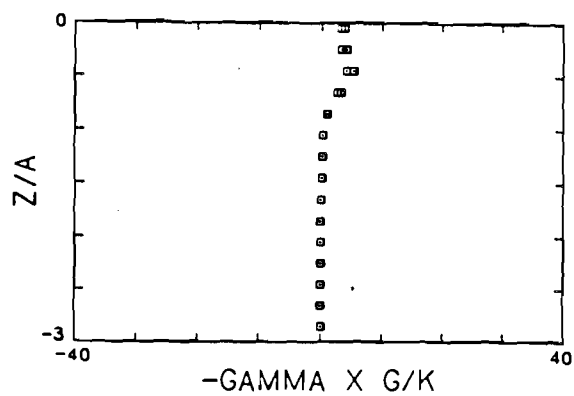
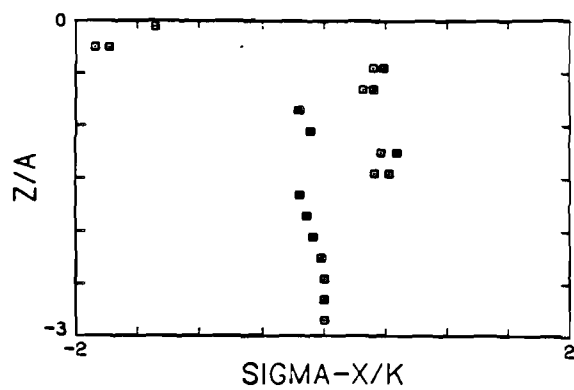


Fig.10 Predictions of two surface model  
for (top)  $p_0/k=2.5\sqrt{3}$  and  
(bottom)  $p_0/k=3.5\sqrt{3}$  for  $q_0=0.3$   
 $p_0$ .

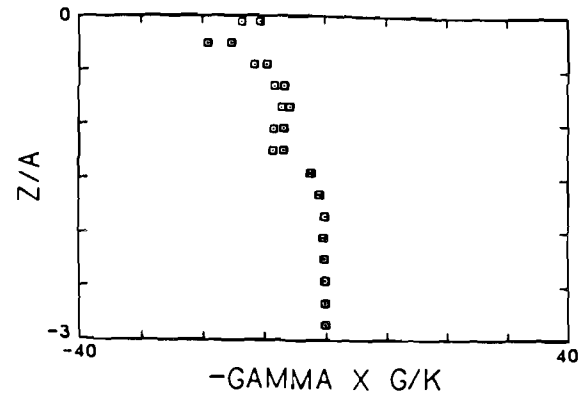
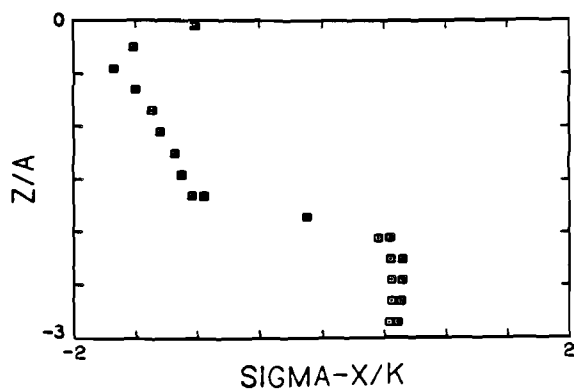


Fig.11 Predictions of two surface model  
for  $p_0/k=3.5\sqrt{3}$  and  $q_0=-0.3 p_0$ .

ON THE NUMERICAL IMPLEMENTATION OF  
CYCLIC ELASTO-PLASTIC MATERIAL MODELS

A THESIS

Presented to

The Faculty of the Division of Graduate Studies

By

Wilfredo Sotolongo

In Partial Fulfillment

of the Requirements for the Degree

Master of Science in the School of Mechanical Engineering

Georgia Institute of Technology

February, 1985

## TABLE OF CONTENTS

	Page
ACKNOWLEDGMENTS . . . . .	ii
LIST OF TABLES . . . . .	v
LIST OF ILLUSTRATIONS . . . . .	vii
NOMENCLATURE . . . . .	ix
SUMMARY . . . . .	xiv
Chapter	
I. INTRODUCTION . . . . .	1
Problem Definition	
Purpose and Outline of Work	
II. MATERIAL MODELING: TIME- AND RATE-INDEPENDENT CYCLIC PLASTICITY. . . . .	8
Drucker's Model	
McDowell's Model	
Krieg's Model with Radial-Return Integration Algorithm	
Abrahamson's Model	
III. NUMERICAL INTEGRATION TECHNIQUES . . . . .	34
Classical Runge-Kutta Method with Gill Coefficients	
Euler's Method with Automatic Step-Size Control	
Iterative Adams Predictor-Corrector Method with Automatic Step-Size Control	
Non-Iterative Adams Predictor-Corrector Method	
Gear's Method	
IV. COMPUTER ANALYSIS. . . . .	50
Material Model Evaluations	
Integration Technique Evaluations	
V. CONCLUSIONS AND RECOMMENDATIONS. . . . .	121



	Page
APPENDICES	
A. SPECIALIZATION TO AXIAL-TORSIONAL LOADING. . . . .	124
B. EXPERIMENTAL PROCEDURE . . . . .	137
C. INTEGRATION TECHNIQUE EVALUATIONS WITH ALTERNATE ERROR CRITERION. . . . .	140
BIBLIOGRAPHY. . . . .	145

## LIST OF TABLES

Table		Page
4-1	Stable Loop Errors and Computation Times for Drucker's Model . . . . .	62
4-2	Stable Loop Errors and Computation Times for McDowell's Model . . . . .	69
4-3	Stable Loop Errors and Computation Times for Krieg's Model. . . . .	75
4-4	Stable Loop Errors and Computation Times for Abrahamson's Model . . . . .	82
4-5	Model Evaluation Summary. . . . .	88
4-6	Actual Computation Times and Number of Function Evaluations Using Gear's Method with Standard Input Parameter Values. . . . .	93
4-7	Runge-Kutta Method Performance Evaluation with $h_{init} = 0.01$ . . . . .	95
4-8	Runge-Kutta Method Performance Evaluation with $h_{init} = 0.005$ . . . . .	95
4-9	Non-Iterative Adams Method Performance Evaluation with $h_{init} = 0.01$ . . . . .	101
4-10	Non-Iterative Adams Method Performance Evaluation with $h_{init} = 0.005$ . . . . .	101
4-11	Euler's Method Performance Evaluation with $E_{max} = 0.001$ , $E_{min} = 0.0001$ . . . . .	107
4-12	Euler's Method Performance Evaluation with $E_{max} = 0.0001$ , $E_{min} = 0.00001$ . . . . .	107
4-13	Iterative Adams Method Performance Evaluation with $E_{max} = 0.001$ , $E_{min} = 0.0001$ , $m = 2$ . . . . .	113
4-14	Iterative Adams Method Performance Evaluation with $E_{max} = 0.0001$ , $E_{min} = 0.00001$ , $m = 2$ . . . . .	113
4-15	Iterative Adams Method Performance Evaluation with $E_{max} = 0.001$ , $E_{min} = 0.0001$ , $m = 10$ . . . . .	116
4-16	Integration Technique Evaluation Summary. . . . .	120

Table		Page
B-1	Type 304 Stainless Steel Chemical Composition . . . . .	139
C-1	Modified Euler's Method Performance Evaluation with $E_{\max} = 0.001$ , $E_{\min} = 0.0001$ . . . . .	141
C-2	Modified Iterative Adams Method Performance Evaluation with $E_{\max} = 0.001$ , $E_{\min} = 0.0001$ , $m = 2$ . . . . .	144

## LIST OF ILLUSTRATIONS

Figure		Page
1-1	Nonproportional and Proportional Loading Paths in Strain Space . . . . .	3
4-1	Program Structure Used for the Solution of the Cyclic Axial-Torsional Loading Problem. . . . .	51
4-2	Experimental Data for History I. . . . .	55
4-3	Experimental Data for History II . . . . .	56
4-4	Experimental Data for History III. . . . .	57
4-5	Experimental Data for History IV . . . . .	58
4-6	Numerical Solution by Drucker's Model for History I. . . . .	64
4-7	Numerical Solution by Drucker's Model for History II . . . . .	65
4-8	Numerical Solution by Drucker's Model for History III. . . . .	66
4-9	Numerical Solution by Drucker's Model for History IV . . . . .	67
4-10	Numerical Solution by McDowell's Model for History I . . . . .	70
4-11	Numerical Solution by McDowell's Model for History II. . . . .	71
4-12	Numerical Solution by McDowell's Model for History III . . . . .	72
4-13	Numerical Solution by McDowell's Model for History IV. . . . .	73
4-14	Numerical Solution by Krieg's Model for History I. . . . .	77
4-15	Numerical Solution by Krieg's Model for History II . . . . .	78
4-16	Numerical Solution by Krieg's Model for History III. . . . .	79
4-17	Numerical Solution by Krieg's Model for History IV . . . . .	80
4-18	Numerical Solution by Abrahamson's Model for History I . . . . .	84
4-19	Numerical Solution by Abrahamson's Model for History II. . . . .	85
4-20	Numerical Solution by Abrahamson's Model for History III . . . . .	86
4-21	Numerical Solution by Abrahamson's Model for History IV. . . . .	87

Figure		Page
4-22	Axial and Shear Stress vs. Time Responses for Histories V and VI Integrated by Gear's Method . . . . .	91
4-23	Axial and Shear Stress Errors vs. Time Responses for Histories V and VI Integrated by Runge-Kutta Method ( $h_{init} = 0.01$ ) . . . . .	96
4-24	Axial and Shear Stress Errors vs. Time Responses for Histories V and VI Integrated by Non-Iterative Adams Method ( $h_{init} = 0.01$ ) . . . . .	103
4-25	Axial and Shear Stress Errors vs. Time Responses for Histories V and VI Integrated by Euler's Method ( $E_{max} = 0.001$ , $E_{min} = 0.0001$ ) . . . . .	109
4-26	Axial and Shear Stress Errors vs. Time Responses for Histories V and VI Integrated by Iterative Adams Method ( $E_{max} = 0.001$ , $E_{min} = 0.0001$ , $m = 2$ ) . . . . .	114
B-1	Tubular Axial-Torsional Specimen . . . . .	139

## NOMENCLATURE

$\tilde{C}$	fourth rank elasticity tensor
$CPU_A$	actual CPU time
$CPU_N$	normalized CPU time
$D_o, D_i$	specimen outside and inside diameters, respectively
$E$	Young's modulus
$\bar{E}$	integration routine single-step error estimate
$\bar{E}_i$	integration routine single-step error estimate for the i-th dependent variable $\tilde{X}_i$
$E_a, E_s$	axial and shear stress errors, respectively
$E_{a,avg}, E_{s,avg}$	axial and shear stress average errors, respectively
$E_{a,max}, E_{s,max}$	axial and shear stress maximum errors, respectively
$E_{max}, E_{min}$	maximum and minimum single-step error estimates, respectively
$\tilde{F}$	ordinary differential system of equations vector
$f$	yield (stress) surface
$G$	shear modulus
$h, h_p$	current and predicted time step-sizes, respectively
$\tilde{I}$	identity tensor
$J_2$	second invariant of deviatoric stress tensor $\tilde{s}$
$k$	shear yield strength
$\tilde{k}_i$	i-th value of Runge-Kutta's intermediate calculation vector $\tilde{k}$
$l_o$	initial specimen gage length
$m, m^*$	current and maximum allowable number of corrector equation iterations at a single time step, respectively

$N$	number of dependent variables in system of ODE's
$N_c$	cummulative number of phenomenological subroutine evaluations
$N_f$	nondimensional number of phenomenological subroutine evaluations
$P$	applied specimen axial force
$\underline{g}_i$	i-th value of Runge-Kutta's intermediate calculation vector $\underline{g}$
$r_m$	mean specimen radius
$\underline{s}$	deviatoric stress tensor
$t, t_f$	current and final values of time, respectively
$T$	applied specimen torque
$W^{pc}$	accumulated plastic work
$\underline{X}, \underline{X}_0$	current and initial dependent variable vectors, respectively.
$\underline{X}_p, \underline{X}_c$	predicted and corrected dependent variable vectors, respectively
$\underline{X}_i$	i-th value of Runge-Kutta's intermediate calculation vector $\underline{X}$
$\underline{\alpha}$	center of yield (stress) surface in deviatoric stress space
$\alpha_{eff}$	uniaxial equivalent value of $\underline{\alpha}$
$\gamma$	engineering experimental shear strain
$\gamma_a$	hysteresis loop engineering shear strain amplitude
$\Delta l$	specimen gage length increment
$\Delta \theta$	specimen twist angle increment
$\epsilon$	engineering experimental axial strain
$\epsilon_a$	hysteresis loop engineering axial strain amplitude
$\underline{\epsilon}, \underline{\epsilon}^e, \underline{\epsilon}^p$	total, elastic, and plastic strain tensors, respectively

$\epsilon_{\text{eff}}$	uniaxial equivalent value of $\epsilon$
$\nu$	Poisson's ratio
$\underline{\sigma}$	stress tensor
$\sigma_{\text{eff}}$	uniaxial equivalent value of $\sigma$
$\sigma_a, \sigma_e$	predicted and experimental values of axial stress, respectively
$\sigma_{\text{max}}$	maximum value of axial stress
$\tau_a, \tau_e$	predicted and experimental values of shear stress, respectively
$\tau_{\text{max}}$	maximum value of shear stress
$\phi$	current measure of nonproportionality
$\phi_{\text{limit}}$	threshold value of $\phi$

#### Drucker's Model

$A, B, G, N,$ $W_0, \gamma, \sigma^*$	experimentally determined model parameters
$R$	axial yield strength
$\bar{\sigma}$	plastic modulus function normalizing stress

#### McDowell's Model

$f^*$	limit surface function
$F$	plastic strain memory surface
$g(x)$	$g(x) = 1$ for $x = 0$ , $g(x) = x$ for $x \neq 0$
$h$	plastic modulus function
$H(F)$	$H(F) = 1$ for $F = 0$ , $H(F) = 0$ for $F < 0$
$J$	instantaneous measure of nonproportionality
$\underline{n}, \underline{n}^*$	yield and strain memory surface unit normals, respectively



$q$	strain memory surface radius
$R, R^*$	yield and limit surface radii, respectively
$\bar{R}, \bar{R}^*$	cyclically stable values of $R$ and $R^*$
$\tilde{s}^*$	corresponding deviatoric stress tensor in limit surface
$u(x)$	Heaviside function of $x$
$\tilde{\alpha}^*$	center of limit surface in deviatoric stress space
$\tilde{\alpha}^p$	center of strain memory surface in plastic strain space
$\Gamma$	scalar function in evolution of $q$
$\epsilon_1, \epsilon_3$	current maximum and minimum principal strains, respectively
$(\dot{\tilde{\epsilon}})_1, (\dot{\tilde{\epsilon}})_3$	current maximum and minimum principal strain rates, respectively
$\eta$	accumulated plastic strain
$\kappa$	asymptotic plastic modulus
$\bar{\kappa}$	cyclically stable value of $\kappa$
$\Lambda(q)$	memory loss-rate function
$\mu, \mu^*$	rate constants
$\dot{\mu}_\alpha$	scalar in kinematic hardening rule
$\tilde{\nu}$	unit normal in Mroz kinematic hardening rule
$\psi, \psi^*$	admissibility functions in isotropic hardening rules
$\psi_\kappa$	asymptotic plastic modulus admissibility function

#### Krieg's Model

$H', W_0, \gamma$	experimentally determined model parameters
$\tilde{N}$	approximated yield surface unit normal in deviatoric stress space
$R$	$\sqrt{2} k$ where $k$ is the shear yield strength

$\beta$	linearizing hardening parameter in isotropic and kinematic hardening rules
$\dot{\epsilon}_{eff}^p$	uniaxial equivalent value of $\dot{\tilde{\epsilon}}^p$
$\zeta$	approximate yield surface normal in deviatoric stress space
$\Lambda$	plastic modulus function in associated flow rule
$\tilde{\xi}^{tr}$	trial yield surface normal
$\tilde{\sigma}^{tr}$	trial stress tensor

#### Abrahamson's Model

$a_1, a_2, a_3,$ $b_1, b_2, b_3,$ $B, c, d_1, d_2,$ $k_0, m, p$	experimentally determined model parameters
$h_\alpha$	hardening term in kinematic hardening rule
$H(I_{\alpha\epsilon})$	isotropic hardening rate adjusting function
$K$	stress surface radius
$Q$	instantaneous measure of nonproportionality
$r_\alpha$	recovery term in kinematic hardening function
$w_2(K)$	recovery term in isotropic hardening function
$\tilde{\epsilon}^n$	inelastic strain tensor
$\dot{\epsilon}_{eff}^n$	uniaxial equivalent value of $\dot{\tilde{\epsilon}}^n$
$\Psi(\phi)$	nonproportional hardening function in isotropic hardening rule

## SUMMARY

Accurate fatigue life prediction of mechanical components subjected to high cyclic loads that cause nonlinear plastic deformation is becoming a design problem of prime importance in today's industry. This thesis compares four constitutive models for cyclic plasticity under conditions of nonproportional, multiaxial loading. It evaluates five numerical solution algorithms from the standpoints of computational accuracy and efficiency.

Drucker's one-surface theory, McDowell's two-surface theory, Krieg's one-surface theory with Radial-Return Integration Algorithm, and Abrahamson's state variable theory are the constitutive models that have been evaluated. Their transient hardening and stable loop responses are compared to experimental data in four different axial-torsional loading cases.

The Classical Runge-Kutta method with Gill Coefficients, Non-Iterative Adams Predictor-Corrector method, Euler's method with Automatic Step-Size Control, Iterative Adams Predictor-Corrector method with Automatic Step-Size Control, and Gear's method are the numerical solution algorithms considered in this study. Their computational efficiency and accuracy are evaluated for two cases of axial-torsional loading.

It is found that the one-surface theories predict with relatively good accuracy the stress-strain responses for proportional loading histories. They are not capable of predicting additional hardening due

to nonproportionality effects. Two-surface and state variable theories with repositories for nonproportional state variables predict rather accurately the material response to proportional and nonproportional loading paths. However, significantly increased computation times result from these gains in predictive accuracy.

For fixed step-size numerical methods like Runge-Kutta and Non-Iterative Adams, it is found that the integrated responses are quite accurate with significant reductions in computation times compared to Gear's method. For low-order, variable step-size methods such as Euler's and Iterative Adams, it is seen that their performance strongly depends on the nonproportionality level of the input history. They are computationally efficient for proportional type histories. Their computation times for nonproportional loadings make them cost-prohibitive as compared to Gear's method.

## CHAPTER I

### INTRODUCTION

#### Problem Definition

Design of mechanical components for finite fatigue life is becoming a common structural design problem encountered in industry today as more stringent design requirements and operating conditions place additional constraints in weight, safety, and reliability of the components to be built. The automotive, aerospace, and nuclear power industries are just a few examples of the areas of applicability of this design philosophy. New technologies are geared toward the design of parts to operate at high cyclic loads and/or high temperatures for a finite length of time. These extreme operating conditions inevitably cause plastic deformation that strongly affects the fatigue life and performance of the component being designed. Turbine engine blades and rocket motor nozzles are two typical examples of current areas of application of this technology where extreme operating temperatures, close dimensional tolerances to be kept, and weight constraints require expertise in design for plastic deformation and finite life. In the ground vehicle industry, it is common to include the effects of overloads which produce cyclic plastic deformation. Most analyses of fatigue failures involve the quantification of cyclic plasticity at critical locations which result in initiation and/or growth of microcracks.

Nonproportional, multiaxial, cyclic plasticity embraces the most general plasticity problem for time- and rate-independent phenomena. This theory is used in applications where the component's operating temperatures are low enough and/or strain rates are high enough to exclude time- and rate-dependent phenomena. At the present moment, cyclic plasticity models valid for the more restricted case of proportional loading are being used in finite element codes to predict plastic deformation behavior. In general, the problem is to predict the stress-strain response at every point of interest in a component or part subjected to cyclic loadings that cause significant plastic deformation. These loadings can be either uniaxial or multiaxial. For example, a simple tension test would impose a uniaxial stress field. Any stress tensor that contains more than one independent component is by definition multiaxial. Proportional loading (straining) is mathematically defined by

$$\dot{\underline{\underline{\epsilon}}}_r = \dot{r} \underline{\underline{\epsilon}}_0 \quad (1.1)$$

where  $\underline{\underline{\epsilon}}_0$  is a constant strain tensor,  $\dot{r}$  is a scalar rate parameter, and  $\dot{\underline{\underline{\epsilon}}}_r$  is the strain rate tensor. Figure 1-1 shows a schematic representation of a proportional loading path (a) and two nonproportional strain paths (b,c). Note that equation (1.1) requires that the strain tensor in nine-dimensional strain space be radial. Stated in words, a proportional loading path is that for which the individual components of the strain tensor change proportionally. Any other path is by definition nonproportional. Physically, a proportional

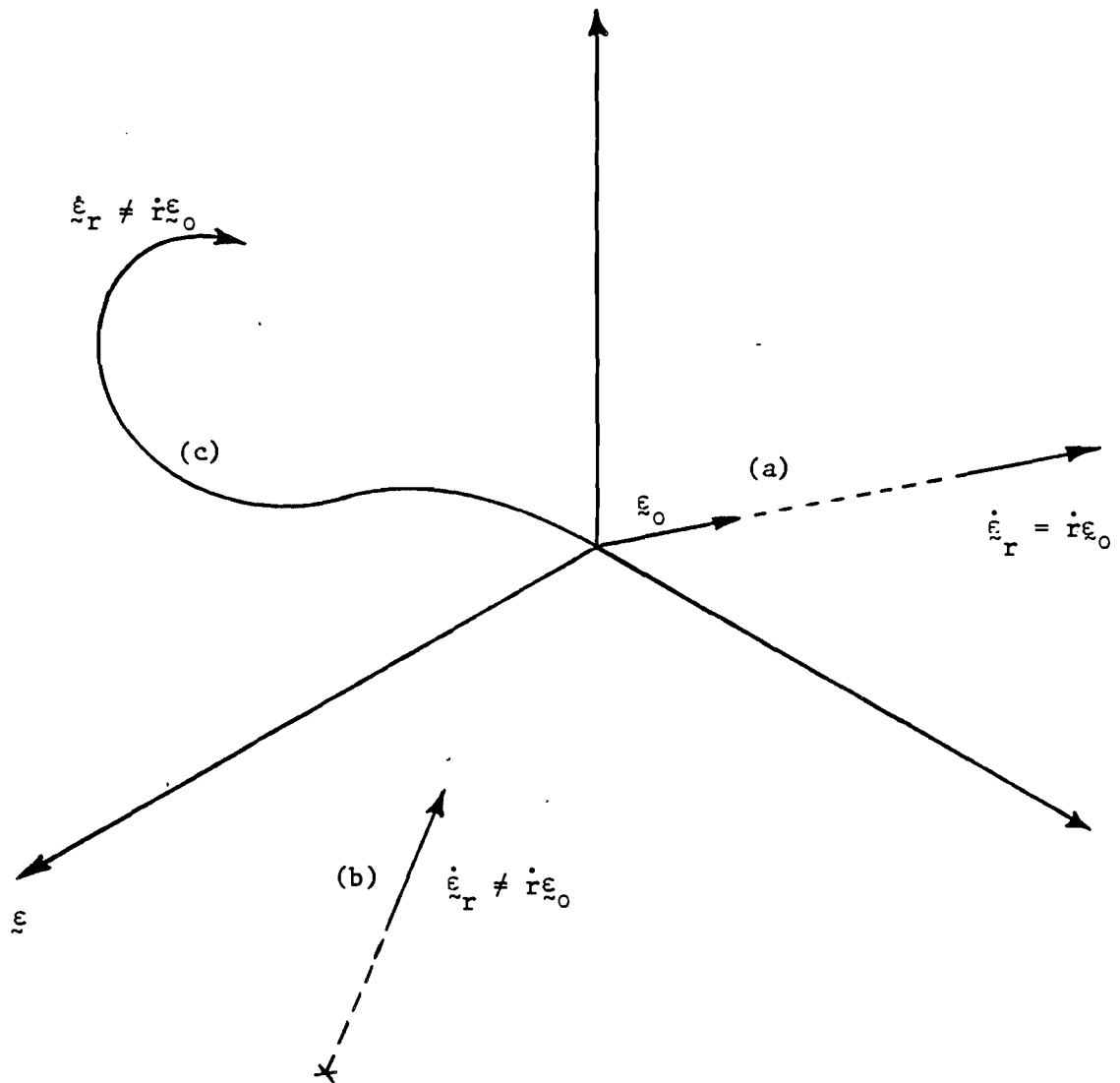


Figure 1-1. Nonproportional and Proportional Loading Paths in Strain Space. (a) proportional loading path; (b) linear nonproportional loading path; (c) nonlinear nonproportional loading path.

loading path activates a discrete set(s) of maximum shear strain planes with constant principal shear strain directions; a nonproportional path continuously changes the directions of maximum shear strain, resulting in an observed increase in hardening (McDowell, 1984f). Obviously, if a general loading case is to be analyzed, nonproportional loading effects have to be taken into account.

The effect of a nonproportional loading path on the predicted stress-strain response is currently an area of concentration for constitutive equations of metals. The dramatic increase in hardening due to nonproportional straining is caused, according to McDowell (1984f), by increased dislocation interactions. The activation of previously inactive slip systems, as the critical resolved shear stress direction is rotated via nonproportional loading, is responsible for the higher uniformity of deformation product observed in specimens. So, the nonproportional, multiaxial, cyclic plasticity problem can be approached from both micromechanical and phenomenological viewpoints.

Solutions for the time- and rate-independent case can give better insight into the solution of the general time- and rate-dependent plasticity and visco-plasticity problems. Hence, it is extremely important to accurately and efficiently (i.e. low cost) predict the stress-strain response for the nonproportional, multiaxial, cyclic plasticity problem.

#### Purpose and Outline of Work

There is a wide variety of cyclic plasticity models available in the literature. Most of the implemented models are capable of properly



modeling only uniaxial or proportional, multiaxial loadings. They are sometimes used for nonproportional straining without basis for knowing if the predicted results are accurate. This approach is less than desirable but has evolved from the lack of knowledge (experimental data) regarding nonproportional loading histories.

This study has two major objectives. First, it will evaluate several generic forms of proposed cyclic plasticity models with respect to their modeling capability for nonproportional, multiaxial, cyclic plasticity. Four different plasticity models will be evaluated and classified based on their accuracy in predicting the stress-strain response for an axial-torsional (biaxial) stress state. This test case was chosen for two reasons. There is extensive experimental data available to serve as the reference in the model evaluation process. Also, McDowell (1984e) has experimentally shown that these biaxial histories incorporate most of the relevant anomalous phenomena that characterizes nonproportional, multiaxial loading. In effect, such biaxial histories are the simplest yet most appropriate step to be followed in the transition from uniaxial to nonproportional, multiaxial straining. It is felt that once the biaxial loading case is fully understood and accurately predicted, the transition toward more complicated stress fields (e.g. triaxial) can be easily achieved.

The second objective of this study is to evaluate a series of numerical solution schemes for the models mentioned above with special attention to changes in the numerical behavior of these models when integrating proportional versus nonproportional histories. Five different ordinary differential equation solvers will be implemented and

categorized according to their computational accuracy and efficiency for each of the models discussed. Special emphasis will be placed on the analysis of the influences of nonproportionality on the integration procedures themselves. The significant coupling between material models and numerical solution schemes will be extensively investigated in this work. This study is intended to be a practical guide for plasticity model users in the selection of the most appropriate combination of material model and integration routine to be used for specific problems in the general area of nonproportional, multiaxial, cyclic plasticity. When dealing with structural cyclic plasticity problems via finite element analysis, a scheme which reduces computational time by 50% can mean thousands of dollars in savings in a single run. This work is the first known to the author to systematically compare several forms of constitutive equations with nonproportional, cyclic experimental results. Also, it is the first work known to critically investigate the behavior of numerical integration techniques for both proportional and nonproportional loadings.

In order to achieve this dual objective, this discussion has been written so that each chapter is somewhat independent. Chapter II presents the general equations, model characteristics, and some mathematical background necessary for the computer implementation of the four models discussed. Drucker's, McDowell's, Krieg's, and Abrahamson's models will be discussed in detail. These models were selected on the basis of their generic representation of the structure of three currently dominant approaches. A general overview of plasticity theory is presented as the introduction to Chapter II. Chapter III summarizes

the numerical integration techniques to be evaluated in the analysis section. Classical Runge-Kutta with Gill Coefficients, Non-Iterative Adams Predictor-Corrector, Euler's with Automatic Step-Size Control, Iterative Adams Predictor-Corrector with Automatic Step-Size Control, and Gear's methods will be discussed in general. The importance of considering coupled effects of material model and integration technique performance is highlighted throughout the chapter. Chapter IV analyzes the material models of chapter II and the integration routines of chapter III in the context of the axial-torsional loading problem. A general overview of the computer system utilized and evaluation procedure used is given early in the chapter. Descriptions of the axial-torsional test input histories are given for both material models and integration routines. Chapter V summarizes the results of chapter IV and classifies the material models and integration routines according to their capabilities. Appendix A is a summary of the axial-torsional forms of the models presented in chapter II. Model parameters, modeling functions, and material constants used in the numerical solution are also listed in this appendix. Appendix B presents general details on the experimental procedure used to gather the experimental data shown in this study. Appendix C deals with the evaluation of Euler's and Iterative Adams methods with automatic step-size control using an alternate error criterion. The results are compared to those shown in chapter IV.

## CHAPTER II

### MATERIAL MODELING: TIME- AND RATE-INDEPENDENT CYCLIC PLASTICITY

The main objective of the mathematical modeling of nonproportional, multiaxial, cyclic plasticity of metals is to predict, as accurately and as efficiently as possible, the inelastic material behavior considered relevant to the application at hand. Most room temperature cyclic plasticity problems encountered in industry today require that just a few aspects of nonlinear material behavior be accurately predicted. The most essential aspects of material behavior to be predicted were defined by Drucker and Palgen (1980) and McDowell (1984a) as:

1. Materials subjected to symmetric cycles of stress or strain will harden or soften until they reach a stable state described by stable hysteresis loops. Whether they harden or soften is dependent on the material and/or its initial state.
2. Materials subjected to unsymmetric cycles of stress in the plastic region will develop progressive deformation in the direction of the applied stress, a phenomenon called ratcheting.
3. Materials subjected to unsymmetric cycles of plastic strain will show stress relaxation toward a mean value of zero for the stress cycle.
4. Materials retain "memory" of prior deformation history which is dependent on the maximum plastic strain range and the degree of

nonproportionality of the previous loading paths.

5. Materials subjected to nonproportional loadings may harden to significantly higher values of stress compared to proportional loadings at the same strain range for cyclic hardening materials. Cross-hardening becomes more noticeable for nonproportional paths.

6. On elastic unloading and subsequent reversed loading, materials yield at stress levels significantly smaller than the current yield stress. This is called the Bauschinger effect.

With these requirements in mind, many researchers have tackled the problem of developing general constitutive equations. In so doing, two schools of thought developed. On one hand, the classical theories were developed which differentiated between plastic and creep strains. On the other hand, unified creep-plasticity models which did not make that distinction appeared. In this work, only time- and rate-independent responses will be considered. Hence, modifications of classical plasticity theories and some limited forms of unified creep-plasticity theories are appropriate for this case.

The classical models themselves can be divided into two groups: "simple" theories and "complex" theories. Their differences reside in the complexity of the concepts and equations used in the modeling process as well as their modeling capabilities. They relate increments of stress to the correspondent increments of strain and thus are called incremental theories. Generally, they have four basic components:

1. The yield surface, a convex surface in nine-dimensional stress space within which the material response is linearly elastic. During plastic flow it will be required that the stress point stay on the yield surface

(consistency condition). The von Mises and the Tresca yield surfaces are the most widely used forms.

2. The flow rule, an equation relating stress increments to increments of plastic strain during plastic flow. In essence, it requires that the plastic strain be in the direction of the outer normal to the yield surface.

3. The hardening rules, a set of equations governing the response of the yield surface in stress space due to a stress increment during plastic flow. The most popular hardening rules are either isotropic or kinematic or a combination of both. Isotropic hardening allows for the yield surface to expand or contract as plastic flow occurs. Kinematic hardening allows for pure translation of the yield surface to model deformation-induced anisotropy or the so-called Bauschinger effect. Many theories use combined isotropic and kinematic hardening in which the yield surface translates and expands/contracts as necessary during plastic flow.

4. The elastic constitutive equations. Since this study deals with isotropic, polycrystalline metals only, linear isotropic elasticity equations are appropriate.

The unified creep-plasticity models invoke a state variable approach. Usually, two or more state variables are used to predict the material response in the form of a system of ordinary differential equations relating stress, strain, temperature, and the chosen internal state variables. Linear isotropic elasticity is applicable in the elastic regime as in the classical models. However, according to Abrahamson (1983), there are some differences between the two

approaches:

1. The stress surface, a surface similar to the yield surface, is generally introduced in the model to define a region in stress space in which the material response will be nearly elastic, but not linearly elastic. The stress point is allowed to be outside of the stress surface in contrast to the yield surface concept.
2. The flow rule, an equation relating the stress increments to the given strain increments, is used to model both elastic and plastic material responses. As a consequence, these theories are characterized by the high stiffness of the resulting systems of ordinary differential equations.
3. The hardening rules, the equations governing the behavior of the stress surface, introduce temperature dependence in the form of added recovery terms. These equations allow for description of creep without distinction between creep and time-independent plastic strains. However, they are also restricted to isotropic and kinematic hardening/recovery as explained above.

With this introduction, the models to be considered in this study will be described. Four models from different categories will be described as follows:

1. Drucker's Model, a "simple" classical theory.
2. McDowell's Model, a "complex" classical theory.
3. Krieg's Model with Radial-Return Integration Algorithm, a "simple" classical theory.
4. Abrahamson's Model, a unified-creep plasticity theory.

The main features of each model will be described using the most

general form of their equations. Their possible advantages and disadvantages will be highlighted to serve as references for chapter IV. Each model will be specialized to its axial-torsional subspace form and implemented in a computer program to analyze its performance in predicting actual data.

#### Drucker's Model

This model was presented for the first time in 1980 by Drucker and Palgen as a relatively simple solution to a rather complex problem. It was intended to satisfy most of the material modeling requirements explained before with a model as simple as possible. Two versions of it were presented. The rounding corner option would predict smooth rounding of the cyclic stress-strain curves. The sharp corner option would predict the correct behavior on reloading after elastic unloading. The first option will be described in the lines to follow since it seemed to predict a more realistic material response for the experimental histories to be considered in this study.

According to Drucker and Palgen (1980), this model uses a von Mises yield surface (yield criterion) given by

$$f = \frac{1}{2}(\underline{s} - \underline{\alpha}) : (\underline{s} - \underline{\alpha}) - \frac{R^2}{3} = 0 \quad (2.1)$$

where  $\underline{s}$  is the deviatoric stress tensor,  $\underline{\alpha}$  is the deviatoric backstress tensor, and  $R$  is the current material yield strength for the uniaxial loading case. In this work, the colon represents the scalar product of two second order tensors.



This model assumes that the increment of plastic strain is always along the normal direction to the yield surface. Its associative flow rule is thus given by

$$\dot{\underline{\underline{\epsilon}}}^p = G \left( \frac{\partial f}{\partial \underline{\underline{\sigma}}} : \dot{\underline{\underline{\sigma}}} \right) \frac{\partial f}{\partial \underline{\underline{\sigma}}} \quad (2.2)$$

when  $f = 0$  and  $\dot{\underline{\underline{\sigma}}} : \partial f / \partial \underline{\underline{\sigma}} \geq 0$ , and where  $\dot{\underline{\underline{\epsilon}}}^p$  is the plastic strain rate tensor,  $G$  is a scalar multiplier, and  $\dot{\underline{\underline{\sigma}}}$  is the stress rate tensor;  $\dot{\underline{\underline{\epsilon}}}^p = 0$  for  $f < 0$  and/or  $\dot{\underline{\underline{\sigma}}} : \partial f / \partial \underline{\underline{\sigma}} < 0$ . Substituting equation (2.1) into (2.2) and assuming  $G$  to be of the form

$$G = A(J_2)^N \quad (2.3)$$

$$J_2 = \frac{1}{2} \underline{\underline{s}} : \underline{\underline{s}} \quad (2.4)$$

it may be shown that

$$\dot{\underline{\underline{\epsilon}}}^p = A(J_2)^N (\underline{\underline{s}} - \underline{\underline{\alpha}}) ((\underline{\underline{s}} - \underline{\underline{\alpha}}) : \dot{\underline{\underline{s}}}) \quad (2.5)$$

where  $A$  and  $N$  are material dependent model parameters.

A Ziegler-type kinematic hardening rule is assumed to be applicable. The center of the yield surface in deviatoric stress space, that is, the backstress tensor, is assumed to evolve according to the following equation:

$$\dot{\underline{\underline{\alpha}}} = \frac{1}{2k^2} (\underline{\underline{s}} - \underline{\underline{\alpha}}) ((\underline{\underline{s}} - \underline{\underline{\alpha}}) : \dot{\underline{\underline{s}}}) \quad (2.6)$$

where  $\underline{\alpha}$  is the backstress tensor and  $k$  is a model parameter that very closely resembles the material yield strength in shear. Equation (2.6) satisfies the consistency condition  $\dot{f} = 0$  during plastic flow with  $R$  taken to be a constant.

Isotropic hardening is achieved by effectively increasing or decreasing the plastic tangent modulus at a given stress level for the hardening or softening cases respectively. This is achieved by modifying equation (2.5) as

$$\dot{\underline{\epsilon}}^p = B \left( \frac{J_2}{\bar{\sigma}^2} \right)^N (\underline{s} - \underline{\alpha}) ((\underline{s} - \underline{\alpha}) : \dot{\underline{s}}) \quad (2.7)$$

where  $\bar{\sigma}$  is a normalizing stress dependent on the accumulated plastic work. The functional form of  $\bar{\sigma}$  was assumed to be of the following form:

$$\bar{\sigma} = \sigma^* (1 \mp \gamma \exp(-\frac{W^{pc}}{W_0})) \quad (2.8)$$

where

$$W^{pc} = \int_t (\underline{s} - \underline{\alpha}) : \dot{\underline{\epsilon}}^p dt \quad (2.9)$$

and  $\gamma$  and  $W_0$  are material dependent model parameters. The upper sign in equation (2.8) applies to hardening materials while the lower sign applies to softening materials. Note that  $W^{pc}$  is a direct measure of the accumulated effects due to plastic deformation; it is the accumulated plastic work. Due to the modifications of equations (2.7)-(2.9), it is necessary to redefine model parameter  $A$  as

$$A = \frac{B}{(\sigma^*)^{2N}} \quad (2.10)$$

Model parameters  $A$ ,  $N$ ,  $k$ ,  $\gamma$ , and  $W_0$  can be determined from uniaxial cyclic stress-strain curves and transient hardening cyclic hysteresis loops at a given maximum strain range. For more details on the determination of the model parameters the reader is referred to Drucker and Palgen (1980).

In the elastic regime, this model assumes that linear isotropic elasticity is valid. So, the stress rate tensor can be expressed as

$$\dot{\underline{\underline{\sigma}}} = \underline{\underline{C}} : (\dot{\underline{\underline{\epsilon}}} - \dot{\underline{\underline{\epsilon}}}^p) \quad (2.11)$$

where  $\underline{\underline{C}}$  is the fourth rank elasticity tensor for isotropic materials. Substituting equation (2.7) into (2.11) will allow a solution for the stress rate tensor, given the strain rate tensor and the current state.

This model was tested by Drucker and Palgen for the uniaxial loading case and it performed very nicely. However, it is unknown to the author if it has been tested for nonproportional multiaxial cyclic loadings. It is expected not to perform adequately because the model parameters are constants independent of maximum plastic strain range and nonproportionality levels. The model will not predict additional hardening due to nonproportionality effects.

For a detailed revision of the axial-torsional form of this model, the material constants, and the model parameters used, the reader is referred to Appendix A.

### McDowell's Model

This model was presented for the first time in 1984 by McDowell as a possible general solution to the nonproportional multiaxial cyclic plasticity problem based on the assumptions of time- and rate-independent plasticity theory. This theory belongs to the class of multiple-surface, modified classical theories. It is based on the concept of a yield surface within which the material response is elastic and a limit surface that "bounds" the material response during plastic flow. In this sense, it could be categorized as a "complex" theory.

According to McDowell (1984b), this model uses von Mises surfaces for the yield and limit surfaces of the following forms:

$$f = \frac{3}{2}(\underline{s} - \underline{\alpha}) : (\underline{s} - \underline{\alpha}) - R^2 = 0 \quad (2.12)$$

$$f^* = \frac{3}{2}(\underline{s}^* - \underline{\alpha}^*) : (\underline{s}^* - \underline{\alpha}^*) - R^{*2} = 0 \quad (2.13)$$

where  $\underline{s}$  is the deviatoric stress tensor,  $\underline{\alpha}$  is the center of the surface in deviatoric stress space (backstress tensor), and  $R$  is the radius of the surface. The asterisk superscript refers to the limit surface.

The flow rule for this model is given by

$$\dot{\underline{\epsilon}}^p = \frac{1}{h}(\dot{\underline{s}} : \underline{n})\underline{n} \quad (2.14)$$

where  $h$  is the plastic modulus,  $\underline{n}$  is the unit normal to the yield surface,  $\dot{\underline{s}}$  is the deviatoric stress rate tensor, and  $\dot{\underline{\epsilon}}^p$  is the plastic strain rate tensor. In essence, the plastic strain rate tensor is normal

to the yield surface as in Drucker's model.

This model has isotropic and kinematic hardening rules for the yield and limit surfaces. For the yield surface, a Mroz-type kinematic hardening rule is assumed:

$$\dot{\tilde{\alpha}} = \dot{\mu}_{\alpha} \tilde{\nu} \quad (2.15)$$

$$\tilde{\nu} = \frac{(\tilde{s}^* - \tilde{s})}{\|\tilde{s}^* - \tilde{s}\|} \quad (2.16)$$

$$\dot{\mu}_{\alpha} = \frac{((\tilde{s} - \tilde{\alpha}) : \dot{\tilde{s}} - \frac{2}{3} R \dot{R})}{(\tilde{s} - \tilde{\alpha}) : \tilde{\nu}} \quad (2.17)$$

where  $\dot{\tilde{\alpha}}$  is the backstress rate tensor,  $\tilde{\nu}$  is the unit vector from  $\tilde{s}$  to  $\tilde{s}^*$ , and  $\dot{\mu}_{\alpha}$  is a scalar function determined by applying the consistency condition,  $\dot{f} = 0$ , to the yield surface. The term  $\dot{R}$  represents isotropic hardening of the yield surface. Note that  $\tilde{s}^*$  is defined as the point at the limit surface with the same outward normal as the yield surface at the current stress state:

$$\tilde{s}^* = \tilde{\alpha}^* + (\tilde{s} - \tilde{\alpha}) \frac{R}{R}^* \quad (2.18)$$

For the limit surface, a Prager-Ziegler type kinematic hardening rule is assumed as

$$\dot{\tilde{\alpha}}^* = \kappa \dot{\eta} \tilde{\eta} \quad (2.19)$$

$$\dot{\bar{\eta}} = (\dot{\bar{\epsilon}}^p : \dot{\bar{\epsilon}}^p)^{1/2} = \| \dot{\bar{\epsilon}}^p \| \quad (2.20)$$

where  $\dot{\bar{\alpha}}^*$  is the backstress rate tensor,  $\kappa$  is the asymptotic modulus,  $\bar{n}$  is the yield surface unit normal given by  $(\bar{s}-\bar{\alpha})/\|\bar{s}-\bar{\alpha}\|$ , and  $\dot{\bar{\eta}}$  is the norm of the plastic strain rate tensor.

The isotropic hardening rules for the yield and limit surfaces have been similarly defined. For the yield and limit surfaces,

$$\dot{\bar{R}} = \mu(\bar{R}(\phi, q) - R)\dot{\bar{\eta}} \quad (2.21)$$

$$\dot{\bar{R}}^* = \mu(\bar{R}^*(\phi, q) - R^*)\dot{\bar{\eta}}^* \quad (2.22)$$

where  $\bar{R}(\phi, q)$  and  $\bar{R}^*(\phi, q)$  correspond to the cyclically stable values of the yield and limit surface radii for the given values of state variables  $\phi$  and  $q$ . State variables  $\phi$  and  $q$  have been introduced in the model to account for nonproportionality and maximum plastic strain range effects, respectively, and will be discussed later.  $\psi$  and  $\psi^*$  are admissibility functions chosen appropriately for the material being used. For non-fading memory of cyclically hardening materials, McDowell recommends to use Heaviside functions  $\psi = u(\bar{R}(\phi, q) - R)$  and  $\psi^* = u(\bar{R}^*(\phi, q) - R^*)$ . For completely fading memory, McDowell recommends  $\psi = \psi^* = 1$ . In equations (2.21) and (2.22),  $\mu$  is a scalar rate parameter experimentally determined from the transient hysteresis response of the material.

McDowell, through experimental testing, has shown that  $\bar{R}(\phi, q)$  and  $\bar{R}^*(\phi, q)$  can be expressed approximately as linear functions of the form

$$\bar{R}(\phi, q) = \phi(\bar{R}(1, q) - \bar{R}(0, q)) + \bar{R}(0, q) \quad (2.23)$$

$$\bar{R}^*(\phi, q) = \phi(\bar{R}^*(1, q) - \bar{R}^*(0, q)) + \bar{R}^*(0, q) \quad (2.24)$$

where  $\bar{R}(1, q)$ ,  $\bar{R}(0, q)$ ,  $\bar{R}^*(1, q)$ , and  $\bar{R}^*(0, q)$  can be experimentally determined. For greater detail on the determination of the model parameters the reader is referred to McDowell (1984c).

An evolution equation for the asymptotic plastic modulus can be written as

$$\dot{\bar{\kappa}} = \mu(\bar{\kappa}(\phi, q) - \kappa) \psi_{\kappa} \dot{\eta} \quad (2.25)$$

where  $\bar{\kappa}(\phi, q)$  corresponds to the cyclically stable values of the asymptotic modulus for given values of variables  $\phi$  and  $q$ .  $\psi_{\kappa}$  is an admissibility function similar to  $\psi$  and  $\psi^*$  which must be experimentally determined. Following the reasoning behind equations (2.23) and (2.24), it is assumed that

$$\bar{\kappa}(\phi, q) = \phi(\bar{\kappa}(1, q) - \bar{\kappa}(0, q)) + \bar{\kappa}(0, q) \quad (2.26)$$

where  $\bar{\kappa}(0, q)$  and  $\bar{\kappa}(1, q)$  can be experimentally determined. With all these parameters known, an experimentally determined function for the plastic modulus can be written as shown in Appendix A.

The most desirable attributes of this model are its capability to accurately predict nonproportionality effects as well as memory of maximum plastic strain range. McDowell (1983) has defined an instantaneous measure of nonproportionality of the loading path as

$$J = \left| \frac{\frac{d}{dt}(\epsilon_1 - \epsilon_3)}{g((\dot{\epsilon})_1 - (\dot{\epsilon})_3)} \right| \quad (2.27)$$

where  $\epsilon_1$  and  $\epsilon_3$  are the largest and smallest principal strains, and  $(\dot{\epsilon})_1$  and  $(\dot{\epsilon})_3$  are the largest and smallest principal strain rates. Here  $g$  is defined as  $g(x) = 1$ , if  $x = 0$  or  $g(x) = x$  if  $x \neq 0$ . It may be proved that for radial or proportional loading paths equation (2.27) gives  $J = 1$ . For the case of sinusoidal tension-torsion tests with a shear to axial strain amplitude ratio of  $\gamma_a/\epsilon_a = (1 + \nu)$  and 90 degrees out-of-phase, equation (2.27) gives  $J = 0$ . This sinusoidal loading path has been experimentally shown to be highly nonproportional in terms of additional hardening.

To be able to account for accumulated effects of nonproportional paths, McDowell (1983) introduced a state variable  $\phi$  which evolves according to

$$\dot{\phi} = \mu^* (1 - J - \phi) \dot{\eta} u(1 - J - \phi_{\text{limit}}) \quad (2.28)$$

where  $\mu^*$  is an experimentally determined scalar parameter and  $u(1-J-\phi_{\text{limit}})$  is a Heaviside function introduced to reduce the effects of proportional path segments in the evolution of  $\phi$ . It can be shown that for proportional straining  $\phi = 0$  while for sinusoidal straining with a phase angle of 90 degrees,  $\phi = 1$ .

To account for memory of maximum plastic strain range, McDowell (1983) also introduced a state variable  $q$  equal to the radius of a strain memory surface in nine-dimensional plastic strain space. For this



surface he also introduced kinematic and isotropic hardening rules. This surface was defined in second invariant form as

$$F = \frac{2}{3}(\underline{\underline{\epsilon}}^P - \underline{\underline{\alpha}}^P) : (\underline{\underline{\epsilon}}^P - \underline{\underline{\alpha}}^P) - q^2 = 0 \quad (2.29)$$

where  $\underline{\underline{\alpha}}^P$  is the center of the strain memory surface in plastic strain space and  $q$  is its current radius. The kinematic hardening rule assumed was of the following form:

$$\dot{\underline{\underline{\alpha}}}^P = \frac{H(F)}{2} (\dot{\underline{\underline{\epsilon}}}^P : \underline{\underline{n}}^*) \underline{\underline{n}}^* \quad (2.30)$$

where  $\dot{\underline{\underline{\alpha}}}^P$  is the time rate of change of position of the center of the strain memory surface,  $H(F) = 1$  if  $F = 0$  and  $H(F) = 0$  if  $F < 0$ , and  $\underline{\underline{n}}^*$  is the unit normal to the strain memory surface at the current state of plastic strain. Its isotropic hardening rule was assumed to be of the following form:

$$\dot{q} = \left( \frac{1}{2} H(F) \Gamma \sqrt{\frac{2}{3}} - \Lambda(q) \right) \dot{\eta} \quad (2.31)$$

where  $\Gamma$  is a scalar parameter and  $\Lambda(q)$  is a function to account for fading memory of maximum plastic strain range. In general, this function has to be experimentally determined. Applying the consistency condition  $\dot{F} = 0$  during plastic flow when the plastic strain point lies on  $F$ , it may be shown that

$$\Gamma = \underline{\underline{n}}^* : \dot{\underline{\underline{n}}}^* + \sqrt{6} \Lambda(q) \quad (2.32)$$

Equations (2.12)-(2.32) make up the main body of McDowell's two-surface theory. However, there are many model parameters and functions that must be experimentally determined. These details are outside the scope of this study and the reader is referred to McDowell (1983,1984b,1984c) for greater details.

As in Drucker's model, one of the assumptions is that linear elasticity is applicable in the elastic regime. By substituting equation (2.14) into equation (2.11) and recognizing that  $\underline{\underline{s}} = \underline{\underline{\sigma}} - \frac{1}{3}(\underline{\underline{\sigma}}:\underline{\underline{I}})\underline{\underline{I}}$  where  $\underline{\underline{I}}$  is the identity tensor, it may be shown that

$$\dot{\underline{\underline{s}}} = 2G(\dot{\underline{\underline{\epsilon}}} - \frac{1}{3}(\dot{\underline{\underline{\epsilon}}}:\underline{\underline{I}})\underline{\underline{I}} - \frac{2G}{h + 2G}(\dot{\underline{\underline{\epsilon}}}:\underline{\underline{n}})\underline{\underline{n}}) \quad (2.33)$$

where  $G$  is the shear modulus and  $h$  is a function defining the plastic modulus.

This model has already been tested for proportional and nonproportional multiaxial cyclic plasticity by McDowell (1984b). It was shown that it predicts accurately most of the relevant aspects of the material response as described at the beginning of this chapter. However, there are two significant inconveniences to this model. Firstly, it requires a great deal of experimental tests to be run so that all model parameters and modeling functions be determined for each different material. This is time consuming and expensive. Secondly, due to the complexity and the number of ordinary differential equations to be solved, finding a solution will require considerably longer computation times when compared to simple theories.

Appendix A shows a summary of the axial-torsional form of this

model, its material constants, the model parameters, and the modeling functions used.

#### Krieg's Model with Radial-Return Integration Algorithm

This model belongs to the class of "simple" classical theories for the time- and rate-independent cyclic plasticity problem. However, by using a radial-return algorithm to solve these equations, it has been separated from the rest of its group. It was introduced by Krieg and Key in 1976 as a fast yet accurate model to be used in applications of the finite element method to the solution of problems where significant plastic deformation occurs. The intention was to present a set of constitutive equations with a good balance of predictive accuracy and computational efficiency.

According to Hughes (1983), this model assumes a von Mises yield surface of the form given by equation (2.1). In order to implement the radial-return algorithm, Krieg and Key introduced a trial stress rate tensor given by

$$\dot{\underline{\underline{\sigma}}}^{\text{tr}} = \underline{\underline{C}} : \dot{\underline{\underline{\epsilon}}} \quad (2.34)$$

where  $\underline{\underline{C}}$  is the fourth rank elasticity tensor and  $\dot{\underline{\underline{\epsilon}}}$  is the total strain rate tensor. In essence, equation (2.34) gives a pseudo-elastic stress increment.

As with other models, it is assumed that the plastic strain rate tensor is along the normal to the yield surface. So, the flow rule is expressed as

$$\dot{\tilde{\epsilon}}^P = \Lambda \tilde{N} \quad \text{if } f = 0 \text{ and } \dot{\tilde{\sigma}}^{tr} : \tilde{N} \geq 0 \quad (2.35)$$

$$\dot{\tilde{\epsilon}}^P = 0 \quad \text{if } f < 0 \text{ or } f = 0 \text{ and } \dot{\tilde{\sigma}}^{tr} : \tilde{N} < 0$$

where  $\Lambda$  is found by applying the consistency condition during plastic flow and  $\tilde{N}$  is the unit normal to the yield surface at the beginning of the time step as approximated by the radial-return algorithm. It can be shown that  $\Lambda$  is given by

$$\Lambda = \frac{1}{2G} \left( \frac{1}{1 + \frac{H'}{3G}} \right) \dot{\tilde{\sigma}}^{tr} : \tilde{N} \quad (2.36)$$

where  $H'$  is the cyclically stable value of the asymptotic plastic modulus of the material at the maximum plastic strain range of interest. This value has to be experimentally determined.

Isotropic and kinematic hardening are assumed to be necessary to appropriately model the material behavior. Krieg and Key assumed a linear combination of isotropic and Prager-type kinematic hardening or softening as given by a model parameter  $\beta$ . Kinematic and isotropic hardening were given by

$$\dot{\tilde{\alpha}} = \frac{2}{3} (1 - \beta) H' \dot{\tilde{\epsilon}}^P \quad (2.37)$$

$$\dot{\tilde{R}} = \sqrt{\frac{2}{3}} \beta H' \dot{\tilde{\epsilon}}_{eff}^P \quad (2.38)$$

where  $\dot{\tilde{\alpha}}$  is the time rate of change of the backstress tensor,  $\dot{\tilde{R}}$  is the

time rate of change of  $R$  (which is given by  $R = \sqrt{2} k$ ),  $\beta$  is the linearizing parameter, and  $\dot{\epsilon}_{eff}^p$  is given by

$$\dot{\epsilon}_{eff}^p = \left( \frac{2}{3} \dot{\epsilon}^p : \dot{\epsilon}^p \right)^{1/2} \quad (2.39)$$

Note that in this model  $k$  corresponds to the material shear yield strength in a similar way as in Drucker's model.

Note that  $\beta$  is a constant that is experimentally determined as pointed out by Key, Krieg, and Stone (1981). This constant is determined by the reversed-loading yield stress in a simple cyclic experiment (Bauschinger effect). However, by letting  $\beta$  be a constant, it is assumed that no saturation of the cyclic stress-strain response occurs as the material hardens or softens. Obviously, this violates point one of the essential material behavior to be modeled as described at the beginning of this chapter. In view of this, it seemed necessary to modify Krieg's model so that it could be fairly evaluated against the other three models presented in this study.

The modification was quite simple. The linearizing parameter  $\beta$  was made a function of the accumulated plastic work. As pointed out by Drucker and Palgen (1980), this is a reasonable assumption. Thus, similarly to equations (2.8) and (2.9), it is assumed that

$$W^{DC} = \int_t (\bar{s} - \bar{\alpha}) : \dot{\epsilon}^p dt \quad (2.40)$$

$$\beta = \gamma \exp\left(-\frac{W^{DC}}{W_0}\right) \quad (2.41)$$

where  $w^{PC}$  is the accumulated plastic work,  $\gamma$  and  $w_0$  are model parameters that must be experimentally determined, and  $\underline{s}$  and  $\underline{\alpha}$  are the deviatoric parts of the stress and backstress tensors respectively.

Krieg and Key (1976) applied the radial-return numerical integration technique to the system of differential equations given by equations (2.34)-(2.39). Including equations (2.40)-(2.41) and applying this algorithm, the system of ordinary differential equations becomes:

$$\underline{\sigma}_{n+1}^{tr} = \underline{\sigma}_n + \underline{C} : \Delta \underline{\epsilon} \quad (2.42)$$

$$\underline{\xi}_{n+1}^{tr} = \underline{\sigma}_{n+1}^{tr} - \underline{\alpha}_n \quad (2.43)$$

$$\underline{\zeta} = \underline{\xi}_{n+1}^{tr} - \frac{1}{3}(\text{trace } \underline{\xi}_{n+1}^{tr})\underline{I} \quad (2.44)$$

with the elastic loading case given by

$$\underline{\epsilon}_{n+1}^p = \underline{\epsilon}_n^p \quad (2.45)$$

$$\underline{\sigma}_{n+1} = \underline{\sigma}_{n+1}^{tr} \quad (2.46)$$

$$\underline{\alpha}_{n+1} = \underline{\alpha}_n \quad (2.47)$$

$$R_{n+1} = R_n \quad (2.48)$$

$$w_{n+1}^{PC} = w_n^{PC} \quad (2.49)$$

$$\beta_{n+1} = \beta_n \quad (2.50)$$

and the plastic loading case given by

$$\Lambda = \frac{1}{2G} \left( \frac{1}{1 + \frac{H'}{3G}} \right) (\|\tilde{\zeta}\| - R_n) \quad (2.51)$$

$$\tilde{\epsilon}_{n+1}^p = \tilde{\epsilon}_n^p + \Lambda \tilde{N} \quad (2.52)$$

$$\tilde{\sigma}_{n+1} = \tilde{\sigma}_{n+1}^{tr} - 2G\Lambda\tilde{N} \quad (2.53)$$

$$\tilde{\alpha}_{n+1} = \tilde{\alpha}_n + \frac{2}{3}(1 - \beta)H'\Lambda\tilde{N} \quad (2.54)$$

$$R_{n+1} = R_n + \frac{2}{3}\beta H'\Lambda \quad (2.55)$$

$$w_{n+1}^{pc} = w_n^{pc} + \Lambda(\tilde{s}_{n+1} - \tilde{\alpha}_{n+1}) : \tilde{N} \quad (2.56)$$

where  $\tilde{\zeta}$  is a tensor approximately normal to the yield surface,  $\tilde{I}$  is the identity tensor,  $\Delta\tilde{\epsilon}$  is the increment in the total strain tensor,  $\|\tilde{\zeta}\|$  is the norm of the tensor  $\tilde{\zeta}$ , and  $\tilde{N} = \tilde{\zeta}/\|\tilde{\zeta}\|$  is the approximated unit normal to the yield surface in deviatoric stress space. Subscripts  $n$  and  $n+1$  refer to the values at the beginning and at the end of the current time step.

It must be emphasized that equations (2.42)-(2.56) include Krieg's simplified model equations, the introduced modification, and the numerical integration algorithm to be used to solve this system. The form of equations (2.42)-(2.56) is such that if all dependent variables at time  $t_n$  are known, their values at the next time step can be calculated with no need of a differential equation solver routine. In essence, an Euler type ordinary differential equation solver is used by expressing (2.42)-(2.56) in their time-discretized form. It is possible

to solve equations (2.34)-(2.41) without using the radial-return algorithm. However, the author deemed it unnecessary due to the existing similarities between this model and Drucker's model; no new information would be gained.

This model will be analyzed from two different points of view. Firstly, its modeling capabilities will be compared to the other three models presented in this study. It is expected to behave similarly to Drucker's model including its inability to correctly predict plastic material behavior when subjected to nonproportional loading paths. Secondly, its computational characteristics will be compared against some standard numerical integration techniques. Due to the simplicity of equations (2.42)-(2.56), it is expected that the radial-return algorithm will present significantly reduced computation times. However, one subtle problem can be immediately seen: the radial-return equations are model-dependent and, therefore, they have to be rederived for each model to be solved. For complex models like McDowell's and Abrahamson's this might be a quite difficult task.

For a detailed version of this model as specialized to the axial-torsional subspace, its model parameters, and the material constants used, the reader is referred to Appendix A.

#### Abrahamson's Model

This model is the result of the application of a two state variable unified creep-plasticity theory to the time- and rate-independent nonproportional, multiaxial, cyclic plasticity problem. It was presented by Abrahamson in 1983 to show the wide range of



applications of unified creep-plasticity models. Although quite general in scope, such unified theories result in highly stiff systems of ordinary differential equations with the capability to model elastic, plastic, time- and rate-independent, and time- and rate-dependent material behavior.

According to Abrahamson (1983), the multiaxial form of this theory can be generalized from the uniaxial case. By definition he used

$$\sigma_{eff} = \left( \frac{3}{2} (\underline{s} - \underline{\alpha}) : (\underline{s} - \underline{\alpha}) \right)^{1/2} \quad (2.57)$$

$$\alpha_{eff} = \left( \frac{3}{2} \underline{\alpha} : \underline{\alpha} \right)^{1/2} \quad (2.58)$$

where  $\underline{s}$  is the deviatoric stress tensor,  $\underline{\alpha}$  is the center of the stress surface in deviatoric stress space, and  $\sigma_{eff}$  and  $\alpha_{eff}$  are the uniaxial equivalent values of stress and backstress, respectively.

The magnitude of the inelastic strain rate tensor is a highly nonlinear function given by

$$\dot{\epsilon}_{eff}^n = a \left( \frac{\sigma_{eff}}{K} \right)^p \quad (2.59)$$

where  $a$  and  $p$  are model parameters and  $K$  is the current radius of the stress surface. Note that this is a scalar equation in which the flow stress is rate-dependent. Similar to classical theories, it is assumed that the direction of the inelastic strain rate tensor is normal to the stress surface. Thus, the flow rule can be expressed as

$$\dot{\tilde{\epsilon}}^n = \frac{3}{2} \left( \frac{\dot{\tilde{\epsilon}}_{eff}^n}{\sigma_{eff}} \right) (\tilde{s} - \tilde{\alpha}) \quad (2.60)$$

As explained in the beginning of the the chapter, this theory uses both isotropic and kinematic hardening rules characterized by the presence of hardening and recovery terms. The hardening terms represent the hardening due to dislocation interactions as plastic flow occurs. The recovery terms represent the effects of recovery processes that become significant as temperature increases. It can be shown that the recovery terms are negligible in modeling the room-temperature tests considered in this study.

Kinematic hardening is achieved by a function of the form

$$\dot{\tilde{\alpha}} = h_{\alpha}(\alpha_{eff}) \dot{\tilde{\epsilon}}^n - \frac{r_{\alpha}(\alpha_{eff})}{B^p} \tilde{\alpha} \quad (2.61)$$

where  $\dot{\tilde{\alpha}}$  is the time rate of change of the center of the stress surface,  $B$  is a temperature correction factor, and  $h_{\alpha}(\alpha_{eff})$  and  $r_{\alpha}(\alpha_{eff})$  are the hardening and recovery functions assumed for the material being modeled. Abrahamson (1983) showed that the following forms are appropriate for these functions:

$$h_{\alpha}(\alpha_{eff}) = \begin{cases} \frac{\exp(-d_2 \alpha_{eff})}{d_1} & \text{if } \dot{\tilde{\epsilon}}^n : \tilde{\alpha} \geq 0 \\ \frac{1}{d_1} & \text{if } \dot{\tilde{\epsilon}}^n : \tilde{\alpha} < 0 \end{cases} \quad (2.62)$$

$$r_{\alpha}(\alpha_{\text{eff}}) = c(\alpha_{\text{eff}})^m \quad (2.63)$$

where  $d_1$ ,  $d_2$ ,  $c$ , and  $m$  are model parameters to be determined experimentally.

The isotropic hardening is achieved by a function of the form

$$\dot{K} = \frac{H(I_{\alpha\epsilon})}{(\psi(\phi))^{1/2}} (\psi(\phi)\alpha_{\text{eff}} - w_2(K))\dot{\epsilon}_{\text{eff}}^n \quad (2.64)$$

where  $\dot{K}$  is the time rate of change of the stress surface radius,  $\psi(\phi)$  is a function that accounts for nonproportionality effects,  $w_2(K)$  is a recovery term, and  $H(I_{\alpha\epsilon})$  is an assumed function necessary to adjust the isotropic hardening rate.

Based on experimental analysis Abrahamson (1983) proposed the following functions for the recovery term  $w_2(K)$  and the adjustment term  $H(I_{\alpha\epsilon})$ :

$$w_2(K) = b_1(b_2 K)^{b_3} \quad (2.65)$$

$$H(I_{\alpha\epsilon}) = \frac{1}{a_1 a_3 \exp(a_1(K - k_0))} \quad (2.66)$$

where  $b_1$ ,  $b_2$ ,  $b_3$ ,  $a_1$ ,  $a_3$  and  $k_0$  are all model parameters to be determined from experimental results.

The function  $\psi(\phi)$  was introduced by Abrahamson to his original model in order to account for the observed increase in hardening for nonproportional loading paths. In his work, Abrahamson used McDowell's

original formulation for the nonproportional state variable  $\phi$ , that is,

$$\phi = \frac{\int_{t_0}^t u(Q_0 - Q) \dot{\epsilon}_{eff}^n Q dt}{\int_{t_0}^t u(Q_0 - Q) \dot{\epsilon}_{eff}^n dt} \quad (2.67)$$

where  $Q$  is exactly equivalent to  $J$  in equation (2.27). In later research, McDowell (1984b) suggested a rate formulation for  $\phi$  as given by equation (2.28). Striving for better results, the author modified Abrahamson's model by using equation (2.28) instead of (2.67) to define  $\phi$ . In view of this change, it was necessary to also change Abrahamson's definition of  $\psi(\phi)$  to the following final form:

$$\psi(\phi) = \exp(4\phi) \quad (2.68)$$

Equations (2.57)-(2.68) form the main body of Abrahamson's model. The procedures to follow for the experimental determination of all the model parameters are explained by Abrahamson (1983) and the reader is referred to him for greater details.

Linear isotropic elasticity is also valid in Abrahamson's model. Assuming  $\underline{\epsilon} = \underline{\epsilon}^e + \underline{\epsilon}^n$  where  $\underline{\epsilon}^e$  is the elastic strain tensor, and substituting equation (2.60) into equation (2.11), the stress rate tensor can be expressed as a function of total strain and the current stress state.

This model in its original form has already been tested for nonproportional multiaxial cyclic plasticity problems. According to

Abrahamson (1983), it predicted to a good first approximation the essential aspects of material behavior that were mentioned at the beginning of this chapter. However, no comments are ever made regarding the computational difficulties that may arise from this highly stiff system of ordinary differential equations. This is seen as one of the critical aspects to be considered in the analysis of unified creep-plasticity theories like this one. Another inconvenience of this model is the tremendous amount of experimental work necessary to determine all the model parameters.

It should be noted that the modified Abrahamson model will go through its first test in this study. For greater details on the axial-torsional form of this model and the corresponding model parameter values, the reader is referred to Appendix A.

## CHAPTER III

## NUMERICAL INTEGRATION TECHNIQUES

Once the different material models have been described, it is necessary to expand on the five numerical integration algorithms used by the author to solve the different systems of ordinary differential equations encountered in this study. The selection of the appropriate numerical solution technique is as critical as the selection of the correct material model. The success in the implementation of any material model depends heavily on the accuracy and efficiency of the solution technique used. Likewise, the performance of the numerical solution technique strongly depends on the numerical behavior of the model to be solved.

In general, the problem is to solve an initial value problem given by a system of ordinary differential equations and the prescribed initial conditions. Mathematically this can be represented as

$$\dot{\tilde{X}} = \tilde{F}(\tilde{X}, t) \quad (3.1)$$

$$\tilde{X}(0) = \tilde{X}_0 \quad (3.2)$$

where  $t$  is the independent variable,  $\tilde{X}$  is the vector of dependent variables, and  $\tilde{F}$  is the vector of functions relating them.

For the time- and rate-independent strain-controlled plasticity

problem, the actual independent variable is the total strain tensor  $\underline{\epsilon}$ . However, the author decided to use time as the independent variable in this study with  $\underline{\epsilon}$  implicitly assumed to be the independent variable. This change was implemented to allow for the introduction of time- and rate-dependent phenomenon to the material model equations. For the models presented in chapter II, the dependent variables are generally the deviatoric stress tensor  $\underline{s}$ , the deviatoric backstress tensor  $\underline{\alpha}$ , the plastic strain tensor  $\underline{\epsilon}^p$ , and the chosen state variables.

The number of numerical integration techniques available for the solution of initial value problems is tremendous. According to Carnahan et. al. (1969), these techniques can be classified in many categories. For example, these methods can be one-step or multiple-step, explicit or implicit, iterative or non-iterative, variable-order or fixed-order, variable step-size or fixed step-size, etc.

This study is concentrated on the integration techniques that seem best suited for the solution of cyclic plasticity problems. The selection was made based on previous research work by others and the author's personal experience. Thus, the following numerical integration techniques were implemented, each one belonging to a different class:

1. Classical Runge-Kutta Method with Gill coefficients, a multiple-step, explicit, non-iterative, fixed-order, fixed step-size method.
2. Euler's Method with Automatic Step-Size Control, a one-step, explicit, non-iterative, fixed-order, variable step-size method.
3. Iterative Adams Predictor-Corrector Method with Automatic Step-Size Control, a one-step, explicit, iterative, fixed-order, variable step-size method.

4. Non-iterative Adams Predictor-Corrector Method, a multiple-step, explicit, non-iterative, fixed-order, fixed step-size method.
5. Gear's Method, a multiple-step, implicit, iterative, variable-order, variable step-size method.

Each integration technique will be described in its most general form, that is, with its equations expressed in vector form. The error control criteria either for step-size changes and/or determination of iterative convergence will also be described. The performance characteristics of each method will be briefly mentioned. Special emphasis will be placed on issues such as computation time, accuracy of solution, complexity of coding, and data storage requirements.

#### Classical Runge-Kutta Method with Gill Coefficients

Runge-Kutta methods have been widely used in the solution of systems of ODE's (Ordinary Differential Equations) that are characterized by their relatively low stiffness. There is a whole family of Runge-Kutta methods but of particular interest is the version as modified by Gill (1950). This method has been organized to require the least amount of data storage at any time step of any of the Runge-Kutta type formulae.

According to Gill (1950), the step-by-step procedure for the solution of a system of ODE's, denoting  $\underline{X}$  at time  $t = t^n$  by  $\underline{X}(t^n) = \underline{X}^n$ , is given by:



$$\underline{g}_0 = \begin{cases} 0 & \text{for } t^n = 0 \\ \underline{g}_4^{n-1} & \text{for } t^n > 0 \end{cases} \quad (3.3)$$

$$\underline{k}_1 = hF(\underline{X}^n, t^n) \quad (3.4)$$

$$\underline{X}_1 = \underline{X}^n + \frac{1}{2}(\underline{k}_1 - 2\underline{g}_0) \quad (3.5)$$

$$\underline{g}_1 = \underline{g}_0 + \frac{3}{2}(\underline{k}_1 - 2\underline{g}_0) - \frac{1}{2}\underline{k}_1 \quad (3.6)$$

$$\underline{k}_2 = hF(\underline{X}_1, t^n + \frac{h}{2}) \quad (3.7)$$

$$\underline{X}_2 = \underline{X}_1 + (1 - \sqrt{\frac{1}{2}})(\underline{k}_2 - \underline{g}_1) \quad (3.8)$$

$$\underline{g}_2 = \underline{g}_1 + 3(1 - \sqrt{\frac{1}{2}})(\underline{k}_2 - \underline{g}_1) - (1 - \sqrt{\frac{1}{2}})\underline{k}_2 \quad (3.9)$$

$$\underline{k}_3 = hF(\underline{X}_2, t^n + \frac{h}{2}) \quad (3.10)$$

$$\underline{X}_3 = \underline{X}_2 + (1 + \sqrt{\frac{1}{2}})(\underline{k}_3 - \underline{g}_2) \quad (3.11)$$

$$\underline{g}_3 = \underline{g}_2 + 3(1 + \sqrt{\frac{1}{2}})(\underline{k}_3 - \underline{g}_2) - (1 + \sqrt{\frac{1}{2}})\underline{k}_3 \quad (3.12)$$

$$\underline{k}_4 = hF(\underline{X}_3, t^n + h) \quad (3.13)$$

$$\underline{X}^{n+1} = \underline{X}_3 + \frac{1}{6}(\underline{k}_4 - 2\underline{g}_3) \quad (3.14)$$

$$\underline{g}_4^n = \underline{g}_3 + \frac{1}{2}(\underline{k}_4 - 2\underline{g}_3) - \frac{1}{2}\underline{k}_4 \quad (3.15)$$

where superscripts  $n-1$ ,  $n$ ,  $n+1$  refer to values at the previous time

step, at the present time step, and at the desired time step increment, respectively. Note that  $h$  is the time-step size and the  $k_i$ ,  $g_i$ ,  $x_i$  are intermediate values that do not have to be stored.

This integration technique introduces single-step errors of the order of  $h^4$ . The exact magnitudes depend on the system of ODE's being solved. As stated by Eraslan (1969), a good check on the truncation error can be obtained by keeping track of the values of  $q_4^n$  at each time step. If at any time step  $t^n$  the value of  $|q_{4i}^n|$  (where the  $i$  subscript refers to the  $i$ -th component of  $q_4^n$ ) is greater than  $h^{10}$ , then this method might be introducing considerable errors. Thus,

$$|q_{4i}^n| \leq h^{10} \quad t \geq 0 \quad (3.16)$$

must be true in order to guarantee accurate results. Essentially, condition (3.16) determines the initial time step-size chosen in the solution of a particular set of ODE's. Because this is a fixed step-size method,  $h$  will then be constant for  $t \geq 0$ .

This method has two attractive advantages. Firstly, it is very simple to code in FORTRAN as presented by equations (3.3)-(3.15). Secondly, it requires very little storage and this is very important for large systems of ODE's. However, its major disadvantage is its inability to accurately solve medium to highly stiff systems of ODE's. Eraslan (1969) showed mathematically that this method becomes unstable as the stiffness of a particular system increases.

### Euler's Method with Automatic Step-Size Control

Euler type methods are the simplest numerical integration techniques used in the solution of systems of ODE's. They are not very accurate unless they are used with very small time step-sizes. So, they are extremely inefficient in solving even mildly stiff systems. However, by implementing them with an automatic step-size control algorithm, they become well suited for the solution of stiff systems.

According to Kumar et. al. (1980), a reasonable step-size control algorithm would involve either doubling or halving the step-size as required by some suitable error criterion and the prescribed error limits. The step-size will then be controlled based on a predicted step-size  $h_p$  and the actual step-size  $h$ . Thus, for the  $n$ -th step the procedure would be as follows:

1. If  $\bar{E} > E_{\max}$ , replace  $h_p$  by  $h_p/2$  and recompute  $\bar{E}$
2. If  $\bar{E} \leq E_{\max}$ , let  $h = h_p$  and compute  $\tilde{X}^{n+1}$
3. If  $E_{\min} \leq \bar{E} \leq E_{\max}$ , let  $h_p = h$
4. If  $\bar{E} \leq E_{\min}$ , let  $h_p = 2h$

where  $E_{\max}$  and  $E_{\min}$  are the prescribed error limits, and  $\bar{E}$  is a suitable error criterion chosen by the user.

Given that the initial conditions at time  $t^n$  are given by  $\tilde{X}(t^n) = \tilde{X}^n$ , the basic Euler's method can be expressed as

$$\tilde{X}^{n+1} = \tilde{X}^n + h\tilde{F}(\tilde{X}^n, t^n) \quad (3.17)$$

where superscripts  $n$  and  $n+1$  refer to values at the beginning and at the end of this time step respectively.

This method introduces single step errors of the order of  $h^2$ . So, it is reasonable to expect smaller step-sizes for this method as compared to any other method under the same accuracy constraints. Kumar et. al. (1980) chose the following error criterion for the automatic step-size control:

$$\bar{E}_i = \left| \frac{h(F_i(\tilde{X}^n, t^n) - F_i(\tilde{X}^{n-1}, t^{n-1}))}{X_i^n} \right| \quad (3.18)$$

where the  $i$  subscript refers to the  $i$ -th dependent variable in the system being solved, i.e. the  $i$ -th component of  $\tilde{X}$ . In this study and for the totality of the system the author chose the following error criterion:

$$\bar{E} = \left[ \sum_{i=1}^N \left[ \frac{h(F_i(\tilde{X}^n, t^n) - F_i(\tilde{X}^{n-1}, t^{n-1}))}{X_i^n} \right]^2 \right]^{1/2} \quad (3.19)$$

where superscripts  $n$  and  $n-1$  and subscripts  $i$  are as defined before. Note that  $N$  is the number of dependent variables in the system.

This method is very simple and easy to code. Its storage requirements are also minimal. Theoretically, this method should be able to solve highly stiff systems as accurately as any sophisticated method by just specifying a small enough maximum acceptable error. However, the time taken to solve them will increase tremendously. Note that in this discussion the round-off errors introduced by the computer are ignored;

as the time step-size becomes smaller, these round-off errors can become an important consideration. For the systems of ODE's being considered, based on the fact that the calculations were executed using a CDC Cyber 855, it is reasonable to ignore this secondary effect.

From the standpoint of computational accuracy, this method is expected to perform well by specifying a small enough maximum acceptable error. From the standpoint of computational efficiency, this method is expected to be slower than desirable due to the small step-sizes achieved through the automatic step-size control algorithm.

#### Iterative Adams Predictor-Corrector Method with Automatic Step-Size Control

The family of Adams type predictor-corrector algorithms for solving systems of ODE's is very extensive and widely used. In general they consist of predictor equations, corrector equations, and an equation relating predicted and corrected values to an acceptable solution for the system. In their basic form (no iterations and no automatic step-size control), they perform quite nicely for non-stiff systems or systems with low stiffness. In order for them to be stable as the stiffness of the system increases, automatic step-size control and/or iterative algorithms must be incorporated into the solution technique. The approach followed here incorporates both features.

Given that the initial conditions at time  $t^n$  are given by  $\tilde{X}(t^n) = \tilde{X}^n$ , the predictor equation is given by

$$\tilde{X}_p^{n+1} = \tilde{X}^n + h\tilde{F}(\tilde{X}^n, t^n) \quad (3.20)$$

where  $h$  is the current time step-size,  $\tilde{X}_p^{n+1}$  is the predicted vector of dependent variables, and superscripts  $n$  and  $n+1$  refer to values at the beginning and at the end of this time step respectively. The corrector equation is given as

$$\tilde{X}_c^{n+1} = \tilde{X}^n + h\tilde{F}(\tilde{X}_p^{n+1}, t^{n+1}) - \frac{h}{2}(\tilde{F}(\tilde{X}_p^{n+1}, t^{n+1}) - \tilde{F}(\tilde{X}^n, t^n)) \quad (3.21)$$

where  $\tilde{X}_c^{n+1}$  is the corrected vector of dependent variables.

As recommended by Kumar et. al. (1980), the step-size control algorithm used in this method is the same as the one described for Euler's method except that an iterative algorithm for the corrector equation must be accounted for in this new procedure. The step-size and iteration algorithms will be controlled based on a predicted step-size  $h_p$ , an actual step-size  $h$ , and the current number of iterations  $m$ . Thus, for the  $n$ -th step the procedure would be as follows:

1. If  $\bar{E} > E_{\max}$ :
  - a. If  $m \leq m^*$ , let  $\tilde{X}_p^{n+1} = \tilde{X}_c^{n+1}$ ,  $m = m + 1$ , and recompute  $\tilde{X}_c^{n+1}$  and  $\bar{E}$
  - b. If  $m > m^*$ , let  $m = 0$ ,  $h_p = h_p/2$ , and recompute  $\tilde{X}_p^{n+1}$ ,  $\tilde{X}_c^{n+1}$ , and  $\bar{E}$
2. If  $\bar{E} \leq E_{\max}$ , let  $h = h_p$  and compute  $\tilde{X}^{n+1}$
3. If  $E_{\min} \leq \bar{E} \leq E_{\max}$ , let  $h_p = h$
4. If  $\bar{E} \leq E_{\min}$ , let  $h_p = 2h$

where  $E_{\max}$  and  $E_{\min}$  are the prescribed error limits,  $\bar{E}$  is a suitable error criterion chosen by the user, and  $m^*$  is the maximum number of iterations allowed at a fixed time step-size. In order to approach

convergence as quickly as possible,  $m^*$  must be kept small to force a reduction in step-size rather quickly. In this study, the maximum number of iterations allowed at a fixed time step varied between two and ten.

Once convergence of the corrector equation has been achieved or the time step has been significantly reduced to keep the error within desirable bounds, the accepted value of the dependent variables at  $t^{n+1}$  becomes

$$\tilde{x}^{n+1} = \frac{4}{5}\tilde{x}_c^{n+1} + \frac{1}{5}\tilde{x}_p^{n+1} \quad (3.22)$$

This method introduces single-step errors of the order of  $h^2$  for the predictor and corrector equations treated individually. However, since they are coupled by the iteration algorithm, it seems reasonable to expect smaller single-step errors. Kumar et. al. (1980) chose the following error criterion for the iteration and automatic step-size control algorithms:

$$\bar{E}_i = \left| \frac{(\tilde{x}_c^{n+1})_i - (\tilde{x}_p^{n+1})_i}{(\tilde{x}_c^{n+1})_i} \right| \quad (3.23)$$

where the  $i$  subscript refers to the  $i$ -th dependent variable in the system. For the whole system of equations the author chose the following error criterion:

$$\bar{E} = \left[ \sum_{i=1}^N \left[ \frac{(X_C^{n+1})_i - (X_P^{n+1})_i}{(X_C^{n+1})_i} \right]^2 \right]^{1/2} \quad (3.24)$$

where  $N$  is the number of dependent variables in the system.

Equations (3.20)-(3.24) with the control algorithm as explained above make up this iterative Adams Predictor-Corrector method. It is attractive from many standpoints. It is relatively simple to code in FORTRAN. It is expected to be able to integrate highly stiff systems of equations due to the increased region of stability achieved through its iteration and step-size control algorithms. The accuracy of the method can be adjusted by just specifying the desired bounds of the error. However, two disadvantages are visible. Firstly, the stiffer the system is, the longer will be the computation time required for the given bounds of the acceptable error. Secondly, this method needs twice the storage capacity of any of the methods already described.

#### Non-iterative Adams Predictor-Corrector Method

As mentioned before, there is a large variety of predictor-corrector pairs that fall in the class of Adams Predictor-Corrector Methods. The non-iterative, explicit versions are the most widely used for non-stiff to mildly stiff systems of ODE's. Thus, it seemed reasonable to investigate an example of such a type to determine its performance characteristics in solving the three elasto-plastic material models presented in this study.

Cash (1979) presents an extensive list of explicit, non-



iterative, second-order, Adams Predictor-Corrector methods. The author selected what Cash calls "scheme three". This method was shown to have an stability interval of more than twice the interval of absolute stability of any other method in its class.

The method consists of one corrector and two predictor equations. Knowing the initial conditions at time  $t^n$ , that is,  $\tilde{x}(t^n) = \tilde{x}^n$ , the sequence of calculations would be as follows:

$$\tilde{x}_p^{n+1} = \tilde{x}^n + hF(\tilde{x}^n, t^n) \quad (3.25)$$

$$\tilde{x}_p^{n+2} = \tilde{x}_p^{n+1} + hF(\tilde{x}_p^{n+1}, t^{n+1}) \quad (3.26)$$

$$\tilde{x}^{n+1} = \tilde{x}^n + h\left(\frac{1}{16}F(\tilde{x}_p^{n+2}, t^{n+2}) + \frac{3}{8}F(\tilde{x}_p^{n+1}, t^{n+1}) + \frac{9}{16}F(\tilde{x}^n, t^n)\right) \quad (3.27)$$

where superscripts  $n$ ,  $n+1$ , and  $n+2$  refer to values at the beginning of the present time step, at the end of the present time step, and at the end of the next time step respectively. Note the  $h$  is the time step-size (constant) and  $\tilde{x}_p^{n+1}$  and  $\tilde{x}_p^{n+2}$  are intermediate predictor values that must be stored.

Even though this method requires just one set of initial conditions, it is essentially a multiple-step method. Looking at equation (3.27) it can be seen that the calculated value of  $\tilde{x}^{n+1}$  is a function of the initial condition  $\tilde{x}^n$  and two predicted values  $\tilde{x}_p^{n+1}$  and  $\tilde{x}_p^{n+2}$ . In effect, this is a three-step method.

This method introduces single-step errors of the order of  $h^2$  for the predictor and corrector equations. Cash (1979) specifies that a good

estimate of the single-step error is given by

$$\bar{E}_i = \left| (\tilde{X}^{n+1})_i - (\tilde{X}_p^{n+1})_i \right| \quad (3.28)$$

where the  $i$  subscript refers to the  $i$ -th dependent variable. The author chose an overall system error estimate of the form

$$\bar{E} = \left[ \sum_{i=1}^N \left[ (\tilde{X}^{n+1})_i - (\tilde{X}_p^{n+1})_i \right]^2 \right]^{1/2} \quad (3.29)$$

where  $N$  is the number of dependent variables. The aim is to maintain  $\bar{E}$  below a specified maximum allowable error  $E_{\max}$ . By determining  $\bar{E}$ , the appropriate initial time step-size can be chosen for a particular system of ODE's. Note that this time step-size will be kept constant and should correspond to the smallest necessary time step-size for the whole solution interval.

Like the iterative Adams Predictor-Corrector method, this technique requires twice the storage used by any of the other methods already discussed. It is very easy to implement. However, its greatest disadvantage resides on its expected inability to accurately integrate highly stiff systems. It is suspected that this technique will be quite accurate and efficient for non-stiff systems while it may be slow or even unstable for stiff systems of ODE's.

### Gear's Method

Gear's method is by far the most widely accepted numerical integration technique for all types of systems of ordinary differential equations. It was developed by Gear in the late 1960's to serve as a general purpose ODE solver. It is a multiple-step, implicit, iterative, variable-order, and variable step-size method whose sophistication guarantees an accurate solution for virtually any system. Since it has become the standard ODE solver, the author decided to use it as the reference solution technique against which all other integration methods will be compared. This point will be discussed extensively in the next chapter.

The mathematical details of this method are lengthy and complicated. So, the author decided to only present the general ideas concerning its operation. For a detailed explanation on the subject the reader is referred to Gear (1969).

The method consists of a  $p$ -th order explicit predictor equation and a  $p$ -th order iterative, implicit corrector equation. The predictor equation is used to obtain the first iterate of the corrector equation. To iterate the corrector equation,  $p$  number of values of the dependent variable vector at distinct points in time must be known. Since the corrector equation is implicit, at each iteration a system of  $N$  simultaneous algebraic equations (where  $N$  is the number of dependent variables) must be solved. Once solved, the single-step error is estimated. If this error is less than the maximum allowable single-step error, the calculated value is returned as the result. Otherwise, one of the following alternatives is chosen: continue iterating, decrease the

step-size, or increase the order of the predictor and corrector equations used. All of these measures are intended to decrease the magnitude of the estimated error. The decision is made based on the status of the solution at the current time step. Briefly stated, the decision process would be as follows:

1. If the number of iterations is less than or equal to three, continue the iteration procedure.
2. If the number of iterations is greater than three but the order of the method is less than twelve, increase the order by one and start the iteration procedure again.
3. If the number of iterations is greater than three and the order of the method is greater than or equal to twelve, decrease the time step-size to one fourth of its original value and start the iteration procedure again.

Whenever the estimated error becomes smaller than some prescribed maximum allowable error, this method returns the last iterate value as the solution for the current time step.

This method has proved itself to be one of the most accurate available for the solution of stiff systems of ODE's. However, it is also one of the slowest methods. Note that for each iteration the Jacobian matrix of the system must be inverted; most of the computation time is spent in this operation. Also note that these operations require increased data storage; in fact, this method requires about 20 times more memory than simple techniques like Euler and Runge-Kutta methods.

When solving systems of ODE's whose numerical behavior is unknown and a guaranteed accurate solution is needed, this method must be used.

This is the approach followed in the first part of chapter IV. When computational efficiency and storage requirements are the major concern, any of the methods already described may be used. This is the approach followed in the second part of chapter IV.

## CHAPTER IV

### COMPUTER ANALYSIS

This chapter presents the numerical solutions found for the axial-torsional plane-stress problem using the material models and numerical solution algorithms presented in chapters II and III, respectively. The objective is to predict, as accurately and as efficiently as possible, the stress-strain response of a thin-walled tubular specimen subjected to cyclic axial-torsional loadings that result in significant plastic deformation.

A series of computer programs were written to implement all possible combinations of material models with numerical integration techniques. Figure 4-1 shows the general program structure used in the solution process. This program structure was standardized to ease the matching of material models and integration routines. This standardization allowed a fair comparison of the material models and integration techniques by largely avoiding solution bias due to specific programming characteristics of the model or integration routine used. A modular approach was taken. The input pre-processor allows the user to generate all the input data for the main program interactively. This data consists of the applied strain and strain rate histories, the initial dependent variable values, initial time step-size, and the tolerances on the acceptable single-step error magnitudes. The main program controls all input/output operations and coordinates the

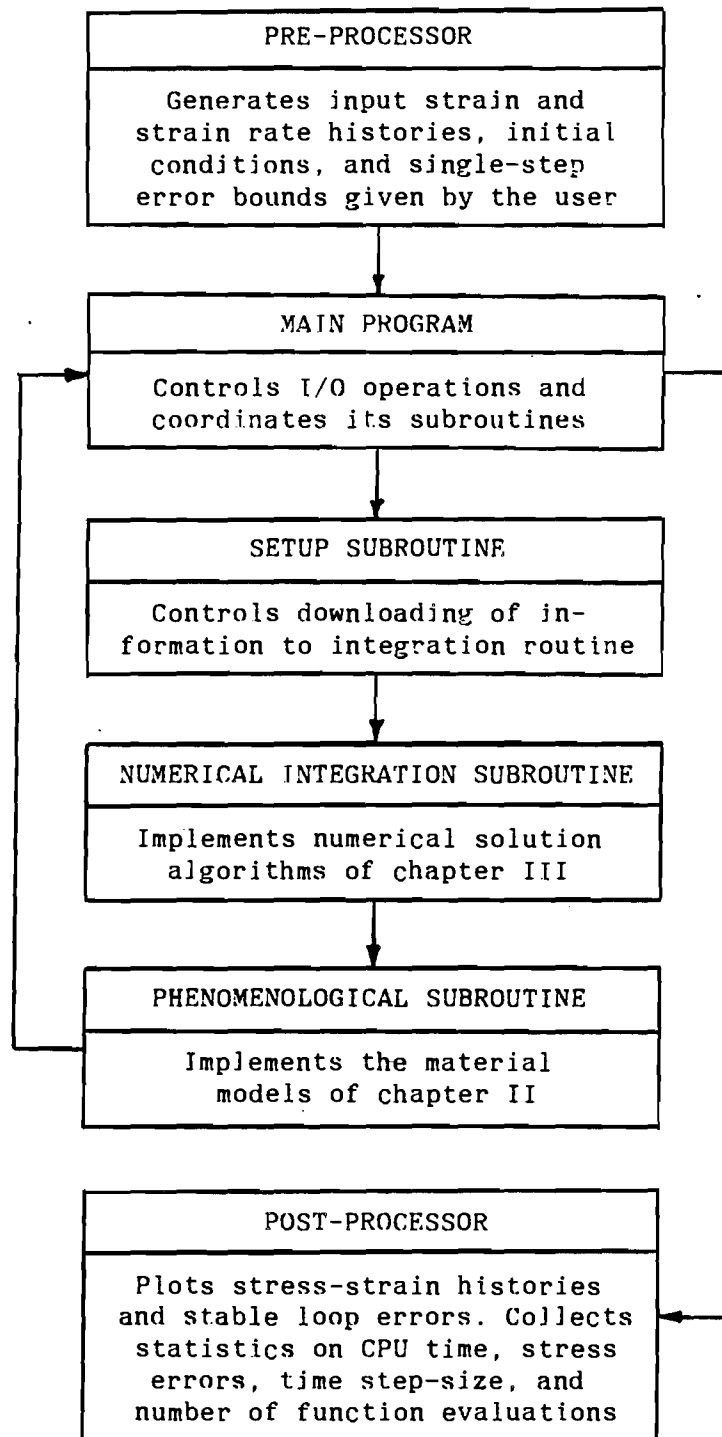


Figure 4-1. Program Structure Used for the Solution of the Cyclic Axial-Torsional Loading Problem.

operation of the three main subroutines. The setup subroutine prepares the input data for downloading into the integration subroutine. The numerical integration subroutines (one for each method) implement the numerical solution algorithms presented in chapter III. The phenomenological subroutines (one for each model) implement the axial-torsional forms of the material models presented in Appendix A. The output post-processor takes the output data from the main program for input into data reduction programs. The resulting output consists of plots of the calculated stress-strain histories, stable loop errors, and integration routine errors. It also collects statistics on computation times, time step-sizes, number of function evaluations, and axial and shear stress integration errors. This program structure was utilized throughout this work with exception of Krieg's model where the integration and phenomenological subroutines are combined into one larger subroutine.

All programs with the exception of the output post-processor were written in FORTRAN and executed on Georgia Tech's CDC Cyber 835. All calculations were done using 64 bits of accuracy to minimize round-off errors. The output post-processor was written in BASIC and executed on an IBM-PC linked to an HP-7470A plotter. Double-precision was not used on the IBM-PC since it was only used for plotting and statistics gathering purposes.

To clarify the analysis, this chapter has been divided into two separate halves. The first half deals strictly with comparisons between the four material models presented in chapter II. With the exception of Krieg's model, all models were solved by using Gear's numerical



integration algorithm. This guarantees an accurate solution and serves as an objective basis for comparison of the computational advantages or disadvantages of each model. The second half compares the five numerical solution algorithms presented in chapter III. Integration routine performance will be evaluated by using Gear's method as the standard of reference. The evaluations will be made in the context of the expected numerical behavior of the models being solved.

#### Material Model Evaluations

Even though experimental data for nonproportional, multiaxial, cyclic plasticity are scarce, McDowell provided the author with sufficient experimental results to make extensive model evaluations. Some general details of the axial-torsional, strain-controlled experimental tests are given in Appendix B.

Figures 4-2 through 4-5 summarize the relevant experimental data that will be used in this study to evaluate the material models. In this study, they will be referenced as histories I, II, III, and IV, respectively. In reality, histories I and II are part of a single history run by McDowell. Likewise, histories III and IV are also part of a different but single strain history. Due to limitations on space, the complete histories cannot be analyzed in this work. The applied shear strain-axial strain curves and the experimentally observed axial stress-axial strain, shear stress-shear strain, and shear stress-axial stress responses are shown for the transient hardening case (left column) and the stable loop or steady state case (right column) for each of the four histories. The tips of the transient shear strain-axial strain plots

have been numbered to denote the sequence of loading. The stable loop plots have been numbered at some locations to denote the starting point ("0") and the ending point ("1") of the stable cycle.

For 304 Stainless Steel at room temperature, the measured values of Young's and shear moduli were  $E = 188$  GPa and  $G = 77$  GPa, respectively. Histories I and II were run on specimen SS01. As shown in Figure 4-2, history I consists of 25 cycles of proportional loading from the virgin state with axial strain amplitude  $\epsilon_a = 0.0041$ , shear strain amplitude  $\gamma_a = 0.0060$ , and constant effective strain rate  $\dot{\epsilon}_{eff} = 0.003$  s<sup>-1</sup>. Observe that very little hardening occurred in this history and that the material stabilized within the first ten cycles. This is a typical response to purely proportional loading. As shown in Figure 4-3, history II consists of 25 cycles of nonproportional loading with the same axial and shear strain amplitudes as history I. Segments 4-1 and 2-3 are proportional in terms of total strain and correspond to the previously applied strain histories for this specimen. Segments 1-2 and 3-4 are nonproportional since the components of the strain tensor change nonproportionally. Note the tremendous increase in hardening achieved by introducing nonproportionality effects even though the maximum plastic strain ranges have not increased. Histories III and IV were run on specimen SS09. As shown in Figure 4-4, history III consists of 25 cycles of nonproportional sinusoidal loading from an initially hardened state (through proportional loading) with 30 degrees phase angle, strain amplitudes  $\epsilon_a = 0.0050$  and  $\gamma_a = 0.0075$ , and an effective strain rate  $\dot{\epsilon}_{eff} = 0.001$  s<sup>-1</sup>. Observe the significant increase in hardening resulting from this "mild" nonproportionality level. Again, very little

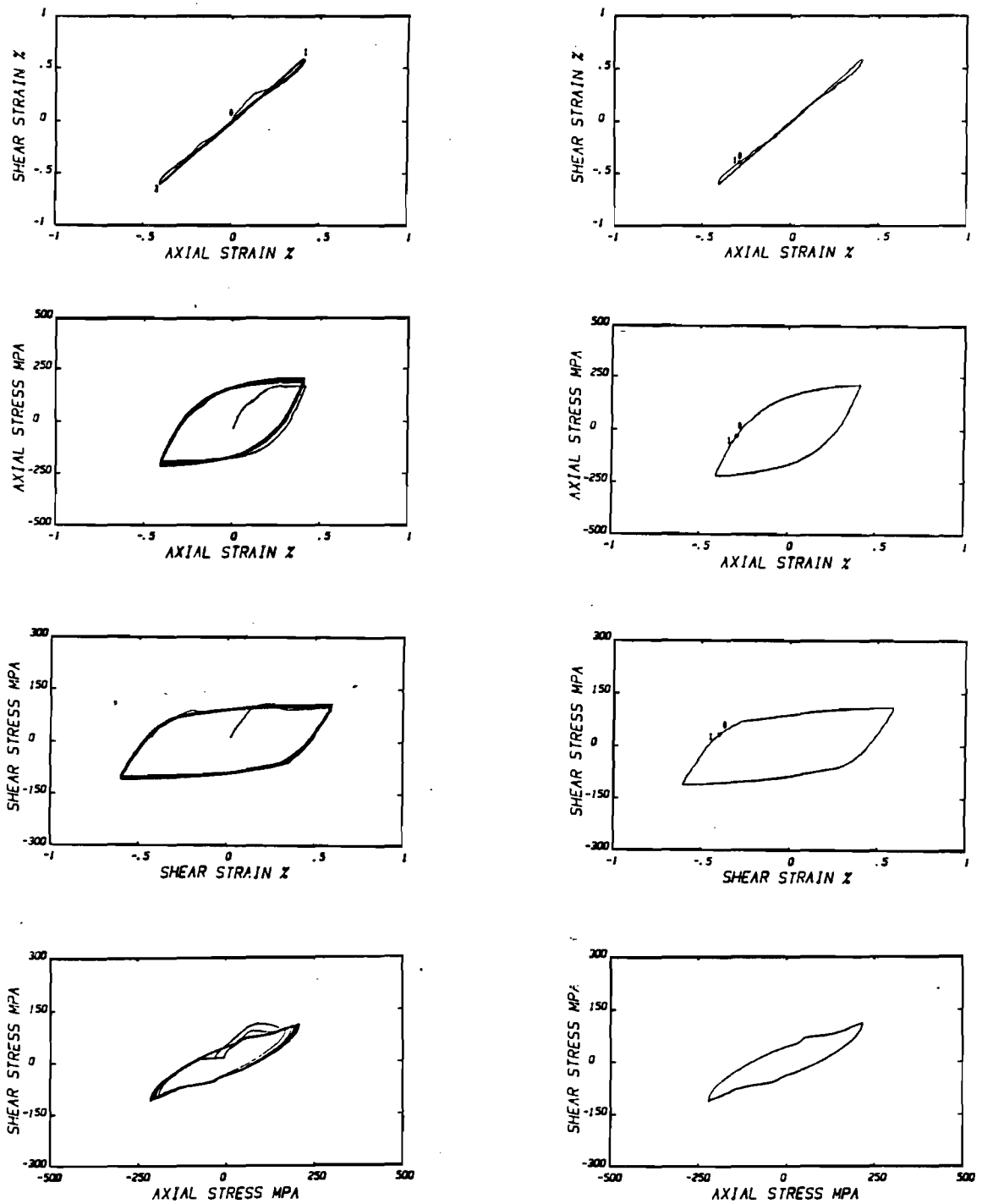


Figure 4-2. Experimental Data for History I.  
 Left column shows transient response (cycles 1-10);  
 right column shows stable loop response (cycle 25).

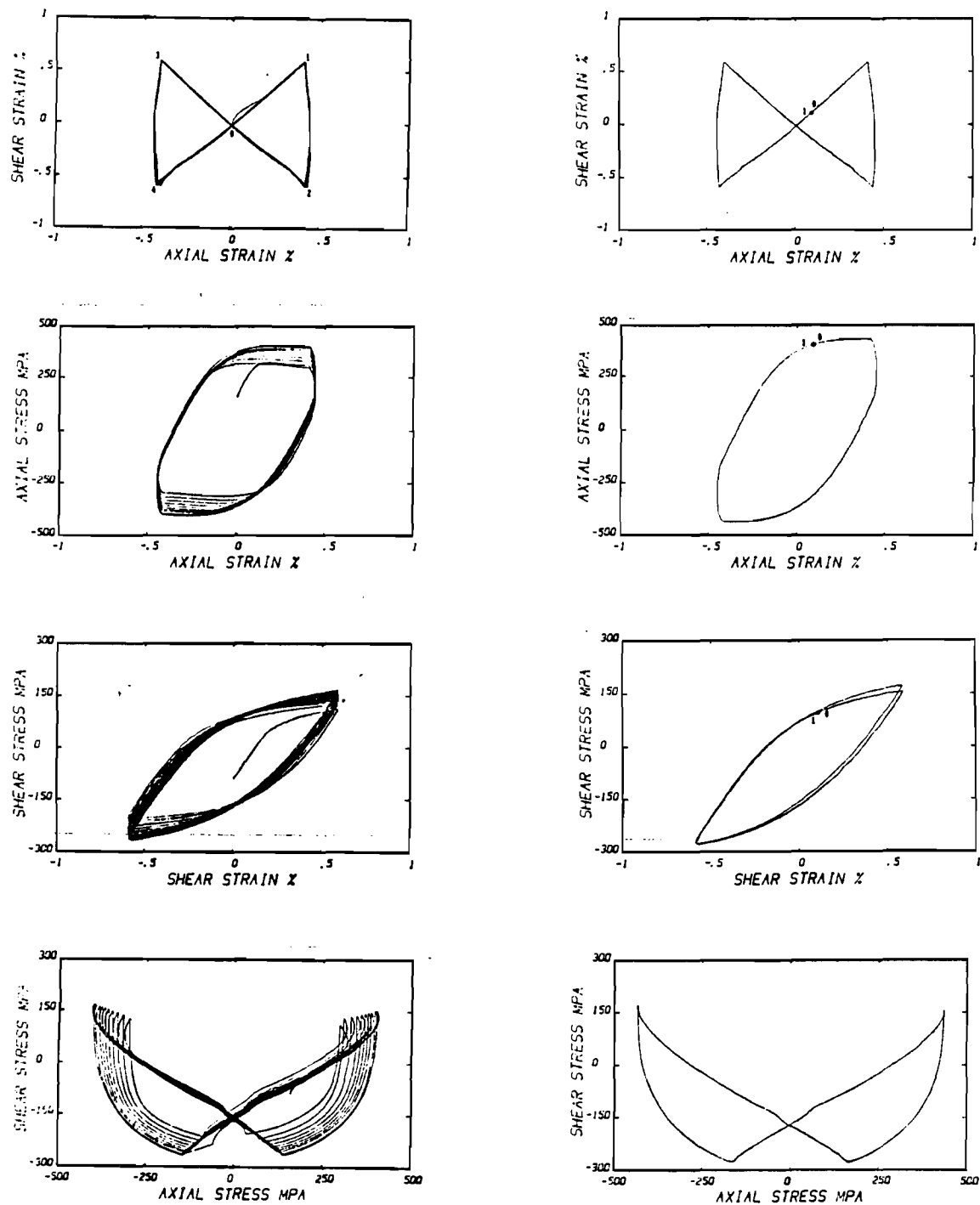


Figure 4-3. Experimental Data for History II.  
 Left column shows transient response (cycles 1-10);  
 right column shows stable loop response (cycle 25).

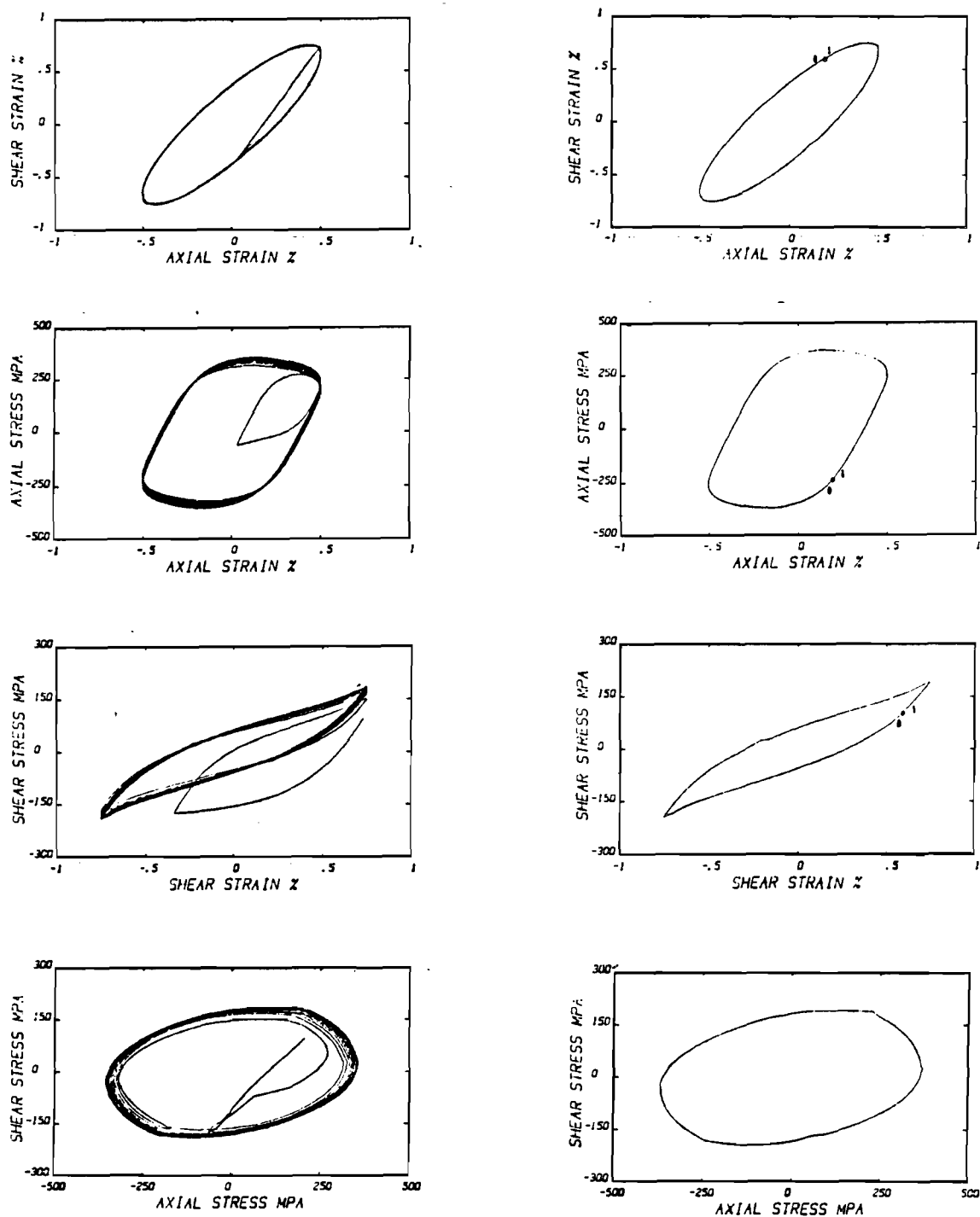


Figure 4-4. Experimental Data for History III.  
 Left column shows transient response (cycles 1-10);  
 right column shows stable loop response (cycle 25).

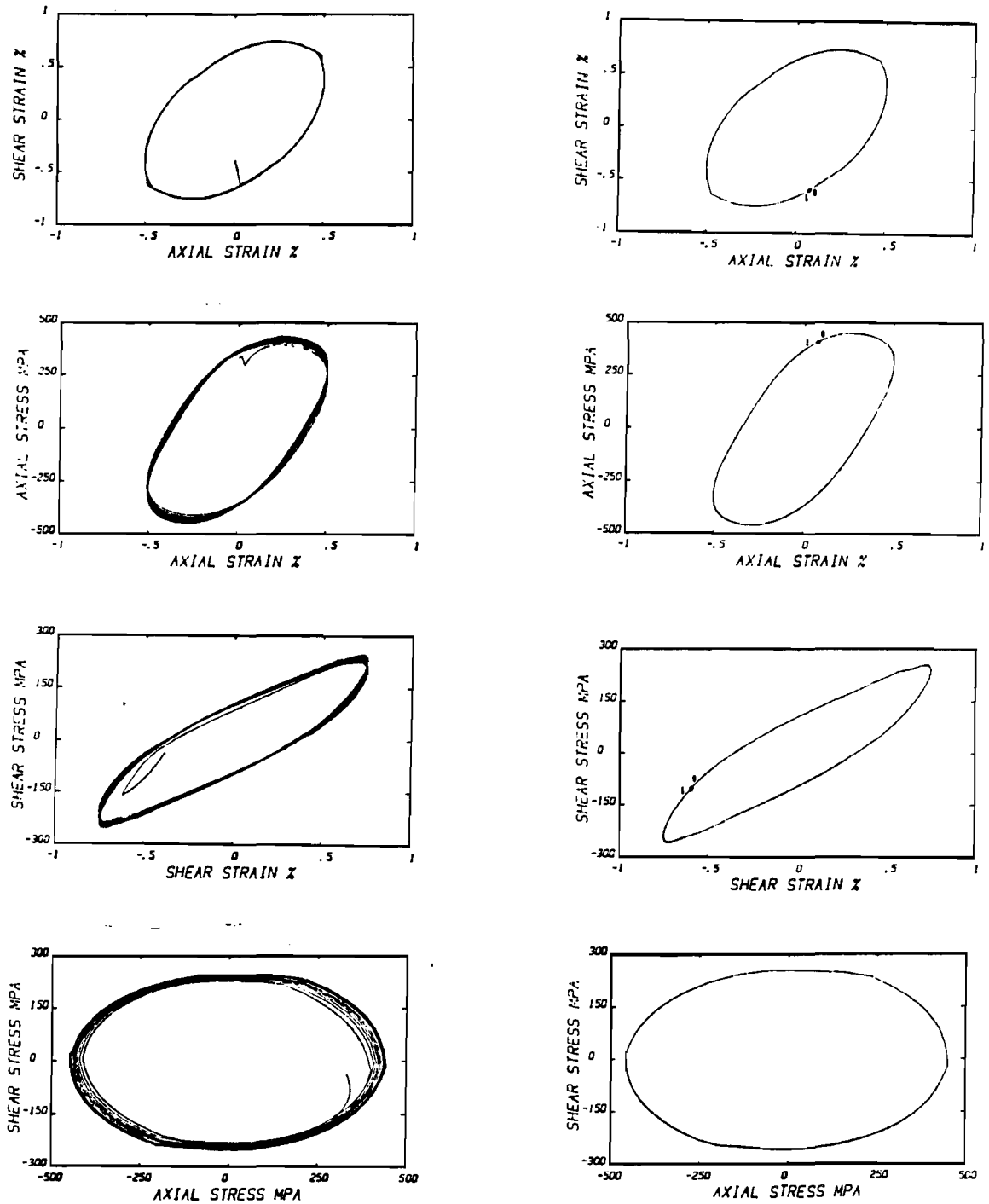


Figure 4-5. Experimental Data for History IV.  
 Left column shows transient response (cycles 1-10);  
 right column shows stable loop response (cycle 20).

hardening occurred between cycles 10 and 25. Finally, Figure 4-5 shows history IV which consists of 25 cycles of nonproportional sinusoidal loading from the history III ending state with 60 degrees phase angle and the same strain amplitudes as in the third history. Notice the increase in hardening achieved by just changing the phase angle of the test. History IV then is a more severe nonproportional path with a consequential hardening increase.

As previously stated, Appendix A summarizes the material constants, model parameters, modeling functions, and axial-torsional forms of the models discussed here. It was assumed that for multiaxial, cyclic plasticity applications the model parameters could be determined on the basis of uniaxial equivalent values. So, the model parameters shown in Appendix A for Drucker's and Krieg's models were determined from experimental history I based on effective axial and shear stresses and strains. The model parameters and modeling functions for McDowell's and Abrahamson's models were taken from their respective analyses on the experimental histories shown in this work.

Each of the four models presented in chapter II will be evaluated for each of the four histories discussed. The numerical solutions will be shown in a format similar to that of Figures 4-2 through 4-5. In addition, plots of the axial and shear stress errors during the stable loop response will be shown. These errors have been defined as follows:

$$E_a(\%) = \frac{\sigma_a - \sigma_e}{\sigma_{\max}}(100) \quad (4.1)$$

$$E_s(\%) = \frac{\tau_a - \tau_e}{\tau_{\max}}(100) \quad (4.2)$$

where  $\sigma_e$  and  $\tau_e$  are the experimental values of axial and shear stresses for given axial and shear strains respectively,  $\sigma_a$  and  $\tau_a$  are the corresponding numerical solutions (at the same axial and shear strains) by the model being considered, and  $\sigma_{\max}$  and  $\tau_{\max}$  are the largest experimental values of axial and shear stresses over the stable loop response. Thus, the axial and shear stress errors  $E_a$  and  $E_s$  are normalized with respect to the same measure for the histories being analyzed.

To further expand the analysis of the stable loop error plots, average and maximum stress errors will be shown in the analysis to follow. The axial stress average error  $E_{a,avg}$  and the shear stress average error  $E_{s,avg}$  correspond to average values calculated over the shown stable loop response. The axial stress maximum error  $E_{a,max}$  and the shear stress maximum error  $E_{s,max}$  are the actual absolute maximums over the stable hysteresis loop. The error criteria chosen might not be the best possible; however, they do show the error trends and relative error magnitudes necessary to evaluate the material models. Due to the cyclic nature of the problem being considered, multiplicity of stress values at a given strain is observed. Furthermore, due to phase lags of the predicted stress behaviors, sudden jumps in the stable loop error plots will be observed as the loading direction changes or as the stress values pass through zero. These are two inconveniences of the error criteria chosen which slightly affect the accuracy of the results shown.

To analyze the computational efficiency of the models, a non-



dimensional CPU time has been defined as follows:

$$CPU_N = \frac{CPU_A}{t_f} \quad (4.3)$$

where  $CPU_A$  is the actual CPU time taken by the Cyber 835 to solve the history under consideration and  $t_f$  is the final value of the independent variable (time) for this execution. Thus, the normalized CPU time  $CPU_N$  is calculated based on the assumption that the computation time varies linearly with the total length of the execution. Due to the cyclic nature of the calculations, this is a reasonable assumption.

#### Drucker's Model

Figures 4-6 through 4-9 show the predicted stress-strain responses for Drucker's model for the four histories considered. Table 4-1 presents general data pertaining to the stable loop error plots and computation times required.

Computation times for Drucker's model seem to be history-independent as seen in Table 4-1. The variances in normalized CPU times are rather small given that all histories are quite different. Notice that the average stable loop errors are smallest for history I (proportional history) and about three times larger for all other histories (nonproportional histories). Also note that the maximum stress errors are considerably larger than the average errors regardless of the applied strain history.

History I. As can be seen from Figure 4-6, the transient hardening response is predicted quite accurately for this proportional loading path. The stabilized axial and shear stress amplitudes are

Table 4-1. Stable Loop Errors and Computation Times for Drucker's Model.

	History I	History II	History III	History IV
CPU <sub>N</sub>	0.71	0.73	0.60	0.60
E <sub>a,avg</sub>	12.0	32.7	30.2	35.3
E <sub>a,max</sub>	43.0	48.7	40.7	51.5
E <sub>s,avg</sub>	8.1	21.5	27.2	34.7
E <sub>s,max</sub>	38.2	43.8	54.5	66.0

predicted very well. However, notice that this model overestimates axial and shear stress values near the region of initial yielding. The sharp yielding shown is not characteristic of the implemented rounding corner option of this model. The stable loop error plots confirm that the peak stress errors always occur near the point of initial yielding and then are driven toward zero as the material deforms into the asymptotic plastic region. Note that the shear stress-shear strain plots exhibit an extraneous material softening followed by increased hardening just after initial yielding. This seems to be a consequence of the sharp yielding.

History II. Figure 4-7 shows that this model does not predict any further hardening due to nonproportional loading paths. Observe that the material shows a saturated response throughout the 25 cycles; hence, the predicted hardening response does not describe experimental results. The stable loop shapes are predicted incorrectly; the asymptotic plastic modulus is considerably underestimated. Notice that in this case the axial stress-axial strain plots exhibit softening followed by increased hardening just after yielding. The stress error plots show that,

contrary to history I, the largest errors occur as the material deforms into the asymptotic plastic region and then are driven back to zero as the material unloads and enters the initial yielding regime. This behavior results from this model's inability to predict the increased isotropic hardening due to nonproportionality effects.

History III. Figure 4-8 shows the numerical solution to the nonproportional 30 degrees out-of-phase sinusoidal strain path. Notice that even though this model predicts hardening, it significantly underestimates the isotropic hardening for the axial stress response. The shear stress response is poorly predicted. The shape of the stabilized shear hysteresis loop is not in agreement with the experimental results. According to McDowell (1984a) this is probably, at least partially, a consequence of using a von Mises yield condition normalized to the axial stress. The axial stress error plot confirms that the largest errors occurred as the material deformed in the asymptotic plastic region. The shear stress error plot shows that this model significantly overestimates the shear stress for the entire stable hysteresis loop.

History IV. As can be seen from Figure 4-9, this model's predictions are quite similar for histories III and IV. First, observe that throughout 25 cycles the model predicts a stabilized stress response. Hardening due to nonproportionality effects is disregarded. The stable loop responses greatly underestimate the actual hardening incurred. The stress error plots show that the largest errors always occur as the material yields into the asymptotic plastic region; this confirms expectations. An interesting point should be made here.

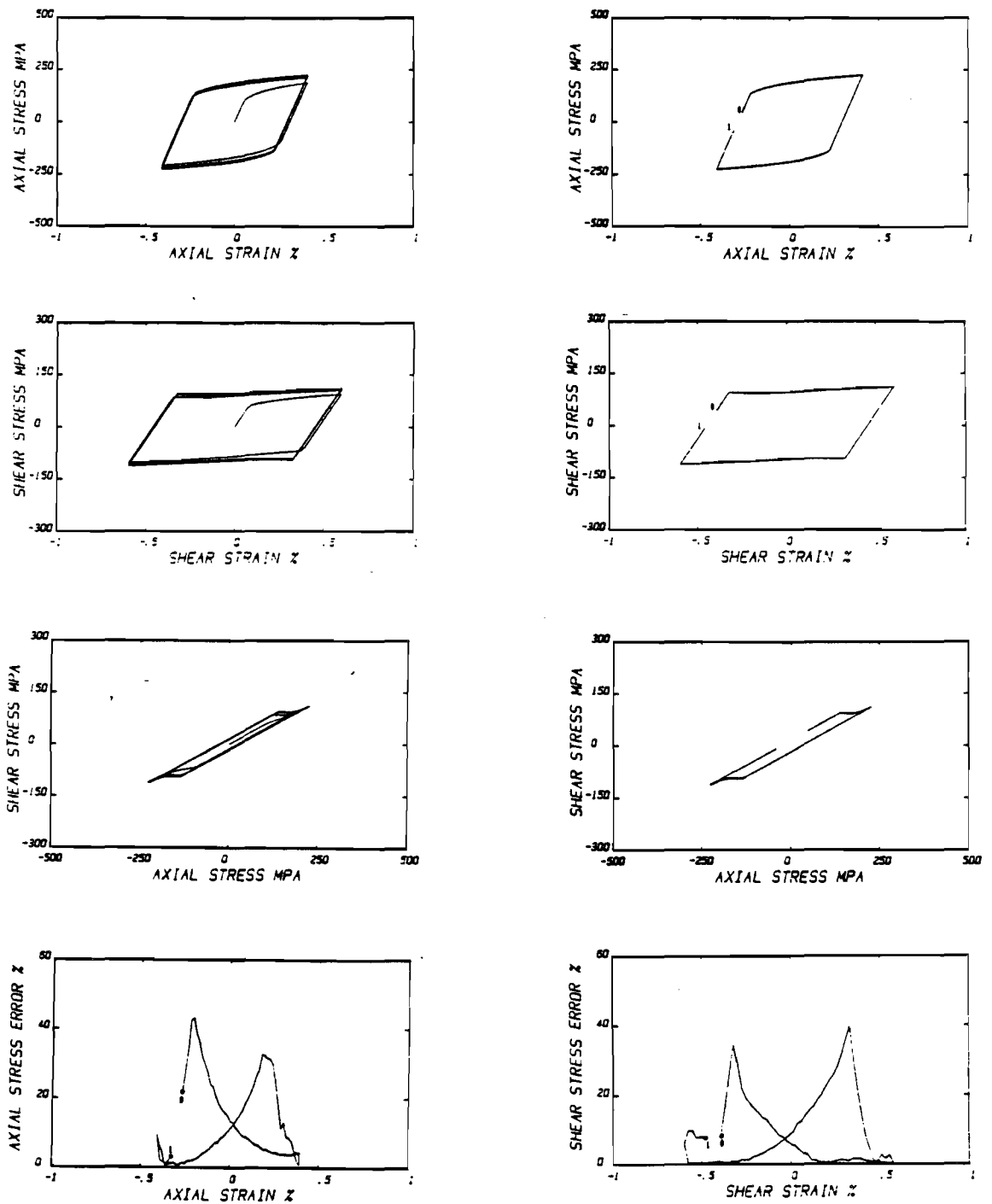


Figure 4-6. Numerical Solution by Drucker's Model for History I. Left column, top three plots show transient response (cycles 1-10); right column, top three plots show stable loop response (cycle 25); bottom row shows stable loop errors compared to experimental data.

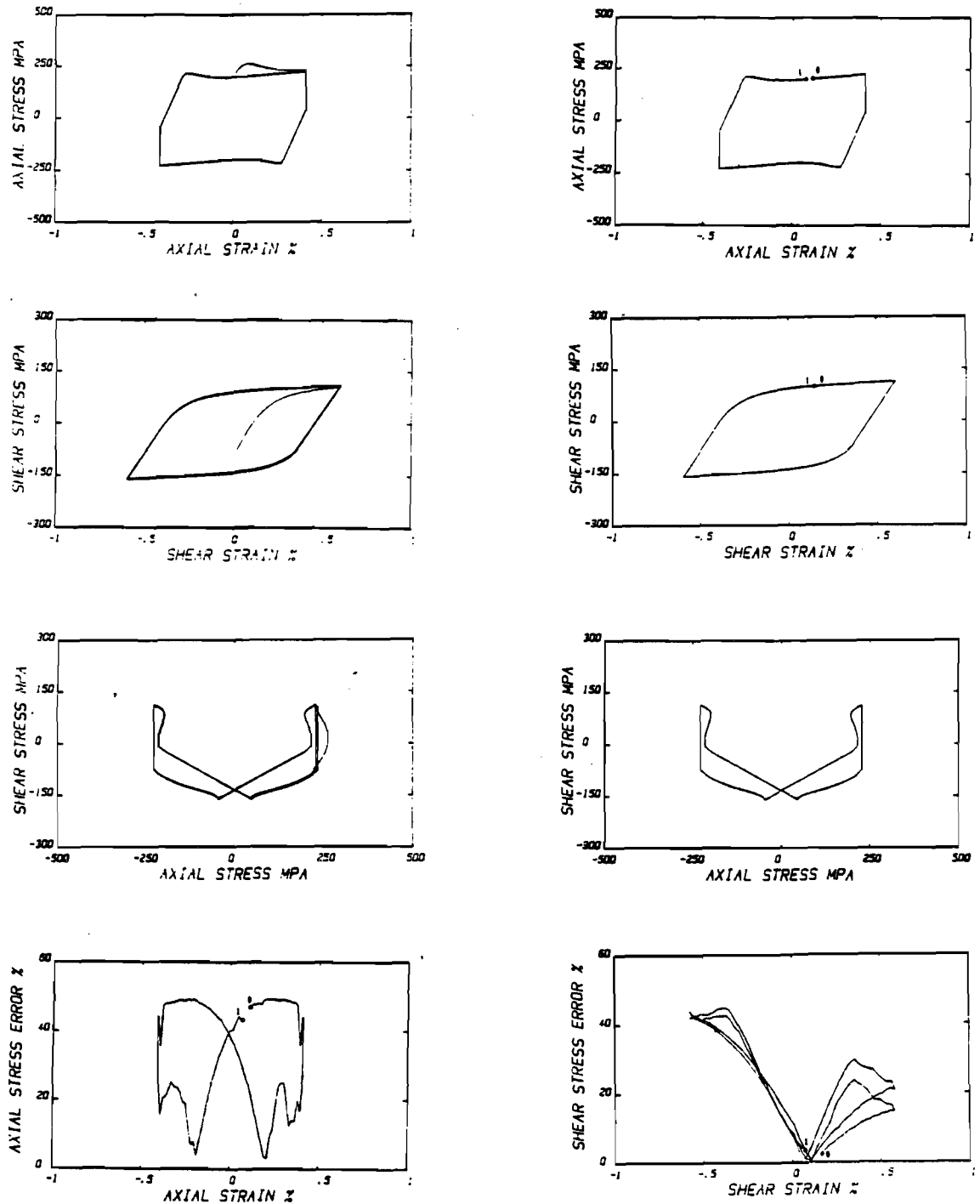


Figure 4-7. Numerical Solution by Drucker's Model for History II. Left column, top three plots show transient response (cycles 1-10); right column, top three plots show stable loop response (cycle 25); bottom row shows stable loop errors compared to experimental data.

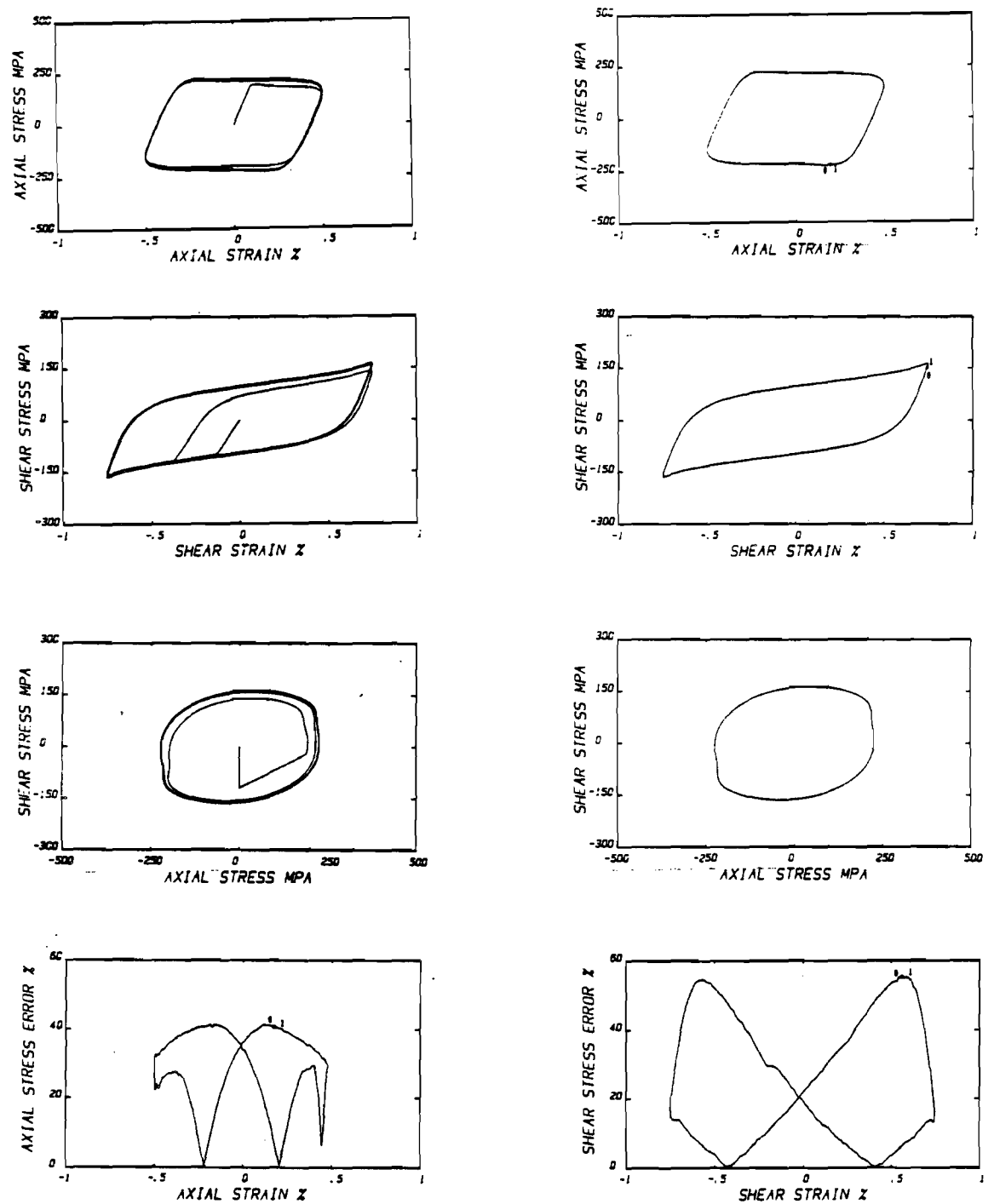


Figure 4-8. Numerical Solution by Drucker's Model for History III. Left column, top three plots show transient response (cycles 1-10); right column, top three plots show stable loop response (cycle 25); bottom row shows stable loop errors compared to experimental data.

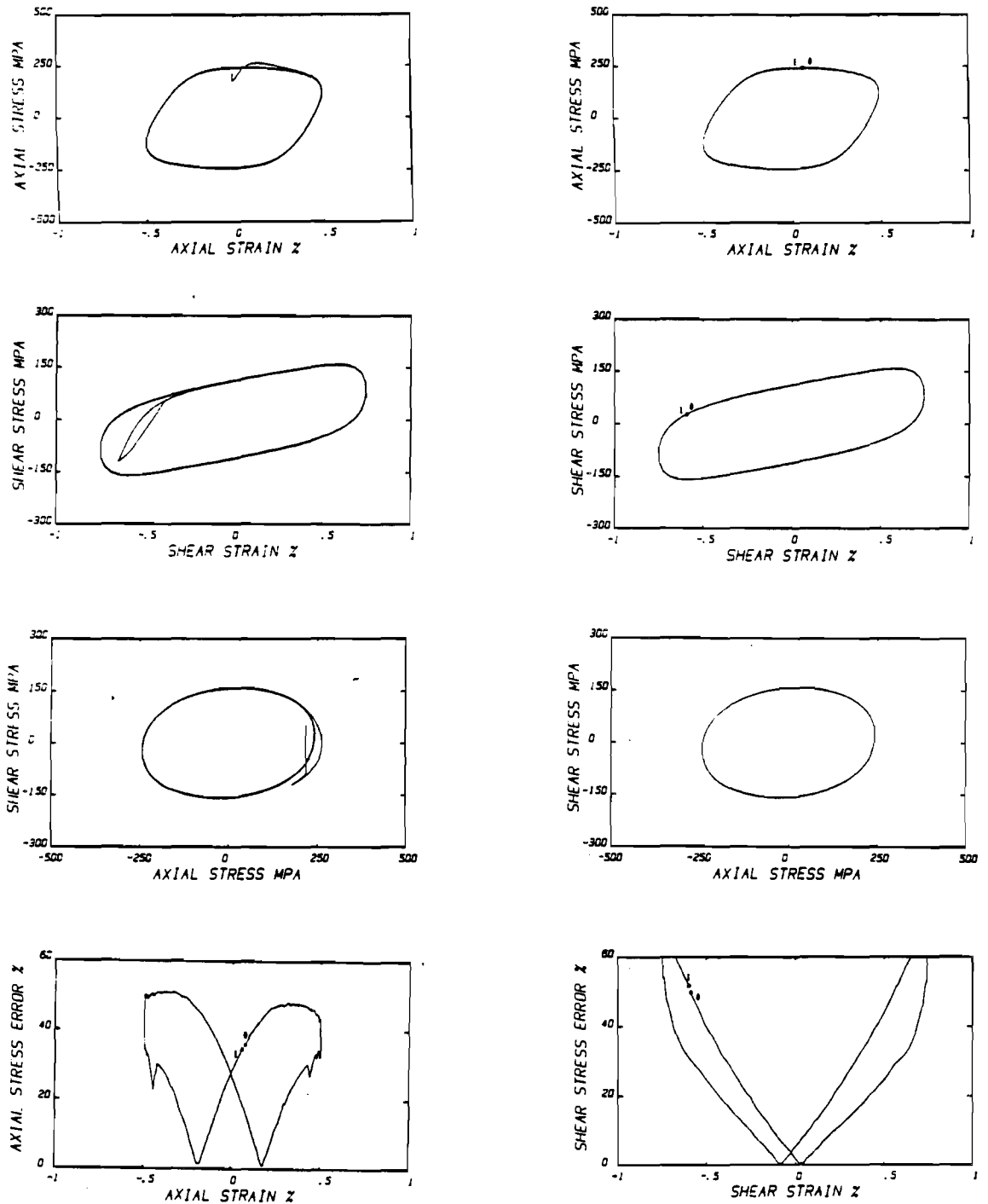


Figure 4-9. Numerical Solution by Drucker's Model for History IV. Left column, top three plots show transient response (cycles 1-10); right column, top three plots show stable loop response (cycle 25); bottom row shows stable loop errors compared to experimental data.

Considering the stress space stable response, it can be seen that, disregarding stress amplitude differences, the predicted response shape is accurate. This suggests the possibility that an improved isotropic hardening rule would significantly increase this model's accuracy with little increase in computational efforts. McDowell (1984d) has shown for these histories that a plastic modulus dependence on effective stress, as assumed in this model, is not a viable description. Hence, loop shape does not seem to be greatly affected by inaccuracies in the plastic modulus function representation. Plastic strain range, however, is apparently greatly affected by the form of the plastic modulus representation under nonproportional loading. This is a very important point to be remembered.

#### McDowell's Model

Figures 4-10 through 4-13 present plots of the predicted stress-strain responses by McDowell's model for the histories under consideration. Table 4-2 shows some statistics with regard to the stable loop error plots and computation times required.

Table 4-2 shows that McDowell's model computation times seem to be history-independent. The normalized CPU time variances do not seem to follow a pattern dependent on history characteristics. On the other hand, the stable loop average errors do follow a clear pattern. For proportional history I the average and maximum errors are quite small. The axial stress average and maximum errors are basically the same for histories II, III, and IV. The shear stress average and maximum errors for histories III and IV are considerably larger than any other error for this model. It is immediately seen that this model has problems



Table 4-2. Stable Loop Errors and Computation Times for McDowell's Model.

	History I	History II	History III	History IV
CPU <sub>N</sub>	1.87	1.87	1.45	1.56
E <sub>a,avg</sub>	4.3	13.6	12.0	15.2
E <sub>a,max</sub>	14.1	19.8	17.3	24.9
E <sub>s,avg</sub>	2.6	7.6	24.9	25.0
E <sub>s,max</sub>	11.2	11.7	38.0	41.5

predicting the shear response of sinusoidal nonproportional histories.

History I. As can be seen from Figure 4-10, this model predicts quite accurately the transient hardening, the transient hardening rate, and the stable hysteresis loop responses for proportional histories. Observe that very realistic smooth yielding is predicted. The stress error plots show that the largest (but still small) errors occur just after initial yielding where this model underestimates the response for both axial and shear stresses.

History II. Figure 4-11 shows the numerical solution predicted by this model. Note that a significant hardening increase due to nonproportionality effects is predicted with sufficient accuracy. The stable loop shear stress amplitude and shape are predicted with very good accuracy. However, the axial stress stable loop amplitude is considerably underestimated at the point of unloading after maximum axial stress loading. This is due to the fact that the model predicts elastic unloading from the yield surface at this point when the experimental plots show this is not true. The axial stress error plot

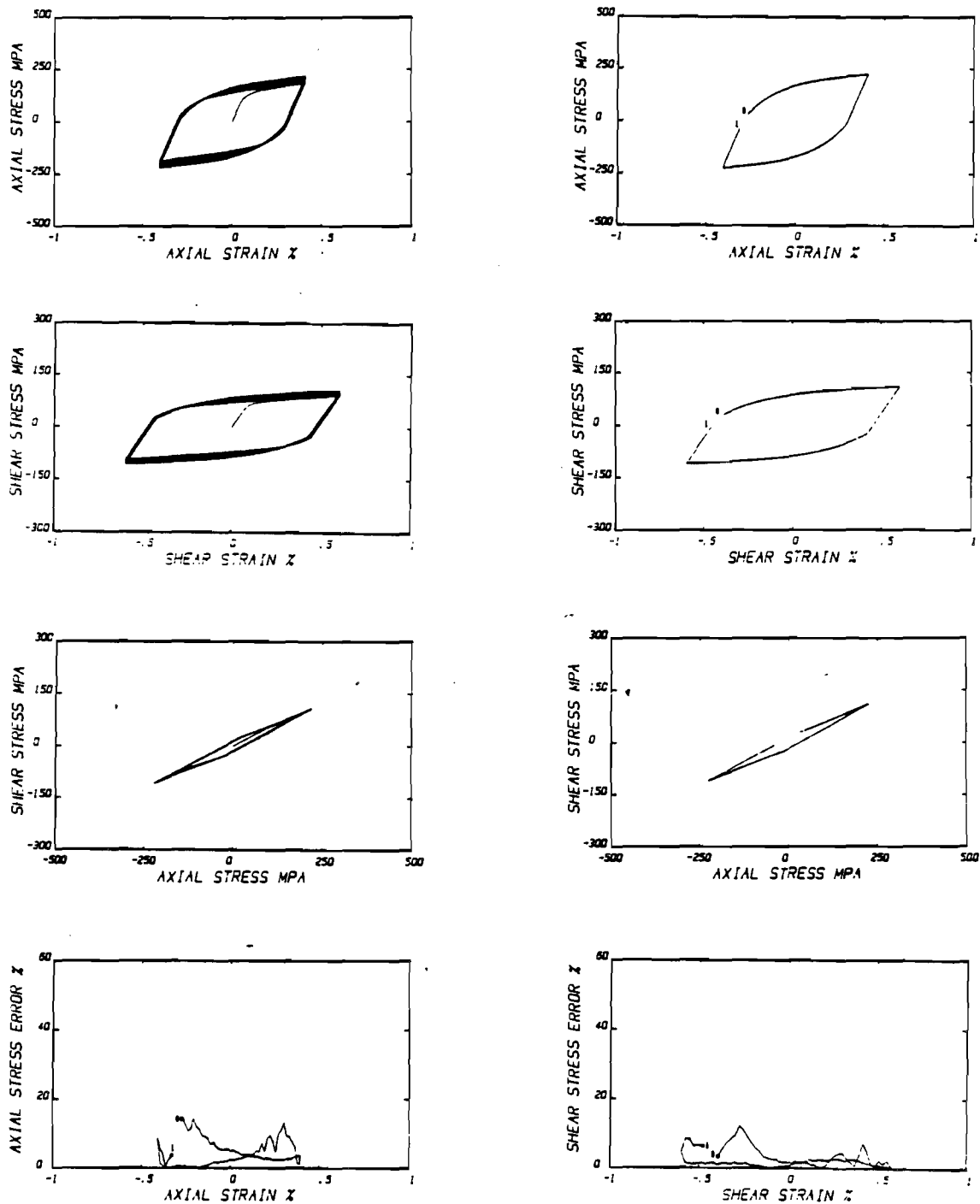


Figure 4-10. Numerical Solution by McDowell's Model for History I. Left column, top three plots show transient response (cycles 1-10); right column, top three plots show stable loop response (cycle 25); bottom row shows stable loop errors compared to experimental data.

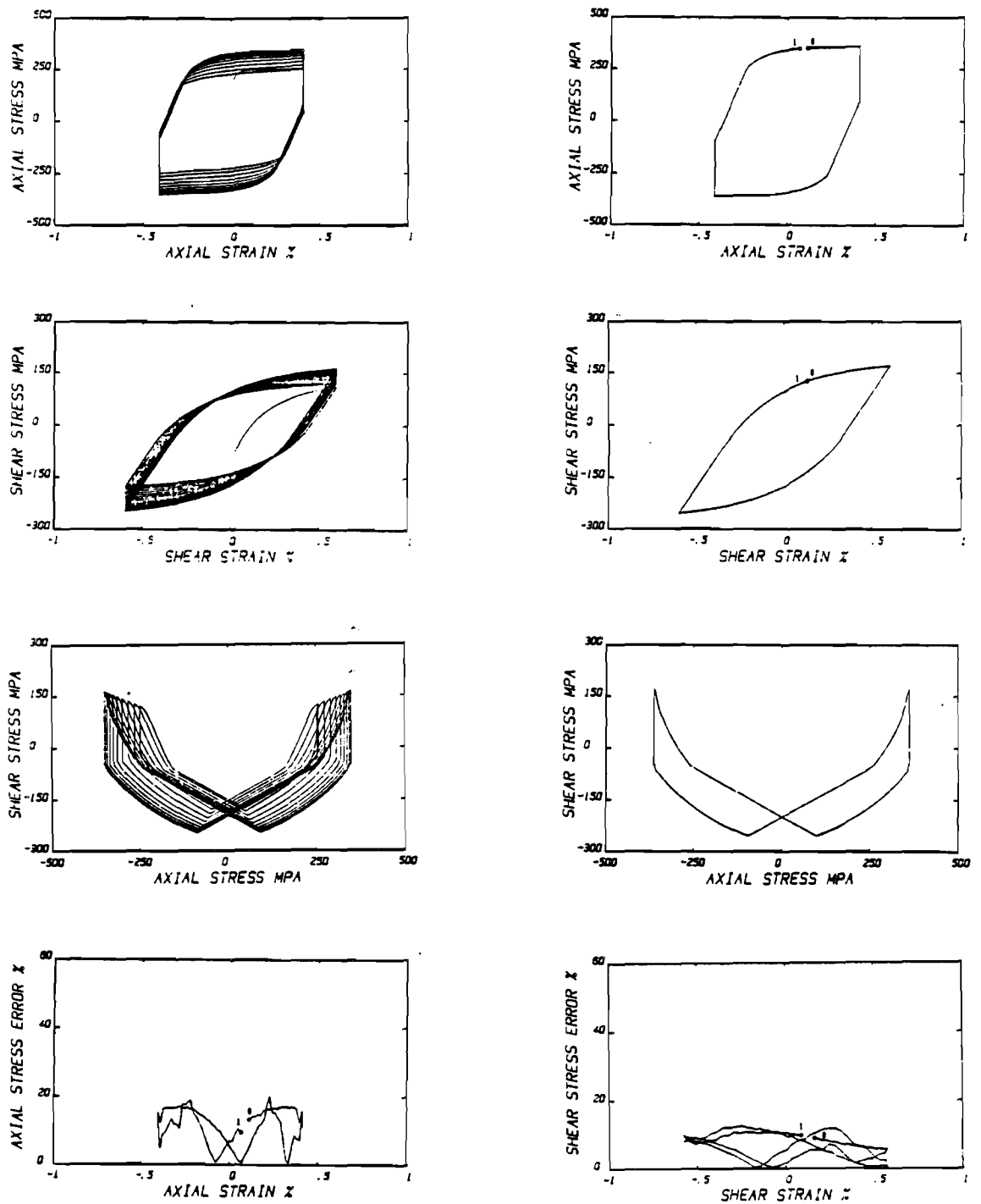


Figure 4-11. Numerical Solution by McDowell's Model for History II. Left column, top three plots show transient response (cycles 1-10); right column, top three plots show stable loop response (cycle 25); bottom row shows stable loop errors compared to experimental data.

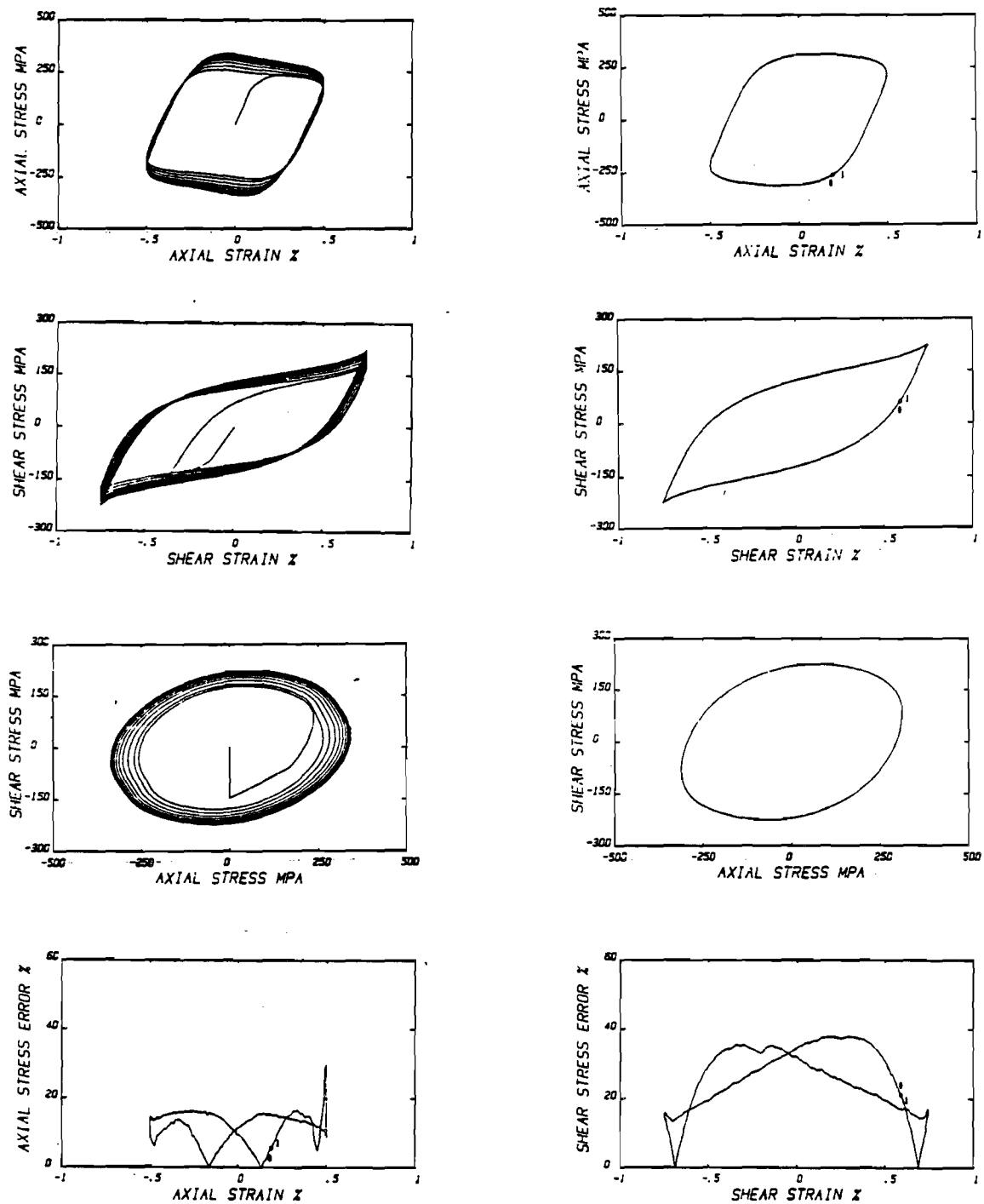


Figure 4-12. Numerical Solution by McDowell's Model for History III. Left column, top three plots show transient response (cycles 1-10); right column, top three plots show stable loop response (cycle 25); bottom row shows stable loop errors compared to experimental data.

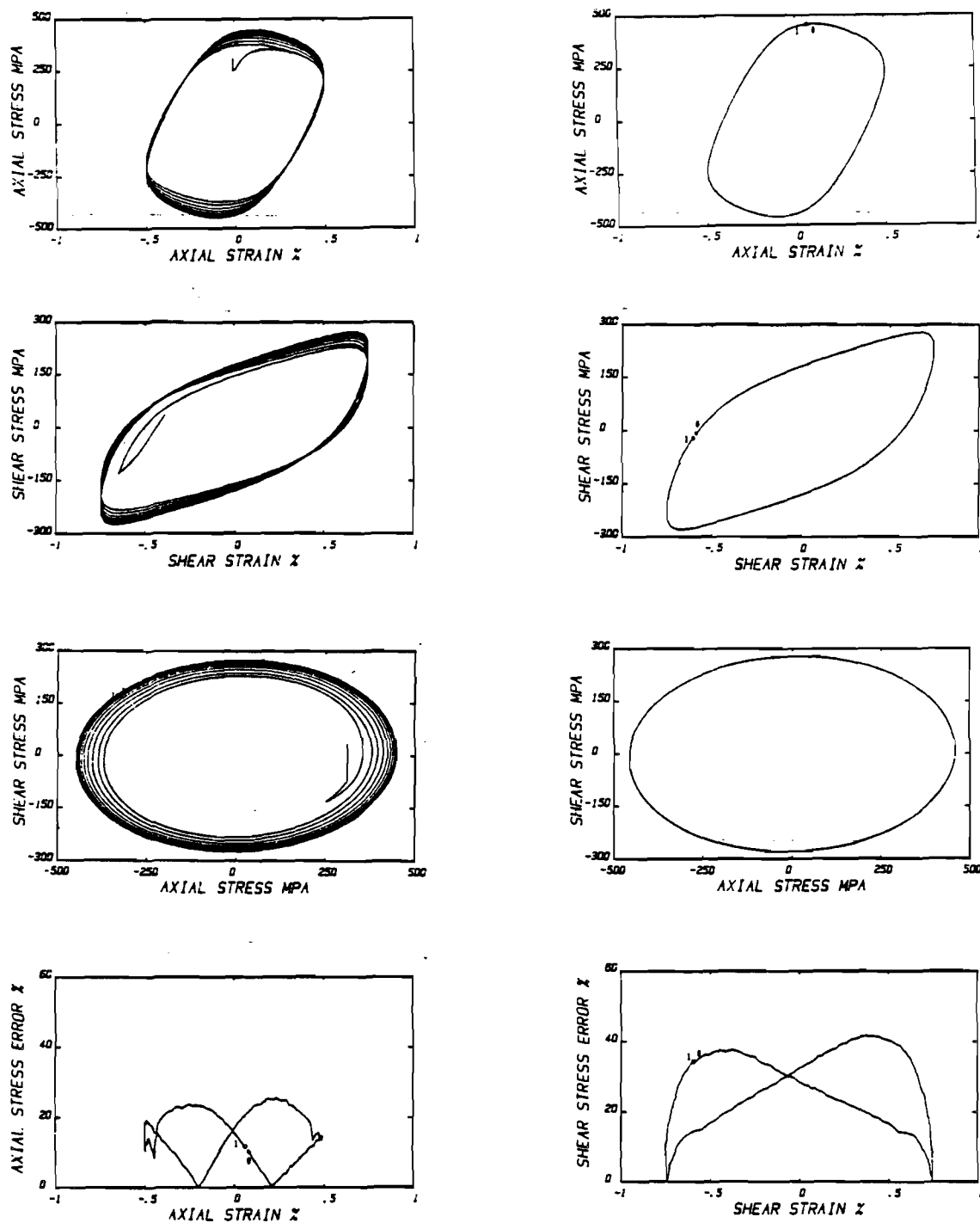


Figure 4-13. Numerical Solution by McDowell's Model for History IV. Left column, top three plots show transient response (cycles 1-10); right column, top three plots show stable loop response (cycle 25); bottom row shows stable loop errors compared to experimental data.

confirms that the maximum errors occur at large values of axial strain. The shear stress errors are seen to vary smoothly around the stable loop with no region of significantly larger errors.

History III. As shown in Figure 4-12, this model is capable of predicting additional hardening due to nonproportional loading. Even though the initial flow stress at yielding is underestimated, the transient hardening response is very well predicted up to the saturated state. The stable axial stress-axial strain loop very closely resembles the shape and amplitude of the experimentally observed values. The axial stress error plot confirms that the largest prediction errors occur at large values of axial strain; note that these errors are still rather small. The stable shear stress-shear strain loop shows rather large deviations from experiment. The shear stress error plot shows that these deviations are due to the "fattening" of the shear response. This fact suggests that a Tresca yield condition may predict a more accurate shear response. Observe that the maximum plastic strain range is overestimated by about 30% and thus, any fatigue life calculations based on this prediction can be significantly in error.

History IV. Comparing Figures 4-12 and 4-13 it is seen that most comments regarding history III apply to this history. Transient hardening is again well-predicted. Predicted axial stress response is more accurate than the shear stress response for the same reasons. Note again that this model predicted with good accuracy the additional hardening due to nonproportional loading.

#### Krieg's Model

The numerical solutions obtained using Krieg's model for the

Table 4-3. Stable Loop Errors and Computation Times for Krieg's Model.

	History I	History II	History III	History IV
CPU <sub>N</sub>	0.17	0.17	0.16	0.16
E <sub>a,avg</sub>	12.9	33.2	31.3	37.5
E <sub>a,max</sub>	40.0	51.5	41.4	52.3
E <sub>s,avg</sub>	23.3	26.8	27.2	37.4
E <sub>s,max</sub>	54.1	53.4	60.9	74.0

test histories under consideration are shown in Figures 4-14 through 4-17. Table 4-3 summarizes some statistics regarding stable loop errors and computer execution times required.

Krieg's model execution time is definitely history-independent as shown in Table 4-3. Note the extremely short computation times needed; this is the primary advantage of this model. Remember that this evaluation incorporates both the material model and the radial-return integration algorithm. Since this is the only model solved without using Gear's method, the radial-return algorithm must be responsible for the tremendous decrease in execution time. Note however that this reduction in computation time results in a sacrifice of predictive accuracy. It is seen that the axial and shear stress stable loop average and maximum errors increase from left to right in the table, from proportional to highly nonproportional loading. It must be pointed out that even for proportional paths this method predicts a response with large errors.

History I. As shown in Figure 4-14, the transient hardening response for this proportional history is very well predicted. It is,

however, the basic response shape what introduces the large errors in this model. Even though the axial stress response shows smooth yielding, this model significantly overestimates the experimental axial stress values at yielding. This is clearly shown by the two peaks in the axial stress error plot; it is also seen that the axial stress error is driven toward zero as the material deforms into the asymptotic plastic region. The predicted shear stress response is totally unrealistic. Firstly, it presents a fictitious material softening just after yielding. This results in significantly underestimated shear stress values in the asymptotic region. Secondly, it overestimates the extent of the elastic regime. This is shown by the two peaks in the shear stress error plot.

History II. Figure 4-15 shows the predicted response for this nonproportional history. Referring to Figure 4-7 the reader will realize the many similarities between Drucker's and Krieg's predicted responses for this history. The predicted response shapes are identical. The only difference resides in the actual magnitude of the stresses. So, the analysis made for Drucker's model is also valid here.

History III. Figure 4-16 shows the predicted results for history III. Again, if the reader compares Figures 4-8 and 4-16, it is evident that Drucker's and Krieg's models behave very similarly for nonproportional loading histories. Notice again that the hysteresis loop shape is fairly accurate. This confirms the contention that the plastic modulus formulation is not very influential on the predicted loop shape for simple models like Drucker's and Krieg's, since their plastic modulus descriptions are different.

History IV. Finally, Figure 4-17 shows the predicted solution



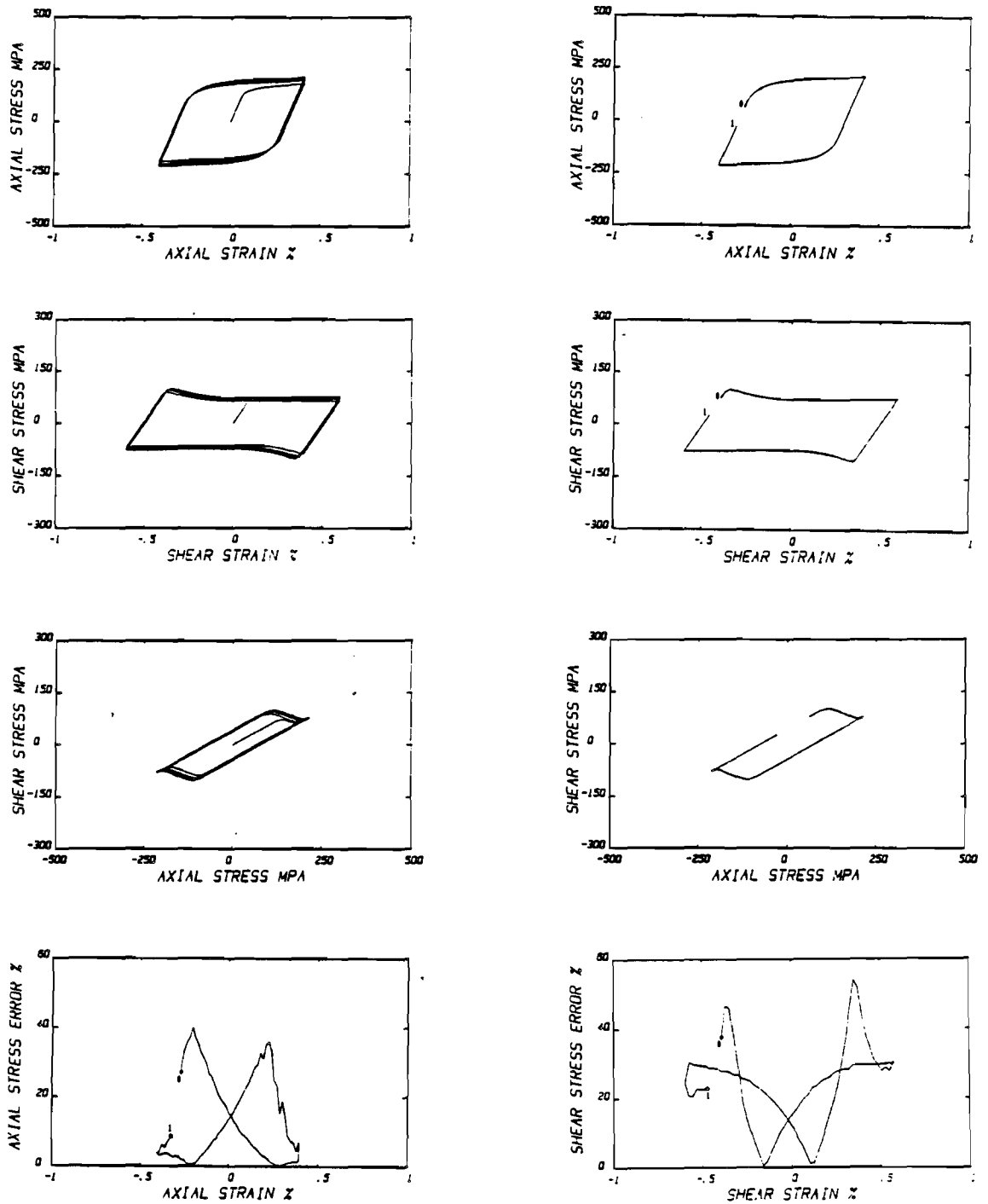


Figure 4-14. Numerical Solution by Krieg's Model for History I. Left column, top three plots show transient response (cycles 1-10); right column, top three plots show stable loop response (cycle 25); bottom row shows stable loop errors compared to experimental data.

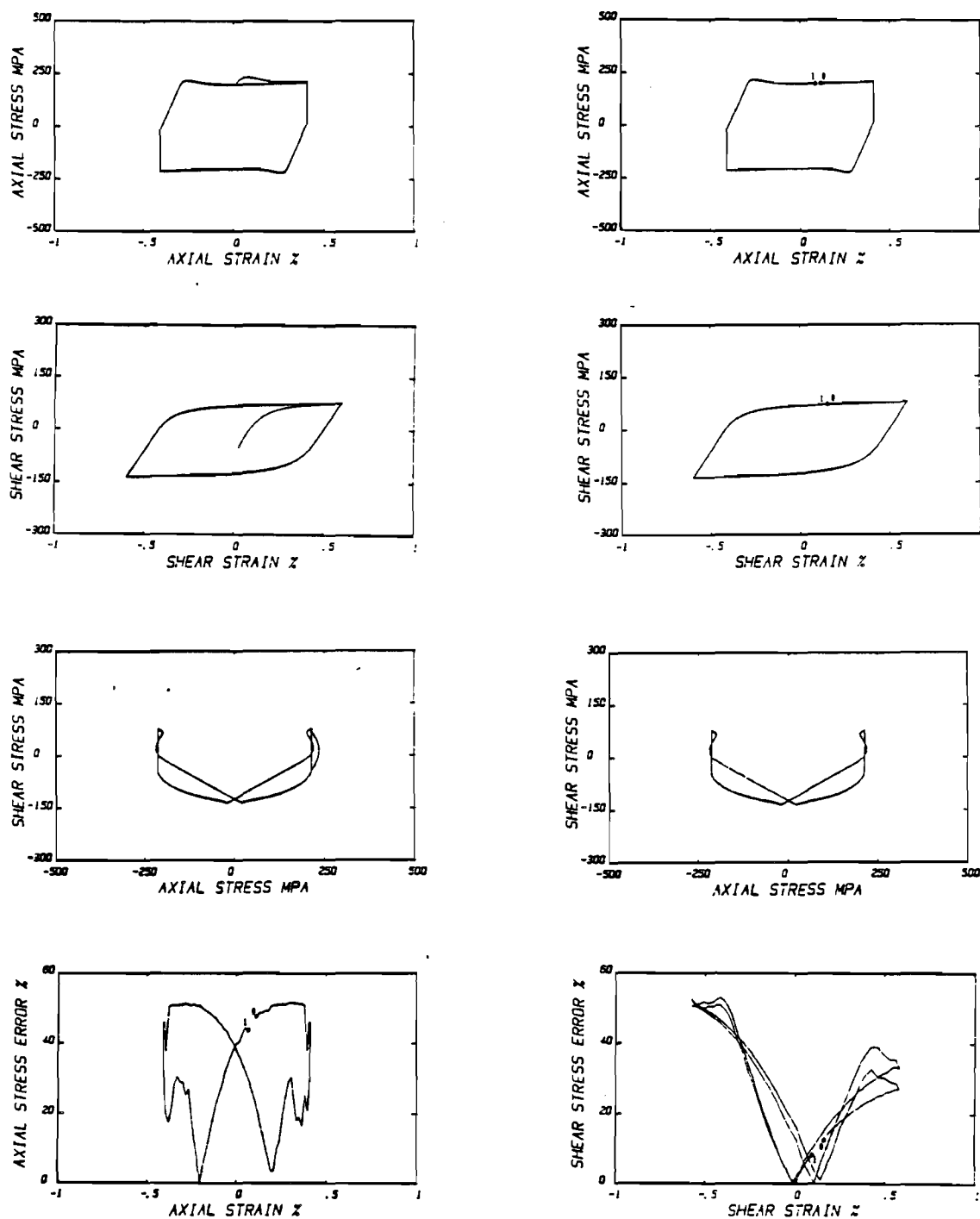


Figure 4-15. Numerical Solution by Krieg's Model for History II. Left column, top three plots show transient response (cycles 1-10); right column, top three plots show stable loop response (cycle 25); bottom row shows stable loop errors compared to experimental data.

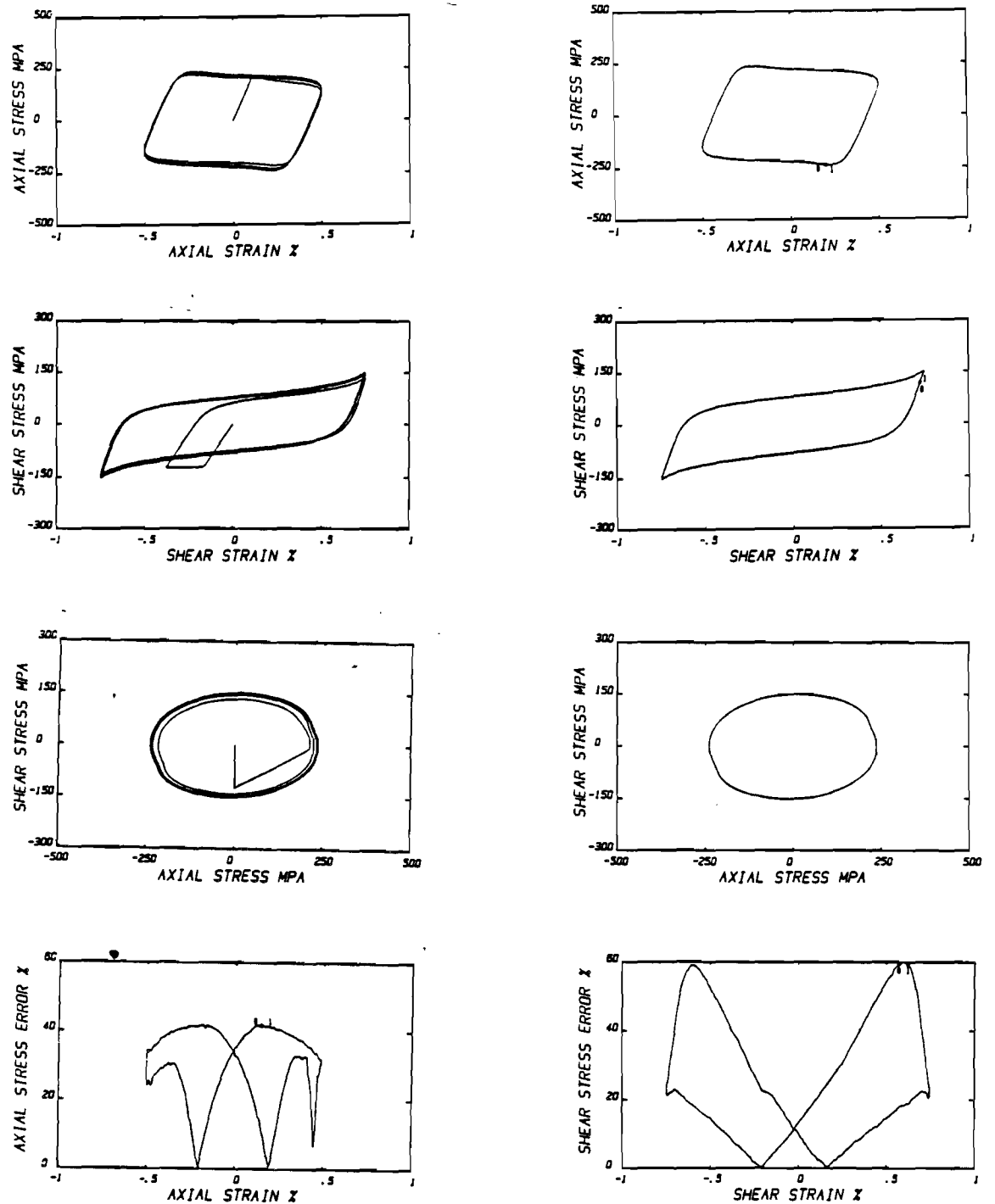


Figure 4-16. Numerical Solution by Krieg's Model for History III. Left column, top three plots show transient response (cycles 1-10); right column, top three plots show stable loop response (cycle 25); bottom row shows stable loop errors compared to experimental data.

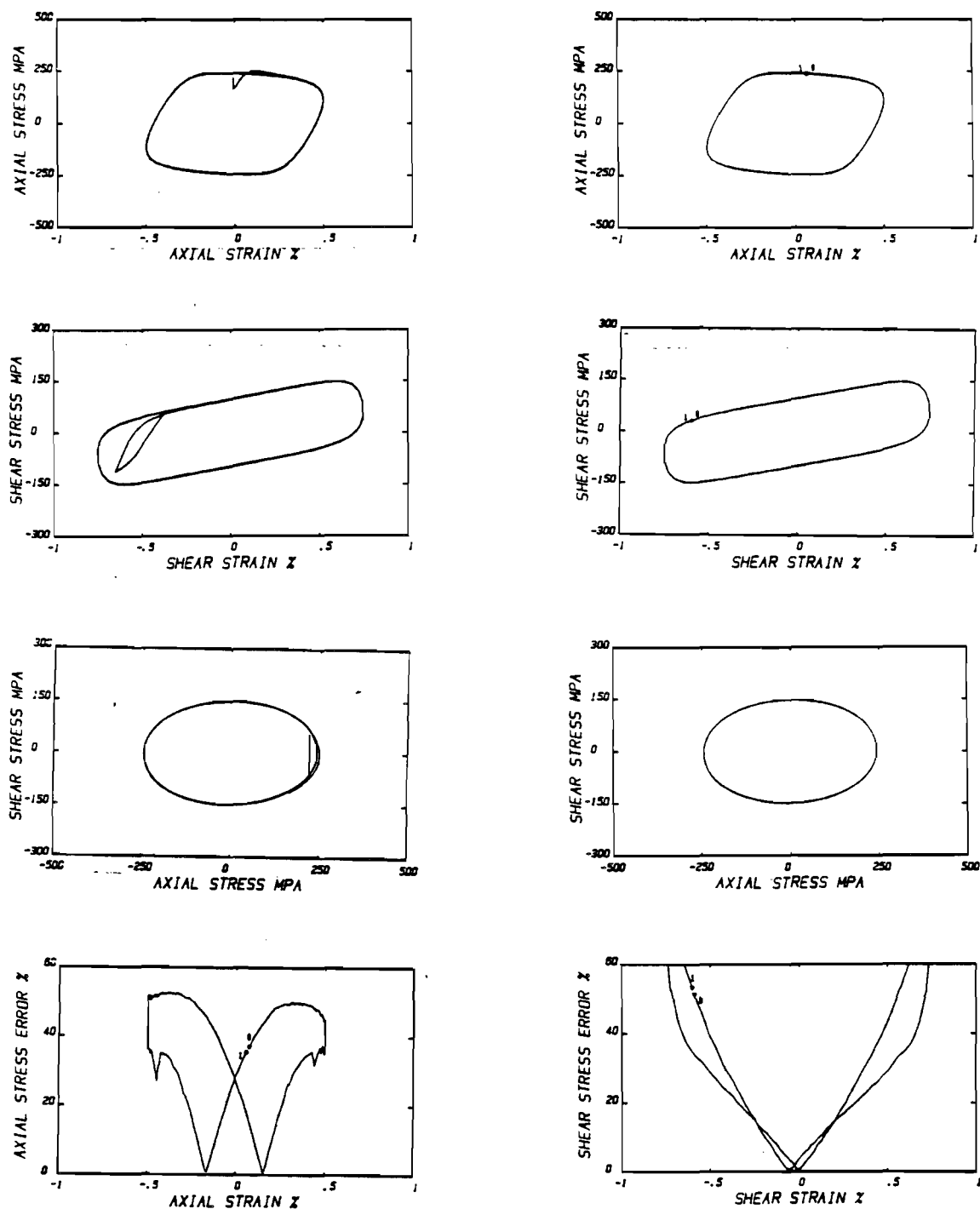


Figure 4-17. Numerical Solution by Krieg's Model for History IV. Left column, top three plots show transient response (cycles 1-10); right column, top three plots show stable loop response (cycle 25); bottom row shows stable loop errors compared to experimental data.

for history IV which, if compared to Figure 4-9, leads to the same conclusion: for nonproportional loading paths, Krieg's and Drucker's models behave effectively the same. In this sense, Krieg's model has the advantage of being computationally more efficient. Note that this is not true for proportional loadings where Drucker's model is considerably more accurate than this model.

#### Abrahamson's Model

Figures 4-18 through 4-21 exhibit the stress-strain response calculated by Abrahamson's model for histories I through IV. Table 4-4 shows the execution times and stable loop error statistics.

Referring to Table 4-4, the reader will note immediately the very large variations in computation time from one history to the other. For example, compare histories III and IV where a 30 degrees phase angle difference results in a 760% increase in computation time. Similarly, compare histories I and II where the addition of two nonproportional segments to the hysteresis cycle result in a 330% increase in computation time. There seems to be a nonlinear relationship between computation time and the level of nonproportionality of the applied strain history. In general, it can only be said that for Abrahamson's model the computation time is history-dependent until further analysis is done. Since this model is a generic form of unified creep-plasticity theory, this path-dependence of computational efficiency probably extends to other particular unified theories.

Similar to McDowell's model, this model predicts the nonproportional axial stress response with greater accuracy than the shear stress response. Table 4-4 shows that the stable loop average

Table 4-4. Stable Loop Errors and Computation Times for Abrahamson's Model.

	History I	History II	History III	History IV
CPU <sub>N</sub>	0.97	3.20	0.95	7.18
E <sub>a,avg</sub>	15.3	12.1	12.6	14.8
E <sub>a,max</sub>	32.5	21.7	24.7	23.0
E <sub>s,avg</sub>	15.5	11.6	25.3	21.6
E <sub>s,max</sub>	39.0	20.1	46.9	39.5

axial stress errors remain essentially constant with increasing nonproportionality. However, the average shear stress errors significantly increase for the two sinusoidal histories.

History I. As shown in Figure 4-18, the transient hardening response is predicted with relatively good accuracy. The stable loop maximum stress amplitudes are within 5% of the experimental values. However, notice that due to the very sharp yielding characteristic of unified creep-plasticity theories, this model underestimates the stress values in the first few cycles; as it hardens, the stable loop response is matched accurately except in the initial yielding regime. The axial and shear stress error plots show that the maximum prediction error occurs just after yielding (notice the two error peaks) and then reduces toward zero as the material deforms into the asymptotic plastic region.

History II. Figure 4-19 shows the resulting numerical solution. It is immediately seen that this model is capable of predicting nonproportional transient hardening rather accurately. Again notice the very sharp yielding observed in the axial stress response which results

in underestimated stresses both during transient hardening and for the stable loop response. The stable loop error plots show that for the axial case the largest errors occur in the asymptotic plastic region while for the shear case (due to "fattening" of the shear plot), they occur just after initial yielding.

History III. Figure 4-20 presents the calculated values for history III. Again, due to the sharp yielding characteristics of this model, it is seen that the transient hardening response significantly underestimates the stress histories for the first few cycles. On the other hand, the stable loop stress amplitudes are matched with better accuracy. Like McDowell's model, the shear stress response is characterized by a hysteresis loop "fattening" that significantly overpredicts the maximum plastic strain range and the stress values just after initial yielding for every cycle.

History IV. Figure 4-21 finally shows the predicted hysteresis loops for history IV. Note that disregarding the "fattening" of the shear stress response, both the transient hardening and the stable loops are predicted rather accurately. Comparing Figures 4-10 through 4-13 to Figures 4-18 to 4-21, the reader will note the existing similarities between McDowell's and Abrahamson's predicted results. Even though these models have radically different structures, the predicted results are quite similar. However, McDowell's model is computationally more efficient while Abrahamson's is more versatile since it can handle time- and rate-dependent phenomena. McDowell (1984a) expresses that, as a general rule, unified creep-plasticity theories are computationally inefficient in solving time-dependent problems.

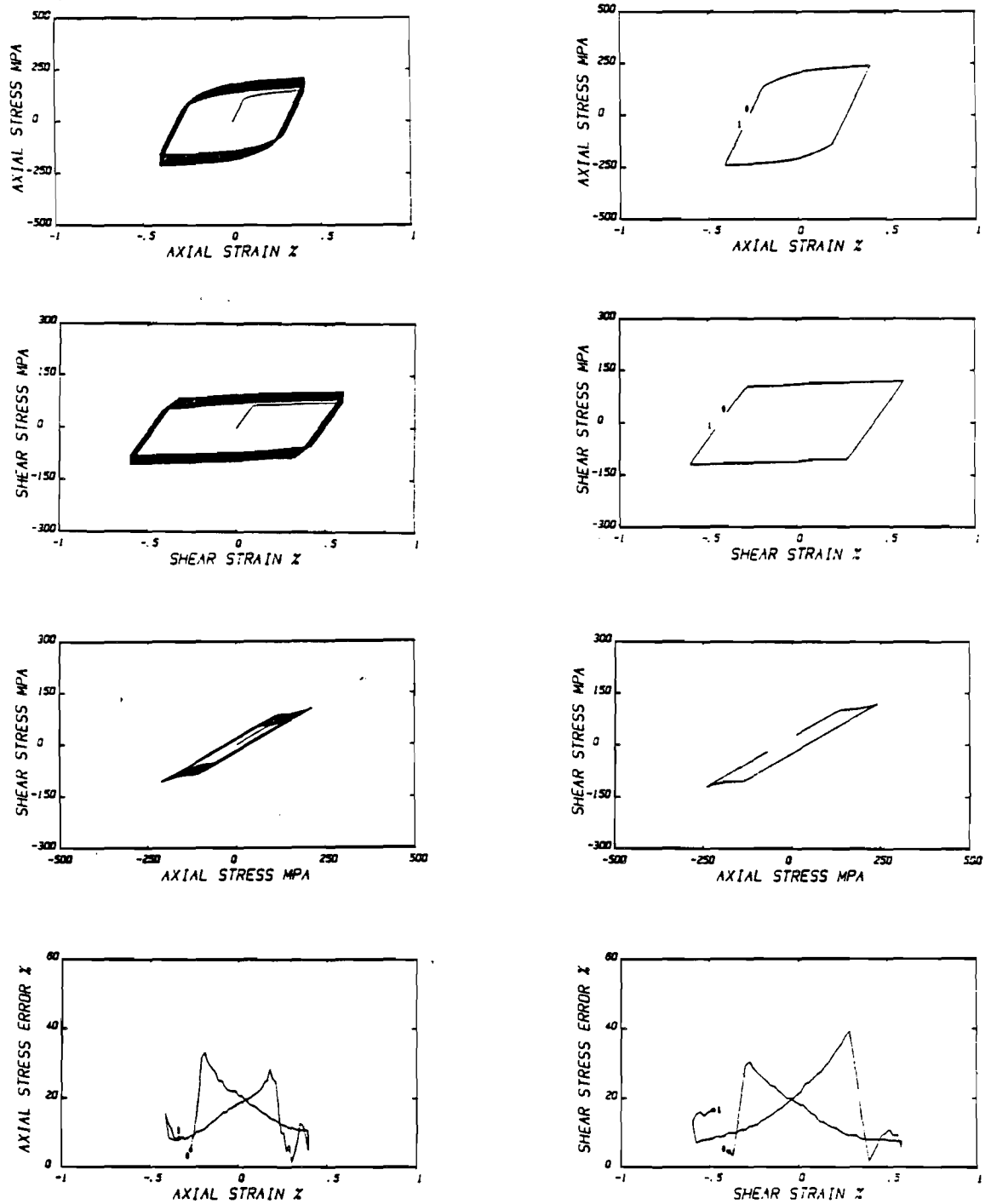


Figure 4-18. Numerical Solution by Abrahamson's Model for History I. Left column, top three plots show transient response (cycles 1-10); right column, top three plots show stable loop response (cycle 25); bottom row shows stable loop errors compared to experimental data.



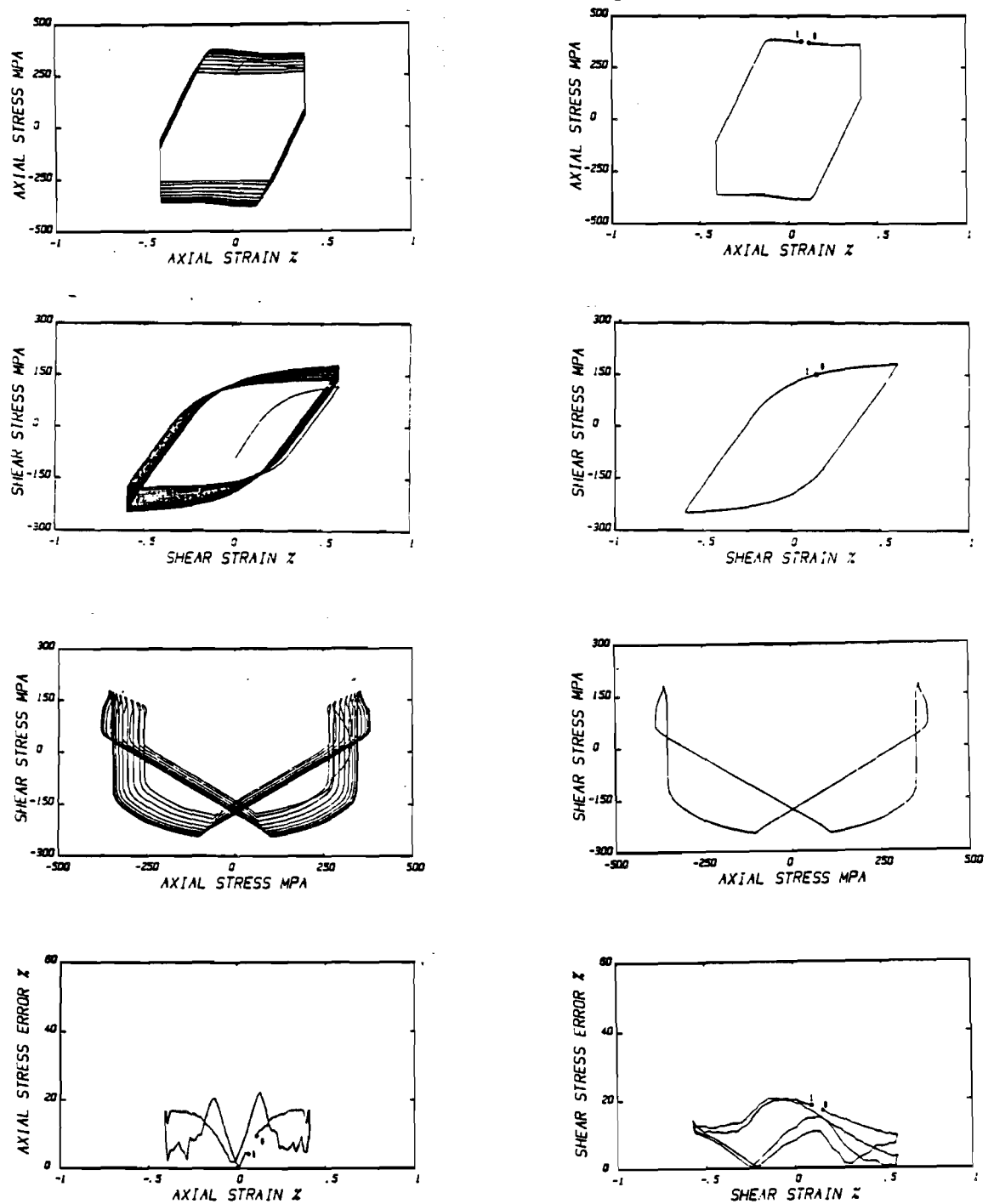


Figure 4-19. Numerical Solution by Abrahamson's Model for History II. Left column, top three plots show transient response (cycles 1-10); right column, top three plots show stable loop response (cycle 25); bottom row shows stable loop errors compared to experimental data.

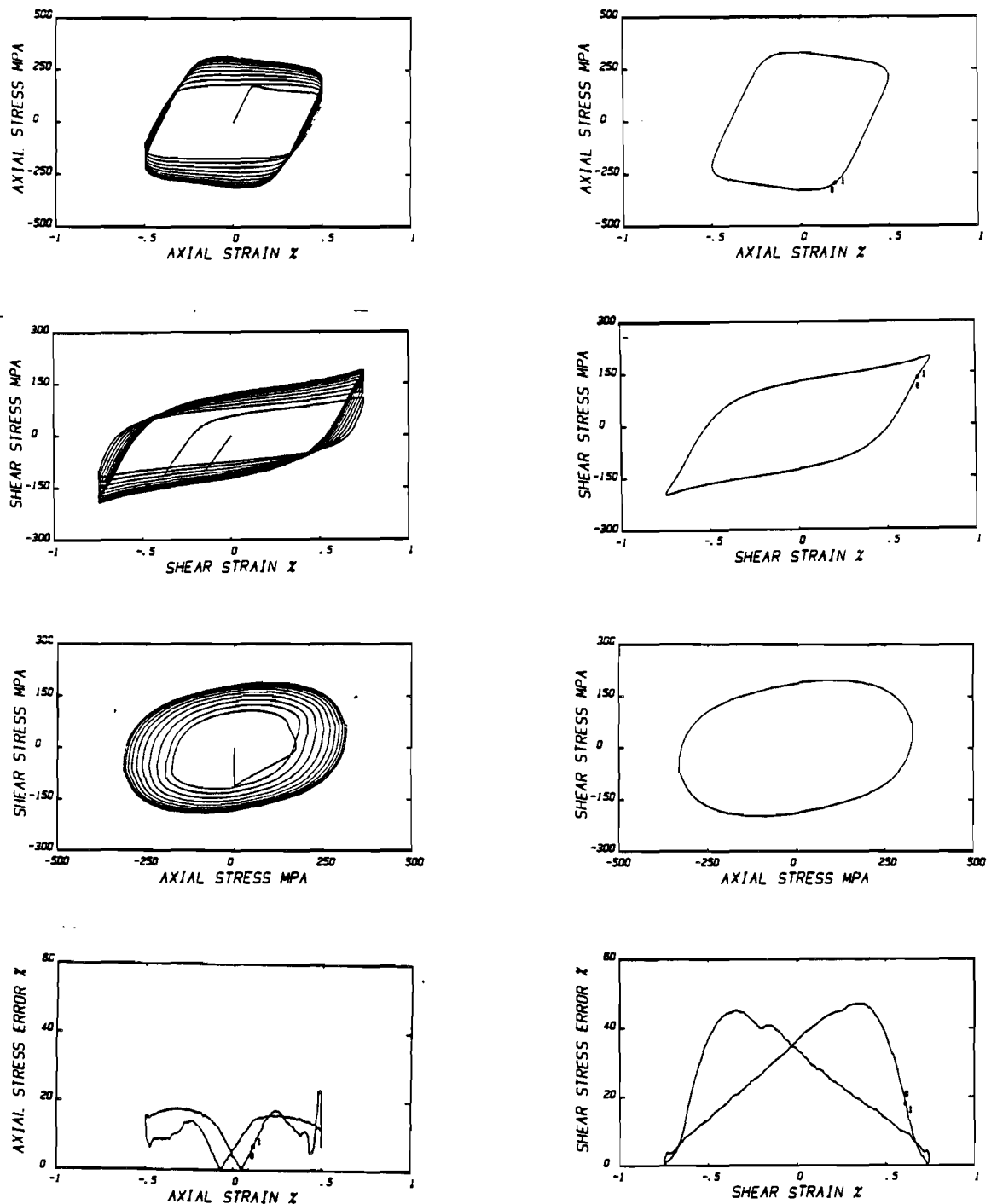


Figure 4-20. Numerical Solution by Abrahamson's Model for History III. Left column, top three plots show transient response (cycles 1-10); right column, top three plots show stable loop response (cycle 25); bottom row shows stable loop errors compared to experimental data.

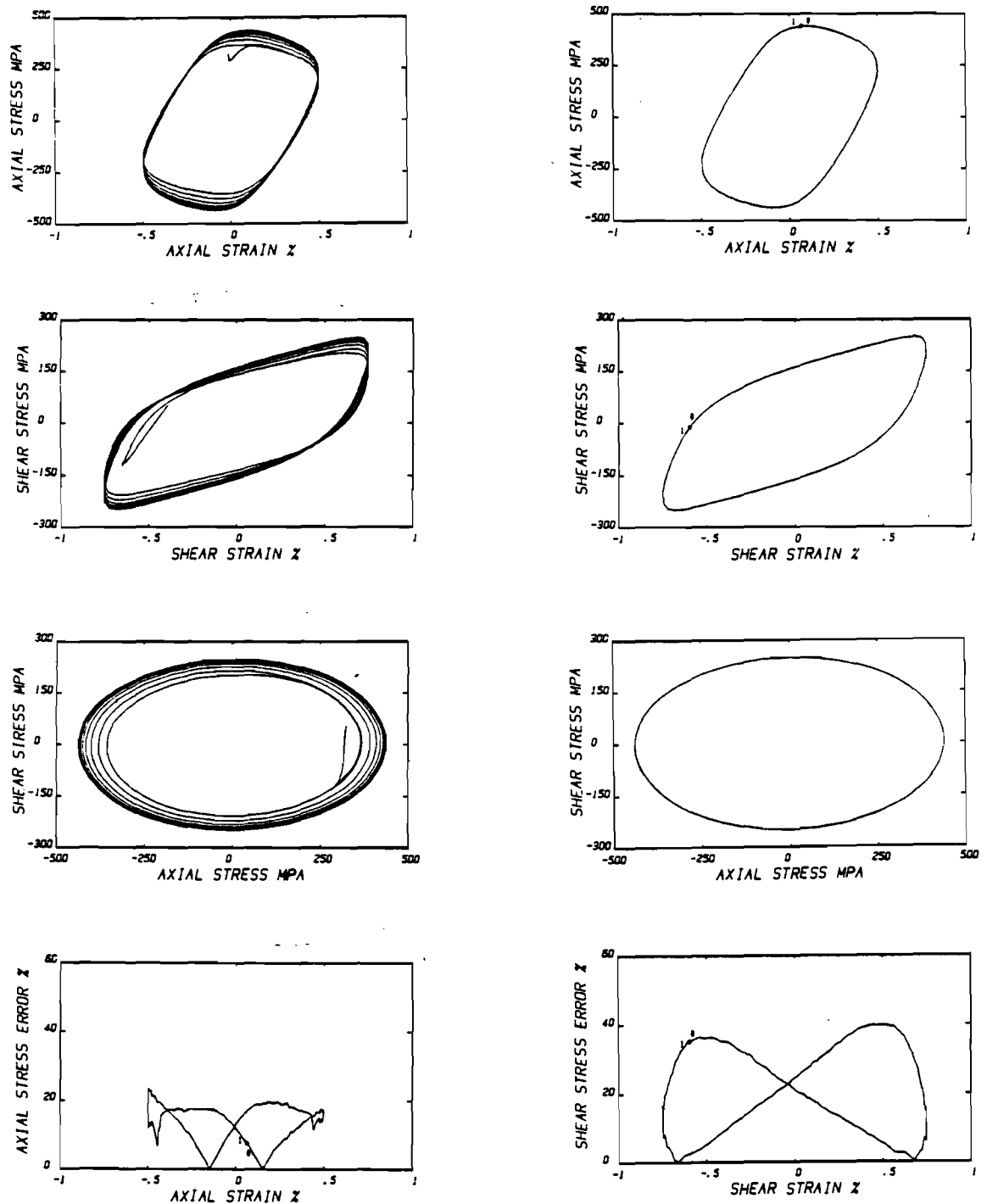


Figure 4-21. Numerical Solution by Abrahamson's Model for History IV. Left column, top three plots show transient response (cycles 1-10); right column, top three plots show stable loop response (cycle 25); bottom row shows stable loop errors compared to experimental data.

It should be noted that for all the models, when subjected to nonproportional strain paths, the predicted plastic strain range does not reflect the experimental results. This is evidenced clearly by the "fattening" of the shear stress responses under nonproportional type loadings. If accurate fatigue life predictions are to be made, it is necessary to engage in further research to develop a model capable of accurately predicting the plastic strain ranges in addition to stress amplitudes. This is seen as the next step for current research and development of these constitutive equations.

#### Model Evaluation Summary

Table 4-5 shows a summarized version of the conclusions that can be drawn from the model evaluations just presented.

Table 4-5. Model Evaluation Summary.

	Proportional Multiaxial Loadings	Nonproportional Multiaxial Loadings	Time- and Rate-dependent Phenomena
Drucker's Model:			
Predictive Accuracy	Good	Inferior	Incapable
Computational Eff.	Medium	Medium	-----
McDowell's Model:			
Predictive Accuracy	Excellent	Good	Incapable
Computational Eff.	Low	Low	-----
Krieg's Model:			
Predictive Accuracy	Regular	Inferior	Incapable
Computational Eff.	Very High	Very High	-----
Abrahamson's Model:			
Predictive Accuracy	Good	Good	Good
Computational Eff.	Medium	Very Low	Very Low

### Integration Technique Evaluations

In the previous section, it was shown that most of the models outlined presented a numerical behavior independent of input strain and strain rate history. With the exception of Abrahamson's model, all models showed little sensitivity to changes in input history from the standpoint of computational efficiency. However, Abrahamson's model's normalized CPU time (a measure of computational efficiency) showed large variations which reflected that radical changes in the numerical behavior of the model were occurring as the input history was changed. This suggests the possibility of the model's numerical behavior changing not only with input strain history but also with the numerical solution algorithm. This section shows that, as suspected, the computational efficiency of the models change with numerical solution algorithm used.

In this section, Krieg's model will not be integrated since it was only introduced in the analysis to show the tremendous computational advantage of the radial-return integration algorithm applied to a constitutive model of the generic form of Drucker's model.

As previously stated, all the numerical integration techniques will be compared against the solutions calculated using Gear's numerical integration algorithm. Therefore, errors reported in this section are computed with respect to Gear's method solution, not experimental results. Two input strain histories were used as the basis for these comparisons. History V consisted of three cycles of proportional straining from the initially annealed state with maximum axial and shear strain amplitudes  $\epsilon_a = 0.0041$  and  $\gamma_a = 0.0060$ , respectively (very similar to history I). The effective strain rate was kept constant at

$\dot{\epsilon}_{\text{eff}} = 0.003 \text{ sec}^{-1}$ . History VI consisted of three cycles of sinusoidal loading with 90 degrees phase angle,  $\epsilon_a = 0.0050$ ,  $\gamma_a = 0.0075$ , and  $\dot{\epsilon}_{\text{eff}} = 0.001 \text{ sec}^{-1}$ . McDowell (1984a) and others have experimentally shown this history to result in the largest observed increase in hardening due to nonproportionality effects for axial-torsional loading. These two contrasting histories were chosen so that any history-dependent model numerical behavior would be clearly exhibited.

Figure 4-22 shows the axial stress-time and the shear stress-time responses predicted for histories V and VI by using Gear's numerical integration method with McDowell's, Drucker's, and Abrahamson's models. These graphs show the predicted results by using Gear's method in its most efficient yet accurate form, as explained next. A series of trial runs were executed with the same input strain histories but variable initial time step-size and maximum allowable single-step error. It was determined that the solution was insensitive to changes in the initial time step-size unless the chosen values were unreasonably large. The best combination of computational accuracy and efficiency was found by keeping the maximum allowable single-step error  $E_{\text{max}} \leq 0.001$ . Choosing  $E_{\text{max}} > 0.001$  resulted in large variations for the calculated stress values as compared to the values predicted with  $E_{\text{max}} \leq 0.001$ . Choosing  $E_{\text{max}} \lll 0.001$  resulted in no significant change of the calculated stress values but tremendously increased the computation times. So, this was chosen as the reference solution used for this analysis.

The integration routines presented in chapter III have been evaluated for both histories V and VI, and for each of the models mentioned above. The standard input values used in the first execution

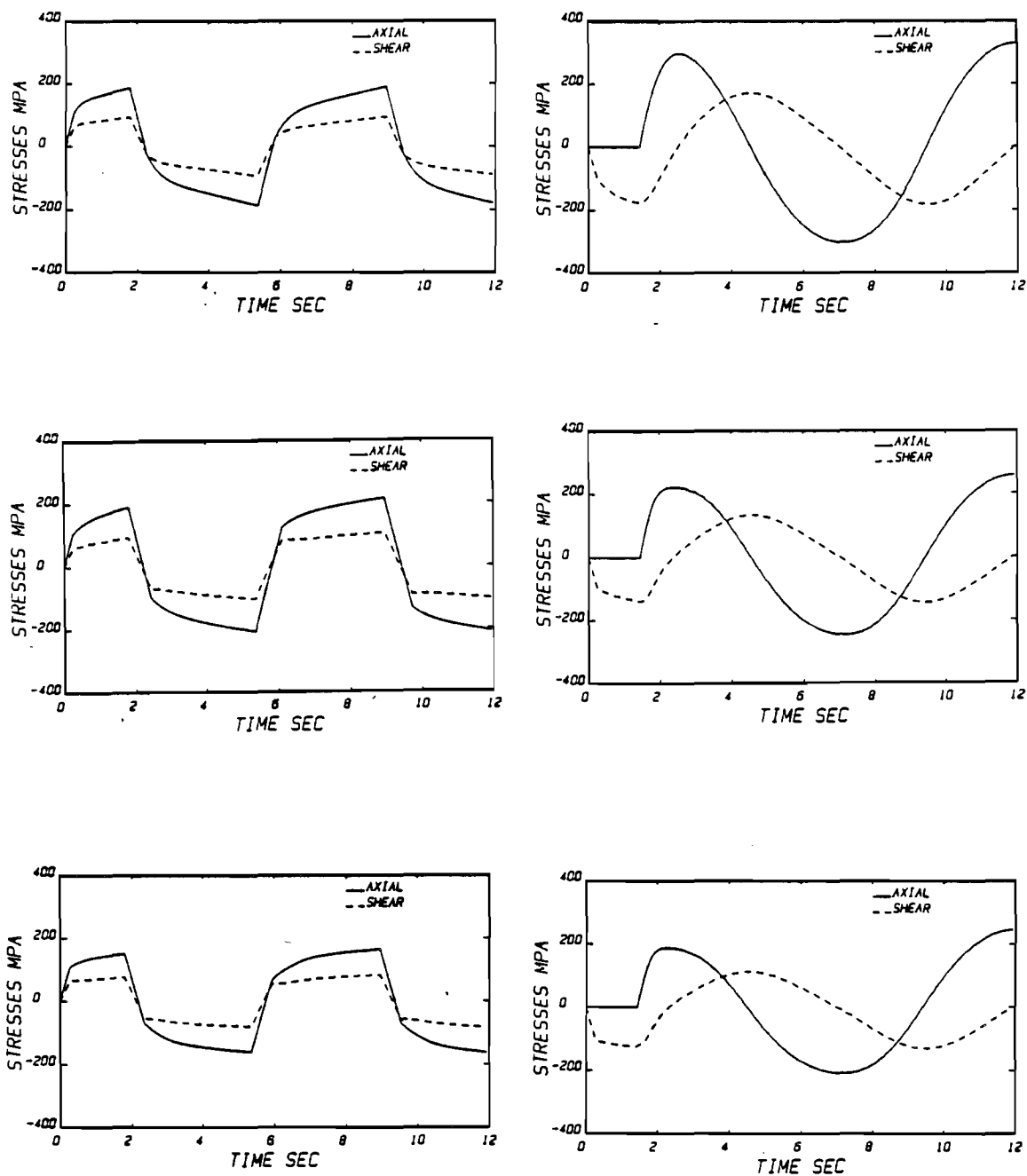


Figure 4-22. Axial and Shear Stress vs. Time Responses for Histories V and VI Integrated by Gear's Method.

Left column, history V; right column, history VI; top row, McDowell's model solution; middle row, Drucker's model solution; bottom row, Abrahamson's model solution.

of each integration routine were chosen as  $E_{\max} = 0.001$ ,  $E_{\min} = 0.0001$ ,  $h_{\text{init}} = 0.01$  sec., and  $m^* = 2$ .  $E_{\max}$ ,  $E_{\min}$ , and  $m^*$  are as defined in chapter III and  $h_{\text{init}}$  is the initial time step-size chosen by the user. Notice that  $m^*$  is a parameter applicable to the Iterative Adams Predictor-Corrector method only. After the first set of executions with standard values, further insight was gained by varying some of these parameters as shown in the sections to follow.

The integration routines will be evaluated based on computational accuracy and efficiency. Efficiency performance evaluation will be based on the normalized CPU time  $\text{CPU}_N$  as defined by equation (4.3) and the number of phenomenological subroutine evaluations  $N_f$  (to be called number of function evaluations) as given by

$$N_f = \frac{N_c}{t_f} \quad (4.4)$$

where  $N_c$  is the total number of function evaluations for the history under consideration and  $t_f$  is the corresponding final value of the independent variable (time). Table 4-6 shows the actual values of  $\text{CPU}_N$  and  $N_f$  for all the models when integrating histories V and VI using the reference Gear's method. As noted in the previous section, the normalized CPU time seems to be insensitive to input history for McDowell's and Drucker's models. This is confirmed by the small variances in the number of function evaluations  $N_f$ . However, note the tremendous increase in execution time for Abrahamson's model when integrating nonproportional history VI. So, as shown in the previous section, the computation times for Abrahamson's model are greatly



Table 4-6. Actual Computation Times and Number of Function Evaluations Using Gear's Method with Standard Input Parameter Values.

Model	McDowell		Drucker		Abrahamson	
History	V	VI	V	VI	V	VI
CPU <sub>N</sub>	7.72	7.08	2.98	2.99	4.05	44.97
N <sub>f</sub>	1494	1354	865	844	920	13974

sensitive to the nonproportionality level of the input strain history. The reader must keep in mind this apparent path-dependence of computational efficiency since it will be shown to be an important parameter in the selection of the best numerical solution algorithm for nonproportional, multiaxial, cyclic plasticity. Tables 4-7 through 4-15 and C-1' through C-2 show values of CPU<sub>N</sub> and N<sub>f</sub> as percentages of the values shown in Table 4-6 to give the reader a relative basis for comparison of the different numerical methods studied.

Integration routine accuracy will be evaluated on the basis of axial stress average error  $E_{a,avg}$ , axial stress maximum error  $E_{a,max}$ , shear stress average error  $E_{s,avg}$ , and shear stress maximum error  $E_{s,max}$ . Axial and shear stress errors are defined by equations (4.1) and (4.2), respectively, with the modifying assumption that the reference is Gear's corresponding numerical solution instead of experimental data. Plots of these errors as they vary with time will be shown to pinpoint segments of large errors and to determine the overall trends of the error patterns.

#### Runge-Kutta Method with Gill Coefficients

As presented in chapter III, this is a multiple-step, explicit,

non-iterative, fourth-order, fixed step-size method. Because this method maintains a constant time step-size, it is insensitive to changes in the numerical behavior of the system of ODE's if viewed from the standpoint of computational efficiency. However, if the fixed time step-size chosen is too large relative to the stiffness of the system being solved, it may render this method unstable or at least it will introduce false oscillations in the predicted results. On the other hand, if the time step-size is small enough so that no oscillations occur, it may still introduce considerable errors.

The standard input values were used in the first execution. It was found that the estimated single-step error as defined in chapter III was well within desirable bounds. So, there was no danger of instability or false oscillations. Table 4-7 summarizes the results obtained for the performance parameters with  $h_{init} = 0.01$ . Table 4-8 shows a similar table for a second set of runs with  $h_{init} = 0.005$ . Figure 4-23 shows axial and shear stress errors vs. time for the first cycle of histories V and VI for all the models with  $h_{init} = 0.01$ .

History V. For proportional type histories, Table 4-7 shows that this method results in computation time savings of the order of at least 70% compared to Gear's method. Such large savings are due to an approximate drop of 65% in the number of function evaluations as shown in Table 4-7. It is seen that the savings incurred apply to all the models tested with the largest savings occurring for McDowell's model. Notice that there is no sacrifice in computational accuracy. The maximum axial stress error observed was in the order of 1% with average error values ranging from 0.05% to 0.45% for all the models. The maximum

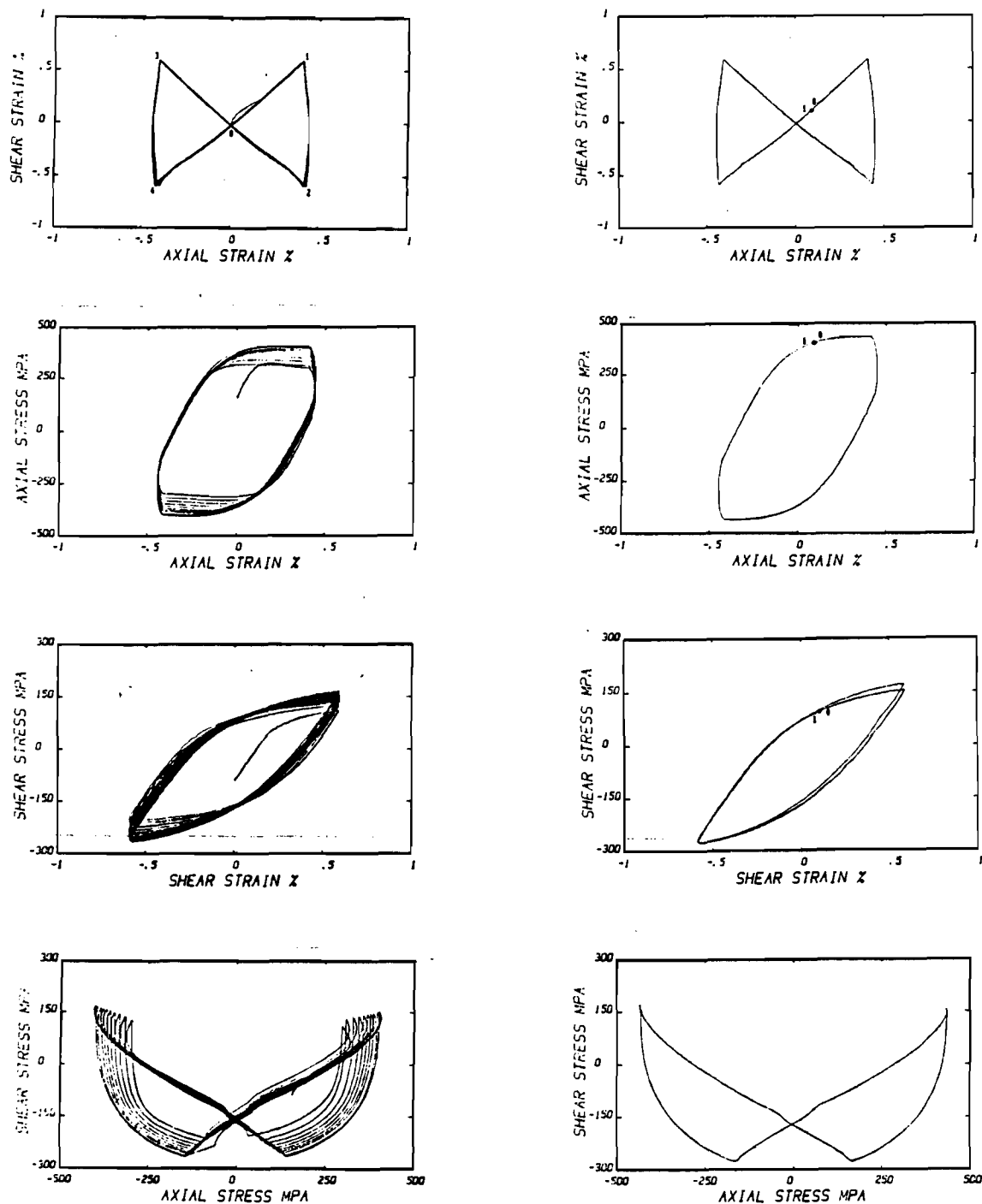


Figure 4-3. Experimental Data for History II.  
 Left column shows transient response (cycles 1-10);  
 right column shows stable loop response (cycle 25).

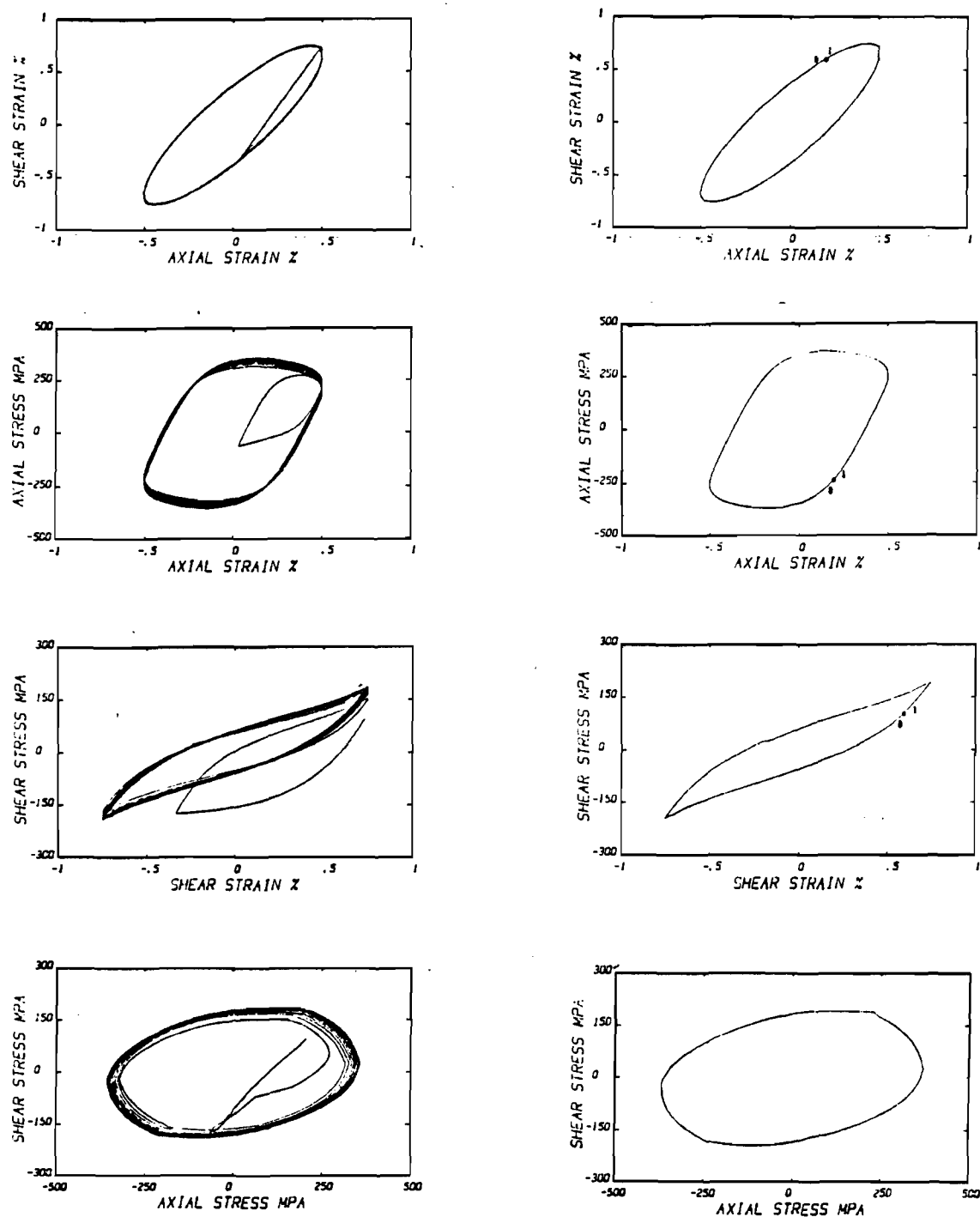


Figure 4-4. Experimental Data for History III.  
 Left column shows transient response (cycles 1-10);  
 right column shows stable loop response (cycle 25).

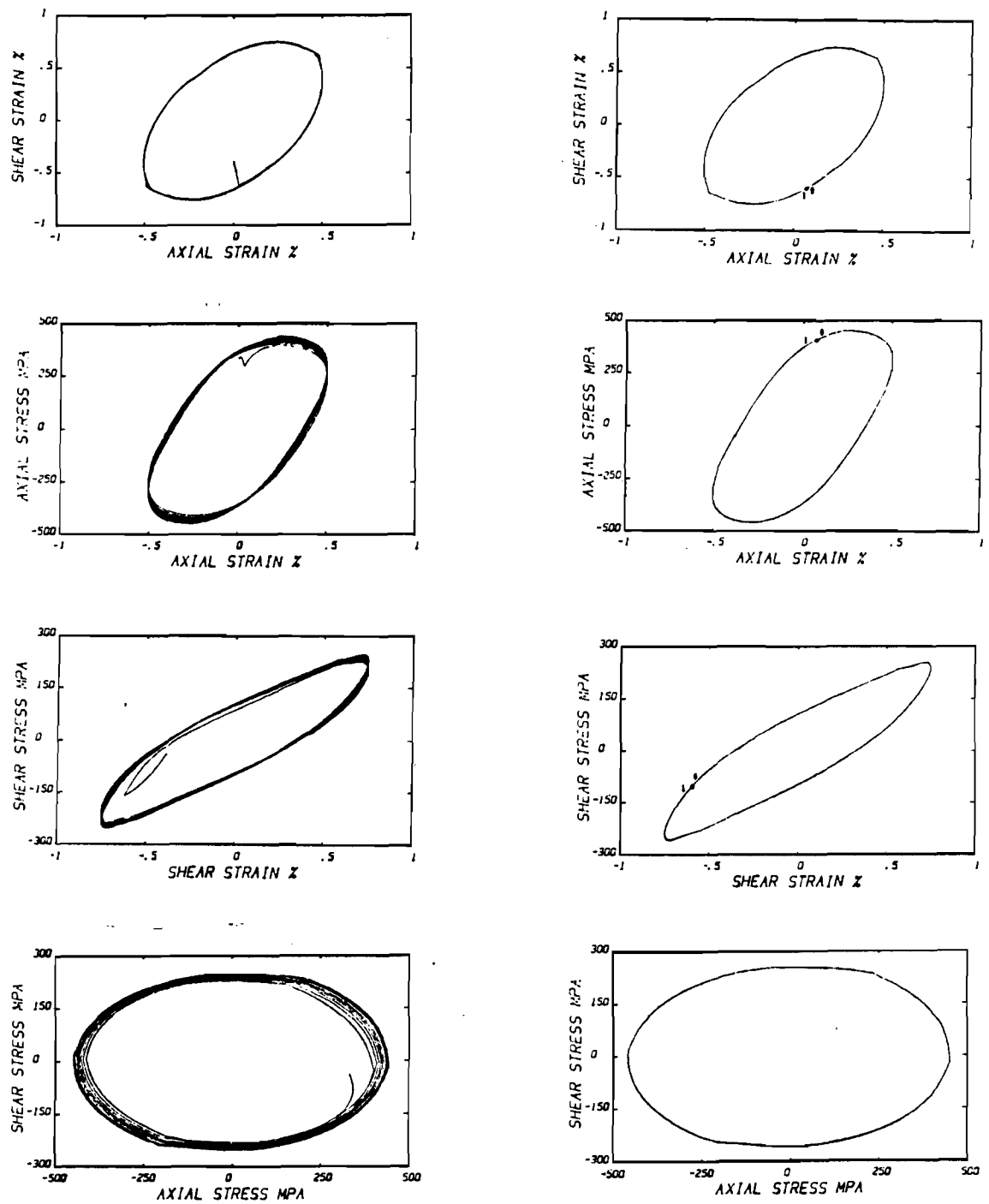


Figure 4-5. Experimental Data for History IV.  
 Left column shows transient response (cycles 1-10);  
 right column shows stable loop response (cycle 20).

hardening occurred between cycles 10 and 25. Finally, Figure 4-5 shows history IV which consists of 25 cycles of nonproportional sinusoidal loading from the history III ending state with 60 degrees phase angle and the same strain amplitudes as in the third history. Notice the increase in hardening achieved by just changing the phase angle of the test. History IV then is a more severe nonproportional path with a consequential hardening increase.

As previously stated, Appendix A summarizes the material constants, model parameters, modeling functions, and axial-torsional forms of the models discussed here. It was assumed that for multiaxial, cyclic plasticity applications the model parameters could be determined on the basis of uniaxial equivalent values. So, the model parameters shown in Appendix A for Drucker's and Krieg's models were determined from experimental history I based on effective axial and shear stresses and strains. The model parameters and modeling functions for McDowell's and Abrahamson's models were taken from their respective analyses on the experimental histories shown in this work.

Each of the four models presented in chapter II will be evaluated for each of the four histories discussed. The numerical solutions will be shown in a format similar to that of Figures 4-2 through 4-5. In addition, plots of the axial and shear stress errors during the stable loop response will be shown. These errors have been defined as follows:

$$E_a(\%) = \frac{\sigma_a - \sigma_e}{\sigma_{\max}}(100) \quad (4.1)$$

$$E_s(\%) = \frac{\tau_a - \tau_e}{\tau_{\max}}(100) \quad (4.2)$$

where  $\sigma_e$  and  $\tau_e$  are the experimental values of axial and shear stresses for given axial and shear strains respectively,  $\sigma_a$  and  $\tau_a$  are the corresponding numerical solutions (at the same axial and shear strains) by the model being considered, and  $\sigma_{\max}$  and  $\tau_{\max}$  are the largest experimental values of axial and shear stresses over the stable loop response. Thus, the axial and shear stress errors  $E_a$  and  $E_s$  are normalized with respect to the same measure for the histories being analyzed.

To further expand the analysis of the stable loop error plots, average and maximum stress errors will be shown in the analysis to follow. The axial stress average error  $E_{a,avg}$  and the shear stress average error  $E_{s,avg}$  correspond to average values calculated over the shown stable loop response. The axial stress maximum error  $E_{a,max}$  and the shear stress maximum error  $E_{s,max}$  are the actual absolute maximums over the stable hysteresis loop. The error criteria chosen might not be the best possible; however, they do show the error trends and relative error magnitudes necessary to evaluate the material models. Due to the cyclic nature of the problem being considered, multiplicity of stress values at a given strain is observed. Furthermore, due to phase lags of the predicted stress behaviors, sudden jumps in the stable loop error plots will be observed as the loading direction changes or as the stress values pass through zero. These are two inconveniences of the error criteria chosen which slightly affect the accuracy of the results shown.

To analyze the computational efficiency of the models, a non-

dimensional CPU time has been defined as follows:

$$CPU_N = \frac{CPU_A}{t_f} \quad (4.3)$$

where  $CPU_A$  is the actual CPU time taken by the Cyber 835 to solve the history under consideration and  $t_f$  is the final value of the independent variable (time) for this execution. Thus, the normalized CPU time  $CPU_N$  is calculated based on the assumption that the computation time varies linearly with the total length of the execution. Due to the cyclic nature of the calculations, this is a reasonable assumption.

#### Drucker's Model

Figures 4-6 through 4-9 show the predicted stress-strain responses for Drucker's model for the four histories considered. Table 4-1 presents general data pertaining to the stable loop error plots and computation times required.

Computation times for Drucker's model seem to be history-independent as seen in Table 4-1. The variances in normalized CPU times are rather small given that all histories are quite different. Notice that the average stable loop errors are smallest for history I (proportional history) and about three times larger for all other histories (nonproportional histories). Also note that the maximum stress errors are considerably larger than the average errors regardless of the applied strain history.

History I. As can be seen from Figure 4-6, the transient hardening response is predicted quite accurately for this proportional loading path. The stabilized axial and shear stress amplitudes are



Table 4-1. Stable Loop Errors and Computation Times for Drucker's Model.

	History I	History II	History III	History IV
CPU <sub>N</sub>	0.71	0.73	0.60	0.60
E <sub>a,avg</sub>	12.0	32.7	30.2	35.3
E <sub>a,max</sub>	43.0	48.7	40.7	51.5
E <sub>s,avg</sub>	8.1	21.5	27.2	34.7
E <sub>s,max</sub>	38.2	43.8	54.5	66.0

predicted very well. However, notice that this model overestimates axial and shear stress values near the region of initial yielding. The sharp yielding shown is not characteristic of the implemented rounding corner option of this model. The stable loop error plots confirm that the peak stress errors always occur near the point of initial yielding and then are driven toward zero as the material deforms into the asymptotic plastic region. Note that the shear stress-shear strain plots exhibit an extraneous material softening followed by increased hardening just after initial yielding. This seems to be a consequence of the sharp yielding.

History II. Figure 4-7 shows that this model does not predict any further hardening due to nonproportional loading paths. Observe that the material shows a saturated response throughout the 25 cycles; hence, the predicted hardening response does not describe experimental results. The stable loop shapes are predicted incorrectly; the asymptotic plastic modulus is considerably underestimated. Notice that in this case the axial stress-axial strain plots exhibit softening followed by increased hardening just after yielding. The stress error plots show that,

contrary to history I, the largest errors occur as the material deforms into the asymptotic plastic region and then are driven back to zero as the material unloads and enters the initial yielding regime. This behavior results from this model's inability to predict the increased isotropic hardening due to nonproportionality effects.

History III. Figure 4-8 shows the numerical solution to the nonproportional 30 degrees out-of-phase sinusoidal strain path. Notice that even though this model predicts hardening, it significantly underestimates the isotropic hardening for the axial stress response. The shear stress response is poorly predicted. The shape of the stabilized shear hysteresis loop is not in agreement with the experimental results. According to McDowell (1984a) this is probably, at least partially, a consequence of using a von Mises yield condition normalized to the axial stress. The axial stress error plot confirms that the largest errors occurred as the material deformed in the asymptotic plastic region. The shear stress error plot shows that this model significantly overestimates the shear stress for the entire stable hysteresis loop.

History IV. As can be seen from Figure 4-9, this model's predictions are quite similar for histories III and IV. First, observe that throughout 25 cycles the model predicts a stabilized stress response. Hardening due to nonproportionality effects is disregarded. The stable loop responses greatly underestimate the actual hardening incurred. The stress error plots show that the largest errors always occur as the material yields into the asymptotic plastic region; this confirms expectations. An interesting point should be made here.

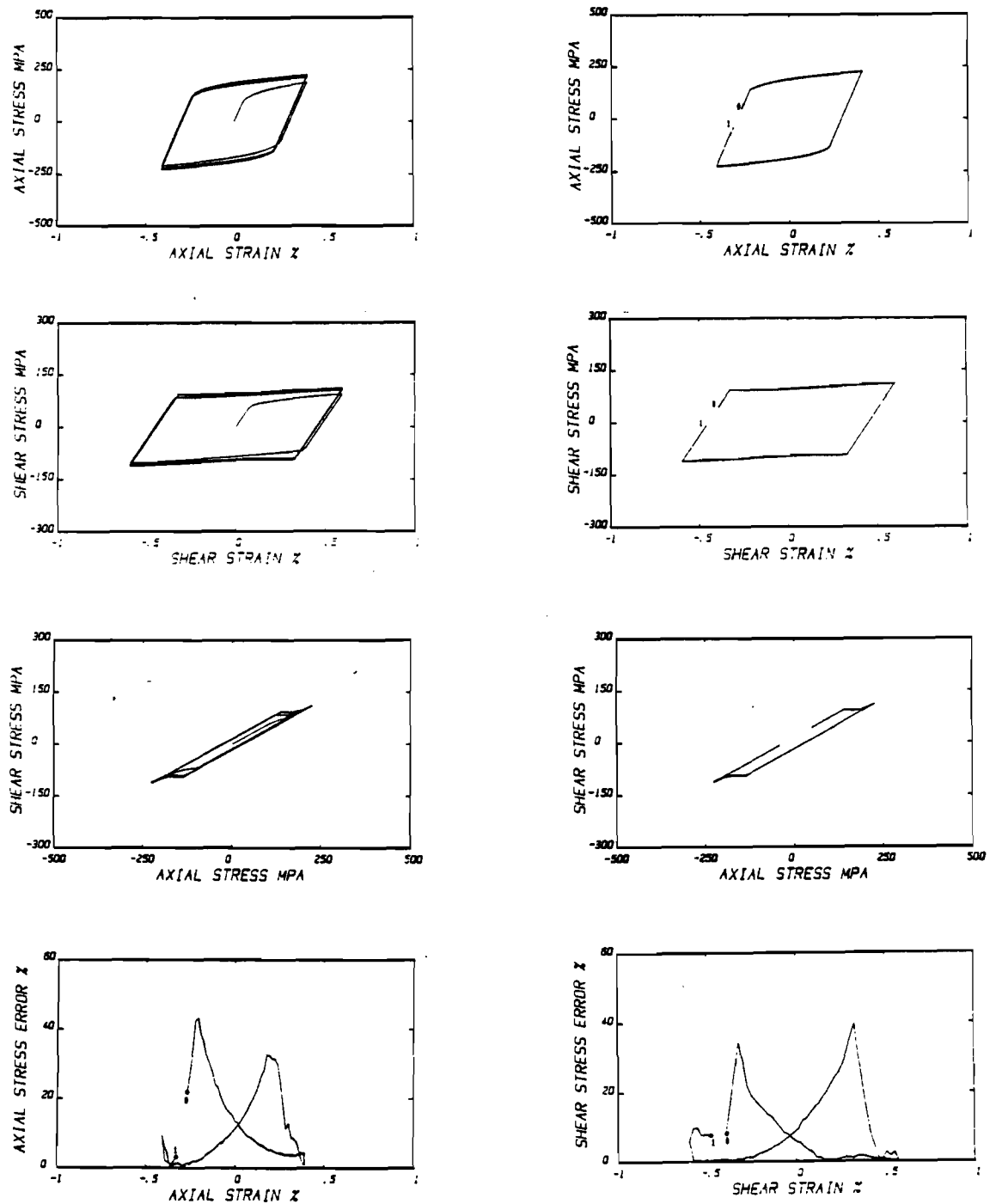


Figure 4-6. Numerical Solution by Drucker's Model for History I. Left column, top three plots show transient response (cycles 1-10); right column, top three plots show stable loop response (cycle 25); bottom row shows stable loop errors compared to experimental data.

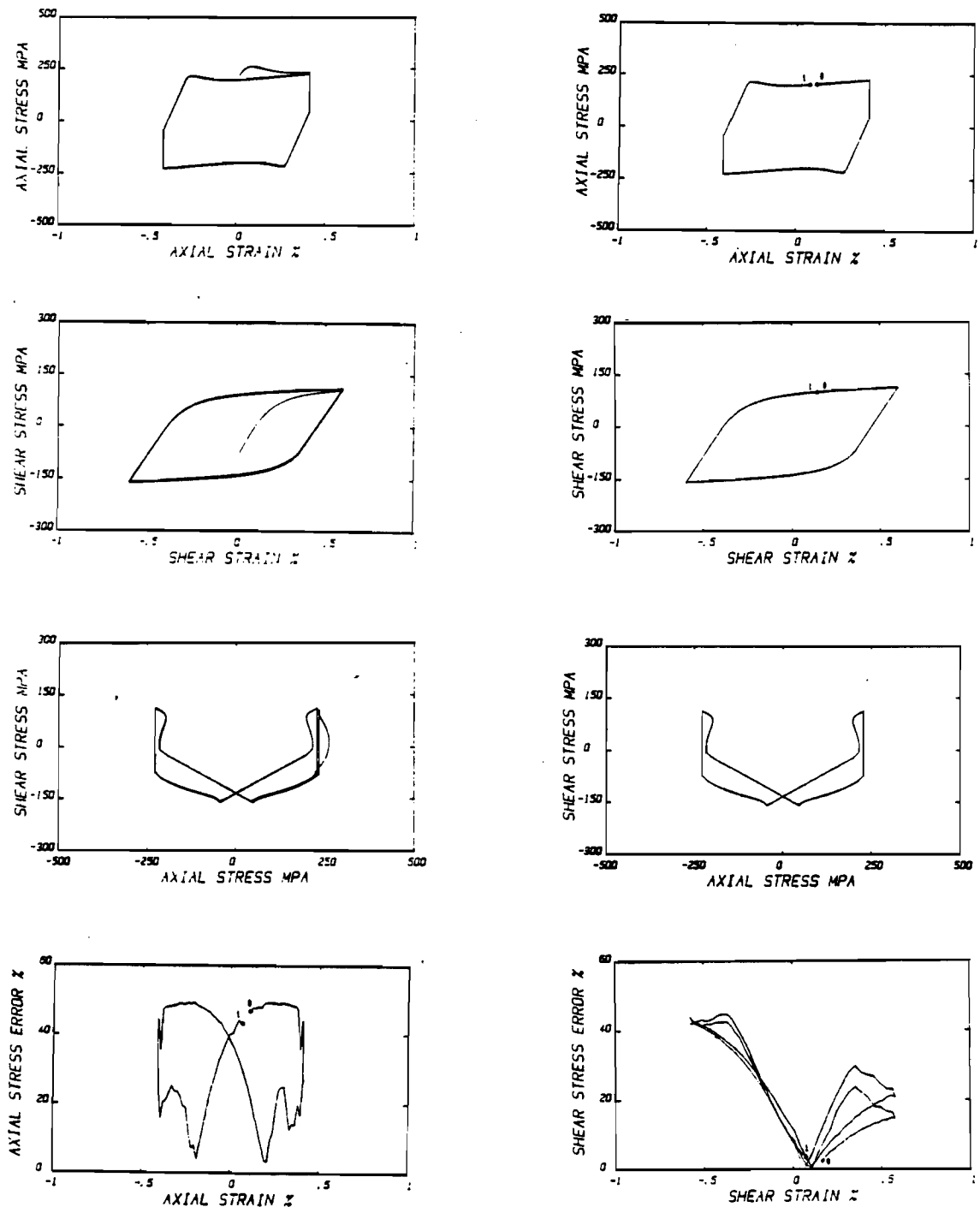


Figure 4-7. Numerical Solution by Drucker's Model for History II. Left column, top three plots show transient response (cycles 1-10); right column, top three plots show stable loop response (cycle 25); bottom row shows stable loop errors compared to experimental data.

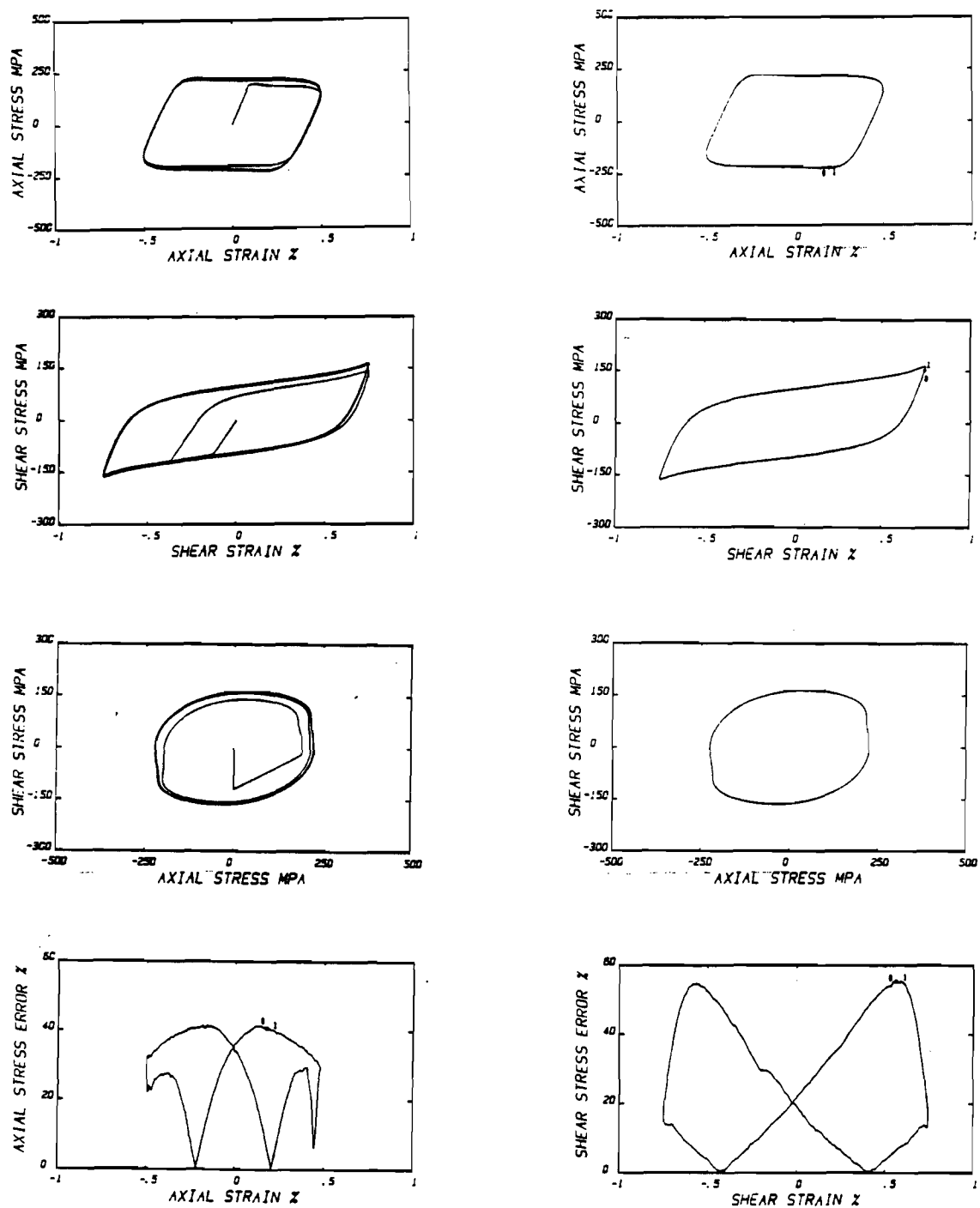


Figure 4-8. Numerical Solution by Drucker's Model for History III. Left column, top three plots show transient response (cycles 1-10); right column, top three plots show stable loop response (cycle 25); bottom row shows stable loop errors compared to experimental data.

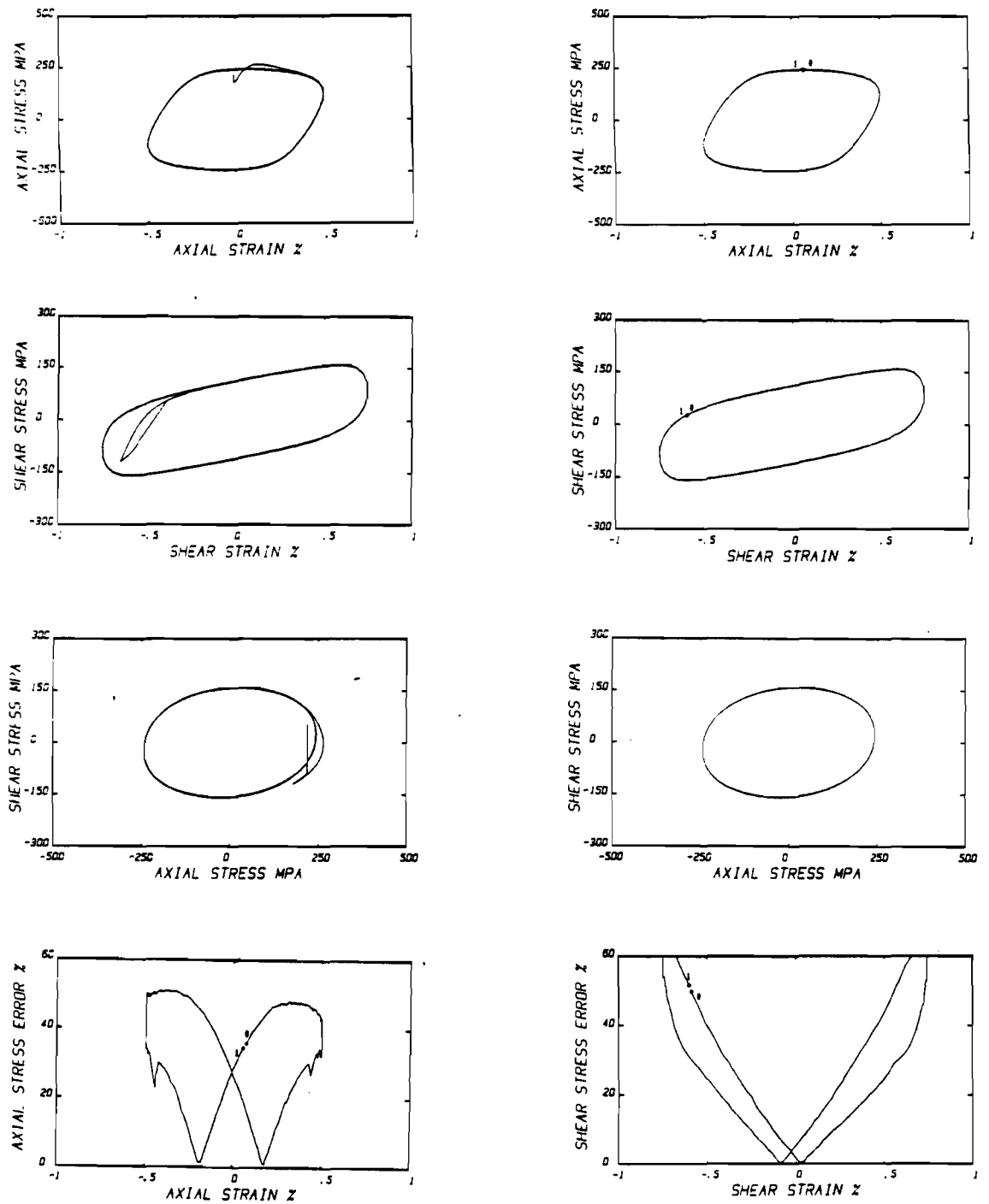


Figure 4-9. Numerical Solution by Drucker's Model for History IV. Left column, top three plots show transient response (cycles 1-10); right column, top three plots show stable loop response (cycle 25); bottom row shows stable loop errors compared to experimental data.

Considering the stress space stable response, it can be seen that, disregarding stress amplitude differences, the predicted response shape is accurate. This suggests the possibility that an improved isotropic hardening rule would significantly increase this model's accuracy with little increase in computational efforts. McDowell (1984d) has shown for these histories that a plastic modulus dependence on effective stress, as assumed in this model, is not a viable description. Hence, loop shape does not seem to be greatly affected by inaccuracies in the plastic modulus function representation. Plastic strain range, however, is apparently greatly affected by the form of the plastic modulus representation under nonproportional loading. This is a very important point to be remembered.

#### McDowell's Model

Figures 4-10 through 4-13 present plots of the predicted stress-strain responses by McDowell's model for the histories under consideration. Table 4-2 shows some statistics with regard to the stable loop error plots and computation times required.

Table 4-2 shows that McDowell's model computation times seem to be history-independent. The normalized CPU time variances do not seem to follow a pattern dependent on history characteristics. On the other hand, the stable loop average errors do follow a clear pattern. For proportional history I the average and maximum errors are quite small. The axial stress average and maximum errors are basically the same for histories II, III, and IV. The shear stress average and maximum errors for histories III and IV are considerably larger than any other error for this model. It is immediately seen that this model has problems

Table 4-2. Stable Loop Errors and Computation Times for McDowell's Model.

	History I	History II	History III	History IV
CPU <sub>N</sub>	1.87	1.87	1.45	1.56
E <sub>a,avg</sub>	4.3	13.6	12.0	15.2
E <sub>a,max</sub>	14.1	19.8	17.3	24.9
E <sub>s,avg</sub>	2.6	7.6	24.9	25.0
E <sub>s,max</sub>	11.2	11.7	38.0	41.5

predicting the shear response of sinusoidal nonproportional histories.

History I. As can be seen from Figure 4-10, this model predicts quite accurately the transient hardening, the transient hardening rate, and the stable hysteresis loop responses for proportional histories. Observe that very realistic smooth yielding is predicted. The stress error plots show that the largest (but still small) errors occur just after initial yielding where this model underestimates the response for both axial and shear stresses.

History II. Figure 4-11 shows the numerical solution predicted by this model. Note that a significant hardening increase due to nonproportionality effects is predicted with sufficient accuracy. The stable loop shear stress amplitude and shape are predicted with very good accuracy. However, the axial stress stable loop amplitude is considerably underestimated at the point of unloading after maximum axial stress loading. This is due to the fact that the model predicts elastic unloading from the yield surface at this point when the experimental plots show this is not true. The axial stress error plot



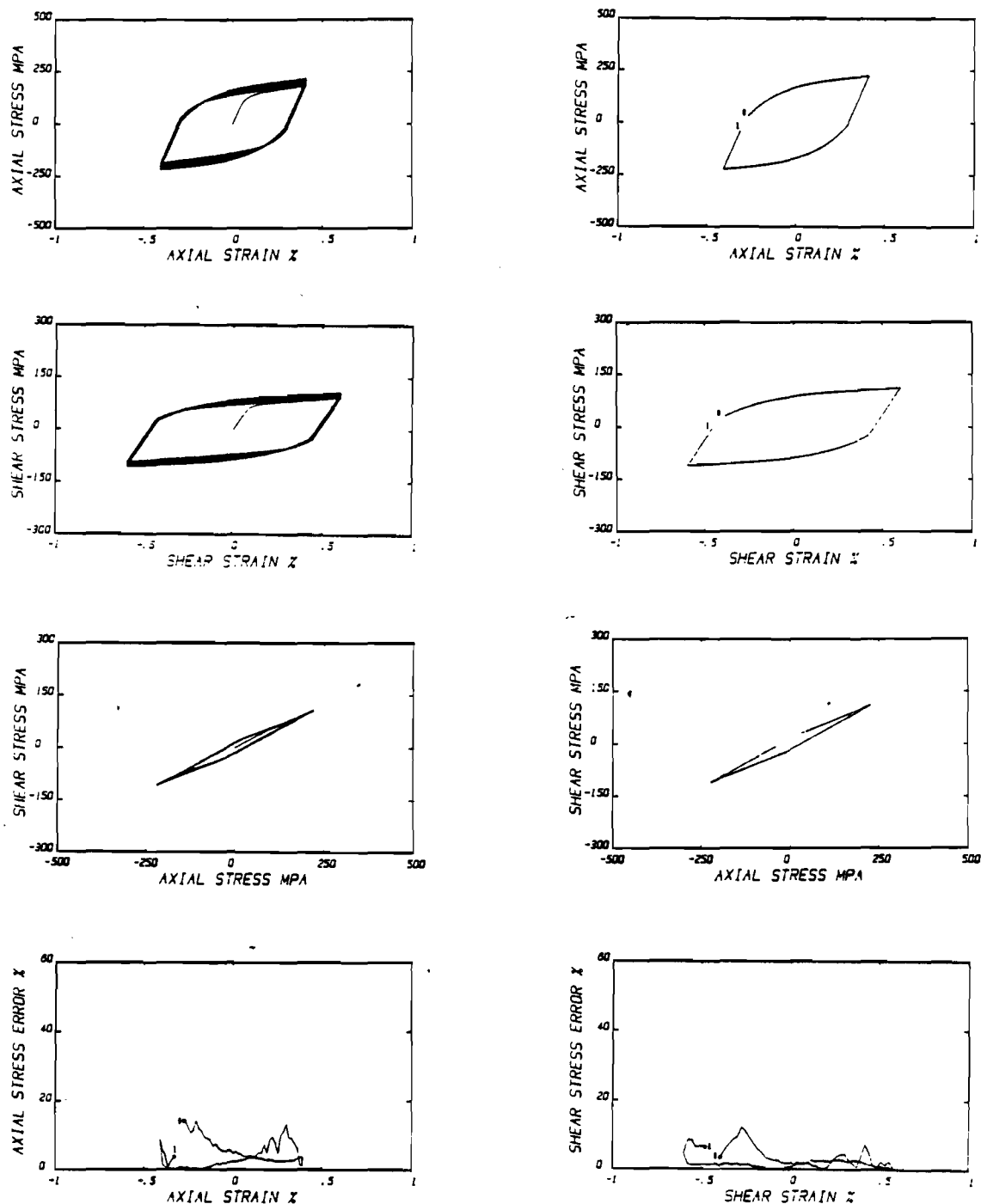


Figure 4-10. Numerical Solution by McDowell's Model for History I. Left column, top three plots show transient response (cycles 1-10); right column, top three plots show stable loop response (cycle 25); bottom row shows stable loop errors compared to experimental data.

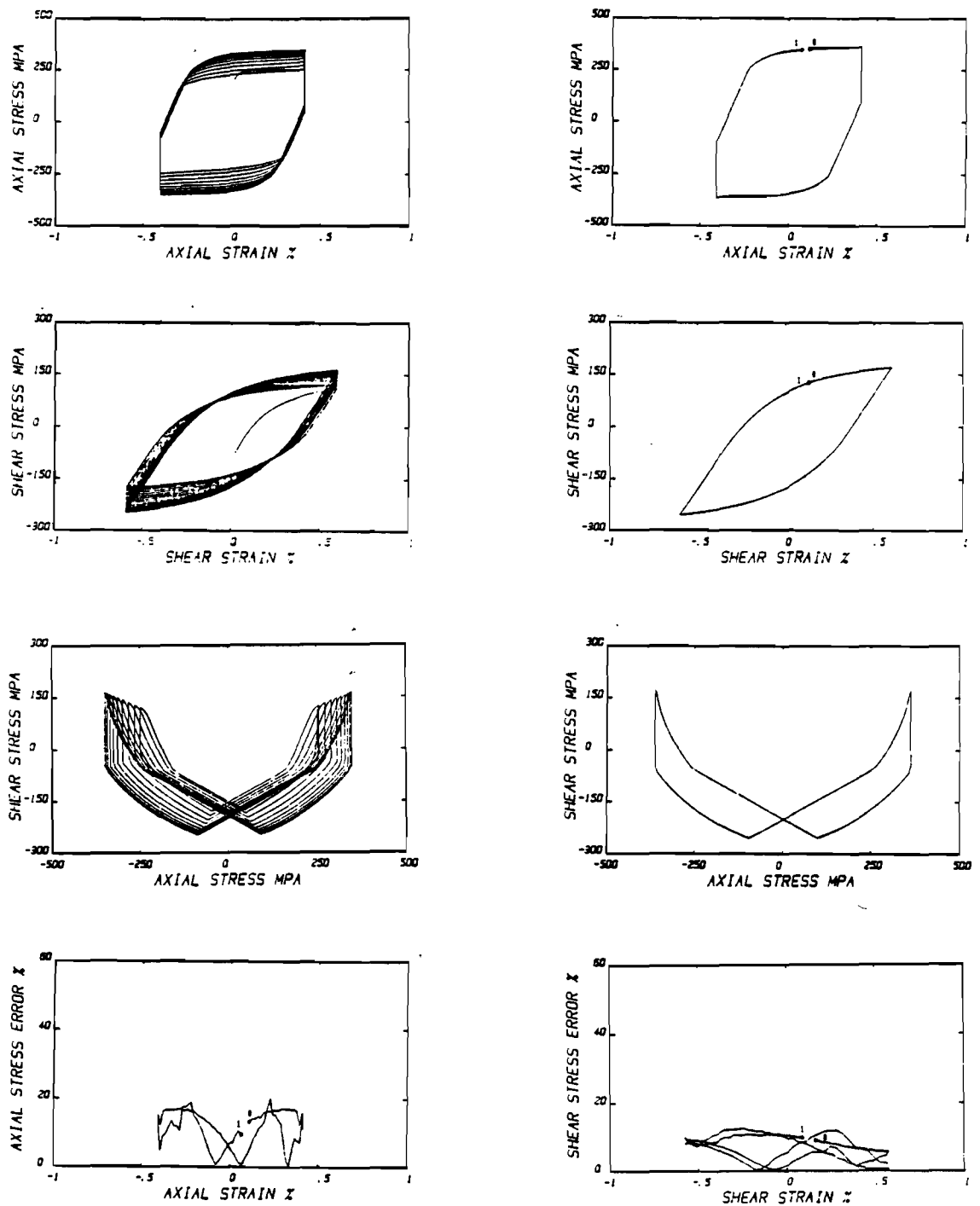


Figure 4-11. Numerical Solution by McDowell's Model for History II. Left column, top three plots show transient response (cycles 1-10); right column, top three plots show stable loop response (cycle 25); bottom row shows stable loop errors compared to experimental data.

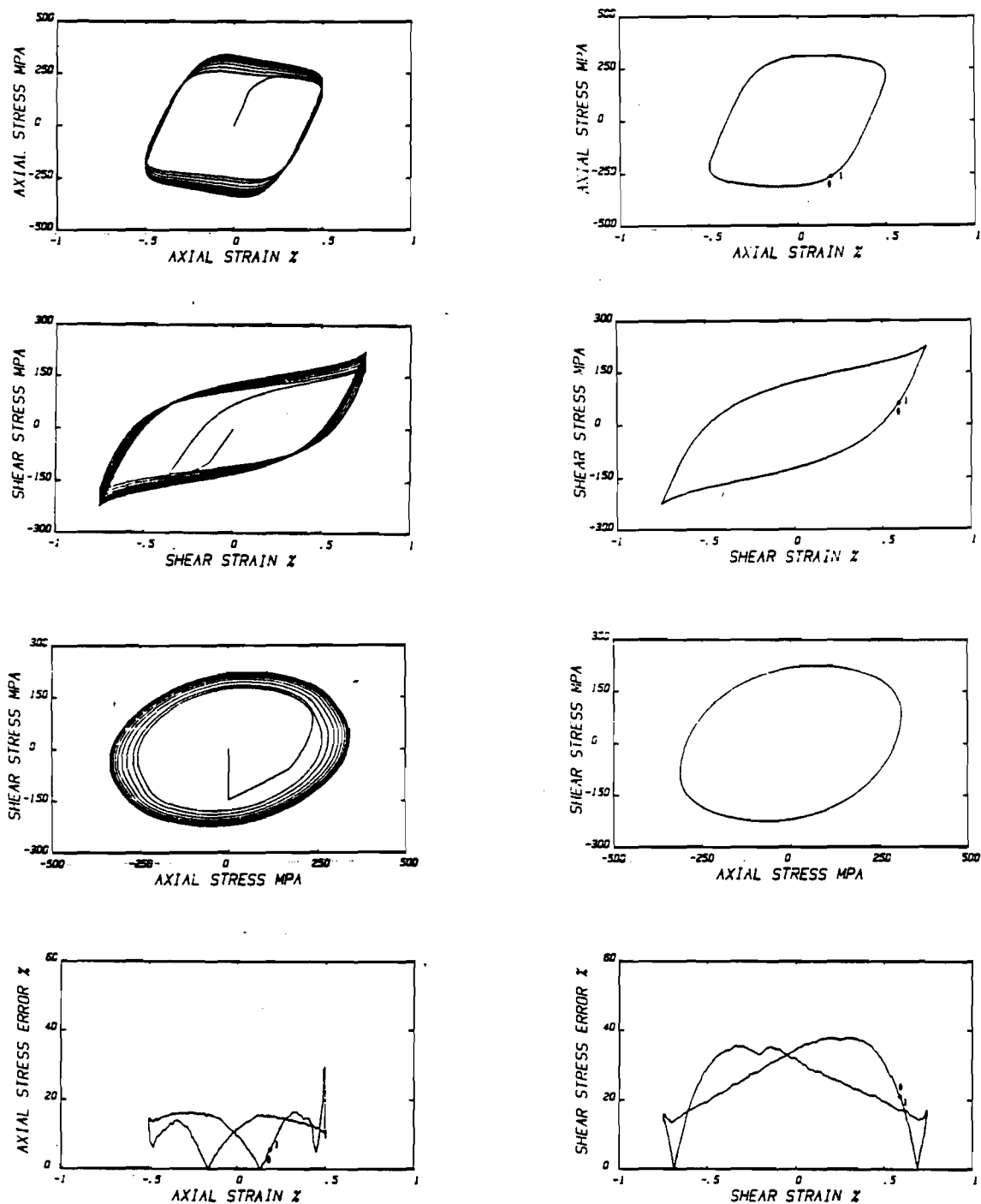


Figure 4-12. Numerical Solution by McDowell's Model for History III. Left column, top three plots show transient response (cycles 1-10); right column, top three plots show stable loop response (cycle 25); bottom row shows stable loop errors compared to experimental data.

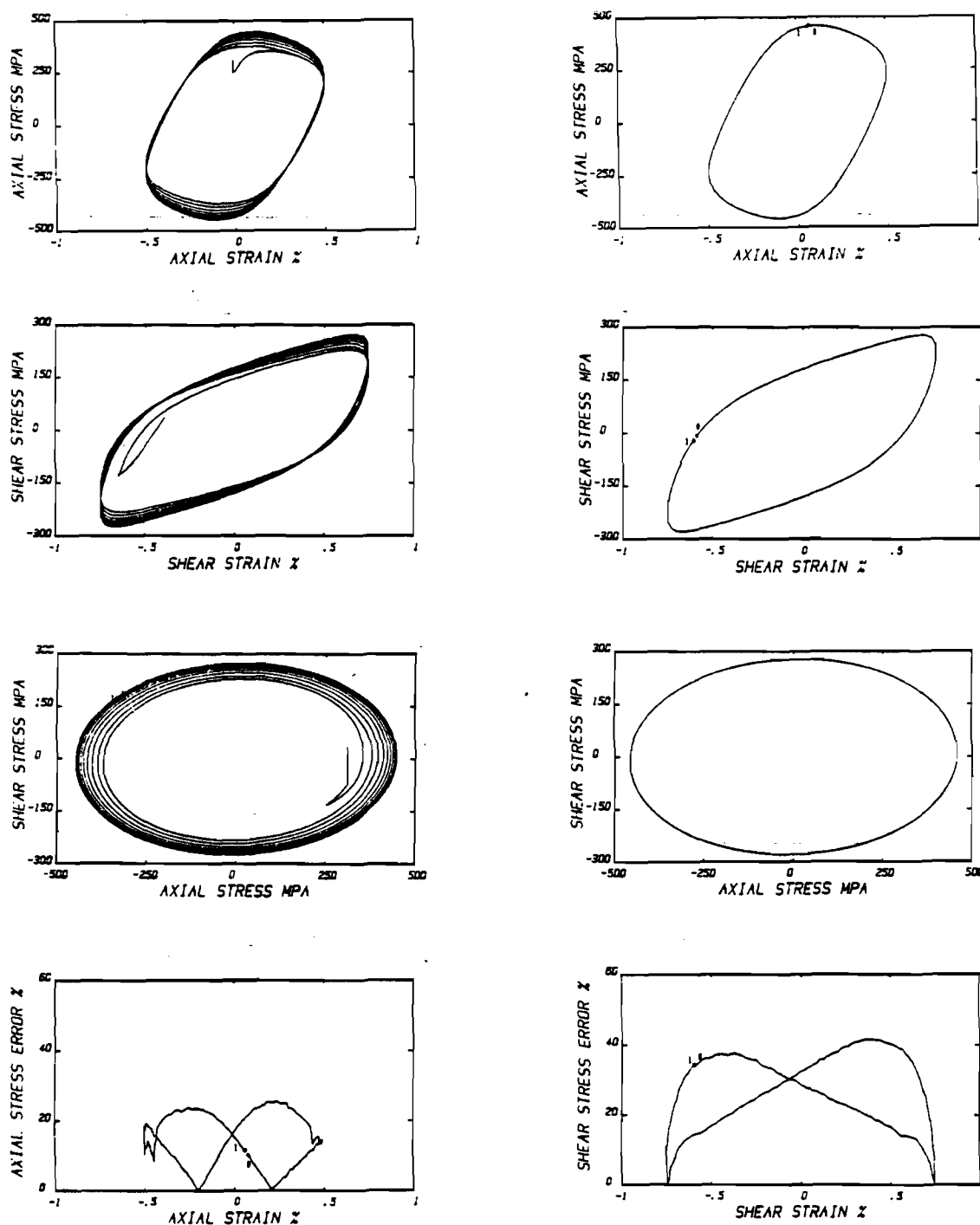


Figure 4-13. Numerical Solution by McDowell's Model for History IV. Left column, top three plots show transient response (cycles 1-10); right column, top three plots show stable loop response (cycle 25); bottom row shows stable loop errors compared to experimental data.

confirms that the maximum errors occur at large values of axial strain. The shear stress errors are seen to vary smoothly around the stable loop with no region of significantly larger errors.

History III. As shown in Figure 4-12, this model is capable of predicting additional hardening due to nonproportional loading. Even though the initial flow stress at yielding is underestimated, the transient hardening response is very well predicted up to the saturated state. The stable axial stress-axial strain loop very closely resembles the shape and amplitude of the experimentally observed values. The axial stress error plot confirms that the largest prediction errors occur at large values of axial strain; note that these errors are still rather small. The stable shear stress-shear strain loop shows rather large deviations from experiment. The shear stress error plot shows that these deviations are due to the "fattening" of the shear response. This fact suggests that a Tresca yield condition may predict a more accurate shear response. Observe that the maximum plastic strain range is overestimated by about 30% and thus, any fatigue life calculations based on this prediction can be significantly in error.

History IV. Comparing Figures 4-12 and 4-13 it is seen that most comments regarding history III apply to this history. Transient hardening is again well-predicted. Predicted axial stress response is more accurate than the shear stress response for the same reasons. Note again that this model predicted with good accuracy the additional hardening due to nonproportional loading.

#### Krieg's Model

The numerical solutions obtained using Krieg's model for the

Table 4-3. Stable Loop Errors and Computation Times for Krieg's Model.

	History I	History II	History III	History IV
CPU <sub>N</sub>	0.17	0.17	0.16	0.16
E <sub>a,avg</sub>	12.9	33.2	31.3	37.5
E <sub>a,max</sub>	40.0	51.5	41.4	52.3
E <sub>s,avg</sub>	23.3	26.8	27.2	37.4
E <sub>s,max</sub>	54.1	53.4	60.9	74.0

test histories under consideration are shown in Figures 4-14 through 4-17. Table 4-3 summarizes some statistics regarding stable loop errors and computer execution times required.

Krieg's model execution time is definitely history-independent as shown in Table 4-3. Note the extremely short computation times needed; this is the primary advantage of this model. Remember that this evaluation incorporates both the material model and the radial-return integration algorithm. Since this is the only model solved without using Gear's method, the radial-return algorithm must be responsible for the tremendous decrease in execution time. Note however that this reduction in computation time results in a sacrifice of predictive accuracy. It is seen that the axial and shear stress stable loop average and maximum errors increase from left to right in the table, from proportional to highly nonproportional loading. It must be pointed out that even for proportional paths this method predicts a response with large errors.

History I. As shown in Figure 4-14, the transient hardening response for this proportional history is very well predicted. It is,

however, the basic response shape what introduces the large errors in this model. Even though the axial stress response shows smooth yielding, this model significantly overestimates the experimental axial stress values at yielding. This is clearly shown by the two peaks in the axial stress error plot; it is also seen that the axial stress error is driven toward zero as the material deforms into the asymptotic plastic region. The predicted shear stress response is totally unrealistic. Firstly, it presents a fictitious material softening just after yielding. This results in significantly underestimated shear stress values in the asymptotic region. Secondly, it overestimates the extent of the elastic regime. This is shown by the two peaks in the shear stress error plot.

History II. Figure 4-15 shows the predicted response for this nonproportional history. Referring to Figure 4-7 the reader will realize the many similarities between Drucker's and Krieg's predicted responses for this history. The predicted response shapes are identical. The only difference resides in the actual magnitude of the stresses. So, the analysis made for Drucker's model is also valid here.

History III. Figure 4-16 shows the predicted results for history III. Again, if the reader compares Figures 4-8 and 4-16, it is evident that Drucker's and Krieg's models behave very similarly for nonproportional loading histories. Notice again that the hysteresis loop shape is fairly accurate. This confirms the contention that the plastic modulus formulation is not very influential on the predicted loop shape for simple models like Drucker's and Krieg's, since their plastic modulus descriptions are different.

History IV. Finally, Figure 4-17 shows the predicted solution

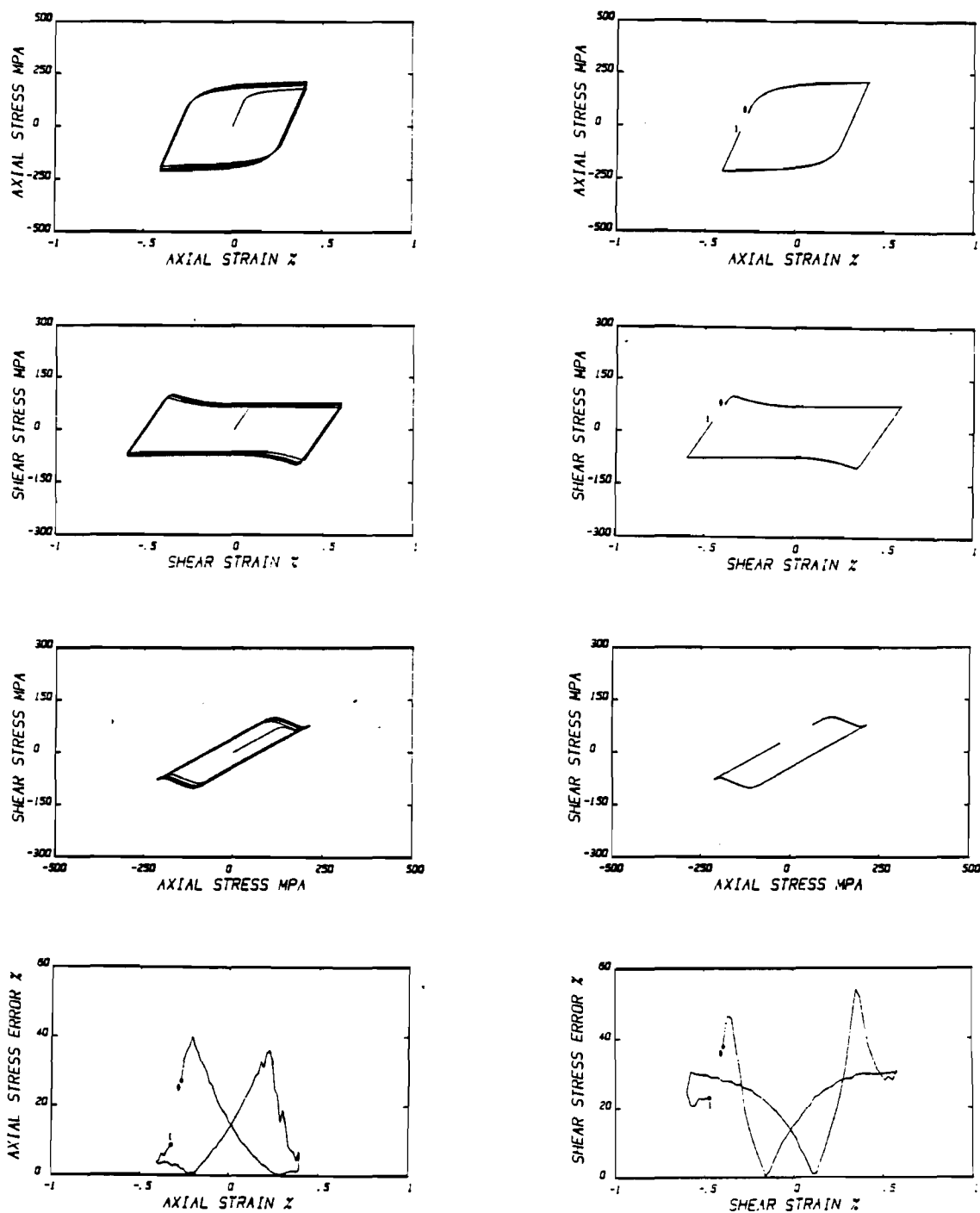


Figure 4-14. Numerical Solution by Krieg's Model for History I. Left column, top three plots show transient response (cycles 1-10); right column, top three plots show stable loop response (cycle 25); bottom row shows stable loop errors compared to experimental data.



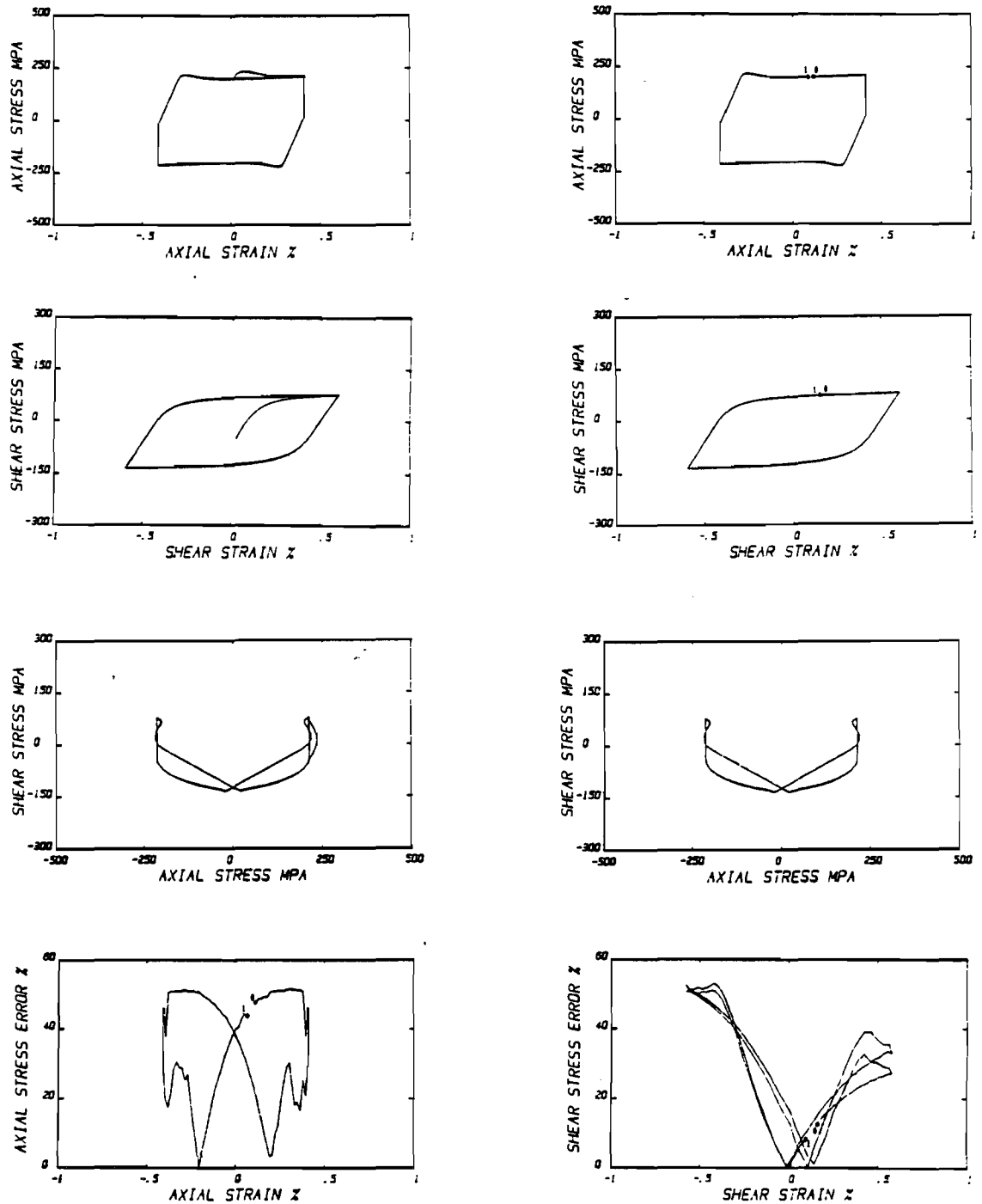


Figure 4-15. Numerical Solution by Krieg's Model for History II. Left column, top three plots show transient response (cycles 1-10); right column, top three plots show stable loop response (cycle 25); bottom row shows stable loop errors compared to experimental data.

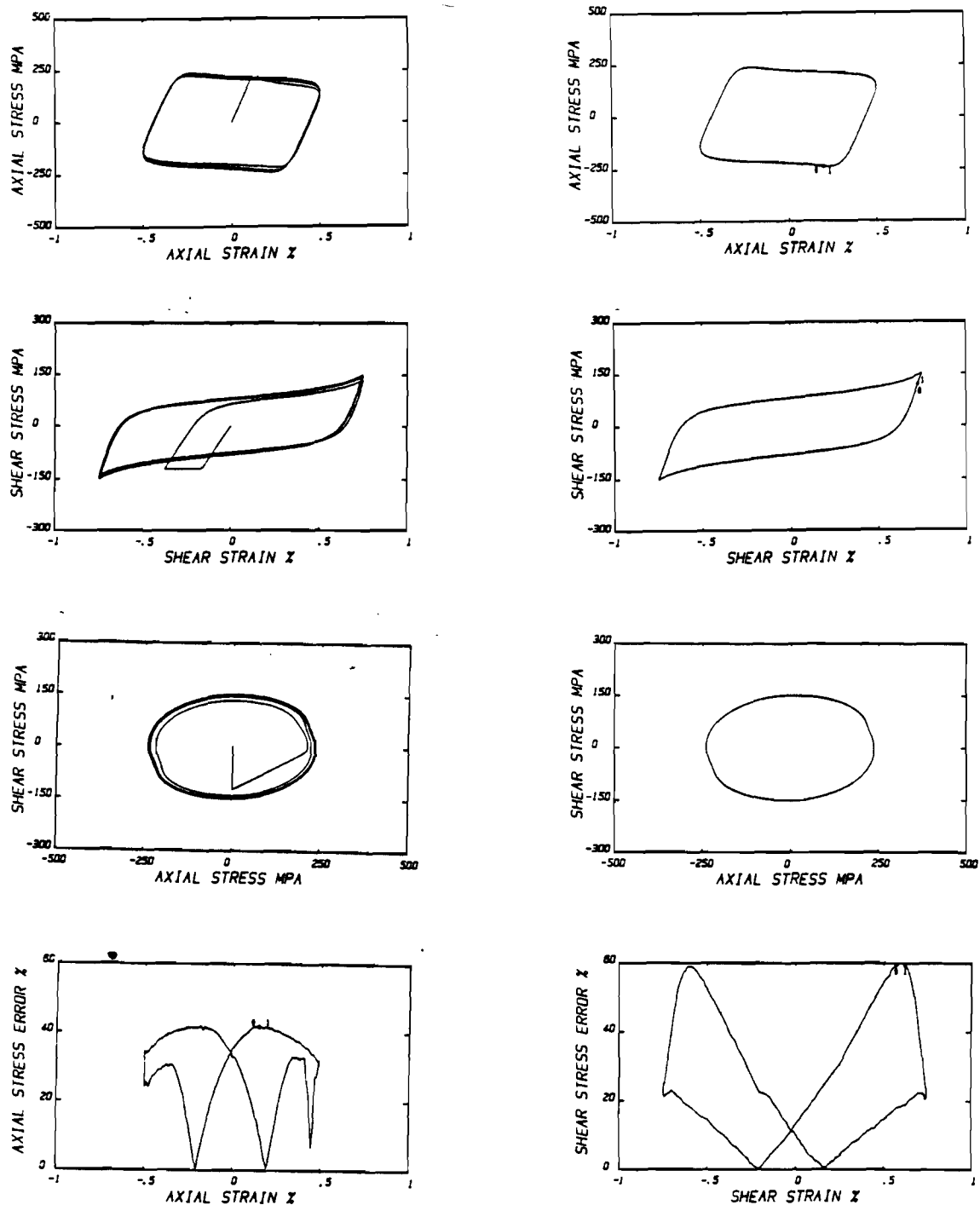


Figure 4-16. Numerical Solution by Krieg's Model for History III. Left column, top three plots show transient response (cycles 1-10); right column, top three plots show stable loop response (cycle 25); bottom row shows stable loop errors compared to experimental data.

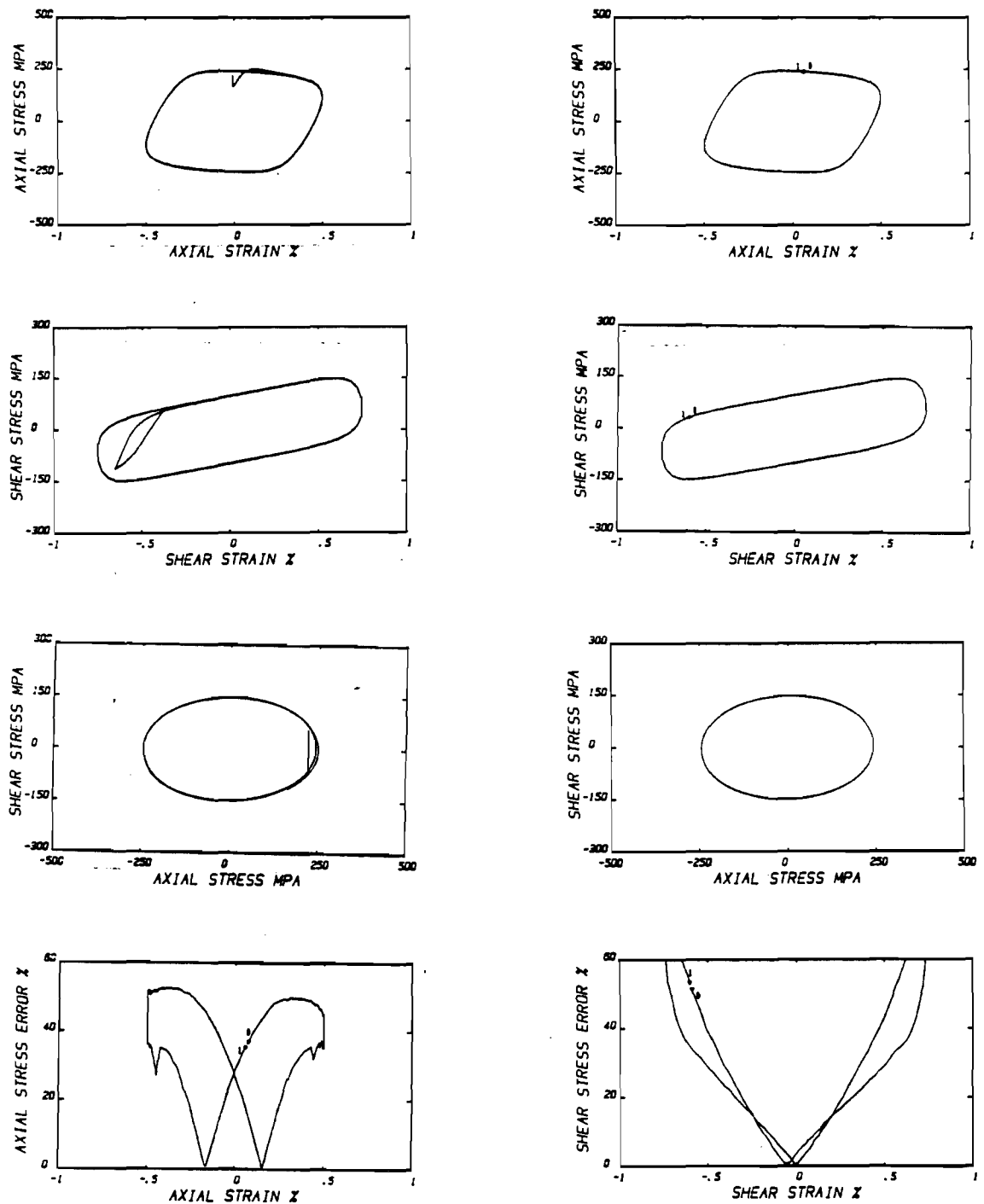


Figure 4-17. Numerical Solution by Krieg's Model for History IV. Left column, top three plots show transient response (cycles 1-10); right column, top three plots show stable loop response (cycle 25); bottom row shows stable loop errors compared to experimental data.

for history IV which, if compared to Figure 4-9, leads to the same conclusion: for nonproportional loading paths, Krieg's and Drucker's models behave effectively the same. In this sense, Krieg's model has the advantage of being computationally more efficient. Note that this is not true for proportional loadings where Drucker's model is considerably more accurate than this model.

#### Abrahamson's Model

Figures 4-18 through 4-21 exhibit the stress-strain response calculated by Abrahamson's model for histories I through IV. Table 4-4 shows the execution times and stable loop error statistics.

Referring to Table 4-4, the reader will note immediately the very large variations in computation time from one history to the other. For example, compare histories III and IV where a 30 degrees phase angle difference results in a 760% increase in computation time. Similarly, compare histories I and II where the addition of two nonproportional segments to the hysteresis cycle result in a 330% increase in computation time. There seems to be a nonlinear relationship between computation time and the level of nonproportionality of the applied strain history. In general, it can only be said that for Abrahamson's model the computation time is history-dependent until further analysis is done. Since this model is a generic form of unified creep-plasticity theory, this path-dependence of computational efficiency probably extends to other particular unified theories.

Similar to McDowell's model, this model predicts the nonproportional axial stress response with greater accuracy than the shear stress response. Table 4-4 shows that the stable loop average

Table 4-4. Stable Loop Errors and Computation Times for Abrahamson's Model.

	History I	History II	History III	History IV
CPU <sub>N</sub>	0.97	3.20	0.95	7.18
E <sub>a,avg</sub>	15.3	12.1	12.6	14.8
E <sub>a,max</sub>	32.5	21.7	24.7	23.0
E <sub>s,avg</sub>	15.5	11.6	25.3	21.6
E <sub>s,max</sub>	39.0	20.1	46.9	39.5

axial stress errors remain essentially constant with increasing nonproportionality. However, the average shear stress errors significantly increase for the two sinusoidal histories.

History I. As shown in Figure 4-18, the transient hardening response is predicted with relatively good accuracy. The stable loop maximum stress amplitudes are within 5% of the experimental values. However, notice that due to the very sharp yielding characteristic of unified creep-plasticity theories, this model underestimates the stress values in the first few cycles; as it hardens, the stable loop response is matched accurately except in the initial yielding regime. The axial and shear stress error plots show that the maximum prediction error occurs just after yielding (notice the two error peaks) and then reduces toward zero as the material deforms into the asymptotic plastic region.

History II. Figure 4-19 shows the resulting numerical solution. It is immediately seen that this model is capable of predicting nonproportional transient hardening rather accurately. Again notice the very sharp yielding observed in the axial stress response which results

in underestimated stresses both during transient hardening and for the stable loop response. The stable loop error plots show that for the axial case the largest errors occur in the asymptotic plastic region while for the shear case (due to "fattening" of the shear plot), they occur just after initial yielding.

History III. Figure 4-20 presents the calculated values for history III. Again, due to the sharp yielding characteristics of this model, it is seen that the transient hardening response significantly underestimates the stress histories for the first few cycles. On the other hand, the stable loop stress amplitudes are matched with better accuracy. Like McDowell's model, the shear stress response is characterized by a hysteresis loop "fattening" that significantly overpredicts the maximum plastic strain range and the stress values just after initial yielding for every cycle.

History IV. Figure 4-21 finally shows the predicted hysteresis loops for history IV. Note that disregarding the "fattening" of the shear stress response, both the transient hardening and the stable loops are predicted rather accurately. Comparing Figures 4-10 through 4-13 to Figures 4-18 to 4-21, the reader will note the existing similarities between McDowell's and Abrahamson's predicted results. Even though these models have radically different structures, the predicted results are quite similar. However, McDowell's model is computationally more efficient while Abrahamson's is more versatile since it can handle time- and rate-dependent phenomena. McDowell (1984a) expresses that, as a general rule, unified creep-plasticity theories are computationally inefficient in solving time-dependent problems.

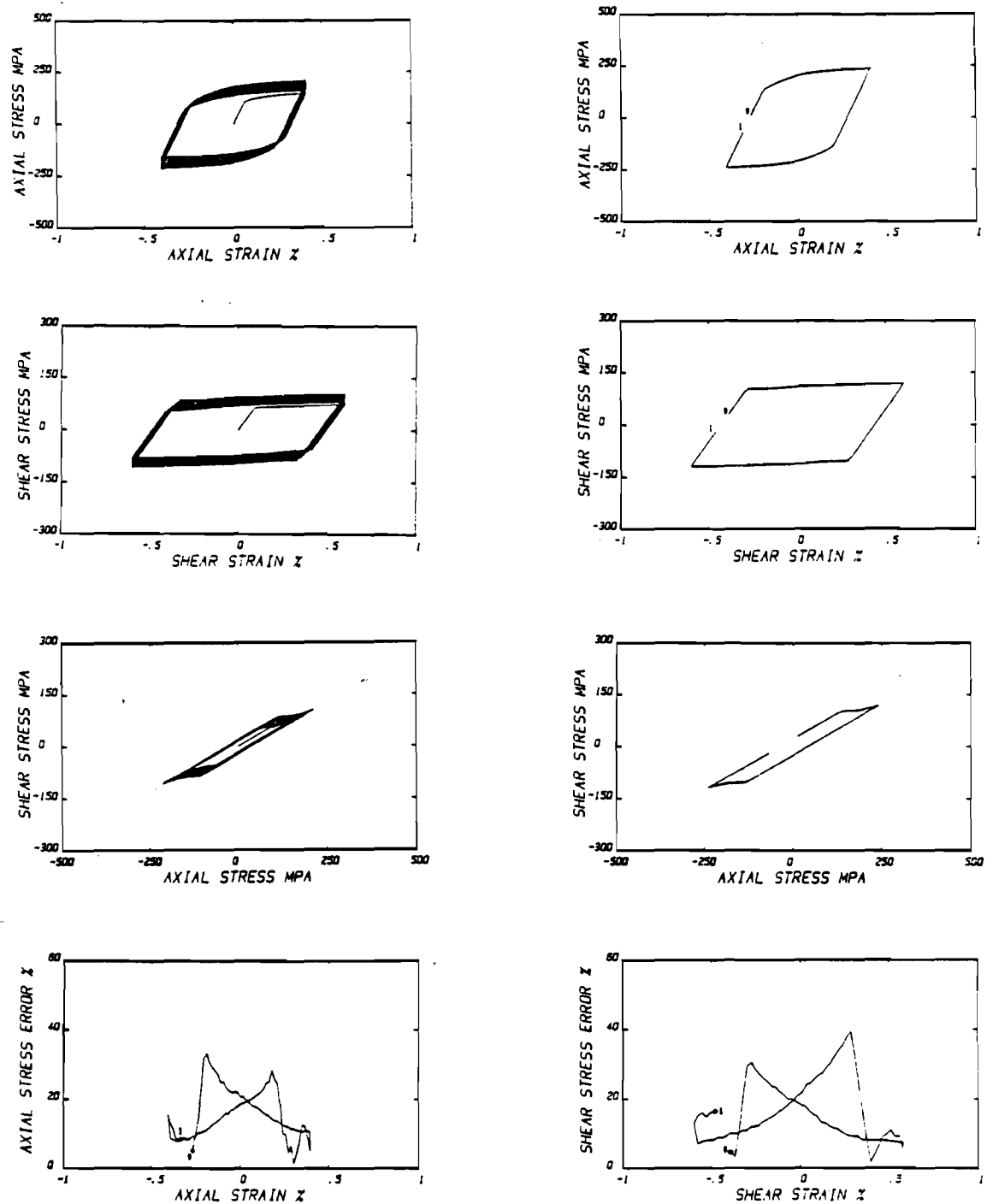


Figure 4-18. Numerical Solution by Abrahamson's Model for History I. Left column, top three plots show transient response (cycles 1-10); right column, top three plots show stable loop response (cycle 25); bottom row shows stable loop errors compared to experimental data.

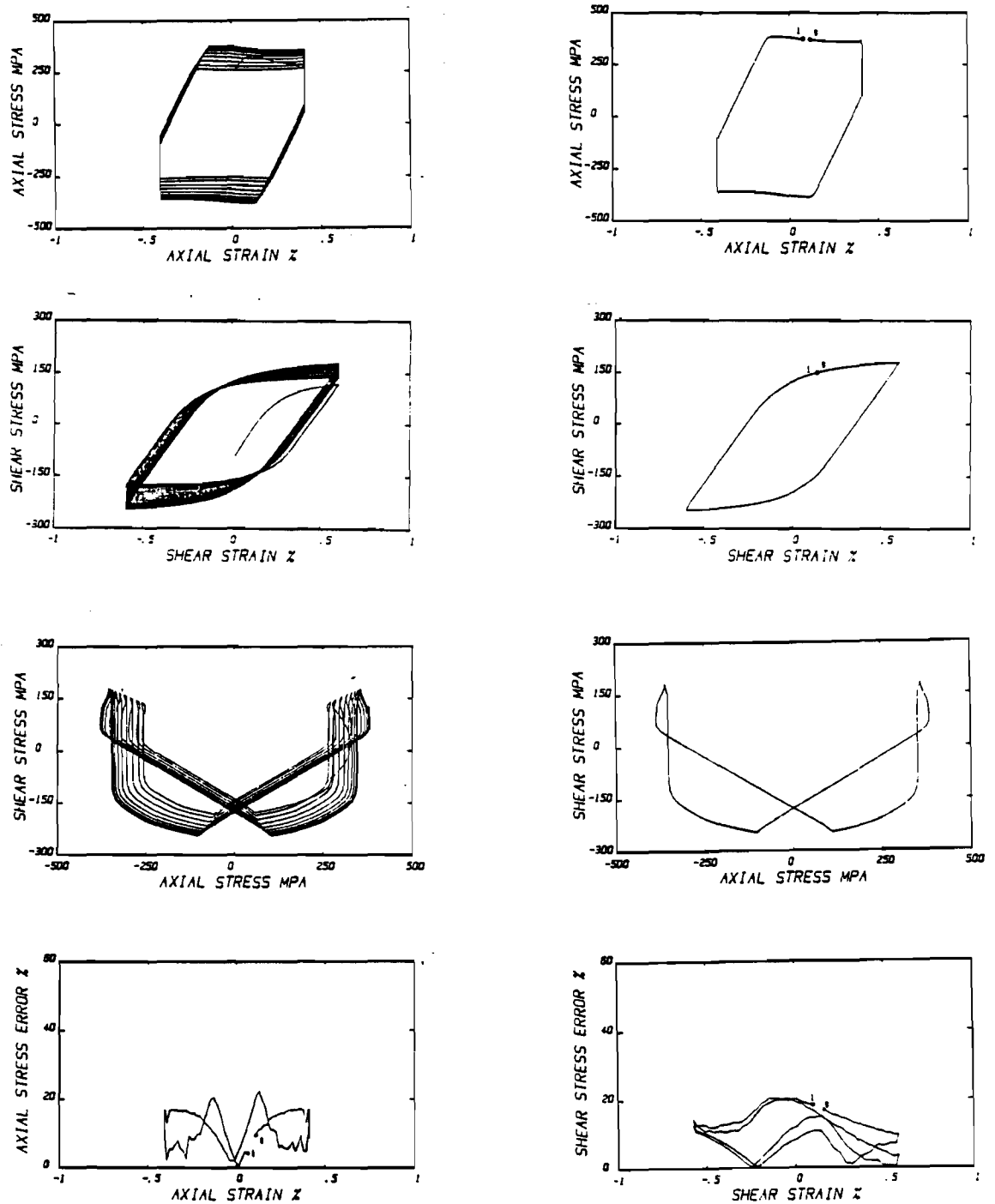


Figure 4-19. Numerical Solution by Abrahamson's Model for History II. Left column, top three plots show transient response (cycles 1-10); right column, top three plots show stable loop response (cycle 25); bottom row shows stable loop errors compared to experimental data.



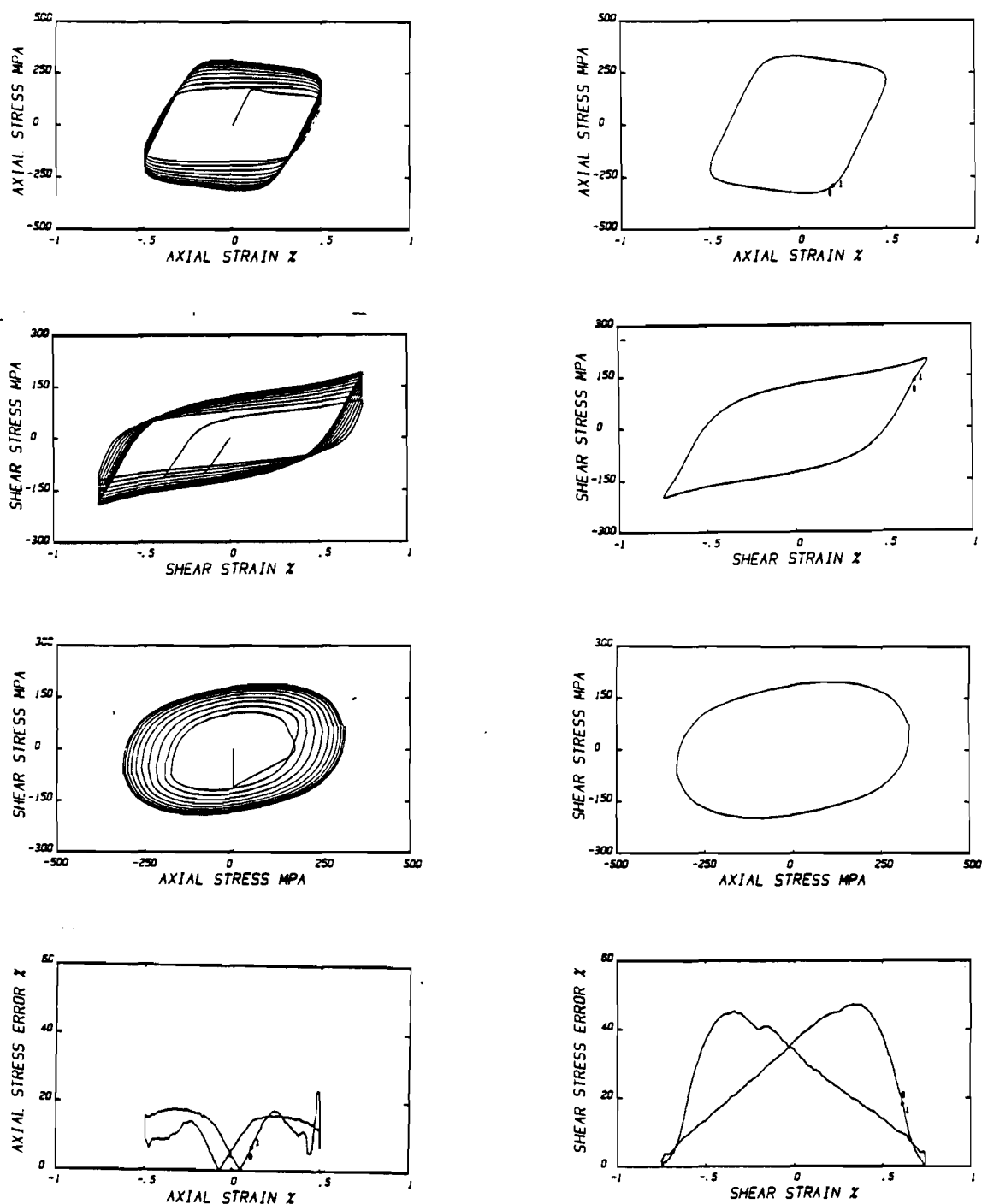


Figure 4-20. Numerical Solution by Abrahamson's Model for History III. Left column, top three plots show transient response (cycles 1-10); right column, top three plots show stable loop response (cycle 25); bottom row shows stable loop errors compared to experimental data.

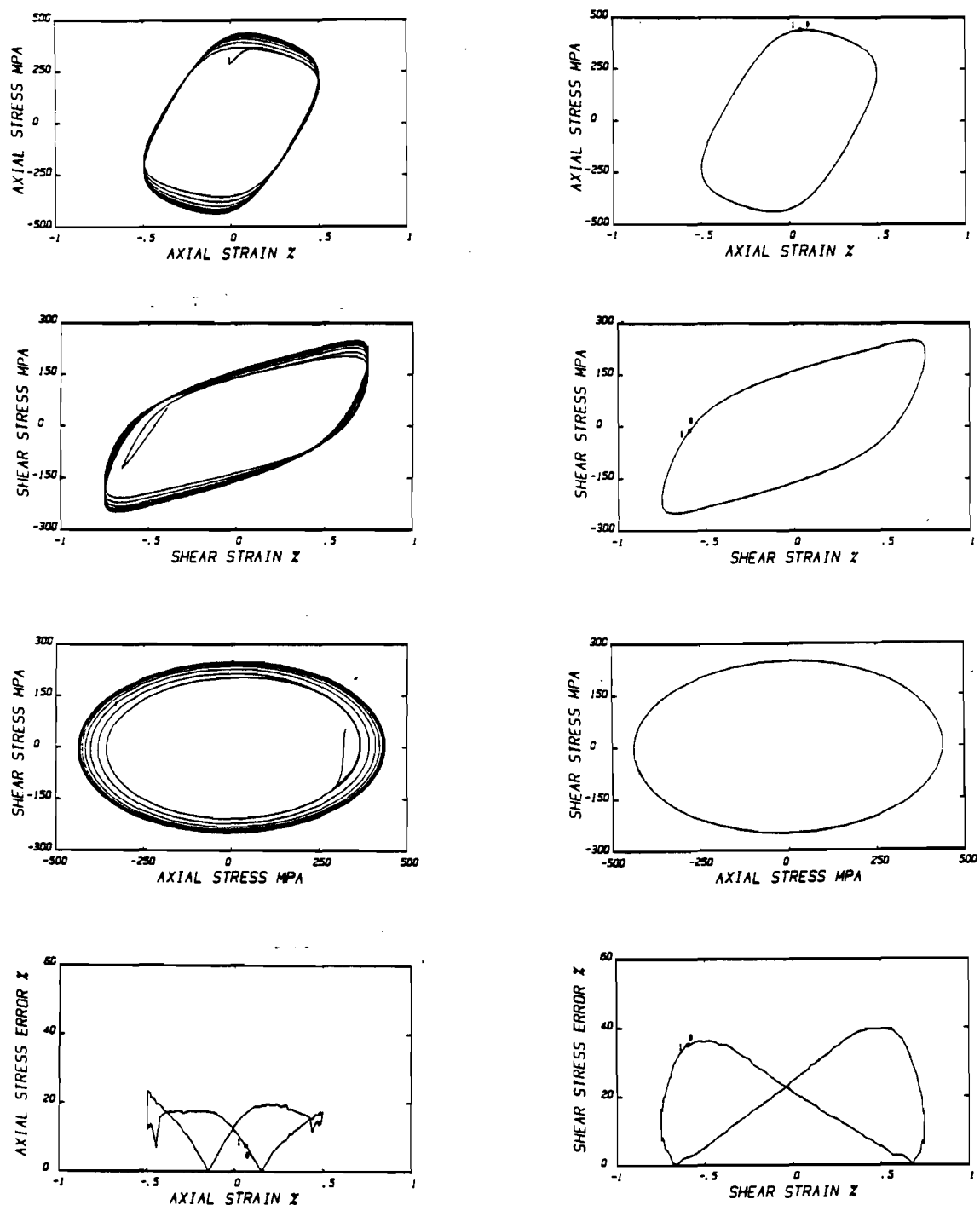


Figure 4-21. Numerical Solution by Abrahamson's Model for History IV. Left column, top three plots show transient response (cycles 1-10); right column, top three plots show stable loop response (cycle 25); bottom row shows stable loop errors compared to experimental data.

It should be noted that for all the models, when subjected to nonproportional strain paths, the predicted plastic strain range does not reflect the experimental results. This is evidenced clearly by the "fattening" of the shear stress responses under nonproportional type loadings. If accurate fatigue life predictions are to be made, it is necessary to engage in further research to develop a model capable of accurately predicting the plastic strain ranges in addition to stress amplitudes. This is seen as the next step for current research and development of these constitutive equations.

#### Model Evaluation Summary

Table 4-5 shows a summarized version of the conclusions that can be drawn from the model evaluations just presented.

Table 4-5. Model Evaluation Summary.

	Proportional Multiaxial Loadings	Nonproportional Multiaxial Loadings	Time- and Rate-dependent Phenomena
Drucker's Model:			
Predictive Accuracy	Good	Inferior	Incapable
Computational Eff.	Medium	Medium	-----
McDowell's Model:			
Predictive Accuracy	Excellent	Good	Incapable
Computational Eff.	Low	Low	-----
Krieg's Model:			
Predictive Accuracy	Regular	Inferior	Incapable
Computational Eff.	Very High	Very High	-----
Abrahamson's Model:			
Predictive Accuracy	Good	Good	Good
Computational Eff.	Medium	Very Low	Very Low

### Integration Technique Evaluations

In the previous section, it was shown that most of the models outlined presented a numerical behavior independent of input strain and strain rate history. With the exception of Abrahamson's model, all models showed little sensitivity to changes in input history from the standpoint of computational efficiency. However, Abrahamson's model's normalized CPU time (a measure of computational efficiency) showed large variations which reflected that radical changes in the numerical behavior of the model were occurring as the input history was changed. This suggests the possibility of the model's numerical behavior changing not only with input strain history but also with the numerical solution algorithm. This section shows that, as suspected, the computational efficiency of the models change with numerical solution algorithm used.

In this section, Krieg's model will not be integrated since it was only introduced in the analysis to show the tremendous computational advantage of the radial-return integration algorithm applied to a constitutive model of the generic form of Drucker's model.

As previously stated, all the numerical integration techniques will be compared against the solutions calculated using Gear's numerical integration algorithm. Therefore, errors reported in this section are computed with respect to Gear's method solution, not experimental results. Two input strain histories were used as the basis for these comparisons. History V consisted of three cycles of proportional straining from the initially annealed state with maximum axial and shear strain amplitudes  $\epsilon_a = 0.0041$  and  $\gamma_a = 0.0060$ , respectively (very similar to history I). The effective strain rate was kept constant at

$\dot{\epsilon}_{\text{eff}} = 0.003 \text{ sec}^{-1}$ . History VI consisted of three cycles of sinusoidal loading with 90 degrees phase angle,  $\epsilon_a = 0.0050$ ,  $\gamma_a = 0.0075$ , and  $\dot{\epsilon}_{\text{eff}} = 0.001 \text{ sec}^{-1}$ . McDowell (1984a) and others have experimentally shown this history to result in the largest observed increase in hardening due to nonproportionality effects for axial-torsional loading. These two contrasting histories were chosen so that any history-dependent model numerical behavior would be clearly exhibited.

Figure 4-22 shows the axial stress-time and the shear stress-time responses predicted for histories V and VI by using Gear's numerical integration method with McDowell's, Drucker's, and Abrahamson's models. These graphs show the predicted results by using Gear's method in its most efficient yet accurate form, as explained next. A series of trial runs were executed with the same input strain histories but variable initial time step-size and maximum allowable single-step error. It was determined that the solution was insensitive to changes in the initial time step-size unless the chosen values were unreasonably large. The best combination of computational accuracy and efficiency was found by keeping the maximum allowable single-step error  $E_{\text{max}} \leq 0.001$ . Choosing  $E_{\text{max}} > 0.001$  resulted in large variations for the calculated stress values as compared to the values predicted with  $E_{\text{max}} \leq 0.001$ . Choosing  $E_{\text{max}} \lll 0.001$  resulted in no significant change of the calculated stress values but tremendously increased the computation times. So, this was chosen as the reference solution used for this analysis.

The integration routines presented in chapter III have been evaluated for both histories V and VI, and for each of the models mentioned above. The standard input values used in the first execution

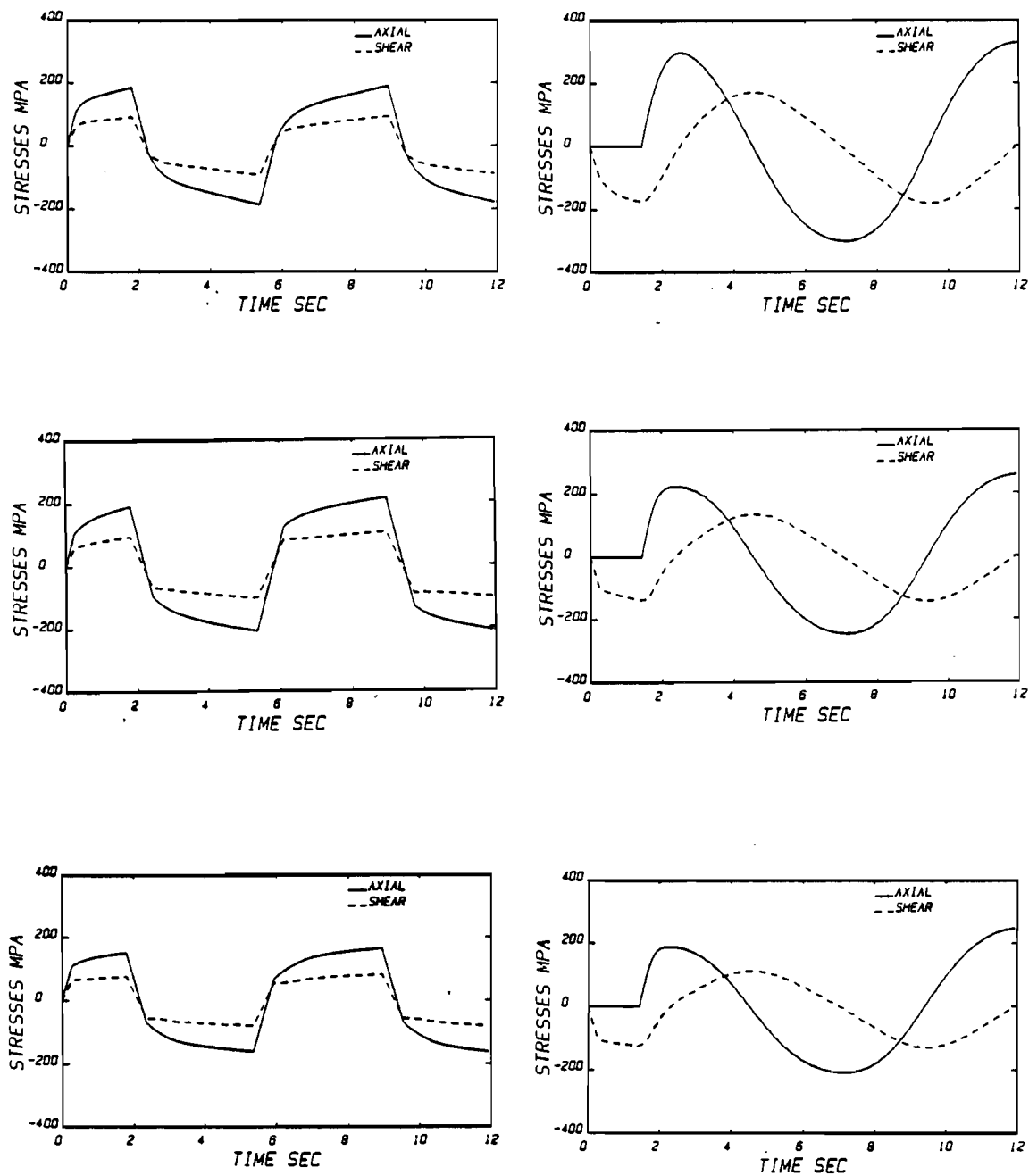


Figure 4-22. Axial and Shear Stress vs. Time Responses for Histories V and VI Integrated by Gear's Method.

Left column, history V; right column, history VI; top row, McDowell's model solution; middle row, Drucker's model solution; bottom row, Abrahamson's model solution.

of each integration routine were chosen as  $E_{\max} = 0.001$ ,  $E_{\min} = 0.0001$ ,  $h_{\text{init}} = 0.01$  sec., and  $m^* = 2$ .  $E_{\max}$ ,  $E_{\min}$ , and  $m^*$  are as defined in chapter III and  $h_{\text{init}}$  is the initial time step-size chosen by the user. Notice that  $m^*$  is a parameter applicable to the Iterative Adams Predictor-Corrector method only. After the first set of executions with standard values, further insight was gained by varying some of these parameters as shown in the sections to follow.

The integration routines will be evaluated based on computational accuracy and efficiency. Efficiency performance evaluation will be based on the normalized CPU time  $\text{CPU}_N$  as defined by equation (4.3) and the number of phenomenological subroutine evaluations  $N_f$  (to be called number of function evaluations) as given by

$$N_f = \frac{N_c}{t_f} \quad (4.4)$$

where  $N_c$  is the total number of function evaluations for the history under consideration and  $t_f$  is the corresponding final value of the independent variable (time). Table 4-6 shows the actual values of  $\text{CPU}_N$  and  $N_f$  for all the models when integrating histories V and VI using the reference Gear's method. As noted in the previous section, the normalized CPU time seems to be insensitive to input history for McDowell's and Drucker's models. This is confirmed by the small variances in the number of function evaluations  $N_f$ . However, note the tremendous increase in execution time for Abrahamson's model when integrating nonproportional history VI. So, as shown in the previous section, the computation times for Abrahamson's model are greatly

Table 4-6. Actual Computation Times and Number of Function Evaluations Using Gear's Method with Standard Input Parameter Values.

Model	McDowell		Drucker		Abrahamson	
History	V	VI	V	VI	V	VI
CPU <sub>N</sub>	7.72	7.08	2.98	2.99	4.05	44.97
N <sub>f</sub>	1494	1354	865	844	920	13974

sensitive to the nonproportionality level of the input strain history. The reader must keep in mind this apparent path-dependence of computational efficiency since it will be shown to be an important parameter in the selection of the best numerical solution algorithm for nonproportional, multiaxial, cyclic plasticity. Tables 4-7 through 4-15 and C-1' through C-2 show values of CPU<sub>N</sub> and N<sub>f</sub> as percentages of the values shown in Table 4-6 to give the reader a relative basis for comparison of the different numerical methods studied.

Integration routine accuracy will be evaluated on the basis of axial stress average error  $E_{a,avg}$ , axial stress maximum error  $E_{a,max}$ , shear stress average error  $E_{s,avg}$ , and shear stress maximum error  $E_{s,max}$ . Axial and shear stress errors are defined by equations (4.1) and (4.2), respectively, with the modifying assumption that the reference is Gear's corresponding numerical solution instead of experimental data. Plots of these errors as they vary with time will be shown to pinpoint segments of large errors and to determine the overall trends of the error patterns.

#### Runge-Kutta Method with Gill Coefficients

As presented in chapter III, this is a multiple-step, explicit,



non-iterative, fourth-order, fixed step-size method. Because this method maintains a constant time step-size, it is insensitive to changes in the numerical behavior of the system of ODE's if viewed from the standpoint of computational efficiency. However, if the fixed time step-size chosen is too large relative to the stiffness of the system being solved, it may render this method unstable or at least it will introduce false oscillations in the predicted results. On the other hand, if the time step-size is small enough so that no oscillations occur, it may still introduce considerable errors.

The standard input values were used in the first execution. It was found that the estimated single-step error as defined in chapter III was well within desirable bounds. So, there was no danger of instability or false oscillations. Table 4-7 summarizes the results obtained for the performance parameters with  $h_{init} = 0.01$ . Table 4-8 shows a similar table for a second set of runs with  $h_{init} = 0.005$ . Figure 4-23 shows axial and shear stress errors vs. time for the first cycle of histories V and VI for all the models with  $h_{init} = 0.01$ .

History V. For proportional type histories, Table 4-7 shows that this method results in computation time savings of the order of at least 70% compared to Gear's method. Such large savings are due to an approximate drop of 65% in the number of function evaluations as shown in Table 4-7. It is seen that the savings incurred apply to all the models tested with the largest savings occurring for McDowell's model. Notice that there is no sacrifice in computational accuracy. The maximum axial stress error observed was in the order of 1% with average error values ranging from 0.05% to 0.45% for all the models. The maximum